

A study of use of mini-bladders in active compression as a treatment for venous disease and lymphoedema

H. M. A. Gayani K. Nandasiri

Nottingham Trent University

A thesis submitted in partial fulfilment of the requirements of
Nottingham Trent University for the degree of
Doctor of Philosophy

To my loving parents for their unconditional love and support
and

To my loving husband, who believed in me and for being my rock throughout this journey...

Copyright statement

This work is the intellectual property of the author. You may copy up to 5 % of this work for private study, or personal, non-commercial research. Any re-use of the information contained within this document should be fully referenced, quoting the author, title, university, degree level and pagination. Queries or requests for any other use, or if a more substantial copy is required, should be directed in the owner(s) of the Intellectual Property Rights.

H. M. A. Gayani K. Nandasiri
July 2019

Acknowledgements

It would not have been possible to complete this PhD journey for the past years if I was not accompanied by many wonderful people who supported me throughout. I am very much privileged to express my gratitude to all of them through this small note of appreciation.

My first and foremost heartfelt gratitude goes to my director of studies Professor Tilak Dias who guided me throughout this journey not only by providing valuable insights into develop this research, but also giving certain inspirational facets about growing as a research scientist. I am enormously grateful to him for giving me the opportunity to finish this research under his guidance.

I would also like to thank my co-supervisor Mr. William Hurley and Dr. Anton Ianakiev for their valuable guidance and support during this research.

I wish to extend my sincere gratitude to Nottingham Trent University for the award of Vice Chancellor bursary and also to my employer, University of Moratuwa, Sri Lanka for providing me the opportunity to undertake this research programme.

I would like to specially thank all the members of Advanced Textiles Research Group; Dr. Dorothy Hardy, Dr. Theodore Hughes-Riley, Mr. Carlos Oliveria, Dr. Pasindu Lugoda, and Mr. Achala Satharasinghe for their support throughout this period. A special mention goes to Mr. Richard Arm and Dr. Arash M. Shahidi for their tremendous support and motivation. I am also very much grateful to my cousins; Mr. Gihan Mohotti, Dr. Dilinee Wijayathunga, Dr. Nagitha Wijayathunga, Mrs. Shiroma Goonaratne and Mr. Sherman Goonaratne for their massive support during my stay in the U.K. I would also like to thank Mr. Chamara Perera and Mrs. Piyumi Perera for giving me a home away from home in Nottingham for the past years.

A special thanks goes to my family; I am forever grateful to my mother, father and brother for their unconditional love and support. Your prayers and motivation kept me going throughout these years. Finally, the words fall short to express my gratitude to my loving husband for believing in me and being my rock throughout this journey. This wouldn't have been possible without his unconditional support.

Abstract

Venous disease of human lower limbs can cause a range of disorders that have a significant impact on the quality of life of patients. The sheer prevalence of varicose veins and its associated costs of treating late complications, such as chronic ulcers, contribute to a higher burden on health care resources as well as affecting the quality of life of people in the western world. The established gold standard of treatment is the application of graduated compression, applied mostly by medical compression bandages (MCB) and graduated compression stockings (GCS). Both systems are passive treatment methods as the pressure is generated by the component of the tangential force created due to the fabric tension resulted by the fabric stretch, which fails to provide uniform pressure around the leg circumference.

This thesis presents the fundamental research of design, development, and evaluation of an active compression system consisting of an array of silicone based inflatable mini-bladders, which can provide a better solution for the treatment of venous disease and also lymphoedema. The mini-bladders were designed with two elastomeric layers; however, the mini-bladder inflation was limited only to one layer when the mini-bladder was filled with air. The mini-bladders could apply a radial force on to the treated surface when inflated, and the pressure in mini-bladders could be determined by measuring the back pressure, thus providing the ability to inflate mini-bladders to a predefined pressure. An array of mini-bladder can be used to apply pressure over a large area with a pre-determined resolution in order to create a graduated pressure profile. The 3-D deformation profile of mini-bladders was analysed using Finite Element Modelling and the simulations showed a good agreement with the experimental results within the pressure region which of interest for the compression therapy. The pressure transmission characteristics of the mini-bladders were investigated, initially on hard surfaces and then extended to a biofidelic leg surrogate. The hexagonal shaped mini-bladders provided the best pressure transmission properties. As a higher packing density can be achieved with hexagonal shaped mini-bladders in a honeycomb structure, a prototype active compression device was designed with hexagonal shape mini-bladders. Moreover, the interface pressure generated by the mini-bladders demonstrated a good linear relationship with the mini-bladder inflation pressure, which could be used as a calibration curve for the mini-bladders to inflate the mini-bladders to apply a predefined pressure. The second

phase of the experiments, were conducted with a biofidelic lower leg surrogate covered with artificial skin and fat layers of different Young's modulus values. To the best of the author's knowledge this type of validation was the first of its kind in compression therapy research. The research has proved that mini-bladders can be used to apply a uniform circumferential pressure irrespective of the position of the lower leg surrogate; which proves the validity of the research hypothesis. The pressure propagation through the fat layers were around 35%-45% of the mini-bladder inflation pressure. Moreover, the propagation of the pressure through the fat layers varied with the modulus of the fat layers; the fat layer having lowest modulus recorded the highest pressure transmission percentage.

A prototype of an active compression system was designed with mini-bladder arrays integrated within a silicone layer, in which the mini-bladders were directly in-contact with the skin. The laboratory experiments demonstrated that the developed active compression system was capable of delivering the required graduated pressure profiles.

Table of contents

List of figures	xv
List of tables	xix
Nomenclature	xxi
1 Introduction	1
1.1 Introduction	1
1.2 Motivation	1
1.2.1 Severity of the problem	2
1.2.2 Existing treatment methods and market size	2
1.2.3 Shortcomings of the existing treatment methods	3
1.3 Research plan	4
1.3.1 Research Aim:	4
1.3.2 Research Questions	4
1.4 Structure of the thesis	5
1.5 Contributed papers	7
2 Literature review	9
2.1 Chronic Venous Disorder	9
2.1.1 Definition	9
2.1.2 Epidemiology	9
2.1.3 The human lower limb venous system	11
2.1.4 Pathophysiology: Effects of damages to the venous system	16
2.1.5 Management of complications related to venous disorder	21
2.2 Compression therapy	23
2.2.1 Current compression therapy	23
2.2.2 Mechanism of compression therapy	24
2.2.3 The optimum interface pressure profile for compression therapy	26

2.2.4	Medical Compression Bandages (MCBs)	26
2.2.5	Graduated Compression Stockings	31
2.2.6	Pneumatic Compression	35
2.2.7	Other active compression techniques	38
2.2.8	Risks involved with compression therapy	40
2.3	Interface pressure measurement	40
2.3.1	Methods of interface pressure measurement	41
2.3.2	Pneumatic based interface pressure measurement systems	42
2.3.3	Flexible piezo-resistive sensors	46
2.4	Hyperelastic behaviour of platinum cured silicones	47
2.4.1	Hyperelastic materials	47
2.4.2	Platinum cured silicones	48
2.4.3	Hyperelastic Models	49
2.4.4	The stretch-stress relationship for uniaxial extension	54
2.5	Chapter summary	57
3	Evaluation of interface pressure measurement systems	59
3.1	Introduction	59
3.2	Study of pressure measurement systems	60
3.3	Study of FlexiForce [®] sensors for interface pressure measurement	61
3.3.1	Calibration of FlexiForce [®] sensors	61
3.3.2	Calibration of FlexiForce [®] sensors using Zwicki [®] tester	65
3.3.3	Evaluation of FlexiForce [®] sensors against the manometer)	68
3.4	Study of AMI Sensors for Interface Pressure Measurement	74
3.4.1	Calibration of AMI sensors	74
3.4.2	Calibration of the main unit and Air-pack sensor	75
3.4.3	Evaluation of AMI air-pack sensors against the manometer	76
3.4.4	Study of PicoPress [®] sensors against the manometer	82
3.5	Selection of a suitable pressure sensor	84
3.6	Chapter Summary	85
4	Material characterisation and designing of mini bladders	87
4.1	Introduction	87
4.2	Achieving uniform pressure using mini-bladders	89
4.2.1	Use of single bladder cuffs	89
4.2.2	Use of mini-bladders	92
4.3	Material properties and geometrical analysis	93

4.3.1	Uniaxial testing of silicone material used to craft mini-bladders . . .	93
4.3.2	Sample preparation	93
4.3.3	Curve fitting of experimental data (uni-axial tension tests)	95
4.3.4	Geometrical analysis and mathematical model	101
4.4	Design and development of mini-bladders	107
4.4.1	Preliminary study to create the mini-bladders	107
4.4.2	Design and development of moulds to manufacture mini-bladders .	109
4.5	Manufacturing process of mini-bladders	111
4.6	Inflation behaviour of mini-bladders	112
4.6.1	Experimental set-up	112
4.6.2	Experimental results and discussion	114
4.7	Numerical modelling of the inflation behaviour	120
4.7.1	FEM modelling of the mini-bladder unit on a flat surface	120
4.7.2	Results of FE simulation	124
4.7.3	Comparison of experimental and numerical data	125
4.8	Chapter summary	128
5	Pressure transmission characteristics of mini-bladders	129
5.1	Pressure transmission behaviour on hard surfaces	129
5.1.1	Stage 1: Study of the pressure transmission on to a flat surface by mini-bladders	130
5.1.2	Stage 2: Study of the pressure transmission onto a cylindrical surface	133
5.2	The effect of fabric tension on mini-bladder inflation	139
5.2.1	Derivation of the pressure function due to fabric tension	139
5.2.2	Experimental set up	140
5.3	Pressure transmission on biofidelic leg surrogate	143
5.3.1	Introduction to modulus of human skin	144
5.3.2	Evaluation of the artificial skin and fat	145
5.4	Evaluation of pressure transmission on the leg surrogate	146
5.4.1	Preparation of the skin and fat layers with sensors embedded	146
5.4.2	Calibration of the AMI Air pack sensors embedded in fat layer . . .	147
5.4.3	Experimental set up	150
5.4.4	Results and discussion	151
5.5	Study of pressure transmission on different types of skin and fat layers . . .	154
5.5.1	Pressure transmittance on a skin with a hard modulus fat layer . . .	154
5.5.2	Results and discussion	155
5.5.3	Pressure transmission in a low modulus fat layer	157

5.5.4	Results and discussion	158
5.6	The pressure transmittance on ankle area of the leg	160
5.7	Comparison of pressure transmission by mini-bladders against GCS	162
5.8	Chapter summary	167
6	Prototype design of mini-bladder unit	169
6.1	Design of mini-bladder array	169
6.2	Design of a bandage to house mini-bladder arrays	172
6.3	Manufacturing of the final prototype design	178
6.3.1	Manufacturing process of mini-bladder unit	179
6.4	Experimental set up to create a graduated compression	181
6.5	Chapter summary	183
7	Summary and Conclusions	185
7.1	Summary	185
7.2	Conclusions	189
7.3	Future work	190
	References	191
	Appendix A	209
	Appendix B	233
	Appendix C	265
	Appendix D	283
	Appendix E	295

List of figures

2.1	CVD abnormalities	10
2.2	Superficial veins	12
2.3	Deep veins	13
2.4	Perforator veins	13
2.5	Blood pressure variation	14
2.6	Muscular pump action	15
2.7	Fluid flow at capillaries	16
2.8	Healthy and incompetent valves	17
2.9	Pressure in leg veins without any action of muscle pump	19
2.10	Effect of walking: normal Vs CVD	20
2.11	How compression works	24
2.12	Tension elongation curves: elastic Vs inelastic	30
2.13	Different measurement positions of the leg	32
2.14	Effect of contours on skin pressure variations	34
2.15	Intermittent pneumatic compression cuffs: Uniform, circuferential	36
2.16	A twelve chamber graded-sequential, whole leg IPC device	37
2.17	NormaTec PULSE technology	38
2.18	A schematic of the EAP placed on a human calf	39
2.19	PicoPress® sensor	42
2.20	AMI air-pack type analyser	43
2.21	Air-pack sensor and its operating sequence	44
2.22	Calibration of the probe using a water column	45
2.23	Oxford Pressure Monitor	46
2.24	FlexiForce® sensor	47
2.25	Platinum catalysed addition curing of Silicones	49
2.26	A cubic differential volume element with tensile stress	54
3.1	Calibration procedure for FlexiForce® sensors	62

3.2	MSA-CAL lite 1.0 software interface	63
3.3	MSA-CAL lite 1.0 software interface;calibration points	63
3.4	MSA-CAL lite 1.0 software calibration file:standard weight	64
3.5	Calibration process of FlexiForce sensors using Zwicki® Roell	66
3.6	MSA-CAL lite 1.0 software calibration file: Zwicki® Roell	67
3.7	Calibration for the Flexiforce® sensor 1	68
3.8	Experimental setup for validation against manometer	69
3.9	FlexiForce® sensors against manometer :Standard weight calibrated	69
3.10	FlexiForce® sensors against manometer: Zwicki® calibrated	70
3.11	Face-reverse readings difference FlexiForce® sensors (weight calibrated)	72
3.12	Face-reverse readings difference FlexiForce® sensors (Zwicki® calibrated)	72
3.13	FlexiForce® sensor readings against manometer (2 nd batch)	73
3.14	Calibration setup for main unit and AMI Air-pack sensor	75
3.15	AMI sensors readings against manometer	77
3.16	AMI sensors readings against manometer -linear relationship	78
3.17	AMI sensors readings against manometer (2 nd batch)	79
3.18	AMI sensors readings against manometer -linear relationship (2 nd batch)	79
3.19	PicoPress® sensor readings against manometer	83
3.20	PicoPress® sensor readings against manometer-linear relationship	83
4.1	Blood pressure measurement cuffs	90
4.2	The non-uniform deformation created by BP measuring cuff	91
4.3	A schematic diagram of bladders in contact with a cylinder	92
4.4	The preparation of silicone samples according to the BS 37: 2011	94
4.5	Zwick Roell® tester used for the uniaxial testing	94
4.6	Curvefit for Mooney Rivlin model:PlatSil® Gel-OO 30 –sample 1	96
4.7	Curvefit for Mooney Rivlin model:PlatSil® Gel-A 10 – sample 1	97
4.8	Curvefit for Yeoh model:PlatSil® Gel-OO 30 – sample 1	99
4.9	Curvefit for Yeoh model:PlatSil® Gel-A 10 – sample 1	99
4.10	The layered view of mini-bladder unit design	102
4.11	Mathematical representation of mini-bladder inflation	103
4.12	Analytically calculated inflation height	105
4.13	Pressure transmittance percentage- different geometries	106
4.14	Sample bladder unit manufactured using Kaolinite	108
4.15	Previously manufactured mini-bladders: curled edges	109
4.16	3D printed two parts of the mould for the hexagonal bladder unit	110
4.17	SolidWorks drawing of top mould part	111

4.18	Experimental setup for measuring the inflation height	113
4.19	Fixation of the mini-bladder unit on surface	113
4.20	The inflation/deflation height for PlatSil® Gel-OO 30-sample 1	115
4.21	The average inflation/deflation height for PlatSil® Gel-OO 30	116
4.22	The relationship between the average inflation/deflation height for PlatSil® Gel-A10	117
4.23	The inflation/deflation height for PlatSil® Gel-A10-sample 1	118
4.24	The inflation deflation heights for normal vs. relaxed :PlatSil® Gel-OO 30 .	119
4.25	The inflation deflation heights for normal vs. relaxed: PlatSil® Gel-A 10 . .	120
4.26	A graphical representation of the mini-bladder unit	121
4.27	ANSYS workbench setup	123
4.28	The specification of boundary conditions	124
4.29	Simulation of the directional deformation- z direction	125
4.30	Comparison of numerical model vs. experimental data	126
4.31	The effect of the woven fabric used inside mini-bladder	127
5.1	The experimental setup for interface pressure measurement-flat surface . . .	130
5.2	Interface pressure variation on a flat surface for hexagonal mini-bladders . .	132
5.3	Pressure transmittance percentage variation on the flat surface	132
5.4	Schematic diagram of the experimental set up- cylindrical surface	133
5.5	Interface pressure variation on cylindrical surface-linear relationship	135
5.6	Interface pressure variation on cylindrical surface-different geometries . . .	136
5.7	Pressure transmittance percentage on cylindrical surface-different geometries	137
5.8	Comparison of interface pressure for flat and cylindrical surfaces	138
5.9	Schematic diagram of the arrangement of the mini-bladder on flat surface .	138
5.10	A sketch of a fabric tension over a circular cross section	139
5.11	Experimental set up to study the effect of the fabric tension	141
5.12	Variation of the interface pressure for inflating and reference bladders . . .	142
5.13	Cross-sectional view of the human lower limb-different curvature zones . .	143
5.14	Structure of collagen fibre in different phases	144
5.15	The placement of the sensors in the fat layer	147
5.16	Calibration of embedded AMI sensors against standard weight	148
5.17	Calibration of embedded AMI sensors-different positions	149
5.18	Experimental set up to evaluate pressure transmittance on modelled leg . .	150
5.19	Interface pressure on the artificial skin layer	152
5.20	Interface pressure on the artificial fat layer	152
5.21	Average pressure transmittance percentage-on skin and fat layers	153

5.22	Interface pressure on the artificial skin layer-high modulus fat	155
5.23	Interface pressure on the artificial fat layer-high modulus fat	156
5.24	Average pressure transmittance percentage-high modulus fat	157
5.25	Interface pressure on the artificial skin layer-low modulus fat	158
5.26	Interface pressure on the artificial fat layer-low modulus fat	159
5.27	Average pressure transmittance percentage-low modulus fat	159
5.28	Interface pressure on the first prepared skin-ankle position	161
5.29	Interface pressure on the modelled leg without skin-ankle position	161
5.30	Comparison of class I compression stocking against mini-bladders	163
5.31	Comparison of class II compression stocking against mini-bladders	164
5.32	Comparison of class III compression stocking against mini-bladders	164
5.33	Comparison of class I stocking against mini-bladders-high modulus fat . . .	165
5.34	Comparison of class II stocking against mini-bladders-high modulus fat . .	165
5.35	Comparison of class III stocking against mini-bladders-high modulus fat . .	166
6.1	The arrangement of mini-bladders arrays	170
6.2	Interface pressure on the leg: array of two mini-bladders	170
6.3	Interface pressure on the leg: array three mini-bladder	171
6.4	The experimental setup for testing different fabric pockets	173
6.5	Interface pressure for a mini-bladder unit housed in -20030 fabric pocket . .	174
6.6	Interface pressure comparison: effect of 20030 fabric pocket	175
6.7	Interface pressure for a mini-bladder unit housed in -6437 fabric pocket . .	175
6.8	Interface pressure comparison: effect of 6437 fabric pocket	176
6.9	Interface pressure for a mini-bladder unit housed in Z2300 fabric pocket . .	177
6.10	Interface pressure comparison: effect of Z2300 fabric pocket	177
6.11	The average interface pressure: comparison of different fabrics	178
6.12	The stencil used to create the top layer of the mini-bladder unit	179
6.13	Manufacturing process of the complete mini-bladder unit	180
6.14	The final prototype: manufactured active compression sleeve	181
6.15	The sensor placement on the cylinder	182
6.16	The experimental setup for final prototype	182
6.17	Interface pressure Vs the position of the cylindrical surface	183

List of tables

2.1	CEAP classification of chronic venous disease	18
2.2	The UK classification of bandage for the Drug Tariffs	27
2.3	Comparison of British and German bandage pressures	28
2.4	Comparison of British standard and European standard	32
2.5	Pressure gradient distribution by different compression classes	33
3.1	Calibration points for FlexiForce [®] sensors using standard weight	64
3.2	Calibration points for FlexiForce [®] sensors using Zwicki	65
3.3	Repeatability and non-linearity error (%) for FlexiForce [®] sensors of batch 1	71
3.4	Mean repeatability error for the 2 nd batch of FlexiForce [®] sensors	74
3.5	Calibration of AMI sensors	76
3.6	Linear relationships:AMI air-pack sensors	80
3.7	Non-linearity and repeatability errors for AMI air-pack sensors	81
3.8	Summary of error (%) for different AMI sensors	81
3.9	Non-linearity and repeatability errors for different PicoPress [®] sensors	82
4.1	Mooney Rivlin two parameter model, PlatSil [®] Gel-OO 30	97
4.2	Mooney Rivlin two parameter model, PlatSil [®] Gel-A 10	98
4.3	Yeoh second order model, PlatSil [®] Gel-OO 30	100
4.4	Yeoh second order model, PlatSil [®] Gel-A 10	100
4.5	The strain percentages calculated at different inflation volumes	104
4.6	Minimum gap distance for different shaped mini-bladders	106
5.1	Linear relationships for pressure transmittance of mini-bladders	135
5.2	Young's modulus of skin:literature data	145
5.3	Mechanical properties of the artificial skin and fat layers	146
5.4	Linear relationships:embedded AMI sensors (standard weight calibrated)	148
5.5	Mechanical properties of the second artificial skin and fat layer)	154
5.6	Linear relationships:AMI sensors (standard weight calibrated)	155

5.7	Mechanical properties of the third artificial skin and fat layer	157
5.8	inflation pressures: mini-bladder and GCS comparison	163
6.1	The details of elastomeric yarns used to knit fabrics	172
6.2	The elastic modulus of elastomeric knitted fabrics	173

Nomenclature

Roman Symbols

a minimum gap distance between the membrane fixing points

C_{ijk}/C_{ij} material constants

D two times the bulk modulus at small strain

ΔA_i error

ΔZ total error

f real-valued function

h inflation height

HP_c capillary hydrostatic pressure

HP_{int} interstitial fluid hydrostatic pressure

I_1, I_2, I_3 principle strain invariants

J Jacobian determinant

J_{el} elastic volume ratio

k filtration constant

L deformed length

L_0 deformed length

N positive integer

n number of bandage layers (—)

n	number of cycles
OP_c	osmotic pressure
OP_{int}	interstitial fluid colloid osmotic pressure
P	pressure
P_{int}	interface pressure (N/m^2)
R	radius of curvature (m)
r	radius of curvature of the inflated membrane
T	temperature
T	tension in bandage (N)
V	volume
W	strain energy function
w	bandage width (m)

Greek Symbols

α_i, μ_i	constants for shear behaviour of the material
ε	engineering strain
$\lambda_1, \lambda_2, \lambda_3$	Principal stretches
λ_m	locking stretch at which the upturn of the stress strain curve would rise significantly
μ	initial shear module
σ	standard deviation
σ_e	engineering stress

Superscripts

i, j, k	variables
-----------	-----------

Subscripts

1, 2, 3	principal directions
---------	----------------------

Acronyms / Abbreviations

BP	blood pressure
CVD	chronic venous disorder
CVI	chronic venous insufficiency
DSI	dynamic stiffness index
EAP	electro-active polymers
EVLT	endovenous laser therapy
FEA	finite element analysis
<i>FS</i>	full scale
GSV	great saphenous vein
MRI	magnetic resonance imaging
<i>NFP</i>	net filtration pressure
IIR	butyl rubber
NR	natural rubber
PDMS	polydimethylsiloxane
PU	polyurethane
RFA	radiofrequency ablation
RTV	room temperature vulcanizing
SBR	styrene-butadiene rubber
<i>SD</i>	standard deviation
<i>SE</i>	standard error
SMA	shape memory alloy
SSI	static stiffness index
SSV	small saphenous vein

Chapter 1

Introduction

1.1 Introduction

The focus of the research documented in this thesis was to investigate the design and development of a wearable active compression system capable of providing a graduated pressure profile for the treatment of venous disease, using inflatable mini-bladders. The research has created the fundamental knowledge base necessary to create inflatable mini bladder units using low modulus Silicones, and to evaluate the suitability of the system in providing a graduated compression profile necessary for the treatment of venous disease and lymphedema. The mini- bladders were designed such that they could apply a radial force when inflated instead of the traditional method of stretching a textile fabric over a human limb to generate the pressure required to ensure venous return; the fabric tension resulting due to stretching acts as the tangential force which generates a radial pressure depending on the radius of curvature of human limb.

The advantage of using mini-bladders is that they are capable of providing a more accurately controlled pressure profile using multiple mini-bladders in a network of discrete points instead of using single bladder cuffs. The designed mini-bladders would also be able to provide a controllable pressure profile, independent of the variation of radius of curvature of the human limb. The use of mini-bladders would make the system wearable and enable to achieve a better pressure resolution than current treatment methods.

1.2 Motivation

This research was motivated by the severity and the prevalence of the venous disease and associated complications among the adult populations, global market requirements for better

treatment devices and the inadequacy of the current treatment systems in meeting the required standards. The intention of the research was to address the drawbacks of the existing treatment methods by proposing a novel concept of active compression for the treatment of venous disease and lymphoedema.

1.2.1 Severity of the problem

Venous diseases of human lower limbs, including varicose veins and chronic venous insufficiency, are common chronic medical conditions, affecting around 5-30% of adult population in the developed countries (Beebe-Dimmer et al., 2005; Callam, 1994; Evans et al., 1994; Kaplan et al., 2003; Kurz et al., 2001; Ruckley et al., 2002). The estimated prevalence of such conditions among adult population in the United Kingdom (UK) is around 20-40% (Michaels et al., 2006) and prevalence of varicose veins among the United States' adult population is reported to be around 23%, mainly affecting the age group of 40-80 years (Hamdan, 2012). Chronic leg ulcers which is a late complication of the venous insufficiency, is found to be affecting around 1% of the adult population in the developed countries (Al Khaburi, 2010; Beebe-Dimmer et al., 2005; Crane and Cheshire, 2004; Criqui et al., 2003; Ruckley et al., 2002). A study carried out in 2007 estimated that around seven million people in the world suffer some form of chronic venous problem in the lower limb, out of which around three million would evolve to venous ulcers (van Gent et al., 2010).

The sheer prevalence of chronic venous disease is often associated with high treatment costs, making significant impacts on healthcare systems of many countries. In the United States the estimated annual treatment costs ranges between USD 1.9-3.5 billion, where one patient demands USD 40,000 per year for treatment (Borges et al., 2016). The annual costs to UK's National Health Service (NHS) attributed to managing venous disease, venous leg ulcers and associated commodities is estimated as £596.6 - £921.9 million (Guest et al., 2017). In categorizing the venous leg ulcer management costs in the UK, according to the 2015 and 2016 statistics, the highest percentage was due to the community nurse visits, which was 78% of the cost of patient management (Guest et al., 2018).

1.2.2 Existing treatment methods and market size

Compression therapy is considered as the mainstay of treatment for the chronic venous disease; the concept is to apply an external pressure against the hydrostatic pressure to improve the venous return (Eberhardt and Raffetto, 2005; Flour et al., 2013; Lim and Davies, 2014; Mosti, 2014; O'Meara et al., 2012). Graduated compression is considered as the most effective form of compression, where the highest pressure is applied at the ankle

and gradually reduced towards the knee. Effective graduated compression would squeeze blood from superficial veins, through perforators back into the deep veins, and push the blood back into the heart. This effective external graduated compression, helps to increase the blood flow velocity, reduce the venous reflux, reduce the swelling, prevent and treat lymphedema/oedema, reduce the risk of deep venous thrombosis and reduce the recovery time from extreme sport activities.

In the medical literature the optimum pressure profile is most commonly describes as 40-45mmHg at the ankle, reducing gradually up to 15-20mmHg towards the knee(Al Khaburi, 2010; Coull et al., 2006; Nelson, 2001; Stemmer et al., 1980). There are five main methods presently using for compression therapy, including medical compression bandaging (MCBs), "graduated compression stockings" (GCSs), "self-adjustable fabric hook and loop fastener devices", "intermittent pneumatic compression (IPC) devices", and hybrid devices (Latz et al., 2015; Partsch, 2014). However, the most common forms of graduated compression treatment systems are four-layer bandaging and graduated compression stockings.

The global market for compression therapy devices is USD 2.4 billion in 2012, and is expected to rise to USD 3.4 billion by 2019 (GBI-Research, 2013). It was found that United States was the largest market for compression therapy devices in 2012, having a 49% of market share for the revenue, and is expected to grow at a compound annual growth rate of 6% in 2019(GBI-Research, 2013). The European market is expected to have 35% market share by 2019, while Asia pacific regions are supposed to have 13% (GBI-Research, 2013). As described in section 1.2.1, besides the high incidence of venous disease the adoption of compression therapy in the treatment of lymphedema and amputations can also be a market driver (GBI-Research, 2013).

1.2.3 Shortcomings of the existing treatment methods

Despite the many studies investigating the effectiveness of different methods of compression therapy, the underpinning physics of how compression therapy works is not yet clearly understood. Compression therapy employing compression bandages, and compression stockings work based on the principle of generating pressure on the surface by a component of the tangential tension developed in the fabric, due to the stretch of the fabric (Fernando, 2010). The generated pressure is proportional to the tension of the fabric, and inversely proportional to the radius of curvature and width of the fabric as described by the Laplace's law (Moffatt, 2005, 2008; Thomas, 1990, 2003; Thomas and Fram, 2003). Human limbs do not have a perfectly circular cross section (Fernando, 2010; Liu et al., 2017), therefore even if compression bandage provides a uniform tension the pressure applied will be different from point to point over the limb circumference due to the changes of radius of curvature.

Due to this indirect application of pressure both the compression bandaging and compression stockings are classified as passive treatment systems capable of providing a static compression. Recent research has demonstrated the advantage of applying a variable compression (time-dependent). Intermittent pneumatic compression (IPC) has been used to create variable compression effectively in the treatment of lymphedema. The systems used in IPC have consequently ranged from large single bladder cuff to complex multi chamber systems employing sequential compression (Feldman et al., 2012; Morris, 2008). However, the size of these pneumatic cuffs makes these devices bulky and less wearable. Many times these are used under the clinical supervision. There have been few other attempts towards developing active compression products, by using electro-active polymers and shape memory alloys. However, these methods could not overcome the effect of radius of curvature variability over the limb circumference, which is one of the main scientific knowledge gaps addressed in this study.

1.3 Research plan

The ambition of this research was to address the above shortcomings of existing compression systems for the treatment of venous disease by creating the scientific knowledge base required to develop an active compression system based on inflatable mini-bladders.

1.3.1 Research Aim:

The aim was to create the fundamental science of utilising the radial force generated by inflatable mini-bladders to generate a graduated compression, and design and development of a wearable active compression system for medical applications.

1.3.2 Research Questions

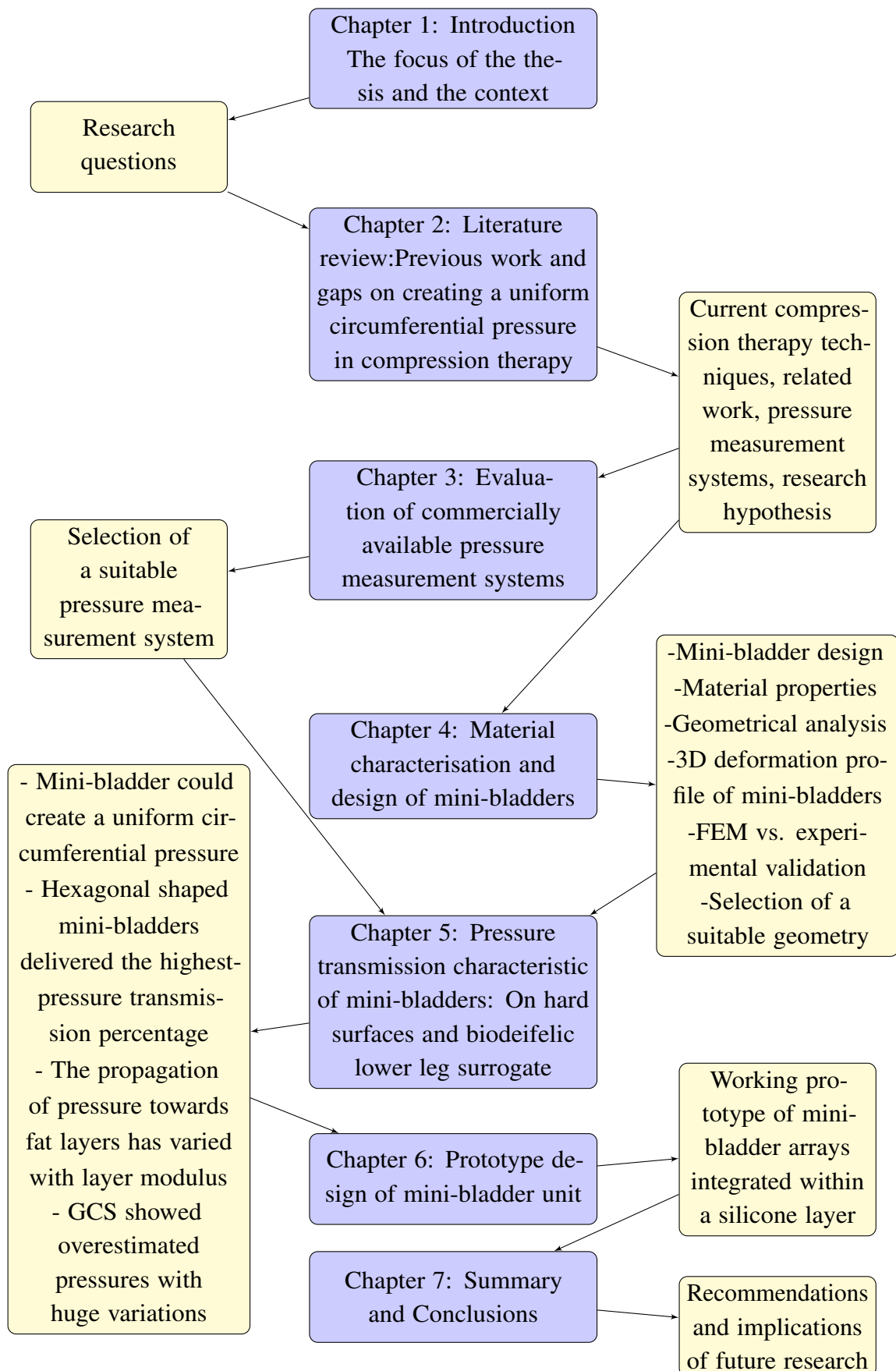
The concept of creating an active compression system was based on the use of inflatable mini-bladders which could be integrated into a wearable bandage. The research questions which had to be addressed are summarised below.

- Formulation of a conceptual design of an active compression system;
The intent was to develop an inflatable bladder preferably in miniature scale, which could be better adopted to the changes of the radius of curvature of the leg and effectively transmit the pressure on to the treated surface.

- Investigation of materials which could be used to craft the inflatable mini-bladders and, parameterise the material characteristics;
In order to select the most appropriate material for the application the stress-strain behaviour, hysteresis, and bio-compatibility of the materials had to be studied and understood. The hyperelastic behaviour of low modulus silicones and the material parameters required for the numerical modelling had to be calculated.
- Investigation of the suitable shape, size and the design of the mini-bladders:
In order to select the most appropriate shape and the size of the mini-bladders, a geometrical analysis together with experimental study was carried out.
- To characterise the inflation behaviour of the mini bladders;
The focus was to study the inflation characteristics of the mini-bladders experimentally and using finite element analysis. Test methods had to be designed to study the inflation/deflation cyclic characteristics of the inflation surface of mini-bladders in order to analyse the performance of the mini-bladders in recurring usage cycles, and hysteresis effects.
- New test rigs had to be developed to study the effectiveness of the mini bladders;
A series of experiments had to be designed to evaluate the pressure transmittance characteristics of the mini-bladders. A suitable interface pressure measuring system need to be selected and experiments had to be extended for flat and curved surfaces.
- Testing of the developed active compression system on a biofidelic leg surrogate and analyse its effectiveness.
The idea was to test the mini-bladders on a biofidelic leg surrogate to study the effectiveness of the designed mini-bladders to transmit pressure on to a human limb. The study should be extended to understand how the applied pressure is propagated through the skin and fat layers using an artificial skin and fat layer.

1.4 Structure of the thesis

The following flow chart summarises the structure of this thesis.



1.5 Contributed papers

This research has been resulted in the following publications;

Conference proceedings

Nandasiri, G. K., Dias T., and Hurley W., “The development of an active compression system for the venous disease using a series of a silicone-based inflatable mini-bladders”, In Proc. of American Association of Textile Colourists and Chemists International Conference, South Carolina, United States, pp 227-240, 2018

Nandasiri, G. K., Dias T., and Hurley W., “Development of an active compression system for treating the venous disease in lower human limb”, In Proc. of Textile Institute World Conference, Leeds, United Kingdom, 2018

Journal papers

Nandasiri, G. K., Ianakiev, A., Arm, R. and Dias T. Hyperelastic properties of platinum cured silicones and its application in active compression treating venous disease-**In preparation to be submitted to Polymers**

Nandasiri, G. K., and Dias T., “The use of mini-bladders in creating an active compression system and its effectiveness”-**In preparation**

Nandasiri, G. K., Shahidi, A.M. and Dias T., “The evaluation of commercially available interface pressure measurement systems for compression therapy”-**In preparation**

Chapter 2

Literature review

2.1 Chronic Venous Disorder

2.1.1 Definition

Chronic venous disorder (CVD) refers to morphological and functional abnormalities of the venous system of long duration, like telangiectasias, blue veins, varicose veins, oedema, pigmentation, eczema, lipodermatosclerosis, and venous ulcers (Al Khaburi, 2010; Bergan et al., 2006; Eberhardt and Raffetto, 2005; Eklof, 2007; Eklof et al., 2009; Langer et al., 2005). Some of these abnormalities are graphically illustrated in the Figure 2.1. CVD is normally caused by primary abnormalities of venous wall and the valves and secondary abnormalities due to previous venous thrombosis that can lead to reflux, obstruction or both (Bergan et al., 2006; Nicolaides, 2000; Nicolaides et al., 2014). Chronic venous insufficiency (CVI) is a term reserved for advanced CVD due to functional abnormalities of the venous system producing oedema, skin changes and venous ulceration (Nicolaides et al., 2014). Varicose veins are a common symptom of CVD and results from the abnormal distensibility of connective tissue in the venous wall (Nicolaides et al., 2014). Varicose veins are subcutaneous dilated veins which equal to or more than 3mm in diameter in the upright position and are usually tortuous (Nicolaides et al., 2014). A venous ulcer is a full thickness defect (open wound) in the epidermis and have a long healing tendency (more than four weeks)(Crane and Cheshire, 2004; Nicolaides et al., 2014).

2.1.2 Epidemiology

Venous disease of human lower limb including varicose veins and chronic venous insufficiency has been one of the most common chronic medical condition reportedly affecting the quality of life of people in the western world (Beebe-Dimmer et al., 2005; Callam, 1994; Evans et al., 1994; Kaplan et al., 2003; Kurz et al., 2001). Early epidemiological studies have shown that CVD has a considerable socio-economic impact in most of the western countries due to its high prevalence, high treatment and investigation costs, along with loss of working days affecting the quality of life (Abenhaim

et al., 1999; Kurz et al., 1999). Chronic leg ulcers which is a common condition developed due to venous disease, estimated to be affecting 0.3% of the adult population in the developed countries, and this number increases to 1% when both healed and active ulcers are considered (Beebe-Dimmer et al., 2005; Crane and Cheshire, 2004; Criqui et al., 2003; Magnusson et al., 2001; Ruckley et al., 2002). The same studies have showed that the leg ulcers are more common in women, of older age groups and there is a noticeable increase with the age. Venous ulcers are considered to be chronic and recurrent, where more than 50% of ulcers require therapy for more than one year (Scott et al., 1995) and around 67%-75% of patients experience recurrent ulcers (Baker et al., 1991; Callam, Harper, Dale and Ruckley, 1987).



Fig. 2.1 CVD abnormalities (Heller and Evans, 2015)(Alguire and Mathes, 1997)(Karadi et al., 2011)(Valencia et al., 2001)

The most common estimates of the prevalence of varicose veins are between 5% and 30% in the adult population, but reports have estimated values ranging from <1% to >70% (Beebe-Dimmer et al., 2005). The varicose veins are present in 25-33% of female and 10-40% of male adult population (Allan et al., 2000; Bradbury et al., 1999; Evans et al., 1999; Fowkes et al., 2001; Ruckley et al., 2002). The sheer prevalence of varicose veins and associated substantial costs of treating late complications such as chronic ulcers contribute to a high burden on healthcare resources. Normally this accounts for 1-3% of total healthcare budget of most western countries with developed healthcare systems (Piazza, 2014).

The socioeconomic impact of CVD could be associated with the substantial number of individuals affected, increased healthcare costs, considerable economic effects reflected in terms of work lost days and diminishing quality of life (Bachoo, 2009; Bergan et al., 2006). Millions of people seek medical

attention annually due to varicose veins, related to the cosmetic appearance or other associated chronic conditions leading to diminishing quality of life. This leads to significant impacts on the healthcare systems, where it is estimated as \$3 billion per year being spent in the USA for treating venous wounds (McGuckin et al., 2002). In the UK, the Healthcare Commission has estimated that chronic venous ulcers cost the NHS £300-600 million per year (O'Meara, Tierney, Cullum, Bland, Franks, Mole and Scriven, 2009).

CVD and venous ulceration can be considered a condition that deteriorate the quality of life, which require long term care, and lifelong need for medical intervention. There are several risk factors associated with CVD, such as family history (genetics), age, standing occupation, gender, pregnancy, obesity, ankle mobility (Bergan, 2007; Bergan et al., 2006; Criqui et al., 2007). The age and the family history (genetics) were supposedly the strongest risk factors for CVD irrespective of the sex. The likelihood of developing varicose veins increases with getting older, as wear and tear on the veins causes the vein walls to weaken and allowing them to enlarge. The peak occurrence age period for venous ulcers is estimated to be between 60 and 80 years (Callam, Harper, Dale and Ruckley, 1987). The hours spent standing or walking is also favourably associated with the formation of varicose veins in both men and women.

2.1.3 The human lower limb venous system

In order to study the pathophysiology of various venous disorders and to understand the treatments required, it is necessary to identify the normal anatomy of the venous system of lower extremities, along with the normal functionalities of its elements and mechanisms.

Composition of the venous system: Veins and venous valves

The peripheral vein system act as a reservoir to store blood and as a channel to carry the deoxygenated blood from the extremities back into the heart. It is estimated that 60 to 75% of the blood in the body is found to be in the veins which are less than 200 μ m in diameter (Bergan and Pascarella, 2007). The venous valves play an important role in this transportation of blood from the lower extremities, back into the heart. The venous blood flow is not steady state but pulsatile and the venous valves undergo opening and closing cycles (Bergan and Pascarella, 2007). The venous valves are cusps attached with their convex edges to the venous wall, and their concave margins lie against the wall when the blood flow is towards the heart (Al Khaburi, 2010; Standring and Wigley, 2005). When the blood flow reverses, the valves close restricting the blood flowing back into the vein compartments. The veins of the lower extremities are divided into three main categories namely, superficial, deep and perforator veins.

Superficial veins

Superficial veins are located between the skin and the superficial fascia. As depicted in Figure 2.2, the two main superficial veins in the lower extremities are the great saphenous vein (GSV) and small saphenous vein (SSV). GSV begins on the dorsum of the foot as a dorsal venous arch and runs along the tibial internal edge (Ricci, 2011). The GSV receives multiple tributaries along its course, and these veins usually lie in a less supported, more superficial plane above the membranous fascia (Goldman and Weiss, 2016; Ricci, 2011). The SSV is the most prominent superficial vein below the knee, which begins at the lateral aspect of the foot and ascend posterior to the lateral malleolus, heads to popliteal fossa and enters the popliteal vein (Goldman and Weiss, 2016; Ricci, 2011; Standring and Wigley, 2005). Communicating veins, which are located in the same compartment connect veins either deep to deep or superficial to superficial (Liu et al., 2017), therefore the communicating veins between GSV and SSV direct the blood flow from SSV to the GSV (Mozes and Gloviczki, 2007).

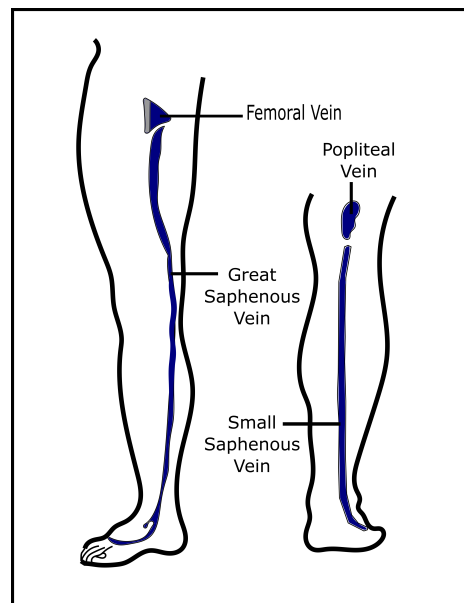


Fig. 2.2 Superficial veins (GSV and SSV)

Deep veins

The venous blood flows from the superficial veins into the deep veins, while the deep veins primarily drain blood flows from muscles (Liu et al., 2017). The unidirectional valves present in the superficial, perforating and deep veins prevent the back flow of the blood supporting the venous return (Caggiati et al., 2002; Kachlik et al., 2012). The deep venous system is located below the muscular fascia and consists of three sets of paired tibial veins : the anterior tibial vein, posterior tibial vein and peroneal vein that merge to become popliteal vein (Eberhardt and Raffetto, 2005, 2014; Meissner, 2005; Standring and Wigley, 2005). Deep veins play a key role in the calf muscle pump function.

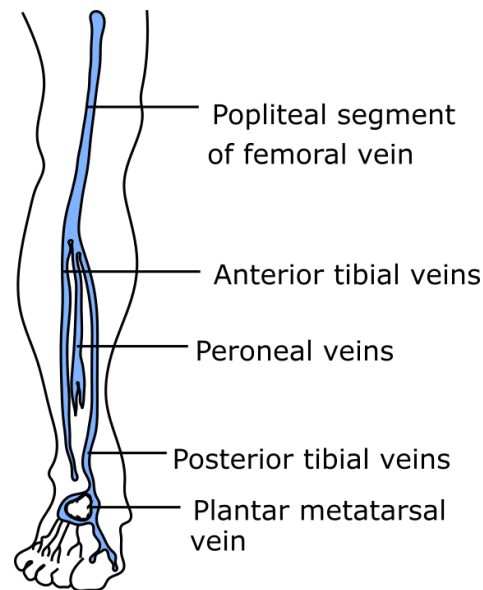


Fig. 2.3 Deep veins

Perforator veins

These veins begin from the superficial veins and connects the superficial veins and deep veins, with one to three valves, directing the flow towards the deep veins from superficial (Figure 2.4) (Meissner, 2005). The calf contains four groups of perforators: the para-tibial perforators which connects the GSV and posterior tibial veins, the posterior tibial perforators and the lateral and anterior leg perforators (Meissner, 2005).

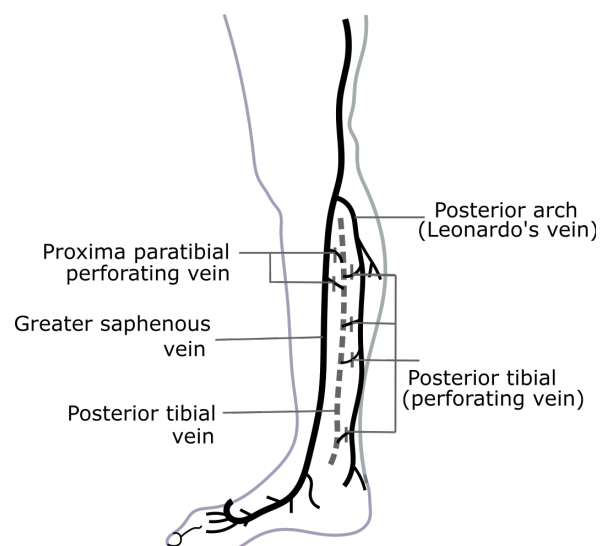


Fig. 2.4 Perforator veins

Venous return

Blood pressure is defined as the force per unit area exerted on a vessel wall by the blood contained inside the vessel (Al Khaburi, 2010). When the blood flows inside a vessel, there exists a resistance to the flow which is a measure of the amount of friction blood encounters as it passes through. The blood flow is directly proportional to the difference in the blood pressure (ΔP) and inversely proportional to the peripheral resistance (R) (this depends on the blood vessel diameter).

Unlike arterial pressure which pulsates, venous blood pressure is steady and subjects to minute changes during the cardiac cycle. According to the Figure 2.5, the pressure gradient in the veins from venules to the venae cavae is about 15mmHg (Marieb and Hoehn, 2007), which is very low and not adequate to promote venous return. For venous return three functional adaptations are critically important, namely the muscular pump, respiratory pump, and sympathetic venoconstriction (Marieb and Hoehn, 2007).

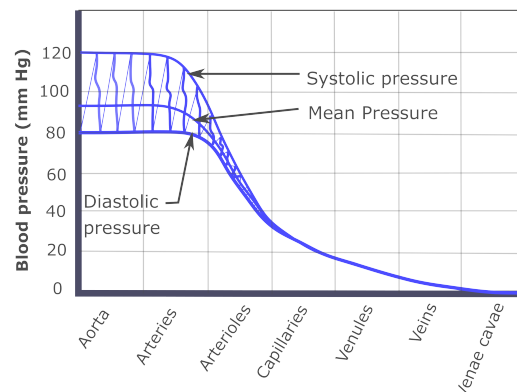


Fig. 2.5 Blood pressure variation in different blood vessels (Marieb and Hoehn, 2007)

Muscular pump: The muscular pump consists of skeletal muscle activity, on contraction and relaxation of the muscles which surrounds the deep veins, they squeeze blood towards the heart and once the blood passes each successive compartment, it doesn't allow to flow back (Figure 2.6) (Marieb and Hoehn, 2007; Moore et al., 2013). The human lower limb consists of three muscular pumps; foot, calf, and thigh out of which calf muscle pump is the most important which has the largest blood capacitance and generates highest pressures (around 200 mmHg) during contraction (Meissner et al., 2007). During the normal motion, foot pump, distal and proximal calf pumps join in to pump the blood back to the heart.

Respiratory pump: This moves the blood upward as the pressure changes in the ventral body cavity during breathing. Upon inhale the pressures in the abdominal increases squeezing the veins and forcing the blood towards the heart, while the pressure in the chest decreases allowing thoracic veins to expand and speeding blood into the right atrium (Al Khaburi, 2010; Marieb and Hoehn, 2007).

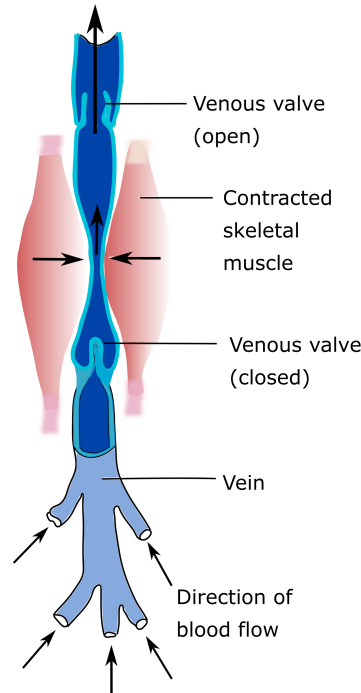


Fig. 2.6 Muscular pump action (Marieb and Hoehn, 2007)

Capillary dynamics

Capillaries are the smallest blood vessels that form a network throughout the bodily tissues, through which the nutrients and gas exchanges occurs. The fluid is deposited from the capillaries at the arterial end and returned back to the bloodstream at the venous end via the lymphatic system (Al Khaburi, 2010; Marieb and Hoehn, 2007). The amount of fluid and the direction of the flow across the capillary walls will depend upon the hydrostatic and osmotic pressures as shown in Figure 2.7. Hydrostatic pressure in the capillaries is identical to the capillary blood pressure and is referred to as capillary hydrostatic pressure (HP_c), which acts to force the liquid through the walls in a process called filtration. The interstitial fluid hydrostatic pressure (HP_{int}), which which oppose the HP_c pushes the fluid back to the capillary. However, this pressure is very low and therefore the net pressure is equivalent to HP_c . Osmotic pressure (OP_c) is generated due to the difference of water concentration between the two sides of the capillary walls. The net filtration pressure can be defined as the net loss of fluid from the blood, and can be summarized in the Starling's equation (Eq. 2.1)

$$NFP = k(HP_c - HP_{int}) - (OP_c - OP_{int}) \quad (2.1)$$

where, OP_c is the osmotic pressure (oncotic pressure), OP_{int} is the interstitial fluid colloid osmotic pressure, and k is a filtration constant (Partsch, 2003).

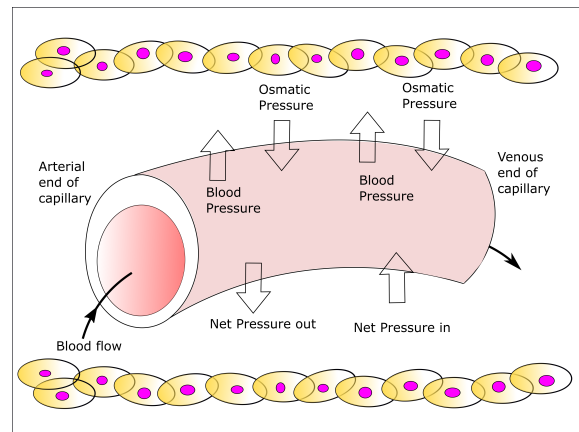


Fig. 2.7 Fluid flow at capillaries (Marieb and Hoehn, 2007)

2.1.4 Pathophysiology: Effects of damages to the venous system

The major feature of CVD pathophysiology is reflux, which is mainly caused due to the valvular incompetence and obstruction. The previously mentioned obstruction and reflux may often exist alone or in combination, and this can be intensified by muscle pump dysfunction or inactivity (Bozkurt et al., 2017). Venous reflux can be based on several mechanisms; the main factors are venous valve incompetence, inflammation of the vessel wall, hemodynamic factors and venous hypertension (Santler and Goerge, 2017). Primary valvular incompetence and primary vein wall weakness, are considered to be the most widely accepted theories of primary varicose vein pathophysiology (Fan, 2005). According to Sir William Harvey's "primary valvular incompetence theory" in 1628, the varicose veins develop as the consequences of central valvular incompetence developed due to the deterioration of valves (Fan, 2005). This results in developing venous hypertension, which will successively impair the adjacent peripheral valves and will contribute towards propagation of varicose transformation in a central to peripheral direction. The competent valves prevent the blood refluxing and backward retrograde flow of blood, while the incompetent valves, as shown in the Figure 2.8, allows the reflux and backward retrograde of blood back into the veins (Al Khaburi, 2010).

This "primary vein wall weakness theory" fails to describe that the valves are strong structures that are capable of withstanding 200mmHg pressure without leakage (Goldman et al., 1999) and varicose veins can occur below or between competent valves (Fan, 2005). On the other hand, the "primary vein wall weakness theory" states that varicose veins develop from a defect in vein wall rather than the valves. A normal vein wall consists of a collagen matrix which provides the strength and three smooth muscle layers that controls the venous tone (Fan, 2005). Histological studies demonstrate that compared to normal veins, varicose veins exhibit a rapid generation of the collagen matrix with disruption of the muscle fibre layers (Rose and Ahmed, 1986). This can cause the vein dilation due to the venous hypertension.

There exists evidence which shows that the primary varicose veins results from an intrinsic genetic defect of collagen synthesis (Fan, 2005), these findings also supports that the primary varicose veins

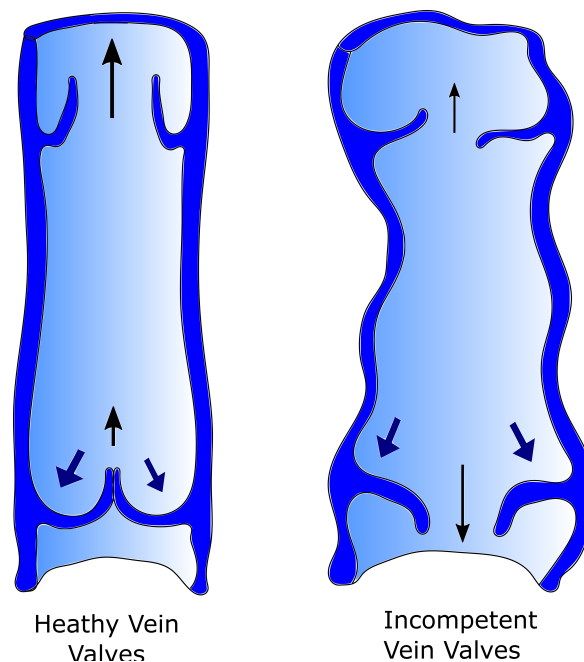


Fig. 2.8 Healthy and incompetent valves (Al Khaburi, 2010)

are developed due to systemic malformation of connective tissue physiology, than a mechanical phenomenon exists at the level of the veins. This malformation of collagen synthesis leads to impairment and expansion of the valve and causes poor leaflet contact and venous reflux (Edwards and Edwards, 1940; Fan, 2005; Goldman et al., 1999). There exist evidence that incompetent perforators have also been considered as a cause of primary varicose veins, as several studies have demonstrated that incompetent perforator veins are larger in diameter than competent ones (Delis et al., 2001; Stuart et al., 2000; Yamamoto et al., 2002). This suggests that perforator reflux develops secondarily accounting to a primary complication with the vein wall integrity (Fan, 2005). As shown in the Figure 2.8, once this condition prevails over a longer time it will result in vein dilation, venous hypertension, and increase of filtration within the capillary beds causing oedema (Al Khaburi, 2010; Armstrong et al., 2006; Nelson, 2001).

Clinical manifestations and CEAP classification

As "CVD" represents a range of conditions from simple varicose veins to more advanced stages like venous ulceration. It is necessary to understand that same clinical manifestations may result from different mechanisms, including incompetent valves, venous obstruction, muscle pump dysfunctions, or combination of these as described above (Eberhardt and Raffetto, 2014). Therefore, manifestation of chronic venous disease should be explored in terms of a well-established clinical classification scheme. Hence, the Clinical, Etiology, Anatomic, Pathophysiology (CEAP) classification scheme was developed to implement a basis for the uniformity in diagnosing, treating and reporting the chronic

venous disease (Eberhardt and Raffetto, 2005; Porter et al., 1995). The detailed explanation of the CEAP classification is given in the Table 2.1 below.

Table 2.1 CEAP classification of chronic venous disease(Youn and Lee, 2019)

Classification	Description/Definition
Clinical classification (C)	
C_0	No venous disease
C_1	Telangiectases or reticular veins
C_2	Varicose veins
C_3	Oedema
C_4	Changes in skin and subcutaneous tissue A Pigmentation or eczema B Lipodermatosclerosis or atrophie blanche
C_5	Healed ulcer
C_6	Active ulcer
Etiologic classification (E)	
E_c	Congenital (e.g. Klippel-Trenaunay syndrome)
E_p	Primary
E_s	Secondary (e.g. postthrombotic syndrome, trauma)
E_n	No venous cause identified
Anatomic classification (A)	
A_s	Superficial
A_d	Deep
A_p	Perforator
A_n	No venous location identified.
Pathophysiologic classification (P)	
P_r	Reflux
P_o	Obstruction, thrombosis
$P_{r,o}$	Reflux and obstruction
P_n	No venous pathophysiology identified

Dilated veins and Ambulatory Venous Hypertension

The failure of valves that occur at the junctions of the deep and superficial systems, let high pressures enter into the the superficial veins which causes vein dilation and formation of varicose veins from the proximal junction down the extremity (Eberhardt and Raffetto, 2005, 2014). Perforator valve incompetence causes the blood to flow from deep veins backward into the superficial system which generates high pressure, this high pressure can produce excess vein dilation and secondary failure of vein valves (Eberhardt and Raffetto, 2005), as a result a cluster of dilated veins would develop at that site and would spread up the leg.

Chronic Venous Insufficiency (CVI) defines the manifestations of venous disease often results from

ambulatory venous hypertension, which is the venous pressure being higher than the normal condition and failure to reduce the venous pressure during exercise (Meissner et al., 2007). Pressure in the veins of the leg is depending on the "hydrostatic component" related to the weight of the column of blood, and "hydrodynamic component" related to the pressure generated by contraction of skeletal muscles of leg and pressure in the capillary network (Al Khaburi, 2010; Moffatt, 2007), where both these conditions are affected by the actions of venous valves.

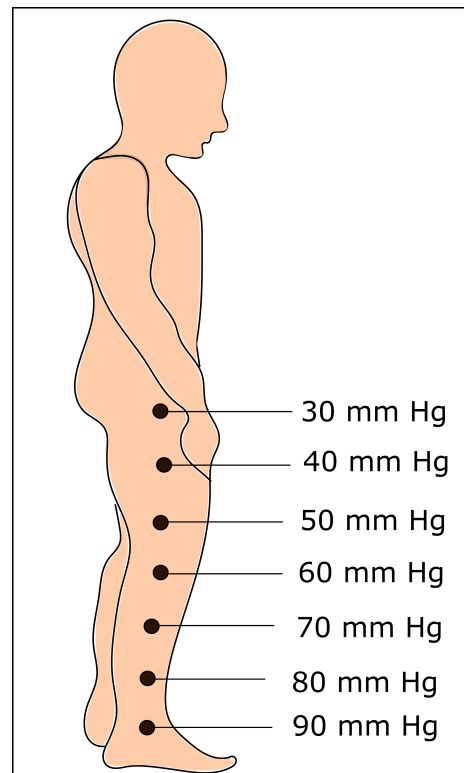


Fig. 2.9 Pressure in leg veins (mmHg), without any action of muscle pump (weight of the blood column) (Moffatt, 2007)

When a patient is standing without any exercise (muscle activity), the venous pressure is determined by "hydrostatic component" (weight of the blood column) and capillary flow, which is higher as 80 – 100mmHg as shown in Figure 2.9. However, during ambulation due to skeletal muscle contraction, the venous pressure transiently increases within the deep leg veins, and competent venous valves, allows the venous blood to flow back into the heart, emptying the deep and superficial venous system which reduces the pressure less than 30mmHg (Bergan et al., 2006) (Figure 2.9).

As shown in the Figure 2.10, a healthy subject with normal venous valve activity, the hydrostatic pressure at standing position is around 80-90mmHg, which drops more than 50% to ambulatory venous pressure of 20-30mmHg, with calf exercise. The return of pressure is gradual, taking more than 20 seconds for the refill. A subject with abnormal venous pressure with venous reflux has a resting/standing pressure higher than normal (Eberhardt and Raffetto, 2014). And the reduction of

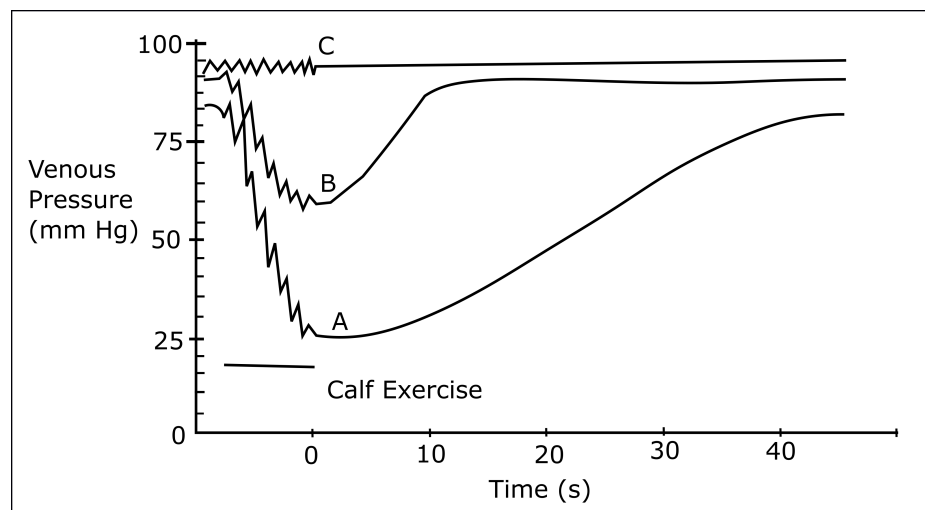


Fig. 2.10 Effect of walking on normal individuals and those with different stages of CVD. A: Normal venous pressure (healthy individuals), B: Abnormal venous pressure, with venous reflux (moderate venous insufficiency), C: Abnormal venous pressure, with venous obstruction (severe venous insufficiency) (Eberhardt and Raffetto, 2014)

pressure with the calf muscle exercise is less than 50%, as well as the return of venous pressure to the resting level is rapid as less than 20 seconds, due to shorter refill times. Subjects with venous obstruction, shows a much higher ambulatory venous pressure in comparison to the normal condition with no or minimal drop in pressure due to exercise. Due to the impotent venous emptying, the immediate post ambulatory venous pressure will be as high as the pressure after prolonged standing (Eberhardt and Raffetto, 2014). These sustained elevated venous pressure conditions results in pathological effects in the skin and subcutaneous tissue such as oedema, pigmentation, and venous ulceration (Meissner et al., 2007).

Oedema and Ulcer formation

As shown in Figure 2.7, net filtration pressure depends on hydrostatic and osmotic pressure in the capillaries and the interstitial space. According to the Staling's equation (equation 2.1) at the arterial end, NFP is positive and the filtration occurs, and at the venous end hydrostatic pressure is less than osmotic pressure, which causes negative NFP allowing the reabsorption of the fluid. However, due to ambulatory venous hypertension the pressure at the venous end of the capillaries is much higher than for a healthy subject (Al Khaburi, 2010), which facilitates more filtration into the interstitial space. This abnormal increase in the interstitial fluid within the tissues causes oedema.

An ulcer can be defined in simple terms as a defect occurred in a previously damaged skin (Caprini et al., 2012). Classically a venous ulcer is defined as "an irregularly shaped ulcer with well-defined borders (often covered with yellow-white exudate) surrounded by erythematous skin" (Crane and Cheshire, 2004, 2008). Considerable leakages of fluid through the venous ulcers may often cause

irritation of the surrounding skin, and if this condition is left untreated it can cause 'mummification' of skin and subcutaneous tissues with darkening and thickening of the skin (Caprini et al., 2012). The formation of venous ulcers may be explained in the following theories.

"Fibrin cuff theory": In 1982 Browse and Burnand introduced the fibrin cuff hypothesis explaining the venous ulceration (Shami et al., 1992), which shows that elevated venous pressure results in elevated capillary pressure and permeability that stretches the pores between endothelial cells linings and capillaries allowing large molecules (fibrinogen) to escape into the interstitial tissue. Thereafter, it polymerizes into "fibrin" to form pericapillary fibrin cuffs, which act as a barrier, preventing the diffusion of oxygen and other nutrients reaching the skin which results in cell death and ulceration (Shami et al., 1997, 1992).

"White cell trapping theory": This theory suggests that due to the venous hypertension, the reduction of the capillary flow rate resulting in trapping white blood cells in the leg due to their slow-moving rates compared to red blood cells. These trapped white blood cells may cause plugging of the capillaries, and release free radicals (toxic oxygen metabolites), proteolytic enzymes and cytokines leading to tissue damage and ulceration (Crane and Cheshire, 2008; Shami et al., 1992).

"The trap hypothesis" (Macromolecules): This theory proposes that fibrin and other macromolecules that leak into dermis, due to venous hypertension "trap" growth factors and other stimulatory or homeostatic substances, and make them unavailable for the tissue integrity and repair process (Crane and Cheshire, 2008; Falanga and Eaglstein, 1993; Santler and Goerge, 2017).

2.1.5 Management of complications related to venous disorder

There exists a wide range of treatment options for CVD, aims to improve venous function, prevent sequelae of complications of CVD, and to promote the ulcer healing. Management of complications related to venous disease should address the progressive nature of the CVD and act against the progression. The treatment consists of both conservative and invasive treatment options, where the conservative treatment includes physical treatment, consisting of compression therapy, manual lymphatic drainage, and physical therapy (exercise). The invasive treatment include standard surgery, stripping techniques, phlebectomy and less invasive treatment options like sclerotherapy, thermal ablation of GSV, and radio frequency ablation (Bachoo, 2009; Boné Salat, 1999; Cabrera et al., 2003; Chandler et al., 2000).

Medical compression therapy is the basis for any treatment of CVD, it counteracts the venous reflux and hypertension, by mechanical venous compression and improving the functionality of the muscle pump. Also compression therapy is considered to be more important in the treatment of the leg ulcers (Dissemond et al., 2016; Stacey et al., 1997). Often compression therapy can play a pivotal role in greatly relieving the symptoms like oedema, and heaviness of legs in the early stages of CVD (Evans et al., 1999; Motykie et al., 1999). Physical therapy can be beneficial in the form of a supplemental therapy, in which the graded exercise programs are used to reinstate the calf muscle function and ankle

mobility(Eberhardt and Raffetto, 2014; Santler and Goerge, 2017). Manual lymphatic drainage with subsequent compression bandaging can be used to reduce chronic leg oedema(Santler and Goerge, 2017).

Sclerotherapy is a treatment in which a liquid is injected into the incompetent veins (varicose veins and venous segments with reflux), that will make inflammation of the endothelium of the vessel wall, which results in localized thrombosis (Santler and Goerge, 2017). This will block the further blood flow through the vessel and it will fade eventually by absorbing to the body. Sclerotherapy can be injected in liquid or foam forms and is easy to carry out, with no restrictions of repeatability (Santler and Goerge, 2017). It can also have side effects like hyperpigmentation and transient pain associated with the area treated, and has recurrence possibilities after five years.

Less invasive treatment options offer good midterm results and have comparable efficacy to stripping (Santler and Goerge, 2017). Amongst them two of the most commonly used endovenous thermal procedures are radiofrequency ablation (RFA) and endovenous laser therapy (EVLT) to ablate the incompetent veins(Santler and Goerge, 2017). The thermal energy is used in either of the above forms of treatment to generate heat, and it will then cause a local thermal injury to the vein wall resulting in venous occlusion. The effectiveness of the both categories are reported to be the same, whereas the radio frequency ablation associated with few side effects but with rapid recovery (Almeida et al., 2009; Goode et al., 2010; Rasmussen et al., 2013). As both systems involve thermal energy there exists a potential risk of nerve damage.

Surgical procedures aim to remove or obliterate incompetent veins or to isolate them. These techniques compared to the conservative measures, provide a significant decrease in the systems. This procedure is often recommended to the patients with persistent discomfort with disability and non-healing venous ulcers. In this procedure the GSV is ligated and dissected from the femoral vein, followed by the removal of tributaries (Eberhardt and Raffetto, 2014; Santler and Goerge, 2017).

Apart from the above methods, there exists novel methods such as venous occlusion using "cyanoacrylate adhesive" and "mechanochemical endovenous ablation" (Almeida et al., 2013; Elias and Raines, 2012; Santler and Goerge, 2017). Cyanoacrylate adhesive can be formulated for rapid polymerisation and high tissue affinity in the presence of blood (Almeida et al., 2017). This causes the closure of the targeted vein by an inflammatory reaction, and encapsulation that leads to fibrosis (Aleksiejew-Kleszczyński and Jagielska-Chwała, 2015; Wang et al., 2006). Mechanochemical endovenous ablation achieves the venous occlusion by a wire rotating within the lumen of the vein at 3500 rpm which abrades and allows a better efficiency of sclerosant (Elias and Raines, 2012). A liquid sclerosant is then inserted near the rotating wire, these two mechanical and chemical combination achieves the venous occlusion. Since the above two methods are quite new in the treatment domain, it is difficult to draw any recommendations, but unlike previous techniques such as RFA, and EVLT, in this method tumescence anaesthesia is not required, while tingling sensations are also occurred less in comparison. As discussed above there exists lots of treatment options for the CVD, and it is much important to consider individual's anatomical conditions, underlying diseases, and patient's wish in deciding the required treatment. However, considering the complexity and the requirement of surgical and other

invasive treatment options compression therapy is considered to be one of the mainstay treatment. It is often considered even with the surgical and endovenous procedures, adequate compression therapy is required. Compression therapy can be considered as a preliminary therapeutic consideration for all CEAP clinical classes of CVD.

2.2 Compression therapy

Compression therapy is the most widely used treatment in preventing adverse effects of chronic venous disease. Although the mechanism of compression therapy is not yet clearly understood, it seems that the external pressure applied raises the interstitial pressure, decreasing superficial venous pressure and thereby improving the venous return (Burnand and Layer, 1986). The evidence of limb compression exists from the 3500BC in the Neolithic period (Mariani, 2009). Descriptions of limb compression therapy are found in 450-350BC, where both Hippocrates and Aurelius Celsus used compression in their treatment of venous disease (Anning, 1976; Moffatt, 2007), as the Greeks used compression to counteract the adverse effects of gravity and upright position (Felty and Rooke, 2005). Guy de Chauliac published the first mention of compression therapy for varicose veins in 1363, whereas in 1440 Savonarola described how bandages should be used from the distal part of the limb and worked upwards (Felty and Rooke, 2005).

In the 17th century description of the circulation of blood by William Harvey led to an understanding of the rationale for limb compression (Felty and Rooke, 2005), and later in the 18th century Johann Theden proposed that compression reduces the flow, stimulating the activity of the skin in the areas of impairment increasing the return flow (Felty and Rooke, 2005). Starting from the ancient times the compression therapy has improved ever since and either active or passive forms of compression have been used as one of the mainstay treatment option exists for CVD. Passive compression is the application of a constant pressure by use of compression garments, while active compression involves the use of intermittent compression.

2.2.1 Current compression therapy

Current compression treatment takes the forms of Medical Compression Bandages (MCB), Medical Compression Stockings (MCS), and Intermittent Pneumatic Compression (IPC) which can be divided into the two main categories of passive and active compression. Compression therapy aims to increase venous and lymphatic return by increasing flow velocity, reduce oedema and ambulatory venous pressure, and improve the effectiveness of the muscle pump (Felty and Rooke, 2005). It is also found that compression increases the healing rates for venous ulcers, with high compression being more effective (O'Meara, Cullum, Nelson et al., 2009). For compression to work effectively, it must be graduated and therefore the graduated compression is considered as the gold standard of treatment, where the higher pressure is applied at the ankle and then it is graduated towards the knee. It is

believed that this would improve the venous return, since an external pressure graduation is provided (O'Meara, Cullum, Nelson et al., 2009).

2.2.2 Mechanism of compression therapy

As mentioned earlier, though it has been an effective treatment, physics behind the compression therapy is not yet fully understood. According to the literature current understanding of the mechanism of the compression therapy can be summarised into the following points (Moffatt, 2007; Nelson, 2001; Partsch, 2003, 2006, 2007; Ramelet, 2002);

- Narrows or occludes superficial/deep veins and improve the venous return

The compression reduces the diameters of both superficial and deep veins (Figure 2.11), which leads to a reduction in the local blood volume, increasing the flow velocity towards the heart redistributing the blood towards the central parts of the body (Moffatt, 2007; Partsch, 2003, 2006, 2007).

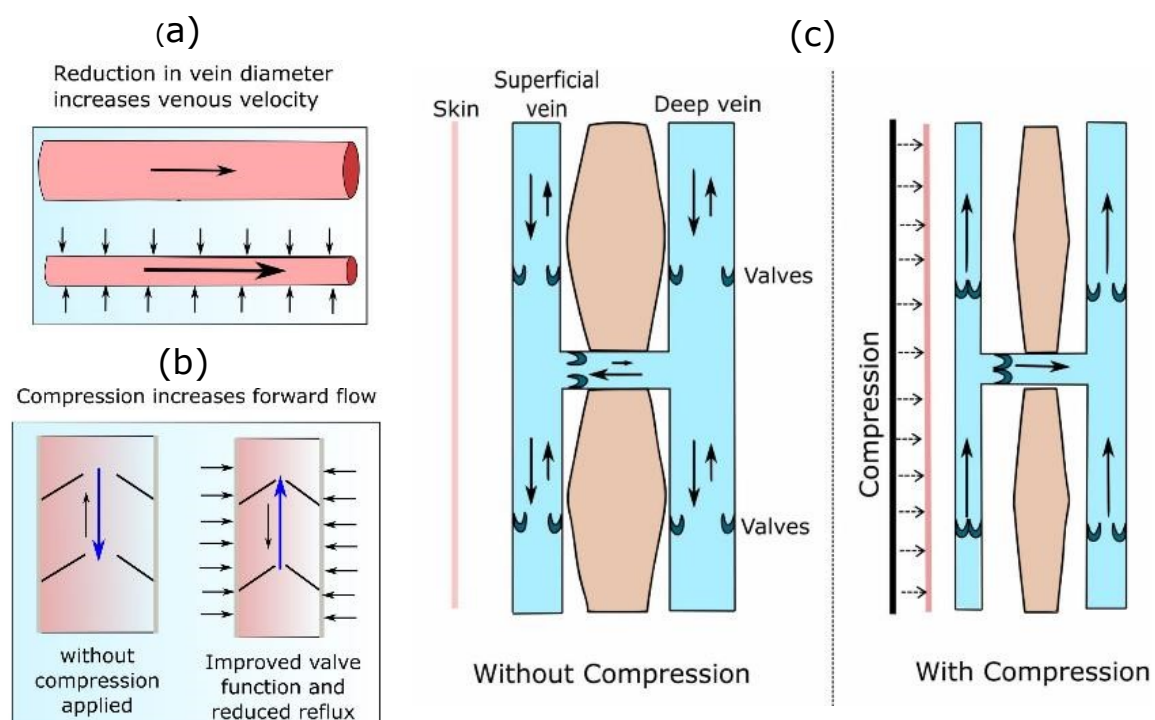


Fig. 2.11 How compression works: a) accelerating the venous flow b) & c) reduction in venous reflux

Because of the reduction in vein diameters, better coaptation of valve cusps leads to reduction in venous reflux (Figure 2.11b). It also contributes towards reducing venous hypertension. The reduction of diameter of veins redistributes the blood from superficial veins to deep veins, which improves muscle pumping and the flow in the deep veins (Born et al., 2014). As the volume of venous blood reduces in the lower extremities it leads to increased volume in the central part of the body and increase

in the preload of the heart (Calne and Moffatt, 2003). With the arterial flow remain unchanged, this will lead to increase in the velocity of the blood flow (Calne and Moffatt, 2003).

Duplex ultrasound, and phlebography has been used to demonstrate the reduction of the diameter of major veins, when the external compression is applied (Lord and Hamilton, 2004; Partsch and Partsch, 2005; Partsch et al., 2000). The clinical importance of the effects described above, rely on the relationship between intravenous-hydrostatic pressure and the compression applied externally. In the supine position around 10 – 15mmHg pressure is sufficient enough to reduce venous stasis, decreasing the vein diameter and increase the blood flow velocity (Partsch and Partsch, 2005; Partsch, 2003). According to Lord and Hamilton (Lord and Hamilton, 2004), the medical compression stockings which are designed to apply 20 – 30mmHg pressure to the limb are able to reduce the diameter of GSV and deep veins in the supine position (Al Khaburi, 2010). However, the same pressure is not significant on the superficial and deep veins in the upright position. In the upright position the pressure in the leg fluctuates during walking between 20 – 100mmHg (Partsch, 2003), which will require around 40 – 50mmHg to exerted in order to mark an effect upon the blood flow. In their study Partsch and Partsch (Partsch and Partsch, 2005) showed that around median of 20mmHg pressure is required in the supine position and 50 – 70mmHg interface pressure is adequate enough to block the leg veins at mid-calf region in the upright position.

Instead of using ultra sound imaging for the studying the effects of compression on vein wall diameter, cross section area and alignment of veins, the magnetic resonance imaging (MRI) technique has proven its effectiveness in the context. According to the study carried out by Downie and others (Downie et al., 2007) using MRI has shown that with the exception of the great saphenous vein, superficial veins were circular in cross section and retained the same shape under compression, while the deep veins cross section was varied between circular and elliptical but remained elliptical after compression. It was also found, that there exists a longitudinal movement in the GSV with compression, which would never have been found if ultra sound imaging was used. The study also concluded that around 64% reduction in deep vein diameters existed, along with 39% reduction in the diameter of superficial veins, when 18 – 21mmHg pressure was applied at the ankle.

- Increasing tissue pressure and improving lymphatic function:

As described in the section 2.1.4, according to Starling's equation, the applied external compression it reduces the filtration caused due to ambulatory hypertension and increase the re-absorption. This reduces the lymphatic fluid in the tissue, and increase the lymphatic transport (Partsch, 2003, 2007). A study has shown that higher compressions can result in 6.7% reduction in the volume of leg with patients suffering from lymphoedema (Damstra et al., 2008). It is found that the sustained compression is more effective, therefore continuation of compression therapy is often advised for people with oedema.

- Microcirculation:

Compression will accelerate the blood flow in microcirculation, this favours the white cell detachment from the endothelium and also prevents further adhesion (Abu-Own et al., 1994; Al Khaburi, 2010).

As described in the section 2.1.4 under white cell trapping theory, this detachment and prevention of further adhesion of white cells promotes the ulcer healing and prevention of formation of venous ulcers.

2.2.3 The optimum interface pressure profile for compression therapy

In the context of the compression therapy the interface pressure is referred to as the pressure exerted by the compression device on the skin surface (Partsch, 2007). The clinicians use millimetres of mercury (mmHg) is used as the unit in measuring the interface rather than using SI units of (N/m^2), where $1\text{mmHg} = 133.33\text{N}/m^2$ (Partsch, 2007).

To have an effective compression therapy, medical experts believe that it should provide an intermittent occlusion of incompetent veins, which will result in an artificial valve that segments the venous reflux (Partsch and Partsch, 2005). The applied external pressure should be large enough, as some of the pressure will be dissipated in the skin and fat. In the medical literature the optimum pressure profile that is most commonly described is a pressure of 40 – 45mmHg at the ankle, reducing gradually to 15 – 20mmHg at the knee (Al Khaburi, 2010; Coull et al., 2006; Nelson, 2001; Stemmer et al., 1980). The main argument of the need for graduated pressure comes from the physical nature of the fluid flow, where in order to push blood from ankle to the knee, there is a need to apply a gradient of pressure which is higher at ankle and graduated towards the knee (Al Khaburi, 2010; Armstrong et al., 2006).

Graduated compression

As described in the section 2.1.4, pressure in the veins of the legs is determined by two components: a "hydrostatic component" which is caused due to the weight of the blood column and a "hydrodynamic component" related to pressures generated mainly due to the contractions of the skeletal muscles. As the pressure inside the veins of a standing subject is mainly hydrostatic, the levels of external pressure require to neutralize this hydrostatic pressure should be progressively reduced up the limb. Therefore, in the case of applying external compression the highest pressure should be applied at the ankle and gradually reduced up on the limb; thus, termed graduated compression therapy.

2.2.4 Medical Compression Bandages (MCBs)

The history of using compression bandages flows back to the era of the ancient Egyptians, who used simple woven fabrics with coated adhesives and resins as dressings to help wound healing (Thomas, 1997). It is also known that the Greeks and Romans used bandaging to treat leg ulcers and to empty the stagnant blood in the superficial veins. In the 17th century, Pierre Dionis described the use of elastic laces and flannel bandages (Mariani, 2009). The existing methods at this point of time (17th century) was not suitable for applying sustained and controlled compression, due to their inelastic nature. The elastic compression bandages appeared very late but long before the elastic stockings, where in the

19th century first elastic bandages were produced using natural rubber in Germany (Mariani, 2009; Thomas, 1997).

In the UK, standards for bandages first emerged as a supplement to the 1911 "British Pharmaceutical Codex", which included a specification for an extensible crepe bandage with cotton and wool yarns (Thomas, 1997). The ideal bandaging system is expected to decrease the oedema at the same time offer higher working pressures but comparatively low resting pressures (Kunimoto, 1999). For patients with venous disease the application of external graduated pressure will help to minimize the previously described impairment and forcing the fluid from the interstitial spaces back to the vascular and lymphatic section.

Classification of MCBs

There are few classifications available for compression bandages, however no consistent international classification is available (Armstrong et al., 2006; Clark, 2003). Some of the available classifications are based on the type of the bandage (elastic or non-elastic), the interface pressure applied by the bandage, number of components available, and stiffness. The UK classification of the bandages for the Drug Tariff is described in the Table 2.2 below, (Al Khaburi, 2010; Moffatt, 2007; Partsch et al., 2008; Thomas, 1997) and few of the other classifications are described later.

Table 2.2 The UK classification of bandage for the Drug Tariffs (Al Khaburi, 2010; Moffatt, 2007; Partsch et al., 2008; Thomas, 1997)

Type 1	Light weight and elastic bandages. Have a long and shallow stress vs. strain curve, having higher degree of elasticity and less power. These apply little or no pressure, and generally used to hold dressings in place	
Type 2	Light support inelastic bandages. Used to prevent oedema and provide support in management of mild sprains. These apply low pressures; however, some may apply moderate pressures	
Type 3: compression bandages	Type 3a	Light compression bandages. Provide lower levels of pressure around 12-17mmHg, and used to manage superficial or early varicose formed during pregnancy
	Type 3b	Moderate compression bandages. These can provide 18-24mmHg pressure and used in treatment for varicose veins during pregnancy and medium severity varices
	Type 3c	High compression bandages. These are capable of providing g 25-35mmHg pressures and are used to treat post thrombotic venous insufficiency and management of venous ulcers
	Type 3d	Extra high compression bandages, capable of applying pressures exceeding 50mmHg. High power of these is capable of applying higher pressures forextended periods, even with most oedematous limbs.

Classification according to interface pressure: The classification of bandages according to the level of pressure can provide an easy interpretation for the clinicians. In general, the interface pressure can be referred to as the pressure applied by the materials in contact, in this context it is the pressure between the bandage and skin surface. The pressures should be measured when the wearer is at supine position, at the medial region of the lower leg. It should be noted that definition of the interface pressure, limiting to one particular point in classification is not based on clinical studies (Al Khaburi, 2010; Partsch et al., 2008). British standard (BS 7505:1995) (British Standards Institution, 1995), and RAL-GZ 387, (Germany)(Deutsches Institut für Gütesicherung und Kennzeichnung e.V., 2008) has used to describe the classification given in Table 2.3

Classification according to elasticity: elasticity of a bandage is the ability of it to return to its original length when the tension is removed. As per that definition bandages can be divided into two categories, in elastic bandages made without elastomers (normally cotton) and elastic bandages which are made out of elastomers such as Lycra (Moffatt, 2007).

Table 2.3 Comparison of British and German bandage pressures

Group RAL-GZ	Type BS 7505	Level of compression	Pressure according to British standard (mmHg)	Pressure according to German standard (mmHg)
1	3a	Light	<20	18.4-21.2
2	3b	Moderate	21-31	25.1-32.1
3	3c	High	31-40	36.4-46.5
4	3d	Extra high	41-60	>59

Classification on components: This depends on whether the bandage is applied alone, or with few layers. Single layer; consists of one type of bandage and multi-layer; consists of number of bandages applied on top of each other (normally three to four) (Partsch et al., 2008), under which most common one is the four layer bandaging system. Four-layer bandaging has been in existence for more than 15 years, where it is considered to be a highly recommended compression bandaging system that incorporates stretch fabric layers to achieve a sustained level of compression over a time period (Moffatt, 2005). The four-layered bandaging system has reported quick heal rates for chronic venous ulcers in comparison to the traditional adhesive plaster bandaging (Buchbinder et al., 1993). The short stretch which exists in four-layer bandaging has made it an effective treatment option to the venous lymphatic disorders (Moffatt, 2005).

Classification according to stiffness: Researchers have shown two methods to evaluate stiffness, which is defined as the increase of compression pressure per centimetre increase in the circumference of the leg (Partsch, 2003). The two methods are Static Stiffness Index (SSI), which is the difference in the pressures under supine and standing conditions, and Dynamic Stiffness Index (DSI) which is the

increase in the pressure when the leg circumference variation equals to 1cm at 1Hz frequency. Elastic bandages are defined to have SSI more than 10mmHg (Mosti and Mattaliano, 2007). Bandages with high stiffness (inelastic) will have low resting pressures (pressure continuously exerted, 40mmHg) and high working pressure (pressure exerted by muscle against the resistance of the bandage, 60 – 70mmHg)(Al Khaburi, 2010; Moffatt, 2007). But low stiffness (elastic) bandages have both high resting and working pressures (40mmHg resting pressure and 40 – 50mmHg working pressure) (Al Khaburi, 2010), which suggests that elastic bandages may be more comfortable in comparison (Moffatt, 2007).

Factors affecting interface pressure applied by MCBs

There are few factors that affect the interface pressure applied by MCBs, out of which few are discussed in detail below.

a. Tension of the fabric

Many researchers have attempted to theoretically predict the interface pressure, while some used trigonometry to relate the interface pressure to tension in the bandage and limb radius of curvature (Thomas, 2003) used the Laplace equation in predicting the interface pressure (Basford, 2002; De Bruyne and Dvořák, 1976). Both methods arrived at the same formula to describe the interface pressure (equation 2.2).

$$P_{int} = \frac{T}{R} \quad (2.2)$$

where, P_{int} is the interface pressure in (N/m^2), T is the tension in bandage (N) for 1m width of fabric and R is the radius of curvature (m). Many research have used the equation 2.2 in calculating the interface pressure or analysing the variations in the interface pressure (Basford, 2002; Gaied et al., 2006; Moffatt, 2008; Schomburg, 2015; Thomas, 2003; Thomas and Fram, 1990, 2003; Wertheim et al., 1999). However, Thomas (2003) extended this model to estimate the interface pressure applied by a multi-layer bandage system given in the equation 2.3 below.

$$P_{int} = \frac{nT}{Rw} \quad (2.3)$$

where, n is the number of bandage layers and w is the bandage width (m). He extended equation 2.3 to make it more appealing to the medical community, denoted in equation 2.4.

$$Pressure (mmHg) = \frac{Tension (kgf) \times Number of layers}{Circumference (cm) \times Bandage width (cm)} \times 4620 \quad (2.4)$$

As shown in equation 2.3, according to Laplace's law the pressure applied by the bandage is proportional to the tension. The tension in the bandage is proportional to the elongation of the fabric, which is illustrated in Figure 2.12 and the relationship isn't linear. In clinical stage, nurses apply the MCBs

controlling the level of stretch (elongation) to achieve the required pressure profiles. This required highly skilled clinical nurses with experience to apply MCBs to correct pressures with consistency. At present some bandages include geometric shapes printed on them which change from one shape to the other (rectangular to square, or oval to circle) at the correct elongation levels, which significantly reduces the variability exists in application by each individual (Thomas and Fram, 2003).

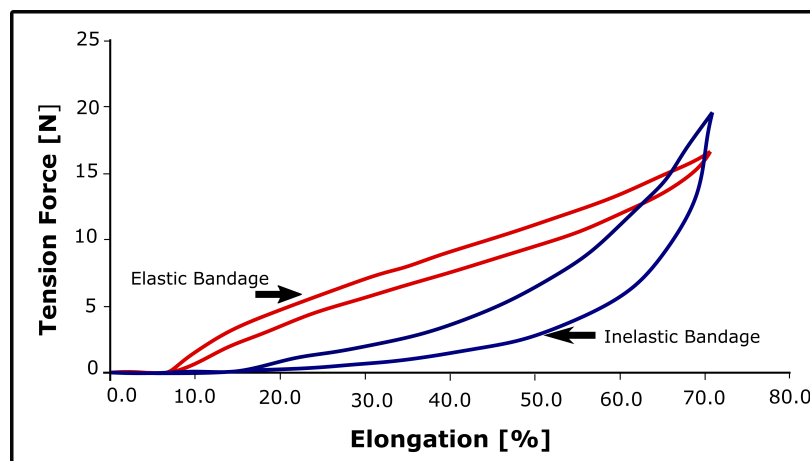


Fig. 2.12 Tension elongation curves for elastic and inelastic bandages (Al Khaburi, 2010)

b. Skill of the operator:

As described above the possibility in which getting the required correct pressure profile is very much dependent on the skill level of the operator. Literature has shown that only 9.5% of 63 nurses who had 10 or less years of experience were able to apply compression bandages with target pressure of 35 – 45mmHg (Al Khaburi, 2010; Ghosh et al., 2008). However, it is reported in several literature that this could be improved significantly by training (Ghosh et al., 2008; Lim and Davies, 2014; Nelson, 2001).

c. Leg dimensions:

According to Laplace's law the pressure applied is inversely proportional to the radius of curvature of the leg (equation 2.3). As the leg circumference increases from ankle to knee, there will be a natural gradient of pressure which will be applied if the bandages were applied with uniform tension (stretch). The leg itself does not have a uniform cross section, which will make the applied pressure to be changed at different position of the leg circumference. Further it implies that there will be higher pressures at bony structures (concave) while lower at convex areas (Moffatt, 2008), and also there are some areas which are considered to be more or less flat on the leg surface which may be experiencing very high pressures. Therefore, a requirement for a wadding layer exists, which could be applied on the concave and flat areas of the leg to fill it and make the limb circumference circular and uniform. But these wadding layers can be uncomfortable and would also result in higher pressures, causing discomfort for the patients.

d. Number of layers:

According to equations 2.3 and 2.4, increasing the number of layers increases the interfacial pressure.

e. Application techniques:

Different application techniques such as spiral technique, and figure of eight technique could be used to apply the bandages at different angles to the leg; hence, will produce different levels of pressure (Al Khaburi, 2010; Moffatt, 2008; Nelson, 2001). When the angle between the bandage and leg decreases the pressure will also decrease (Al Khaburi, 2010; Moffatt, 2008).

2.2.5 Graduated Compression Stockings

The first medical elastic compression stocking was manufactured with rubber threads in 1848 in England by William Brown (Liu et al., 2017). These are made according to the standards (British Standard: BS 6612:1985, European Standard, DIN EN12719:1997) which guarantees a defined and graduated pressure along the limb. The compression stockings work by the principle of exerting a higher pressure at the ankle, and gradually decreased pressure up towards the knee. Therefore, these are commonly referred to as Graduated Compression Stockings (GCS) or medical compression stockings, and commonly comes in knee high, mid high and pantyhose with open and closed toe designs.

Classification of GCSs

GCSs are commonly classified according to the interface pressure applied by the garment at the ankle level (Lim and Davies, 2014). Due to the possibility of delivering a wide range of pressures, currently GCSs are produced to deliver three different classes of graduated pressures. The degree of pressure applied is classified into several standards however, there isn't any single standard used worldwide as it was for MCBs. The current British Standard, BS 6612:1985 and the European standard DIN EN 12719 (RAL-GZG standard) for medical compression stockings are summarised in the Table 2.4.

In contrast to the compression bandaging which has high working pressures, compression stockings exert a resting pressure. Unlike the compression bandages, the daily build-up of the pressure is controlled by the limited ability of the stretch in the stocking. This limited ability of the stretch controls the build-up of pressure resulting in a resting pressure (Kouka et al., 2004). Compression stockings have to be worn on a daily basis in order to prevent recurrence of venous ulcers (Stemmer et al., 1980). Studies have shown that even after removal of the stockings disease will not completely disappear (Stemmer et al., 1980), therefore graduated compression stockings are useful in prevention and maintaining the results obtained.

All the GCS classifications are based on the pressure exerted at the ankle B level (Fig 2.13, Table 2.5). Also pressure gradient distributions differ with different compression classes. Hence, there should be a better understanding on how the pressures are defined at different positions of the leg.

RAL-GZ 387/1 standard for medical compression stockings (Deutsches Institut für Gütesicherung und Kennzeichnung e.V., 2008; Liu et al., 2017), provides an detail understanding of where the pressure gradient levels are applied and the residual pressure ratios in percentages of pressures exerted at the ankle (Table 2.5)

Table 2.4 Comparison of British standard and European standard (British Standards Institution, 1985; Deutsches Institut für Gütesicherung und Kennzeichnung e.V., 2008; Iwama et al., 2000; Mosti et al., 2012; Partsch et al., 2012)

Class DIN EN12719 RAL387/1Class	Class BS6612	Level of compression	Pressure according to British standard (mmHg)	Pressure according to European/German standard (mmHg)
I	I	Light	14-17	15-21 (EU) 18-21 (German)
II	II	Medium	18-24	23-32
III	III	Strong	25-35	34-46
IV	IV	Very strong	N/A	>49

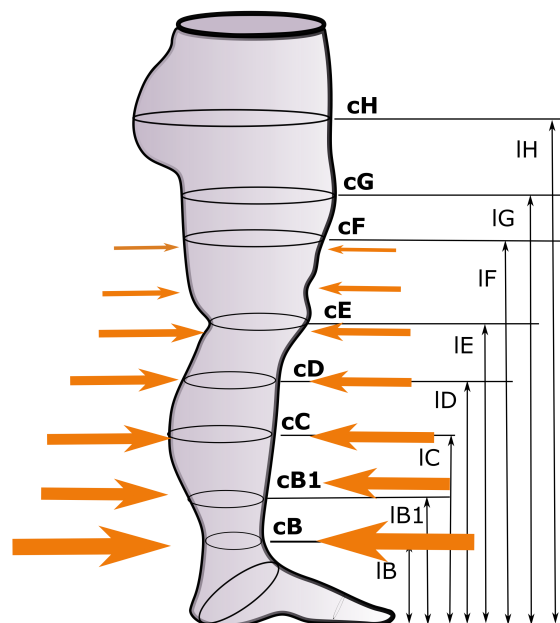


Fig. 2.13 Different measurement positions of the leg in defining the pressure distribution ratios (Liu et al., 2017)

Characteristics of medical compression stockings: Few of the characteristics of medical compression stockings according to Mariani (2009) and Qin (2015) are;

Table 2.5 Pressure gradient distribution by different compression classes (Deutsches Institut für Gütesicherung und Kennzeichnung e.V., 2008; Liu et al., 2017)

Gradient level	Residual pressure ratio as a % of the pressure inserted at ankle			
	Class I	Class II	Class III	Class IV
At F or G	20-60%	20-50%	20-40%	20-40%
At C	50-80%	50-80%	50-70%	50-70%
At B1	70-100%	70-100%	70-100%	70-100%
At B	100%	100%	100%	100%

- manufactured using circular or flat knitting, but most generally by circular knitting
- extensibility of the knit in both directions to facilitate joint movement
- aerated fabric to allow evaporation
- perfect adaptability to the shape of the limb
- knitted heel to allow an anatomical position of the ankle

Measurements for compression stockings

The measurements of limb circumferences should be taken accurately, otherwise elastic support of wrong size will exert completely different pressure profiles from the desired and sometimes it might not even be graduated. Incorrect measurements can sometimes lead to discomfort, trauma and even ulceration (Fernando, 2010).

Three measurements are normally taken during the selection of the stocking with the patient's feet flat on the floor and also both legs are measured where the dimensions might change slightly for the two legs (Fernando, 2010). Three basic measurements are (Johnson, 2002; Ruckley, 1992):

- Circumference of the ankle at the narrowest point above the ankle bone
- Length between the base of the heel to just below the knee
- Circumference of the calf at its widest point

According to the above measurements the correct size of stocking is selected, if the measurement falls outside the available range, a made to measure stocking is required (Fernando, 2010). The correct selection of the stocking is critical as the high pressures could restrict the blood flow to the leg and may cause more damage.

Scan to Knit: When a compression stocking is worn the normal forces at each point will define the pressure, as it will depend on the elongation and the radius of curvature of the leg surface at each point. Since the radius of curvature on individual leg is unique, it is difficult to define the exact

pressure profile without measuring the stocking on patient's leg. This brings out to the patented technology of "Scan to Knit" (Tilak et al., 2006; Van Langenhove, 2007), which defines shape (by way of generating a plurality of discrete points –a point cloud, which define the part of the body) and pressure characteristics of garment, by specifying the knitting pattern, calculating the yarn feed data for knitting pattern to produce the defined shape, and manufacturing the garment according to the fed data.

Problems associated with compression stockings

Generally graduated compression stockings are safe to use with relatively few complications and problems associated with them (Lim and Davies, 2014).

a. Leg dimensions resulting in nonuniform pressure

As described under section 2.2.4, the pressure generated by the compression stockings also depend on the tension of the fabric, which is caused due to its stretch. Therefore, according to Laplace's law (equation 2.3), the pressure generated by the compression stockings also depend on the radius of curvature of the limb (R). Because of the contours of different positions (Figure 2.14) of the leg pressure variations can exist, which makes the system unable to apply a uniform pressure.

b. Poor fitting stockings

As described earlier the leg measurements are quite important in manufacturing GCSs, as the poorly fitting stockings can cause discomfort at worst can cause pressure necrosis (Lim and Davies, 2014). Even using GCSs on patients with impaired arterial flow can worsen ischemia (Callam, Ruckley, Dale and Harper, 1987). Sometimes these can extremely deform the leg, or make unusual leg shape.

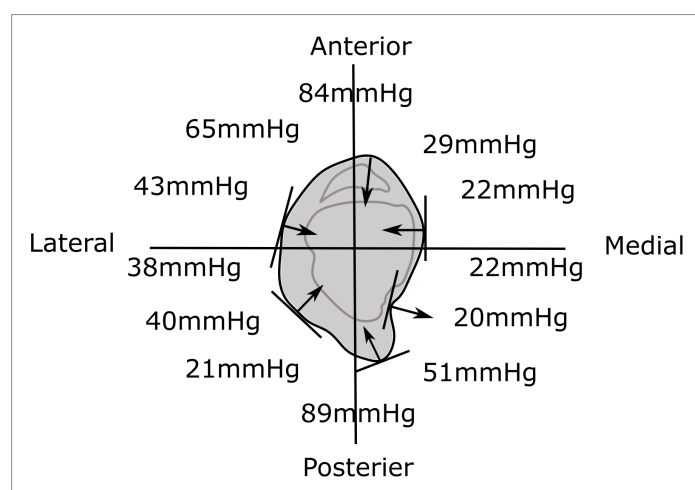


Fig. 2.14 Effect of contours on skin pressure variations (Liu et al., 2017)

c. Non-compliance

The non-compliance rate for GCSs, is reported to be 30 – 65% (Raju et al., 2007; Shingler et al., 2013), and the commonly cited reasons include pain, discomfort, perceived ineffectiveness, excessive heat, skin irritation and appearance (Palfreyman and Michaels, 2009; Raju et al., 2007; Ziaja et al., 2011).

d. Difficulty in donning and doffing

The elastic stockings have inherent difficulty in pulling them up through the ankle which requires quite lot of strength. There are devices developed to assist in putting the stocking. However, considering most of those who wear these stockings are in the aged category this inherent disadvantage of the system would call it to be replaced by an easily wearable stocking.

e. Allergy to stocking material

These conditions can make the patients to develop contact dermatitis, skin discolouration, and blistering (Lim and Davies, 2014). Many of the above complications excluding the non-uniform pressure distribution could be easily overcome by refitting the stockings, changing the material, applying an emollient and reducing the level of compression (Lim and Davies, 2014).

2.2.6 Pneumatic Compression

Pneumatic compression devices are based on an intermittent inflation of air bags which can be used for the management of oedema (Falanga and Eaglstein, 1986; Kirsner and Eaglstein, 1993) and to promote wound healing (Kolari et al., 1988; Mulder et al., 1990). These were mainly developed to prevent the of deep venous thrombosis, especially for bedridden elderly or inactive patients or for the patients with severe lymphoedema (Parsch, 1991; Richmand et al., 1985; Zelikovski et al., 1983). Intermittent pneumatic compression (IPC) is considered as an active compression treatment system, which mimics the action of the calf muscle pump (Comerota, 2011). Various forms of intermittent compression techniques have a 70-year history of published clinical effectiveness (Morris, 2008). In spite of being low tech these are effective due to the capability of mimicking the intermittent compression of the lower limb during muscle contraction (Morris, 2008). This has a history of being used effectively in the treatment for lymphoedema as the compression empties the lymphatics and drain the fluid from the interstitium (Delis et al., 2000; McGeown et al., 1988).

Classification of intermittent pneumatic compression devices

Intermittent pneumatic compression systems differ in terms of the number of constituting segments of the device and also due to the inflation sequences.

a. Single bladder cuffs

These systems use large single bladder cuffs applying compression to the whole limb (Figure 2.15) (Morris, 2008). However, these are unable to produce a pressure gradient, as the single cuff expands and contracts applying pressure against the whole limb. This requires a considerable input of air, to get in contact with the limb prior to the device starts to apply compression (Chang and Cormier, 2013; Morris, 2008).

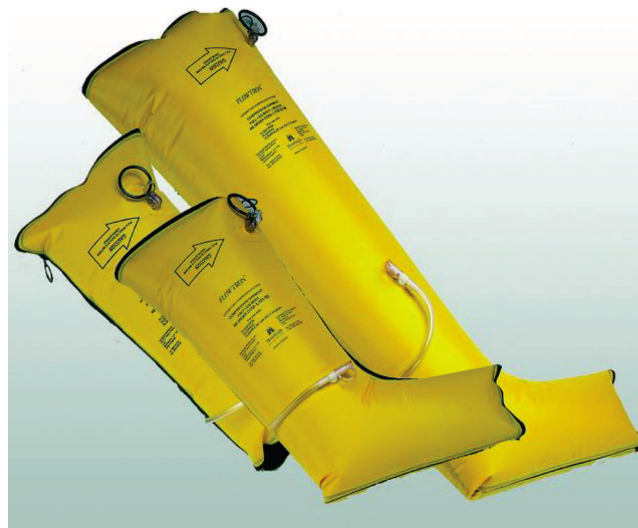


Fig. 2.15 Uniform, circumferential, calf, thigh length intermittent pneumatic compression cuffs (Morris, 2008)

b. Multi-chamber cuffs

These type of devices commonly have three to four chambers, but sometimes may have twelve or 36 chambers (Figure 2.16) (Feldman et al., 2012), which inflate sequentially from distal to proximal of the leg and then deflate all together. This type of IPCs can either be:

- I. Sequential: A single pressure is applied to parts of the limb in a sequence (normally from distal to proximal) (Morris, 2008). Typically, pressure is not independently adjustable and pressure gradient is achieved by the naturally existing limb contours. One distinctive feature is that all the distal chambers remain inflated, when the next proximal bladder inflates (Morris, 2008), resulting whole limb is compressed once the last chamber is inflated.

- II. Graded sequential: Each bladder is inflated to different pressures in order to achieve a gradient of pressure. This pressure gradient is achieved by applying higher pressure at the distal position and lower pressures at the proximal chambers (Figure 2.16). These may include at least three zones, but some may extend up to 36 (Feldman et al., 2012). These are manually programmable and facilitate the adjustment of the compression level and the location (Chang and Cormier, 2013; Feldman et al., 2012).

Also there exist advanced compression systems with digital programming, simulating the action of manual lymphatic drainage, only using 2-5 chambers which are active at different times as the compression progresses in distal to proximal direction (Chang and Cormier, 2013; Feldman et al., 2012)



Fig. 2.16 A twelve chamber graded-sequential, whole leg IPC device for oedema (Morris, 2008)

- III. Peristaltic sequence: In here the distal chamber deflates while others are inflating, so that each chamber will provide compression for the same period (Morris, 2008). During the pre-inflation cycle, the chambers would inflate to a level which makes it to exact body shape, then each segment will compress in a pulsating manner and then will release the pressure (Sands et al., 2015). This technique has been effectively used in treating the recovery of high performance athletes developed by the NormaTec, which is referred to as NormaTec PULSE recovery system (Figure 2.17a) with their patented PULSE technology. In this system pulsing happens instead of a static compression effectively mimicking the muscle pump as shown in Figure 2.17b (Sands, 2014; Sands et al., 2015).

The range of pressures mostly recommended is 35 – 180 mmHg, even though some pumps could provide pressures as high as 300 mmHg (Morris, 2008). However, it is advisable not to exceed pressures of 40 – 60 mmHg (Mariani, 2009). The above pressure range is advised to be used, for the treatment of oedema and then in later maintenance phase to use an elastic stocking with suitable

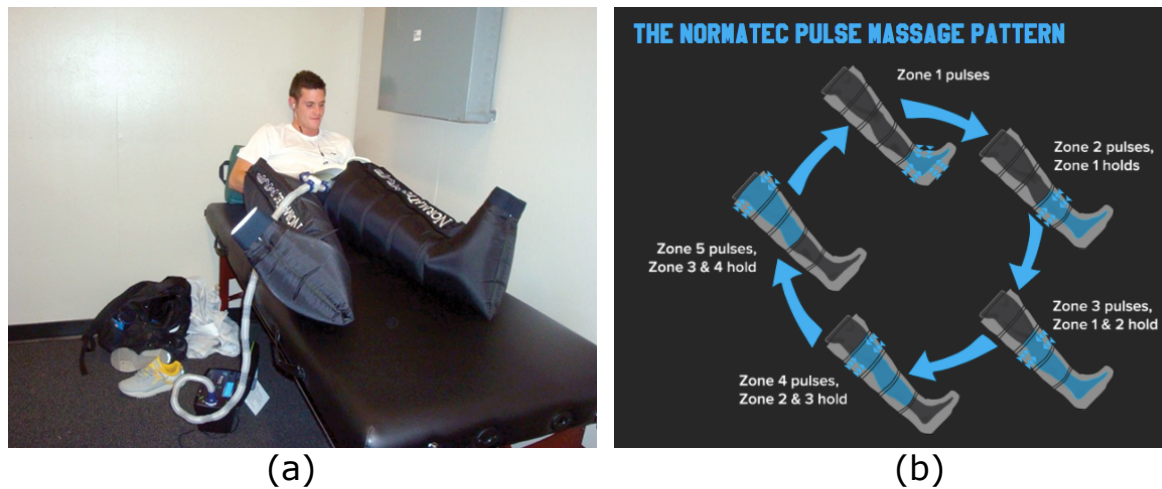


Fig. 2.17 (a) Using NormaTec PULSE for recovery (b) the functioning process (Sands, 2014)

compression level. Kendall SCDTM has introduced a sequential device with three chambers and six compartment which provides 45mmHg at the ankle, 40mmHg at the calf and 30mmHg at thigh level (Mariani, 2009). The construction of a sequential intermittent compression system is more complex, in an engineering perspective (Morris, 2008). There is no certainty that the same pressure and timing would serve every patient though that is currently what most systems offer. Pneumatic compression systems could also be used in treating for leg ulcers, where the same type of multi-chamber sequential compression is used. The literature demonstrates clinical success of trialling pneumatic compression for treating ulcers (Berliner et al., 2003; Kumar et al., 2002; Mani et al., 2001; Pekanmäki et al., 1987).

However, one could not find evidence of the clinical use of this technique for treating venous disease effectively, as a stand-alone treatment system. Also there is neither a clear single best practice guideline for IPC, nor universal consensus notes with the applied pressure ranges (Feldman et al., 2012). Also, variable pressures could be achieved using IPC, which is a further development towards active compression. However, the sizeable pneumatic cuffs make the IPC bulky and less wearable. Therefore, the future efforts must be combined with design and engineering along with the clinical research to determine the most appropriate designs for the application, considering the cost factor as well.

2.2.7 Other active compression techniques

As described under section 2.2.4 and 2.2.5, MCBs and GCSs are considered to be passive since they provide a static compression. But many studies have shown the importance of the variable compression (time-dependent) and that it is more efficient in comparison to static compression. Therefore, several attempts have been made in the recent past in developing active compression systems to overcome the identified drawbacks of the existing treatments.

Pourazadi (Pourazadi et al., 2014) have suggested a novel approach towards an active compression bandage using Electro-Active Polymers (EAPs), which are actuated with the application of external electric stimuli (Figure 2.18). He further claims that the bandage could be tuned to apply a gradient or constant pressure along the length of the leg. The working principle is as such once the bandage is activated by applying an electrical voltage the bandage reduces its thickness, resulting a reduction of the circumferential compression around the calf (Pourazadi et al., 2014).



Fig. 2.18 A schematic of the EAP placed on a human calf (Pourazadi et al., 2014)

There is also few research carried out using shape memory alloys in developing active compression products. Few US patents have described their attempts in achieving this objective (Holschuh et al., 2015; Pamplin and Dennis, 2015). The US patent 2015/0073318 (Holschuh et al., 2015), awarded to Massachusetts Institute of Technology, Cambridge, MA, USA claims that it is the first to represent the technology that incorporate integrated shape changing materials to create compression textile garments having controllable pressure (Holschuh et al., 2015). They have claimed a compression garment comprising at least one passive flexible member, one active actuator including shape memory alloy (SMA) being able to apply or remove compression upon the presence or absence of an applied stimulus. They also describe few possible configurations for the SMA to be used in.

The other patent describes a similar context, where it includes forming a segmented flex frame and installing a SMA on struts of the frame, then connecting the SMA to an electrical connection (Pamplin and Dennis, 2015). The electric current will then be applied on continuous or intermittent phase, generating heat which will cause SMA to reach a target transition temperature either to lengthen or

shorten in size. The shortening will exert the compression on to the limb and the pressure will be released once it is lengthened. Although the above methods could overcome some of the drawbacks of passive compression, still these active systems apply compression depending on a force which is generated due to the tangential force (tension), and radius of curvature of the limb. Therefore, they have not taken into consideration the factor of non-uniformity and irregularity exist in the limb circumference in their designs.

2.2.8 Risks involved with compression therapy

There are several risks associated with compression therapy which are,

- a. Reduction of the arterial flow: failure to recognise arterial disease will make unsafe application of higher compressions, as the compression therapy reduces arterial flow.
- b. Increase the pre-load of the heart: compression therapy results in shifting the blood into the central compartment of the body (estimated to preload heart by 5%) (Al Khaburi, 2010; Partsch, 2007), which can be dangerous for people with cardiac failures.
- c. Damage in skin tissue and formation of ulcers: according to Kosaik (Kosiak, 1959) high pressures for short period of time can result in skin damages. However, there are number of studies suggesting that incorrect (high) compression could lead to severe skin necrosis and even amputation (Callam, Ruckley, Dale and Harper, 1987; Moffatt, 2007; Nelson, 2001)

2.3 Interface pressure measurement

The accurate interface pressure measurement has been considered as one of the challenges faced in the field of medical and biomedical engineering fields. Its importance also extends to the fields like sports science, diabetes, prosthetics, and human joint studies (Buis and Convery, 1997; Polliack et al., 2000; Rikli et al., 2007; Wilson et al., 2003; Woodburn and Helliwell, 1996). The measurement of the interface pressure applied by the compression devices are required for range of reasons including,

- a. study the efficiency of the compression product in treatment for CVD
- b. to study the working principles of compression therapy
- c. to evaluate the applied pressures of MCBs, to improve training of nurses with the feedback on their bandaging techniques
- d. to design better compression treatment systems
- e. to study the effect of different postures of patients on the applied pressures
- f. to study the influence of different materials on the applied pressures

There are several systems available for the interface pressure measurement of the compression products. They differ in working principle, sensitivities to temperature, hysteresis, dimensions, accuracy levels, ability in dynamic measurements and other factors. As defined in an international consensus meeting in Vienna, 2005 (Burke et al., 2014; Partsch et al., 2006) an ideal pressure measurement system should be,

- a. easy to calibrate before each measurement
- b. insensitive to changes in temperature and humidity
- c. providing a linear response to the applied pressure
- d. long lasting, reliable and accurate
- e. having a low hysteresis
- f. thin, flexible and small in size
- g. having simple electronics

This definition should be used as an evaluation criterion and a guideline in analysing the existing pressure measurement systems and developing future pressure measurement systems. However, this definition gives a vague understanding on the accuracy, reliability, hysteresis and the size of the sensors as it has not defined a numerical figure for those.

2.3.1 Methods of interface pressure measurement

There are many pressure measurement systems which are commercially available to measure the interface pressure which could be categorised into,

- a. Pneumatic based interface pressure measurement systems
- b. Flexible piezo resistive sensors
- c. Fluid based interface pressure measurement systems
- d. Electrical pressure devices

These would be reviewed in detail in the following section.

2.3.2 Pneumatic based interface pressure measurement systems

These systems use air as a medium to transfer the forces applied via compression, to an air pressure which will be converted to an electrical signal using transducers (Al Khaburi, 2010). These sensors use bladders or compartments which are filled with a small amount of air (Flaud et al., 2010) and connected to the transducer and kept sealed as a closed system. As the bladder is compressed due to the compressive forces applied via compression material, the volume of air will be decreased and then the connected transducer will detect the pressure accordance with the volume change. These are considered to be the most popular type of pressure measurement associated with compression therapy (Burke et al., 2014). There are few type of commercially used sensors available such as, PicoPress[®] AMI air-pack type analyzer (AMI Techno), Kikuhime, and Oxford Pressure Monitor. These sensors have advantageous features such as thin sensors (probes), cheaper, having good repeatability. However, they have the difficulties regarding dynamic pressure measurement (simultaneous measurement).

a. PicoPress[®]

This is a portable pneumatic pressure measuring system manufactured by Microlab Electronica, Ponte S. Nico PD, Italy. It has a sensor of a 50mm diameter and 3mm thickness once inflated and 0.2mm when not inflated (Figure 2.19 a, b). The device could be used to measure a range of 0 – 200mmHg pressures. There is a possibility of storing the recorded data in the device and/or can be transferred to a computer, which will enable the dynamic pressure measurement (Mosti and Rossari, 2008).

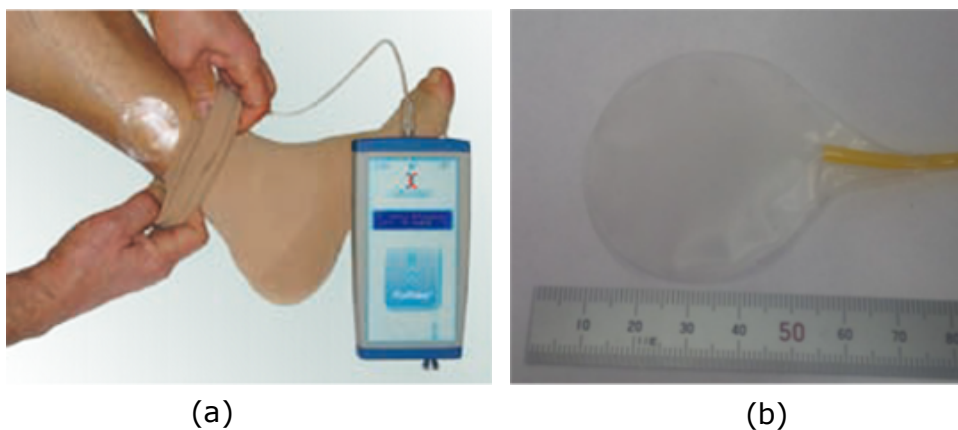


Fig. 2.19 a) PicoPress[®] measuring unit (Microlab-Electronica, 2014) b) sensor/bladder dimensions

It has found that this system has very good linearity and repeatability (Mosti and Rossari, 2008), it was found to have repeatable results within ± 3 mmHg (Parsch et al., 2006). However, these sensors are considered to be sensitive to the curvature, which could lead to overestimated pressures (Burke et al., 2014).

b. Air-Pack Type Analyzer model A0905-SA-35k (AMI Techno)

This is an interface pressure measurement system developed by AMI Techno, Japan with a 20mm diameter (standard) thin sensor/bladder (1mm thickness) (AMI-Techno, 2009b). There are other size probes available such as 15mm, 25mm and 30mm. However, it is considered that reproducibility is good in 20mm (standard) probe, where it is considered only the centre part of the bag contacts with the measuring point when sensor is too large (e.g. 30mm diameter). It has a measurement range of 0 – 150 mmHg (0 – 20 kPa) with the standard probe. However, there is less evidence of the use of this measurement system in dynamic measurement. As shown in Figure 2.20 this measurement system consists of (Figure 2.20):

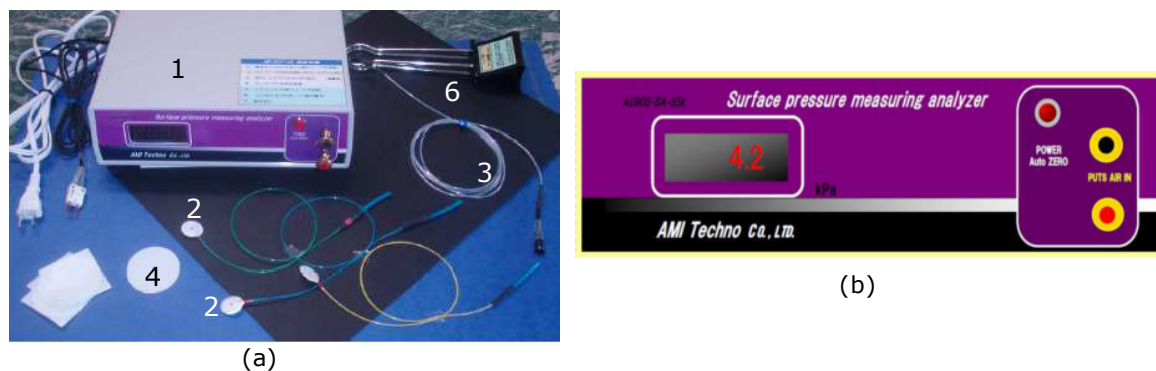


Fig. 2.20 AMI air-Pack type analyser Model 3037, $\phi = 20$ mm, main unit model AMI 0905-SA-35K (a) measurement system with components 1) main unit, 2) Air-pack sensors 3) relay tube 4) covering tape 5) press tester (b) The main unit, with two knobs (black and red) for the two semi-auto air cylinder (AMI-Techno, 2009a)

- main unit with display, DC output and auto zero adjustment function
- air-pack sensors of 20mm diameter, 0.5m-1m length variations
- relay tube of 1.5m length
- covering tape
- press tester

Features of Air-pack sensors:

- Flexible but non-elastic probes

the probes are made such with flexible film of least possible elasticity, and air is enclosed in to the thickness of 1mm. The change of the pressure of this enclosed air is measured externally due to the compression between the contacted surfaces. The non-elastic material does not allow the probe to expand as shown in the Figure 2.21.

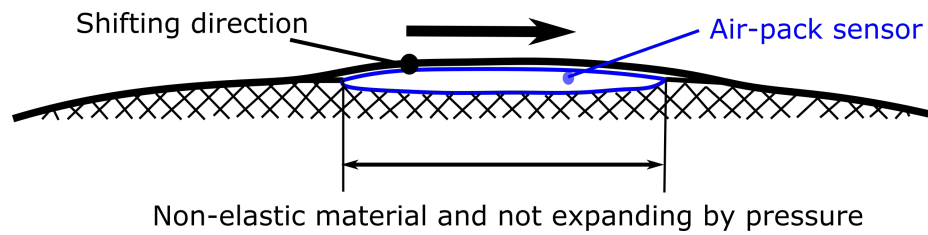


Fig. 2.21 Air-pack sensor and its operating sequence (AMI-Techno, 2009a)

- Influence of heat:

The probes were reported to be shown a very low (0.1kPa) sensitivity to a large temperature change (temperature change of 40°C), therefore the thermal effect is considered to be negligible (AMI-Techno, 2009a). This can be explained in the following manner according to the manufacturer (AMI-Techno, 2009a)

- Even though the thermal expansion factor of air is changed due to the temperature rise, which may cause a volume increase, it would have a very little impact on the Air-pack sensor thickness direction due to its flat shape
- The amount of air enclosed in the probe is smaller than the maximum volume capacity of the sensor, thus, there exist a sufficient capacity inside for the probe to absorb a swell in the air enclosed
- In the actual measuring condition, a swell to the thickness direction of the air-pack sensor is absorbed by its flexibility.

- has two semi-auto air cylinders:

This allows to select the air amount to be infused to the air-pack sensor. The red knob is pulled when testing over soft living body and black knob is pulled when testing with hard surfaces.

- measurement accuracy of 20mm standard probe is 1.5 mmHg (0.2kPa)
- measuring accuracy of the main unit in 23°C, 1.5mmHg (0.2kPa)
- auto zero adjustment
- easy to stick to each part of living body and between the measured surface.

Calibration of the unit:

The air-pack sensors and the measurement units require a separate calibration using a water column, which will be explained in detail under chapter 4. In here the calibration tries to imitate the actual situation. In the calibration, the air-pack sensor is mounted to the bottom plate of the t-shaped bar, and submerged into a cylinder filled with water at 23-30°C. However, it is not necessary to calibrate

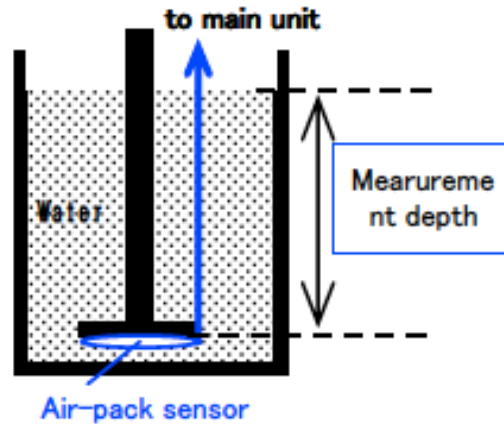


Fig. 2.22 Calibration of the probe using a water column (AMI-Techno, 2009a)

before each measurement, but the probes and the measurement unit should be calibrated before the experiment.

c. Kikuhime

This pressure sensor is a portable unit, which has an air filler flexible probe connected to a pressure transducer (Al Khaburi, 2010). The standard probe is 30mm in diameter and 3mm in thickness. It was widely used over the past in measuring sub bandage pressure (Damstra et al., 2008; Mosti and Mattaliano, 2007; Partsch, 2005). Partsch (2005), reported that the sensor has a good accuracy at higher pressures, and it tends to overestimate the pressures in the range of 20 – 60mmHg, with a coefficient of variation of 7.1% (maximum) at 20mmHg. This was further confirmed by Mosti and Rossari (2008), where they reported higher error levels at 20 mmHg.

d. Oxford Pressure Monitoring system (OPM)

This is developed by Talley medical Group Ltd, UK and operates under the same principle as a, b, and c. but has 12 small plastic probes of 14mm diameter and 1.5mm thickness, which allows dynamic measurement for 12 points (Figure 2.23). It has been used in several studies and is reported to have an accuracy of ± 4 mmHg (Finnie, 2000; John et al., 2007; Wildin et al., 1998).

However, none of the studies have reported a proper evaluation for the system (Al Khaburi, 2010), where the earlier version of the system reported to have an accuracy error of 12% calculated using equation 2.5 (Allen et al., 1993).

$$\text{error} = \frac{\text{measured value} - \text{expected pressure}}{\text{expected pressure}} \quad (2.5)$$



Fig. 2.23 Oxford Pressure Monitor (Al Khaburi, 2010)

2.3.3 Flexible piezo-resistive sensors

These sensors are flexible and manufactured from flexible conductive thin polymer sheets. The working principle is based on the resistance change of the material (decrease in resistance), when the compressive force is applied (Ashruf, 2002). There are several sensor types available in the market under this category, such as FlexiForce[®] and FSR[®]. However, in general they are considered to have high non-linearity, high hysteresis, creep problems, poor stability, temperature and humidity dependency, and low durability (Ashruf, 2002).

a. FlexiForce[®] sensors

Produced by Tekscan, Inc. USA, has the usage in both force measurements and pressure measurement. FlexiForce is the Tekscan's single point measuring product (while most of the others were grids) given for measuring the interface pressure. Tekscan is probably the one entity, whose thin film pressure sensors are most reportedly used in pressure mapping and force measurement in the medical field (Ashruf, 2002; Macintyre et al., 2004; Polliack et al., 2000; Wilson et al., 2003) such as F-Scan, I-Scan.

The sensor is around 0.203mm in thickness, and is constructed using two layers of thin polyester film with silver conductive material applied over it followed by a pressure sensitive ink material as shown in Figure 2.24a (Al Khaburi, 2010). Two adhesive layers are used to laminate the two polyester layers to form the sensor, whereas silver is used to extend from the sensing area to the other end for the connection forming conductive leads (Tekscan®, 2016).

When the force is applied on the sensing area, the resistance decreases, leading to an increase in conductance. The sensors come with three different ranges of force, where the lowest being 0 – 4N (Tekscan®, 2017), which is capable of measuring 0 – 462.6mmHg pressure range. These sensors

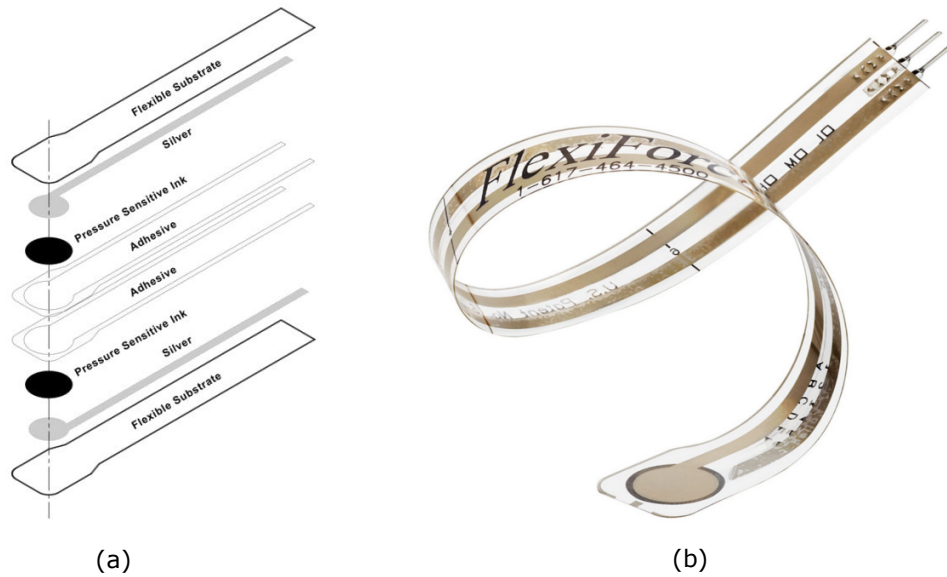


Fig. 2.24 a) FlexiForce® sensor layer construction (Tekscan®, 2016) b) FlexiForce® sensor, made with flexible thin film

have been widely used in studies for compression garments (Burke et al., 2014; Ferguson-Pell et al., 2000; Komi et al., 2007; Lebosse et al., 2008; Liu et al., 2007, 2005; Vecchi et al., 2000) .

Tekscan claim that 11b(4N) sensors have a repeatability within 5% and linearity within 5% and hysteresis less than 4.5% of the full scale, but none of the information are given on the curvature effect (Ferguson-Pell et al., 2000). However, Ferguson-Pell (Ferguson-Pell et al., 2000) claimed that hysteresis was 5.4% on average, but the linearity was recorded to be higher as 9.9% at lower forces values compared to higher forces values, which could be due to the low sensitivity of the sensor in lower force ranges (Ferguson-Pell et al., 2000).

It was also found that sensor should not be recommended to use over curvatures with radius of curvatures less than 32mm (Ferguson-Pell et al., 2000). Furthermore, there is minimum load necessary to excite the sensor, which means that the sensor is unreliable for measuring pressures under 15mmHg (Lao, 2016). Also due to the errors attributed in repeatability, hysteresis, and linearity the total error of sensor is often approximated to be ± 10 mmHg (Burke et al., 2014).

2.4 Hyperelastic behaviour of platinum cured silicones

2.4.1 Hyperelastic materials

Materials which are characterised by relatively low elastic modulus and high bulk modulus are of wide use today. These materials undergo large elastic strains and deformations for smaller volume changes (Kumar and Rao, 2016). The "Hyperelastic materials" are still elastic materials which return to its

original shape when forces are removed. However, they are also "Cauchy-elastic", which implies that the stress is determined solely by the current state of deformation, and not by the path or the history of the deformation. The behaviour of these materials is described by using Hyperelastic constitutive laws. These laws are extensively used to model materials that respond elastically to very large strains and account for both nonlinear behaviour and large deformations.

The linear elastic models could not used to accurately describe the experimentally observed behaviour of many materials such as rubber. The stress-strain relationship for rubber is non-linear, isotropic, and incompressible (Jakel, 2010). The concept of "hyperelasticity" provides a means of modelling the stress-strain behaviour of these type of materials. A material is said to be hyperelastic if there exists an elastic strain energy function that is a scalar function of strain deformation tensors, whose derivatives with respect to strain components determine the corresponding stresses (Kumar and Rao, 2016). Unlike plasticity, hyperelasticity is not defined as a rate formulation, instead total stress vs. total strain relationship is defined via a strain energy potential (W) (Xu et al., 2003). The details of the strain energy potential and the existing models developed to describe the behaviour of Hyperelastic materials are discussed in following sections.

2.4.2 Platinum cured silicones

Silicones, known to chemists as polydiorganosiloxanes, consist of an inorganic backbone built with alternating silicon and oxygen atoms. The other two bonds of silicon are usually occupied with organic groups (Fig. 2.25), preferably methyl (De Buyl, 2001). These organic groups are responsible for the semi-organic nature of silicones. Silicone polymers are transformed into a three-dimensional network and an elastomer via a cross linking reaction which is also known as vulcanization or curing. The Room Temperature Vulcanization (RTV) of Silicone rubber can be carried out in two different ways:

- condensation curing which is performed with an organotin catalyst generating alcohol as the by product.
- addition curing that uses platinum catalyst.

The second method does not produce any by-products (De Buyl, 2001). As shown in Fig. 2.25, during platinum-catalysed addition curing, Si-H groups of the cross linker react with the vinyl groups of the polymer to form a 3-D network. The condensation cured silicones are also referred to as one-part RTV, whereas the addition cured silicones are referred to as two-part RTV. In two-part RTVs one part consists of the catalyst and the other contains a silicon hydride- functional cross linker and an inhibitor to increase the curing time.

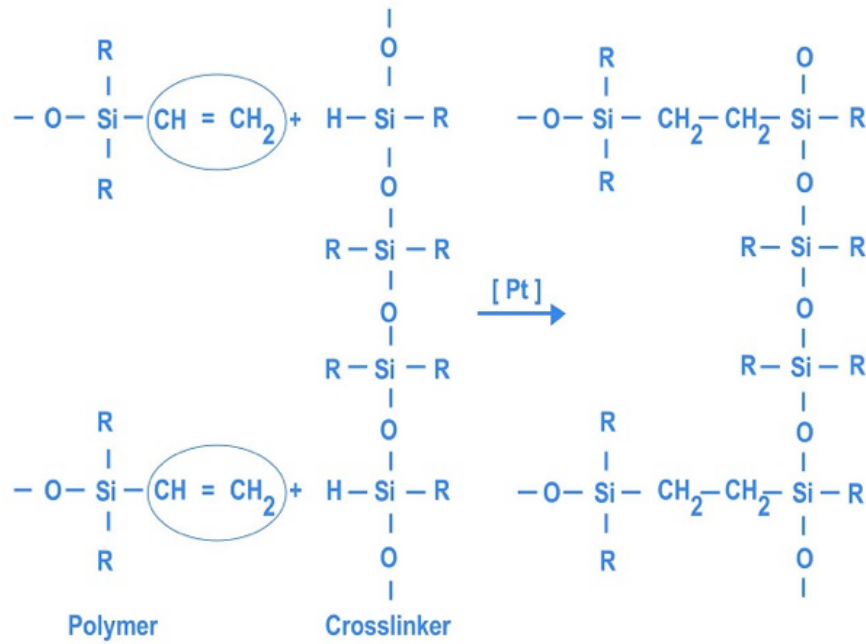


Fig. 2.25 Platinum catalysed addition curing of Silicones(TBL-Plastics, 2018)

2.4.3 Hyperelastic Models

Hyperelastic models have been widely used in analysing rubber like materials such as silicones, skin, soft tissues and other elastomeric materials (Manan et al., 2015). Among the existing models "Mooney-Rivlin", "Neo Hookean", "Ogden", "Arruda-Boyce", "Yeoh" and "Polynomial model" are the ones that commonly used for analysis of hyperelastic behaviour. Moreover, these models have been included in commercially available finite element analysis (FEA) software packages such as ANSYS, ABAQUS (Manan et al., 2015). The common characteristic of all the above mentioned models is that they all involve some material related constants that need be determined by experiments (Shahzad et al., 2015). The choice of the model depends on the application it is used, related variables and available data (Kumar and Rao, 2016). Prior to the use, the validity of possible models should be evaluated and the simplest model with a high accuracy and less materials parameters should be selected (Kumar and Rao, 2016; Lemaitre, 2001). The constitutive behaviour of hyperelastic material is derived from "strain energy function" W , which is based on three "strain invariants" I_1, I_2, I_3 (Shahzad et al., 2015).

$$W = f(I_1, I_2, I_3) \quad (2.6)$$

This theory provides a mathematical frame work to describe the behaviour of an elastomer based on continuum mechanics (Ali et al., 2010). The three invariants of the green deformation tensor are expressed in terms of principle extension ratios given by,

$$I_1 = \lambda_1^2 + \lambda_2^2 + \lambda_3^2 \quad (2.7)$$

$$I_2 = \lambda_1^2 \lambda_2^2 + \lambda_2^2 \lambda_3^2 + \lambda_3^2 \lambda_1^2 \quad (2.8)$$

$$I_3 = \lambda_1^2 \lambda_2^2 \lambda_3^2 \quad (2.9)$$

Equation (2.7) can be written as,

$$W = \sum_{i+j+k=1}^{\infty} C_{ijk} (I_1 - 3)^i (I_2 - 3)^j (I_3 - 3)^k \quad (2.10)$$

Most of the rubber like materials are considered incompressible. Hence, for these type of materials $I_3 = 1$, therefore the equation (2.10) reduces to;

$$W = \sum_{i+j=1}^{\infty} C_{ij} (I_1 - 3)^i (I_2 - 3)^j \quad (2.11)$$

The equation (2.11) has been the basis for most of the available models for Hyperelastic materials. The subsequent sections of this thesis discuss the existing models.

Polynomial model

The Polynomial model was first introduced by Rivlin and Saunders (Rivlin and Saunders, 1951). It was formulated in terms of the two strain invariants of the left Cauchy-Green tensor. The strain energy function for a compressible material is defined as,

$$W = \sum_{i+j=1}^N C_{ij} (I_1 - 3)^i (I_2 - 3)^j + \sum_{i=1}^N \frac{1}{D_i} (J_{el} - 1)^{2i} \quad (2.12)$$

where C_{ij} denotes material constants. For isotropic and incompressible rubber like material, $J_{el} = 1$ therefore the polynomial model reduces to;

$$W = \sum_{i+j=1}^N C_{ij} (I_1 - 3)^i (I_2 - 3)^j \quad (2.13)$$

where C_{ij} are material constants with, $C_{00} = 1$ and I_1 and I_2 are first and second strain invariants respectively, and N is a positive integer determining the number of terms in the strain energy function

(e.g. $N = 1, 2, 3$). This model is also referred to as the generalized Rivlin model (Hartmann, 2001; Laksari et al., 2012).

Mooney Rivlin Model

This is a two parameter phenomenological model known to work well for moderately large strains in uniaxial elongation and shear deformation (Mooney, 1940; Rivlin, 1948; Sujendra et al., 2018). The strain energy function could be reduced from the equation 2.13 for different conditions as follows (Kumar and Rao, 2016).

Mooney Rivlin Two parameter model;

$$W = C_{10}(I_1 - 3)^1 + C_{01}(I_2 - 3)^1 \quad (2.14)$$

Mooney Rivlin three parameter model;

$$W = C_{10}(I_1 - 3)^1 + C_{01}(I_2 - 3)^1 + C_{11}(I_1 - 3)^1(I_2 - 3)^1 \quad (2.15)$$

Mooney Rivlin five parameter model;

$$W = C_{10}(I_1 - 3)^1 + C_{01}(I_2 - 3)^1 + C_{11}(I_1 - 3)^1(I_2 - 3)^1 + C_{20}(I_1 - 3)^2 + C_{02}(I_2 - 3)^2 \quad (2.16)$$

Neo Hookean Model

The Neo-Hookean model is an extension of Hook's Law for the large deformations. It is based on the statistical thermodynamics of cross-linked polymer chains and is possible to use for rubber like materials for initial range of strains (Kim et al., 2012). It is known that cross linked polymers act in a Neo Hookean manner in the linear states (Lin, 2016). However, after a certain stretch, the polymer chains will be allowed to make covalent cross links which will result in a dramatic increase in the modulus (Kim et al., 2012; Lin, 2016). Therefore, Neo-Hookean model is not suitable in predicting the elastic behaviour in larger strain regions. In the polynomial model proposed by Rivlin and Saunders 2.12 when only the first term is retained, the strain energy of an incompressible material is equivalent to;

$$W = C_{10}(I_1 - 3)^1 + \frac{1}{D_i}(J_{el} - 1)^2 \quad (2.17)$$

For an incompressible material $J_{el} = 1$, and the equation 2.17 reduces to;

$$W = C_{10}(I_1 - 3)^1 \quad (2.18)$$

Yeoh Model

This hyperelastic model developed by Yeoh (1993) only depends on the first strain invariant. This is also a series expansion similar to the polynomial model. The definition of strain energy for an incompressible material is define by;

$$W = \sum_{i+j=1}^n C_{i0}(I_1 - 3)^i \quad (2.19)$$

In the original model formula Yeoh (1993) truncated the series after first three terms. However, more general definition is used nowadays (Selvadurai, 2006).

$$W = \sum_{i+j=1}^3 C_{i0}(I_1 - 3)^i \quad (2.20)$$

Within the continuum mechanics framework for the strain energy function as proposed by Rivlin (2.10, use of higher order terms has shown to work effectively in capturing the deformation states of moderate to large deformations (Guo, 2006). The first order, second order, and third order models developed by Yeoh (1993) are given in Eqs. 2.21 to 2.23.

Yeoh first order model;

$$W = C_{10}(I_1 - 3) \quad (2.21)$$

Yeoh second order model;

$$W = C_{10}(I_1 - 3) + C_{20}(I_1 - 3)^2 \quad (2.22)$$

Yeoh third order model;

$$W = C_{10}(I_1 - 3) + C_{20}(I_1 - 3)^2 + C_{30}(I_1 - 3)^3 \quad (2.23)$$

Yeoh (1993) model is considered to be providing a good fit for a wide range of deformations, within a larger range of strains. It can also simulate various deformation modes using limited amount of data (Renaud et al., 2009). This model is capable of predicting the stress strain behaviour for different deformation modes, using the data obtained from only one mode of deformation like uniaxial extension (Ali et al., 2010) hence, requires lesser material testing experiments.

Ogden Model

The model proposed by Ogden (1972) is also a phenomenological model. However, it is different to other models because to a certain extent as it defines the strain energy directly as a function of stretch ratios instead of strain invariants. This model accurately describes the behaviour of rubber for larger ranges of deformation capturing the upturn of the stress strain curve (Shahzad et al., 2015). The proposed strain energy function for a compressible material is of the form;

$$W = \sum_{i=1}^N \frac{2\mu_i}{\alpha_i^2} (\bar{\lambda}_1^{\alpha_i} + \bar{\lambda}_2^{\alpha_i} + \bar{\lambda}_3^{\alpha_i} - 3) + \sum_{i=1}^N \frac{1}{D_i} (J_{el} - 1)^2 i \quad (2.24)$$

where,

$$\bar{\lambda}_i = J^{-\frac{1}{3}} \lambda_i$$

J = The Jacobian determinant

λ_i = Principal stretches

J_{el} = The elastic volume ration

For an incompressible material, $J_{el} = 1$. Therefore, for an incompressible material the equation 2.24 can be rewritten as;

$$W = \sum_{i=1}^N \frac{\mu_i}{\alpha_i} (\lambda_1 + \lambda_2 + \lambda_3 - 3) \quad (2.25)$$

where, $\lambda_i = \lambda$

The constants μ_i and α_i describe the shear behaviour of the material. The calculation of the invariant derivatives of the Ogden's energy function is more computationally intensive than the polynomial form (Martelli and Dusi, 1999). When using the experimental data for curve fitting, this model can be more accurate when data from multiple experiments exists such as uniaxial, biaxial and shear (Korochkina et al., 2005).

Arruda Boyce Model

This model falls under the category of physical models, which is based on an description of a molecular chains network. The strain energy is assumed to be equivalent to the sum of the strain energies of the individual chains which are randomly oriented in the space (Stolz and Bourgeois, 2005). This is also referred to as Arruda- Boyce eight chain model, since it was developed based on representative volume element where the eight chains stem from the centre to the corners of the volume (Arruda and Boyce, 1993). This is also based on the first strain invariant and therefore can be used with limited test data. The defined strain energy function for a compressible material is;

$$W = \mu \sum_{i=1}^5 \frac{C_i}{\lambda_m^{2i-2}} (\bar{I}_1^i - 3) + \frac{1}{D} \left(\frac{J_{el}^2 - 1}{2} - \ln(J_{el}) \right) \quad (2.26)$$

where,

μ = Initial shear modulus

λ_m = Locking stretch at which the upturn of the stress strain curve would rise significantly

D = Two times the bulk modulus at small strain ($D = \frac{2}{k}$)

As discussed above these models should be calibrated with experimental data to select the best available model to analyse the behaviour of the bladder unit. For this purpose, we have used uniaxial

extension tests. The Development of stretch-stress relationship for this test under the above models is discussed in the following section.

2.4.4 The stretch-stress relationship for uniaxial extension

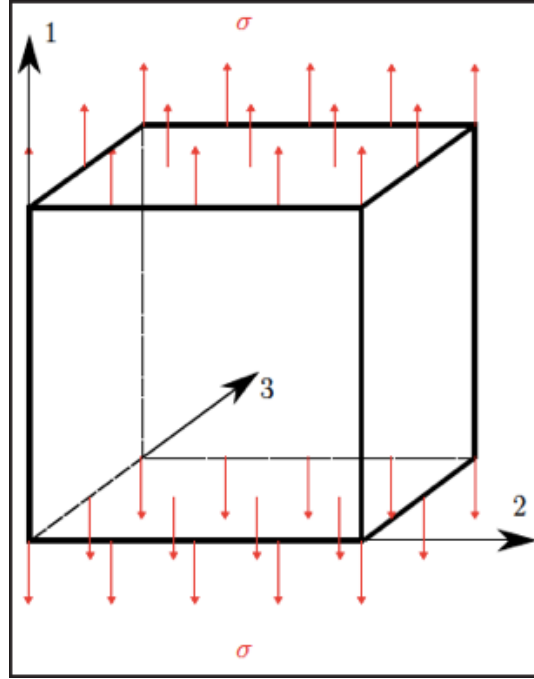


Fig. 2.26 A cubic differential volume element with tensile stress σ in a Cartesian coordinate system (Rackl, 2015)

For deriving the stress stretch relationships for uniaxial tension a cubic differential element as shown in fig. 2.26 is considered (Rackl, 2015). As shown in the fig. 2.26, the volume is subjected to an uniaxial tensile stress of σ , and is allowed to deform in the given Cartesian coordinate system. The three principal stretches in the three directions can be written as, $\lambda_1, \lambda_2, \lambda_3$ where λ_1 is along the direction of the uniaxial tensile stress. In uniaxial extension, it is evident that the stretches in both directions 2 and 3 becomes equal. i.e. $\lambda_2 = \lambda_3$,

If $\lambda_1 = \lambda$, and the material is considered to be incompressible it satisfies the relation;

$$\lambda_1^2 \lambda_2^2 \lambda_3^2 = 1 \text{ (Shahzad et al., 2015)}$$

Hence, λ_2 and λ_3 can be written as;

$$\lambda_2 = \lambda_3 = \frac{1}{\lambda^{\frac{1}{2}}} \quad (2.27)$$

According to Rivlin (Rivlin, 1948, 1956), the relationship between engineering stress and stretch for an incompressible material under tension/ compression can be written as;

$$\sigma_e = 2\left(\lambda - \frac{1}{\lambda^2}\right)\left(\frac{\partial W}{\partial I_1} + \frac{1}{\lambda}\left(\frac{\partial W}{\partial I_2}\right)\right) \quad (2.28)$$

where;

W = Strain energy

I_1, I_2 = Strain invariants

σ_e = Engineering stress

λ = Stretch in the direction of uniaxial tension

According to the definition of stretch ratio;

$$\lambda = \frac{L}{L_0} \quad (2.29)$$

where;

L = deformed length

L_0 = initial length

The engineering strain is defined as;

$$\varepsilon = \frac{L - L_0}{L_0} \quad (2.30)$$

$$\lambda = 1 + \varepsilon \quad (2.31)$$

Deducing the stretch, strain relationship for Yeoh model-uniaxial tension

Case 1: Yeoh first order model;

$$W = C_{10}(I_1 - 3) \quad (2.32)$$

According to equation 2.28,

$$\sigma_e = 2\left(\lambda - \frac{1}{\lambda^2}\right)\left(\frac{\partial C_{10}(I_1 - 3)}{\partial I_1}\right) + \frac{1}{\lambda}\left(\frac{\partial C_{10}(I_1 - 3)}{\partial I_2}\right) \quad (2.33)$$

$$\sigma_e = 2\left(\lambda - \frac{1}{\lambda^2}\right)C_{10} \quad (2.34)$$

Case 2: Yeoh second order model;

$$W = C_{10}(I_1 - 3) + C_{20}(I_1 - 3)^2 \quad (2.35)$$

According to equation 2.28,

$$\sigma_e = 2\left(\lambda - \frac{1}{\lambda^2}\right)\left(\frac{\partial[C_{10}(I_1 - 3) + C_{20}(I_1 - 3)^2]}{\partial I_1} + \frac{1}{\lambda}\left(\frac{\partial[C_{10}(I_1 - 3) + C_{20}(I_2 - 3)^2]}{\partial I_2}\right)\right) \quad (2.36)$$

$$\sigma_e = 2\left(\lambda - \frac{1}{\lambda^2}\right)(C_{10} + C_{20}(I_1 - 3)) \quad (2.37)$$

Hence, $I_1 = \lambda_1^2 + \lambda_2^2 + \lambda_3^2$ and
 $I_1 = \lambda^2 + 2\lambda_2^2$

$$I_1 = \lambda^2 + \frac{2}{\lambda} \quad (2.38)$$

$$\sigma_e = 2\left(\lambda - \frac{1}{\lambda^2}\right)(C_{10} + C_{20}(\lambda^2 + \frac{2}{\lambda} - 3)) \quad (2.39)$$

Deducing the stretch, strain relationship for Mooney Rivlin model-uniaxial tension

Case 1: Mooney Rivlin two parameter model;

$$W = C_{10}(I_1 - 3)^1 + C_{01}(I_2 - 3)^1 \quad (2.40)$$

According to equation 2.28,

$$\sigma_e = 2\left(\lambda - \frac{1}{\lambda^2}\right)\left(\frac{\partial[C_{10}(I_1 - 3) + C_{01}(I_2 - 3)]}{\partial I_1} + \frac{1}{\lambda}\left(\frac{\partial[C_{10}(I_1 - 3) + C_{01}(I_2 - 3)]}{\partial I_2}\right)\right) \quad (2.41)$$

$$\sigma_e = 2\left(\lambda - \frac{1}{\lambda^2}\right)(C_{10} + \frac{1}{\lambda}C_{01}) \quad (2.42)$$

Case 2: Mooney Rivlin three parameter model;

$$W = C_{10}(I_1 - 3)^1 + C_{01}(I_2 - 3)^1 + C_{11}(I_1 - 3)^1(I_2 - 3)^1 \quad (2.43)$$

According to equation 2.28,

$$\sigma_e = 2\left(\lambda - \frac{1}{\lambda^2}\right)\left(\frac{\partial[C_{10}(I_1 - 3) + C_{01}(I_2 - 3) + C_{11}(I_1 - 3)(I_2 - 3)]}{\partial I_1} + \frac{1}{\lambda}\left(\frac{\partial[C_{10}(I_1 - 3) + C_{01}(I_2 - 3) + C_{11}(I_1 - 3)(I_2 - 3)]}{\partial I_2}\right)\right) \quad (2.44)$$

$$\sigma_e = 2\left(\lambda - \frac{1}{\lambda^2}\right)(C_{10} + C_{11}(I_2 - 3) + \frac{1}{\lambda}(C_{01} + C_{11}(I_2 - 3))) \quad (2.45)$$

Hence, $I_2 = \lambda_1^2 \lambda_2^2 + \lambda_2^2 \lambda_3^2 + \lambda_3^2 \lambda_1^2$ and

$$I_1 = \lambda^2 \lambda_2^2 + 2\lambda_2^4 + \lambda_2^2 \lambda$$

since; $\lambda_2^2 = \lambda_3^2 = \frac{1}{\lambda}$

$$I_2 = 2\lambda + \frac{1}{\lambda^2} \quad (2.46)$$

$$\sigma_e = 2\left(\lambda - \frac{1}{\lambda^2}\right)(C_{10} + C_{11}(2\lambda + \frac{1}{\lambda^2} - 3) + \frac{1}{\lambda}(C_{01} + C_{11}(\lambda^2 + \frac{2}{\lambda} - 3))) \quad (2.47)$$

$$\sigma_e = 2C_{10}\left(\lambda - \frac{1}{\lambda^2}\right) + 2C_{01}\left(1 - \frac{1}{\lambda^3}\right) + 6C_{11}\left(\frac{1}{\lambda^2} + \frac{1}{\lambda^3} - \frac{1}{\lambda^4} - 1 - \lambda + \lambda^2\right) \quad (2.48)$$

Deducing the stretch, strain relationship for Neo Hookean model-uniaxial tension

$$W = C_{10}(I_1 - 3)^1 \quad (2.49)$$

According to equation 2.28,

$$\sigma_e = 2\left(\lambda - \frac{1}{\lambda^2}\right)\left(\frac{\partial[C_{10}(I_1 - 3)]}{\partial I_1} + \frac{1}{\lambda}\left(\frac{\partial[C_{10}(I_1 - 3)]}{\partial I_2}\right)\right) \quad (2.50)$$

$$\sigma_e = 2C_{10}\left(\lambda - \frac{1}{\lambda^2}\right) \quad (2.51)$$

2.5 Chapter summary

This chapter presents the previous work carried out in the area of compression therapy for the treatment of venous disease and lymphedema; including various treatment methods and their inherent advantages and disadvantages. However, these existing treatment systems have failed to produce a solution which could deliver uniform circumferential pressures on to the human lower limb. Thus, it suggests the importance of designing and developing an active compression treatment system capable of generating the correct uniform circumferential pressures with a pressure graduation. Out of the theoretical models analyzed to describe the hyperelastic behaviour of silicone Yeoh second order model is capable of predicting the stress strain behaviour for different deformation modes using one set of experimental data like uniaxial extension.

Chapter 3

Evaluation of interface pressure measurement systems

In developing a compression treatment system for Venous disease, it is important to specify the amount of pressure it could deliver to the treatment surface for different conditions. Hence, the characterisation of pressure transmission properties of the proposed active compression system including mini-bladders is important. Thus, selecting a suitable pressure measurement system for accurate measurement of the interface pressure is a vital element of this research study. This chapter presents the evaluation of commercially available interface pressure measurement systems for their accuracy and reproducibility of the test results. The objective of the study was to select a pressure measurement system which could be used to quantify the pressure transmitted by the mini-bladders when inflated to different pressure levels.

A range of pressure sensors are available to measure the interface pressure on a surface, however, some could not provide reproducible results and had large repeatability errors. Therefore, the pressure sensors were calibrated using a liquid manometer. The analysis of test data showed that AMI Air-pack sensors (Model 3037, $\phi = 20$ mm, main unit model AMI 0905-SA-35K) was suitable to determine the interface pressure due to their reproducibility, linearity and the accuracy compared to the other available sensors.

3.1 Introduction

It is important to quantify the percentage of the pressure transferred via the mini-bladders (justification for using the mini-bladders is established in the subsequent chapters of this thesis) on to the contact surface to evaluate the efficiency of the mini-bladder performance. In real life scenario this depicts, the mini-bladders in contact with the human skin should be able to deliver the required graduated pressure profile over the human limb when inflated with different volumes of air. This is the key feature to be considered when engineering the air supply necessary to inflate the mini-bladders in the

active compression system.

In the present study, a series of experiments were designed to quantify the pressure transmittance characteristics of the mini-bladders by expressing contact surface pressure as a function of the pressure inside the mini-bladders. These obtained relationships can be used as calibration curves to determine the pressure necessary to inflate the mini-bladders in order to obtain the required interface pressure; the pressure inside the mini-bladder is influenced by the volume of the inflatable space of a mini-bladder and the volume of air pumped into it. It was necessary to use a pressure sensor to measure the interface pressure between the mini-bladders and the contact surface. Therefore, to select a suitable pressure sensor for this application the most commonly used interface pressure measurement systems, Picopress (Microlab-Electronica, 2014), AMI (AMI-Techno, 2009*a,b*), and Flexiforce (Tekscan®, 2016; Tekscan®, 2017; Tekscan®, 2018) were analysed (Al Khaburi, 2010; Lai and Li-Tsang, 2009; Liu et al., 2017; McLaren et al., 2010; Tyler, 2015). Based on the repeatability of the sensor results, linearity, hysteresis and the size of the sensor, the most suitable system was selected and then used for the further studies.

3.2 Study of pressure measurement systems

Sensors and probes are used to determine the interface pressure distribution of compression garments which is important in understanding the efficiency of the product. Pressure is defined as the force applied over a unit area. The aim of the research is to employ mini-bladders to create a pressure profile, and when a mini-bladder in contact with the human body is inflated a compressive force will be experienced by the body. The average interface pressure developed due to the inflated mini-bladders can be calculated by the total force divided by the area of the mini-bladder in contact with the skin surface.

As explained under section 2.3 of the previous chapter, there are several commercial skin interface pressure measurements systems available, with different working principles such as pneumatic based, piezoresistive, and capacitive. From the commercially available sensors PicoPress® (Microlab Electronica, Ponte S. Nico PD, Italy), AMI air-Pack type analyser (Model 3037 $\phi = 20\text{mm}$, main unit model AMI 0905-SA-35K, AMI Techno Ltd), and FlexiForce® ($\phi = 9.53\text{mm}$ Tekscan Inc., USA) sensors were available for the evaluation. These three systems were analysed for their linearity and repeatability of the results. Based on the results obtained the most suitable pressure sensor for the research was selected.

3.3 Study of FlexiForce® sensors for interface pressure measurement

Before using the sensors for the pressure measurement application, they have to be calibrated. Calibration can be identified as a process of comparing the output of a measurement system against standard of known accuracy (Al Khaburi, 2010). Different pressure sensors have different calibration procedures specified by the manufacturers, and provides a good platform to study the accuracy, linearity and repeatability of the sensors.

3.3.1 Calibration of FlexiForce® sensors

The standard method in calibrating these sensors is by using a set of standard weights. The FlexiForce® (A-201) 1lb (4N) sensors (UbSenthoff, Germany) was selected to use in the interface pressure measurement. The ideal interface pressure measurement system should include the sensors which are thin and flexible (Finnie, 2000; Lai and Li-Tsang, 2009; Ng, 1995). These reasons have made the FlexiForce® sensors produced by Tekscan Inc. to be popular in measuring the pressures delivered by medical compression products in the recent years (Buis and Convery, 1997; Ferguson-Pell et al., 2000; Macintyre, 2007, 2011; Mann et al., 1997). These sensors are produced by the Tekscan is a solution for measuring interface pressure; the applied force to the sensitive area results in a decrease of the resistance which corresponds to the increase in conductance (Al Khaburi, 2010). FlexiForce® (A-201) 1 lb (4.4 N) sensor has the smallest range of the pressure out of the three ranges available (1 lb-4.4 N, 25lb-111N, and 100 lb-445 N), which can be used to measure 0 – 463 mmHg range of pressure (Tekscan®, 2016). Since the interface pressures recorded in compression therapy are low; i.e. in the range of 0 – 60 mmHg (maximum), the sensor with the smallest range of measuring pressure was considered. However, these sensors would not be directly reading the pressure as an output since these are force sensors, hence the force value would be converted in to pressure by;

$$\text{applied pressure} = \frac{\text{force}}{\text{contact surface area}} \quad (3.1)$$

$$\text{applied pressure (mmHg)} = \frac{\text{weight (kg)} \times 9.81(\text{ms}^{-2})}{\text{contact surface area (mm}^2\text{)}} \times 7500.638 \quad (3.2)$$

The diameter of the circular sensing area of FlexiForce® (A-201) 1 lb (4.4 N) sensor was 9.53 mm, which equates to a contact surface area equivalent to 71 mm², hence;

$$\text{applied pressure (mmHg)} = \frac{\text{weight (kg)} \times 9.81(\text{ms}^{-2})}{71 (\text{mm}^2)} \times 7500.638 \quad (3.3)$$

CEBO-MSA 64 multi sensor measurement box (CESYS GmbH, Germany) was used with the sensors for the pressure measurement. It allows to read eight sensors at once, and the built in CeboMSAlab

(CESYS GmbH, Germany) software helps to operate in both calibration and the measurement modes. The recommended calibration procedure was to position a range of weights on the circular sensing area of the sensor using a circular Teflon peg (9.53 mm diameter 3 mm height) in order to concentrate the loading of the sensor by the weights accurately (see Figure 3.1). The recommended procedure by the manufacturer is given in Appendix A.

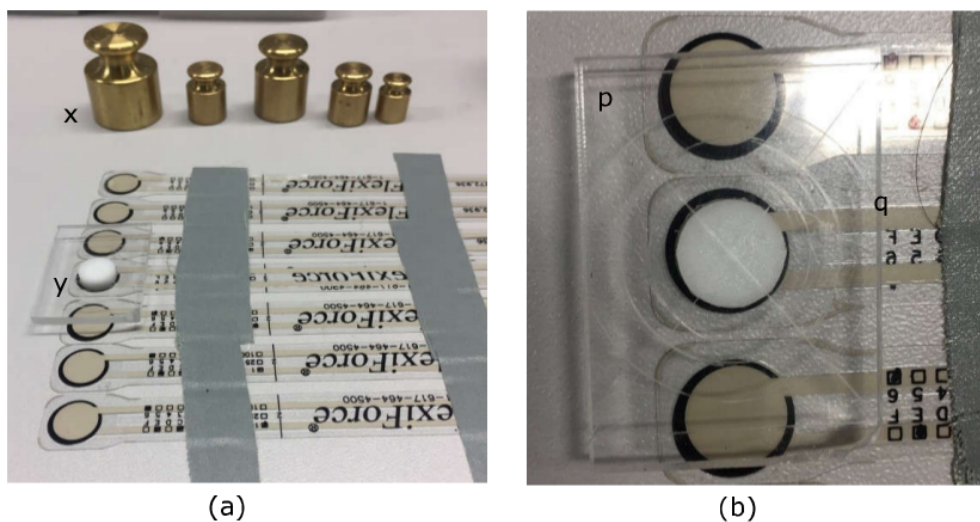


Fig. 3.1 Calibration procedure for FlexiForce® sensors (a) placement of the Teflon peg and the Perspex sheet (x: set of standard weights, y: Teflon peg). (b) The demarcations of different weights on the sheet (p: Perspex sheet, q: demarcations)

Further to the calibration process explained in Appendix A, to avoid the misalignment of the weights out of the centre, it was decided to use a Perspex sheet with the demarcations of the base of the standard weights 20 g, 50g, and 100g (Fig. 3.1b). These demarcations would ensure the weights are aligned with the centre line, providing a better repeatability to every sensor calibration. MSA-CAL lite 1.0 software has an interface which contains eight columns (Fig.3.2) corresponding to the eight input channels, to which the sensors were attached. During the calibration, the sensor was plugged to the corresponding port and as shown in Fig. 3.2, “calibrate” option should be selected to start the calibration. Thereafter, the calibration points specified in the Table 3.1 should be added starting from the zero (Fig. 3.3 (a)). It was recommended by the manufacturer to use at least three data points during the calibration, however, it was decided to use six data points as listed in the Table 3.1 below to analyse the sensor accuracy. As denoted in Fig. 3.3 (b), when the 20 g weight was placed on the sensor, the column displayed a yellow bar height corresponding to the pressure value. The calculated pressure value corresponds to 20 g weight was added according to the Table 3.11 (24.31 mmHg), which was displayed as a percentage value of the bar (5%).

The calibration was continued to all six points for the selected sensor and the file has to be saved before the next sensor is calibrated. The software does not allow to calibrate two sensors at the same time. Figure 3.4 shows the display when all the sensors were calibrated one by one.

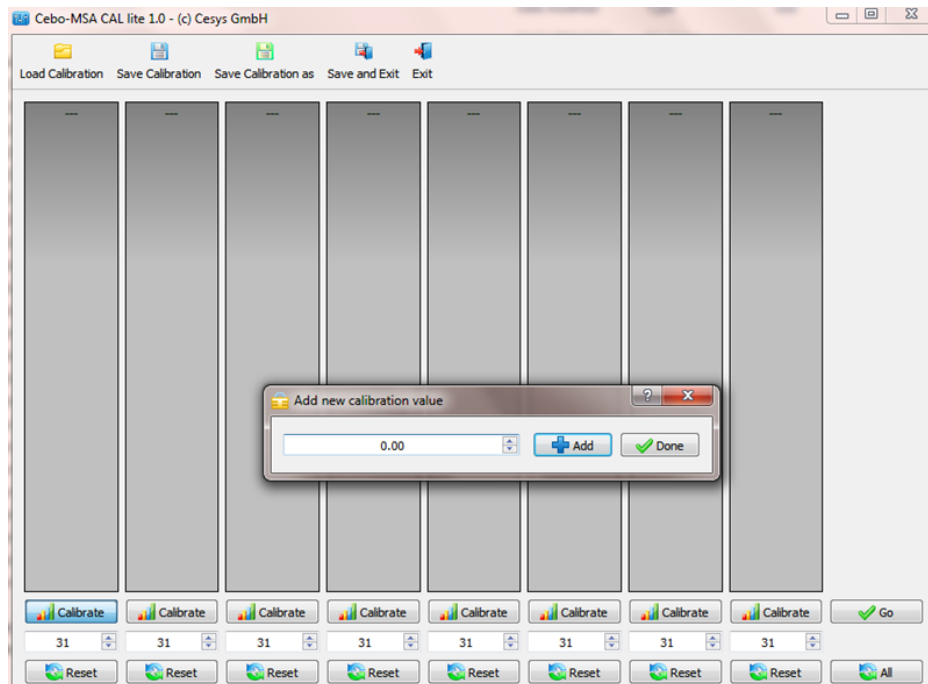


Fig. 3.2 MSA-CAL lite 1.0 software interface, showing eight different columns for, the eight input channels. The first sensor was selected to calibrate (calibrate option highlighted).

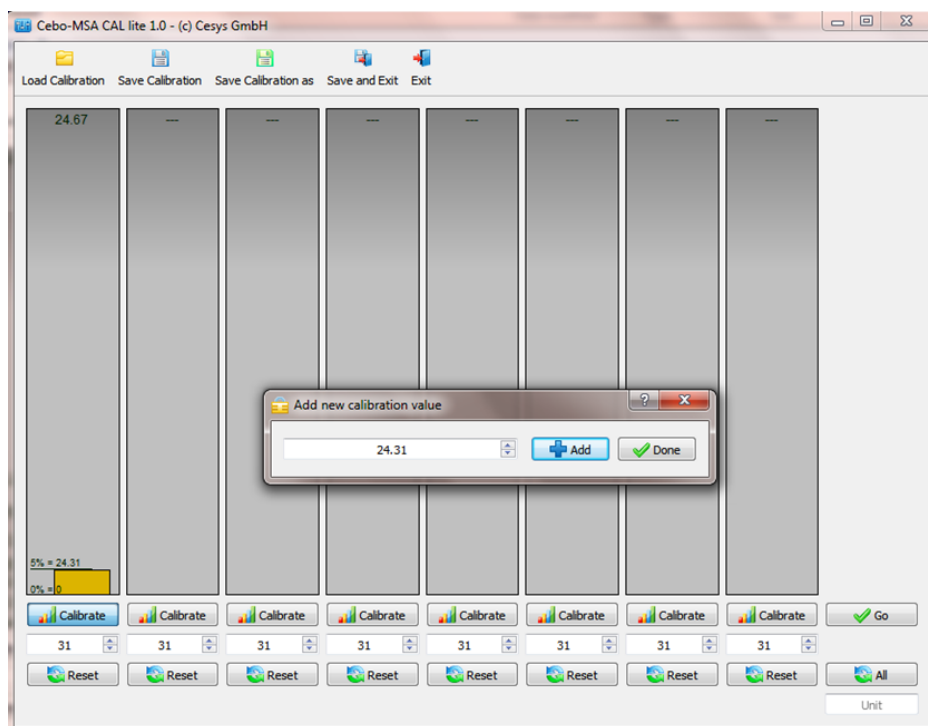


Fig. 3.3 MSA-CAL lite 1.0 software interface; the calibration process; addition of calibration points
(a) 0 mmHg (b) 24.31 mmHg

Table 3.1 The calibration points used with FlexiForce® sensors using standard weight

Constant weight (Peg and Perspex sheet unit)(g)	Standard Weight (g)	Total Weight (g)	Force (N) (weight(kg) $\times 9.98 \text{ ms}^{-2}$)	Pressure (N/mm ²)	Pressure (mmHg)
3.463	20	23.463	0.23012	0.003241	24.31
3.463	40	43.463	0.426242	0.006003	45.03
3.463	50	53.463	0.524312	0.007385	55.39
3.463	70	73.463	0.720452	0.010147	76.11
3.463	80	83.463	0.818522	0.011529	86.48
3.463	100	103.463	1.014662	0.014291	107.20

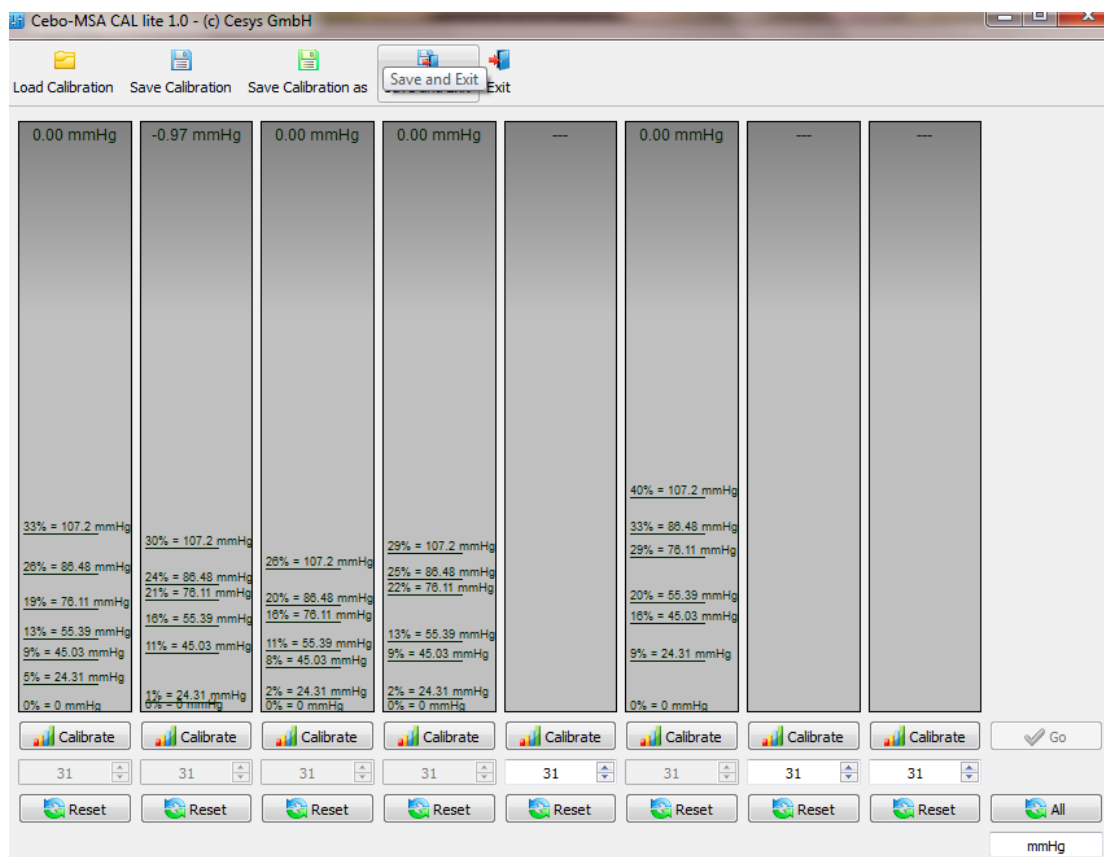


Fig. 3.4 The calibration file for five different FlexiForce® sensors using standard weight

It can be seen from Fig. 3.4 that the different sensors have shown different percentage values for the same six calibration points used. If the first calibration point (24.31 mmHg) is considered, the percentage values have shown a maximum variation of more than 5% within each other. This clearly indicates that FlexiForce® sensors show a considerable variation within sensor to sensor in measuring the interface pressure.

During this calibration by using standard weights, the placement of weights along the centre line of the peg was crucial, as otherwise could deliver faulty readings. As described above by demarcating the base of the weight on the Perspex sheet, it was ensured that this objective was achieved. However, since the weights were placed manually it cannot be assured that the weights were placed along the centre line. Therefore, it was suggested to use the Zwicki® tester in calibration of the sensors, as it's jaw could apply the force on to the sensor along its centre line with a higher precision than the manual placement of the weight.

3.3.2 Calibration of FlexiForce® sensors using Zwicki® tester

The same sensors used above were calibrated using Zwicki 2.5kN (Zwicki Roell®, Ulm, Germany) tensile tester to apply a maximum force of 2 N on to the sensor surface in intervals as shown in Table 3.2. The corresponding pressure values were calculated in mmHg according to the equation 3.4, and the detailed calculation of the pressures are included in the Appendix A.

$$\text{applied pressure (mmHg)} = \frac{\text{peg weight (kg)} \times 9.81\text{ms}^{-2} + \text{Force (N)}}{71\text{mm}^2} \times 7500.638 \quad (3.4)$$

Table 3.2 Calibration points and the corresponding pressure values used in calibration

Force (N)	Corresponding pressure (mmHg)
0	0
0.3	32
0.5	54
0.8	85
1.0	106
1.3	138
1.5	159
1.8	191
2.0	211

The FlexiForce® sensor was glued on to a metal plate which was mounted to the bottom jaw of the Zwicki® tester as shown in Fig. 3.5. A small peg of 0.9192 g was used to concentrate the loading accurately during the calibration. Thereafter, the top jaw (consisting of a wooden cylinder) was lowered on to the peg to apply the force in intervals specified in the Table 3.2; the Zwicki tester was

programmed for the top jaw to stop at each force value for 20 secs and the pressure value given by the sensor was recorded with the MSA-CAL lite 1.0 software provided by the FlexiForce[®] manufacturer. Five sensors in total were tested. The obtained calibration file from MSA-CAL lite 1.0 software, is shown in Fig. 3.6. Each sensor was tested for three loading cycles, and the percentage values given in the calibration bar of MSA-CAL software for the loading cycle was plotted against the calculated input pressure corresponding to the force applied. It is evident from the results shown in Fig. 3.6 the

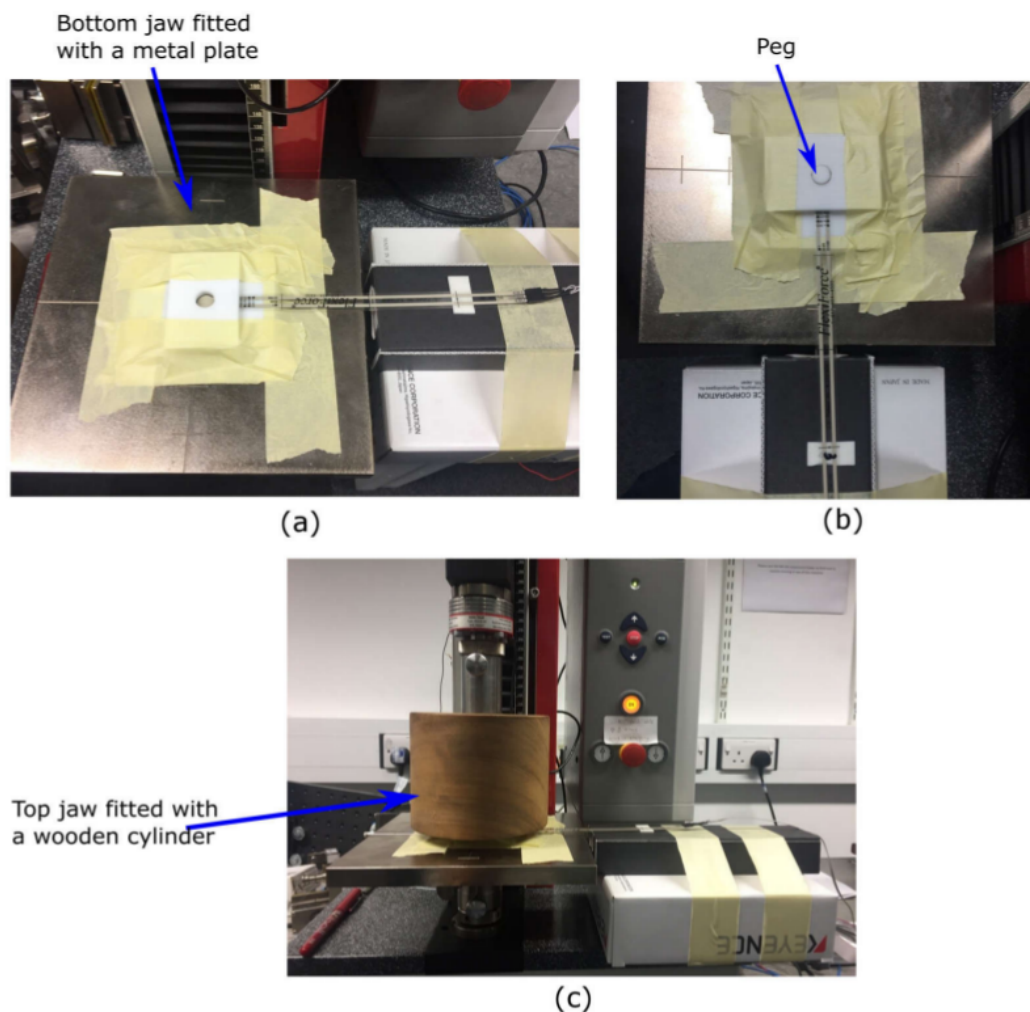


Fig. 3.5 Calibration process of FlexiForce[®] sensors using Zwicki[®] Roell, (a) placement of the FlexiForce[®] sensor on the bottom jaw (b) placement of the peg on sensing surface (c) top jaw applying pressure on the sensor

that each sensor has performed differently; different percentage values were observed. Also the results obtained using this method were different to the results obtained using the standard weight calibration method recommended by the sensor manufacturer. The results obtained for both calibration systems (use of standard weights and Zwicki[®]) for one FlexiForce[®] sensor is shown in Fig. 3.7 and the results

for the other sensors are included in Appendix A.

Also a linear relationship between the percent values recorded by the software and the pressure applied on to the sensor (calibrated from equation 3.4), could not be observed for most of the sensors in both the calibration systems used. As depicted in Fig. 3.7, the calibration points showed a considerable difference to each other for both the calibration methods adopted. This difference was much higher at the higher applied pressure values, comparatively to lower applied pressures. The sensor to sensor variation in calibration points existed in both the calibration methods, and the maximum variation was more than 10% in the Zwicky[®] calibrated sensors. However, as depicted in the Fig.3.7, the Zwicky[®] calibration have shown a better linearity in sensor 1 compared to the calibration obtained for it using standard weights.

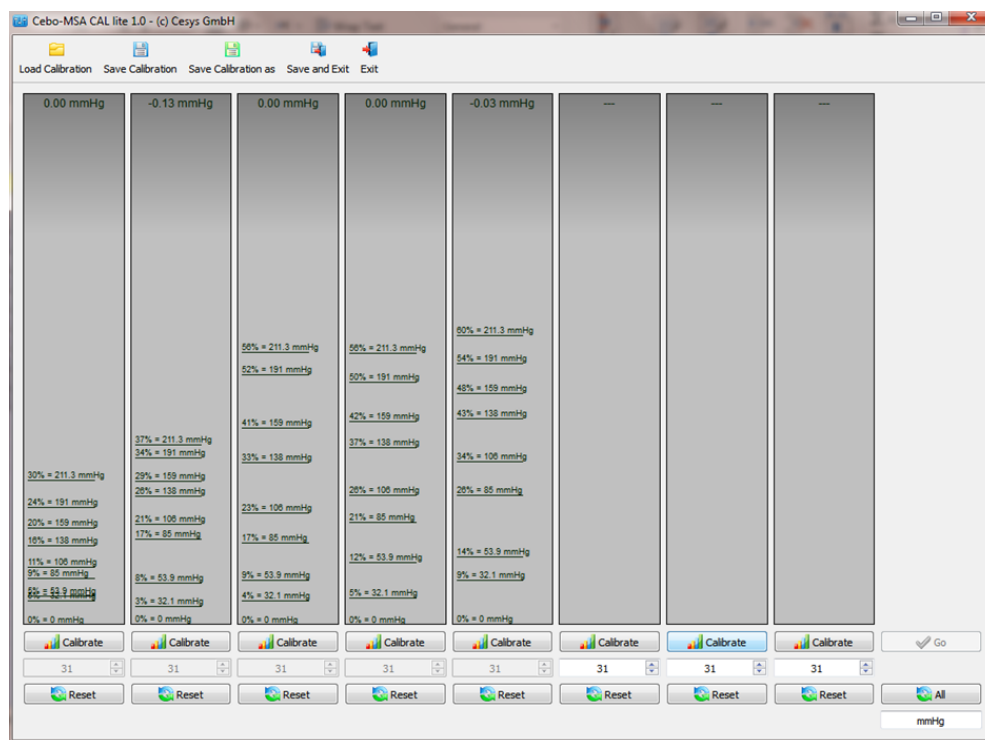


Fig. 3.6 MSA-CAL lite 1.0 software calibration file for the calibration carried out using Zwicky[®] tester

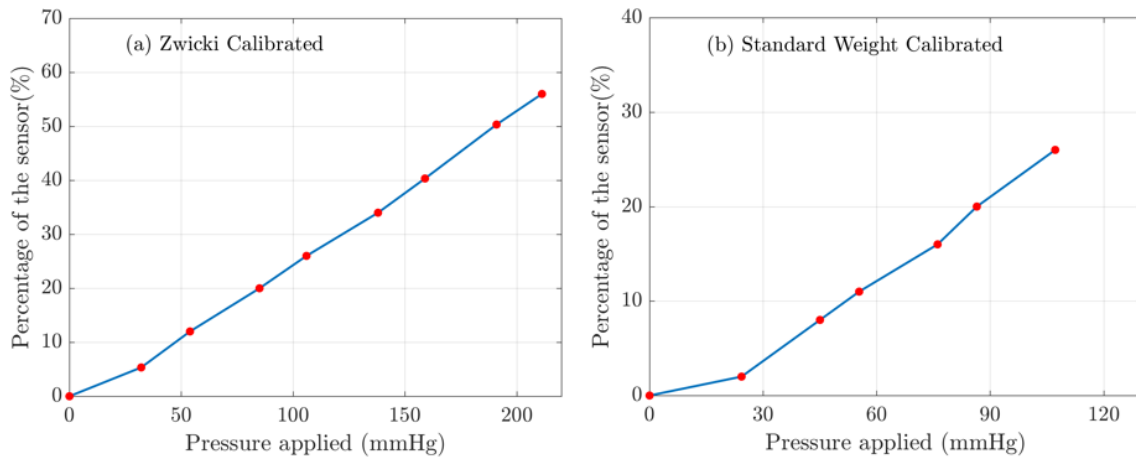


Fig. 3.7 The percent values recorded by the software (% of the calibration bar) against the applied pressure used in the calibration for the sensor 1. (a) Zwicky® tester calibrated (b) Standard weight calibrated

As such it was decided to conduct further tests to understand whether the discrepancies in the above results were associated with the design and manufacture of these sensors, or due to the inaccuracies in the calibration method or the data acquisition system (CEBO-MSA 64 multi sensor measurement box) supplied by CESYS (CESYS, 2017). It was decided to test all the four sensors against a liquid column manometer, which is considered as the gold standard for the pressure measurement. The calibration against the manometer would provide a better understanding on the sensor behaviour, while providing an extra validation for the sensor calibration.

3.3.3 Evaluation of FlexiForce® sensors against the manometer)

The validation of the FlexiForce® sensors was carried out using a vertical liquid column manometer TJ600, measuring range 0 – 130 mbar, filled with Volt 1S manometer liquid of 1.86 gcm^{-3} density (KIMO Instruments, Kent, UK). The test apparatus used in the calibration process is shown in Fig. 3.8. The concept of the test method was to apply a pressure using an inflatable bladder. The bladder was positioned inside a wooden box and inflated by a hand operated air-pump and the pressure inside the bladder was measured with the liquid manometer which was connected in series with the air-pump. The principle behind this experimental set up is that a pressure will be applied to the sensor due to the expansion of the bladder when a volume of air is pumped into the bladder. It was presumed that the pressure inside the bladder to be equivalent to the external pressure applied to the FlexiForce® sensor. The sensor was placed in the middle of the bladder avoiding the shape deformation of the bladder at the edges, thus eliminating possible errors caused due to irregularity of the inflation of the bladder. Hence, it was assumed that a uniform pressure was applied over the sensor surface due to the inflation of the bladder.

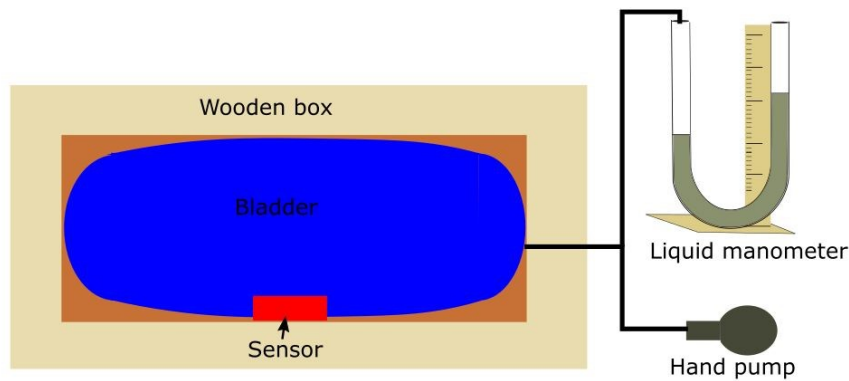


Fig. 3.8 Schematic diagram for the experimental setup for re-calibration (validation) of sensor readings against manometer.

The bladder was inflated in steps of 10 mbars (7.5 mmHg), starting from a pressure of 0 mbar (0 mmHg) up to a pressure of 115 mbar (86.26 mmHg) and the corresponding pressure readings of the sensor was recorded using the CEBO MSA DAQ lite 1.0 software (data acquisition mode of the CEBO software). The above procedure was repeated three times for each sensor, and the average of the readings was calculated. This analysis was repeated for both calibration files obtained from standard weight calibration, and Zwicky[®] calibration. The results for two FlexiForce[®] sensors from the same batch for each calibration set are shown in Figs.3.9 and 3.10, respectively (the figures for other sensors are included in the Appendix A).

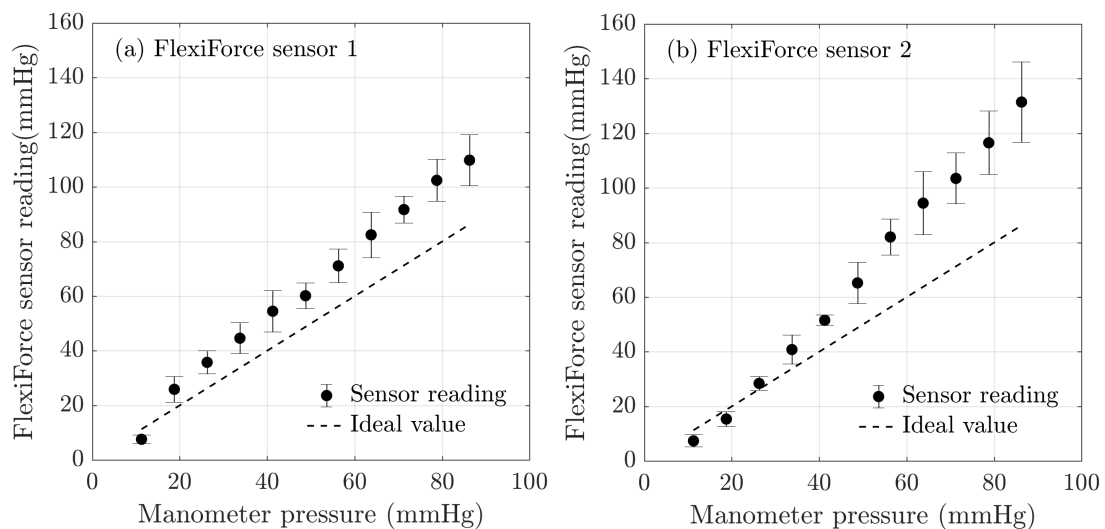


Fig. 3.9 The results obtained using the bladder test, validation of FlexiForce[®] sensors readings against the manometer reading (Standard weight calibrated). The error bars represent the 95% confidence interval.

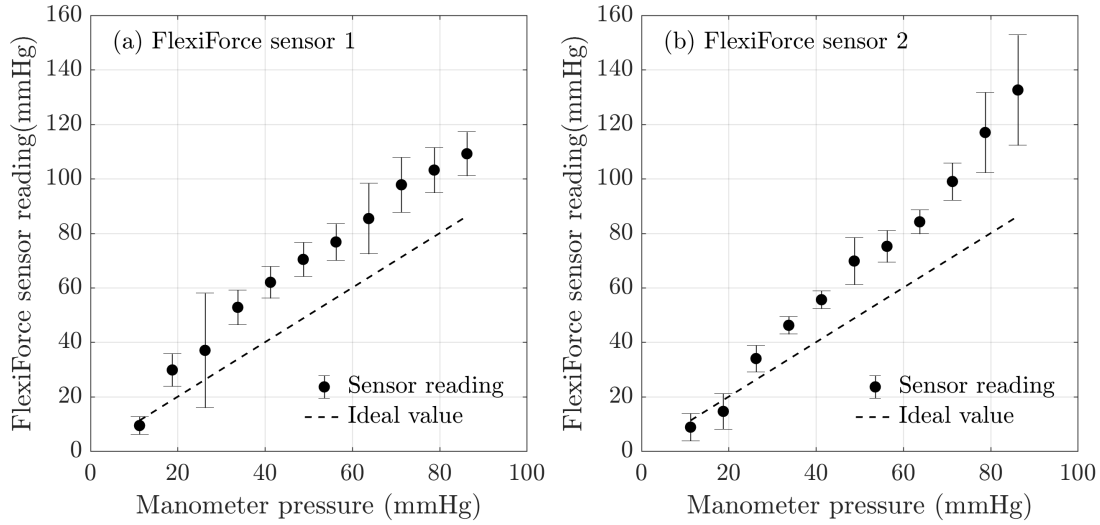


Fig. 3.10 The results obtained using the bladder test, validation of FlexiForce[®] sensors readings against the manometer reading (Zwicky[®] tester calibrated). The error bars represent the 95% confidence interval.

As it can be seen from the Figs. 3.9 and 3.10, the pressure sensor readings have deviated highly from the ideal line, making it clear that the sensors display a huge error in their reading. It was also evident that there exists a large variation of the sensor measured pressured from the ideal line in the high pressure regions. In both calibrations, the measured sensor values have overestimated the pressure readings on average by more than 15 mmHg. This margin of overestimation of pressure values could draw wrong conclusions in the proposed research.

It was important to quantify the repeatability error for each sensor, as the proposed active compression system required frequent, periodic pressure measurements. Generally, the repeatability error is used to quantify the ability of a measurement system to provide the same result for repeated measurements (Al Khaburi, 2010; Bolton, 1996). It can be calculated as expressed in equation 3.5 (Al Khaburi, 2010). According to the equation 3.5, the repeatability error was also calculated for the FlexiForce[®] sensors and included in the Table 3.3

$$\text{Repeatability error} = \text{average} \left(\frac{1.96 \times SD(\text{output})}{FS(\text{output}) \times 100} \right) + \left[t \times SE \left(\frac{1.96 \times SD(\text{output})}{FS(\text{output}) \times 100} \right) \right] \quad (3.5)$$

where,

SD- Standard deviation

FS (output)- Full scale (Maximum output value recorded during the calibration)

SE- Standard error ($SE = SD/\sqrt{n}$), where *n* is equal to the number of readings

t- *t* value from the ‘*t*-distribution’, for 95% confidence interval

Non-linearity error is defined as the error that occurs as a result of assuming a linear relationship between the input and the output over the working range (Bolton, 1996). Non-linearity error is also often defined as a maximum non-linearity which could lead to incorrect information caused due to an outlier of data (Dunn, 2014). Hence, in this study the non-linearity error was calculated for the full span as defined in equation 3.6 (Al Khaburi, 2010). The non-linearity error was calculated for these sensors, and have summarised the results in the Table 3.3.

$$\text{nonlinearity error} = \text{average} \left(\frac{|\text{actual output} - \text{ideal output}|}{FS(\text{out put})} \times 100 \right) + \left[t \times SE \left(\frac{|\text{actual output} - \text{ideal output}|}{FS(\text{out put})} \right) \times 100 \right] \quad (3.6)$$

Tekscan[®] claims that the sensor's non linearity error is less than $\pm 3\%$ FS (Full Span) and repeatability error is less than $\pm 2.5\%$ FS (Full Span) (Tekscan[®], 2018). It can be seen from the results in Table 3.3, that the FlexiForce[®] sensors have shown a higher repeatability error percentage than specified by the manufacturer. Also, it can be observed from Table 3.3, that the relationship existed with the manometer readings have shown a huge non-linearity error; on average above 20% which is almost 7 times than the manufacturer's claimed percentage. However, it was decided to test few more sensors of the same type before making the conclusion that it is an inherent disadvantage of the FlexiForce[®] sensor.

Table 3.3 Repeatability and non-linearity error (%) for FlexiForce[®] sensors of batch 1

FlexiForce (FF) sensor	Repeatability error (%)		Non-linearity	
	Standard weight calibration	Zwicki calibration	Standard weight calibration	Zwicki calibration
FF-Sensor 1	7.49	12.26	15.82	19.65
FF-Sensor 2	9.51	10.71	20.86	19.69
FF-Sensor 3	6.87	8.36	20.19	45.19
FF-Sensor 4	6.59	8.01	13.85	14.11

Both sides of the FlexiForce[®] sensor can be used to measure pressure. As such the two sides of each sensor were validated using the procedure described earlier, which would be referred to as manometer test method in the thesis. The results for two FlexiForce[®] sensors obtained by using standard weight and Zwicki[®] tester calibration data are shown in Fig. 3.11 and 3.12 respectively. It is evident from the data that the difference of the recorded pressure value for face and reverse side of the sensor were insignificant (results of all four sensors are included in the Appendix A).

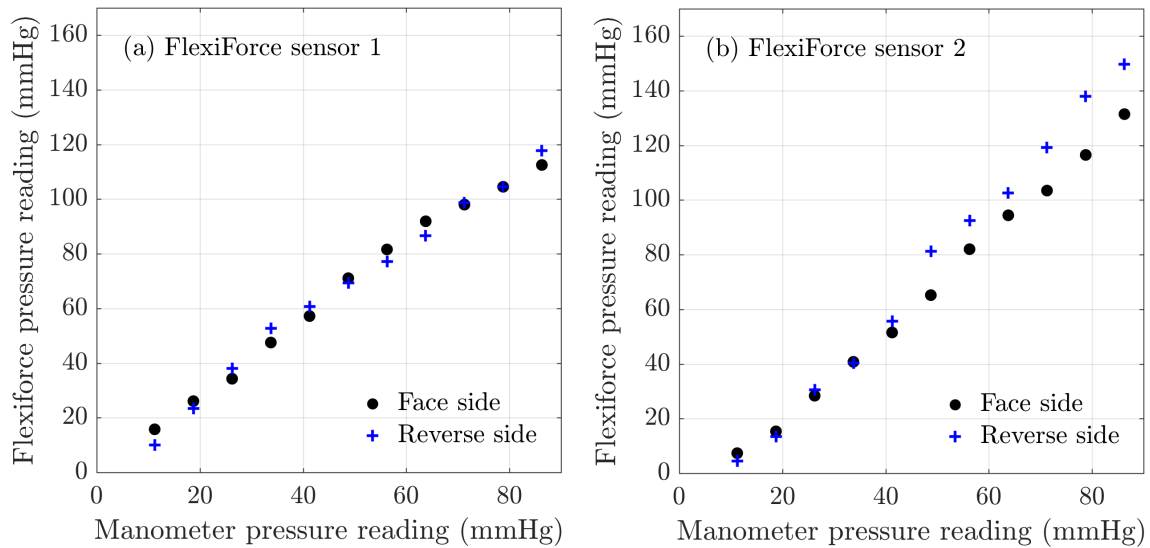


Fig. 3.11 The results obtained for the face and reverse side of the FlexiForce[®] sensors readings against the manometer reading (Standard weight calibrated).

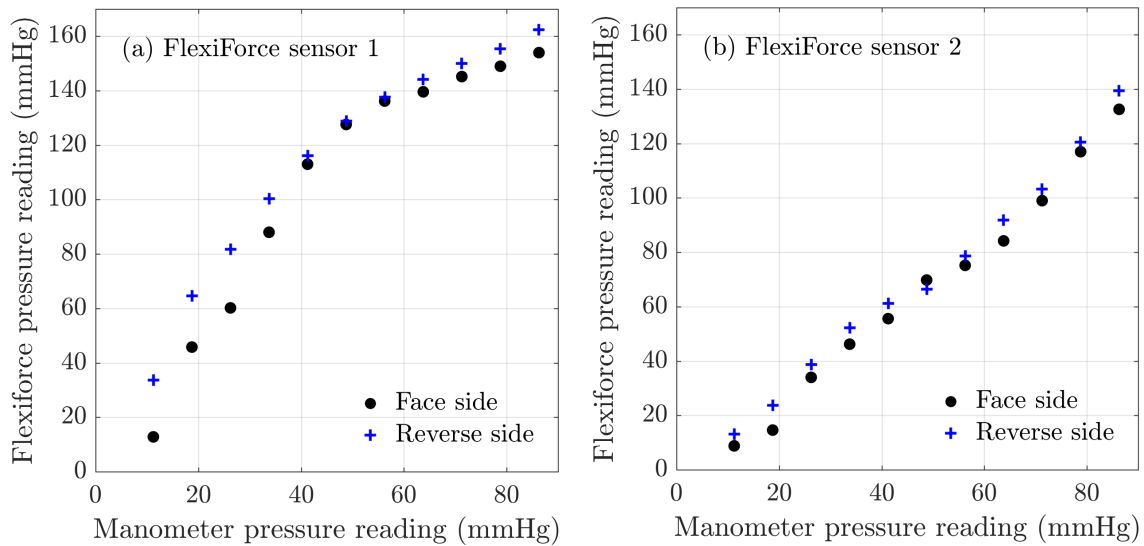


Fig. 3.12 The results obtained for the face and reverse side of the FlexiForce[®] sensors readings against the manometer reading (Zwicki[®] tester calibrated).

Calibration of the second batch of five FlexiForce® sensors

Due to the variations observed with the five sensors tested it was decided to purchase new set of five FlexiForce® sensors and evaluate them. The new five sensors were calibrated using the standard weight method described in the section 3.3.1, and calibration data was used in the data acquisition mode of the software.

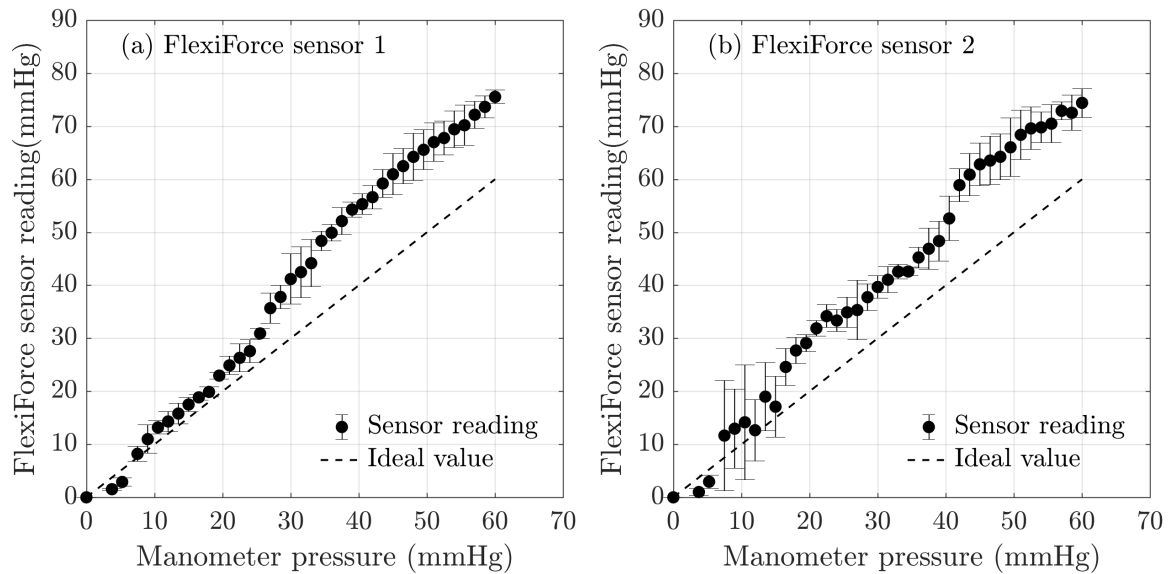


Fig. 3.13 The results obtained using the bladder test, validation of FlexiForce® sensor (2nd batch) readings against the manometer reading (standard weight calibration). The error bars represent the 95% confidence interval.

These sensors were then evaluated against the manometer as described in the section 3.3.3, and the results for two of the new set of sensors are shown in Fig. 3.13 (results for all five sensors are included in Appendix A. The bladder was inflated in steps of 2 mbar (1.5 mmHg), starting from a pressure of 0 mbar (0 mmHg) up to a pressure of 80 mbar (60 mmHg). Then, the repeatability error was calculated for these sensors as per the equation 3.5 and the results were tabulated in Table 3.4. Although the repeatability error was higher than the manufacturer specified value for the new set of sensors, the values were comparatively lower than the previous set of sensors. However, the pressures recorded with the new set of sensors were higher compared to the manometer readings as can be seen from Fig. 3.13. The dashed line in Fig 3.13 shows the correct reading that sensor should read to match with the manometer reading, which clearly indicates that the sensor is over-estimating the pressure value. It was also evident from Fig. 3.13 that the relationship between the manometer reading and the sensor reading could be hardly deduced to a linear relationship. The calibration curve for the manometer and the sensors has shown a quadratic relationship, which would make it difficult for detailed analysis required for the research. The evaluation of the sensors also demonstrated that the FlexiForce® sensors have a higher repeatability error than the value specified by the manufacturer and recorded overrated pressure values. It was also evident that individual FlexiForce® sensors exhibited significant

Table 3.4 Mean repeatability error for the 2nd batch of FlexiForce[®] sensors

Second batch of FlexiForce [®] sensors	Mean repeatability error (%)
FF-Sensor 1	2.98
FF-Sensor 2	4.97
FF-Sensor 3	4.98
FF-Sensor 4	4.16
FF-Sensor 5	3.30

variations, which could lead to errors when measuring pressure at different points simultaneously. It could be noted that there existed a significant variation from batch to batch in these FlexiForce[®] sensors, this could also lead to errors of measuring pressures simultaneously, using more than five sensors. Since both the repeatability and non-linearity error percentages obtained were significantly higher than the manufacturer specified values and also the batch to batch variation existed for the sensors were also higher, it was decided that these sensors are not suitable for this application. Hence, the hysteresis error was not calculated for these sensors.

As per the results obtained from the validation of FlexiForce[®] sensors with the liquid manometer, it was evident that the pressure readings were highly non-linear and always overrated. The pattern described above existed for all the sensors tested, and this was communicated to the manufacturer of hardware CESYS GmbH, Germany (CEBO-MSA 64 multi sensor measurement box). Although their recommendation to address the issue was implemented (email communications given in Appendix A, an improvement in pressure measurement could not be observed. Another shortcoming of the FlexiForce[®] sensors was that any bending of the sensors gave faulty readings. Due to all the above shortcomings of the FlexiForce[®] sensors it was decided not to utilise these for measuring interface pressure in this study.

3.4 Study of AMI Sensors for Interface Pressure Measurement

3.4.1 Calibration of AMI sensors

The AMI pressure measurement system consists of pneumatic sensors (AMI 3037 air-pack sensors $\phi=20\text{mm}$, AMI Techno, Japan) and the control unit (Model: A0905-SA-35k, AMI Techno, Japan). The AMI air-pack sensors were calibrated according to the procedure recommended by the equipment manufacturer. This method was used in calibrating the AMI sensors to evaluate whether there exists a large difference in the calibrated readings accordance with the specified accuracy by the manufacturer. The calibration procedure is described below as specified by the manufacturer (the full calibration manual is included in Appendix A).

3.4.2 Calibration of the main unit and Air-pack sensor

A schematic of the calibration set up specified by the manufacturer is shown in the Fig. 3.14. The cylinder (A) shown in the Fig. 3.14 (a), was filled with warm water (20° ~ 30° C) up to the red line level (B) marked on the cylinder Fig.3.14 (b). The water temperature below 20° C should not be used, as the accuracy values specified by the manufacturer would be only valid in the given temperature range. The air pack sensor (C) was mounted on to the bottom plate of the T-shaped bar (D) as shown in Fig. 3.14 (c). Then, the air pack sensor (C) was inflated, using the main unit and the T-shaped bar (D) was submerged into the cylinder (A). The water depth was measured using the scale (E) printed inside the T-shaped bar (D). At the same time the corresponding pressure reading indicated on the main unit was also obtained. Thereafter this measured water depth was converted into mmHg pressure using the equation 3.7 and the “calculated pressure” values were obtained. This procedure was repeated for three times for each sensor, and the mean “calculated pressure” values and the mean “displayed pressure” values were obtained for each sensor. The obtained calibration results are tabulated in Table 3.5.

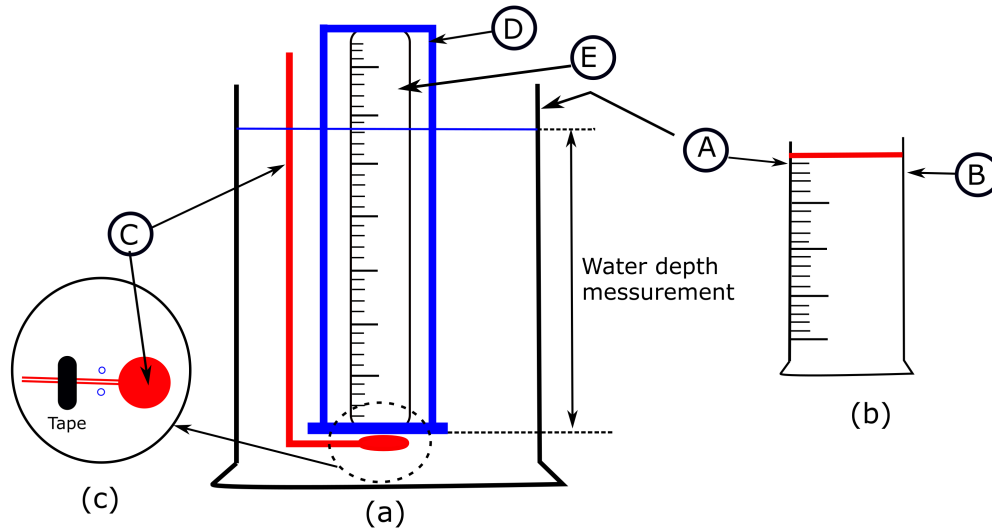


Fig. 3.14 (a) The schematic diagram of the calibration setup for main unit and air-pack sensor (b) water level marked in the cylinder (c) placement of the AMI air-pack sensor on the bottom plate of T-shaped bar. (A)- cylinder (B)- red level marked on the cylinder (C) AMI air-pack sensor (D) T-shaped bar (E) scale printed inside the T-shaped bar.

$$\text{Measured Pressure (mmHg)} = \left(\frac{7.5}{102} \right) \times \text{measured water depth (mm)} \quad (3.7)$$

where, 102mm H₂O = 7.5 mmHg

Table 3.5 Calibration of AMI sensors

Sensor	Measured water depth (mm)	Calculated pressure value (mmHg)	Displayed pressure value in main unit (mmHg)	Accuracy (mmHg) [Manufacturer specified]
First batch				
1	407	29.93	31	+/(0.75-1.5)
2	408	30.00	31	+/(0.75-1.5)
3	408	30.00	30	+/(0.75-1.5)
4	407	29.93	30	+/(0.75-1.5)
5	408	30.00	31	+/(0.75-1.5)
Second batch				
1	407	29.93	30	+/(0.75-1.5)
2	408	30.00	30	+/(0.75-1.5)
3	408	31.00	30	+/(0.75-1.5)
4	408	30.00	30	+/(0.75-1.5)

Only one air-pack sensor could be connected to the control unit; as such all the air-pack sensors were calibrated sequentially. As it is important to measure the pressure at different points during this study it was required to obtain at least eight sensors; where the pressures were required to be measured at anterior, posterior, lateral and medial position on the skin surface and inside the fat layers. Hence, it was decided to get two batches of AMI air pack sensors, as the batch to batch variations that could exist in these sensors could also be evaluated.

As it can be observed from the Table 3.5, the accuracy values specified by the manufacturer is in the range of $\pm 0.75 - 1.5$ mmHg from the displayed pressure value in the main unit. The maximum variation existed in the sensors was about 1 mmHg, which shows that the calculated pressure values are in the range of the displayed pressure in the main unit. Therefore, the sensors could be used for further measurement since the calibration was successfully performed.

3.4.3 Evaluation of AMI air-pack sensors against the manometer

After calibration the AMI interface pressure system was evaluated against a manometer using the method described in section 3.3.3. The bladder was inflated in steps of 2.0 mbars (1.5 mmHg), starting from a pressure of zero mbar (0 mmHg) up to a pressure of 80.0 mbar (60.0 mmHg). Also, after the bladder was inflated up to a pressure of 80.0 mbar (60.0 mmHg), then it was deflated in steps of 2.0 bars (1.5mmHg) to test the hysteresis of the sensors. The validation step enabled a relationship between the air-pack sensor (display value of the control unit) and the manometer reading

to be obtained. The results for two AMI air-pack sensors for both inflation and the deflation cycles were plotted against the manometer pressure and is shown in Fig. 3.15 (results for other sensors are included in Appendix A. Also as shown in Fig. 3.16, a linear relationship between the air-pack sensor reading and the manometer reading is evident from the results. In comparison with the FlexiForce[®] sensors the AMI air-pack sensors demonstrated a higher accuracy, i.e. the error between the sensor and manometer readings were less with the AMI pressure measurement system. The repeatability errors for AMI sensors were also calculated using the equation 3.5, and the results are tabulated in Table 3.7. The repeatability error for AMI sensors was lower compared to the FlexiForce[®] sensors. Therefore, Air-pack sensors were more suitable for the research despite somewhat larger sensing area of the AMI air-pack sensor (the area of AMI air-pack sensors is 314mm^2 while the FlexiForce[®] sensors have 71mm^2 sensing area). Also the air-pack sensors showed a low repeatability error between sensors (see Table 3.7) Because of the favourable results, it was decided to further investigate on the hysteresis error and the non-linearity error of the AMI Air-pack sensors. The hysteresis error is defined as the difference in the output for the same value of the quantity being measured according to whether that value has been reached by continuously increasing change or decreasing change (Al Khaburi, 2010; Bolton, 1996). The hysteresis error is often quantified in terms of maximum hysteresis expressed as percentage of full scale of the output (Dunn, 2014). However, this calculation can give wrong information due to the presence of outlier data, thus the equation 3.8 was adopted (Al Khaburi, 2010) to determine the hysteresis error in the present study.

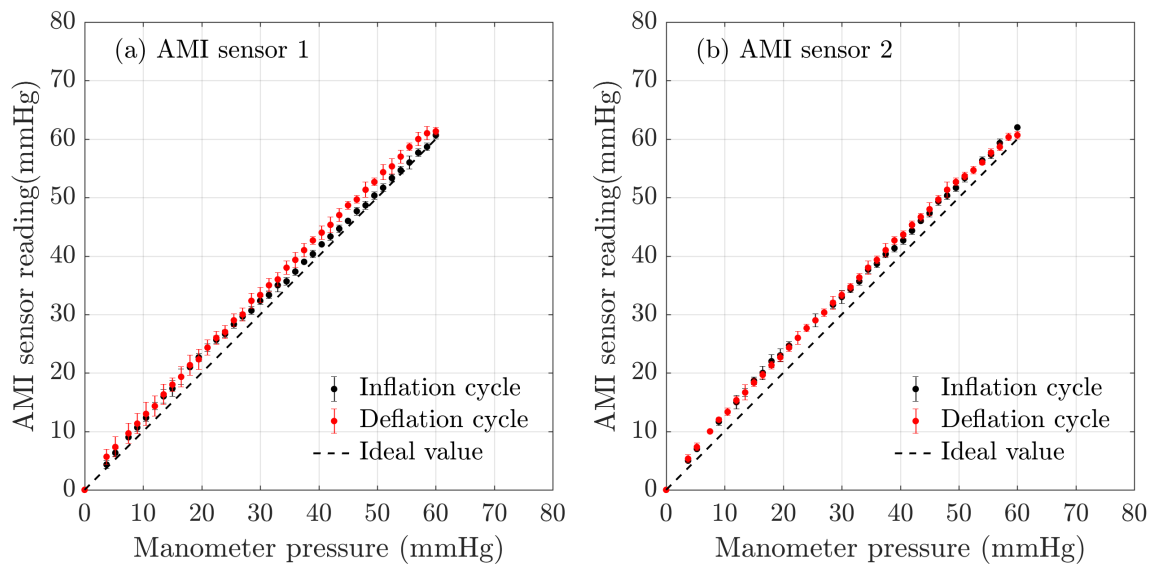


Fig. 3.15 The results obtained using the bladder test, validation of AMI air-pack sensor readings against the manometer reading for inflation and deflation cycles. The error bars represent the 95% confidence interval.

The hysteresis error was calculated for all the AMI air-pack sensors as discussed above, and the results obtained were tabulated in Table 3.7. It can be observed that the hysteresis error for these sensors

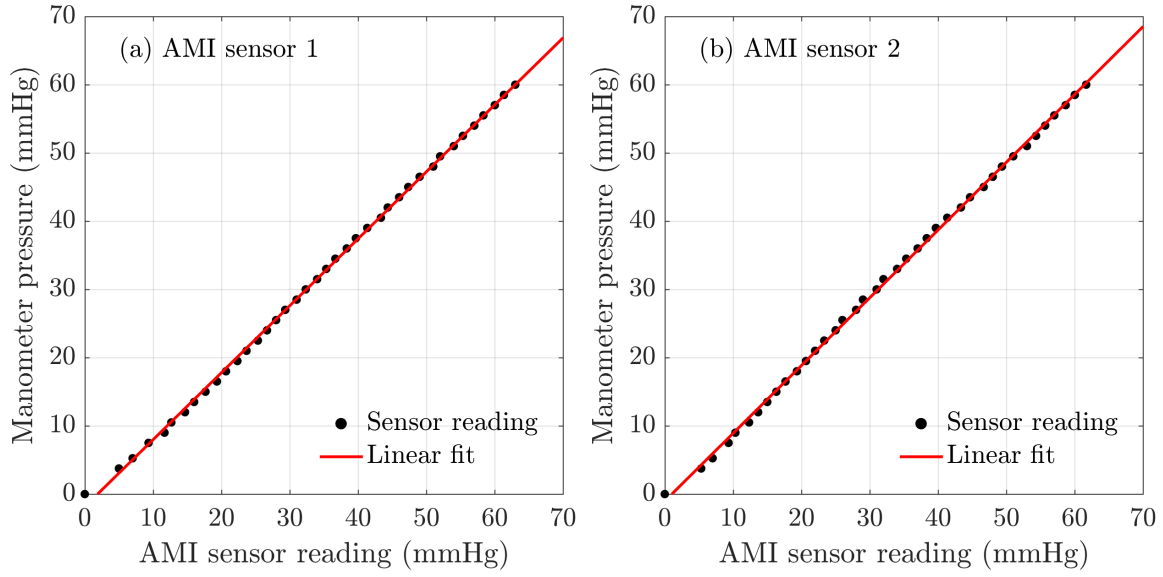


Fig. 3.16 Validation of AMI air-pack sensors readings against the manometer reading-linearity relationship plot for the inflation cycle

were also low except for the sensor 5 of the first batch; which recorded 4.19 %. However, all the other sensors have shown a hysteresis error percentage lower than 3 %. Hence, the sensor 5 could be omitted from the subsequent pressure measurements carried out during this research.

$$\text{hysteresis error} = \text{average} \left(\frac{|\text{loading output} - \text{unloading output}|}{FS(\text{output})} \times 100 \right) + \left[t \times SE \left(\frac{|\text{loading output} - \text{unloading output}|}{FS(\text{output})} \right) \times 100 \right] \quad (3.8)$$

The above analysis demonstrated that AMI pressure measuring system could be used for subsequent pressure measurement experiments of the research. However, there were only five air-pack sensors were available for the analysis and it was envisaged that at least eight sensors would be required for the research. Therefore, a new batch of four air-pack sensors were purchased and calibrated as described in the section 3.4.2 and validated against the manometer as described in section 3.4.3; the test results for two air-pack sensors are shown in Fig. 3.17 and 3.18, where Fig. 3.18 depicts the linear relationship obtained (results of all the sensors are included in Appendix A. The linear relationships with the manometer readings, for all the air-pack sensors (both batch 1 and 2) are given in the Table 3.7. As the manometer is considered to be the gold standard for the pressure measurement by the medical community and medical device manufacturers, these relationships have been used to correct the pressure sensor readings obtained in future experiments carried out for interface pressure measurement.

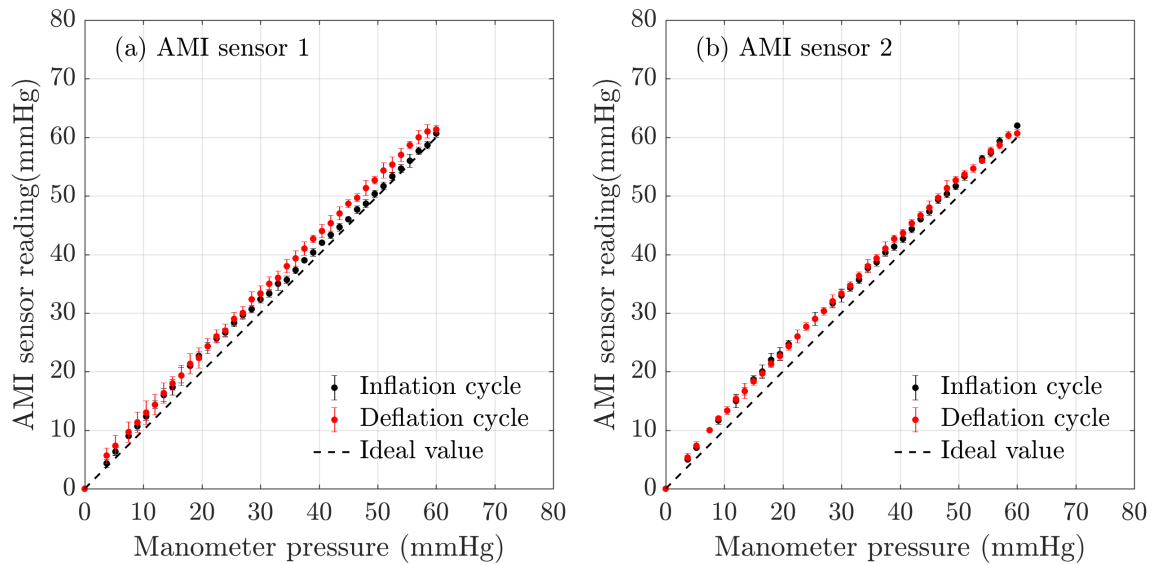


Fig. 3.17 The results obtained using the bladder test, validation of AMI air-pack sensors readings against the manometer reading inflation and deflation cycles for the second batch of sensors. The error bars represent the 95% confidence interval.

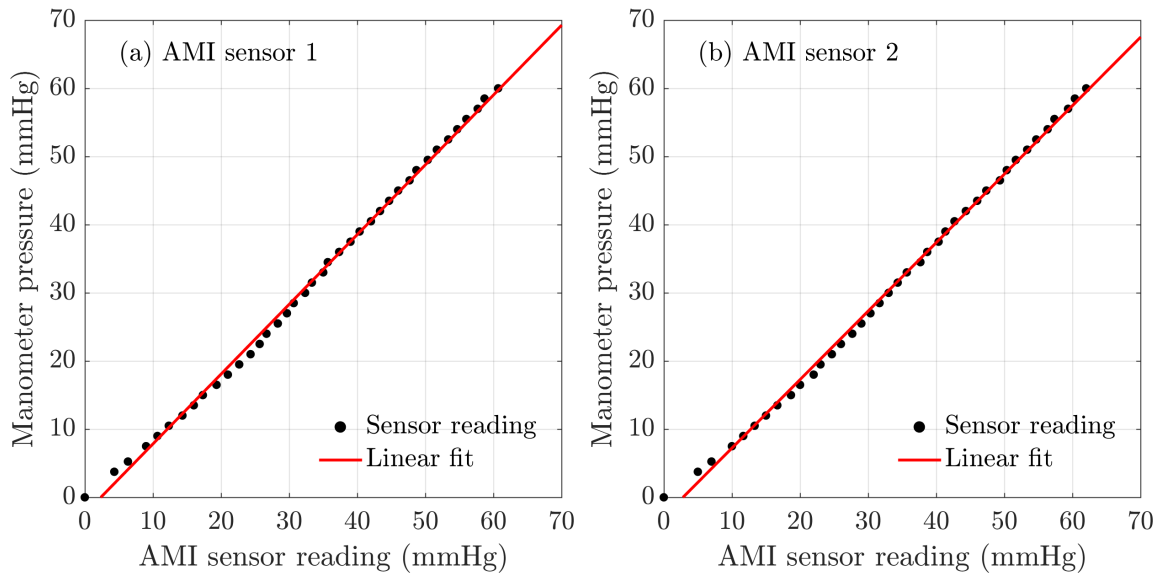


Fig. 3.18 Validation of second batch of AMI air-pack sensors readings against the manometer reading-linearity plot.

Table 3.6 Linear relationships obtained for different AMI air-pack sensors and their statistical analysis

AMI sensor	Linear relationship $P_{Manometer} = a \times P_{Sensor} + b$	R^2	RMSE
First batch of sensors			
Sensor 1	$P_{Manometer} = 0.9818 \times P_{Sensor} - 1.843$	0.9993	0.452
Sensor 2	$P_{Manometer} = 0.9983 \times P_{Sensor} - 1.667$	0.9979	0.808
Sensor 3	$P_{Manometer} = 0.9955 \times P_{Sensor} - 1.814$	0.9992	0.501
Sensor 4	$P_{Manometer} = 0.9884 \times P_{Sensor} - 1.341$	0.9997	0.296
Sensor 5	$P_{Manometer} = 0.9937 \times P_{Sensor} - 1.031$	0.9994	0.446
Second batch of sensors			
Sensor 1	$P_{Manometer} = 1.024 \times P_{Sensor} - 2.414$	0.9977	0.833
Sensor 2	$P_{Manometer} = 1.005 \times P_{Sensor} - 2.836$	0.9981	0.774
Sensor 3	$P_{Manometer} = 0.9915 \times P_{Sensor} - 2.868$	0.9982	0.738
Sensor 4	$P_{Manometer} = 0.9982 \times P_{Sensor} - 2.600$	0.9972	0.924

The mean non-linearity errors obtained for these sensors are tabulated in Table 3.8 below along with their repeatability and hysteresis errors for a better comparison. It could be noted from the results listed in Table 3.8, the AMI Air pack sensors have shown a very low non-linearity error (%); which was less than 1.5%. This shows that the AMI sensors have shown a better linearity than the FlexiForce[®] sensors. These sensors have also reported very low repeatability error (%) than the FlexiForce[®] sensors making it more suitable for the application.

Accuracy of a measurement system can be defined as the extent to which the readings provided by the system might be wrong and can be quantified by summing all the possible errors that are likely to occur (Al Khaburi, 2010; Bolton, 1996). The error can be summed up using the general equation given as equation 3.9 (Al Khaburi, 2010; Bolton, 1996).

$$\Delta Z = \sqrt{\sum (\Delta A_i)^2} \quad (3.9)$$

where, ΔZ = total error, ΔA_i = error

Hence, the reported accuracy of the AMI air-pack sensors could be defined as the combination of errors of repeatability, non-linearity and hysteresis. The calculated accuracy values for the AMI air-pack sensors were tabulated in the Table 3.7.

As it can be seen from the results shown in Table 3.8, the AMI sensors have shown an average accuracy of ± 2.2 mmHg, and all the sensors have shown an accuracy less than ± 3 mmHg. Although the manufacturer's specified accuracy for the sensor is ± 1.5 mmHg at 23 °C, it was shown from the results that actual accuracy is slightly lower than the manufacturer specified value. However, comparatively all the tested AMI air-pack sensors have shown a close approximation to the manufacturer's specified

Table 3.7 Mean non-linearity error (%), mean repeatability error (%) and mean hysteresis error (%) for the two batches of AMI air-pack sensors used.

AMI sensors	non-linearity error (%)	repeatability error (%)	hysteresis error (%)
First batch of sensors			
Sensor 1	1.22	3.62	2.37
Sensor 2	0.52	1.48	1.60
Sensor 3	0.64	2.60	3.39
Sensor 4	0.31	2.00	3.18
Sensor 5	0.66	1.61	4.19
Second batch of sensors			
Sensor 1	1.17	2.08	2.69
Sensor 2	0.97	2.08	0.91
Sensor 3	0.88	3.07	1.39
Sensor 4	1.27	2.67	1.91

Table 3.8 Mean non-linearity error (%), and mean repeatability error (%), mean hysteresis error (%) and accuracy for different AMI air-pack sensors

AMI sensors	Non-linearity error (%)=A	repeatability error (%)=B	Hysteresis error (%)=C	Accuracy (%)	Accuracy \times Full Span (mmHg)
1st batch					
Sensor 1	1.22	3.62	2.37	4.50	2.67
Sensor 2	0.52	1.48	1.6	2.24	1.41
Sensor 3	0.64	2.60	3.39	4.32	2.65
Sensor 4	0.31	2.00	3.18	3.77	2.35
Sensor 5	0.66	1.61	4.19	4.54	2.80
2nd batch					
Sensor 1	1.17	2.08	2.69	3.60	2.18
Sensor 2	0.97	2.08	0.91	2.47	1.53
Sensor 3	0.88	3.07	1.39	3.48	2.19
Sensor 4	1.27	2.67	1.91	3.52	2.19

accuracy.

When measuring skin interface pressure the sensors would be in contact with the human body, where the temperature is around 37 °C. Since the AMI air-pack sensors are calibrated using 20 – 30 °C warm water which is less than the human body temperature one could argue that a measurement error is evident, which can be explained with "Combined Gas Law" shown in equation 3.10

$$\frac{PV}{T} = k \quad (3.10)$$

where,

P = Pressure (N/m²),

T = Temperature (K),

V = Volume (m³)

However, as mentioned in the section 2.3.2, the sensors have reportedly shown a very low sensitivity (0.1kPa) to temperature change of 40 °C. Furthermore, in comparison to standard testing environment, temperature change in real testing environment would only be a maximum of 7 – 10 °C, where the impact could consider to be negligible.

3.4.4 Study of PicoPress[®] sensors against the manometer

As specified by the manufacturer PicoPress[®] sensors need not to be calibrated before the use of measurement (Microlab-Electronica, 2014). Thereafter, similar to the above discussed validation procedure for FlexiForce[®] and AMI sensors, PicoPress[®] sensor (Microlab Electronica, Ponte S. Nico PD, Italy) was also calibrated against the manometer and the obtained results are shown in Fig. 3.19 and 3.20. The figures show that the PicoPress[®] sensor readings demonstrated a very good agreement with the manometer data, and a linear relationship. The calculated non-linearity errors and the repeatability errors are tabulated in Table 3.9. Of all the three pressure measuring systems studied, PicoPress pressure measuring system had the lowest repeatability and nonlinearity errors, demonstrating that it was the most reliable pressure measurement system.

Table 3.9 Mean non-linearity error (%) and mean repeatability error (%) for different PicoPress[®] sensors

PicoPress [®] sensors	non-linearity error (%)	repeatability error (%)
Sensor 1	0.57	0.84
Sensor 2	0.81	0.73

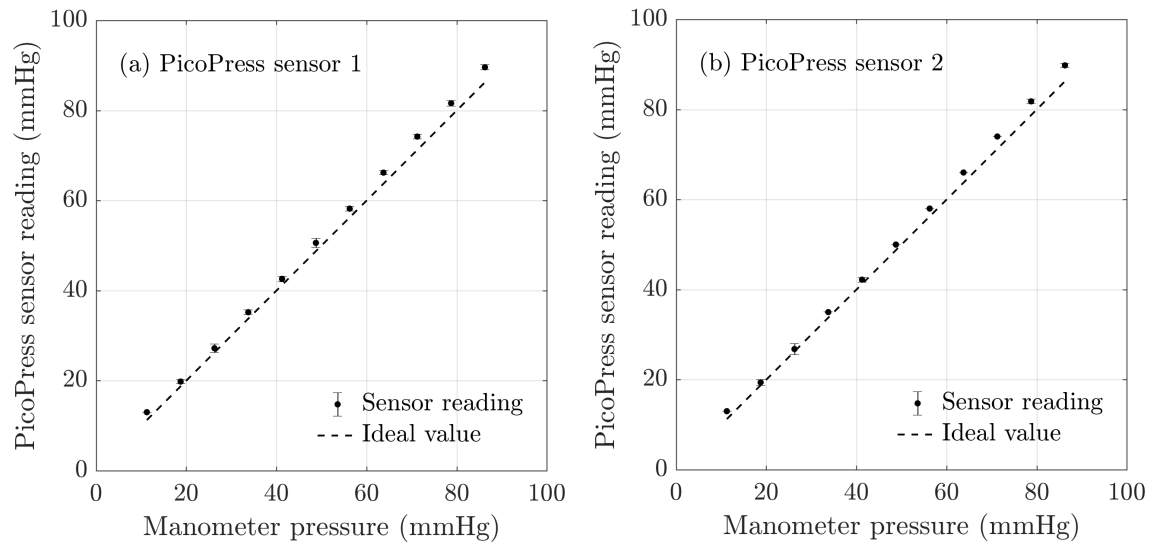


Fig. 3.19 The results obtained using the bladder test, validation of two PicoPress® sensor readings against the manometer reading. The error bars represent the 95% confidence interval.

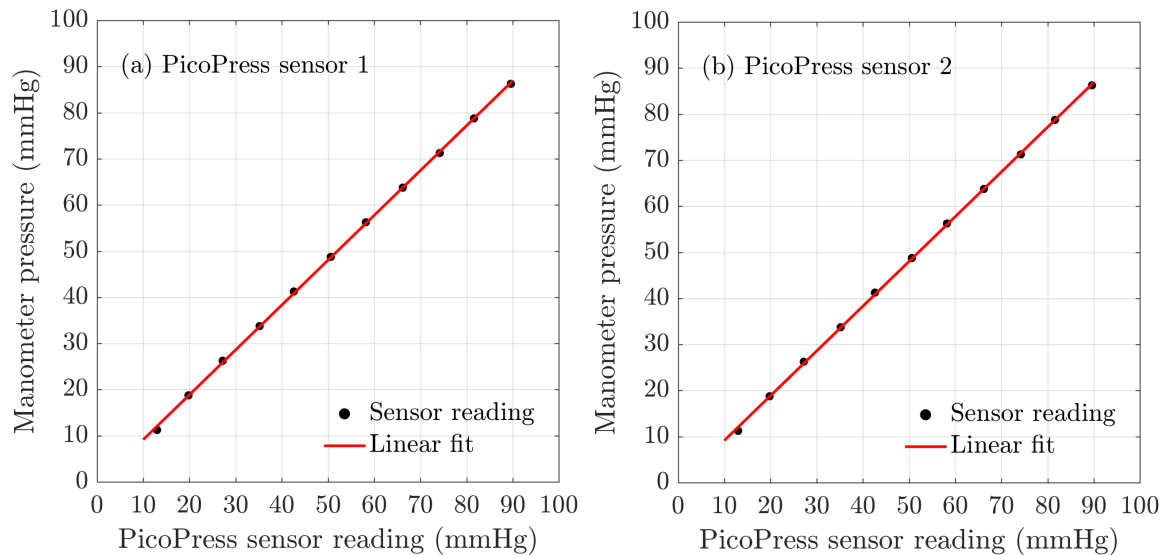


Fig. 3.20 The results obtained using the bladder test, validation of two PicoPress® sensor readings against the manometer reading-linearity relationship plot

3.5 Selection of a suitable pressure sensor

The selection of the interface pressure measuring system for the research of developing an active compression system, the following criteria had to be considered:

- a. the sensor dimensions must be compatible with the dimensions of the mini-bladders used to create the active compression;
- b. higher repeatability of the sensor data;
- c. good linearity of the sensor data;
- d. low hysteresis.

As described above, among the available pressure measurement systems it was evident that even though the FlexiForce[®] sensors were the most compatible sensor with the dimensions of a mini-bladder, its performance was not that accurate compared to the other two tested interface pressure measurement systems. Even though several methods of calibration were considered, repeatability errors as high as 12% (Table 3.3) were observed during the validation of FlexiForce sensors against the manometer. It was also observed that obtaining a linear relationship between the manometer reading and the sensor reading led to higher non-linearity errors, and the data had to be fitted on to a higher degree polynomial in order to obtain a good fit. This is a disadvantage as the calibration step would require a complex relationship that would make it challenging for the further procession of the data. Also a significant variation between the FlexiForce[®] sensors were observed which could result in errors when measuring interface pressure simultaneously at different positions as demanded by the research. The validation of the sensors against the manometer showed that FlexiForce[®] sensors recorded overstated pressure values. In comparison of the repeatability the best results were noted for PicoPress[®] sensors. The repeatability error as low as 0.84%. The study of the three pressure measurement systems showed that the most reliable results against the validation with manometer were obtained with PicoPress[®] sensors. However, PicoPress[®] sensors have a relatively large sensor area of 1964mm^2 (circular geometry of diameter of 50 mm). As hexagonal mini-bladders were designed, with side length of 11 mm (contact areas equivalent to 314mm^2) to create the active pressure PicoPress[®] sensors were too large to be used in the research. Therefore, AMI air-pack sensors with a sensor area of 20 mm diameter were used for the subsequent testing of this research. The maximum repeatability error recorded for AMI air-pack sensor was 3.6%, while on average it was 2.4%, which is low, and the measured data were reproducible. AMI air-pack sensors also showed a very good linearity, with an average non-linearity error of 1%. The average hysteresis error recorded by the AMI air-pack sensors was 2.4%, which is a low and it assured that the pressure measurement is least affected by the sensor hysteresis.

3.6 Chapter Summary

This chapter presented results of the study of three most popular interface pressure measurement systems commercially available. The inaccuracies and limitations of the pressure measurement system could over/under estimate pressure readings leading to fault conclusions which could hinder the future analysis and lead to incorrect conclusions. Therefore, this study was conducted to identify the most suitable interface pressure measurement system for the research considering the criteria discussed. Although PicoPress[®] sensors demonstrated the lowest non-linearity error percentages they could not be used due to their larger sensor area which was not compatible to the geometry of the mini-bladders utilised in the current research to create active pressure. FlexiForce[®] sensors were the most geometrically compatible sensor to the size of the mini-bladders. However, higher repeatability errors were evident with these sensors, and often overstated the pressure measurement value. Also significant variations in pressure values were observed between sensors, which would result in errors when measuring interface pressure at different locations simultaneously. Hence, it was decided to use the AMI air-pack sensors as the pressure measurement system in the research due to its geometrical compatibility with the size of the mini-bladder, low non-linearity error, higher repeatability of the measurement, less variation from sensor to sensor and easy to use with the pressure measurement processing unit.

Chapter 4

Material characterisation and designing of mini bladders

This chapter presents the materials and methods used for manufacturing inflatable mini-bladders that can be employed in the design of the active compression system. In order to improve the pressure transmission, it was decided to design a mini-bladder consisting of only one inflating surface; a novel concept that has not been explored before. Several materials and designs have been investigated, and then the most suitable material was selected considering elastic properties required for the application and the suitability for medical applications, considering the bio-compatibility. The final design of the mini-bladders was formulated after preliminary studies. A mathematical model was created using Finite Element Analysis (FEA) to define the inflation behaviour of the mini-bladder unit. The mathematical model was then validated by comparing the model simulation results with experimental data. The model showed more than 80% agreement with the experimental data over the range of 0 – 60 mmHg inside pressure of the mini-bladders.

4.1 Introduction

The manufacturing of the mini-bladders required investigation of possible materials that could be used to craft them, providing the required/desired properties for the intended application. The most important material properties were the elastic behaviour and the bio-compatibility of the material so that it be used as a medical treatment device in the future. Polymers are often used in manufacturing bladders for different applications. Polyurethane and rubber are the most commonly used polymers up to date in manufacturing different kind of bladders. An example of a widely manufactured bladder is the bicycle tube, which is made mostly from natural and synthetic rubber. Another widely used bladder is the blood pressure measurement cuffs, where most of the time they are produced with polyurethanes.

Elastomers are unique polymers which exhibit extraordinary reversible extension with low hysteresis

and minimal permanent set (Shanks and Kong, 2013; Visakh et al., 2013). Elastomers exhibit large strains, which can be due to the chemical bond stretching, bond angle deformation or crystal structure deformation (Visakh et al., 2013). The strain reversibility is often associated with the crosslinking ability. Natural rubber (NR) is an elastomer with a basic monomer of cis-1,4 isoprene. Styrene-butadiene rubber (SBR) and butyl rubber (IIR) are synthetic rubber derivatives which are made from co-polymers of styrene-butadiene, isobutylene-isoprene respectively (Visakh et al., 2013). Natural rubber exhibits around 100 – 700% elongation at break, showing a good elasticity. However, the stress strain behaviour of rubber is non-linear, and it exhibits hysteresis effect. Hysteresis is identified as the difference in stress relaxation, caused by internal friction, which resists both extension and contraction. Hysteresis vary with the elastomer type, and is lower in unreinforced natural rubber and larger in most of the other elastomers (Bauman, 2012). However, the rubber and latex products cannot be used in direct contact with the skin, as they tend to give allergic reactions, and banned in the U.K for medical applications.

Polyurethane (PU) rubbers were discovered by Otto Bayer in Germany in 1937 (Sharmin and Zafar, 2012). PU elastomers exhibit good elasticity in a wide hardness range, and exhibit high strength of plastics with elasticity and toughness of rubber (Zhang et al., 2008). PU is formed by chemical reaction between a di/poly isocyanate and a diol or polyol forming repeating urethane groups in the presence of a catalyst and/or chain extender (Sharmin and Zafar, 2012; Zafar and Sharmin, 2012). The structure of PU is highly influenced by inter-molecular forces, such as hydrogen bonding, polarizability, "Van der Waals" forces, stiffness of the polymer chain and cross linking (Shanks and Kong, 2013; Visakh et al., 2013). PU exhibits a high hysteresis effect due to its polar structure, stipulating intermolecular interactions that result in deviations from ideal elastomer response (Shanks and Kong, 2013; Visakh et al., 2013). This is same for the NR and SBR, except that strain hardening in PU is such that the repetitive cycles does not appear exactly overlaid (Shanks and Kong, 2013; Visakh et al., 2013). This process can be explained in steps; as the strain increases, the random polymer coils get elongated, inter-molecular forces become more favourable and, thus the stress required for the particular strain would increase. The biggest drawback of PU is its higher modulus compared to NR, and the permanent set of 2-5% when elongated within its elastic limits at 300% (Shah, 2001). Although PU are chemically inert in their fully reacted form, there could exists a risk of asthmatic symptoms on exposure to human skin and organs even in smaller concentrations due to the volatility of isocyanate groups (Sharmin and Zafar, 2012; Zafar and Sharmin, 2012) and some isocyanates are considered as carcinogens (Sharmin and Zafar, 2012).

Polysiloxane elastomers commonly known as silicone rubber is based on a silicone and oxygen backbone instead of organic carbon chain. Frederic Stanley Kipping, the father of silicone science achieved extensive synthesis of silicone compounds (Shanks and Kong, 2013; Visakh et al., 2013). As described under 2.4.2, the most common siloxane compound is polydimethylsiloxane (PDMS), also known as Silicone. They exhibit a low modulus of elasticity, high mechanical dissipation factor (Shanks and Kong, 2013; Visakh et al., 2013), resilience, stretchability, and more stability than NR (Shah, 2001). Silicone has been first used in medical applications during the 1950s, and is one of

the most biocompatible synthetic materials available (Shah, 2001), which is also hydrophobic and has a pleasant touch (Shanks and Kong, 2013). Silicone has a higher elongation than PU (around 600%-1100%), and a very good memory especially the low modulus silicone types of soft grade silicones (Shah, 2001). Medical devices made out of silicones exhibit low bacteria adhesion and thrombogenicity making it an ideal material for an applications where a prolonged contact exists with body tissue (Shah, 2001).

The suitability of the material for the application of manufacturing mini-bladders, required elasticity, low modulus and bio-compatibility. As described above, PU and rubber derivatives exhibited better elasticity properties. However, both these materials have shown hysteresis effect which can be a disadvantage for the application (Buckley et al., 2010). Comparably, silicones show better mechanical properties with low modulus varieties being available for the application. Most importantly silicones are considered to be the most bio-compatible material in comparison to the other two elastomeric materials (Shah, 2001). Therefore, even though silicones are expensive in comparison to PU and rubber derivatives it was selected as the material for the development of the active compression system.

4.2 Achieving uniform pressure using mini-bladders

To achieve the objective of creating a radial pressure a series of mini-bladders are to be used. The advantage of using mini-bladders instead of using single large bladder is that the ability to control them individually as well as to avoid the pressure irregularities caused due to the shape distortion of a large single bladder wrapped over a 3D surface such as an arm or a leg.

The main function of these mini-bladders is to deliver a radial force (pressure) at the point of contact, and to increase the energy transmission efficiency. Therefore, one of the key design criteria was to prevent the inflation on one side of the bladder, so that the air inserted into the mini-bladder will only inflate the side of the mini-bladder in contact with the skin.

4.2.1 Use of single bladder cuffs

As stated earlier, currently, the medical community uses single large bladders to apply pressure; the most widely used application is in blood pressure (BP) measuring cuff. Therefore, preliminary experiments were carried out to study the inflation of a commercially available blood pressure measuring cuff, which uses an electronically controlled pneumatic pump to inflate the bladder, and then measure the back-pressure generated by the bladder to determine the pressure of the air in the bladder. The problem associated with the bladders used in BP measuring cuffs is that it is difficult to apply a uniform pressure over the circumference of a human limb. Two types of bladders are employed in current BP measuring cuffs; a fabric bladder or rubber bladder. Two examples of commercial BP measuring cuffs are given in Figure 4.1 (a) and (b) (Naqvi et al., 2017)

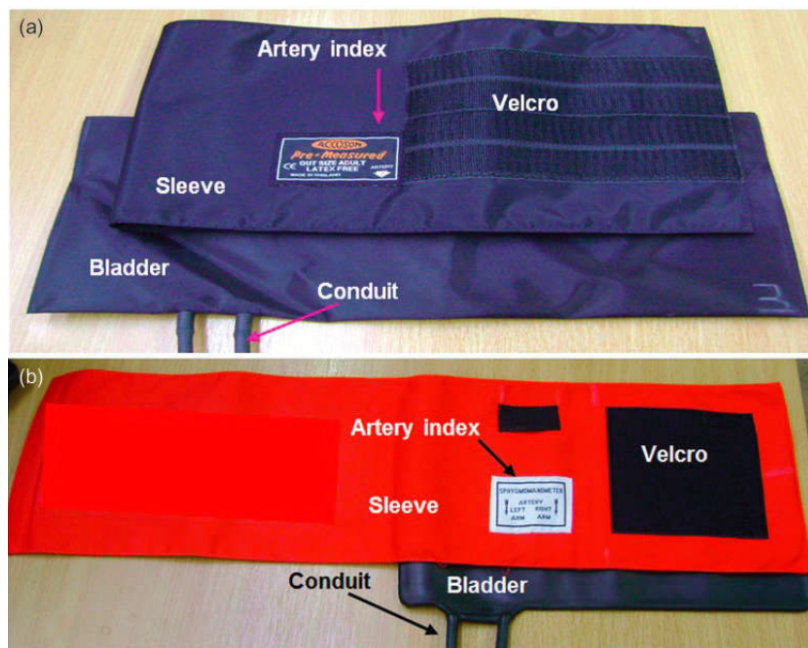


Fig. 4.1 Blood pressure measurement cuffs: Single cuff with (a) fabric bladder (b) rubber bladder (Naqvi et al., 2017)

A typical BP cuff is an assembly of an external sleeve containing an inflatable single bladder and an outer sleeve made of woven textile fabric to accommodate the bladder. In constructing the cuff sleeve two fabric layers are fused together by using radio frequency welding from four sides (Naqvi et al., 2017) in order to create a pocket for the bladder. Therefore, these bladders are normally made in rectangular shaped cuffs.

Investigation of pressure distribution in BP cuffs with single large bladder

The preliminary test was carried out with a BP measuring cuff (Durocic BPM450, Durocic, Romford, UK) wrapped around a plastic bottle filled with water, which was then inflated to different pressures using the electronic inflation unit provided by the manufacturer, and the deformation of the plastic bottle was investigated to study the shape distortion of the bladder. Figure 4.2 shows different stages of inflation of the BP cuff and the resultant deformation of the plastic bottle. According to the deformation of the plastic bottle one can clearly identify the uneven deformation of the plastic bottle at different stages of inflation. This clearly suggests that the BP cuff applied different pressures around the circumference of the plastic bottle. In a similar experiment Naqvi et al. (2018) have determined the pressure distribution at different locations around the bottle which is included in the Appendix B. It is evident from Fig. 4.2 and the pressure distribution data given in Appendix B, a single large bladder cannot provide a uniform pressure distribution over a cylindrical surface; certain areas will be deformed while certain areas are not deformed at all.

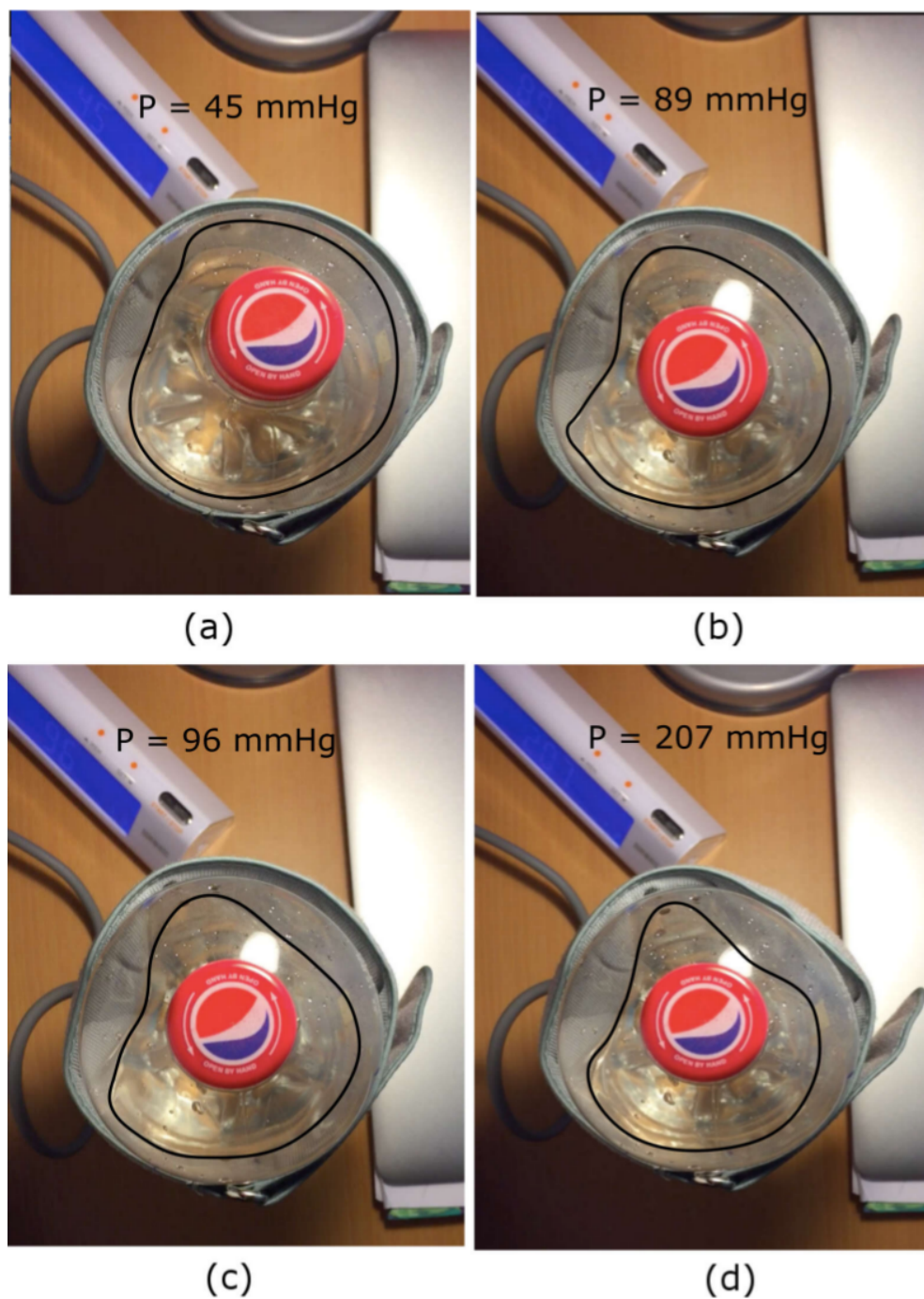


Fig. 4.2 The non-uniform deformation of the cylindrical bottle surface on application of pressure using BP measuring cuff (Duronc BPM450, Duronic, Romford, UK). Deformed shape is demarcated in black coloured line, (a) at 45 mmHg pressure, (b) at 89 mmHg pressure (c) at 96 mmHg pressure (d) at 207 mmHg pressure showed the different stages of the deformation.

4.2.2 Use of mini-bladders

The bladders used in BP measuring cuffs are made with two rectangular rubber layers sealed at the edges by using ultrasonic welding techniques. The BP cuff is usually rapped around the surface of the upper arm, and the bladder is allowed to inflate from both sides which can be considered as a large single bladder. A schematic representation of a large inflated bladder and a mini-bladder in contact with a cylindrical surface is shown in Fig. 4.3; it is clear that the cylindrical contact surface would influence the inflation profile of the bladder.

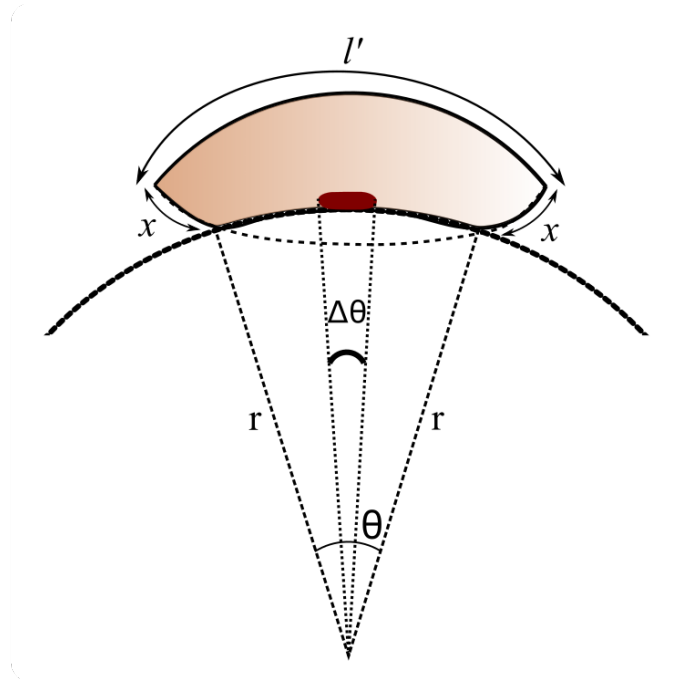


Fig. 4.3 A schematic diagram of a large bladder and a mini-bladder in contact with the cylindrical surface. r = radius of curvature of the surface, θ = contact angle, x = non-contact region length, l' = uniformly deformed bladder length (one side), $\Delta\theta$ = contact angle made by the mini-bladder

The length of the bladder that is in contact with the cylindrical surface ($r\theta$) depends on the angle θ as shown in the Fig.4.3. If it is assumed that the large bladder inflates uniformly on the both sides, the lengths of both sides should ideally be equal to l' . As shown in Fig. 4.3, $r\theta$ deviates more from l' for the large bladder. Hence, it will result in a non-uniform deformation of the bladder resulting in non-uniform pressure distribution. In contrast when a mini-bladder is used, contact angle it makes with the surface becomes smaller ($\Delta\theta$), which make $r\theta$ closer to l' , hence the deviation from the original profile would be less compared to the large bladder. Therefore, the strain values of the deformed surface of the bladder would not be largely varying from point to point, thus making a uniform pressure distribution. Also, when the mini-bladders are considered, the curvature of the cylindrical contact surface is quite large in comparison with the size of mini-bladder. Therefore, deformation of the mini-bladder is minimum with respect to the radius of curvature of the contact

surface. Hence, the mini-bladders would be able to provide a uniform pressure on a cylindrical surface rather than a large bladder. Smaller the mini-bladder, curvature effect would be minimal however there are practical limitations to the size of mini-bladders. Hence, the size and the shape of the mini-bladders should be decided based on maximum pressure transmission and considering the geometrical parameters. Also, this would be limited according to the geometric size of the best available pressure sensor for interface pressure measurement as discussed in chapter 3 of this thesis.

4.3 Material properties and geometrical analysis

The conceptual design of the active compression system is to use a grid of inflated mini-bladders to generate the required pressure profiles. The generated pressure will depend on the elastic behaviour of the mini-bladders; thus it is important to study the inflation characteristics of the silicone layer that would be in contact with the skin. Standard characterisation tests have been developed to measure the stress strain response of rubber and rubber like materials (Adeel et al., 2012; Vahapoglu et al., 2011; Xu et al., 2010). Amongst, the most popular and widely used method being the uniaxial testing, which provides an understanding on the stress-strain behaviour of the materials. The traditional dog boned uniaxial tension test is widely used due to its simplicity. Since silicone is a hyperelastic material, first the material was tested experimentally using uniaxial extension (tension) to determine the material parameters, which were later used in modelling the behaviour of the silicone elastomer.

4.3.1 Uniaxial testing of silicone material used to craft mini-bladders

The uniaxial tension experiments are common for elastomers. To achieve a state of pure tensile strain, the specimen should be longer compared to the width and the thickness (Miller, 2004) the objective being to minimise lateral constraint to specimen thinning during the test. There are several standards for testing of elastomers in tension. ASTM D412 and BS 37:2011 are the standards available for testing rubber, and ASTM D638 and BS 527 are used for testing plastics. However, the most appropriate test methods are not clearly defined for elastomers such as silicones. When comparing different test standards, most of the testing procedures defined are the same, although the defined specimen sizes differ. The stress-strain properties of the silicones used in the research were determined using a tensile tester Zwicki 2.5 kN (Zwicki Roell®, Ulm, Germany) with 200 N load cell, according to the BS 37:2011[12] standard and the type 1A specimen size. The test speed used was 500 mm/min.

4.3.2 Sample preparation

RTV silicone types PlatSil® Gel-OO 30 (Shore OO 30 hardness) and PlatSil® Gel-A 10 (Shore A 10 hardness) were tested. These RTV silicones were selected since they are the commonly available low modulus silicones having low shore hardness values. The selection of a low modulus silicone

will reduce the energy dissipation due to the expansion of the membrane during the inflation of mini-bladders using a volume of air. Both of these RTVs are two-part silicones, and were mixed to a 1:1 ratio (part A: part B), with 3% PlatSil® 71/73-part R retarder (MouldLife, Suffolk, UK) without any other additives. The mixture was then degassed using a 26 L vacuum degassing chamber (Easy composites, Staffordshire, UK) to remove any trapped air bubbles, and poured into the mould manufactured according to the BS 37:2011 (ISO, 2011) type 1 A specimen size (Fig. 4.4 a).

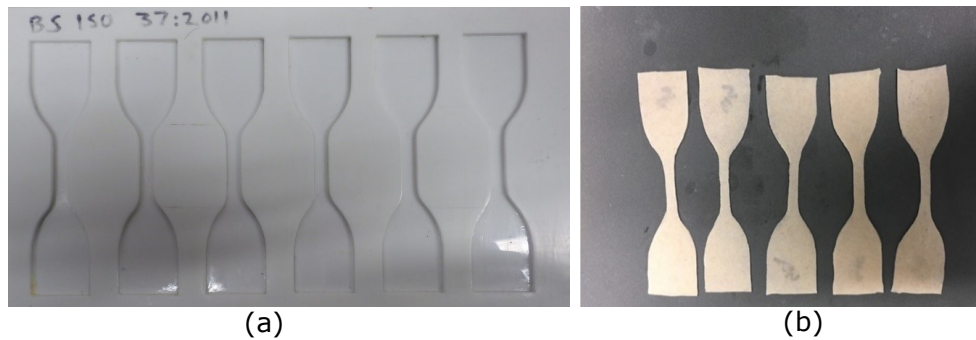


Fig. 4.4 The preparation of silicone samples according to the BS 37: 2011 type 1a specimen type (a) moulds prepared for making the samples (b) prepared samples for testing.



Fig. 4.5 Zwick Roell® tester used for the uni-axial tension while the samples are being tested for uni-axial extension

Thereafter a flat acrylic sheet was placed on top of the moulds to flatten the surface and remove the excess silicone and get a uniform layer of material casted to the required shape and were left to cure for three hours and scraped out of the mould after curing. The test samples were conditioned for

about three hours before testing, in the ambient temperature and humidity due to the unavailability of a conditioned room. Five samples from each type of silicones were tested according to the standard. The samples which did not break in the middle were discarded. An example of a test sample under uniaxial tension is shown in Fig. 4.5.

4.3.3 Curve fitting of experimental data (uni-axial tension tests)

The experimental results obtained from the uniaxial tests of silicone were analysed using the hyperelastic models discussed in section 2.4.3 to determine the best hyperplastic model which describes the stress - strain behaviour of both types of silicones. The curve fitting technique was used to determine the material parameters required for Mooney Rivlin two parameter and Yeoh 2nd order models. Engineering stress-strain relationship for the uniaxial condition for both Yeoh 2nd order model (equation 2.39) and Mooney Rivlin two parameter model (equation 2.42) was used to analyse the results (Polygerinos et al., 2013; Rackl, 2015). Curve fitting was carried out using the curve fitting tool in MATLAB (version: MATLAB R2016b, MathWorks® Inc., USA). It is also possible to determine the model parameters using the uniaxial data with ANSYS Workbench (ANSYS Academic, version 18.1, ANSYS Inc., Canonsburg, USA). However, the accuracy of the model parameters calculated were relatively low in comparison with the curve fitting results given by MATLAB (version: MATLAB R2016b, MathWorks® Inc. USA). Therefore, curve fit results obtained with MatLab was used in the subsequent analysis. (The results obtained from ANSYS are included in Appendix B, including the email conversation with ANSYS team). The experimental data and the MatLab curve fitting results for both silicone materials are discussed in the subsequent sections.

The results obtained from curve fitting of the experimental data for two different models are summarised below. Each case below shows curve fitting results for the particular model with experimental data from 9 different testing samples (5 PlatSil® Gel-OO 30 samples and 4 PlatSil® Gel-A 10 samples; one sample of PlatSil® Gel-A 10 did not break in the middle during the test and was omitted from the curve fitting). At the end of each case/model curve fitting results and statistical measures of the fits are summarised in a table (Table 4.1 to 4.4).

Case 01: Mooney Rivlin two parameter curve fitting model

The stress state of the hyperelastic material is determined by taking the derivatives of the strain energy density with respect to the strain components (Kumar and Rao, 2016). Since the stress-strain curve obtained from the uniaxial tests shows a single curvature and does not contain any reflection points, the Mooney Rivlin two parameter model is used to describe the stress strain behaviour of the samples (Kumar and Rao, 2016). The Mooney-Rivlin model is known to work well for moderately high strains, but the disadvantage of this model is that since the stress depends on both first and second strain invariants, uniaxial tests are not enough to fully describe the material behaviour and require bi-axial testing. The curve fitting plots for Mooney Rivlin two parameter model of the two silicones PlatSil® Gel-OO 30, and PlatSil® Gel-A 10 (one set of data for each silicone type) are shown in Fig. 4.6 and

Fig. 4.7 (curve fitting plots for the other samples are included in Appendix B. The results of curve fit and the statistical parameters of the Mooney Rivlin two parameter model for samples of PlatSil[®] Gel-OO 30 and PlatSil[®] Gel-A 10 respectively are summarised in Tables 4.1 and 4.2.

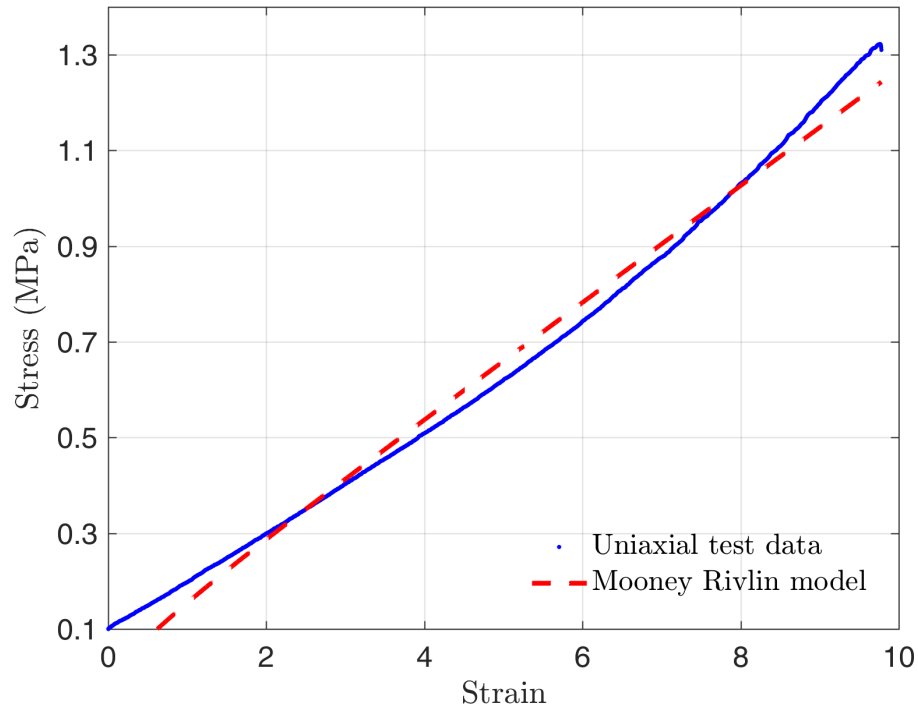


Fig. 4.6 Experimental data and Mooney Rivlin two parameter model curve fit for PlatSil[®] Gel-OO 30 – sample 1.

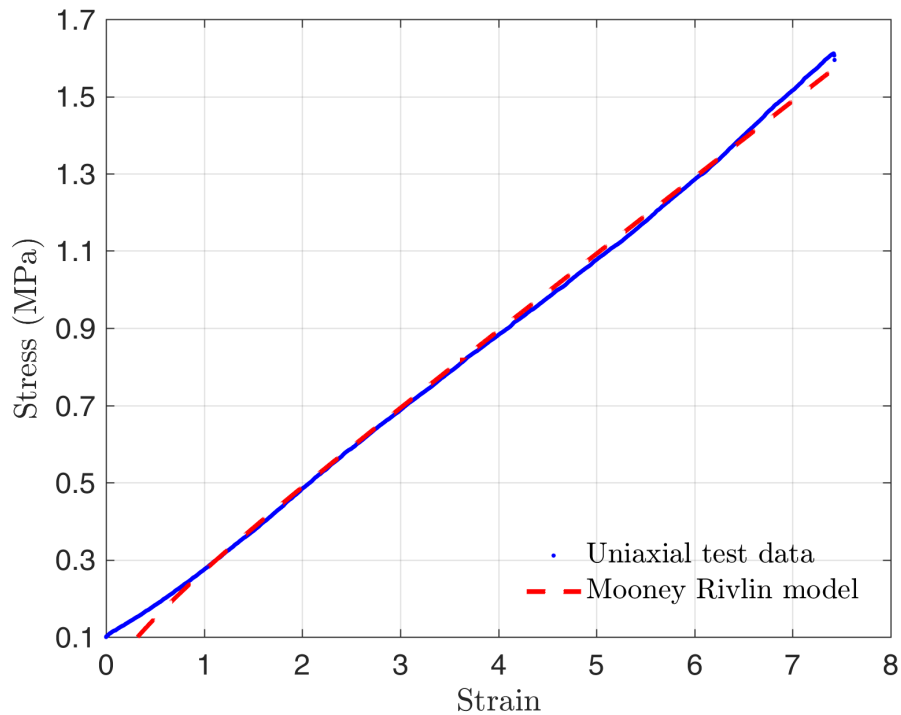


Fig. 4.7 Experimental data and Mooney Rivlin two parameter model curve fit for PlatSil® Gel-A 10 – sample 1.

Table 4.1 Curve fitting results summary for Mooney Rivlin Two parameter model, PlatSil® Gel-OO 30

Sample Number	Material constants		Statistical data		
	C_{10} (MPa)	C_{01} (MPa)	RMSE	SSE	R^2
S1	0.05598	-0.01856	0.03360	3.615	0.9869
S2	0.06079	-0.03321	0.04052	5.914	0.9866
S3	0.06040	-0.02582	0.03512	4.163	0.9874
S4	0.06224	-0.03427	0.03889	5.385	0.9867
S5	0.06174	-0.02762	0.03562	4.370	0.9877
Average	0.06023	-0.02790	0.03675	4.6894	0.9871

RMSE - Root Mean Square error

SSE - Sum of Squared Errors

R^2 – Regression coefficient

C_{10} and C_{01} are empirically determined (by curve fitting using experimental data) material constants for Mooney Rivlin model. These material constants characterise the deformation of the material. In this model to satisfy the stability criterion, the condition $C_{01} \geq 0$ should be satisfied (Kumar and Rao, 2016).

Table 4.2 Curve fitting results summary for Mooney Rivlin two parameter model, PlatSil® Gel-A 10

Sample Number	Material constants		Statistical data		
	C_{10} (MPa)	C_{01} (MPa)	RMSE	SSE	R^2
S1	0.09842	-0.04174	0.02505	1.601	0.9968
S2	0.10360	-0.06854	0.03699	4.110	0.9957
S3	0.09275	-0.03225	0.02363	1.112	0.9953
S4	0.09787	-0.04415	0.03905	0.084	0.9941
Average	0.09816	-0.04667	0.03118	1.727	0.9955

The average material parameters calculated for Mooney-Rivlin model were $C_{10} = 0.06023$ MPa, and $C_{01} = -0.0279$ MPa for PlatSil® Gel-OO 30 and $C_{10} = 0.0982$ MPa, and $C_{01} = -0.0467$ MPa for PlatSil® Gel-A10. The calculated C_{01} material parameter of Mooney-Rivlin model resulted in negative values for both silicone types. However, according to the literature (Kumar and Rao, 2016) Mooney-Rivlin model should satisfy the stability criterion in order to produce real behaviour of the material, and this includes the condition of $C_{01} \geq 0$; which has not been satisfied by the results in the Tables 4.1 and 4.2.

Case 02: Yeoh second order model fit

The Fig. 4.8 and Fig. 4.9 depicts the curve fitting plots for Yeoh second order curve fitting model for both silicone types; only one set of data for each silicone type is included here and the results of the rest of the tests are included in the Appendix B. The Yeoh model provides a good fit for a wide range of deformations, over a larger strain range and can simulate various modes of deformation with limited data. Also, the Yeoh model is capable of predicting the stress strain behaviour for different deformation modes even from the data obtained from only one simple mode of deformation like uniaxial extension (Ali et al., 2010).

The Table 4.3 and 4.4 The Table 4.3 and 4.4 summarise the results of curve fit and the statistical parameters for the Yeoh second order model for samples of PlatSil® Gel-OO 30 and PlatSil® Gel-A 10, respectively. As observed from the plots of curve fitting results the strain percentage before break for PlatSil® Gel-OO 30 was between 800% – 1000% (Fig.4.6 and the figures given in Appendix B and for PlatSil® Gel-A 10 was between 600% – 800% (Fig. 4.7 and the figures given in Appendix B, demonstrating that PlatSil® Gel-OO 30 has a higher elongation at break. The test samples show that the maximum stress before breakage for PlatSil® Gel-OO 30 was in the region 1.0 MPa to 1.2 MPa and 1.2 MPa to 2.0 MPa for PlatSil® Gel-A 10. Therefore, it can be concluded that the PlatSil® Gel-OO samples of shore OO 30 hardness are much more extensible compared to PlatSil® Gel-A10 samples of shore A 10 hardness silicone.

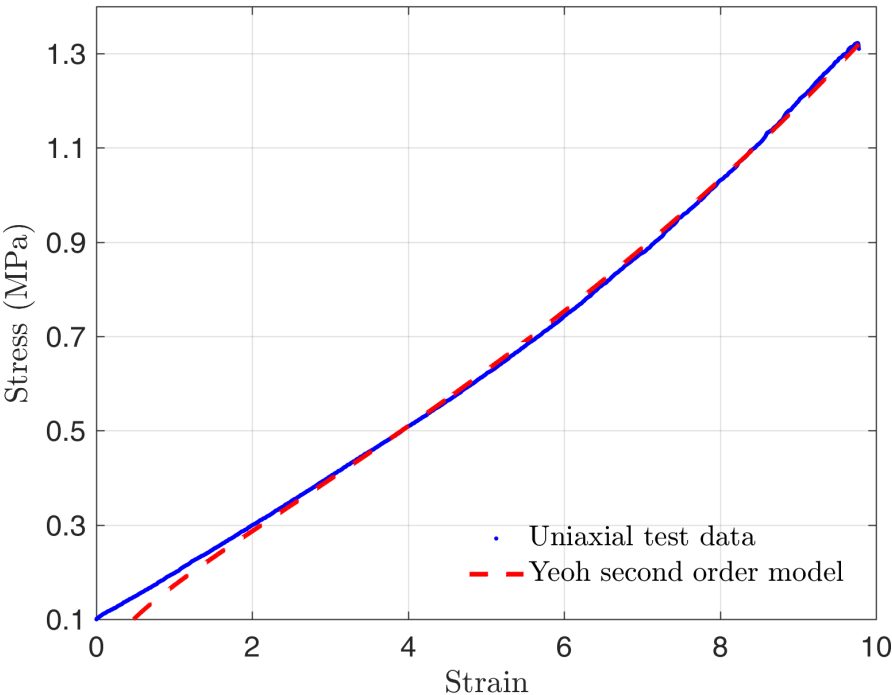


Fig. 4.8 Experimental data and Yeoh second order model curve fit for PlatSil® Gel-OO 30 – sample 1.

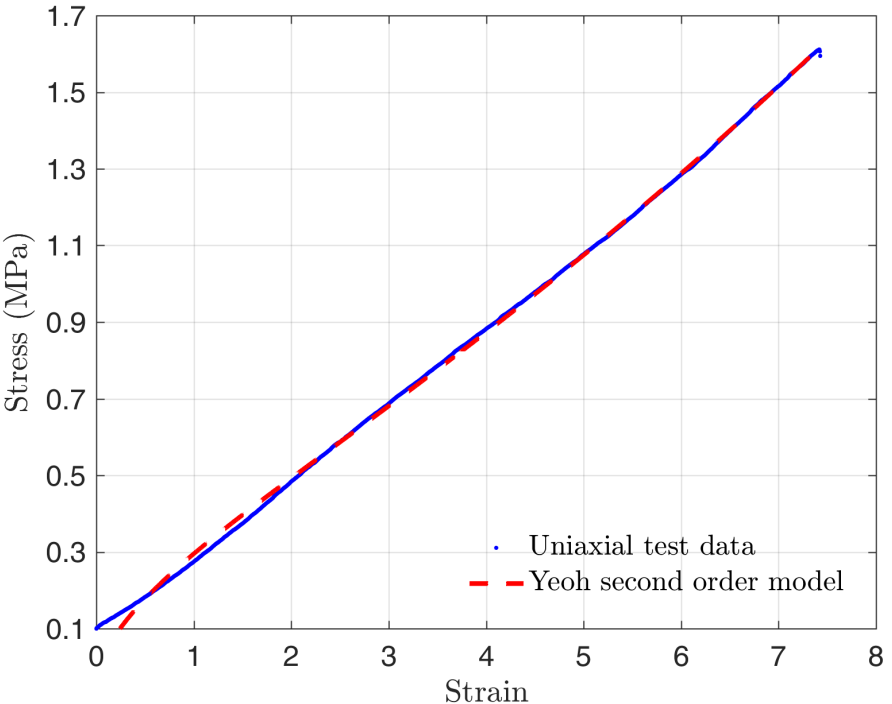


Fig. 4.9 Experimental data and Yeoh second order model curve fit for PlatSil® Gel-A 10 – sample 1.

Table 4.3 Curve fitting results summary for Yeoh second order model, PlatSil® Gel-OO 30

Sample Number	Material constants		Statistical data		
	C ₁₀ (MPa)	C ₂₀ (MPa)	RMSE	SSE	R ²
S1	0.04791	0.0000476	0.02316	1.710	0.994
S2	0.04895	0.0000543	0.02208	1.756	0.996
S3	0.05018	0.0000579	0.02201	1.634	0.995
S4	0.04976	0.0000631	0.02156	1.656	0.996
S5	0.05106	0.0000596	0.02225	1.704	0.995
Average	0.04957	0.0000565	0.02221	1.692	0.995

Table 4.4 Curve fitting results summary for Yeoh second order model, PlatSil® Gel-A 10

Sample Number	Material constants		Statistical data		
	C ₁₀ (MPa)	C ₂₀ (MPa)	RMSE	SSE	R ²
S1	0.08408	0.0000886	0.01981	1.001	0.9980
S2	0.08273	0.0000917	0.01878	1.059	0.9989
S3	0.08060	0.000101	0.02282	1.037	0.9956
S4	0.08065	0.0001068	0.02249	0.003	0.9981
Average	0.08202	0.0000969	0.020975	0.775	0.9977

As can be observed from the Fig 4.6 the Mooney Rivlin curve fit for PlatSil® Gel-OO 30 silicone is deviating highly from the experimental results in comparison to the Yeoh curve fit model. For PlatSil® Gel-A 10 samples the Mooney Rivlin curve fitting model provides better fit for the experimental data when compared with the experimental results of PlatSil® Gel-OO 30 (Fig. 4.6, and Fig 4.7). However, it can be observed that the clear deviations exist below 100%, and over 700% strain percentages. The statistical data of the curve fitting given in Tables 4.1 and Tables 4.2, further confirms this by having lower R² value and higher RMSE value for PlatSil® Gel-A 10.

The Figures 4.8 and 4.9 show that the Yeoh second order curve fitting model provides a good fit for the experimental data for both PlatSil® Gel-OO 30 and PlatSil® Gel-A 10 samples compared to Mooney Rivlin curve fitting model. However, one could identify a noticeable variance from the experimental values for strains below 100% for PlatSil® Gel-OO 30 samples and a noticeable variation in strains in the range of 0 – 50% for PlatSil® Gel-A 10 samples. The Yeoh second order curve fitting model values are more in accordance with the experimental data for the strains values above 100%. In the current application the silicone membrane would be inflated in the strain ranges of 110% – 330% (further details are discussed in the section 4.3.4, page 104), and the Yeoh model shows a better agreement with the uniaxial test data in that region. The statistical data summarised in Tables 4.3 and

4.4 validates the relevance of model fit to experimental data demonstrating a R_2 value of 0.99, which is very closer to 1, and a much smaller RMSE value around 0.02 for both types of silicones.

Based on this analysis, as summed up in Tables 4.1 to 4.4, the Yeoh model was found to be the best fit to the experimental data for both type of silicones used in the experiments (depending on the regression coefficient). As per the results summarised in Table 4.3 and 4.4, Yeoh second order model can be used to fully describe the behaviour of the material with $C_{10} = 0.0496$ MPa, and $C_{20} = 0.00005649$ MPa for PlatSil® Gel-OO and $C_{10} = 0.082$ MPa, and $C_{20} = 0.00009693$ MPa for PlatSil® Gel-A10. Since, the PlatSil® Gel-OO silicones has lower modulus value compared to PlatSil® Gel-A10 silicone type, it was selected in manufacturing the mini-bladders

4.3.4 Geometrical analysis and mathematical model

The mini-bladders were specifically designed to have one side of the mini-bladder inflated fully while inflation of the other side was restrained. As shown in the Figure 4.10 (a), the extensible layer (top elastomer layer A), which fully inflates, delivers the required pressures once in contact with the skin. A less extensible bottom layer (bottom elastomer layer B), was used as the base of the mini-bladder unit and yet was sufficiently flexible to minimise the rigidity of the whole mini-bladder. The top layer of the mini-bladder unit will fully inflate while the bottom layer will have less/no inflation, when a volume of air is inserted into the unit. As the layers are sealed (welded) from the sides, there would not be any inflation in the sides of the mini-bladders. The inextensible layer was manufactured by submerging a woven fabric (151.69 GSM, 62 epi, 60 ppi) of 0.38 mm thickness having a Young's modulus of 0.964 MPa calculated according to (Penava et al., 2014), (the details are included in Appendix B).

The relationship between inflation height and the geometry of the mini-bladders was explored using the Yeoh second order model, with the experimentally calculated coefficients C_{10} and C_{20} . The incompressibility of the mini-bladder unit across the thickness was assumed and hence $\lambda_3 = 1$. since $\lambda_1\lambda_2\lambda_3 = 1$; where $\lambda_1, \lambda_2, \lambda_3$ are principal stretch ratios. Let $\lambda_1 = \lambda$, then,

$$\lambda_2 = \frac{1}{\lambda} \quad (4.1)$$

Using the Yeoh second order model the strain energy density function for a hyperelastic material can be written as;

$$U = C_{10}(I_1 - 3) + C_{20}(I_1 - 3)^2 \quad (4.2)$$

As the first strain invariant I_1 can be written as;

$$I_1 = \lambda_1^2 + \lambda_2^2 + \lambda_3^2 \quad (4.3)$$

For each mini-bladder the Yeoh model becomes the form of;

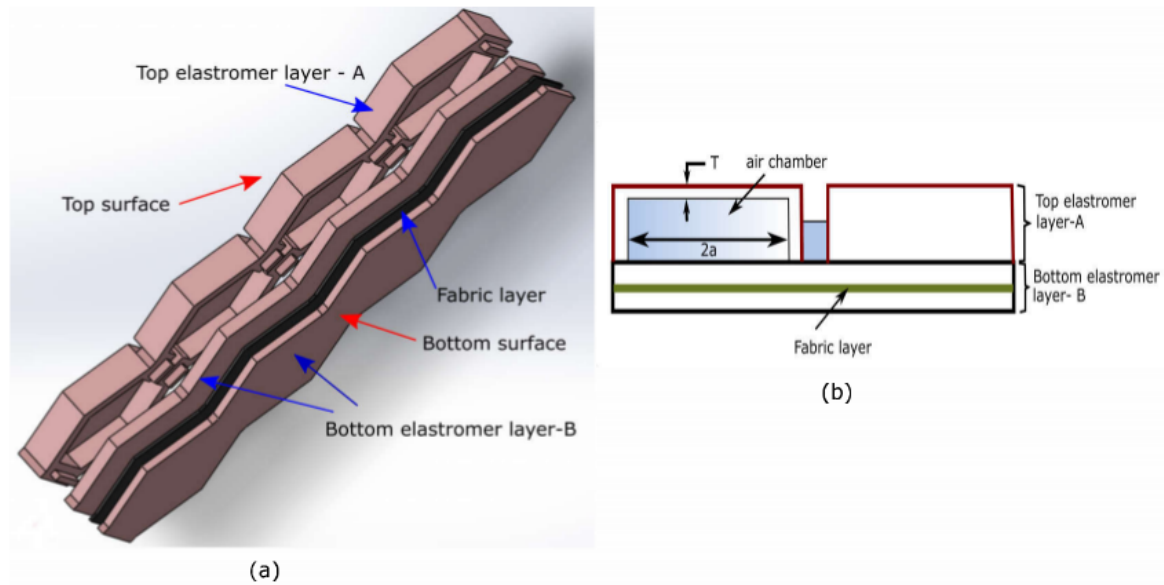


Fig. 4.10 (a) The layered view of mini-bladder unit design, each single mini-bladder is connected through a common air-channel (b) cross sectional view of the mini-bladder unit with consisting layers and the air chambers.

$$U = C_{10} \left[\lambda^2 + \frac{1}{\lambda^2} - 2 \right] + C_{20} \left[\lambda^2 + \frac{1}{\lambda^2} - 2 \right]^2 \quad (4.4)$$

Then the stress can be calculated as;

$\sigma = \frac{\partial U}{\partial \lambda}$, which gives;

$$\sigma = 2 \left[\lambda - \frac{1}{\lambda^3} \right] \left[C_{10} + 2C_{20} \left(\lambda^2 + \frac{1}{\lambda^2} - 2 \right) \right] \quad (4.5)$$

Mathematical representation of the inflation of mini-bladder

A simplified mathematical model was formulated to define the strain rate of the mini-bladder surface during the inflation. Based on the experimental observations it was assumed that the inflation profile of the top layer of a mini-bladder is dome shaped, although the base of the mini-bladder is of hexagonal shape, as shown in the Fig. 4.11. Hence, it was assumed that the radius of curvature at each point of the inflated membrane remained the same. It was also assumed that there is no interference between the inflation of the neighbouring mini-bladders.

Therefore, using basic geometry the following relations could be obtained,

$$r^2 = (r - h)^2 + a^2 \quad (4.6)$$

where; r - radius of curvature of the inflated membrane (mm)

$2a$ - minimum gap distance between the membrane fixing points (mm) when not inflated

h - inflation height (mm)

2θ - contact angle (in radians) Equation 4.6 can be rearranged to get,

$$r = \frac{(h^2 + a^2)}{2h} \quad (4.7)$$

$$\sin \theta = \frac{a}{r} \quad (4.8)$$

From equations 4.7 and 4.8, θ can be calculated as,

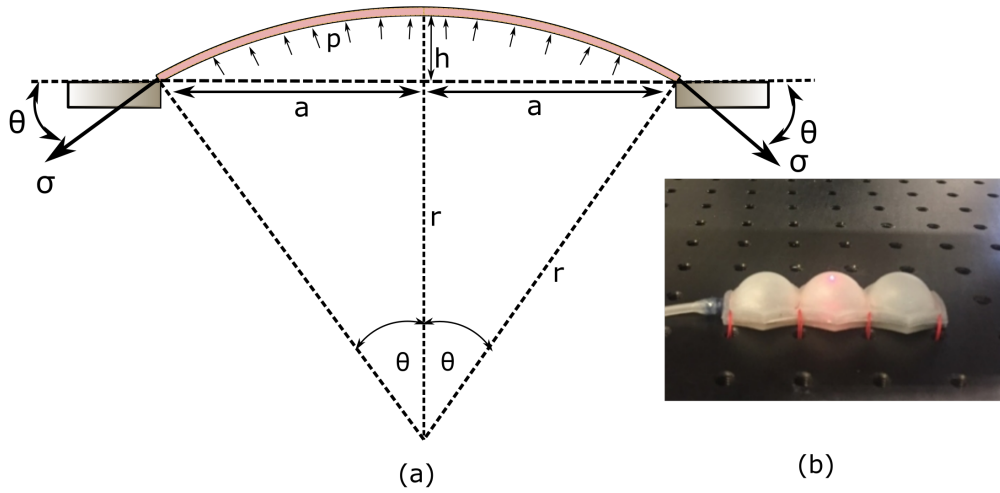


Fig. 4.11 (a) Schematic diagram of the mathematical representation of the inflation of the mini-bladder, (b) a photograph of inflated mini-bladder unit.

$$\theta = \sin^{-1} \left(\frac{2ah}{a^2 + h^2} \right) \quad (4.9)$$

Using the basic geometry, the arc length S of the inflated membrane could be written as

$$S = r \times 2\theta \quad (4.10)$$

The stretch ratio λ can be written as; $\lambda = \frac{S}{2a}$. Substituting from equations 4.10 and 4.8,

$$\lambda = \frac{\theta}{\sin(\theta)} \quad (4.11)$$

Substituting, θ from equation 4.9, yields,

$$S = \left(\frac{h^2 + a^2}{h} \right) \times \sin^{-1} \left(\frac{2ah}{a^2 + h^2} \right) \quad (4.12)$$

In relations given in equation 4.9 and equation 4.12 we have the following conditions (Christensen and Feng, 1986),

For $\frac{h}{a} \leq 1$, $\sin^{-1}(\frac{2ah}{a^2+h^2})$ is in the first quadrant

For $\frac{h}{a} \geq 1$, $\sin^{-1}(\frac{2ah}{a^2+h^2})$ is in the second quadrant

The strain percentage (%), which the membrane has undergone can be calculated as,

$$\text{strain (\%)} = \frac{S - 2a}{2a} \times 100 \quad (4.13)$$

Using the equations 4.13 and 4.12, and the experimentally obtained mean inflation height values for the mini-bladders the strain rates at different inflation volumes could be calculated and the results are shown in the Table 4.5 below.

Table 4.5 The strain percentages calculated at different inflation volumes for the mini-bladder unit made of PlatSil® Gel-OO 30

Inflation volume (ml)	Stain percentage (%)			
	Mini-bladder 1	Mini-bladder 2	Mini-bladder 3	Mini-bladder 4
2	111.94	109.59	109.57	110.87
4	129.18	122.96	122.80	124.44
6	147.89	137.56	136.48	139.65
8	166.54	152.35	150.98	155.38
10	184.75	167.73	166.05	172.17
12	201.53	182.51	179.78	187.62
14	218.12	196.74	193.36	201.55
16	234.48	212.00	208.35	219.00
18	250.15	228.77	224.11	235.72
20	268.57	245.13	238.73	252.40
22	287.58	263.36	255.01	271.47
24	309.57	282.75	273.49	292.81
26	330.92	301.44	290.18	315.26

All the strain percentage values for the mini-bladders ranged from 100 – 330%. As discussed in section 4.3.3, the material behaviour falls in the strain regions (100% – 700%) where the Yeoh second order model showed a good agreement with the uniaxial tension data. Therefore, for further modelling of the inflation behaviour of the mini-bladder unit, the Yeoh second order model was used with FEA. A relationship could be obtained between the stress in the membrane (σ) and the air pressure (ΔP) inside the mini-bladder using the force balance, as shown in the Fig. 4.11 (a);

$$\Delta P \pi a^2 = \sigma \sin \theta \times 2 \pi a t \quad (4.14)$$

$$\sigma = \frac{(a^2 + h^2) \Delta P}{4th} \quad (4.15)$$

where t is the thickness of the membrane.

ΔP is the pressure difference

After solving the equation 4.15 together with equations 4.5 and 4.11 a relationship between the inflation height (h), membrane thickness (t) and the minimum gap between the membrane fixing points (a) could be achieved. These set of equations can be solved using a simple numerical method such as bisection method to calculate the inflation heights for different membrane thicknesses and minimum gap distances, at a certain supplied air pressure. This could be used as a guideline to design the geometry and the size of the mini-bladders. The size and the thickness of the mini-bladder should be designed such that it should be able to achieve a certain minimum height that is required to establish a connection between the skin and the compression sleeve.

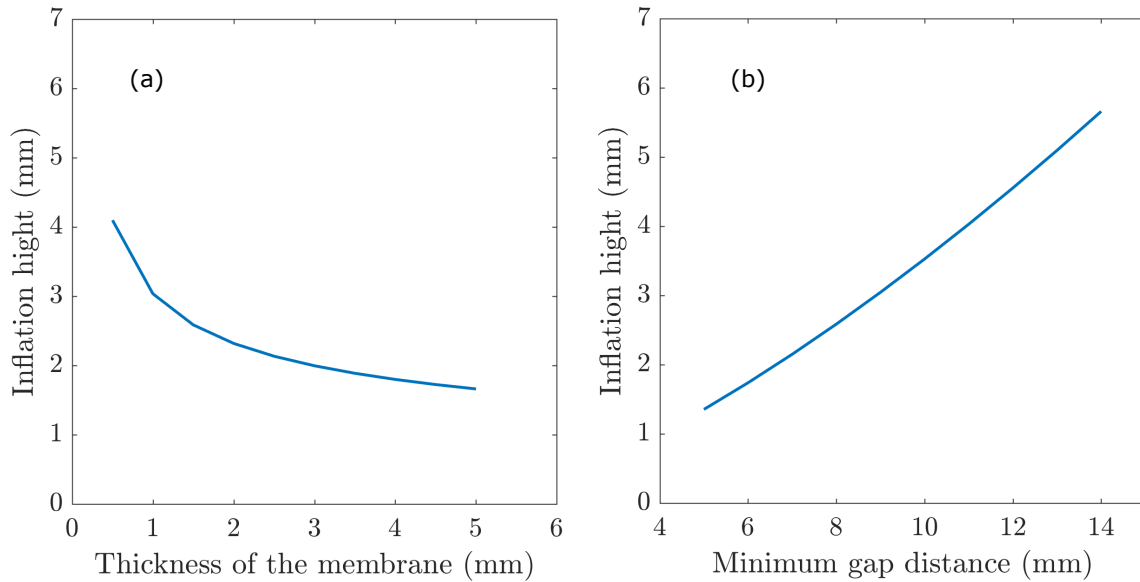


Fig. 4.12 The relationship between the inflation height with (a) thickness of the membrane (b) minimum gap distance (size of the mini-bladder), at supplied air pressure of 40 mmHg

According to Fig. 4.12a, smaller membrane thicknesses would provide higher inflation heights, however to avoid the rupture and increase the stability while reducing the total thickness of the unit, the top membrane thickness was selected as 1.5 mm. The inflation height has shown a positive correlation with the minimum gap between the membrane fixing points (Fig. 4.12 (b)). The minimum gap between the membrane fixing points depends on the size and the geometry of the mini-bladders. If the mini-bladders are hexagonal shaped the minimum gap distance would be $\sqrt{3} \times \text{sidelength}$, circular shaped mini-bladders the minimum gap distance equals to the diameter, and for square shaped mini-bladders it equals to the side length. The minimum gap length for different shaped mini-bladders

are given in the Table 4.6

Table 4.6 Minimum gap distance for different shaped mini-bladders

Geometric shape	Minimum gap length (mm)
Square	12.9
Circular	14.6
Hexagonal	13.9

According to the Table 4.6, largest minimum gap distance was recorded for the circular shaped mini-bladders closely followed by hexagonal shaped mini-bladders. Hence to obtain a higher inflation height, compared to square shaped mini-bladders either hexagonal or circular shaped mini-bladders could be used. However, the hexagonal shaped mini-bladders would give the most efficient packing by arranging them into a honeycomb structure. Furthermore, experimental evidence obtained from pressure transmission tests depicted in Fig. 4.13 illustrate that the hexagonal shaped mini-bladders provide the maximum pressure transmission efficiency (Further details of these experiments are discussed in chapter 5). Considering all the above factors it was decided to select hexagonal geometrical shape for the final design.

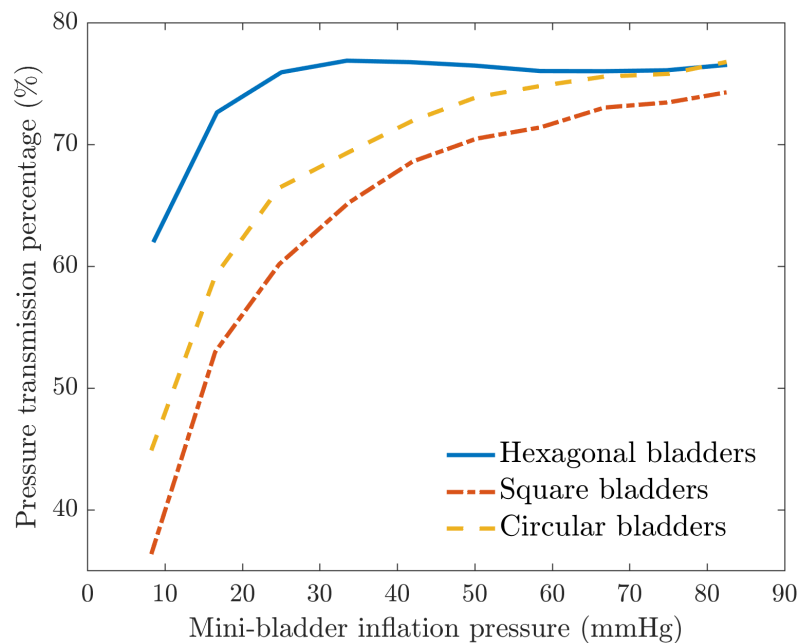


Fig. 4.13 Pressure transmittance percentage on cylindrical (constant radius of curvature) surface against the mini-bladder inflation pressures for different shaped mini-bladders

According to Fig. 4.12 (b), to obtain a minimum inflation height of 1 mm at 40 mmHg pressure the minimum gap distance should be more than 6 mm. However, reducing the side length of the

mini-bladders to such extent would increase the manufacturing errors due to the manual assembling of the mini-bladder unit. Therefore, it was decided to use hexagonal mini-bladders of 8 mm size. The total thickness of the mini-bladder unit should be kept as minimum as possible to avoid the bulkiness of the final design, in order to make it wearable. Thus, to keep the total mini-bladder unit thickness a minimum at the same time provide the required stability, the bottom layer thickness was decided to keep as 3 mm, while the top layer thickness was kept as 4 mm, having an air chamber with a height of 2.5 mm.

4.4 Design and development of mini-bladders

As discussed above, the concept for the design of mini-bladders was to create a single surface inflatable bladder; i.e. only one surface of the mini-bladder could be inflated while all the other surfaces are restricted, in order to maximise the pressure transmission efficiency of the mini-bladder. This required the design of a bladder with an extensible layer (top surface) that can be inflated to deliver the required pressure profile once in contact with the skin, and a less extensible, yet sufficiently flexible bottom layer to minimise the rigidity so that a unit consisting of several mini-bladders could be crafted. As discussed earlier under section 4.1, considering the favourable properties of silicone such as elasticity, low modulus, and bio-compatibility, it was decided to use medical grade silicones to create the two layers of the mini-bladders.

4.4.1 Preliminary study to create the mini-bladders

During this preliminary stage the two layers of the mini-bladder were manufactured separately using two moulds and then both layers were fused at the edges together to craft the mini-bladders. The two layers of the mini-bladders were formed using following two silicone materials with different elastic properties:

- a. The extensible layer (top layer of the mini-bladder): a low hardness/low modulus silicone (PlatSil® Gel-OO 30 –shore OO hardness 30, and PlatSil® Gel-A 10-shore A 10 hardness)
- b. The less extensible layer (bottom layer of the mini-bladder):
 - i. a high hardness/high modulus silicone (Transil® A 20- shore A 20 hardness, and Transil® A 40- shore A 40 hardness)
 - ii. mixing Kaolinite ($\text{Al}_2\text{Si}_2\text{O}_5(\text{OH})_4$), a fine powder with low modulus silicone (PlatSil® Gel-OO 30 –shore OO hardness 30) to reduce the extensibility of silicone.

Figure 4.14, shows the mini-bladders created at the preliminary stage using Kaolinite ($\text{Al}_2\text{Si}_2\text{O}_5(\text{OH})_4$) to form the less extensible layer, and its different stages of inflation. The arrangement of the mini-bladders were such that it could closely replicate the honeycomb structure. This mini-bladder unit

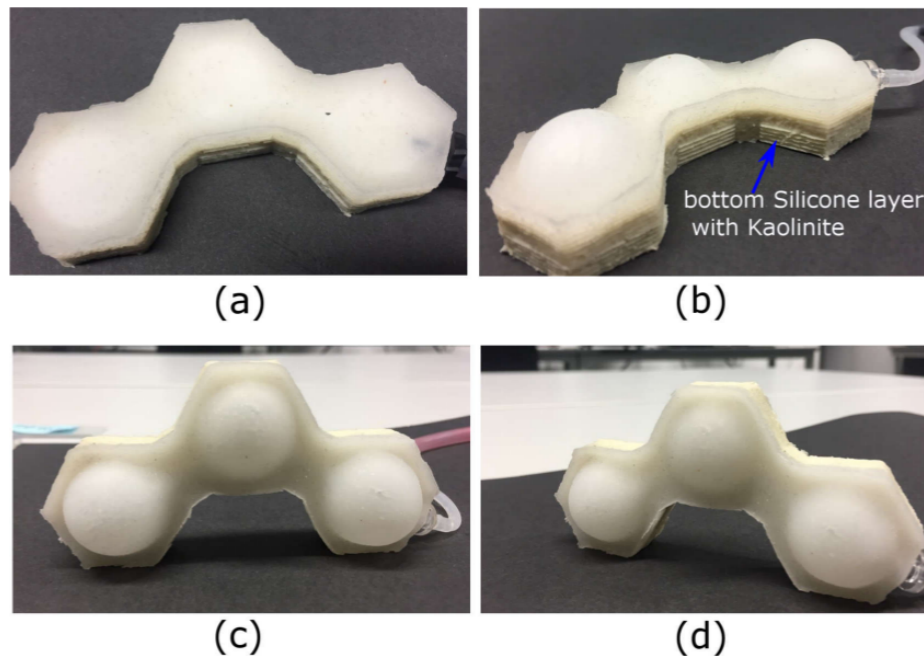


Fig. 4.14 a three mini-bladder unit manufactured by using PlatsilOO gel and Kaolinite at different stages of inflation (a) 0 ml of air volume, (b) 10 ml of air volume, (c) 20 ml of air volume and (d) 30 ml of air volume. All three mini-bladders are connected in series using an internal air channel, and the geometry is designed to closely replicate the honeycomb structure.

was inflated step wise using air volumes of 2 ml increments, and deflated using the same air volume decrements. This design could achieve the desired feature, that is to limit the inflation in less extensible layer however, there were few other problems associated with the design:

- The rigid bottom layer made the unit less flexible, and not suitable for the end application;
- The mini-bladder unit was manufactured using two separate layers, and then connected together at the edges using silicone; this resulted in thicker edges and increased the size of the mini-bladders

It was observed that only the top layer of the mini-bladders inflated when air was pumped into the mini-bladder unit, however this caused the overall unit to bend due to different elastic modulus of the top and the bottom layers; when pumped with air the top layer inflated more than the bottom layer causing the bottom layer to bend. The Fig. 4.15 shows a photograph of two mini-bladder units after inflating for 20 – 25 cycles. It shows that the mini-bladder units have permanently curled upside.

The above preliminary study on crafting mini-bladders demonstrated that it is not suitable to use two different types of silicone to create mini-bladders with an elastic layer and a stiff layer. Therefore, it was decided to use one type of silicone (PlatSil® Gel-OO 30 –shore OO hardness 30) to form both layers of the mini-bladder; however, to combine one of the layers with a strong woven fabric (0.964 MPa Young's modulus, 151.69 GSM, 62epi, 60ppi, and 0.38 mm thickness) in order to restrict this

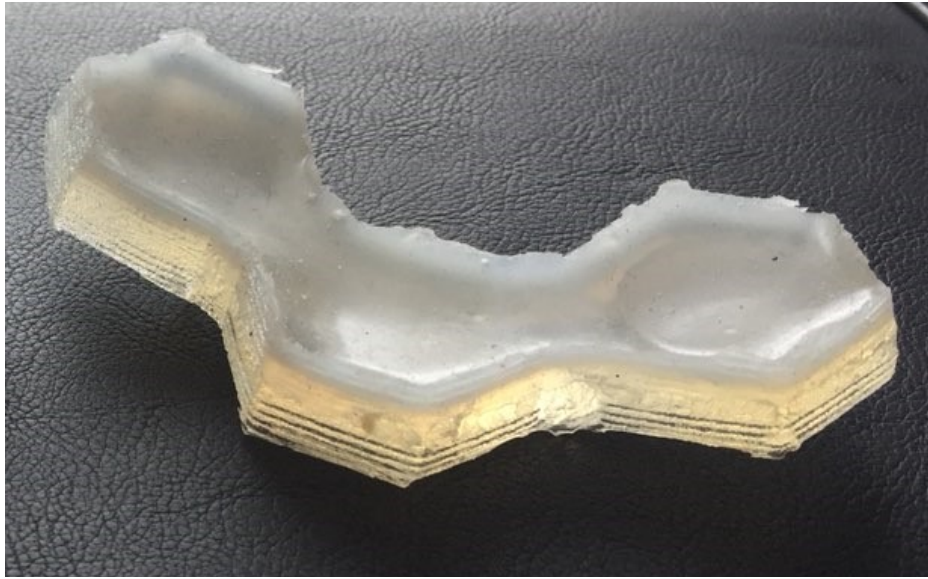


Fig. 4.15 Previously manufactured mini-bladder, using two different types of modulus materials for top and bottom layers of the mini-bladders (after 20 – 25 inflation cycles). The edges have curled to upside

layer from inflating when the mini-bladder is supplied with air.

During the preliminary stage, it was decided to manufacture mini-bladder units consisting of three to four internally connected mini-bladders. The final array of mini-bladders was envisaged to manufacture by combining these mini-bladder units together. However, in the arrangement depicted in Fig. 4.14 would provide much complicated design of the air inlets and the inflation of the mini-bladder units. Hence, it was decided to arrange these mini-bladders inline connected in series via a common air channel to avoid the complex pneumatic circuit.

4.4.2 Design and development of moulds to manufacture mini-bladders

Moulds were used to simplify the manufacture of mini-bladders. Two different moulds were designed to manufacture the top layer (Fig. 4.16 (a)) and the bottom layer of the entire bladder unit (Fig. 4.16 (b)). The moulds were designed using Dassault Systèmes SolidWorks (Dassault Systèmes, version 2016, France) and then 3D printed with a clear acrylic resin using FormLabs Form 2, 3D printer (GoPrint3D, Ripon, UK). Once the moulds have been printed, they were washed in IPA (99.9% Iso Propyl Alcohol) (MouldLife, Suffolk, UK) bath for about 20 minutes to remove any residue resin on the moulds. Thereafter the moulds were placed in a UV curing chamber approximately for an hour to cure the resin and stabilise the mould.

As shown in the Fig. 4.16 a, few special features are used in designing of these moulds, negative square features (Fig. 4.16 (a), 3) were embarked onto the mould in order to achieve the effective sealing of the two layers to avoid any possible leakages. Two parts of the top mould shown in Fig.

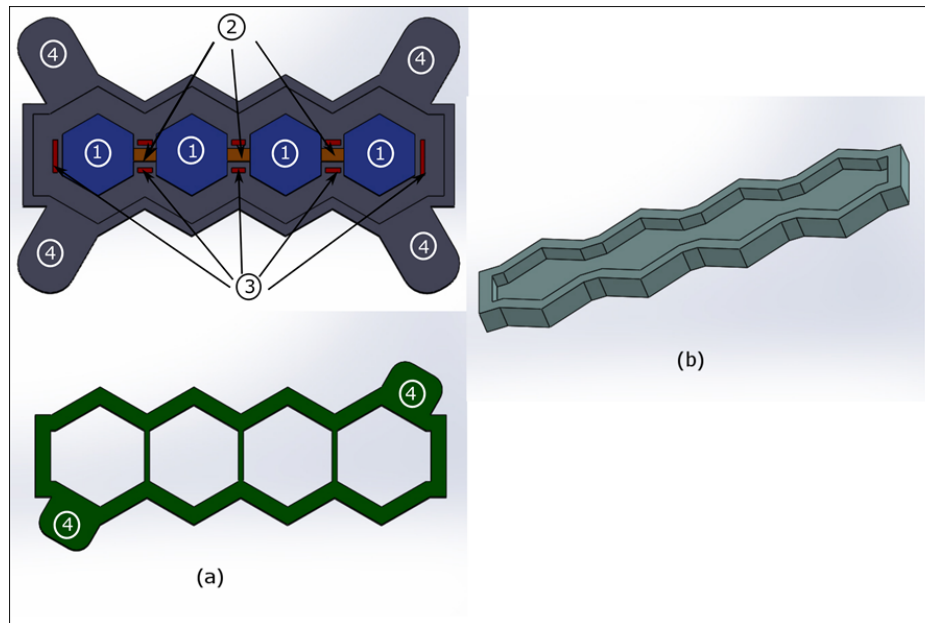


Fig. 4.16 3D printed moulds used to craft the mini-bladder unit (a) two-part mould to craft the top layer of the mini-bladder (b) base mould used to craft the bottom layer. The special features of the moulds used to craft mini-bladders; (1) hexagonal air chamber (positive) feature (2) central air channel (positive feature) (3) negative square feature (4) protruding curved segments at the edge of the moulds.

4.16 (a) were put on top of each other and poured the silicone which make a top layer having air chambers and small protruding parts (pegs). The unit is designed with small pegs coming out of the bottom surface of the mould at equal intervals. These pegs will act as connecting body between the top and the bottom layers, so that the top layer could fit precisely on top of the bottom layer, avoiding any leakages into the air chamber and to the air channel. When designing the top mould, the both top and bottom layers were given a protruding curved segment at the edges, in order to make it easier to lift the top part (Fig. 4.16, (a), 4) of the mould and peel off the silicone layer made with air chambers from the bottom part. With the improved mould designs it was easy to peel off the finished silicone layers (top layer) and connect them with the bottom layer. It was also designed to have different shaped moulds like square and circular in the same manner to manufacture square and circular bladders.

In designing mini-bladder units, which are connected internally on to each other as per the Fig. 4.17, the manufacturing of the top part of the bladder unit, was carried out carefully with mentioned features to improve its performance and avoid the air leakages while assembling. The feature (a) of 1 mm wide in Fig. 4.17 is to allow the bladder unit to bend, without any restriction and to maintain its flexibility. The central air channel (Fig. 4.17 (c)) was designed as 2 mm deep and 2.5 mm wide channels considering the commercially available air tubes. The peg part (Fig. 4.17 (b)) which protrudes will allow the top part of the bladder to fit in to the bottom layer well, preventing excess silicone leaking into either the air channel or to individual mini bladder chambers. As explained in section 4.3,

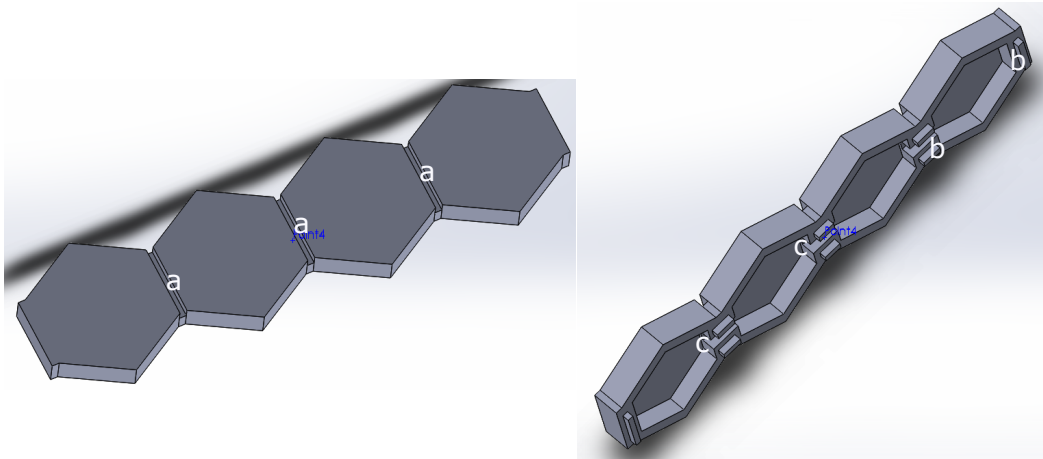


Fig. 4.17 SolidWorks drawing of top mould part of the Silicone bladder with distinguished features. (a) the separation lines of 1 mm thickness for each mini bladder unit (b) Protruding pegs (c) central cut of 2.5 mm wide, 2 mm deep running through all four mini bladders, facilitating the central air channel.

chamber height was decided to be 2.5 mm in order to reduce the thickness of the whole bladder unit, while the wall thickness of the chambers was designed to 1.5 mm, permitting the total thickness of the top layer to be 4.0 mm. The bottom layer was made to a thickness of 3.0 mm, which totals out the thickness of the bladder to be 7.0 mm.

4.5 Manufacturing process of mini-bladders

It was required to manufacture a less extensible, yet sufficiently flexible bottom layer to minimise the effect of rigidity of the whole mini-bladder unit. To produce this less extensible layer, a woven fabric was submerged into the bottom silicone layer, i.e. the entire mini-bladder unit was produced using only one type of silicone (same shore hardness). In the preliminary stage a Greige woven fabric (cotton, plain view, 151.69 GSM, 62 epi, 60 ppi, Young's modulus of 0.964 MPa) was submerged on to the silicone layer in order to reinforce bottom layer. Later in this study, a strong camouflage woven fabric (234 GSM, 50 epi, 37 ppi, Young's modulus of 1.648 MPa) which had a higher Young's modulus than the previous was used to reinforce bottom layer. This change was made to observe whether there exists a considerable change in the inflation height of the top layer, which was studied later under section 4.7.3. The key steps in mini-bladder manufacturing process is discussed below.

A two-part mould (Fig. 4.16a) is used to craft the top layer of the mini-bladder unit. The casting of the mini-bladder was made using PlatSil® Gel-OO 30 (shore OO 30), by mixing part A and part B of the resin in 1:1 ratio with 3% PlatSil® 71/73-part R retarder (MouldLife, Suffolk, UK) and degassed the mixture for 5 minutes until a clear liquid was formed. The degassing procedure ensures that the casted elastomer parts are free of trapped air bubbles. Thereafter the degassed mixture was poured inside the moulds. Then the moulds were placed inside the autoclave at 60 °C for about 5-10 minutes

to accelerate the curing.

The base mould (Fig. 4.16 b) was half filled with PlatSil® Gel-OO 30 (shore OO 30) and a piece Greige woven fabric (151.69 GSM, 62 epi, 60 ppi, Young's modulus of 0.964 MPa) was embedded into it. On top of the fabric layer one last thin layer of elastomer PlatSil® Gel- OO 30 (shore OO 30) was poured, and then the previously cured top layer was immersed deep enough to create a sealed connection with the bottom layer of the mini-bladder unit. Then the whole mini-bladder unit was placed on the autoclave at 60 °C for about 5 – 10 minutes to accelerate the curing (the detailed step wise manufacturing of the mini-bladder unit is included in Appendix C.

4.6 Inflation behaviour of mini-bladders

After designing and manufacturing the mini-bladder units of hexagonal shape, an experimental rig was developed to characterise and quantify the mini-bladders with respect to their inflation deflation height as shown in Fig. 4.18. Three mini-bladder units were manufactured, with each unit consisting of four individual mini-bladders as shown in Figure 4.17. The inflation and deflation height of each mini-bladder against the inlet air volume and back-pressure was examined to determine whether the mini-bladders inflate uniformly as well as to identify any hysteresis effects.

4.6.1 Experimental set-up

The test rig was designed with a laser displacement sensor LK-G 82, with class II laser of 650 nm wavelength (Keyence, Milton Keynes, UK) mounted on to a stepper motor controlled linear translation stage LTS 150 (Thorlabs, Ely, UK). The LK-G 82 had a measuring range of 30 mm with an accuracy of 0.0001 mm, and was used to determine the inflation and deflation height of mini-bladders. The linear translation stage had a traverse of 150 mm with a 5.0 μ m on-axis accuracy and enabled to determine the inflation/deflation height of mini-bladders at different points accurately (The specifications of LK-G 82 and LTS 150 are included in Appendix B.

The laser displacement sensor was connected to LK-G3000 controller and used with supporting LK-Navigator software (Keyence, Milton Keynes, UK) to determine the height of mini-bladders during both inflation and deflation cycles. The experiments were carried out with bladder units, each consisting of four internally connected hexagonal shape mini-bladders. The bladder units were attached to a breadboard as shown in Fig 4.19 using thin coated wires (0.65 mm thick, 1.60 mm wide) (KLOUD City, UK) to secure their position during testing and the bladder unit was connected to external air supply as shown in Fig 4.18. The air supply was connected a Y connector, with one end connected to a 60 ml syringe and the other end to a vertical liquid column manometer (TJ600) with measuring range of 0 – 130 mbar, and Volt 1S manometer liquid of 1.86 specific gravity (KIMO Instruments, Kent, UK) as illustrated in Fig 4.18. A vertical column liquid manometer was used to pressure measurement, as it is considered the gold standard for pressure measurements in comparison to other pressure gauges.

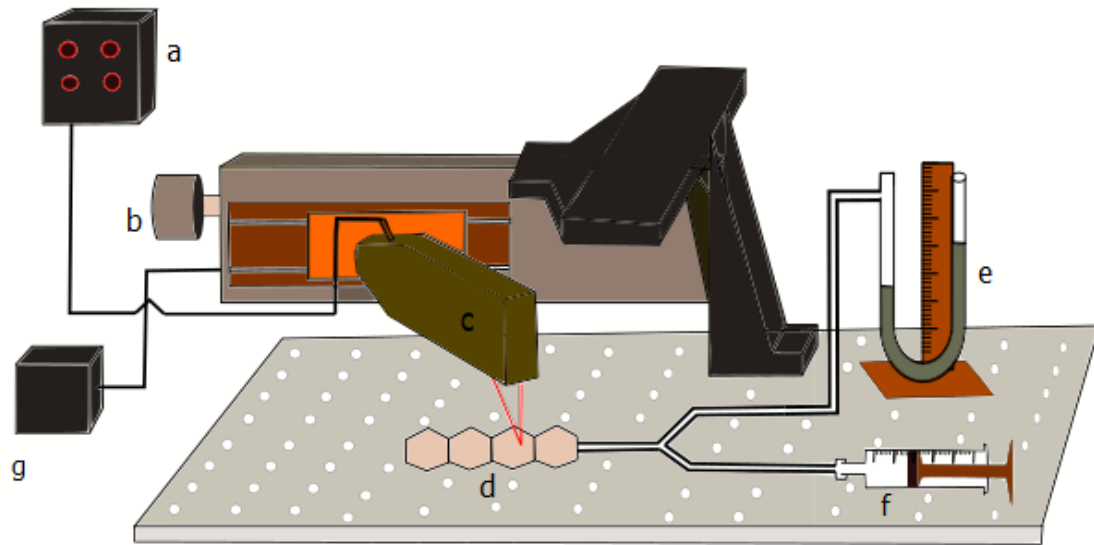


Fig. 4.18 Experimental setup for measuring the inflation height against input air volume. (a) Height measurement display panel and controller, (b) linear translation stage, (c) laser displacement sensor (d) inflatable hexagonal mini- bladder unit, (e) liquid manometer, (f) syringe, and (g) power supply

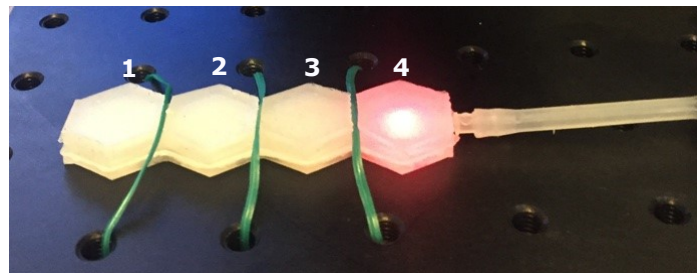


Fig. 4.19 Hexagonal mini bladder unit, tied on to the breadboard surface with mini-bladder numbers for reference

In the first set of experiments mini-bladder inflation height was recorded for three hexagonal mini-bladder sample units made out of each of the two different type of silicones (PlatSil® Gel-OO 30 and PlatSil® Gel-A 10). The air volume inside the bladders were increased in 2 ml increments. The bladder height was measured during both inflation and deflation cycles. For the height measurement LK-G 82 laser measurement head was fixed on to the linear stage so that it could move along the centre axis of the mini-bladder unit. The LK-G 82 was fixed, such that the laser point coincides with the centre line position of each mini-bladder. Then LTS 150 stage could be accurately moved from the mid point of one mini-bladder to the next by specifying the distance on the software. This process could also be carried out by manually by marking the mid-point of each mini-bladder. After inflating the mini-bladders to a certain pressure, it was allowed to stabilise for 1 minute and the mid-point height was measured for each component mini-bladder subsequently. Each test was repeated for

five cycles to evaluate the accuracy and the repeatability of the results. Thereafter, one mini-bladder unit made from each Silicone type was subjected to 48hrs of relaxation under standard laboratory conditions and the same test procedure was repeated to measure the inflation-deflation heights.

4.6.2 Experimental results and discussion

As explained in the section 4.6.1, the inflation occurred in the extensible layer which is the top layer of the mini-bladder. During inflation the hexagonal mini-bladders deformed to a dome shape with the highest inflation height at the midpoint of the mini-bladder, thus the midpoint-height was measured with the LK-G 82 laser displacement sensor during the inflation and deflation cycles. The laser displacement sensor was calibrated so that all height measurements were relative to the top surface of the breadboard, i.e. the zero value setting of the sensor.

Figure 4.20 depicts the results of the sample one (S1) of the hexagonal mini-bladder unit made out of PlatSil® Gel-OO 30 silicone (results for other two samples are included in Appendix C). The midpoint-heights of the four component mini-bladders of the mini-bladder unit were measured during both inflation and deflation cycles at 2 ml volume increment/decrement step. The error bars in the Fig. 4.20 represent the standard error related to the five repeated inflation and deflation cycles. Figure 4.21 shows the variation of the average inflation/deflation height against the inlet air volume averaged over all three hexagonal mini-bladder units made of PlatSil® Gel-OO 30 silicone, with error bars representing the standard error for the three different samples. The standard error was calculated based on, the equation 4.16,

$$\text{Standard error} = \frac{\sigma}{\sqrt{n}} \quad (4.16)$$

where, σ = standard deviation and n = number of cycles.

The average inflation height varied between 0 – 7 mm for the samples prepared from PlatSil® Gel-OO 30 silicone. Mini-bladder one had the highest inflation height, followed by mini-bladder two and three. However, mini-bladder four showed slightly higher inflation height than mini-bladder two and three, and a value closer to mini-bladder one. This may have been caused due to the method used to secure the mini-bladder unit on to the flat surface of breadboard.

As shown in Fig. 4.19, the mini-bladder unit was not fixed from the both ends, instead it was tied in the middle to the breadboard of the experimental rig. Because the ends of the mini-bladder unit were not fixed to the breadboard it may have curved slightly upward during inflation. Also, it can be noted that the deviations between the tested samples were low (standard error was less than 0.5 mm). During the inflation/deflation cycle the back pressure (measured at the inlet of the air channel) of the mini-bladder unit varied from 0-83 mmHg (since the mini-bladders in the unit were internally connected it was assumed that all component mini-bladders are in the same pressure) (The height vs. pressure for the PlatSil® Gel-OO 30 samples are included in Appendix C.

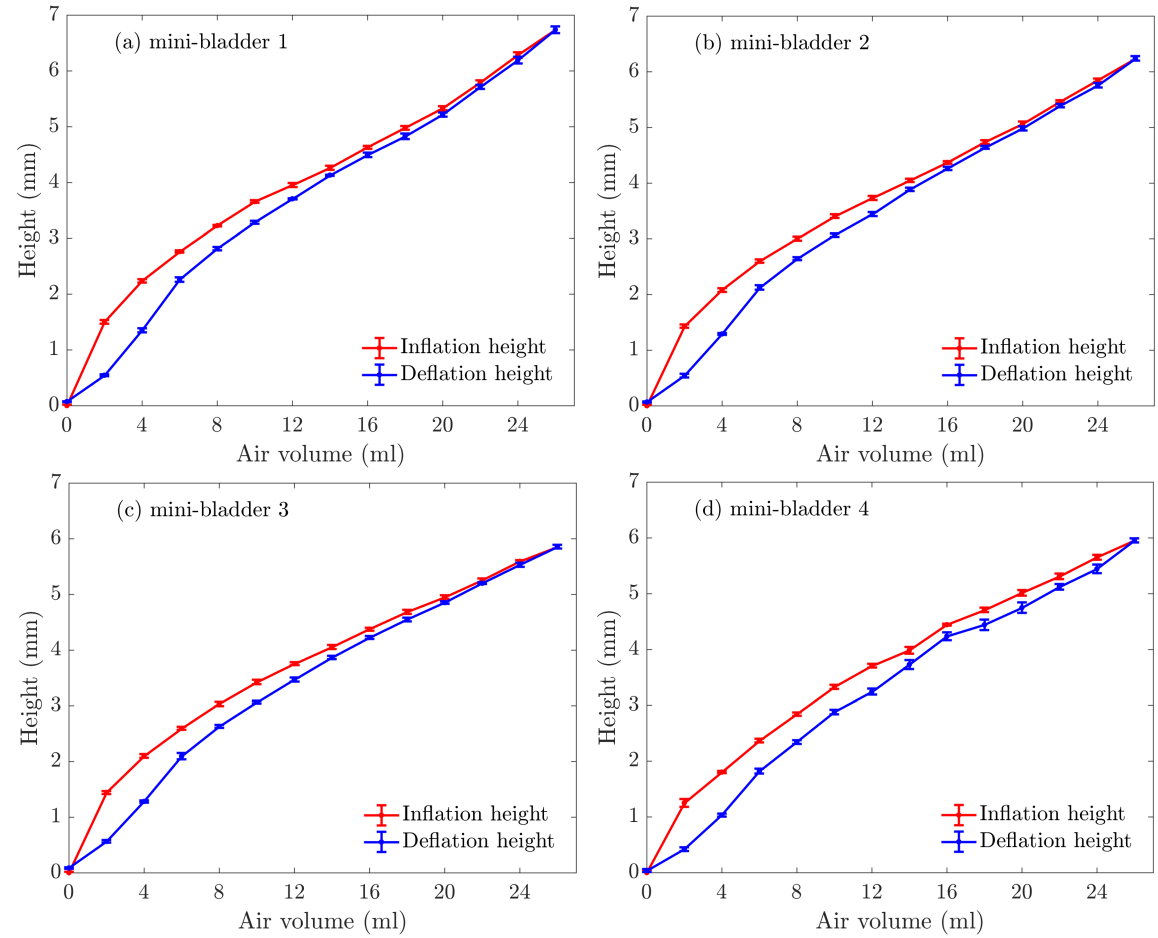


Fig. 4.20 The inflation/deflation height vs. inflating air volume, for mini-bladder unit 1 made from PlatSil® Gel-OO 30. (a) mini-bladder 1, (b) mini-bladder 2, (c) mini-bladder 3, and (d) mini-bladder 4

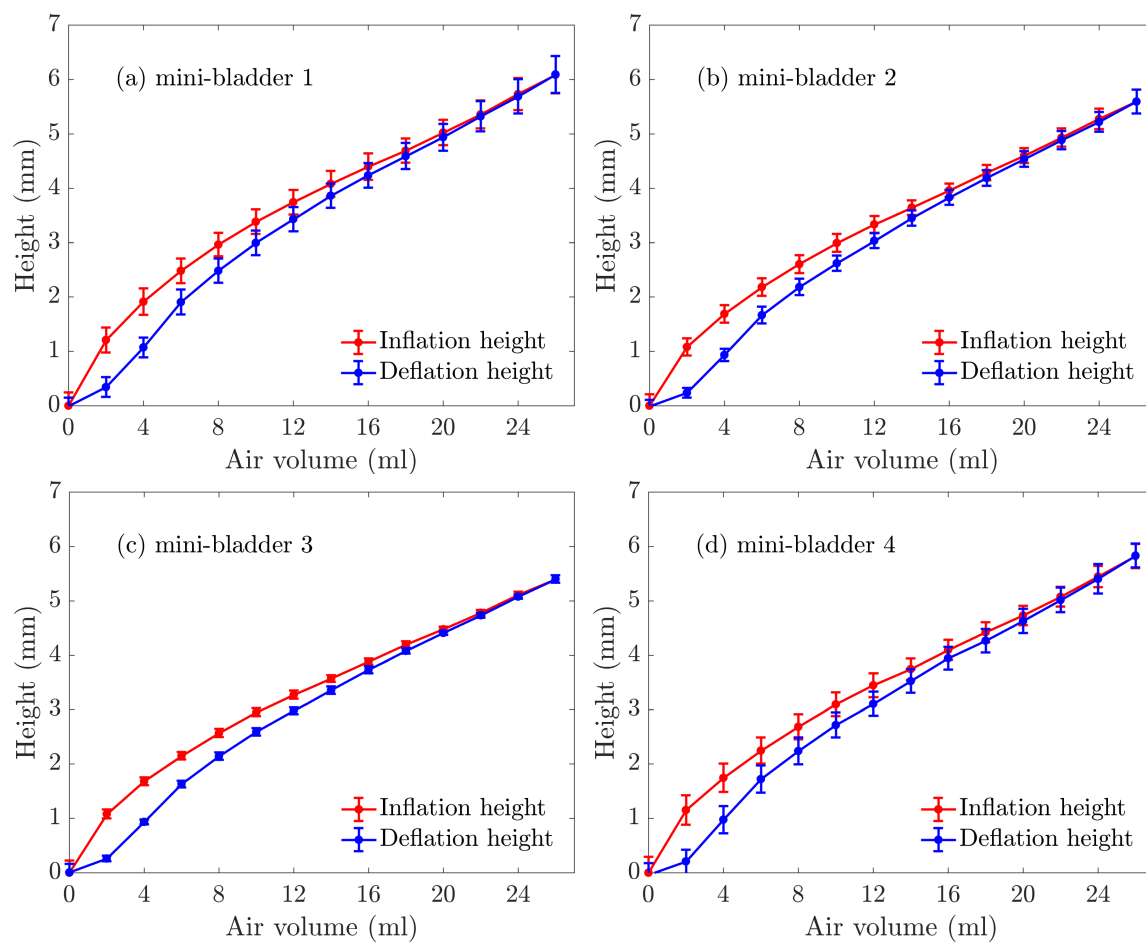


Fig. 4.21 The relationship between the average inflation/deflation height of the mini-bladders and the air volume supplied to the mini-bladder unit made with PlatSil® Gel-OO 30. (a) mini-bladder 1, (b) mini-bladder 2, (c) mini-bladder 3, and (d) mini-bladder 4

The same series of experiments were conducted with three mini-bladder units produced from PlatSil® Gel-A10 and the results are demonstrated in Fig 4.22, which shows the relationship between the average midpoint-height of the hexagonal mini-bladders and the inlet air volume during inflation/deflation cycle for all the three mini-bladder units. The error bars represent the standard error for the three different mini-bladder units. Fig. 4.23, shows the inflation-deflation height against the air volume for one mini-bladder unit, with error bars representing the standard error related to the five repetitive cycles (results for other two mini-bladder units are included in Appendix C).

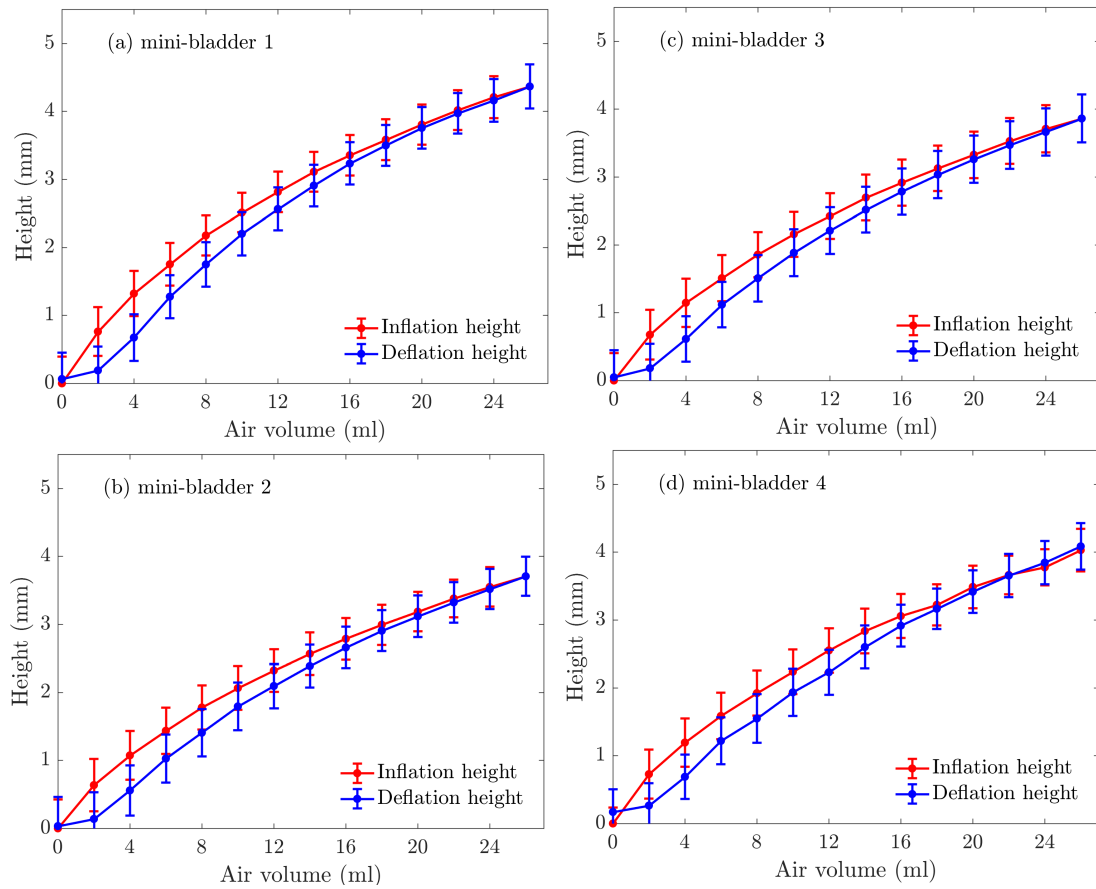


Fig. 4.22 The average inflation/deflation height vs. inflating air volume, for mini-bladder unit made with PlatSil® Gel-A10. (a) mini-bladder 1, (b) mini-bladder 2, (c) mini-bladder 3, and (d) mini-bladder 4

As can be seen from the Figs. 4.22 and 4.23, the inflation-deflation pattern of the PlatSil® Gel-A 10 is similar to that observed for mini-bladder units made from PlatSil® Gel-OO 30. The first mini-bladder of the mini-bladder unit recorded the highest midpoint-height, the second and third slightly less while the fourth mini-bladder showed a higher midpoint-height than the second and third mini-bladders of the mini-bladder unit. This is the same inflation pattern observed with the mini-bladders of mini-bladder units produced with PlatSil Gel-OO 30.

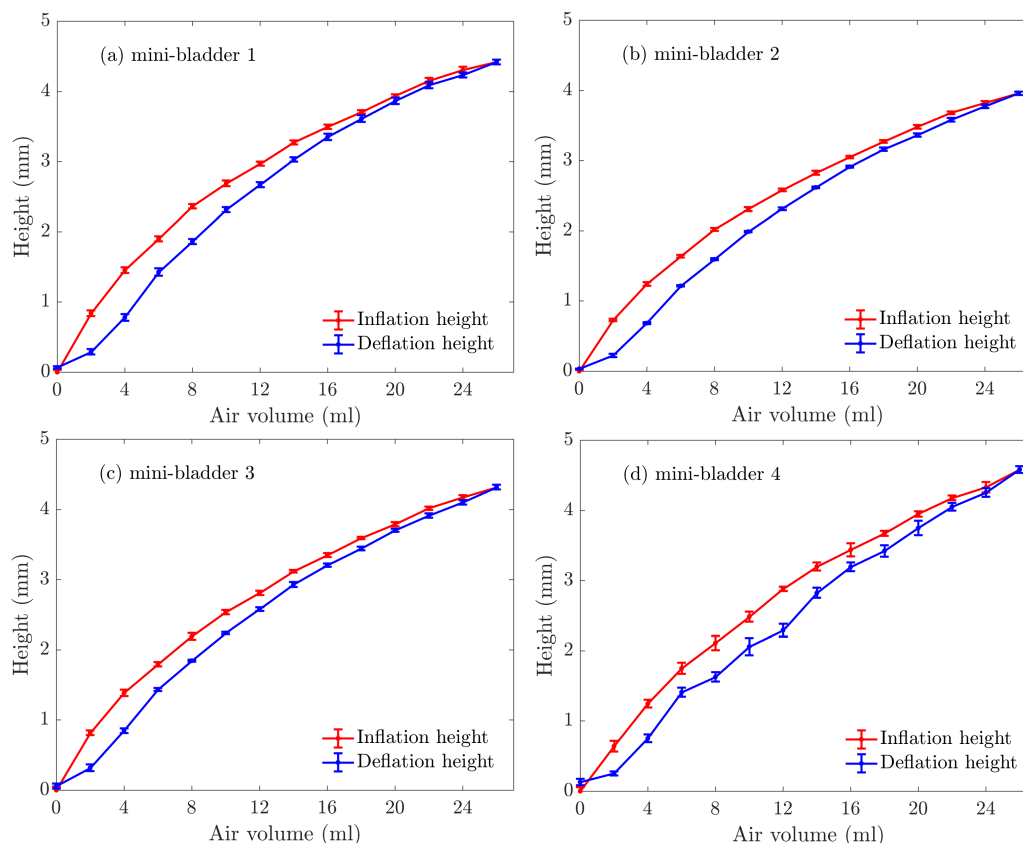


Fig. 4.23 The inflation/deflation height vs. inflating air volume, for mini-bladder unit 1 made out of PlatSil® Gel-A 10 (a) mini-bladder 1, (b) mini-bladder 2, (c) mini-bladder 3, and (d) mini-bladder 4

The inflation-deflation height of the mini-bladders made with PlatSil® Gel-OO 30 (shore OO 30) varied from 0 mm-7.0 mm. The mini-bladders made of PlatSil® Gel-A10 (shore A10) showed lower maximum inflation height (0-5.0 mm) compared to mini-bladders made with PlatSil® Gel-OO 30. This could be explained by the modulus of the two silicones types used; the silicone with shore A10 has a higher modulus than a silicone of shore OO 30 hardness. During the inflation/deflation cycle the pressure inside the mini-bladders varied between 0-90 mmHg (The height vs. pressure for the PlatSil® Gel-A10 samples are included in Appendix C).

The mini-bladder units were allowed to relax for 48 hrs in standard room temperature and pressure and retested. The results of mini-bladder inflation-deflation height characteristics are shown in Fig. 4.24, and Fig. 4.25 for mini-bladder units made from PlatSil® Gel-OO 30 and PlatSil® Gel-A 10 respectively. The results demonstrate a similar pattern of inflation and deflation height characteristics for the mini-bladders, however, a very slight difference to the results prior to 48 hrs relaxation could be observed. This showed that the mini-bladder inflation-deflation behaviour does not deteriorate with time and that after relaxation the material performance was not compromised.

Furthermore, the mini-bladders made of PlatSil® Gel-A 10 silicone mini-bladders also exhibited a similar behaviour to those made of PlatSil® Gel-OO 30 silicone. The inflation-deflation heights

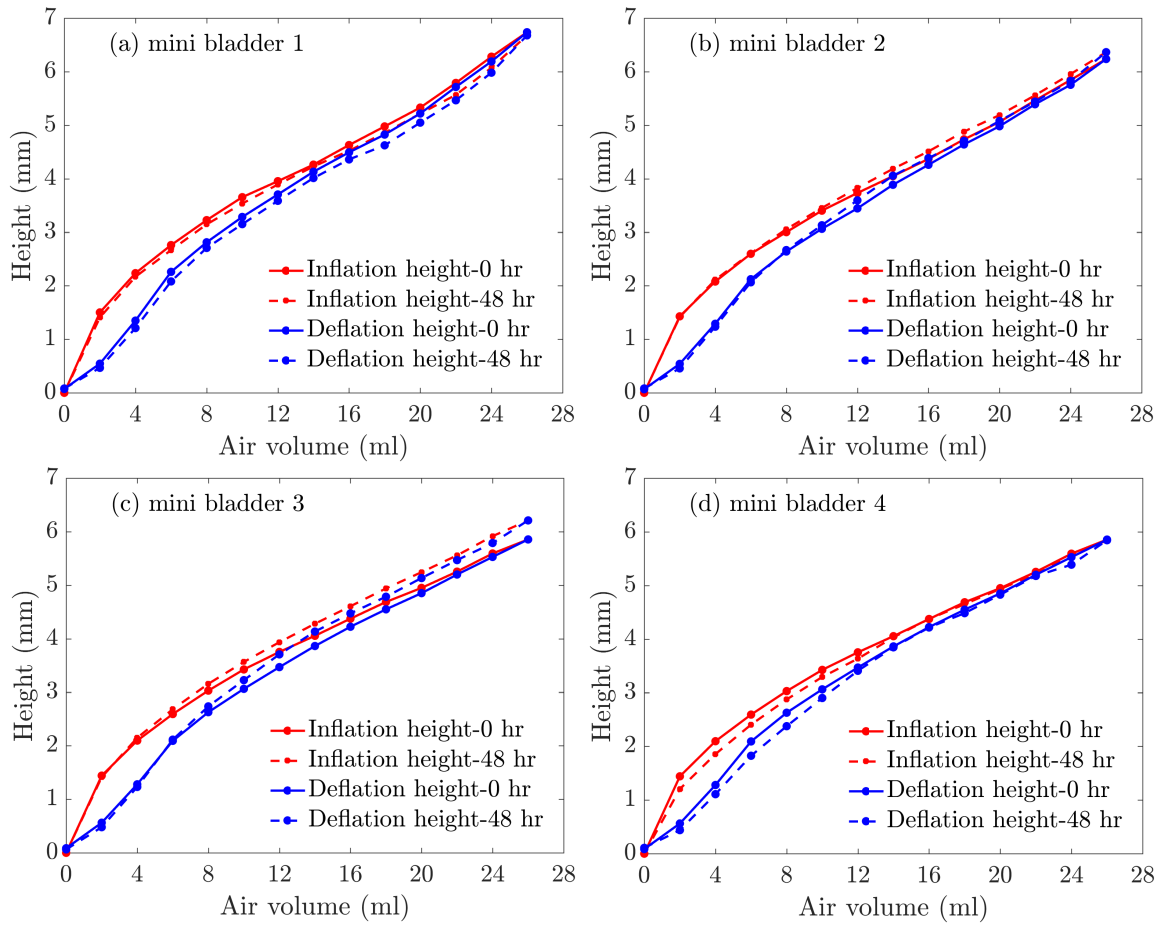


Fig. 4.24 The inflation-deflation heights and inflation air volume function of the four mini-bladders of the mini-bladder units made out of PlatSil® Gel-OO 30 silicone before and after relaxation for 48 hrs. (a) mini-bladder 1 (b) mini-bladder 2 (c) mini-bladder 3 (d) mini-bladder 4.

recorded for the relaxation cycle showed the same pattern as prior to relaxation, however the difference in inflation-deflation heights measured were less than the values observed for mini-bladders made of PlatSil® Gel-OO 30 silicone. Therefore, it could be concluded that after the relaxation, material properties have not deteriorated, which proves that the mini-bladder units can be used for repetitive times without experiencing deteriorated performance.

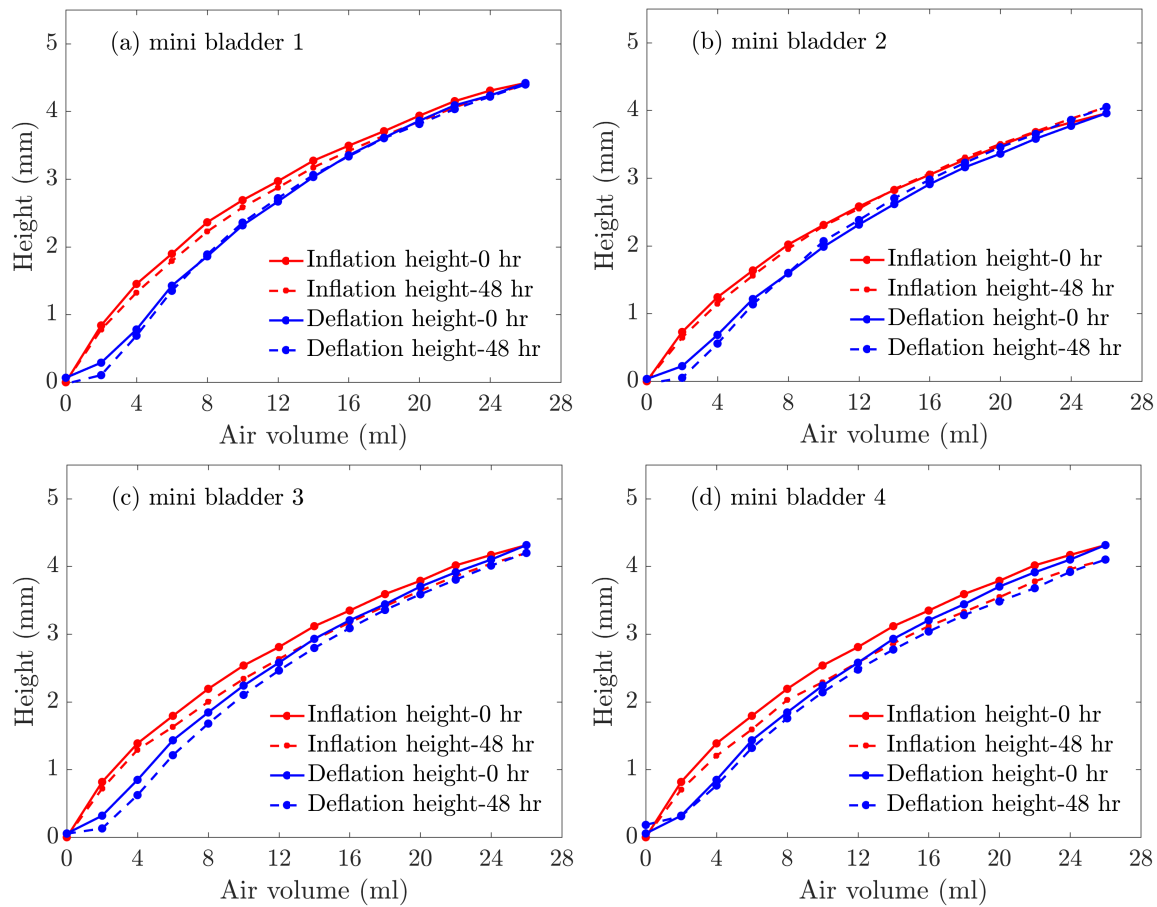


Fig. 4.25 The inflation-deflation heights and inflation air volume function of the four mini-bladders of the mini-bladder units made out of PlatSil® Gel-A 10 silicone before and after relaxation for 48 hrs. (a) mini-bladder 1 (b) mini-bladder 2 (c) mini-bladder 3 (d) mini-bladder 4.

4.7 Numerical modelling of the inflation behaviour

The inflation behaviour of the mini-bladder unit was simulated using finite element analysis (FEA) to understand the behaviour of the mini-bladders of a mini-bladder unit. The development of a numerical model can be used to simulate the inflation behaviour of a mini-bladder unit in different conditions. For the modelling, ANSYS Workbench (ANSYS Academic, version 18.1, ANSYS Inc., Canonsburg, USA) was used. Yeoh second order model was used to build the geometrical modelling and the required material parameters were calculated using the uniaxial tests described under section 4.3.3 for the PlatSil® Gel-OO 30 silicone type.

4.7.1 FEM modelling of the mini-bladder unit on a flat surface

The objective was to simulate the experimental results of the inflation-deflation heights of the mini-bladders of the mini-bladder unit against the inlet air pressure/air volume (experiments discussed in

section 4.6). To be consistent with the experiments, the modelling was based on the assumption that the mini-bladder unit was fixed onto the surface of a breadboard. Therefore, a geometrical model of the mini-bladder unit and the breadboard was created in SolidWorks (Dassault Systèmes SolidWorks, version 2016, France). The geometrical model was created by assembling the layers in SolidWorks, in four layers (Fig. 4.26).

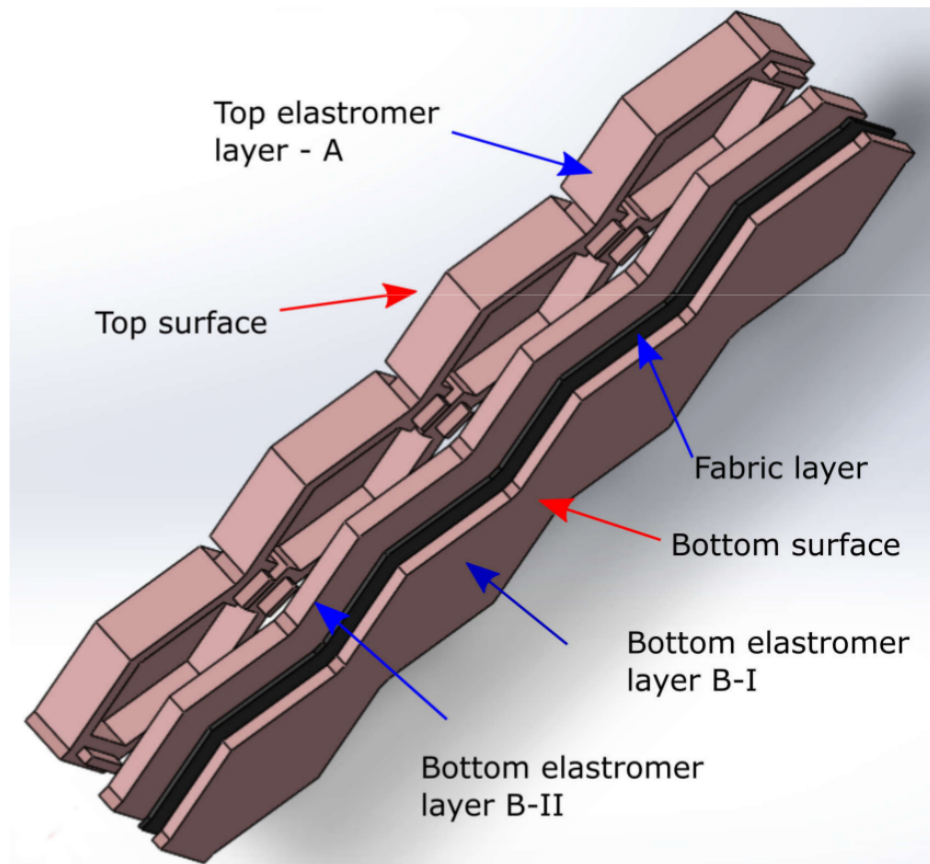


Fig. 4.26 The four constituent layers created in SolidWorks to define the geometrical model of the mini-bladder unit

The four layers as shown in Fig. 4.26 are:

- 1) Bottom elastomer layer B-I: 0.62 mm thick elastomer layer, which represents the bottom most elastomer layer,
- 2) Fabric layer- 0.38 mm thick layer of hexagonal shape to represent the woven fabric layer which will be sandwiched between the bottom elastomer layers,
- 3) Bottom elastomer layer B-II: 2.0 mm thick elastomer layer, which will be in between the top layer A and the fabric layer,
- 4) Top elastomer layer A: with air chambers - 4.0 mm thick elastomer layer, including air chambers of 2.5 mm height.

To represent the breadboard to which the mini-bladders were fixed on during the experiments, another layer was introduced after the bottom elastomer layer B-I. The entire assembly was developed in SolidWorks and then converted to the IGES format in order to process this further on ANSYS workbench.

On the ANSYS workbench the following previously identified material properties and parameters were specified for each layer.

- Silicone layers made from PlatSil® Gel-OO 30 were specified as a hyperelastic material and defined using Yeoh second order model with material parameters $C_{10} = 0.049572$ MPa and $C_{20} = 0.00005649$ MPa and density of 1100kgm^{-3}
- The fabric layer was specified as a linear elastic material, with Young's modulus of 0.964 MPa and 151.69 GSM (62 epi, 60 ppi), density of 0.4kgm^{-3} , and Poisson's ration of 0.3 (approximated value);
- Later the fabric layer was replaced with a strong camouflage military fabric, with Young's modulus of 1.648 MPa and 234 GSM (50 epi, 37 ppi), Young's modulus of 1.648 MPa, density of 0.6kgm^{-3} , and Poisson's ration of 0.3 (approximated value).

Thereafter the connections between each surfaces of the mini-bladder unit and the breadboard surface (Fig. 4.27) were specified. In the FEM analysis the contacts between layers were defined to closely replicate the experimental setup used and are described as follows:

- Bonded contact between top elastomer layer A and the bottom elastomer layer B-II;
- Bonded contact between the bottom silicone layer B-II and the fabric layer;
- Bonded contact between the fabric layer and the bottom elastomer layer B-I silicone layer;
- Frictional contact (coefficient of frictional 0.5) between the bottom elastomer layer B-I and the breadboard surface.

After specifying the contacts between individual layers a mesh of 1.0 mm resolution was created for the mini-bladder unit; 1.0 mm resolution was deemed to be an appropriately high resolution for the mini-bladder unit that was ~ 50 mm across length.

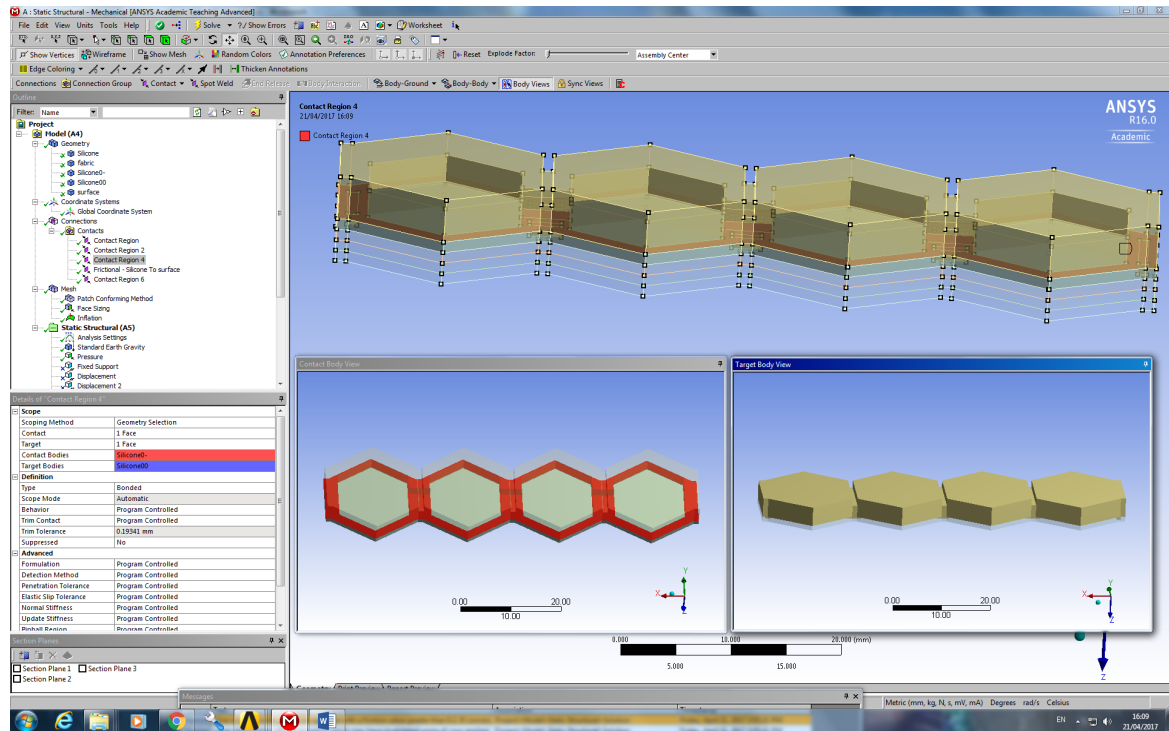


Fig. 4.27 ANSYS workbench setup under the contacts specifying each solid body, and contact surface specifying the contact type - Top silicone layer to first bottom silicone layer (contact type –Bonded)

Thereafter the boundary conditions were defined to represent the experimental conditions discussed in section 4.6; the critical boundaries are shown in Fig 4.28 below.

The defined boundary conditions are as follows:

- Displacement 1 & 2: (The displacement here refers to one or more faces or edges displaced relative to their original location): This is to represent the edges of the mini-bladder unit on the breadboard surface (Fig. 4.28, a and b). At these edges of the mini-bladder unit their movement is constrained on y direction, however they could still move in the x and z directions. Therefore, x and z directions displacement were set as free and y was set to zero;
- Displacement 3: This represents the 12 edges of 6 in each side of the mini-bladder unit which were used to tie the mini-bladder unit on to the breadboard surface using thin chords. These 6 edges on one side represents the top most edge on the top silicone layer and the bottom most edge of the bottom elastomer layer B-I (Fig. 4.28, c). Since the mini-bladder unit is tied on to the surface of the breadboard its movement in y and z directions were restricted, while allowing a possible movement in the x direction. Therefore, displacement in x direction was set as free, while y and z were set zero;
- Thereafter, a force was introduced on the edges to represent the force induced by the tension of the thin wires used to attach the mini-bladder unit to the breadboards as specified in Fig. 4.28 c.

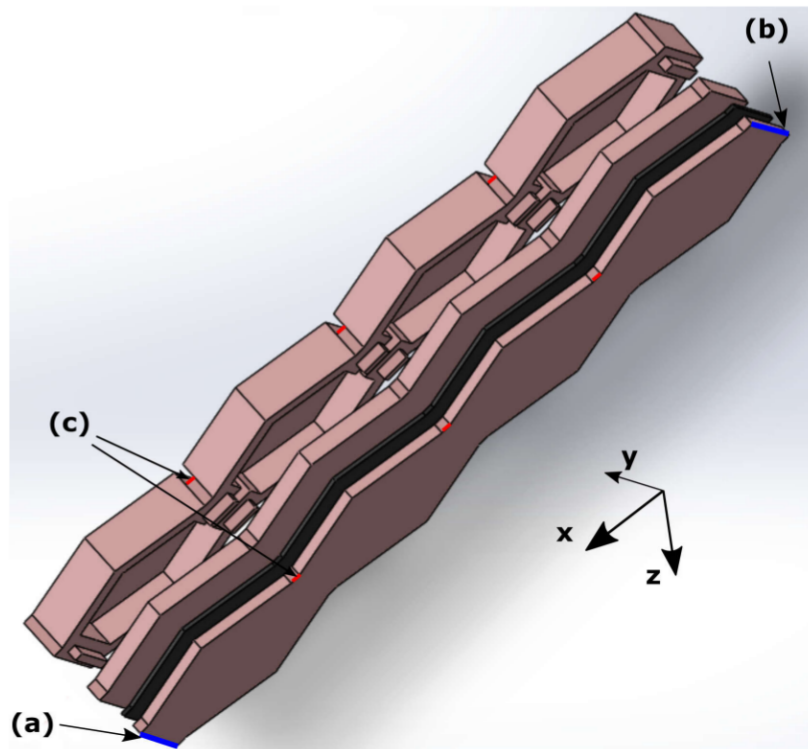


Fig. 4.28 The specification of boundary conditions associated with the mini-bladder unit

As an approximation an absolute value of 0.10 N was used for the force with the following components $X = 0.0$ N, $Y = 0.10$ N, $Z = 0.10$ N on one side and $X = 0.0$ N, $Y = 0.10$ N, $Z = 0.10$ N on the opposite side.

- Then air pressure was applied to all internal surfaces of the air chambers of the mini-bladders including the air channels between the mini-bladders.

4.7.2 Results of FE simulation

After applying the pressure on all the internal surfaces of the air chambers, the simulations were carried out for the range of average input pressures that was used in the experiments described in section 4.6, for mini-bladder unit made of PlatSil® Gel-OO 30. A simulation of the directional deformation was executed up to a pressure of 10,840 Pa (81.3 mmHg), which was the highest pressure the mini-bladder unit was inflated to during the experiments. It was observed that the slight curling of the mini-bladder unit at both edges which were not tied on to the breadboard surface (Fig 4.29).

The numerical simulations were also extended to different sized mini-bladder units and different membrane thicknesses in order to observe the maximum deformation height of the mini-bladder unit with regards to the changes in geometrical size. These numerical predictions could be used as

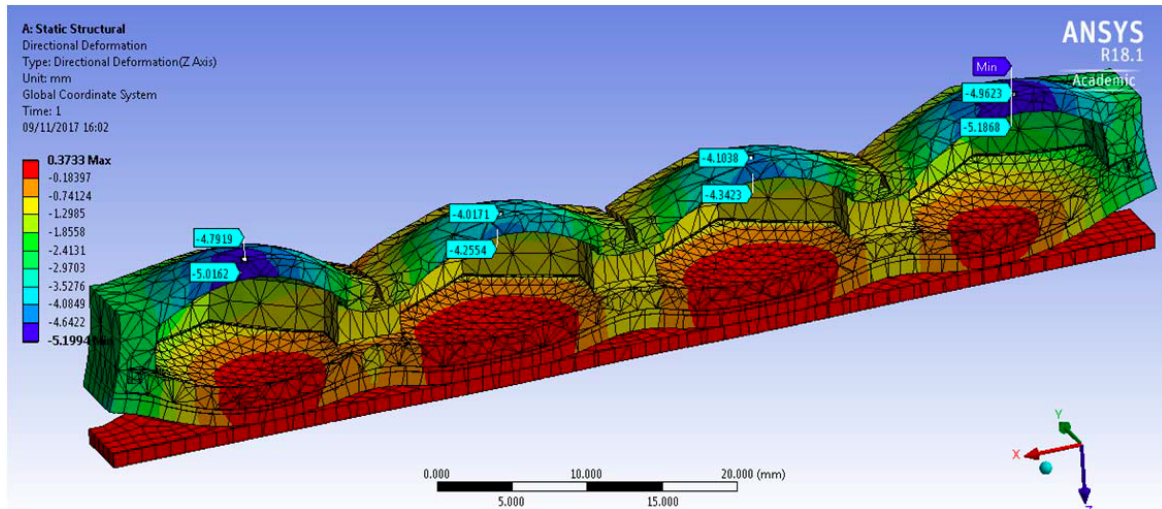


Fig. 4.29 Simulation of the directional deformation (deformation in z direction) of PlatSil® Gel-OO mini-bladder unit for pressure of 10,840 Pa (81.3 mmHg). The maximum deformation is shown in the legend.

designing guidelines as discussed in the section 4.3.4, in designing the mini-bladder units and the final prototype. The results obtained for these simulations are included in Appendix C.

4.7.3 Comparison of experimental and numerical data

The deformation value for the midpoint of the PlatSil® Gel-OO 30 mini-bladder unit was obtained from the results of the model simulation, and plotted against the experimental height increase, averaged over three samples, for each inflation pressure; the results are shown in the Fig. 4.30.

It can be seen from the Fig. 4.30, that the FEM results of the mini-bladders showed more than 80% agreement (on the average) with the experimental data for inlet pressures from 0 – 60 mmHg demonstrating that the numerical model is a good representation of the mini-bladder unit in this pressure range. As it can be seen from the Fig. 4.30, the numerical values from the model start to deviate from the experimental results at pressure above 60 mmHg. This could be due to approximation errors of parameters such as coefficient of friction, which was deduced based on the data available in the public domain; the frictional forces could have a significant impact at high pressure conditions due to occurrence of slippage.

In latter stages of manufacturing mini-bladder units, it was decided to use a much stronger woven fabric (camouflage fabric), to further reduce the inflation of the bottom layer of the mini-bladder unit by reinforcing it. Thus, separate simulations were carried out with strong woven fabric to identify the effect of the mechanical properties of the reinforcing the fabric on the inflation of the mini-bladders. Figure 4.31, shows the comparison for the two different types of fabrics used to reinforce the bottom layer of mini-bladder units. It is evident that there is not much noticeable difference for the both fabric types.

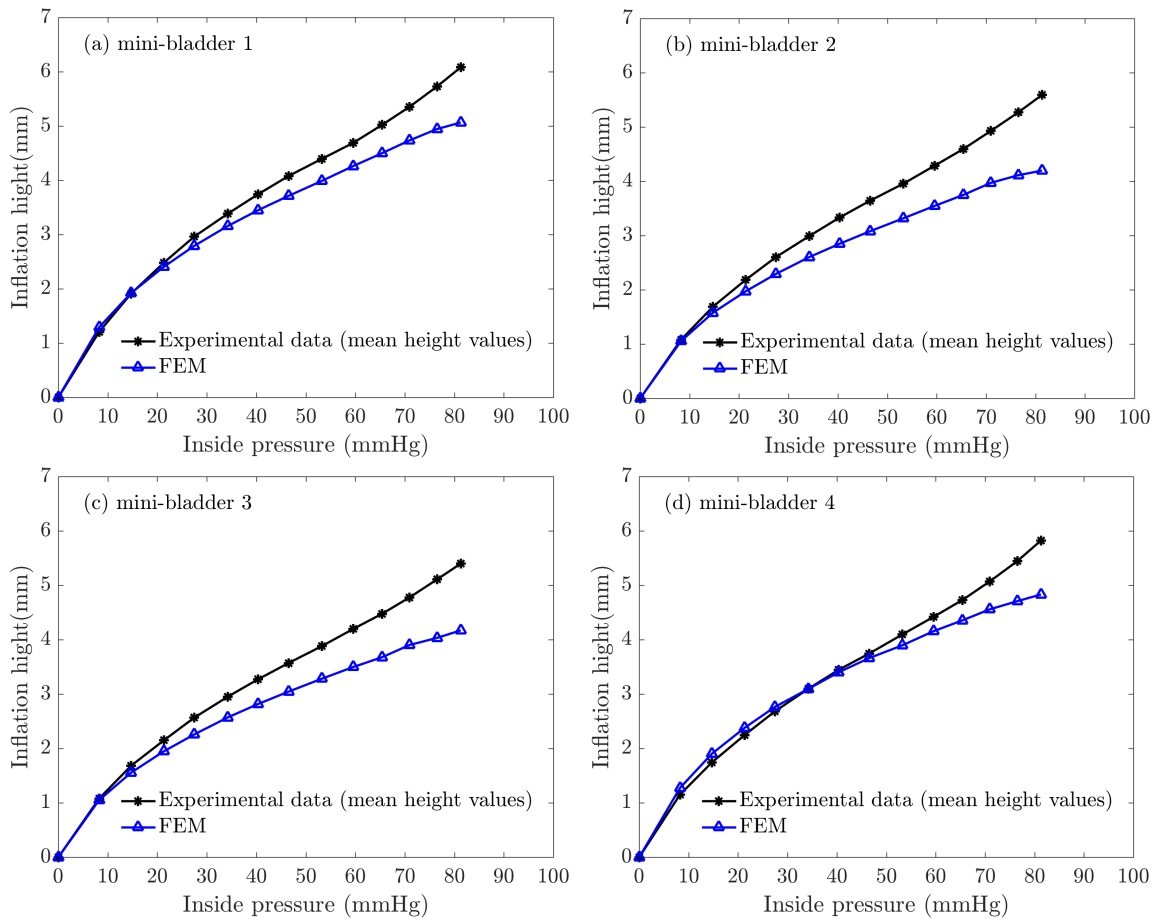


Fig. 4.30 Comparison of Yeoh second order numerical model value (FEA) for inflation height and experimental mean height of PlatSil® Gel-OO 30 sample against the pressure between 0 mmHg and 85 mmHg.

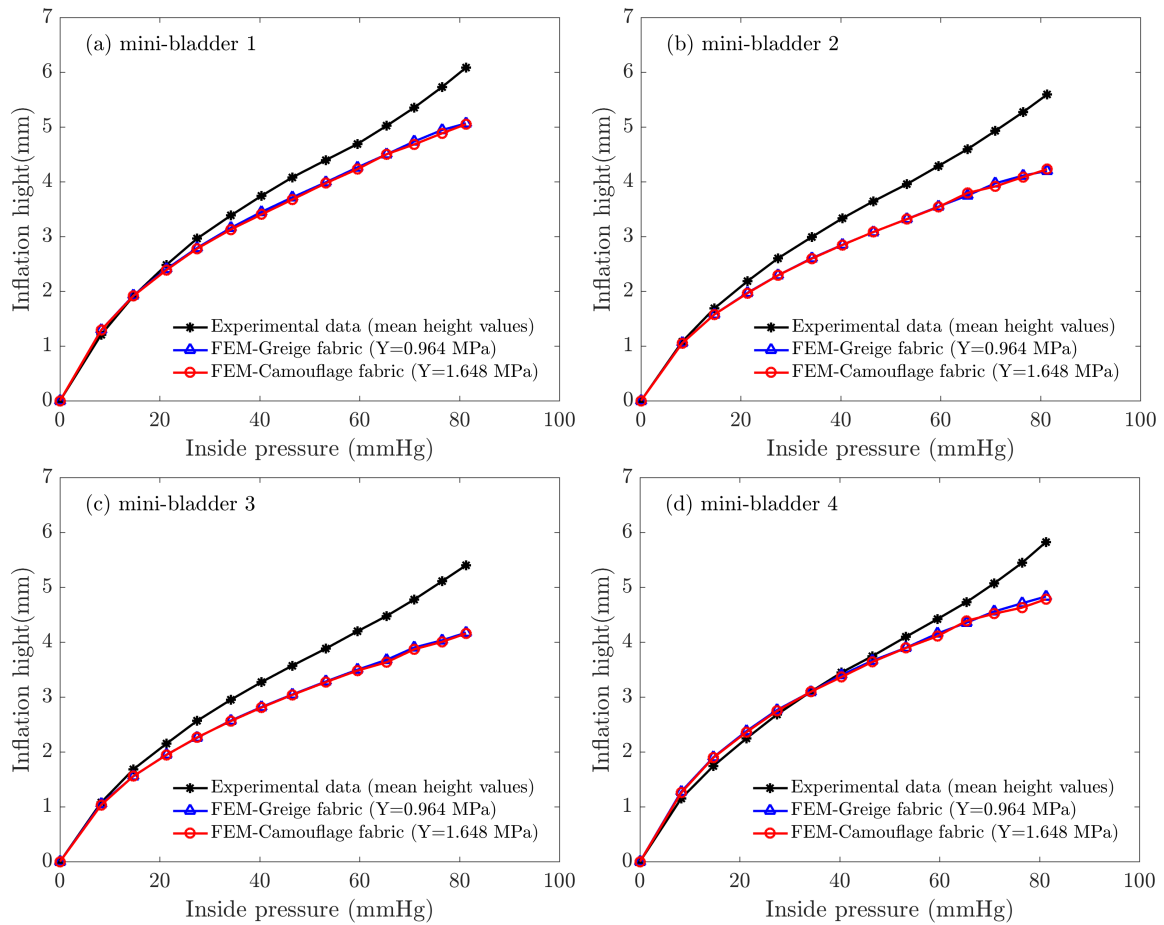


Fig. 4.31 Comparison of Yeoh second order numerical model value (FEA) for inflation height with two different woven fabrics used and experimental mean height different of PlatSil® Gel-OO 30 sample against the pressure between 0 mmHg and 85 mmHg.

4.8 Chapter summary

Previous studies have shown that using a large single bladder, it is difficult to obtain a uniform pressure profile on a cylindrical surface, due to non-uniform deformation the bladder undergoes in contact with the surface (Naqvi et al., 2017). To overcome the effect of shape deformation of large single bladders wrapped around a human limb during its inflation an array of mini-bladders was designed and tested. Such a solution will enable the creation of a uniform pressure profile over the surface of a limb. In order to select an appropriate geometrical shape for the mini-bladders circular, hexagonal and square mini-bladders were crafted and inflation characteristics were studied. The experimental results showed that hexagonal shaped mini-bladders provided the best pressure transmission properties. Hence the hexagonal shape mini-bladders were used in designing the final prototype design. The mini-bladders were manufactured in both single and as an array of four mini-bladders in units.

Materials suitable for manufacturing the mini-bladders were investigated and a low modulus silicone was selected due to its good elastic properties, low hysteresis and the biocompatibility. Since the silicones are hyper-elastic materials, mathematical models available to characterise hyper-elastic materials were used to determine the material behaviour and the material properties using uniaxial tensile tests.

In order to enhance the pressure transmission efficiency. The mini-bladders were designed with only one inflatable surface and a new method has to be developed to manufacture them. Generally, bladders balloon during inflation. The mini-bladders were designed with an extensible layer capable of inflating freely and an inextensible layer fashioned by reinforced with a woven fabric to restrict extension during inflation. In order to maintain the repeatability of the manufacturing mini-bladders, special moulds were designed.

A special experimental rig was designed to characterise and quantify the inflation behaviour of the mini-bladder unit with respect to the volume of air pumped into the mini-bladders. The inflation height of a mini-bladder on the highest inflation point was measured and plotted against the inflation air volume for mini-bladder units made from two type of silicones (PlatSil® Gel-OO 30 andr PlatSil® Gel-A 10). A difference of the inflation heights of the mini-bladders of a mini-bladder unit were recorded; a mini-bladder unit consists of four mini-bladders interconnected with an air supply channel for inflation.

The inflation behaviour of the mini-bladders was modelled using Finite Element Analysis (FEA). The results obtained from the numerical model simulations were then compared with the experimentally observed data. The model showed more than 80% agreement with the experimental data over the range of 0 – 60 mmHg inside pressure of the mini-bladders.

Chapter 5

Pressure transmission characteristics of mini-bladders

This chapter presents the analysis of the capability of mini-bladders to transfer pressure onto a contact surface and to evaluate the mini-bladder efficiency to transfer pressure. Corresponding to the real life scenario this will depict how effective the inflatable mini-bladders are in delivering the required pressure profile and create a graduated compression over the human limb. In the present study, a series of experiments were designed to quantify the pressure transmission characteristics of the mini-bladders by expressing contact surface pressure as a function of the back pressure generated in the mini-bladder during inflation to evaluate the pressure transmission efficiency of the mini-bladders. Initially pressure transmission on to a hard flat surface was studied and then it was extended to a curved surface to assess the effect of radius of curvature.

The experiments were further extended to a biofidelic lower leg surrogate to observe the pressure transmission behaviour at different positions of the leg. The surface of the lower leg surrogate was covered with artificial skin and fat layers in order to evaluate the pressure transmission through the surface skin layers and fat layers, which has not been studied in previous research.

5.1 Pressure transmission behaviour on hard surfaces

The primary objective of developing an active compression system is to effectively deliver the required pressure profiles. Therefore, it was important to study the capability of the mini-bladders to induce pressure onto a contact surface, and this was carried out in following two stages:

1. Study of the pressure transmission on to a flat surface;
2. Study of the pressure transmission on to a cylindrical surface (surface with constant radius of curvature).

The preliminary tests of the mini-bladders were conducted on a hard flat surface and then on a hard cylindrical surface before they were tested against lower leg surrogate with artificial skin and fat layers (soft material). This approach provided a better understanding of the effect of radius of curvature and soft material layers on pressure transmission using the mini-bladders.

5.1.1 Stage 1: Study of the pressure transmission on to a flat surface by mini-bladders

The experimental setup used for this investigation is described in Fig. 5.1. The mini-bladder (q) was fastened using two 0.5 mm diameter red colour wires (RS PRO Red Hook up wire; metal wire with a polymer sleeve, 0.5 mm diameter, RS components UK Ltd, Nottingham, UK) on to a thin aluminium plate (20.35 mm width, 70.12 mm length, 0.69 mm thickness; 7.73 g weight) with its extensible layer (inflation side) facing away from the surface of the aluminium plate. The AMI air-pack type pressure sensor (Model 3037 $\phi = 20$ mm; Main unit model 0905-SA-35K, AMI Techno, Tokyo, Japan) was glued on to a breadboard (MB6060/M, Thorlabs, Ely, UK) using single sided tapes (Tesa[®] Premium acrylic coated cloth tape, 50 mm \times 50 m, 0.31 mm thick, RS components UK Ltd, Nottingham, UK). The aluminium plate with the mini-bladder was placed on the air-pack sensor with the inflatable surface of the mini-bladder overlaying the sensor area and it was secured to the breadboard using green coloured chords (Multi-function Sturdy Garden Plant Twist Ties, KLOUD City, Amazon, UK). Four spacers (t) made of hard silicone (Transil 20, MouldLife, Suffolk, UK) were positioned between the aluminium plate and the breadboard to stabilise the aluminium plate and also to prevent any loading of the air-pack sensor due to the weight of the aluminium plate. The schematic of the experimental setup is shown in Fig 5.1 b.

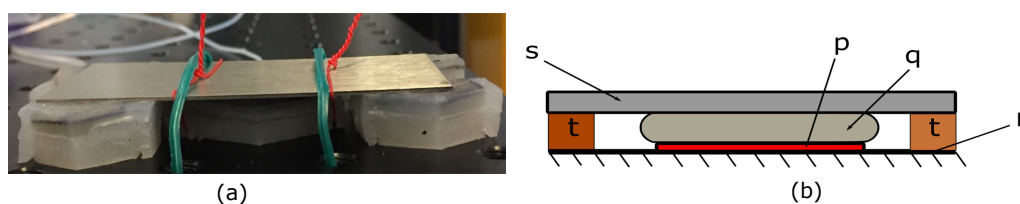


Fig. 5.1 The experimental setup for the measurement of interface pressure (a) photograph of the actual setup (b) schematic diagram of the setup, where p-AMI Air-pack sensor, q-mini-bladder, r-aluminium breadboard, s-aluminium plate, and t-spacers made of silicone

The outlet of a 60 ml syringe (Medicina Oral/Enteral syringe, Amazon, UK) was attached to a Y connector using a 3 mm diameter silicone tube (translucent platinum cured 60 shore, 3 mm outer diameter, 1.5 mm inner diameter, Silex Silicones Ltd., Hampshire, UK), and one of the Y connector's outlet was affixed to the air inlet of the mini-bladder and the second connected to a vertical liquid column manometer (TJ600, Volt 1S liquid of 1.86 specific gravity KIMO Instruments, Kent, UK) to measure the pressure inside the mini-bladder. Thereafter the mini-bladder was inflated by pumping

air into it in 2.0 ml increments with the syringe. The interface pressure induced on to the surface of the breadboard due to the inflation of the mini-bladder was measured using the air-pack sensor. The results obtained were then plotted against the mini-bladder inflation pressure (back pressure).

For these experiments individual bladders were manufactured, which were of hexagonal shape with a 14.0 mm outer-side length and 11.0 mm inner-side length with a 314.0 mm² effective inflation surface area. The size of the mini-bladders was selected to align with the sensor area of the AMI Air-pack sensor whose principle of operation is based on the measurement of back pressure; when a force is applied to the sensor filled with a defined amount of air. The pressure reading would depend on the area of the sensor covered by the mini-bladder. Therefore, it was important that the entire sensor area is encompassed by the inflatable surface of the mini-bladder during the pressure measurement and thus the minimum dimensions of the mini-bladders for the research was defined by the sensor area of the AMI air pack pressure sensor.

Five samples of hexagonal shaped mini-bladders made of PlatSil® Gel-OO 30 silicone were tested. All samples were made from the same batch of silicone, and the number of samples was restricted to five due to limitations on the 3D printer available for the research. The interface pressure obtained using the AMI air-pack sensors were recorded, and the sensor readings were then corrected according with the sensor calibration against manometer values as described in Table 3.6 (page 80). The correction was applied to extract the correct pressure sensor reading as described in Table 3.6. Each mini-bladder sample was tested five times. The average pressure recorded by air pack sensor during the step wise inflation of the mini-bladders, were plotted against the mini-bladder inflation pressure, and the results are shown in Fig. 5.2. The results for individual mini-bladder for the five repeated cycle inflation are included in the Appendix D. The room temperature during the experiment was measured and was recorded as 22.9 °C on average during the tests.

The results shown in Fig. 5.2 demonstrates a linear relationship between the pressure inside the mini-bladders and interface pressure. This linear relationship can be expressed with the equation 5.1, and the linear fit shows a very good correlation factor of $R^2 = 0.9996$, with a very low root mean square error (RMSE) of 0.54. It is also evident that the error bars are very small, which shows that all the samples have inflated in the same manner.

$$P_{interface} = P_{inside} \times 0.875 - 0.976 \quad (5.1)$$

The pressure transmission percentage of mini-bladders provides a better performance indicator of the pressure transmission characteristics of a mini-bladder. The pressure transmission percentage is defined by the equation 5.2 below.

$$Pressure\ transmission\ percentage = \frac{P_{interface}}{P_{inside}} \times 100\% \quad (5.2)$$

The results of the calculated pressure transmission percentages are shown in Fig. 5.3, and it can be seen that the recorded maximum pressure transmission efficiency was around 80% – 90%, and it drops to around 70% – 80%, in the lower pressures ranging from 0 – 20mmHg.

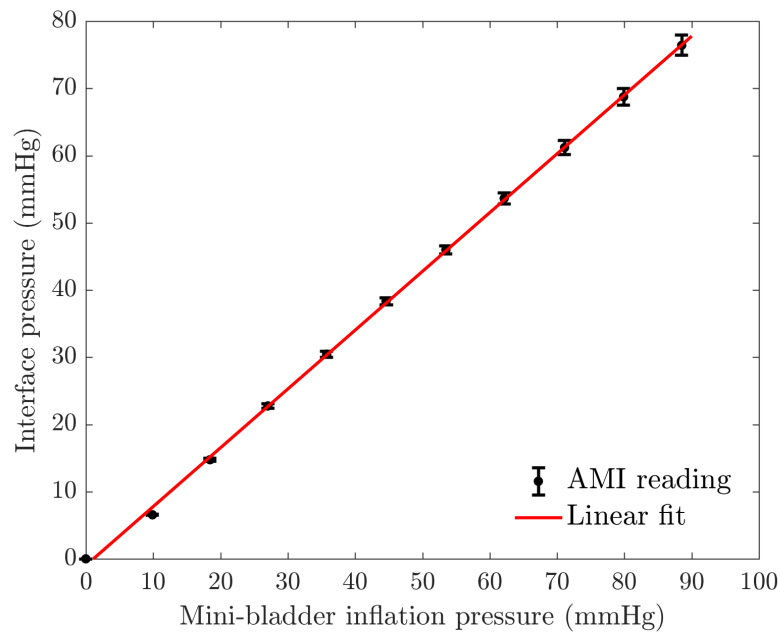


Fig. 5.2 Interface pressure on a flat metal surface against the pressure inside hexagonal shaped mini-bladders. The points marked in black, represents the experimental data and the error bars here represent the standard error for five different samples. The linear relationship obtained for interface pressure and the pressure inside the mini-bladder is shown in red.

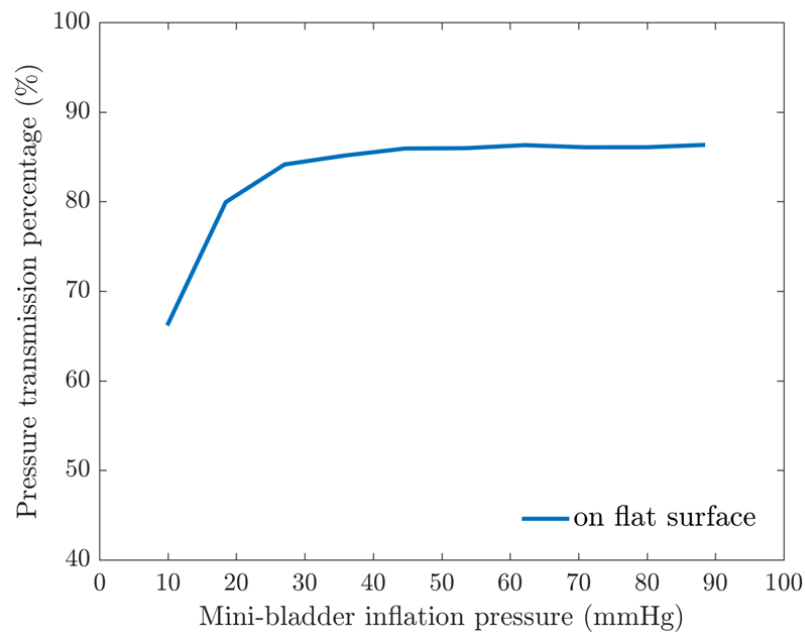


Fig. 5.3 Calculated pressure transmission percentage on the flat surface against the mini-bladder inflation pressure for hexagonal shaped mini-bladders.

5.1.2 Stage 2: Study of the pressure transmission onto a cylindrical surface

A key application of the active compression is for the treatment of venous disease and lymphodema, therefore the performance of mini-bladders was evaluated on a cylinder. The experimental setup used is described in the schematic shown in Fig. 5.4. A transparent acrylic hollow cylinder (The Clear Plastic Shop, Chesterfield, UK) of 180 mm diameter was employed to determine the pressure transmission efficiency of mini-bladders. A transparent cylinder was selected so that the mini-bladder could be aligned accurately with the air pack pressure sensors with the mini-bladder surface covering the air pack sensor as shown in Fig. 5.4.

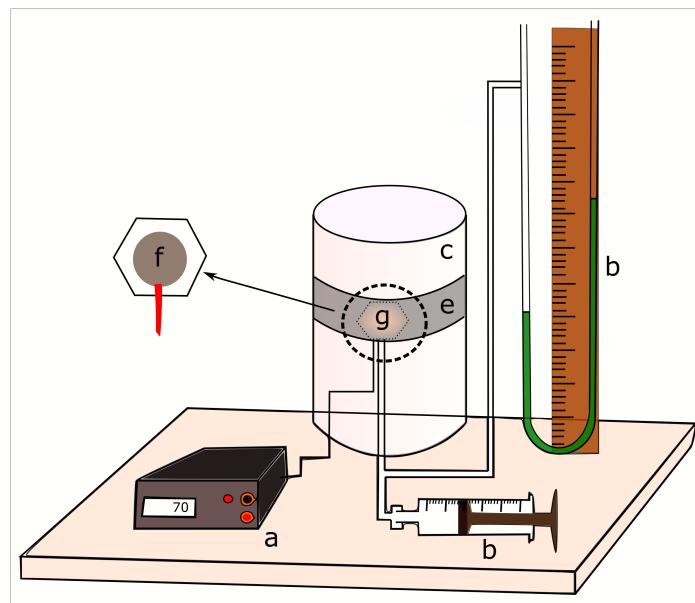


Fig. 5.4 Schematic of the experimental set up. The single mini-bladder attached to a woven fabric, and wrapped around a transparent acrylic cylinder. a-AMI pressure controller unit, b-manometer, c-transparent acrylic cylinder, d-syringe, e-woven fabric strip, f-AMI air pack sensor mounted on the surface of the acrylic cylinder, and g-mini-bladder.

For interface pressure measurement an AMI air-pack sensor (Model 3037 $\phi = 20$ mm; Main unit model 0905-SA-35K, AMI Techno, Tokyo, Japan) was used. The sensor was mounted onto the cylinder by using single side tapes (Tesa[®] Premium acrylic coated cloth tape, 50 mm \times 50 m, 0.31 mm thick, RS components UK Ltd, Nottingham, UK).

Mini-bladders of three different geometries, i.e. hexagonal, circular and square, were manufactured and the mini-bladders were stitched onto (40 mm \times 445 mm) strips from a woven fabric. Five mini-bladders were manufactured for each geometrical shape, and these were stitched onto fabric strips; i.e. each fabric strip had only one mini-bladder. A strong woven fabric of 1.648 MPa Young's modulus was used to minimize possible effect of a pressure being induced on to the pressure sensor due to the stretch of the fabric during the inflation of mini-bladder, and a larger diameter cylinder

was also selected to minimise fabric tension effect on the air pack sensor reading. The fabric strip with a mini-bladder was wrapped around the cylinder. The tension in the fabric would increase due to stretching of the fabric during inflation of the mini-bladder forcing the mini-bladder onto the air pack sensor during testing creating an additional pressure component onto the contact surface.

The mini-bladder was inflated using the air-syringe in 2.0 ml increments and the corresponding interface pressure reading of the air-pack sensor was noted and the indicated pressure value corrected according to the calibration curve obtained in the Table 3.6 (page 80); which represented the relationship between the pressure reading of the air-pack sensor and the manometer reading. The above experimental procedure was repeated with all the mini-bladders in order to determine the impact of the mini-bladder shape on the pressure transmission. Different shape mini-bladders manufactured had the same inflation surface area, so that their interface pressure transmission could be compared.

Five samples of hexagonal shaped mini-bladders made from PlatSil® Gel-OO 30 silicone were tested as described in the previous paragraph and each sample was tested repeatedly for five cycles to assess their ability to replicate the pressure transmission and hysteresis. Similarly, for circular and square shaped mini-bladders, five samples of each shape were made from PlatSil® Gel-OO 30 from the same batch of silicone which was used to manufacture hexagonal shaped mini-bladders, in order to eliminate errors which may have resulted due to variations in different silicones batch. The same test procedure was implemented to evaluate the pressure transmission of circular and square shaped mini-bladders. The room temperature was recorded using a thermistor, and the temperature was 22.8 °C. during the testing.

The results of the mini-bladder inflation pressures were plotted against the average interface pressure (corrected air-pack sensor values) and the results are shown in Figs. 5.5 (a), (b) and (c) for hexagonal, square and circular shape mini-bladders, respectively. Figure 5.5 demonstrates a good linearity between the mini-bladder inflation pressure and the interface pressure for hexagonal, circular and square shaped mini-bladders. The error bars for all mini-bladders of different shapes are insignificant, indicating a good consistency in the mini-bladder samples manufactured for the analysis. The linear relationships obtained for the mini-bladders of different shapes and their goodness of fit values are tabulated in Table 5.1. All the linearity functions showed a good correlation factors (0.997 – 0.999) for mini-bladders of different geometries; however the RMSE value for the hexagonal mini-bladders was the lowest (0.40). The linear relationships given in Table 5.1 can be used as calibration curves, for mini-bladders to determine the pressure required to inflate them to obtain the required interface pressure value.

Figures 5.6, and 5.7 show comparisons of how the interface pressure and pressure transmission percentages vary for the three different shaped mini-bladders. It can be observed that the hexagonal shaped mini-bladders have the highest pressure transmission efficiency around 70% – 80%, for inflation pressures higher than 20 mmHg. However, for circular and square shaped mini-bladders, the transmission efficiencies varied between 60% – 75%.

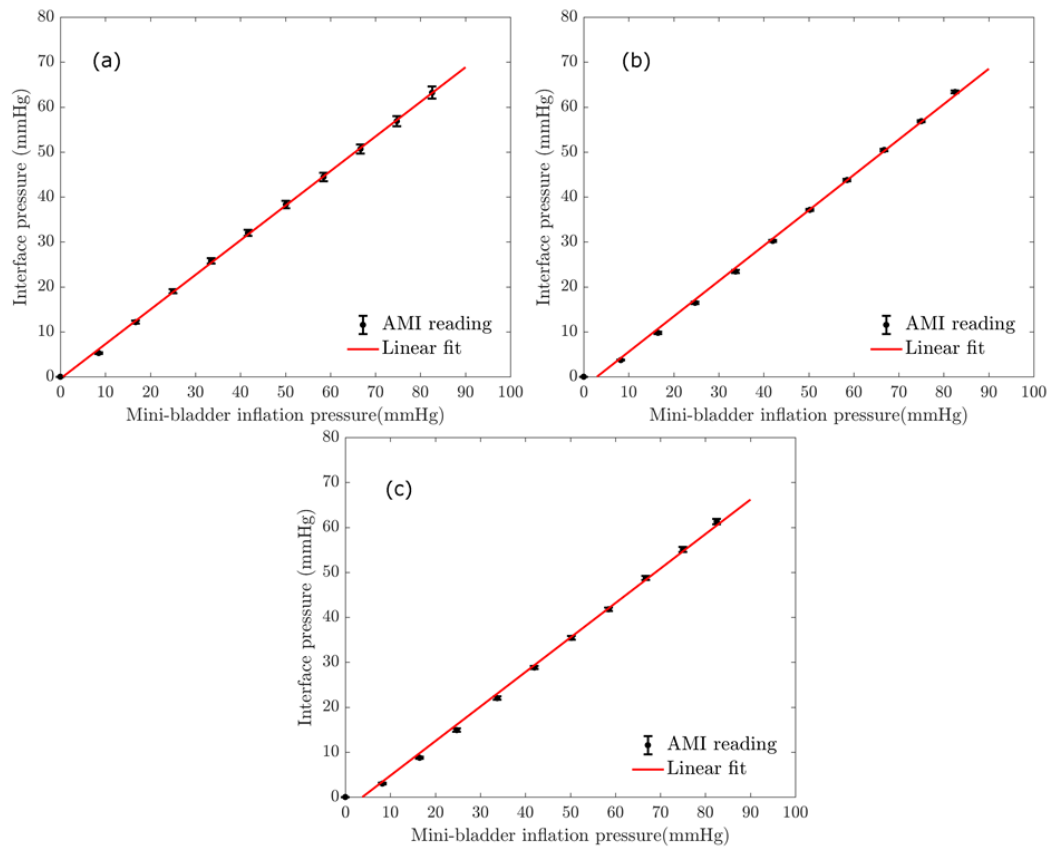


Fig. 5.5 Interface pressure on the cylindrical surface (constant radius of curvature) against the mini-bladder inflation pressure of different geometrical shapes. (a) hexagonal shaped mini-bladders (b) circular shaped mini-bladder (c) square shaped mini-bladders. The points marked in black, represents the experimental data and the error bars here represent the standard error for different samples used. The linear relationship obtained for interface pressure and the the mini-bladder inflation pressure is shown in red.

Table 5.1 Linear relationships obtained for the pressure transmission behaviour of three different shaped mini-bladders (hexagonal, square, and circular)

Bladder shape	Linear fit	Goodness of fit	
		R ²	RMSE
Hexagonal	$P_{inside} = \frac{P_{interface} + 0.4462}{0.7698}$	0.9997	0.40
Square	$P_{inside} = \frac{P_{interface} + 2.919}{0.7679}$	0.997	1.23
Circular	$P_{inside} = \frac{P_{interface} + 2.321}{0.7855}$	0.998	0.97

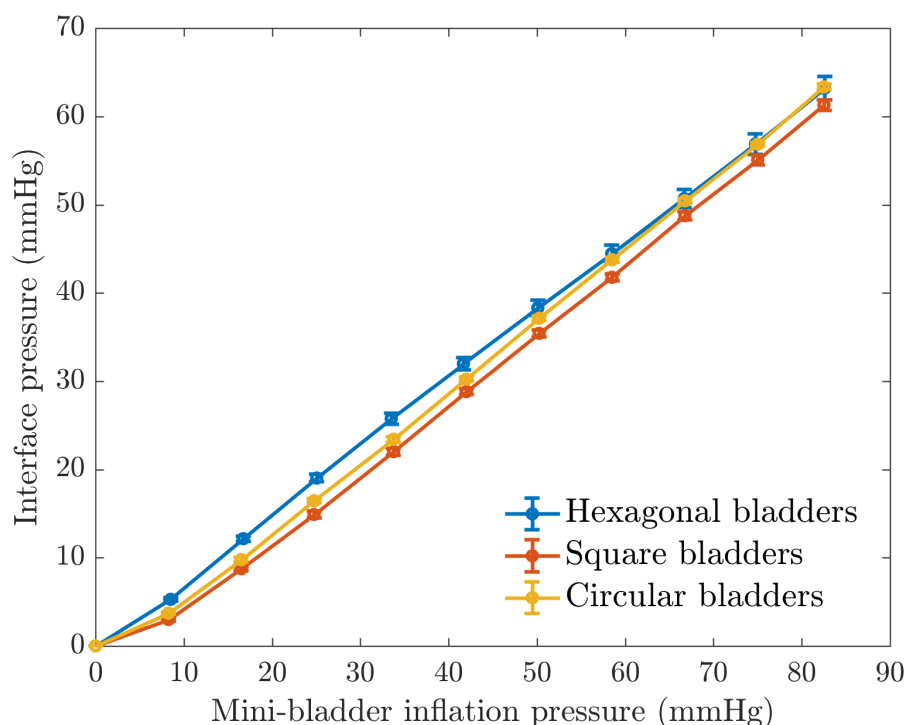


Fig. 5.6 Interface pressure on the cylindrical (constant radius of curvature) surface against the mini-bladder inflation pressure for different shaped mini-bladders

This may be due to the effective contact surface area of different mini-bladder geometries. As discussed in sections 4.3.4 (page 104) the inflation height depends on the minimum gap distance of the membrane fixing points. The minimum gap distance in square shaped mini-bladders was the lowest (17.7 mm), hence the inflation height was also the lowest in-comparison to the other two geometrical shapes. The lower inflation heights will not be able to maintain a sufficient contact with the surface, which will result in lower interface pressures, at low mini-bladder inflation pressures. However, the minimum gap distance for circular and hexagonal shaped mini-bladders were almost identical (circular 20 mm and hexagonal 19.1 mm), thus theoretically the circular and hexagonal shaped mini-bladder should have shown similar pressure transmission characteristics. However, according to the experimental data the hexagonal shaped mini-bladders have the highest pressure transmission efficiency. Even if the circular shaped mini-bladders were selected for the final design, it would be difficult to achieve a compact packing of the mini-bladders in an array. The hexagonal shaped mini-bladders can be arranged into a honey-comb structure, which increases the surface area and provides compact packing of the mini-bladders. Hence, the hexagonal shaped mini-bladders were selected to be used for the final prototype design.

The optimum interface pressure profile for compression therapy as specified in the medical literature is around 40 – 45 mmHg at the ankle, reducing gradually to 15 – 20 mmHg at the knee (Al Khaburi, 2010; Coull et al., 2006; Nelson, 2001; Stemmer et al., 1980). However, slightly higher pressure may

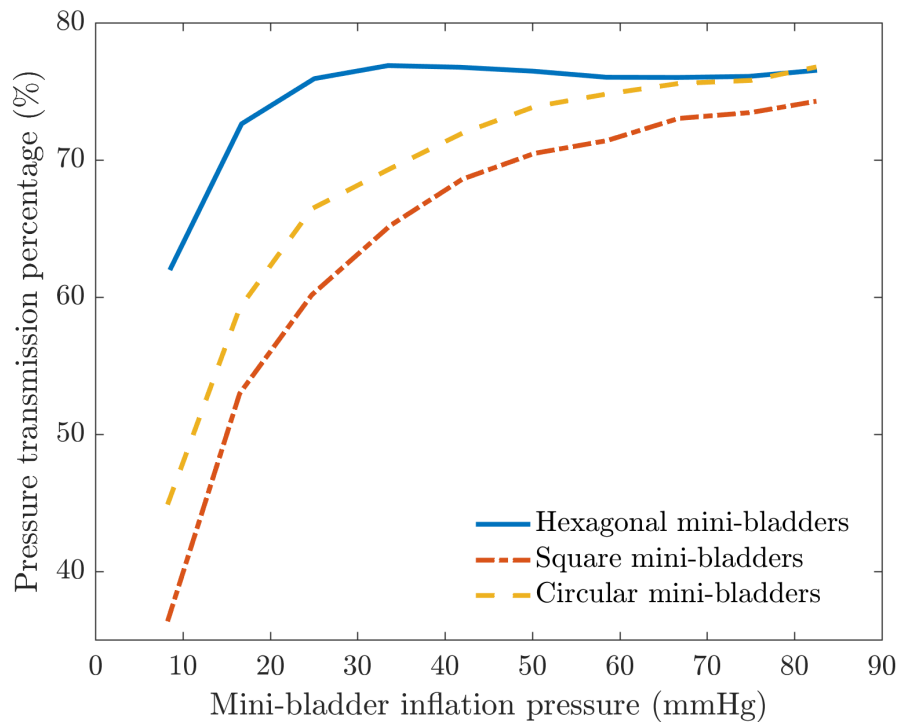


Fig. 5.7 Pressure transmission percentage on cylindrical (constant radius of curvature) surface against the mini-bladder inflation pressure for different shaped mini-bladders

have to be applied to compensate for the skin and fat layers. Therefore in this research the maximum pressure to be applied on to a limb by mini-bladders was limited to 45 mmHg, and the pressure required to inflate the mini-bladders to achieve this was calculated using the linear relationship given in the Table 5.1 and for hexagonal shaped mini-bladders this was around 60 mmHg. Therefore, the focus of the subsequent analysis of the active pressure system was limited to the pressure range 0 – 60 mmHg.

The test results given in Fig. 5.8 show that hexagonal mini-bladders transmitted a higher pressure on to the flat surface than to the circular surface. This increase in pressure transmission onto flat surface is mainly due to the aluminium strip used in the experimental setup (Figs. 5.1 and 5.9) to prevent the mini-bladder moving during inflation (Figs. 5.1 and 5.9). As depicted in Fig. 5.9, during inflation the mini-bladder would attempt to move against the thin aluminium plate (Fig. 5.9-s) which, however is restricted. This would result in a reaction force being applied onto the pressure sensor causing a higher value being recorded by the air-pack pressure sensor. However, when the mini-bladder is positioned onto the cylindrical surface using a fabric strip this outward movement away from the cylindrical surface would be more due to the ability of the fabric strip to stretch; as a strong woven fabric was used this would have been less (High modulus woven fabric $Y = 1.648 \text{ MPa}$). Therefore, a much lesser reaction force would have been applied onto the air-pack sensor compared to the aluminium plate, thus low interface pressure readings were recorded for cylindrical surface.

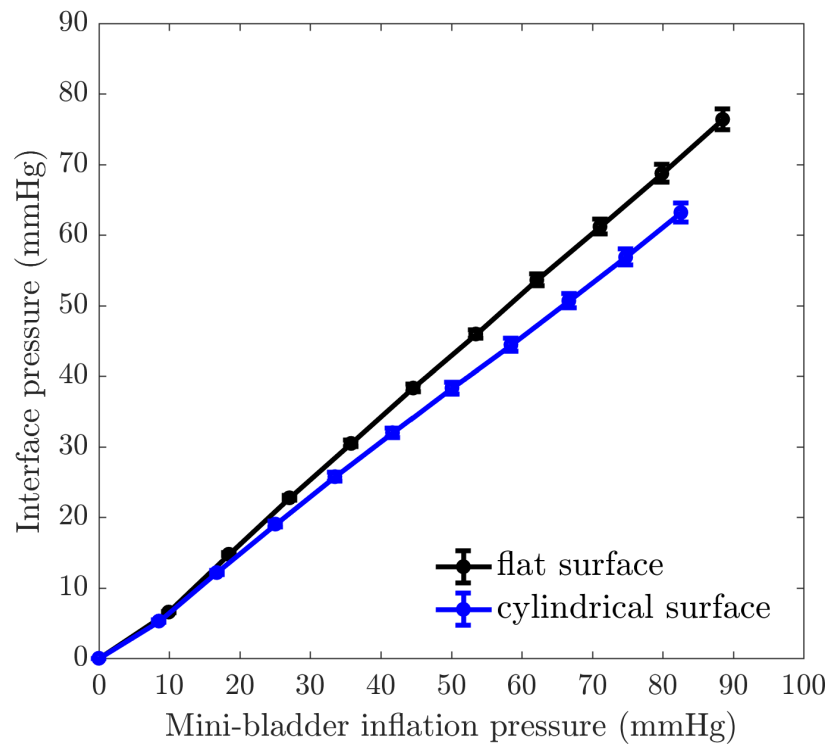


Fig. 5.8 Comparison of interface pressure against the mini-bladder inflation pressure for different shaped mini-bladders on cylindrical (constant radius of curvature) surface and flat surface

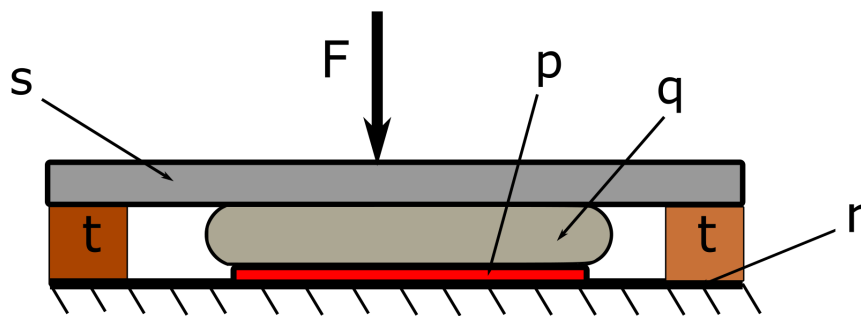


Fig. 5.9 Schematic diagram of the arrangement of the mini-bladder on the flat surface, F represents the resultant force that will act on the mini-bladder to counteract the movement against the metal strip on outward direction. p-AMI Air-pack sensor, q-mini-bladder, r-aluminium breadboard s-aluminium plate t-spacers made of silicone F-reaction force.

5.2 The effect of fabric tension on mini-bladder inflation

The interface pressure readings recorded from the AMI-air pack sensors can be affected by the tension in the woven fabric employed to position the mini-bladder on the cylindrical surface. The principle of operation of the mini-bladder is that a radial force is applied onto the circular surface, by the mini-bladder due to its inflation, resulting in an interface pressure being created subject to the mini-bladder contact area. However, this interface pressure could be affected by an additional pressure component induced by the tension in the fabric used to house the mini-bladder; this pressure component can be calculated with Laplace's equation as shown in Fig. 5.10, and equation 5.3. Therefore, the effect of fabric tension on the interface pressure was investigated using a purpose built test rig described in section 5.2.2. The design of the test rig was built on the findings of a theoretical analysis on how the fabric tension housing the mini-bladders could influence the interface pressure; explained in section 5.2.1.

5.2.1 Derivation of the pressure function due to fabric tension

When a fabric is stretched over a surface with a radius of curvature r , the resultant pressure on the surface can be calculated as described below.

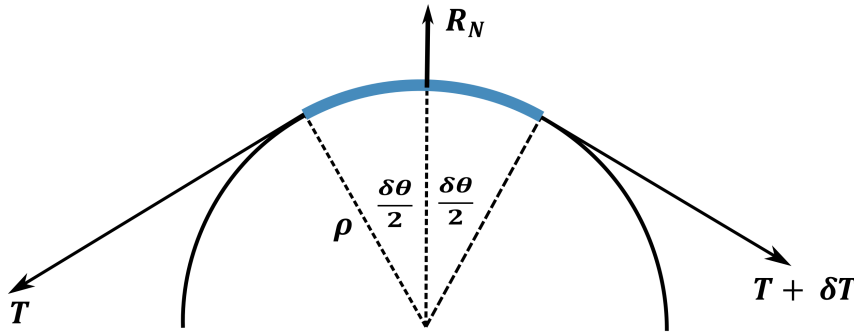


Fig. 5.10 A schematic demonstrating the radial force produced when a fabric is tensioned over a circular cross sectional area. $R_N(N)$ -the normal reaction force, $T(N)$ - the fabric tension, $\delta T(N)$ - incremental of the tension, $\delta\theta(radians)$ – minute angle formed by the fabric segment on the curved surface with ρ - radius of curvature.

Figure 5.10 shows a minute segment of fabric stretched over a circular surface, forming an angle of $\delta\theta$ (radians) with the radius of curvature ρ . The fabric tension will be affected due to surface frictional force which can be calculated using Capstan equation;

$$\frac{T_2}{T_1} = e^{\mu\theta} \quad (5.3)$$

T_1 and T_2 - tensions at the ends of the fabric ($T_2 > T_1$)

μ - frictional coefficient

θ -angle formed by the fabric segment

Hence, a small increment of the tension could be defined as δN (N), and the normal reaction force on the small fabric segment can be defined as R_N (N) and the fabric segment is in equilibrium under the forces T , $T + \delta T$, and R_N (Fernando, 2010).

Resolving the forces vertically for the equilibrium,

$$R_N = (T + \delta T) \times \sin\left(\frac{\delta\theta}{2}\right) + T \times \sin\left(\frac{\delta\theta}{2}\right) \quad (5.4)$$

For minute values of θ ,

$$\sin\left(\frac{\delta\theta}{2}\right) = \left(\frac{\delta\theta}{2}\right) \quad (5.5)$$

Therefore,

$$R_N = 2T \times \left(\frac{\delta\theta}{2}\right) + \delta T \times \left(\frac{\delta\theta}{2}\right) \quad (5.6)$$

Since δT , and $\delta\theta$ are very small values,

$$\delta T \times \left(\frac{\delta\theta}{2}\right) \approx 0 \quad (5.7)$$

Therefore,

$$R_N = T (\delta\theta) \quad (5.8)$$

The pressure generated can be written as,

$$Pressure = \frac{Force(Normal)}{Area} \quad (5.9)$$

$$Pressure = \frac{T (\delta\theta)}{r\delta\theta a} \quad (5.10)$$

where a is the width of the small fabric strip. Hence equation 5.10, could be written as,

$$Pressure = \frac{T}{ra} \quad (5.11)$$

5.2.2 Experimental set up

As per equation 5.11, the effect of pressure induced by the tension of the fabric carrying mini-bladders can be minimised by wrapping it around a circular surface with large radius of curvature. Therefore, a transparent acrylic cylinder (The Clear Plastic Shop, Chesterfield, UK) of 180 mm diameter was used in the experimental setup described in Fig. 5.11. A woven fabric strip (Young's modulus 1.648 MPa, 234 GSM, 50 epi, 37 ppi) embedded with two hexagonal mini-bladders made from PlatSil® Gel-OO

30 silicone was wrapped around the cylinder with the mini-bladders being positioned on opposite side of the cylinder. Two AMI air-pack sensors were positioned between the mini-bladders and the cylinder surface to measure the interface pressure.

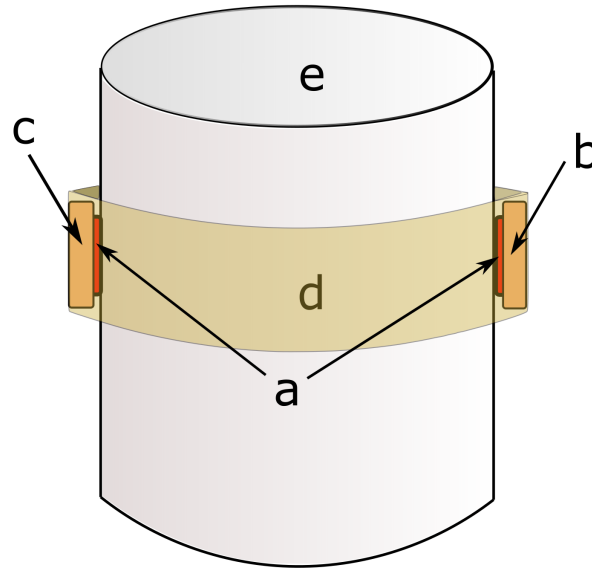


Fig. 5.11 Schematic of the experimental set up used to study the effect of the fabric tension on interface pressure due to inflation of mini-bladder a-AMI air-pack sensors b-inflating bladder (continuously inflating) c-reference bladder d-fabric strip, and e-cylinder.

Out of the two mini-bladders, one was used as the reference (Fig. 5.11, c), which was inflated with a predetermined volume of air at the beginning of the experiments and kept constant, while the opposite mini-bladder (Fig. 5.11, b) was inflated continuously. The interface pressure stimulated by the two mini-bladders were recorded using two separate AMI air-pack sensors. The reference mini-bladder was inflated to three different inflation pressures, i.e. 5mmHg, 10mmHg and 30mmHg while the second mini-bladder was continuously inflated from 0 to 60 mmHg in equal air volume (2ml) intervals. Each test was repeated for five cycles to evaluate the repeatability; the room temperature during the experiments was recorded as 23 °C during the experiment. If there is no effect from the fabric tension, ideally reference mini-bladder should stimulate a constant pressure throughout the experiments. However, due to the inflation of opposite mini-bladder it creates an additional fabric tension resulting a reaction force on the reference mini-bladder, which results in slight increase of the interface pressure recorded by the reference mini-bladder.

The results are shown in Fig. 5.12, where Fig. 5.12 (a) shows the relationship between the inside pressure (inflation pressure) of the inflating mini-bladder and the interface pressure between the cylinder surface and the mini-bladder, for different reference mini-bladder inflation pressures. It is evident that the changes in interface pressure due to the presence of reference mini-bladder are insignificant compared to the results obtained from the experiments without a reference mini-bladder

(green curve in Fig. 5.12a) in the pressure range of 0 – 60 mmHg. The maximum pressure difference recorded was in the range of ± 3 mmHg. However, a slight deviation was observed at inflation pressures above 60 mmHg, which was within the range of ± 5 mmHg.

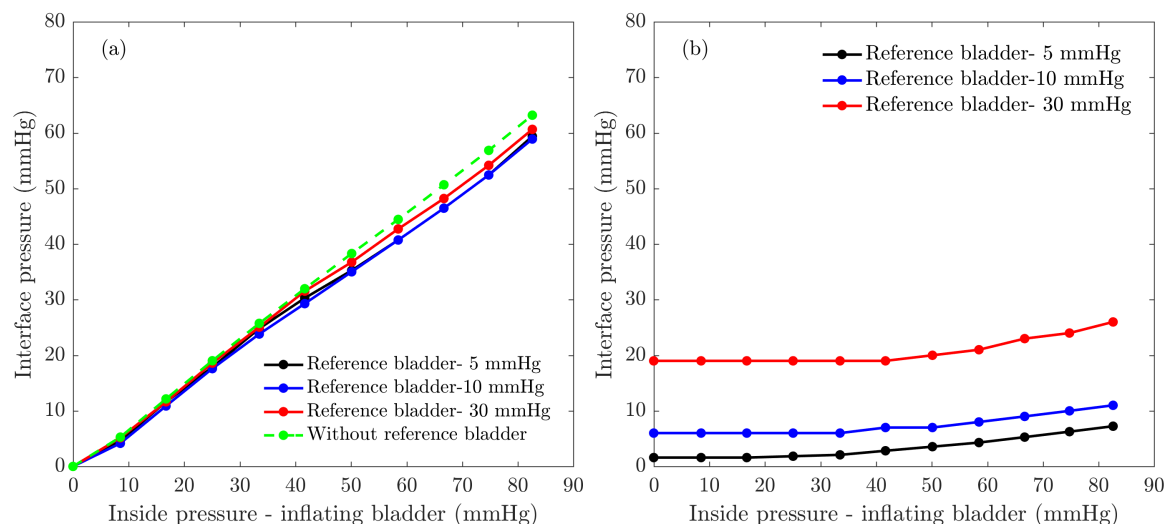


Fig. 5.12 The relationship of interface pressure against the pressure inside the mini-bladder (mini-bladder inflation pressure) (a) inflated mini-bladder and (b) reference mini-bladder inflated to three pre-determined pressures. The coloured lines show the pressure induced onto the cylinder surface by the inflating mini-bladder for different experimental conditions.

In Fig. 5.12(a) the green curve shows the results of the experiments carried out without a reference mini-bladder; black curve shows when reference mini-bladder was inflated to 5 mmHg pressure; blue curve shows when the reference mini-bladder was inflated to 10 mmHg; and red curve shows when the reference mini-bladder was inflated to 30 mmHg. Figure 5.12 (b) shows the variation in the interface pressure developed by the reference bladder when the opposite mini-bladder was continuously inflated. It can be seen that the pressure curves show similar interface pressures in the pressure range of 0 – 60 mmHg, with maximum pressure increase of 2 mmHg at 60 mmHg. In comparison to the commonly used maximum interface pressure range of 40 – 45 mmHg, the corresponding interface pressure difference due to fabric tension change was less than 5% and can be considered as insignificant. Therefore, one can conclude that the impact of the tension in the fabric utilised to support the mini-bladder on the interface pressure is not that significant for the pressure range of interest. When considering the full range of the inflation pressure of (0 – 85 mmHg) the overall change of the interface pressure was 2 mmHg-7 mmHg (reference mini-bladder inflated to 5 mmHg), 6 mmHg-11 mmHg (reference mini-bladder inflated to 10 mmHg), and 21 mmHg-28 mmHg (reference mini-bladder inflated to 30 mmHg), which however, is less than 10 % of the pressure induced by the inflating mini-bladder on to the cylinder surface (interface pressure). Therefore, one can conclude that the effect of the fabric tension is not that significant even for the higher pressures.

5.3 Pressure transmission on biofidelic leg surrogate

The above experiments carried out on a cylindrical surface was then extended on to biofidelic lower leg surrogate in order to replicate a scenario closer to real life application. The cylindrical surface provided a constant radius of curvature, whereas the human lower leg does not form a constant radius of curvature surface. As shown in the Fig. 5.13, the human lower limb profile has an irregular cross section with hollow zones (nearly flat, with large radius of curvatures Fig. 5.13 a), where the pressure applied by a stretch bandage would be low or even non-existing according to the Laplace's law (Eq.5.11). It also consists of bony prominent zones (Fig. 5.13 b), where higher pressures would result due to low radius of curvature in these areas.

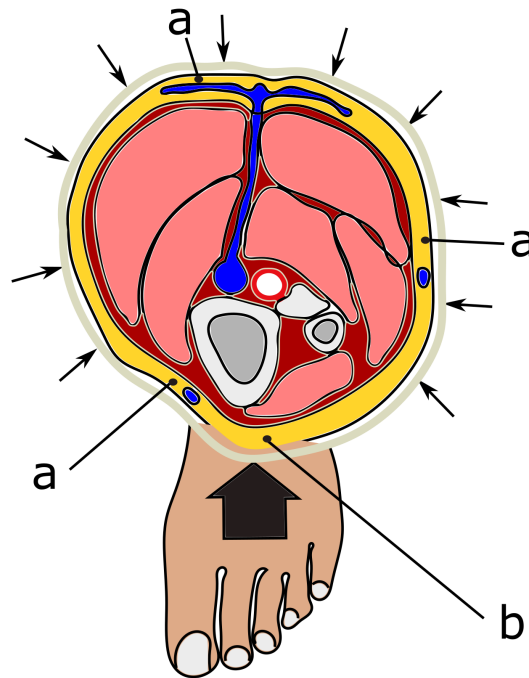


Fig. 5.13 The cross-sectional view of the human lower leg signifying different radius of curvature zones

According to the research hypothesis (ability of mini-bladders to deliver uniform pressure), the developed system using inflatable mini-bladders should be capable of providing a uniform pressure irrespective of the radius of curvature. Therefore, it would be insufficient to draw conclusions from the tests carried out on the cylindrical surface. Hence an anatomically correct shaped leg was used for further evaluation and it was covered with an artificial skin and a fat layer manufactured using Platsil® Gel A10 hardness silicone mixed with additives to resemble the tactile properties of the human skin and fat. These silicone layers were tested for their modulus to compare their mechanical properties to human skin.

5.3.1 Introduction to modulus of human skin

The human skin is a highly organised stratified structure consisting of three main layers called epidermis, dermis, and hypodermis (Geerligs, 2006; Groves, 2012; Hendriks, 2001), and the outermost layer, the epidermis acts as a skin barrier. The most superficial layer of the epidermis is the stratum corneum which is $15\text{ }\mu\text{m}$ thick, very firm but pliable and naturally wrinkled (Zahouani et al., 2009). Beneath the epidermis lies the 1mm thick dermis, which is elastic (Zahouani et al., 2009). in nature comprising mainly of collagen; which is about 75% of the fat free dry weight and 18 – 30% of the volume of dermis (Ebling et al., 1992; Hendriks, 2001). These layers lie on the hypodermis or the subcutaneous fat, whose thickness ranges from 1mm to more than 5cm and behaves like a protective cushion and an insulating layer (Hendriks, 2001; Zahouani et al., 2009). The thickness of this layer varies with the age, sex, race, and nutritional status of the individual (Hendriks, 2001).

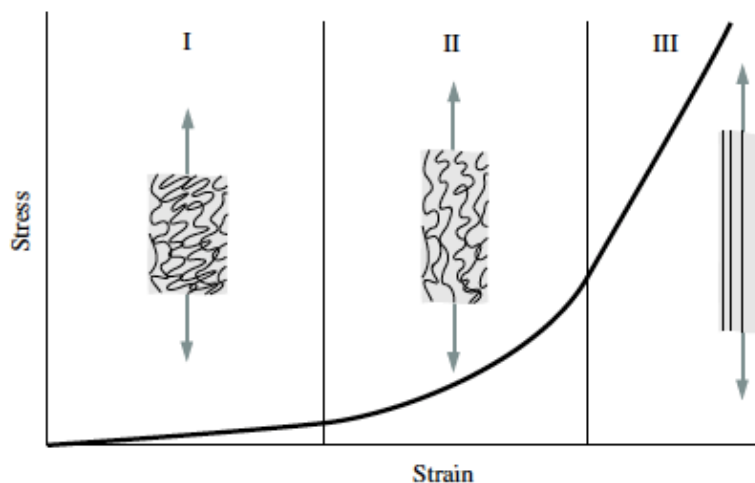


Fig. 5.14 Structure of collagen fibre in different phases (Holzapfel et al., 2001)

The skin is a highly non-linear, anisotropic, viscoelastic and nearly incompressible material (Annaidh et al., 2012), where the typical stress-strain graph of skin exhibits a non-linear behaviour (Figure 5.14) and is characteristically explained in three phases (Annaidh et al., 2012; Holzapfel et al., 2001; Kalra et al., 2016). In the initial loading phase the skin is very compliant, and fibres are largely unaligned (Annaidh et al., 2012) offering a linear stress-strain relationship and a low Young's modulus. In phase 2, the collagen fibres begins to stretch and they start to align themselves in the direction of the load applied (Annaidh et al., 2012; Kalra et al., 2016). In the final phase, which is the almost linear phase where the collagen fibres are mostly aligned and depicts the linear relationship between the stress and strain (Annaidh et al., 2012; Kalra et al., 2016).

Young's modulus of the skin is a vital parameter to estimate the characteristics of the skin. There are many different methods of testing the Young's modulus such as tensile, indentation, suction tests (Geerligs, 2006; Hendriks, 2001; Kalra et al., 2016). Out of all the skin's mechanical testing

methods, suction tests are the most common choice (Kalra et al., 2016). The skin is found to be anisotropic and viscoelastic with a range of Young's modulus between 5 kPa and 140 MPa (Kalra et al., 2016). However, the reported values for Young's modulus of the skin have a large variation between each reported study. This can be expected for biological tissues because of the biological variability between subjects, anisotropic nature of skin, sensitivity of the biological tissues to test conditions (Annaidh et al., 2012). The literature shows a large range for the Young's modulus of the skin at different locations of the human body, and the findings are summarised in Table 5.2 below, (Annaidh et al., 2012; Diridollou et al., 2000).

Table 5.2 Comparison of results obtained from the literature for the Young's modulus of skin (Annaidh et al., 2012; Diridollou et al., 2000)

Author	Test type	Young's modulus (MPa)	Site	Age
(Khatyr et al., 2004)	In vivo tension	0.13-0.66	Tibia	22-68
(Diridollou et al., 1998)	In vivo suction	0.12-0.25	Abdomen and forehead	22-30
(Agache et al., 1980)	In vivo torsion	0.42–0.85	Back	3-89
(Jacquemoud et al., 2007)	In vivo tension	19.5-87.1	Forehead and arm	62-98
(Barel et al., 1998)	In vivo suction	0.13-0.17	Forearm	N/A
(Barel et al., 1998)	In vivo suction	0.20-0.32	Forehead	N/A
(Vogel, 1987)	In vivo tension	15-150	Various	0-90
(Pailler-Mattei et al., 2008)	In vivo indentation	0.0045-0.008	Arm	30
(Zahouani et al., 2009)	In vivo indentation	0.0062-0.0021	Arm	55-70

The above results demonstrate that the Young's modulus varies between 0.0045 – 150.0 MPa. However, the results also show that in majority the Young's modulus of the skin was in the range 0.1 MPa to 1 MPa; therefore, it was decided to manufacture the artificial skin within this range.

5.3.2 Evaluation of the artificial skin and fat

The artificial skin and fat layers made out of PDMS silicone was manufactured according to a special recipe, where it resembles the tactile properties of the human skin and fat to an extent. The author wishes to highlight that the design of an exact replica of artificial skin and fat layers is beyond of the scope of this research. The artificial skin and fat layers were employed to create a biofidelic lower leg surrogate using an anatomically correctly shaped mannequin leg, in order to evaluate the performance of the mini-bladders. The percentages of the components (Smith's prosthetic deadener, PlatThix thickener, polyester flock percentage, and silicone oil percentage) of the original recipe taken from Arm R. were changed in order to obtain different mechanical properties for the artificial skin and fat layers and these results are included in the Appendix D.

It was necessary to study the mechanical behaviour of the manufactured artificial skin and fat layers even though they resembled the tactile properties of the human skin closely, in order to understand their suitability to be used as the human skin of the biofidelic lower leg surrogate. Therefore, uniaxial tensile tests were carried out for the prepared skin and the fat layers according to the BS 37:2011 test standard (ISO, 2011), as explained in the section 4.3.1.

The artificial skin layer was manufactured to a thickness of 1 mm, while the fat layer was manufactured to a thickness of 2mm (according to the literature values in section 5.3.1). Therefore, for the uniaxial tests, 1 mm and 2 mm thick dog-bone shaped samples were prepared by using the process described in section 4.3.2 for the skin and fat layer respectively, and the Young's moduli were determined with uniaxial tests (results are included in appendix D. The linear region of the stress-strain diagram was used to calculate the Young's moduli from the gradient at the midpoint of the linear region. The average value obtained from five test samples was used as the Young's modulus and the calculated values are listed in the Table 5.3. It can be seen that the obtained values for Young's modulus fall within the values specified in the literature for skin and fat layers as shown in Table 5.2.

Table 5.3 Mechanical properties of the prepared artificial skin and fat layers

Component	Young's modulus (MPa)
Skin layer	0.22
Fat layer	0.03

5.4 Evaluation of pressure transmission on the leg surrogate

The research hypothesis suggests that the proposed active compression system using inflatable mini-bladders, should be able to generate uniform pressure irrespective of the position of the leg. Therefore, to test this particular hypothesis it was decided to measure the interface pressure generated by the mini-bladders at four different positions of the biofidelic lower leg surrogate leg, namely anterior (front), posterior (back), lateral (outward side) and medial (inward side). If the interface pressures recorded at these four positions are the same, it could be concluded that the research hypothesis is proven.

5.4.1 Preparation of the skin and fat layers with sensors embedded

It was also decided to study the effect of the pressure transmission through the layers of the skin as this would provide a better understanding on the propagation of the skin contact pressure in the leg; this is a knowledge gap in current compression therapy. This was achieved by embedding AMI

air-pack pressure sensors in the fat layer. In preparation of the biofidelic lower leg surrogate, the outer most skin layer was prepared first and allowed to cure under room temperature. Then, the artificial fat layer was prepared according to the recipe and was poured on top of the previously prepared skin layer. Four AMI Air-pack sensors were embedded on to the surface of the fat layer corresponding to the anterior, posterior, lateral and medial positions of the surrogate leg. Since it was decided to test the pressure measurements in the close proximity of the knee region, the distances corresponding to each of the anterior, posterior, lateral and medial positions at the knee region was measured and the sensors were placed at appropriate distances (Fig. 5.15). The sensors were not pushed far into the fat layer, but placed more towards the outermost edge of the fat layer. Then the fat layer was allowed to cure at the room temperature.

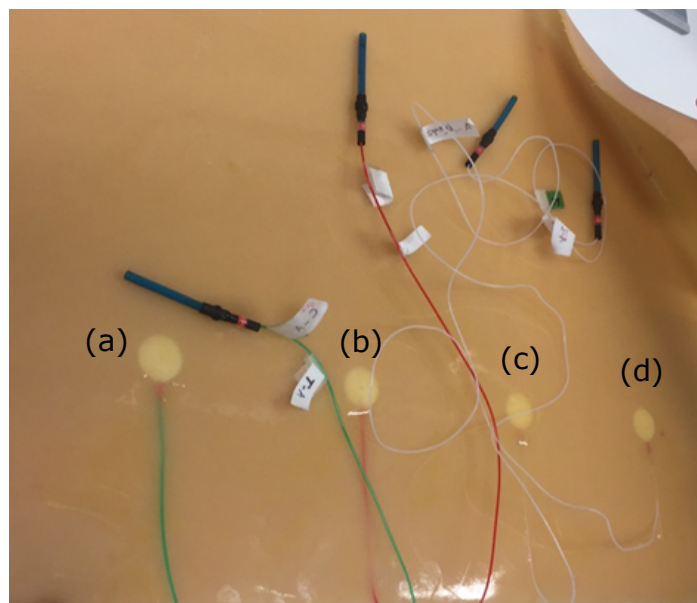


Fig. 5.15 The placement of the sensors in the fat layer, (a) medial, (b) posterior, (c) lateral, and (d) anterior. The embedded AMI sensors, placed at specified positions (medial, posterior, lateral, anterior).

5.4.2 Calibration of the AMI Air pack sensors embedded in fat layer

As discussed in detailed in the chapter 3, these pressure sensors have been calibrated according to the manufacturer specifications and also against the manometer (pages 74 – 79). However, those calibration methods did not account for the pressure sensors being embedded in a silicone layer, and thus the embedded sensors need to be re-calibrated. Since, the sensors were embedded into the fat layer it was difficult to calibrate those against the manometer, hence were calibrated using standard weights.

As shown in Figure 5.16 , a small Teflon disk of 2.1595 g weight, cut to the same size of an AMI air-pack sensor was placed on top of the AMI air-pack sensor embedded in the silicone layer, and

standard weights were placed on the Teflon disk to calibrate the sensors. The weights were applied in 10g increments up to 100g, and the corresponding sensor readings were recorded. The obtained results were used to generate the calibration curves for the all four sensors, using linear regression. The calibration curves obtained for the four embedded sensors and their linear fits are included in Fig. 5.17. The correction for the AMI Air pack sensor reading was applied for the interface pressure experiments based on the linear relationships specified in the Table 5.4.

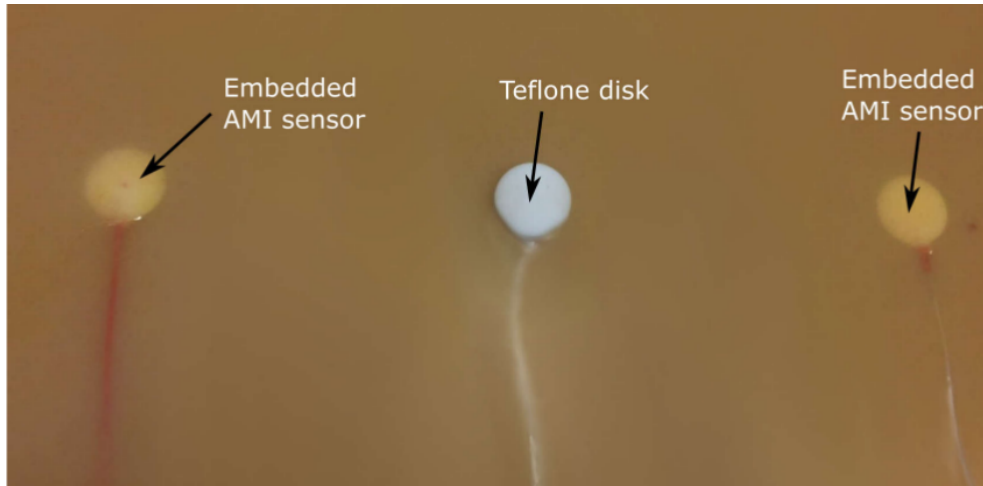


Fig. 5.16 Calibration of embedded AMI air-pack sensors against standard weights

Table 5.4 Linear relationships obtained for embedded AMI air-pack sensors calibrated using standard weights

AMI sensor position	Linear relationship $P_{weight} = a \times P_{Sensor} + b$	R2	RMSE
Anterior	$P_{weight} = 0.9372 \times P_{Sensor} - 0.4533$	0.9951	0.5626
Posterior	$P_{weight} = 0.9770 \times P_{Sensor} - 0.1348$	0.999	0.2543
Lateral	$P_{weight} = 0.9935 \times P_{Sensor} + 0.1374$	0.9988	0.2831
Medial	$P_{weight} = 0.9733 \times P_{Sensor} - 0.2535$	0.9975	0.3992

The linearity relationships showed a good correlation factors (0.995 – 0.999) for the AMI sensors embedded in fat layers at different positions of the leg. Also, the root mean square error (RMSE) value for the four embedded sensors were recorded low, indicating a good linear calibration curve.

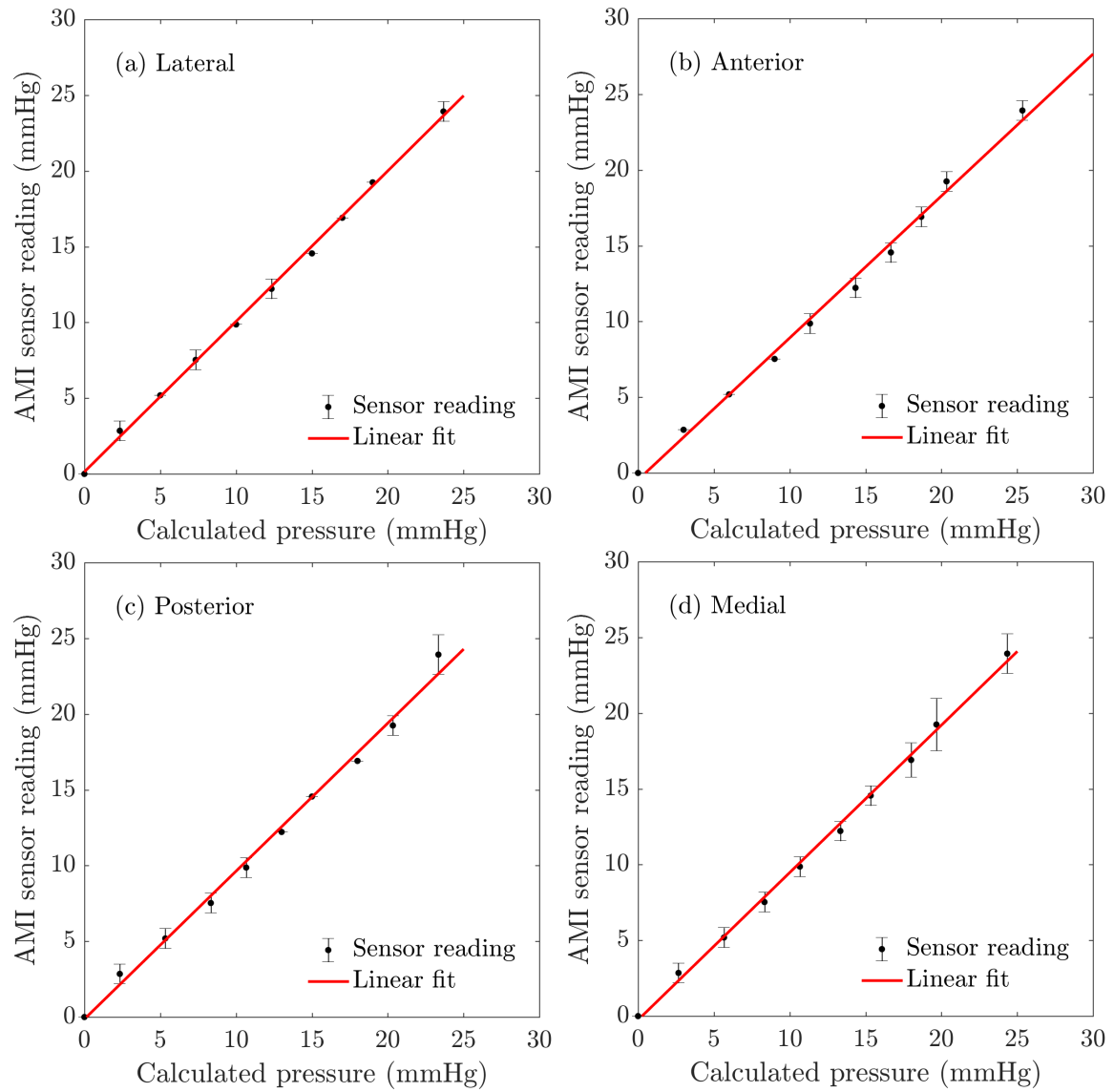


Fig. 5.17 The calibration curves obtained for the four embedded sensors at different positions, with their linear fits at different positions of the leg surrogate (a) lateral (b) anterior (c) posterior (d) medial.

5.4.3 Experimental set up

After the calibration of embedded pressure sensors, the prepared skin and fat layer was wrapped around the anatomically correct shaped mannequin leg to create the biofidelic lower leg surrogate. This was achieved by wrapping skin and fat layer around the mannequin leg carefully that the embedded sensors were correctly placed at anterior, posterior, lateral and medial positions of the surrogate leg. This biofidelic lower leg surrogate was used to evaluate the pressure transmission efficiency at four different positions of the surrogate leg i. e. the skin interface pressure and the corresponding pressure in the fat layers were measured.

Figure 5.18 shows the experimental set up for evaluating the pressure transmission efficiency of the inflated mini-bladders using the biofidelic lower leg surrogate. AMI air-pack pressure sensors were placed on the surface of the skin layer aligned with the AMI air-pack sensors embedded in the fat layer. As it can be seen from the Fig. 5.18b, the sensor embedded in the fat layer could be identified on the skin surface of the leg surrogate which aided the alignment of an AMI air-pack pressure sensor to measure the interface pressure applied by an inflated mini-bladder.

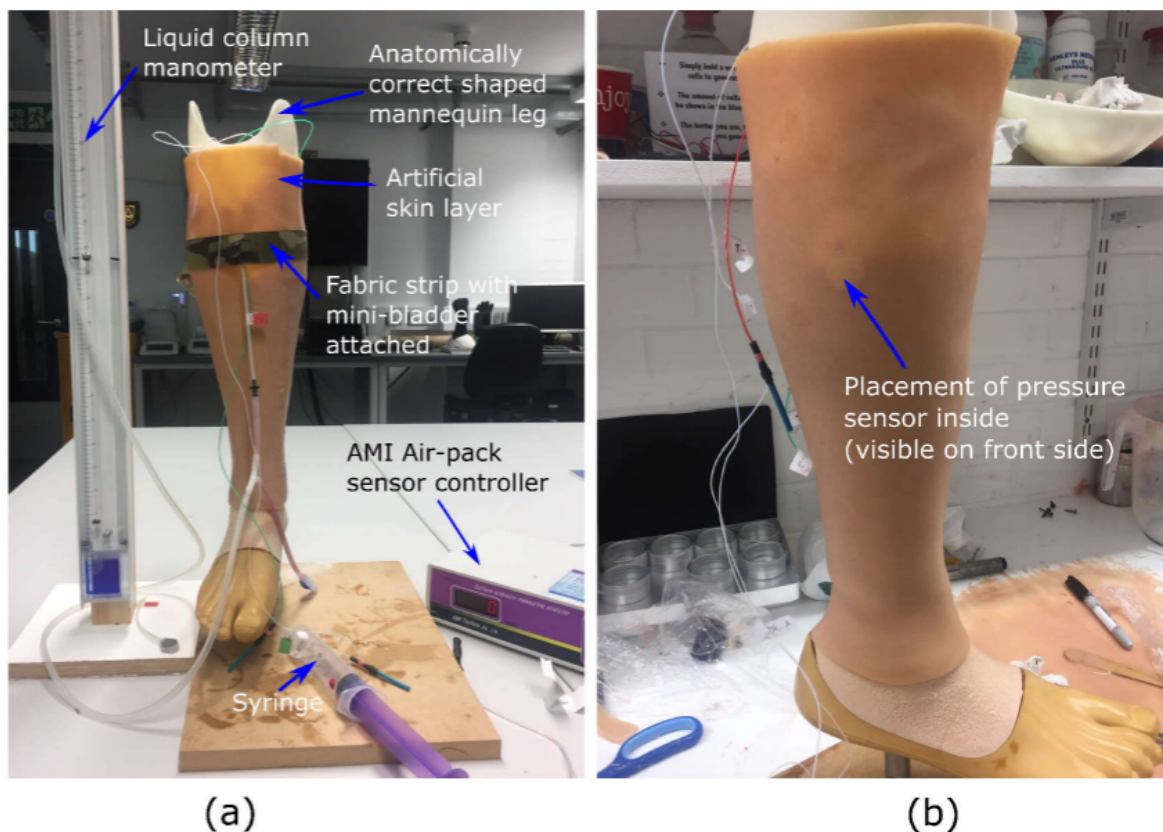


Fig. 5.18 The experimental set up used to evaluate the pressure transmission efficiency, (b) the AMI sensor embedded in the fat layer visible through the skin layer.

The same hexagonal shaped mini-bladders used in the experiments described under section 5.1.1 (pages 128 – 137), were employed in this new set of experiments in order to avoid variations that may result due to the use of different batches of silicones. The mini-bladder was then attached to the same camouflage woven fabric strips and it was wrapped around the leg surrogate ensuring that the mini-bladder has covered the AMI air-pack sensor positioned on the skin layer.

The mini-bladder was inflated with air in 2 ml increments and the corresponding AMI air-pack sensor readings were recorded; the corresponding manometer reading provided the mini-bladder inflation pressure. These readings were obtained for anterior, posterior, medial and lateral positions of the leg surrogate. The tests were repeated for five cycles for each position and five different hexagonal shaped mini-bladders were used for the testing and the average values for the five samples were included in the results.

5.4.4 Results and discussion

The results obtained for the interface pressure on surface of the artificial skin layer and the mini-bladder pressure are shown in Fig. 5.19. The different coloured lines show the interface pressure at anterior, posterior, lateral and medial positions of the leg surrogate. It is evident from the results that irrespective of the position of the leg surrogate the interface pressure values were the same with a maximum variation of 2.5 mmHg. This maximum variation is not that significant considering the range of pressure the mini-bladders inflation pressures. Therefore, it can be concluded that the mini-bladders can be used to apply an uniform circumferential interface pressure, which is not possible with current passive compression products such as stretch bandaging, compression sleeves and stockings. It was also evident that the interface pressure and the mini-bladder inflation pressure continued to demonstrate a linear relationship (for all positions measured). As explained under section 5.1.2, this linear relationship can be used as a calibration curve, to find out the pressure to which the mini-bladder should be inflated to obtain the required interface pressure.

A similar relationship was observed with the AMI air-pack sensors embedded in the fat layer. As shown in Fig. 5.20, the pressure lines for anterior, posterior, lateral and medial positions closely follow each other with a maximum variation of 3 mmHg in the interested pressure range for compression therapy. Therefore, it again confirms that the pressures generated by the mini-bladders were independent of the position of the leg surrogate. However, this deviation begins to increase after 70 mmHg of the mini-bladder inflation pressure with a maximum variation of 4.7 mmHg recorded at the highest mini-bladder pressure value of 95 mmHg applied. Still this variation of pressure lies under ± 5 mmHg, which is the generally accepted tolerance in pressure measurement. Therefore, it can be concluded that the proposed active compression system using mini-bladders can deliver a uniform circumferential pressure irrespective of the radius of curvature.

In order to quantify the transmission of the pressure applied by the mini-bladder through skin and fat layers the pressure transmission percentages on the skin and fat layer were calculated using equation 5.2. Since the pressure lines for the different positions of the leg surrogate were very comparable

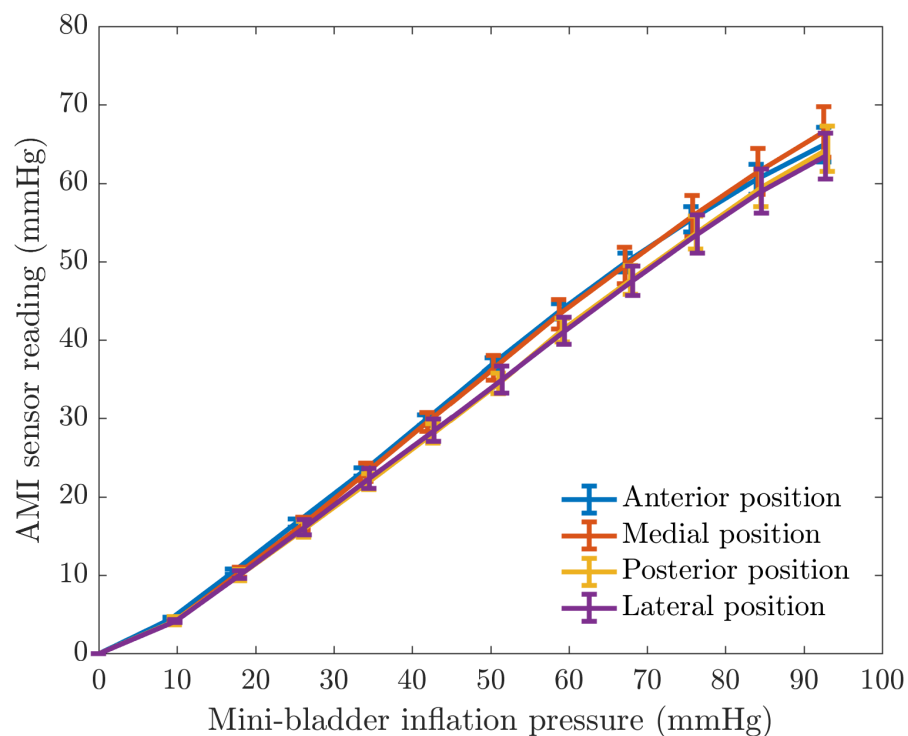


Fig. 5.19 The relationship between the interface pressure on the artificial skin layer (Young's modulus 0.22 MPa) and the mini-bladder inflation pressure. The different colours show the different positions of the leg surrogate as denoted in figure legend.

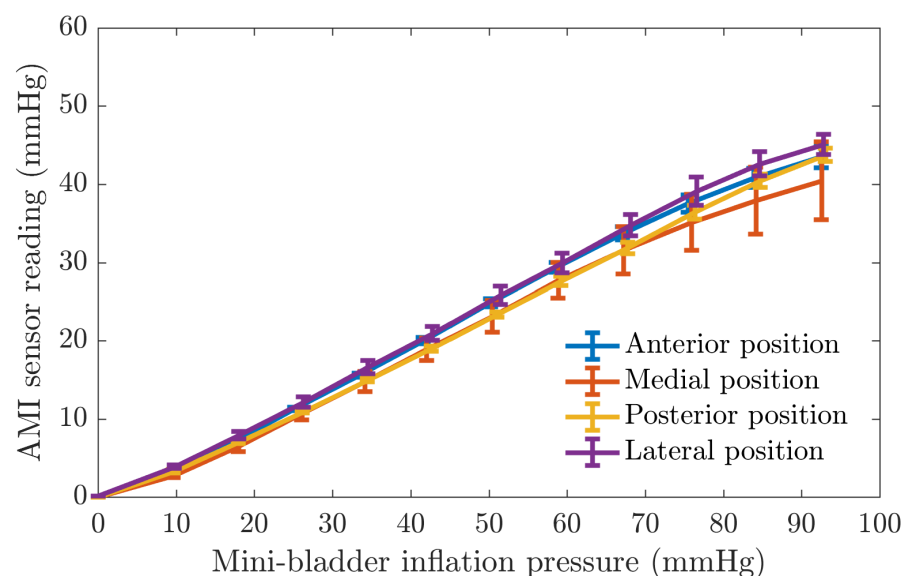


Fig. 5.20 The relationship between the pressure recorded by AMI air-pack sensor embedded in the fat layer (Young's modulus 0.03 MPa) and mini-bladder inflation pressure. The different colours show the different position of the leg surrogate as denoted in figure legend.

the averages of skin interface pressure and pressure readings of AMI air-pack sensors embedded in the fat layers, at those different positions were used to calculate an average interface pressure and average pressure of sensors embedded in the fat layers. This average pressures are used to calculate the average pressure transmission percentage as defined by the equation 5.2. The relationship between the mini-bladder inflation pressure and pressure transmission percentage is shown in Fig. 5.21.

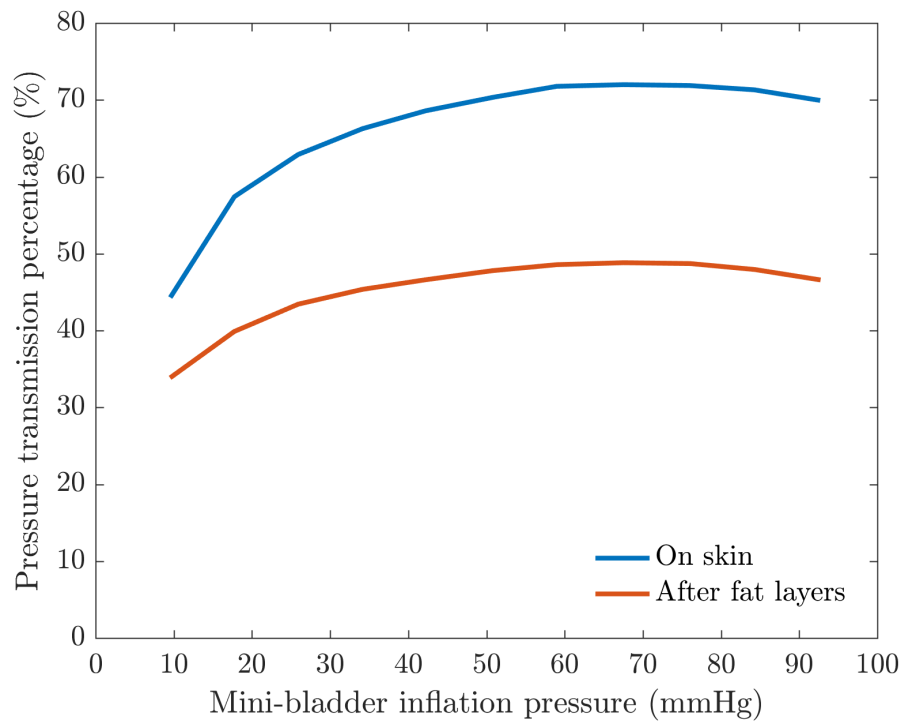


Fig. 5.21 Average pressure transmission percentage against the average mini-bladder inflation pressure, for outer skin layer and the inside fat layer of the leg surrogate.

According to Fig. 5.21, 50%- 70% of the pressure applied by the mini-bladder would be transmitted onto the surface of the leg surrogate (i.e. artificial skin surface). This pressure transmission percentage is lower to the values obtained for the hard cylindrical surface, due to the softness of the artificial skin layer used to cover the leg surrogate.

Figure 5.21 also demonstrates that the pressure transmission percentage in the fat layer is in the range of 35% -45% of the mini-bladder pressure; i.e. in a clinical context only about 35-45% of the force applied on to the surface of skin (in this case by mini-bladders) of a human leg would be available after the fat layer to compress the veins. This finding is important for compression treatment systems in estimating the pressures to be applied at the skin surface of a human limb in order to achieve an effective compression of the veins for the treatment of venous return.

The results show that even though a higher skin interface pressure is recorded, the pressure inside the leg would be much lower. Hence, one could argue to use a higher skin interface pressures during the treatment of venous return. However, this would depend on the stiffness of the skin, and fat muscle

layers of a limb. This must be considered in deciding the inflation of the mini-bladders in clinical practice, which is beyond the scope this research.

5.5 Study of pressure transmission on different types of skin and fat layers

The experimental data presented in the previous section demonstrates the importance of understanding the pressure transmission through skin and fat layers. The literature estimates a range of modulus values for skin and the subcutaneous fat layers through experimental studies (Barel et al., 1998; Kalra et al., 2016; Khatyr et al., 2004). Therefore, the pressure transmission efficiency of artificial skin and fat layers were investigated by using skin and fat layers of different moduli wrapped around the leg surrogate. However, the study has to be limited to two different layers manufactured with different modulus values for skin and fat layers, in order to remain within the scope of this research.

5.5.1 Pressure transmittance on a skin with a hard modulus fat layer

The artificial skin and fat layers were prepared as explained in section 5.3.2. The skin layer was prepared using the silicone recipe described in Appendix D and the hard fat layer was prepared by changing the oil percentage of the silicone used to produce the fat layer for the previous experiments (section 5.3.2), and the Young's moduli of both layers were determined as described in section 5.3. The calculated modulus values are tabulated in Table 5.5.

Table 5.5 Mechanical properties of the second artificial skin and fat layer

Component	Young's modulus (MPa)
Skin layer	0.222
Fat layer	0.15

It can be seen from the Table 5.5, the Young's modulus of the fat layer was five times higher compared to the previous fat layer as shown in Table 5.3, and the skin layer had almost identical modulus value. Due to the limited number of AMI sensors available for the research they were not embedded on to the fat layer, instead were mounted on the surface of leg surrogate to determine the interface pressure between the fat layer and the mannequin leg. The placement and positioning of the AMI air-pack sensors were carried out as described earlier in section 5.3.1. The AMI air-pack sensors used to determine the interface pressure between the fat layer and the leg surrogate at the four positions of the leg surrogate were calibrated against the manometer as described in section 3.4.3, and the results are shown in Table 5.6. (All the experiment data are included in the Appendix D.

The same hexagonal shaped mini-bladders used in the experiments described under section 5.1.1,

Table 5.6 Linear relationships between mounted AMI air-pack sensors and manometer pressure readings calibrated using standard weights

AMI sensor position	Linear relationship $P_{manometer} = a \times P_{Sensor} + b$	R2	RMSE
Anterior	$P_{manometer} = 1.024 \times P_{Sensor} - 2.414$	0.9977	0.83
Posterior	$P_{manometer} = 0.9982 \times P_{Sensor} - 2.6002$	0.9972	0.924
Lateral	$P_{manometer} = 0.9915 \times P_{Sensor} - 2.868$	0.9982	0.738
Medial	$P_{manometer} = 1.005 \times P_{Sensor} - 2.836$	0.9981	0.774

were used. The experimental procedure described in section 5.4 was followed to determine the pressures and the average values of the five mini-bladder samples are included in the results.

5.5.2 Results and discussion

The results of the interface pressure measured by AMI sensor versus the mini-bladders inflation pressure for the skin layer is shown in Fig. 5.22.

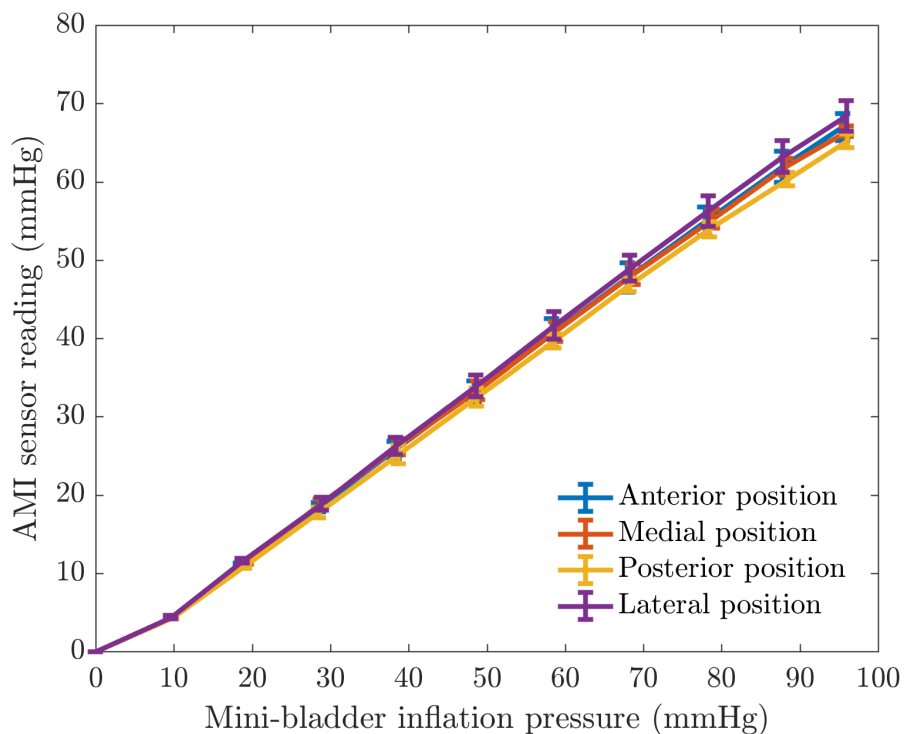


Fig. 5.22 Interface pressure on the surface of the artificial skin layer (Young's modulus 0.222 MPa) against the mini-bladder inflation pressure. The different colours show the different position of the leg surrogate as denoted in figure legend.

The mini-bladder inflation pressure against the interface pressure between the fat layer and leg surrogate surface is shown in Fig. 5.23. In both figures different coloured lines illustrate the pressures at different positions of the leg surrogate (anterior, posterior, lateral and medial). The pressure lines overlap with a maximum difference of 2 mmHg in the region of 0 – 70 mmHg (interested pressure range for compression therapy) mini-bladder pressure, which is not significant within the measured pressure range.

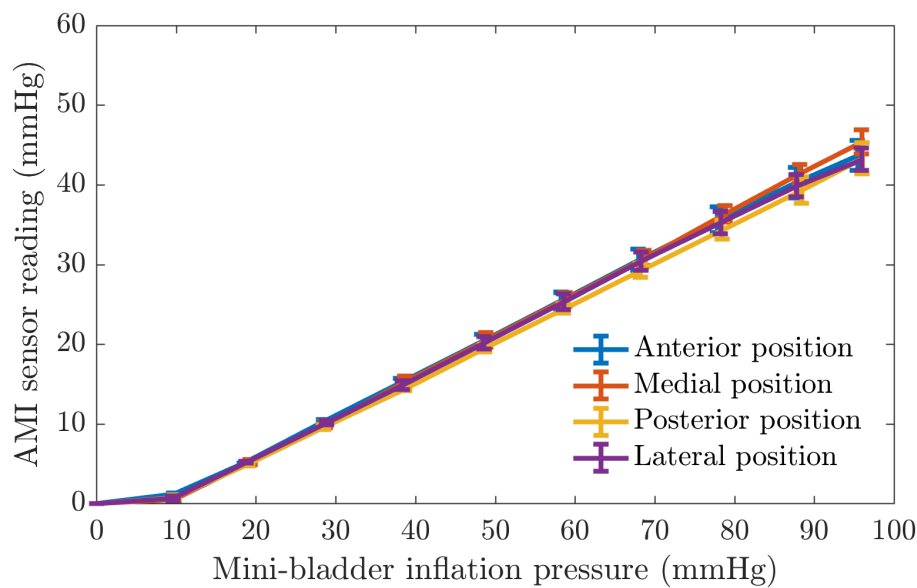


Fig. 5.23 The relationship between the pressure recorded by AMI air-pack sensors on the fat layer (Young's modulus 0.15 MPa) and mini-bladder inflation pressure. The different colours show the different positions of the leg surrogate as denoted in figure

The pressure transmission percentages of the skin layer and the high modulus fat layer are demonstrated in Fig. 5.24., which confirms that 50%- 70% of the mini-bladder inflation pressure can be utilised to apply pressure on to the skin. The pressure transmission percentage value was exactly the same as that obtained for the previously prepared skin layer, as the skin layer were produced with the same silicone composition; i.e. similar modulus value for the skin layer. However, the pressure transmission percentage in the fat layer was in the range of 30%-40%, for the mini-bladder inflation pressures of 20-70 mmHg. This shows that the pressure transmission percentage on the high-modulus fat layer was lower than the low modulus fat layer used earlier in section 5.4. This may be due to the high modulus fat layer's ability to absorb more energy. Another interesting observation is that in 0-20 mmHg mini-bladder inflation pressure range only 10% - 30% of the applied pressure is available after the high modulus fat layer whereas 30% of applied pressure was available even at 10 mmHg mini-bladder inflation pressure.

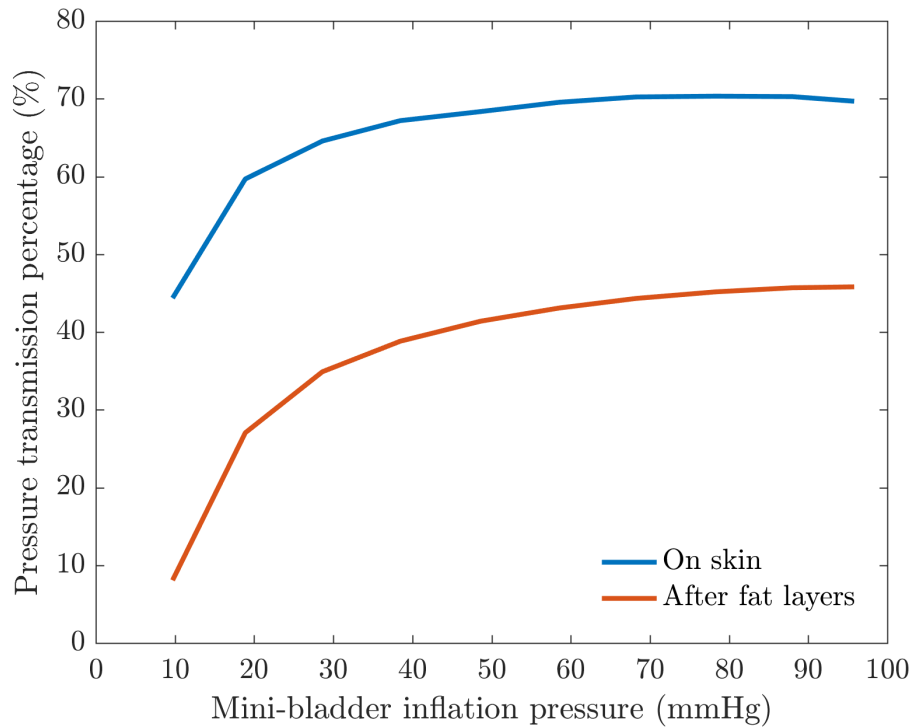


Fig. 5.24 Average pressure transmission percentage against mini-bladder inflation pressure for skin layer and the inside fat layer for the skin layer and high modulus fat layer of the leg surrogate.

5.5.3 Pressure transmission in a low modulus fat layer

The artificial skin and fat layers were prepared as explained in section 5.3.2, the soft skin layer was prepared using the recipe described in Appendix D by increasing the percentage of the slacker. The softer fat layer was prepared by changing the silicone oil percentage used to produce the fat layer for the previous experiment (section 5.5.4), and the Young's moduli of both layers were determined by using the same method described in section 5.3.2. The calculated values are tabulated in Table 5.7.

Table 5.7 Mechanical properties of the third artificial skin and fat layer

Component	Young's modulus (MPa)
Skin layer	0.084
Fat layer	0.0153

It can be seen from the Table 5.7, the Young's modulus values of both the skin and fat layers were half of the modulus of the first skin and fat layer (Table 5.3). Similar to the previous experimental set up (section 5.5.1) sensors were mounted on the leg surrogate to determine the interface pressure between the fat layer and the leg surrogate. The same sensors used in the previous experiment were used to avoid variations of the pressure readings, while the placement and positioning of the sensors

were carried out as described earlier in section 5.4.1.

The same hexagonal shaped mini-bladders, used in the experiments described under section 5.4, were used. The experiment procedure described in section 5.4 was followed to determine the interface pressures and the average percentage transmission values of the five mini-bladders and are included in the results.

5.5.4 Results and discussion

The results of the interface pressure between the mini-bladder and skin layer versus the mini-bladder inflation pressure is shown in Fig. 5.25. The mini-bladder inflation pressure against the interface pressure between the fat layer and leg surrogate surface is shown in Fig. 5.26. In both figures the different coloured lines depicts pressures at different positions of the leg surrogate (anterior, posterior, lateral and medial). Similar to the previous experimental results the pressure lines overlap with maximum difference of 2 mmHg in the region of 0-70 mmHg mini-bladder pressure, which is not significant within the measured pressure range.

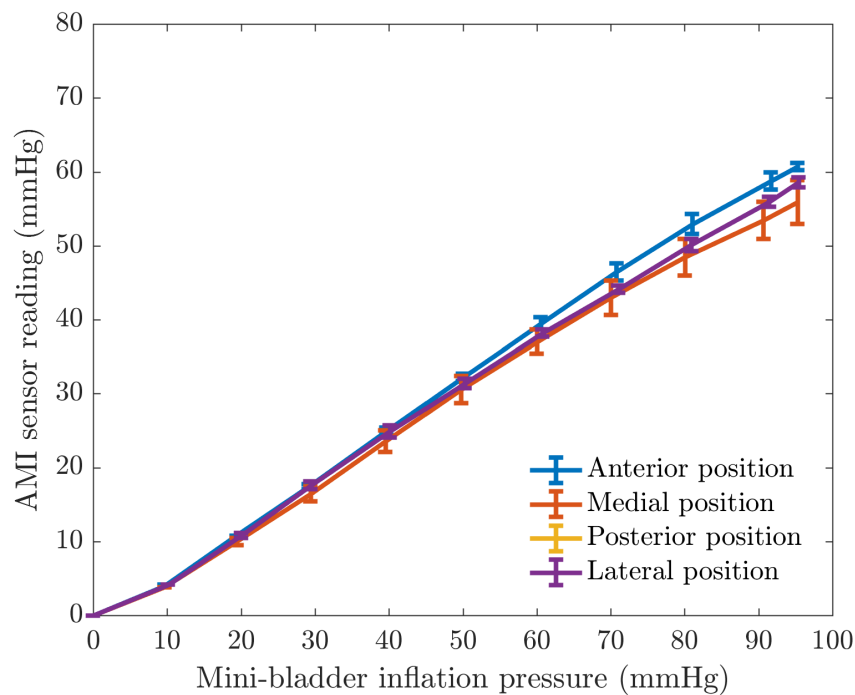


Fig. 5.25 Interface pressure on the surface of the artificial skin layer (Young's modulus 0.12 MPa) against the mini-bladder inflation pressure. The different colours show the different position of the leg surrogate as denoted in figure legend.

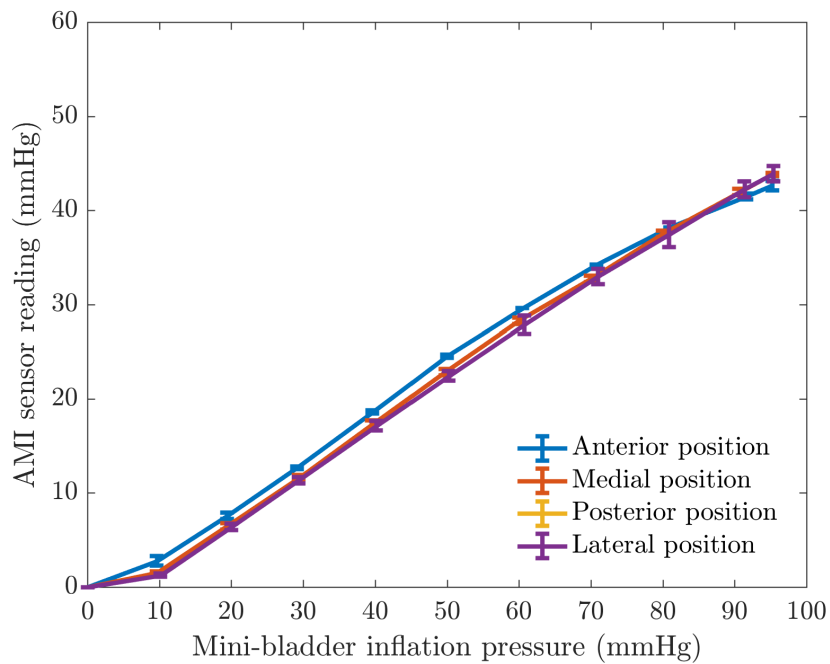


Fig. 5.26 The relationship between the pressure recorded by AMI air-pack sensors on the fat layer (Young's modulus 0.015 MPa) and mini-bladder inflation pressure. The different colours show the different positions of the leg surrogate as denoted in figure.

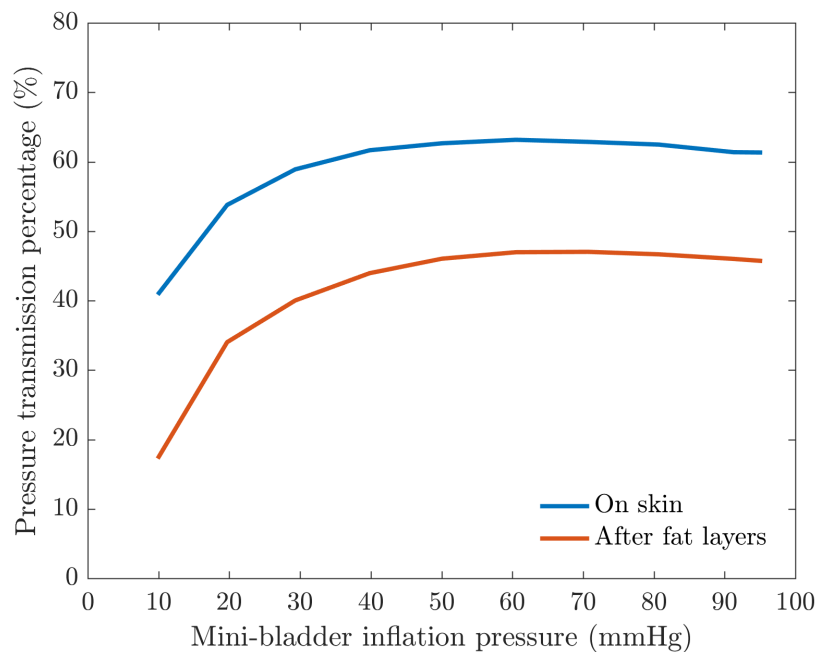


Fig. 5.27 Average pressure transmission percentage against the mini-bladders inside pressure for outer most skin layer and the inside fat layer for the third skin prepared with low modulus skin and fat layers.

The results obtained from all three experiments concludes that the proposed active compression system using mini-bladders could provide a uniform pressure profile irrespective of the position of the leg surrogate. The average pressure transmission percentages of the low modulus skin and fat layers are demonstrated in Fig. 5.27, which confirms that 40%-60% of the mini-bladder inflation pressure can be utilised to apply pressure on the skin layer. The pressure transmission value was lower compared to the previously prepared skin layers, as this skin layer was prepared using a different recipe i.e. lower modulus value for the skin layer. The pressure transmission percentage in the fat layer was in the range of 35%-50%, for the mini-bladder inflation pressures of 20-70mm Hg. This shows that the transmission percentage on the low modulus fat layer was higher than the high modulus fat layers used in sections 5.4 and 5.5.

Similarly, in 0-20 mmHg mini-bladder inflation pressure range only 20%-30% of the applied pressure is available after the low modulus fat layer. The percentage of the pressure transferred via the layers of the skin, would depend on how much energy would be absorbed by the layers of the skin. The results obtained for the three types of skin and fat layers concludes that the percentage of transmission for the lowest modulus fat layer (Young's modulus 0.015 MPa) is recorded to be the highest, followed by the medium modulus fat layer (Young's modulus 0.03 MPa) and then the hard modulus fat layer (Young's modulus 0.15 MPa) in 20-70 mmHg mini-bladder inflation pressure range. However, this variation has changed in the lower mini-bladder pressures (0-20 mmHg), where the medium hard modulus fat layer has shown a higher transmission percentage than the softest modulus fat layer. This may be due to the measurement errors that might occur due to the embedding of the sensors inside the silicone layer. However, one can conclude that the pressure transmission has varied with the modulus of the skin and fat layers.

5.6 The pressure transmittance on ankle area of the leg

In compression therapy ankle is considered as one of the most important area due to its shape and relatively small radius of curvature. As explained in Fig.5.13 the pressure applied with a bandage will vary around the circumference at any given cross-section on the leg, and this variation is most significant in the ankle region due to bony prominence such as malleolus (ankle bone) and tibial crest (shin) (Thomas, 1997). Therefore, extra padding is applied to the leg to minimise localised areas of higher pressures generated due to variations of the radius of curvatures in four-layer bandaging.

The research hypothesis claims that an uniform circumferential pressure can be applied using mini-bladders irrespective of their position on the leg, and the hypothesis has to be validated for the ankle region. Therefore, the experimental procedure described in section 5.4 was carried out to measure the skin interface pressures at four different positions anterior (shin), posterior (back of the ankle), medial and lateral (ankle bone). The same hexagonal shaped mini-bladders were used for the testing and the results are shown in Figs. 5.28 and 5.29 .

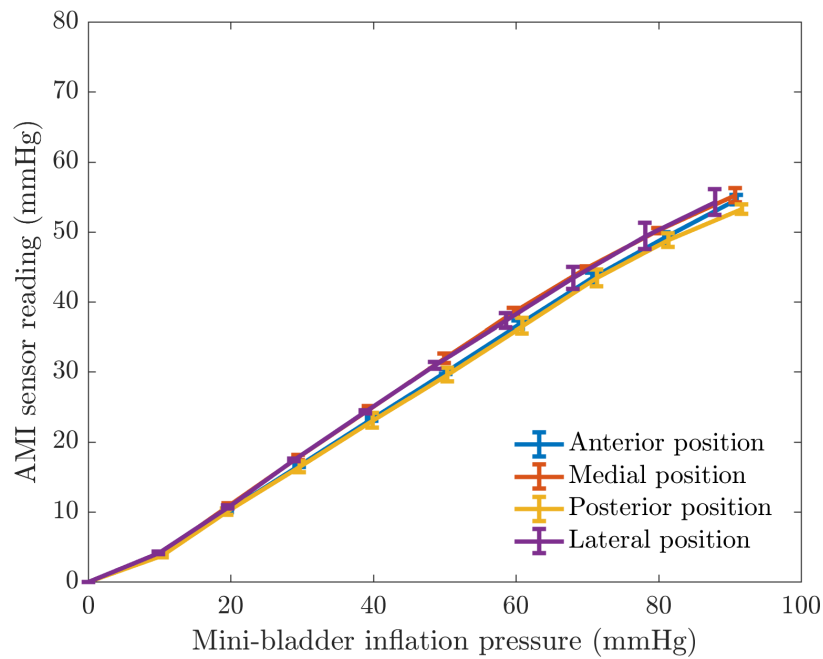


Fig. 5.28 Interface pressure against mini-bladder inflation pressure measured on the leg surrogate with the first artificial skin layer at the ankle position. The different colours show the different position of the leg as denoted in figure legend.

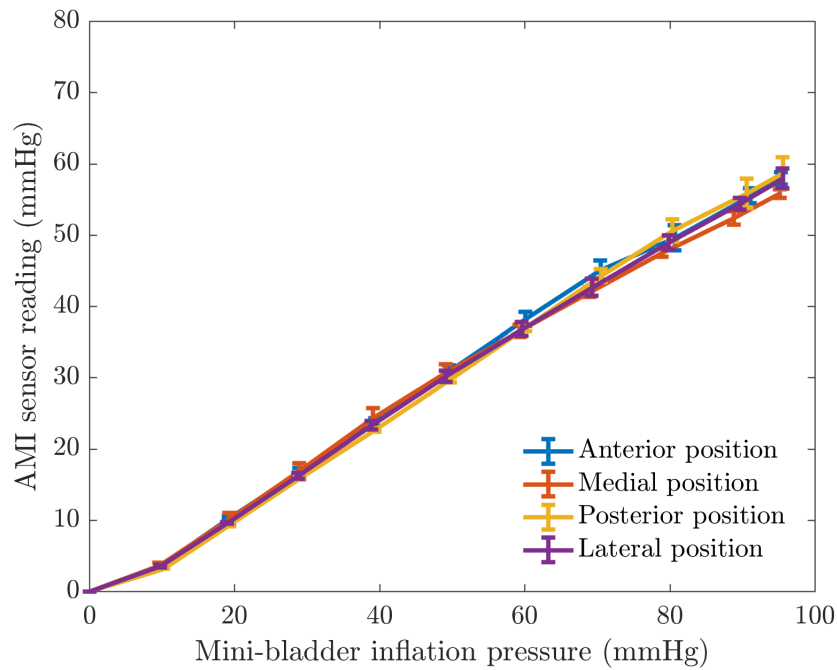


Fig. 5.29 Interface pressure against mini-bladder inflation measured on the leg surrogate without the artificial skin at the ankle position. The different colours show the different position of the leg as denoted in figure legend.

As it can be seen from the Fig. 5.28, the pressure lines almost overlap indicating an uniform circumferential interface pressures at different positions; a pressure difference of ± 2 mmHg for the pressure region 0 – 70 mmHg of mini-bladder inflation pressure. Therefore, one can conclude that the mini-bladders can be used to apply an uniform circumferential pressure irrespective of the position on the leg. This is a significant improvement compared to compression stockings or four-layer bandaging as the ankle area is considered to be a region where it is very difficult to provide uniform defined pressure. This results further confirm that mini-bladders can be used to apply uniform circumferential pressure irrespective of the radius of curvature of the limb. Figure 5.29 shows how the interface pressure on the leg surrogate surface varies with the mini-bladder inflation pressures without artificial skin and fat layers, which demonstrates a similar pattern observed when the leg surrogate was covered with skin and fat layers. All the experimental data presented in sections 5.4, 5.5, and 5.6 proves that the mini-bladders can be used to deliver a uniform pressure around the leg circumference irrespective of the radius of curvature of the leg.

5.7 Comparison of pressure transmission by mini-bladders against GCS

The graduated compression stockings (GCS) generate the pressure depending on the fabric tension and the radius of curvature according to the Laplace's law and therefore, fundamentally cannot provide a uniform circumferential pressure at any position of the leg. However, it was decided to test the pressure performance of a GCS on the leg surrogate covered with artificial skin and fat layers, and the results were compared with the mini-bladders pressure results. For this investigation, Class I, II and III stockings made for the leg surrogate with skin and fat layers were sourced from Urgo Medical Ltd, Loughborough, UK, who manufactures made-to-measure compression stockings. The interface pressure on the skin layer and the fat layer was measured after applying the stockings to the leg surrogate, and the results obtained for the three different classes of stockings were compared with the corresponding interface pressure values obtained with the mini-bladders. The pressures with the GCS were measured at the same position on the leg surrogate. Table 5.8 lists mid pressure of the manufacturer specified interface pressure ranges for the three classes of GCS. It was calculated that to achieve such levels of interface pressure using the mini bladders the inflation pressures were 24.84, 32.03 and 43.54 mmHg, respectively. The required mini-bladder inflation pressures were calculated by linear interpolation of pressure data obtained for the mini-bladder in section 5.4.4.

Table 5.8 The calculated mini-bladder inflation pressures required to achieve the same skin interface pressure as GCS.

Compression stocking	Interface pressure (mmHg)	Mini-bladder inflation pressure (mmHg)
Class I (14-17mmHg)	15.5	24.84
Class II (18-24mmHg)	21	32.03
Class III (25-35mmHg)	30	43.54

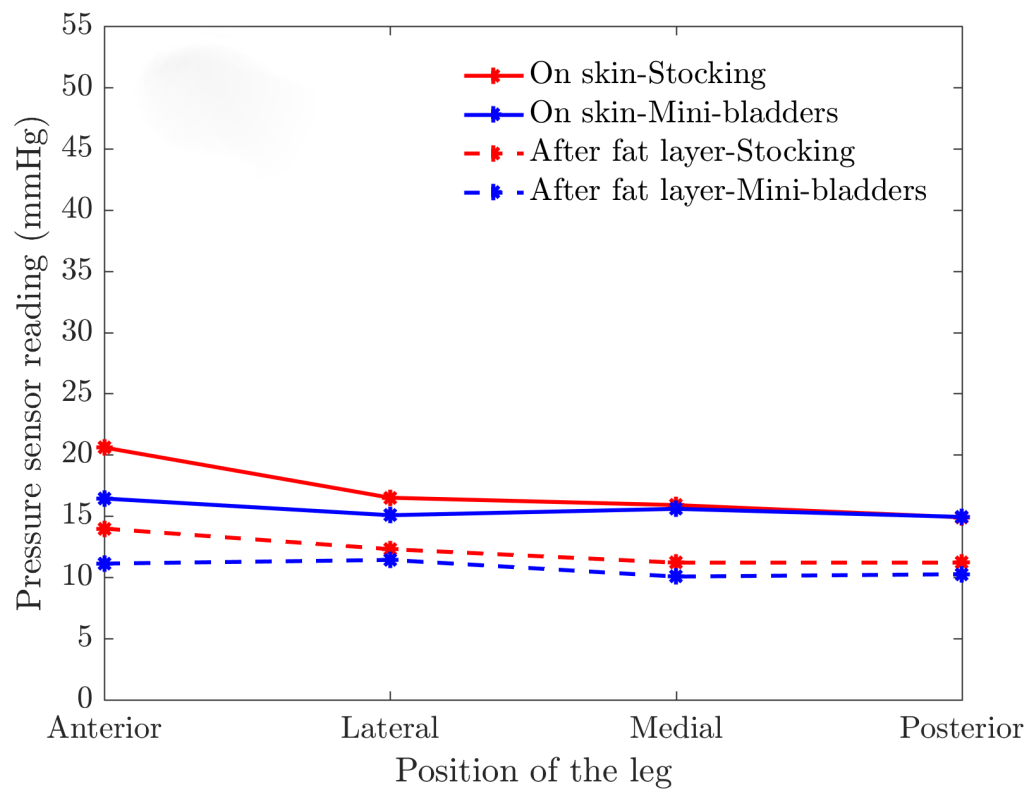


Fig. 5.30 The comparison of class I GCS and the mini-bladder pressure performance (firstly prepared skin and fat layer)

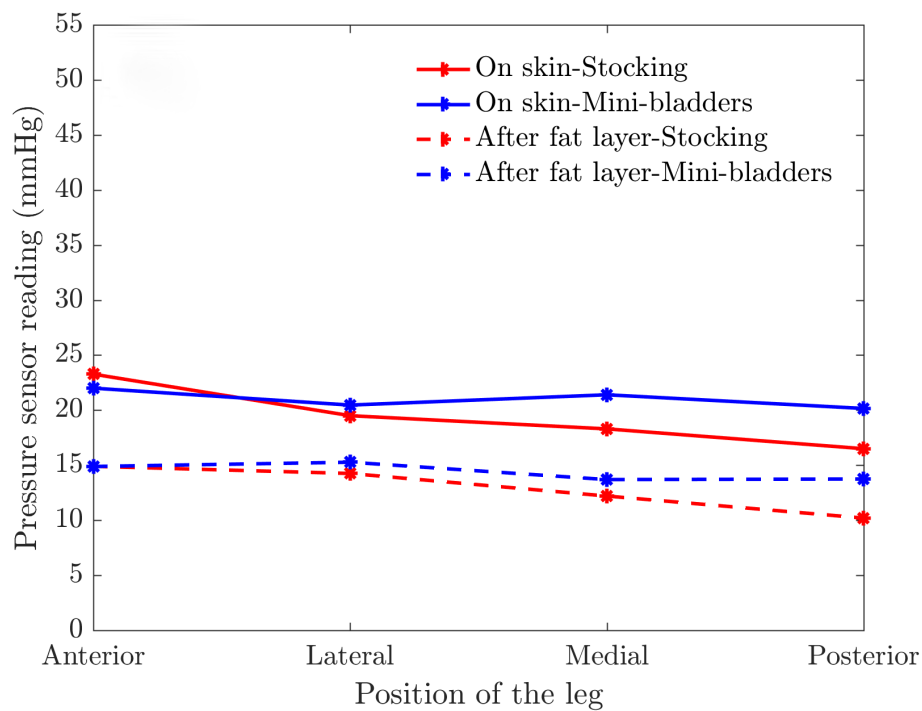


Fig. 5.31 The comparison of class II GCS and the mini-bladder pressure performance (firstly prepared skin and fat layer)

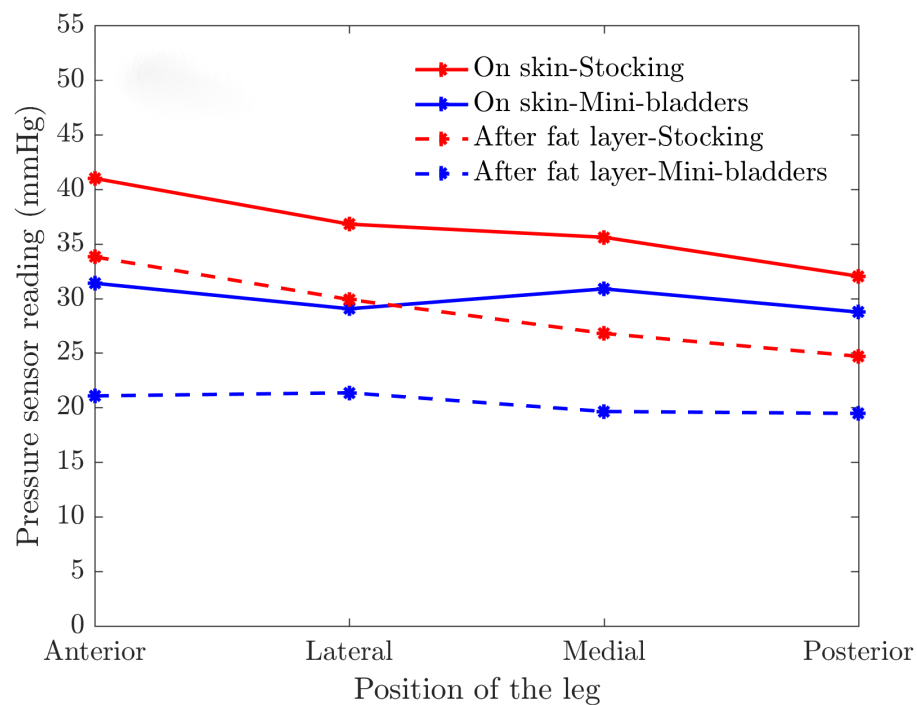


Fig. 5.32 The comparison of class III GCS and the mini-bladder pressure performance (firstly prepared skin and fat layer)

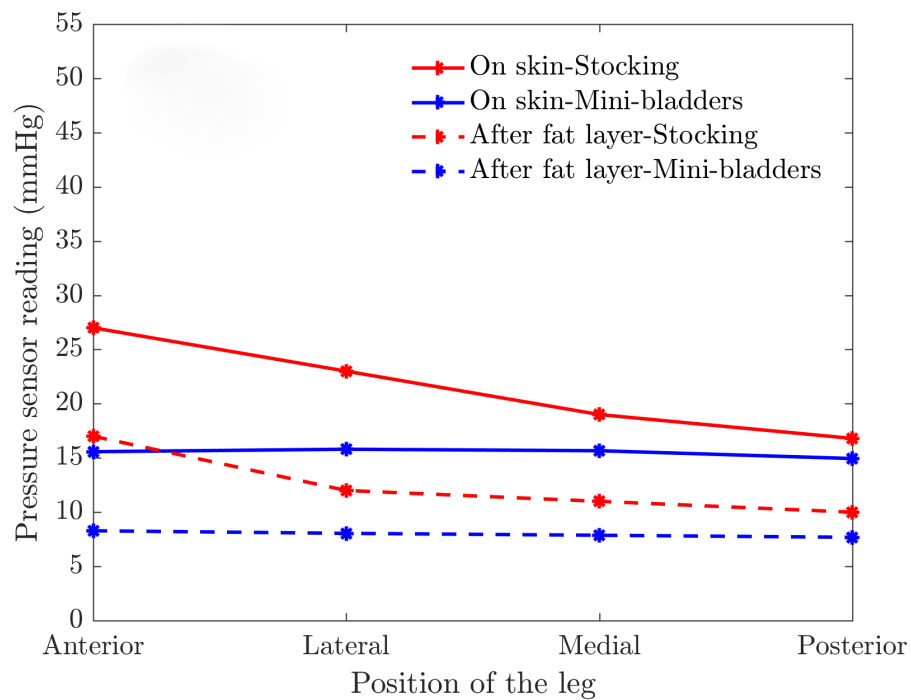


Fig. 5.33 The comparison of class I compression stocking and the performance of mini-bladders in the corresponding pressure range (skin prepared with the layer of hard fat)

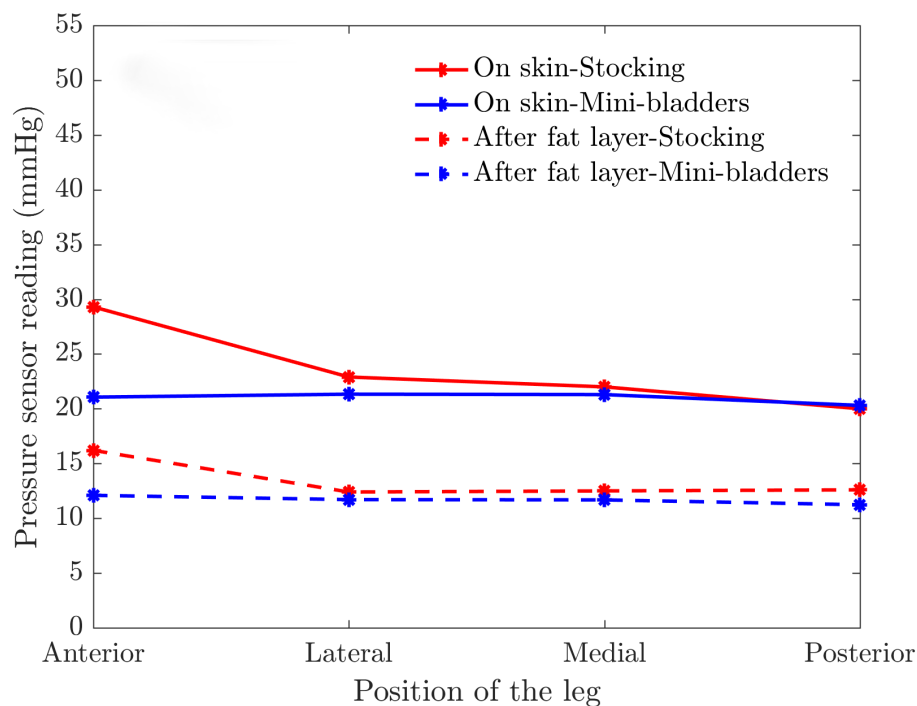


Fig. 5.34 The comparison of class II compression stocking and the performance of mini-bladders in the corresponding pressure range (skin prepared with the layer of hard fat)

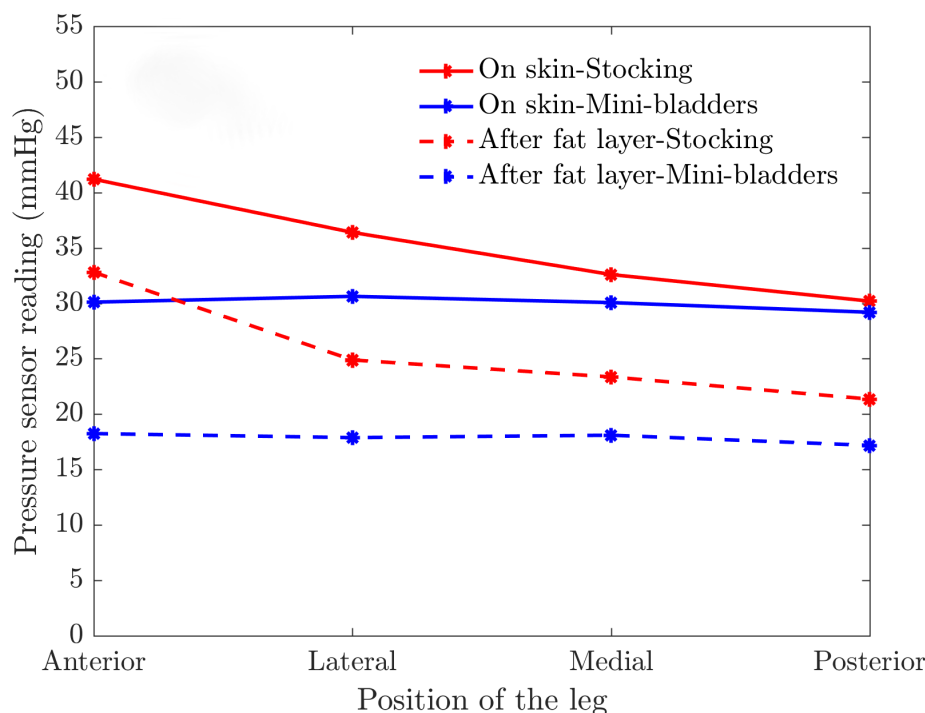


Fig. 5.35 The comparison of class III compression stocking and the performance of mini-bladders in the corresponding pressure range (skin prepared with the layer of hard fat).

The results are shown in Figs. 5.30, 5.31, 5.32 for the class I, class II and class II GCS respectively measured on the leg surrogate covered with the skin and fat layer produced for the experiments described in section 5.4. The results for the GCS show significantly large variation around the circumference of the leg surrogate. It also shows that GCSs have always exerted higher pressures than the manufacturer specified pressure values. However, the mini-bladders have provided correct pressures with the flexibility of achieving higher pressures by changing the inflation pressure range. The same set of experiments were carried out with the skin layer produced with the hard fat layer (high modulus silicone, in section 5.5), and the results are shown in Figs. 5.33, 5.34 and 5.35 for class I, class II and class III GCS respectively.

A similar pattern of large variations around a given circumference of the leg surrogate is evident for GCS, whereas the mini-bladders demonstrated a uniform circumferential pressure. It can be observed that all the different classes of made to measure compression stockings (Class I, Class II, Class III) have shown higher pressure values than what it was defined in the standard; which implicates that they do not provide the correct pressures. The mini-bladders have shown that it could be used to apply the correct pressures, which is important in the treatment system.

5.8 Chapter summary

The primary objective of developing an active compression system using mini-bladders is to apply the correct pressures on to the human lower limb. Hence, it was important to study the capability of mini-bladders to transfer pressure on to a contact surface; which was carried out in two stages. During the first stage the pressure transmission was measured on hard surfaces, which later was extended on to biofidelic lower leg surrogate to closely replicate the real life scenario. Three different geometries of mini-bladders were tested on a cylindrical surface, out of which the hexagonal shaped mini-bladders have shown the highest pressure transmission efficiency which was 70%-80% for inflation pressures higher than 20 mmHg. The interface pressure recorded by the mini-bladders of all three geometries have shown good linear relation with the mini-bladder inflation pressure.

The second phase of the experiments were carried out on a biofidelic lower leg surrogate, to observe the pressure transmission behaviour at different positions of the leg. The surface of the lower leg surrogate was covered with artificial skin and fat layers of different Young's modulus values in order to evaluate the propagation of the skin contact pressure in the leg, which is a knowledge gap in current compression therapy. The mini-bladders were able to apply an uniform circumferential interface pressure (proving the research hypothesis), which was not possible with the current passive compression products.

The pressure transmitted on to the surface of the leg surrogate was about 50%-70% of the pressure applied by the mini-bladder, which was lower compared to the hard cylindrical surface. The pressure transmission percentage in the fat layer was in the range of 35%-45% of the mini-bladder pressure. It was concluded that the pressure transmission has varied with the modulus of the fat layers; the lowest modulus fat layer has recorded to the highest pressure transmission percentage.

In comparison to the graduated compression stockings (GCS), the mini-bladders have demonstrated that it could apply correct uniform circumferential pressure values, whereas GCS have always shown higher interface pressure values with huge variations at different positions of the leg surrogate. Hence it can be concluded that mini-bladders could be used effectively as an active compression treatment system, which could deliver correct uniform circumferential pressures.

Chapter 6

Prototype design of mini-bladder unit

This chapter focuses on designing the prototype of the active compression unit to generate a graduated compression profile. This includes the analysis of the arrangement of mini-bladders, whether to use single mini-bladders or internally connected mini-bladder arrays, and the number of mini-bladders to be included in the mini-bladder unit. This chapter also discusses different arrangements, their pressure transmission characteristics and development of a sleeve consisting of mini-bladders that could be used to provide graduated compression.

6.1 Design of mini-bladder array

The analysis of pressure transmission characteristics reported in Chapter 5 has established that the hexagonal shaped mini-bladders provided the maximum efficiency. Therefore, it was decided to utilise hexagonal shaped mini-bladders to develop the active compression system. The other important advantage of hexagonal shaped mini-bladders is that it provides effective stacking of the mini-bladders in an array. When manufacturing the final prototype design, these hexagonal shaped mini-bladders should be arranged in an array, to generate a graduated compression along the leg profile. Manufacturing of an array of individual mini-bladders would also give the possibility of controlling these mini-bladders separately to generate a predetermined pressure profile.

To achieve the maximum controllability, it is required to have a separate air channel for each mini-bladder. However, this would add large number of air channels, making a complex pneumatic circuit. If the mini-bladders can be arranged in a unit with single air inlet, where mini-bladders are internally connected it would reduce the complexity of the design. This arrangement has the advantage of using less number of air channels to inflate the mini-bladders compared to using separate air channels to activate individual mini-bladders. However, long arrays of internally connected mini-bladders would influence the control of the mini-bladder inflation, whereas the inflation of single mini-bladders would be less demanding. A fact to be considered in designing the mini-bladder array is that slight differences in mini-bladder inflation heights were evident for four internally connected mini-bladders

in experiments described in chapter 4. Therefore, initial stages of testing were carried out using the biofidelic leg surrogate for arrays consisting of two mini-bladders and three mini-bladders to determine the interface pressure transmission characteristics.

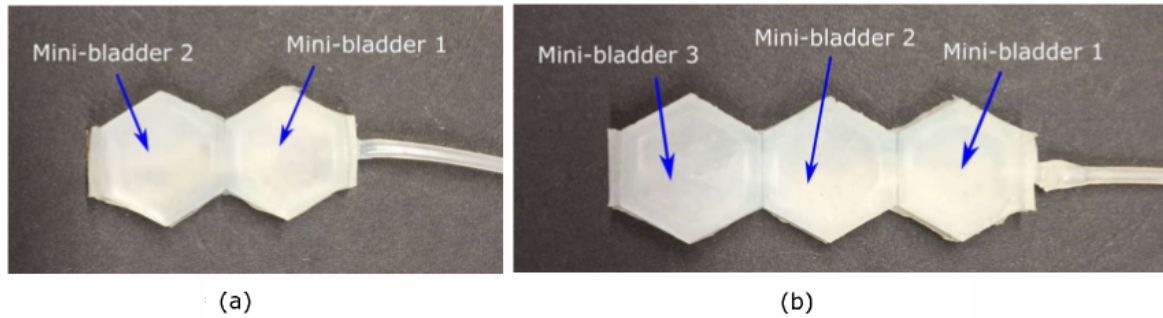


Fig. 6.1 The arrangement of two and three mini-bladders arrays and the composition mini-bladders

The experiments were conducted as elucidated in the section 5.4.3 with sensors placed on the surface of the leg surrogate covered with the artificial skin and fat layer.

The mini-bladder arrays were stitched onto 95 mm wide strips of the woven fabric described in section 5.4.3. These were then placed longitudinally (parallel to the axis of the leg surrogate) and laterally in a ring like fashion on the skin surface of the biofidelic leg surrogate to measure the interface pressure generated by each mini-bladder of the array. The results are summarised in Figs. 6.2 and 6.3, respectively.

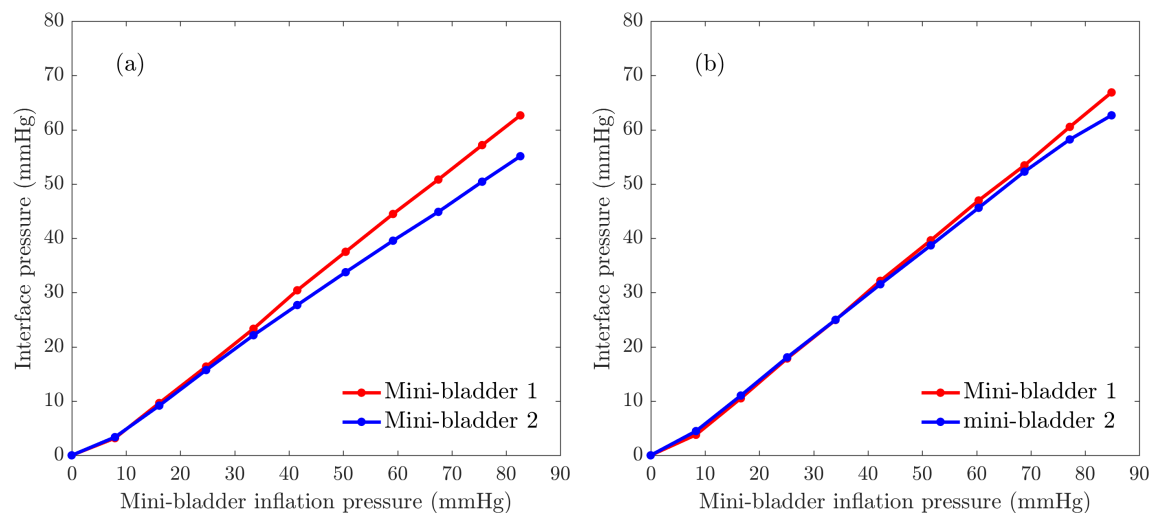


Fig. 6.2 Interface pressure against the mini-bladder inflation pressure for an array with two mini-bladders. (a) lateral arrangement of the mini-bladder array, (b) longitudinal arrangement of the mini-bladder array.

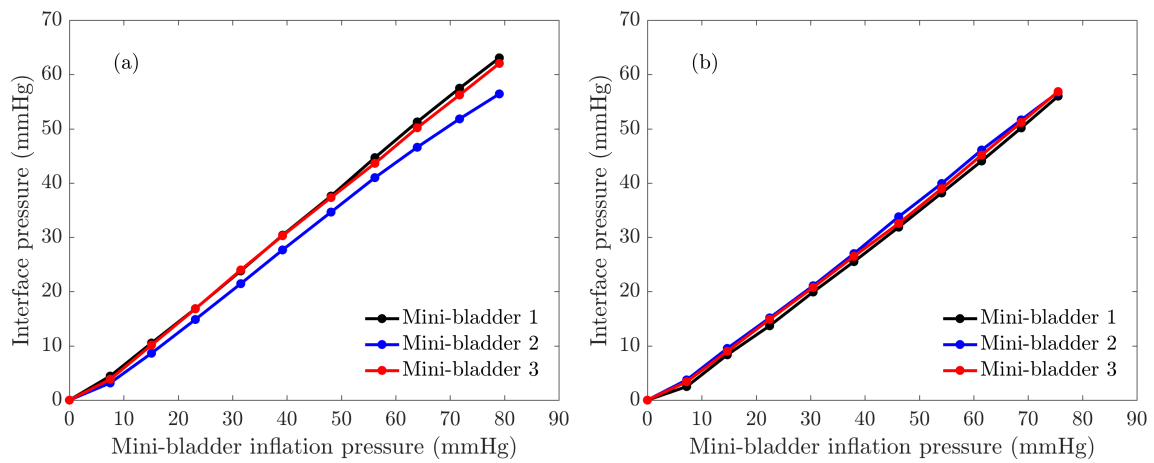


Fig. 6.3 Interface pressure against the mini-bladder inflation pressure for an array with three mini-bladders (a) lateral arrangement of the mini-bladder array (b) longitudinal arrangement of the mini-bladder array.

In Figs. 6.2 (a) and (b), the pressure curves overlap in the mini-bladder inflation pressure range of 0-60 mmHg. For the lateral arrangement of the two mini-bladder array a maximum difference of ± 4 mmHg between interface pressures induced by the two mini-bladders could be determined. However, an insignificant difference between the interface pressures induced by the two mini-bladders was evident when the two mini-bladder array was sited longitudinally on the biofidelic leg surrogate.

Figure 6.3, shows the similar results for three mini-bladder array with internally connected air supply. Again an insignificant difference in interface pressures induced by the three mini-bladder's of the array was evident when the array was located longitudinally on the biofidelic leg surrogate, and a difference of ± 3 mmHg interface pressures was recorded when the mini-bladder array was arranged laterally. The results demonstrate that an uniform interface pressure could be induced with the longitudinal arrangement of an array of mini-bladders. The insignificant interface pressure differences created by mini-bladders, when the array is positioned longitudinally around the biofidelic leg surrogate, could have been caused by the tension in the fabric used to house the mini-bladder array in relation to the variation in radius of curvature within the circumference of the biofidelic leg surrogate

Based on the test results obtained for the mini-bladder unit it was concluded that having an internally connected common air channel to all the mini-bladders in the unit, would be less effective in the lateral arrangement. Therefore, to improve the controllability of individual mini-bladders, it was decided to use separate air inlets to each mini-bladder in the final design, which are arranged in the form of a honeycomb structure. However, to reduce the complexity of the pneumatic circuit, mini-bladders in the same level are connected to a common air channel rather than having separate air channels for each mini-bladder.

6.2 Design of a bandage to house mini-bladder arrays

In the final design, the mini-bladder arrays need to be integrated with a textile fabric in order to create a wearable active compression system. This was achieved with a bandage consisting of two fabric layers with a pocket to house a mini-bladder array; in the present study the design was limited to one mini-bladder array. Two fabric layers of different moduli were utilised in the design of the bandage; a high elastic fabric to be in contact with the surface of the leg surrogate not to restrict the inflation of mini-bladders and a stiff (high modulus, woven) fabric outer layer. Three extensible fabric layers were knitted from different types of covered yarns and pockets were constructed in the bandage by stitching together the two fabric layers as shown in Fig. 6.4(b). The 1×1 rib knitted structure was selected due to its good stretch and dimensional stability properties. The effect of the pocket on pressure transmission characteristics of mini-bladders were evaluated by wrapping the bandage with a mini-bladder around the biofidelic leg surrogate as shown in Fig. 6.4(a). The details of the three yarns used to knit the elastic fabric is tabulated in the Table 6.1, and their uniaxial tensile properties are included in the Appendix E. As listed in Table 6.1 three types of elastic yarns of different power were

Table 6.1 The yarns used to manufacture the elastomeric knitted fabric layers, and their elastic properties

Yarn code	Manufacturer	Fibre type		Yarn count and composition		Elastic modulus (N/dtex)
		Core	Covering	Core	Covering	
20030	W. Zimmermann Gmbh & Co. KG	Lycra	PA (Polyamide)6,6	44 dtex	78/68/1 dtex	7.44
6437	W. Zimmermann Gmbh & Co. KG	Lycra	Yarn1: PA (Polyamide)6,6 Yarn 2: PA (Polyamide)6,6	165 dtex	22/7/1 dtex 22/7/1/dtex	9.23
Z2300	Stretchline (Pvt). Ltd	Lycra	PA (Polyamide)6	22 dtex	33/34/1 dtex	3.73

used to produce 1×1 rib knitted fabrics;

1. 20030 yarn code:single covered yarn with a Lycra core of 44 dtex yarn count and covering yarn of Polyamide 6,6 of 78 dtex yarn count with 68 filaments
2. 6437 yarn code: a double covered yarn having a Lycra core of 165 dtex yarn count and two covering yarns for s and z directions of 22 dtex yarn count with 7 filaments
3. Z2300 yarn code: single covered yarn with a Lycra core of 22 dtex yarn count and a covering yarn of Polyamide 6,6 of 33 dtex yarn count and 34 filaments

In order to evaluate effect of the elastomeric fabric on the interface pressure induced due to the inflation of the mini-bladders. The elastic modulus details of the manufactured elastic fabrics out of the above described yarns are listed in Table 6.2 (the details of uniaxial tensile tests are included in

the Appendix E). The mini-bladder array was placed in longitudinally on the biofidelic leg surrogate using the bandages, since the earlier experiments showed that this arrangement provided interface pressures with minimum variation. The tests were repeated five times and mini-bladder arrays with two mini-bladders and three mini-bladders were used.

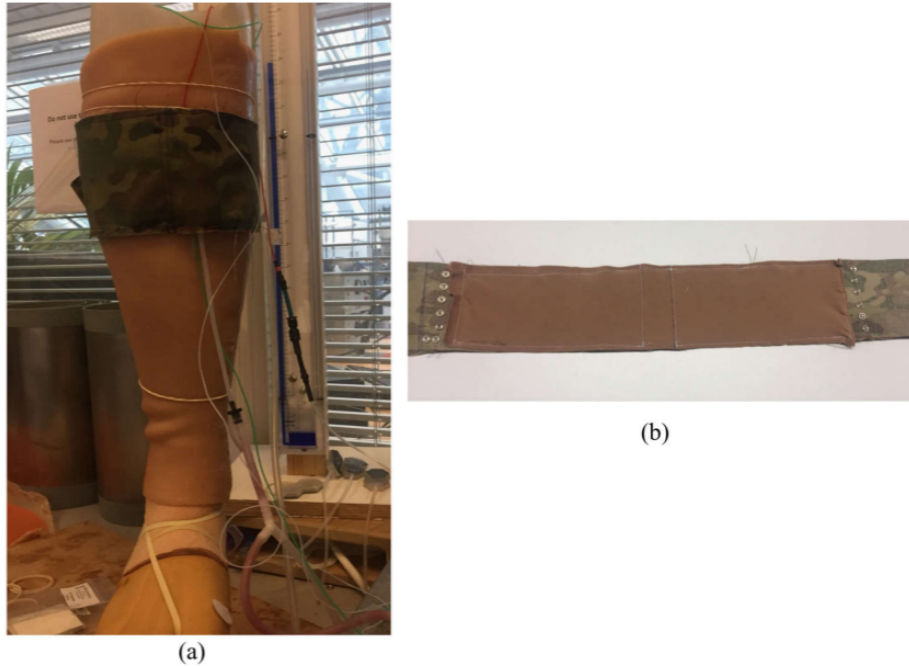


Fig. 6.4 The experimental setup for testing different fabric pockets (a) the fabric panel including the mini-bladder unit wrapped over leg as a bandage (b) pocket made with fabric manufactured from single covered yarns

Table 6.2 The elastic modulus of the manufactured elastomeric knitted fabrics

Fabric type	Yarn code used to manufacture the fabric	Elastic modulus (MPa)
1x1 rib	6437	0.238
1x1 rib	20030	0.183
1x1 rib	Z2300	0.169

Figures 6.5 (a) and (b) shows the interface pressures induced by inflating the mini-bladders incorporated in the bandage made with the elastomeric fabric knitted from yarn code-20030 single covered yarn.

It is evident from Fig. 6.5 (a) that similar interface pressures are induced by both mini-bladders for mini-bladder inflation pressures between 0 mmHg and 60 mmHg. Within this inflation pressure range one could apply an interface pressures between 0 mmHg and 40 mmHg, which is the clinically

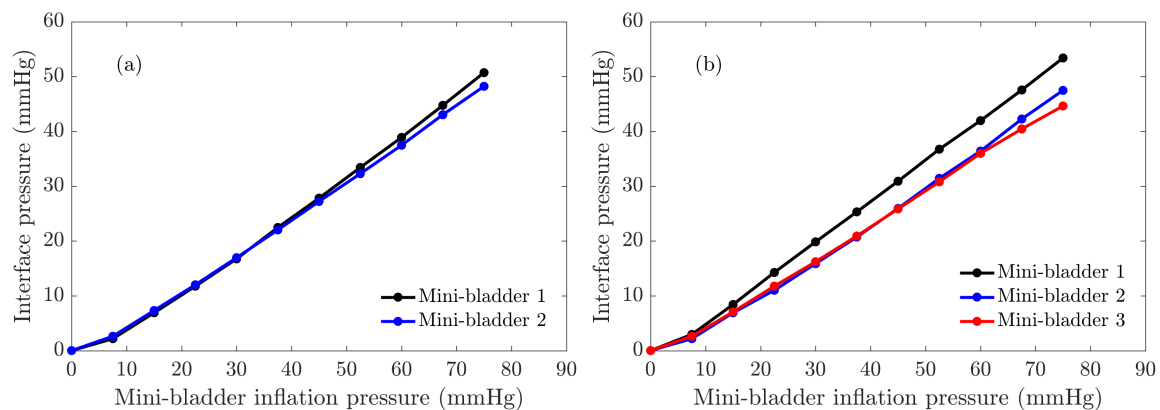


Fig. 6.5 Interface pressure against mini-bladder inflation pressure for mini-bladder array retained in the bandage draped around the biofidelic leg surrogate and the bandage made with elastomeric fabric knitted from 20030 single covered yarns, (a) array with two mini-bladders connected internally with shared air channel, (b) array with three mini-bladders connected internally with shared air channel.

accepted pressure region. However, the interface pressures induced by the three mini-bladder array demonstrated in Figure 6.5 (b) evidence a slightly different behaviour, where the interface pressures induced by the second and the third mini-bladders were lower than that of the first in the array. This might have been due to the series air channel used to inflate all the three mini-bladders and may be resolved by the appropriate engineering of the air channel, which was outside the remit of this research program.

The results of the mini-bladders of the arrays were averaged and shown in Fig. 6.6 (black colour curve) against mini-bladder inflation pressures. The interface pressures attained for the same mini-bladder arrays stitched directly onto the high modulus woven fabric bandage (without a fabric pocket) and located on the biofidelic leg surrogate at the same longitudinal location are referenced in Fig. 6.6 (blue curve) for comparative analysis.

It is evident from Figs. 6.6 that for both mini-bladder arrays, the interface pressure recorded with the bandage made with the stiff woven fabric and elastomeric knitted fabric (1×1 rib knitted with 20030 single covered elastomeric yarn) the interface pressures were less than the values measured with the single layer woven fabric. A difference of ± 10 mmHg in interface pressure was evident for the range of 0 – 60 mmHg mini-bladder inflation pressures. This difference exceeds 10 mmHg for pressures greater than 60 mmHg mini-bladder inflation pressures. Therefore, it can be deduced that the inflation of the mini-bladders is restricted by the knitted elastomeric fabric used.

The experimental procedure described above was repeated with two layer bandages made from the stiff woven fabric and fabrics knitted with the double covered yarn (6437-yarn code) and the single covered yarn (yarn code-Z2300). The experimental results are summarised below.

It is evident from Figs. 6.7 that similar interface pressures are induced by both mini-bladders one and two for mini-bladder inflation pressures between 0 mmHg-60 mmHg; which could apply an

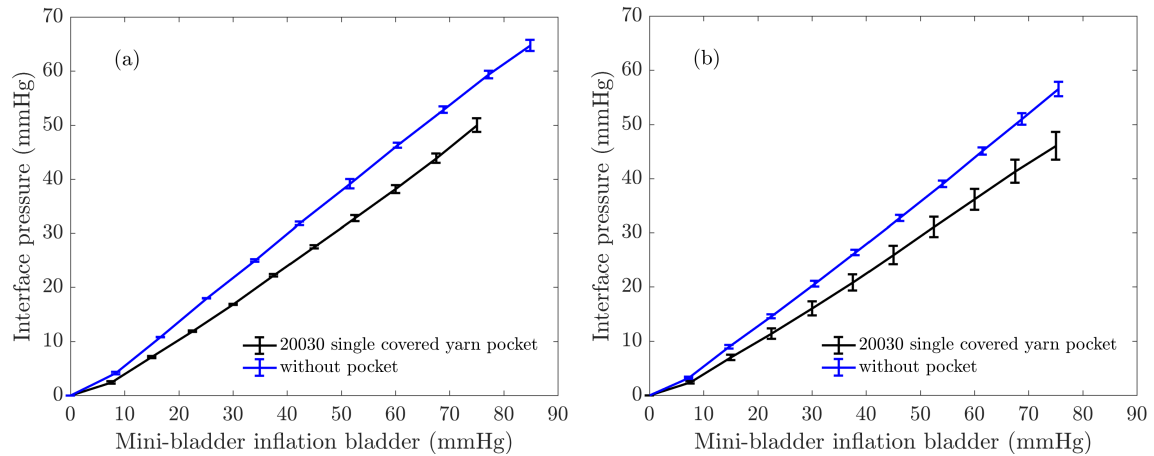


Fig. 6.6 The average interface pressure against the mini-bladder inflation pressure when the mini-bladder arrays were retained in single and two fabric (knitted from 20030 single covered yarn) layer bandage. (a) two mini-bladder array, (b) three mini-bladder array.

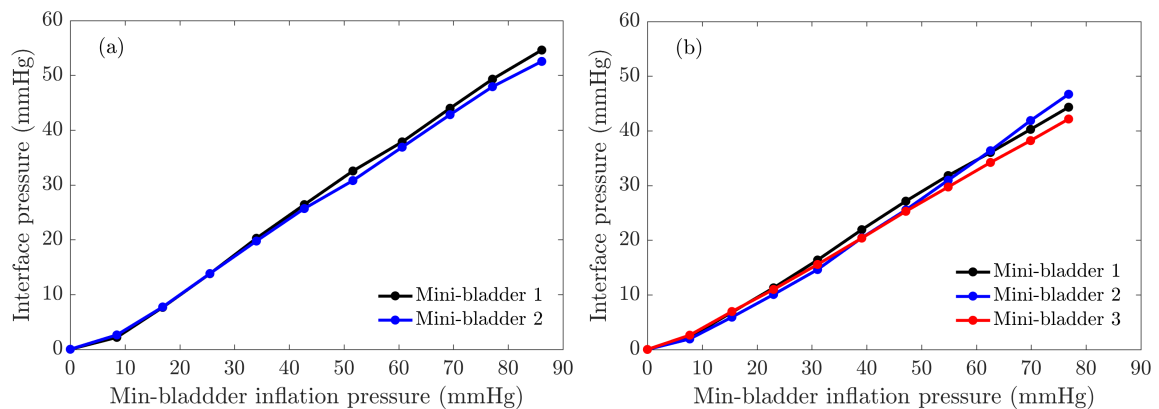


Fig. 6.7 Interface pressure against the mini-bladder inflation pressure for mini-bladder array retained in the bandage draped around the biofidelic leg surrogate and the bandage made with elastomeric fabric knitted with 6437 double covered yarns, (a) array with two mini-bladders connected internally with a shared air channel (b) array with three mini-bladders connected internally with shared air channel.

interface pressure between 0 mmHg-40 mmHg that is clinically accepted. However, the interface pressures induced by three mini-bladder arrays have shown a slight variation (Fig. 6.7 (b)); where the second and third mini-bladders have induced a lower pressure than the first mini-bladder. The results of the mini-bladders of the arrays were averaged and shown in Figs. 6.8 (a) and (b) (black colour curve). The blue curve in Figs. 6.8 a and b represents the interface pressures attained for the same mini-bladder arrays directly stitched onto the high modulus woven fabric bandage (single layer/no pocket). It is evident from Figs. 6.8 for both mini-bladder arrays, the interface pressure recorded with the stiff woven fabric and elastomeric knitted fabric bandage were less than the single layer bandage ; with a difference of ± 10 mmHg in 0 mmHg-60 mmHg mini-bladder inflation pressures. Similarly, to the elastomeric fabric made with single covered yarns (yarn code-Z2300), the difference exceeds 10 mmHg for pressures greater than 60 mmHg mini-bladder inflation pressures. Hence, it further confirms that the inflation of the mini-bladders is restricted by the knitted elastomeric fabric of two-layer bandage irrespective of the yarn type used.

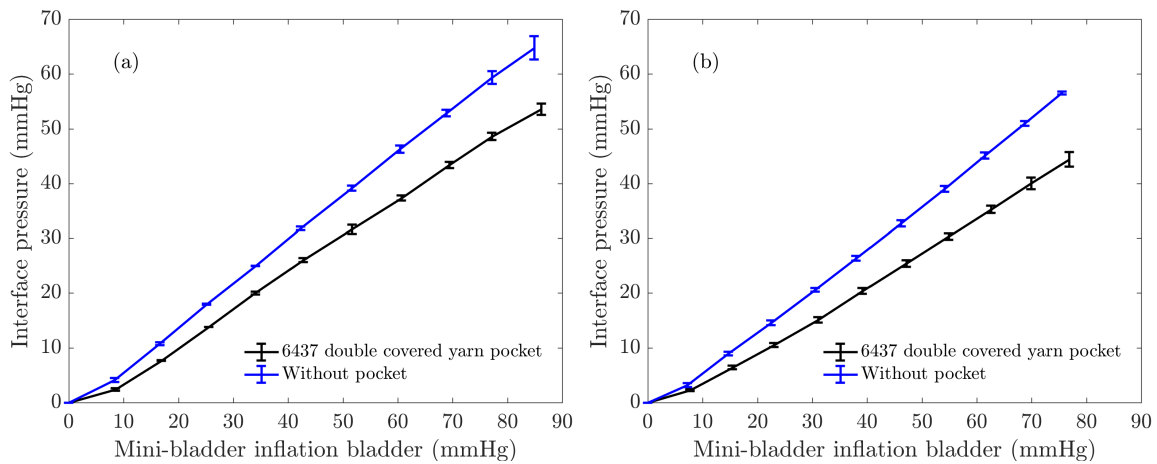


Fig. 6.8 The average interface pressure against the mini-bladder inflation pressure when the mini-bladder arrays were retained in single and two-layer fabric (knitted from 6437 double covered yarn) bandage (a) two internally connected bladder unit, (b) three internally connected bladder unit.

Figure 6.9 shows that similar interface pressures are induced by the component mini-bladders of the mini-bladder arrays, for inflation pressures between 0 mmHg-60 mmHg. However, the interface pressures induced by both two and three mini-bladder arrays have shown less deviation in the higher pressures than 60 mmHg. The results of the mini-bladders of the arrays were averaged and shown in Fig. 6.10. The blue curve in Figs. 6.10 (a) and (b) represents the interface pressures attained for the same mini-bladder arrays directly stitched onto the high modulus woven fabric bandage (single layer/no pocket). It is evident from Figs. 6.10 (a) and (b) for both mini-bladder arrays, the interface pressure recorded with the stiff woven fabric and elastomeric knitted fabrics (knitted from Z2300 single covered yarn) bandage were less than the single layer bandage; with a difference of ± 5 mmHg in 0 mmHg-60 mmHg mini-bladder inflation pressures. However, this difference is the lowest compared to the other two yarn types; which denotes that the double layer bandage made from Z2300

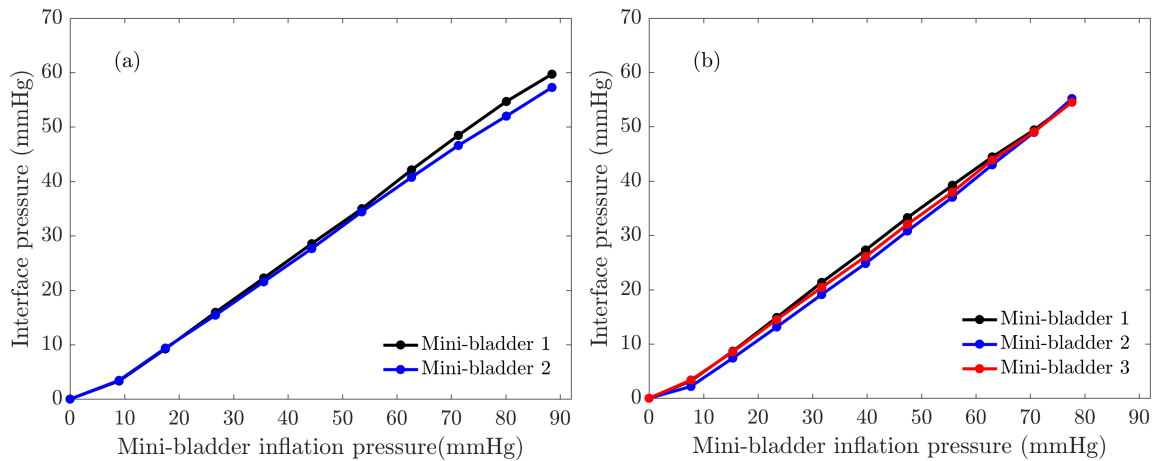


Fig. 6.9 Interface pressure against the mini-bladder inflation pressure for mini-bladder array retained in the bandage draped around the biofidelic leg surrogate and the bandage made with elastomeric fabric knitted with Z2300 single covered yarns, (a) array with two mini-bladders connected internally with a shared air channel (b) array with three mini-bladders connected internally with shared air channel

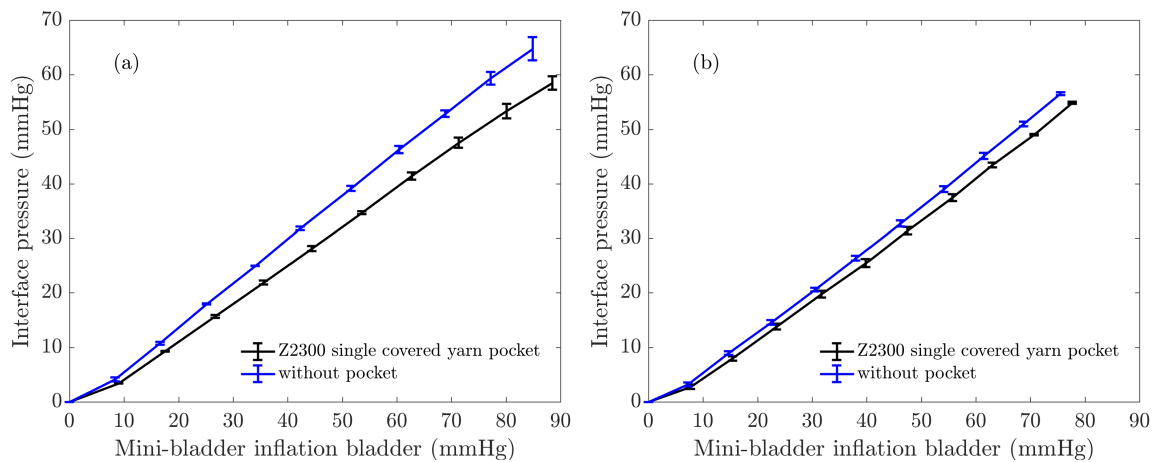


Fig. 6.10 The average interface pressure against the mini-bladder inflation pressure when the mini-bladder arrays were retained in single and two-layer fabric (knitted from Z2300 single covered yarn) bandage (a) two internally connected bladder unit, (b) three internally connected bladder unit.

single covered yarn has shown the least restriction towards the inflation of the mini-bladders.

For a better comparison of the influence of three different bandage types used to accommodate the mini-bladder arrays the interface pressures against the mini-bladder inflation pressures were plotted in Figs. 6.11. It is evident that the use of bandages with two fabric layers will reduce the interface pressures induced by inflating the mini-bladders. It is also clear that the bandage made with the fabric knitted with the double covered 6437 yarn (highest young's modulus 0.238 MPa) induced the lowest interface pressures and the bandage made with the fabric knitted with the single covered Z2300 yarn (lowest young's modulus 0.169 MPa) induced the highest interface pressures as expected.

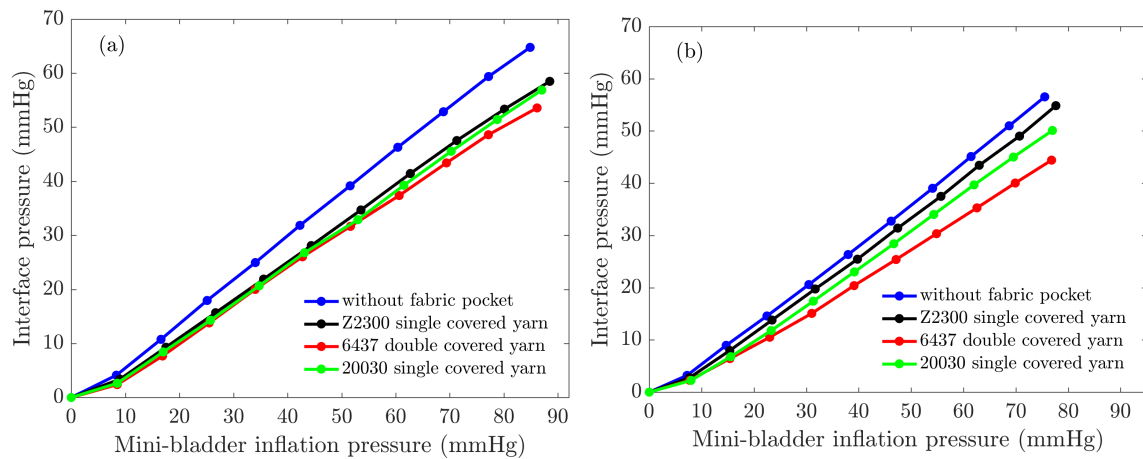


Fig. 6.11 The average interface pressure against the mini-bladder inflation pressure when the mini-bladder arrays were retained in single and two-layer (pocket) fabric; knitted from 6437 double covered yarn, 20030 single covered yarn, and Z2300 single covered yarn bandage (a) two internally connected bladder unit, (b) three internally connected bladder unit.

The above experimental results demonstrate that the use of a textile bandage to house the silicone mini-bladders would negatively influence the interface pressure induced by inflating the mini-bladder. Therefore, in the final prototype of the active compression system was designed with the mini-bladder arrays integrated within a silicone layer. Silicone was selected due to its bio-compatibility enabling the inflating surfaces of the mini-bladders can be directly in contact with the skin; this would facilitate the direct pressure transfer between the skin and the mini-bladder surface. The mini-bladder arrays were arranged laterally to human limb to create a graduated pressure profile, and to minimise pressure variations observed in the internally connected mini-bladders arrays separate air channels were designed for inflating the mini-bladders individually. The details of the final prototype design are discussed in subsequent sections.

6.3 Manufacturing of the final prototype design

The analysis established in the previous section has proven that the use of mini-bladders in serial arrangement has provided variations in the interface pressure between component mini-bladders. Hence, it was decided to create separate air channels to inflate the component mini-bladders individually. However, to avoid the complexity of providing individual air channels to each mini-bladder, a common air channel is introduced to each mini-bladder array having individual inlets to component mini-bladders as shown in Fig. 6.12.

The final prototype was designed with the mini-bladder arrays integrated in a silicone layer, according to the principle described in the chapter 4; having a top extensible layer and an bottom inextensible layer including a strong fabric layer. The mini-bladder array was designed using SolidWorks (Dassault

Systèmes SolidWorks, version 2016, France), and then was laser cut to manufacture a stencil as depicted in Fig. 6.12 to create the top extensible layer of the mini-bladder unit.

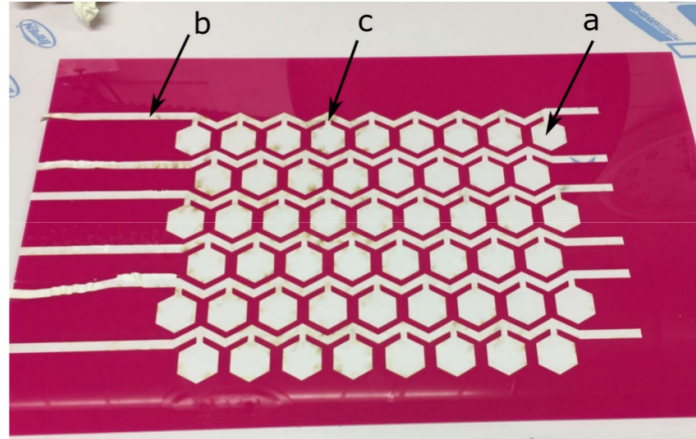


Fig. 6.12 The stencil used to create the top layer of the mini-bladder unit

6.3.1 Manufacturing process of mini-bladder unit

The detailed manufacturing process is described as follows; It was required to manufacture a less extensible, yet sufficiently flexible bottom layer to minimize the effect of rigidity of the final prototype design. To produce this first a 0.5 mm thin PlatSil® Gel-OO 30 silicone layer was prepared and allowed to cure under room temperature. Then a strong camouflage woven fabric (234GSM, 50 epi, 37 ppi, Young's modulus of 1.648 MPa) was immersed into this silicone layer, when it was set half way. Thereafter another layer of 1mm thick PlatSil® Gel-OO 30 silicone layer was poured on top of the previous layer to complete the bottom layer and allowed it to cure. The stencil (Fig. 6.12) was placed on top of the cured bottom layer and a layer of wax (Vaseline Petroleum Jelly, Boots UK Ltd., Nottingham, UK) was applied in the areas of the hexagonal array design by using a paint brush as shown in Fig. 6.13 (c) and (d), to act as an inhibitor to prevent the two silicone layers (top and bottom) gluing to each other. The top layer was manufactured by pouring PlatSil® Gel-OO 30 on top of the previous layer to a thickness of 1.5 mm and allowing it to cure in the room temperature. Then, connectors were fixed to the ends of each air channel. Finally, two Velcro strips were placed (Velcro black hook and loop tape 20 mm /times 10 m, RS components UK Ltd, Nottingham, UK) at the distance required to cover the cylindrical surface and were bonded to the silicone layer (A more detailed manufacturing process is included in Appendix E.

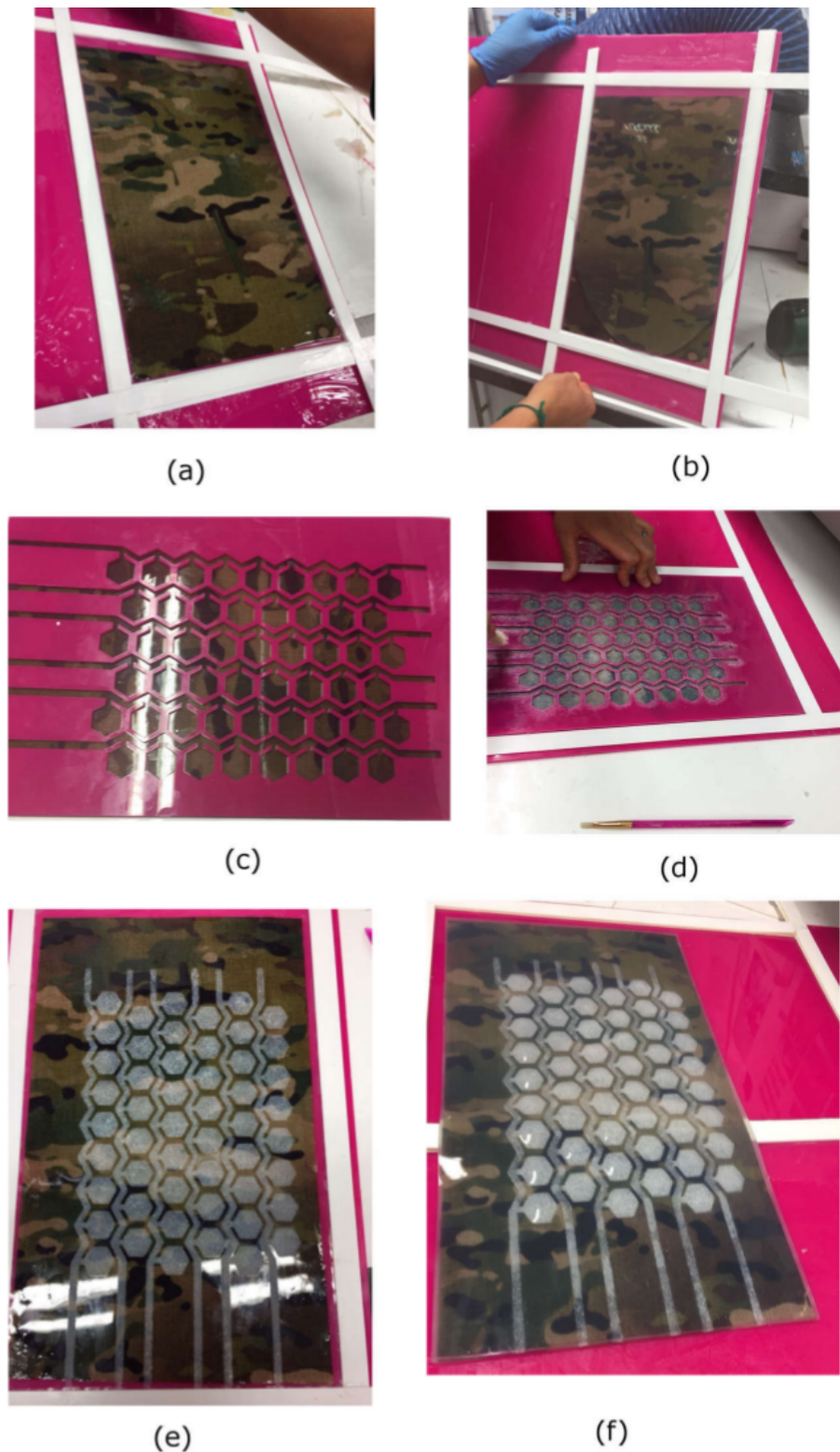


Fig. 6.13 Manufacturing process of the complete mini-bladder unit; (a) and (b) preparation of the thin bottom layer including a strong woven fabric slanting the frame to control the thickness, (c) placement of the stencil cut according to the mini-bladder array design, (d) applying wax using the stencil (e) the mini-bladder array design on the bottom layer after the application of wax (f) the final mini-bladder array prototype

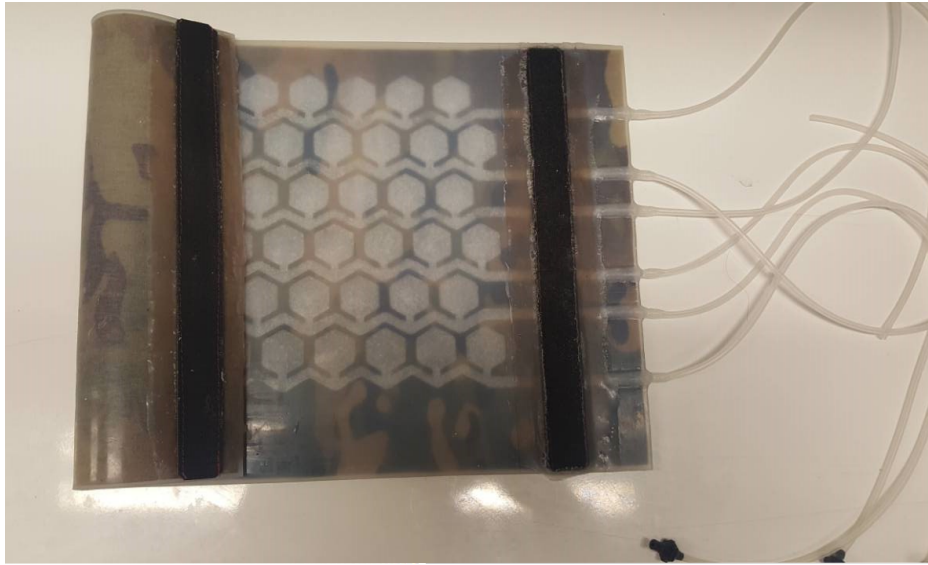


Fig. 6.14 The final prototype of the manufactured active compression sleeve, with the inlet tubes connected to each row of mini-bladders to create a graduated compression. The Velcro strips have been used to wrap this unit around the testing surface.

6.4 Experimental set up to create a graduated compression

The manufactured sleeve could be used to generate a graduated pressure on the contact surface. The test rig was designed with, a cylinder (RS components UK Ltd, Nottingham, UK) of diameter 70 mm and the AMI air-pack sensors (Main unit model A0905, $\phi = 20$ mm, AMI Techno, Tokyo, Japan) which were mounted on to the cylinder using tapes (Tesa® Premium acrylic coated cloth tape, 50 mm \times 50m, 0.31 mm thick, RS components UK Ltd, Nottingham, UK). The design of the mini-bladder array was drawn in a paper and it was wrapped around the cylinder to get the correct positioning of the sensors. The sensors were placed on the marked positions (Fig. 6.15), of each row closer to the middle of the row, to avoid any difference that could exist in the end of the rows. Thereafter, the sleeve was wrapped around the cylinder (the final experiment set up is denoted in Fig. 6.16).

Each mini-bladder row of the array was inflated using the air syringe to a range of different inside pressures, and was measured using the liquid manometer. The bottom most row was inflated to 90 mmHg inside pressure and each row above were inflated with 10 mmHg decrements resulting inside pressures at each row 90 mmHg, 80 mmHg, 70 mmHg, 60 mmHg, 50 mmHg and 40 mmHg to achieve a graduated compression. After each row of the mini-bladders was inflated to the above denoted pressures, air channels were closed and the interface pressures were measured using the AMI air pack pressure sensors. The experiment was repeated for four times and the average interface pressure readings plotted against the position of the cylindrical surface and is shown in Fig. 6.17

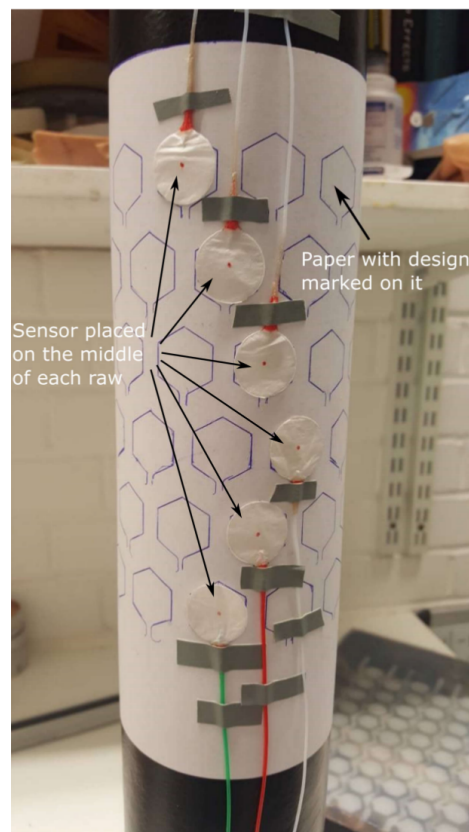


Fig. 6.15 The sensor placement on the cylinder

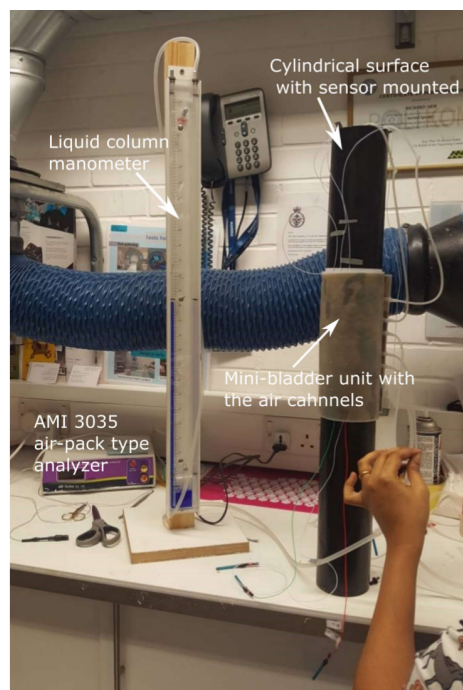


Fig. 6.16 The experimental setup to test the final prototype

Figure 6.17, depicts that the interface pressure has shown a graduation of the pressure along the vertical position of the cylinder. It can also be noted that the graduation over these six rows of mini-bladders has shown an interface pressure changing from 51 mmHg to 18 mmHg. However, these interface pressures can be adjusted by changing the mini-bladder inflation pressures of each rows and can achieve the graduation of the pressure required by the patient for the treatment.

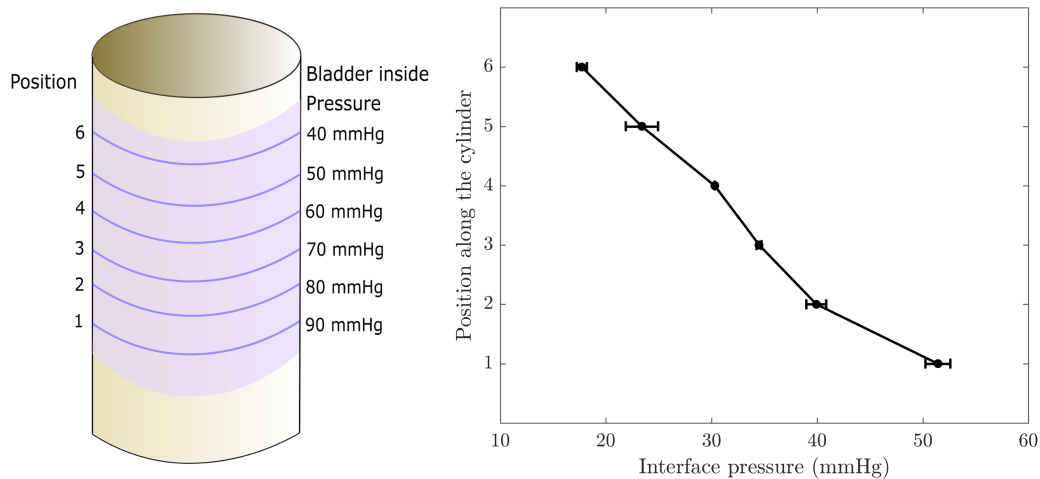


Fig. 6.17 The results of the interface pressure against the position of the cylindrical surface. The error bars show the standard error for the four different cycles the experiment was repeated.

6.5 Chapter summary

This chapter discusses the final prototype design of the active compression system with mini-bladder arrays integrated into a silicone layer. It investigated effectiveness of different arrangements of the mini-bladder arrays. The series of internally connected arrays of mini-bladders with a common air channel showed differences in pressure transmission of individual mini-bladders. Further, the use of a textile bandage with a stiff outer layer and an extensible inner layer made with elastomeric yarn, to house the mini-bladders showed a negative influence on the pressure transmission. Hence, the final prototype was designed with the mini-bladder arrays integrated within a silicone layer, where the mini-bladders can be directly in-contact with the skin. The mini-bladder arrays were arranged laterally to human limb in the final design with separate air channels to each mini-bladder. The developed prototype was able to deliver the required graduated pressure profile with uniform circumferential pressures.

Chapter 7

Summary and Conclusions

This chapter summarises the findings of the research and the conclusions that can be derived from the results. Furthermore, it suggests future research direction of this study. The conclusions and future research directions would provide an insight into design guidelines for developing a smart wearable active compression device.

7.1 Summary

Compression therapy is considered to be the most effective treatment system for the venous disease and lymphoedema by providing an external pressure to improve the venous return. The current compression therapy takes the forms of "Medical Compression Bandages" (MCB), "Graduated Compression Stockings" (GCS) and "Intermittent Pneumatic Compression" (IPC), out of which MCBs and GCSs can be considered as passive treatment systems. Both these passive treatment methods work based on the principle of generating a pressure on the skin surface by the tangential tension developed in the fabric due to its stretch. It is known that the pressure generated by MCBs and GCSs is proportional to the tension of the fabric and inversely proportional to the radius of curvature of the limb. However, the human lower limbs do not define a perfectly circular cross section hence, even if the MCBs and GCSs would provide a uniform fabric tension, the geometry of the limb will result in pressure variations due to the differences in radius of curvature. In addition, these passive treatment systems have their own disadvantages; losing their elasticity over time owing to wrong pressures, difficulty in donning and doffing of GSCs and the requirement of high skilled nursing staff to apply MCBs resulting in higher costs.

The focus of the research elucidated in this thesis was to understand how mini-bladders could be used to develop an active compression system which could overcome the limitations existed in the current treatment options, and establish the scientific knowledge base required. The research investigated the materials, which could be used to craft mini-bladders, manufacturing of the mini-bladders, empirical characterisation of mini-bladder inflation behaviour and the experimental validation of

the mathematical representation of mini-bladder inflation. In addition, the commercially available interface pressure measurement systems were evaluated and the pressure transmission characteristics of the mini-bladders were analysed. Finally, an active compression systems consisting of mini-bladder array was designed, produced and its performance was characterised.

Chapter 2 presented a review of literature on work related to the compression therapy for the treatment of venous disease and lymphoedema. None of the existing studies report on a compression system for the treatment of venous disease and lymphoedema, which could deliver a uniform circumferential pressure irrespective of the radius of curvature. The existing treatment systems include both passive and active compression systems; the most popular treatment systems (MCBs, GCSs) are considered to be passive and current IPC systems use either large single bladder cuffs or multi chamber cuffs to apply compression to the entire limb. There have been some recent attempts to develop active compression systems (Holschuh et al., 2015; Pamplin and Dennis, 2015; Pourazadi et al., 2014) using "Electro Active Polymers" (EAPs) and "Shape Memory Alloys" (SMAs). However, these existing treatment systems have failed in delivering uniform circumferential pressures. The literature review has demonstrated the importance of developing a compression system capable of creating a uniform circumferential pressure, which can be achieved using inflatable mini-bladders; the research hypothesis of the thesis. This chapter also permitted the formulation of the following research questions (RQ):

- RQ1: Formulation of conceptual design of an active compression system;
- RQ2: Investigation of materials to craft the mini-bladders and parameterise the material characteristics
- RQ3: Characterisation of the inflation behaviour of the mini-bladders
- RQ4: Development of new test rigs to study the effectiveness of the mini-bladders
- RQ5: Development of an active compression system using mini-bladders and testing on a biofidelic leg surrogate to analyse its effectiveness etc.

The chapter 3 of the thesis presents the evaluation of commercially available interface pressure measurement systems for their accuracy and reproducibility for compression therapy applications. The pressure sensors available from Microlab Electronica (PicoPress®), AMI Techno Ltd (AMI air-pack sensor), and Tekscan Inc. (FlexiForce®) were evaluated against a manometer by applying pressure using a bladder inflated by a hand operated air-pump and pressure inside the bladder was measured using the manometer. The FlexiForce® sensors have shown a higher repeatability error than specified by the manufacturer and recorded an overestimated pressure reading on average by more than 15 mmHg, which could draw wrong conclusions in the current research. Moreover, it showed a higher non-linearity error as well as significant variations within two batches that could have led to errors when measuring pressures simultaneously.

The PicoPress® sensor was found to have the lowest non-linearity and repeatability errors. However,

PicoPress® sensors have a relatively larger sensing area which was not compatible with the geometry of the mini-bladders used in the research. Hence, the 20 mm diameter AMI air-pack sensors were selected to be used as the pressure measurement system in this study, due to its geometrical compatibility with the mini-bladder size. Furthermore, the AMI air-pack sensors showed a very good linearity (non-linearity error 0.85%), a higher repeatability of the measurement (repeatability error 2.4%) and a lower hysteresis error (hysteresis error 2.4%). A lesser variation between sensors were observed with an easy to use pressure measurement processing unit. Temperature variation in air had insignificant effects on the AMI air-pack sensor readings, hence the calibration of the sensors in ambient conditions was sufficient.

In previous studies it has been proven that a large single bladder could not be used to obtain a uniform circumferential pressure profile on a cylindrical surface due to the non-uniform deformation it undergoes during inflation (Naqvi et al., 2017). Further these bladders balloon during inflation causing energy loss and also the bladder units are large. To overcome the limitations of large single bladders, an array of mini-bladders was designed and tested in the chapter 4 of this thesis. These mini-bladders were designed with only one inflatable surface; an extensible layer capable of inflating freely and an inextensible layer fashioned by reinforcing with a woven fabric to restrict extension during inflation. These mini-bladders can apply a radial force on to the contact surface when inflated and the pressure inside the mini-bladders could be measured using the back pressure. Hence, this solution would enable the creation of a uniform pressure profile over the limb circumference, with a higher pressure transmission efficiency. Furthermore, materials suitable for manufacturing the mini-bladders were investigated and a low modulus silicone was selected due to its good elastic properties, low hysteresis and the bio-compatibility. In order to characterise the hyper-elastic material properties of the silicones required for FEM modelling, uniaxial tensile tests were carried out.

The 3-D deformation profile of the mini-bladders was geometrically analysed and predicted using finite element modelling (FEM). The 3-D deformation profile of mini-bladders was experimentally studied using a special experiment rig designed to measure the inflation height of a mini-bladder on the highest point with respect to the volume of air pumped into the mini-bladders. Moreover, different geometrically shaped mini-bladders (hexagonal, circular and square) were crafted and the experimental results showed that hexagonal shaped mini-bladders provided the best pressure transmission properties. Hence the hexagonal shape mini-bladders were used in designing the final mini-bladder design. The mini-bladders were manufactured in both single and as an array of four mini-bladders in units. The results obtained from the FEM simulations were then compared with the experimentally observed data. The model showed more than 80% agreement with the experimental data over the range of 0 – 60 mmHg mini-bladder inflation pressures.

The key objective of developing an active compression system using mini-bladders is to apply the correct pressures on to the human limb. Therefore, the capability of mini-bladders to transfer pressure on to the contact surface was quantified using the interface pressure and the pressure transmission. The experiments explained in the chapter 5 were carried out in two stages; in the first stage the pressure transmission was measured on hard surfaces, and later it was extended on to a biofidelic lower leg

surrogate, which is the first of its kind developed for compression therapy according to the literature review. As explained above out of the three different geometries, hexagonal shaped mini-bladders have shown the highest pressure transmission efficiency of 70%-80% for the mini-bladder inflation pressures higher than 20 mmHg, on a cylindrical surface. Moreover, all the three geometries have shown a good linear relationship with the mini-bladder inflation pressure. During the second phase of the experiments, the surface of the lower leg surrogate was covered with artificial skin and fat layers of different Young's modulus values. The pressure propagation through the artificial skin and fat layers were evaluated. The pressure transmitted on to the surface of the leg surrogate was about 50%-70% of the mini-bladder inflation pressure. However, the pressure propagated through the fat layer was around 35%-45% of the mini-bladder inflation pressure. The results also showed that mini-bladders were able to apply a uniform circumferential interface pressure irrespective of the position of the leg; which proves the research hypothesis. This is very promising as it is not possible with the current passive compression products in the market. The mini-bladders were also able to apply uniform circumferential interface pressure in the ankle region of the biofidelic lower leg surrogate, which is difficult to achieve using the conventional MCBs and GCSs due to the significant variation of leg circumference in the ankle region. Moreover, the propagation of the pressure through the fat layers have varied with the modulus of the fat layers; the fat layer having lowest modulus recorded the highest pressure transmission percentage. In comparison to the GCS, the mini-bladders have demonstrated that they could apply the correct pressures. The evaluation of GCS showed overestimated interface pressure values with large variations.

The final design of the mini-bladder system is discussed in chapter 6, where different arrangements of the mini-bladders are considered. The series of internally connected arrays of mini-bladders with a common air channel showed differences in pressure transmission in individual mini-bladders. Moreover, the use of a textile bandage to house the mini-bladders negatively influenced the pressure transmission properties of the mini-bladders. Hence, the active compression system was designed with the mini-bladder arrays integrated within a silicone layer, where the mini-bladders can be directly in-contact with the skin. The mini-bladder arrays were arranged laterally to human limb in the final design and also to minimise pressure variations observed in the internally connected mini-bladders arrays, a separate air channels were designed for inflating the mini-bladders individually. The laboratory experiments demonstrated that the prototype developed was able to deliver the required graduated pressure profile with uniform circumferential pressures.

7.2 Conclusions

- Mini-bladders designed with only one inflatable surface have avoided the ballooning and have proven to be used in applying a uniform circumferential interface pressure irrespective of the positions of the leg.
- The mini-bladders could be used to apply a radial force on to the contact surface when inflated and the pressure inside the mini-bladders could be accurately measured using the concept of back pressure.
- The pressure transmitted on to the surface of the lower leg surrogate was around 50%-70% of the mini-bladder inflation pressure. However, the pressure propagated through the fat layer was about 35%-45% of the mini-bladder inflation pressure. Moreover, the propagation of the pressure through the fat layers varied with the modulus of the fat layers.
- In comparison to the GCS, the mini-bladders can apply correct pressures, whereas GCS always applied an overstated interface pressure with huge variations at different positions of the lower leg surrogate.
- The hexagonal shaped mini-bladders showed the highest pressure transmission efficiency for mini-bladder inflation pressures higher than 20 mmHg, on a cylindrical surface.
- The hexagonal shaped mini-bladders were selected for the final prototype design based on the pressure transmission characteristics, and its arrangement in a honeycomb structure which provides compact packing of the mini-bladders.
- The 3-D deformation profile of the mini-bladders, which was geometrically analysed and predicted using finite element modelling (FEM) had shown more than 80% agreement in the range of 0 – 60 mmHg mini-bladder inflation pressures.
- The use of a textile bandage to house the mini-bladders negatively influenced the pressure transmission properties.
- The prototype made with mini-bladder arrays integrated within a silicone layer, showed a good pressure transmission characteristics and was able to deliver the required graduated compression pressures and uniform circumferential pressures.
- AMI air-pack sensors of 20 mm diameter have outperformed the other two sensors (FlexiForce® and PicoPress®), due to their accuracy and the geometric compatibility with the mini-bladder. They had a very good accuracy (± 2.2 mmHg), with a lesser variation between different sensors and sensor batches.
- The FlexiForce® sensor was found to have shown lower accuracy in terms of higher repeatability and non-linearity errors. It overestimated pressure reading on average by more than 15 mmHg. In addition, there were significant variations between different sensors and sensor batches.

- The PicoPress[®] sensor showed a very good accuracy and the lowest non-linearity and repeatability errors. However, PicoPress[®] sensors has a larger sensing area which was not compatible with the geometry of the mini-bladders used.

7.3 Future work

The findings of the current research could lead to the following future work:

- The active compression system developed within the programme of research should be integrated with an intelligent pneumatic controller unit, to create a self-controlled, wearable, and smart compression treatment system for treating venous disease and lymphedema.
- This study should be extended to clinical trials to analyse the performance of the developed active compression system.
- This concept of mini-bladder could be used in commercially available intermittent pneumatic compression systems to improve their performance.
- The concepts of active compression using mini-bladders could be also applied in other applications such as; wound therapy, pressure controlling in anti-g suits etc.

References

- Abenhaim, L., Norgren, L. and Clement, D. (1999), 'The management of chronic venous disorders of the leg: an evidence-based report of an international task force', *Phlebology* **14**, 1–126.
- Abu-Own, A., Shami, S. K., Chittenden, S. J., Farrah, J., Scurr, J. H., Smith, P. D. C. et al. (1994), 'Microangiopathy of the skin and the effect of leg compression in patients with chronic venous insufficiency', *Journal of vascular surgery* **19**(6), 1074–1083.
- Adeel, Y. J., Muhammad, A. I. and Zeeshan, A. (2012), Characterization of hyperelastic (rubber) material using uniaxial and biaxial tension tests, in 'Advanced Materials Research', Vol. 570, Trans Tech Publ, pp. 1–7.
- Agache, P., Monneur, C., Leveque, J. and De Rigal, J. (1980), 'Mechanical properties and young's modulus of human skin in vivo', *Archives of dermatological research* **269**(3), 221–232.
- Al Khaburi, J. A. J. (2010), *Pressure mapping of medical compression bandages used for venous leg ulcer treatment*, University of Leeds.
- Aleksiejew-Kleszczyński, T. and Jagielska-Chwała, M. (2015), 'Varicose veins of lower extremities, hemodynamics and treatment methods', *Adv. Clin. Exp. Med.* **24**, 5–14.
- Alguire, P. C. and Mathes, B. M. (1997), 'Chronic venous insufficiency and venous ulceration', *Journal of general internal medicine* **12**(6), 374–383.
- Ali, A., Fouladi, M. H. and Sahari, B. (2010), 'A review of constitutive models for rubber-like materials', *American Journal of Engineering and Applied Sciences* **3**(1), 232–239.
- Allan, P., Bradbury, A., Evans, C., Lee, A., Ruckley, C. V. and Fowkes, F. (2000), 'Patterns of reflux and severity of varicose veins in the general population—edinburgh vein study', *European Journal of Vascular and Endovascular Surgery* **20**(5), 470–477.
- Allen, V., Ryan, D., Lomax, N. and Murray, A. (1993), 'Accuracy of interface pressure measurement systems', *Journal of biomedical engineering* **15**(4), 344–348.
- Almeida, J. I., Javier, J. J., Mackay, E., Bautista, C. and Proebstle, T. M. (2013), 'First human use of cyanoacrylate adhesive for treatment of saphenous vein incompetence', *Journal of Vascular Surgery: Venous and Lymphatic Disorders* **1**(2), 174–180.
- Almeida, J. I., Javier, J. J., Mackay, E. G., Bautista, C., Cher, D. J. and Proebstle, T. M. (2017), 'Thirty-sixth-month follow-up of first-in-human use of cyanoacrylate adhesive for treatment of saphenous vein incompetence', *Journal of Vascular Surgery: Venous and Lymphatic Disorders* **5**(5), 658–666.

- Almeida, J. I., Kaufman, J., Göckeritz, O., Chopra, P., Evans, M. T., Hoheim, D. F., Makhoul, R. G., Richards, T., Wenzel, C. and Raines, J. K. (2009), 'Radiofrequency endovenous closurefast versus laser ablation for the treatment of great saphenous reflux: a multicenter, single-blinded, randomized study (recovery study)', *Journal of Vascular and Interventional Radiology* **20**(6), 752–759.
- AMI-Techno (2009a), *Air-pack type contact contact surface pressure measurement system*.
- AMI-Techno (2009b), *Pressure measuring system for stockings/ bandages*.
- Annaidh, A. N., Bruyère, K., Destrade, M., Gilchrist, M. D. and Otténio, M. (2012), 'Characterization of the anisotropic mechanical properties of excised human skin', *Journal of the mechanical behavior of biomedical materials* **5**(1), 139–148.
- Anning, S. (1976), 'The historical aspects', *The Pathology and Surgery of the Veins of the Lower Limb. Edinburgh: Churchill-Livingstone* pp. 34–43.
- Armstrong, D., Caprini, J., Comerota, A., Franks, P., Harding, K., Moffat, C., Partsch, H., Phillips, T., Vanscheidt, W. and Vin, F. (2006), *Chronic Venous Insufficiency and Venous Ulceration: Aetiology and Treatment*, 1st editio edn, ConvaTec.
- Arruda, E. M. and Boyce, M. C. (1993), 'A three-dimensional constitutive model for the large stretch behavior of rubber elastic materials', *Journal of the Mechanics and Physics of Solids* **41**(2), 389–412.
- Ashruf, C. (2002), 'Thin flexible pressure sensors', *Sensor Review* **22**(4), 322–327.
- Bachoo, P. (2009), 'Interventions for uncomplicated varicose veins', *Phlebology* **24**(1_suppl), 3–12.
- Baker, S., Stacey, M., Jopp-McKay, A., Hoskin, S. and Thompson, P. (1991), 'Epidemiology of chronic venous ulcers', *British Journal of Surgery* **78**(7), 864–867.
- Barel, A., Lambrecht, R. and Clarys, P. (1998), Mechanical function of the skin: state of the art, in 'Skin Bioengineering', Vol. 26, Karger Publishers, pp. 69–83.
- Basford, J. R. (2002), 'The law of laplace and its relevance to contemporary medicine and rehabilitation', *Archives of physical medicine and rehabilitation* **83**(8), 1165–1170.
- Bauman, J. T. (2012), *Fatigue, Stress, and Strain of Rubber Components: Guide for Design Engineers*, Carl Hanser Verlag GmbH Co KG.
- Beebe-Dimmer, J. L., Pfeifer, J. R., Engle, J. S. and Schottenfeld, D. (2005), 'The epidemiology of chronic venous insufficiency and varicose veins', *Annals of epidemiology* **15**(3), 175–184.
- Bergan, J. (2007), Risk factors, manifestations, and clinical examination of the patient with primary venous insufficiency, in 'The Vein Book', Elsevier, pp. 119–124.
- Bergan, J. J., Schmid-Schönbein, G. W., Smith, P. D. C., Nicolaides, A. N., Boisseau, M. R. and Eklof, B. (2006), 'Chronic venous disease', *New England Journal of Medicine* **355**(5), 488–498.
- Bergan, J. and Pascarella, L. (2007), Venous anatomy, physiology, and pathophysiology, in 'The vein book', Elsevier, pp. 39–45.
- Berliner, E., Ozbilgin, B. and Zarin, D. A. (2003), 'A systematic review of pneumatic compression for treatment of chronic venous insufficiency and venous ulcers', *Journal of vascular surgery* **37**(3), 539–544.

- Bolton, W. (1996), *Measurement and instrumentation systems*, Butterworth-Heinemann.
- Boné Salat, C. (1999), 'Tratamiento endoluminal de las varices con laser de diodo: estudio preliminar', *Rev Patol Vasc* **5**, 35–46.
- Borges, E. L., Ferraz, A. F., Carvalho, D. V., Matos, S. S. d. and Lima, V. L. d. A. N. (2016), 'Prevention of varicose ulcer relapse: a cohort study', *Acta Paulista de Enfermagem* **29**(1), 9–16.
- Born, D.-P., Holmberg, H.-C., Goernert, F. and Sperlich, B. (2014), 'A novel compression garment with adhesive silicone stripes improves repeated sprint performance—a multi-experimental approach on the underlying mechanisms', *BMC sports science, medicine and rehabilitation* **6**(1), 21.
- Bozkurt, K., Rabe, E. and Sharkawy, M. I. (2017), 'Chronic venous insufficiency: Management and treatment: Summary of selected presentations from the chronic venous disease and haemorrhoidal disease', *EMJ Dermatol* **5**(2), 2–13.
- Bradbury, A., Evans, C., Allan, P., Lee, A., Ruckley, C. V. and Fowkes, F. (1999), 'What are the symptoms of varicose veins? edinburgh vein study cross sectional population survey', *Bmj* **318**(7180), 353–356.
- British Standards Institution (1985), *British Standard Specification for Graduated Compression*, bs 6612:19 edn, British Standards Institution, London.
- British Standards Institution (1995), *Specification for the elastic properties of flat, nonadhesive, extensible fabric bandages*, bs 7505:19 edn, British Standards Institution, London.
- Buchbinder, D., McCullough, G. M. and Melick, C. F. (1993), 'Patients evaluated for venous disease may have other pathologic conditions contributing to symptomatology', *The American journal of surgery* **166**(2), 211–215.
- Buckley, C., Prisacariu, C. and Martin, C. (2010), 'Elasticity and inelasticity of thermoplastic polyurethane elastomers: Sensitivity to chemical and physical structure', *Polymer* **51**(14), 3213–3224.
- Buis, A. and Convery, P. (1997), 'Calibration problems encountered while monitoring stump/socket interface pressures with force sensing resistors: techniques adopted to minimise inaccuracies', *Prosthetics and orthotics international* **21**(3), 179–182.
- Burke, M., Murphy, B. and Geraghty, D. (2014), Measurement of sub-bandage pressure during venous compression therapy using flexible force sensors, in 'SENSORS, 2014 IEEE', IEEE, pp. 1623–1626.
- Burnand, K. and Layer, G. (1986), 'Graduated elastic stockings.', *British medical journal (Clinical research ed.)* **293**(6541), 224–225.
- Cabrera, J., García-Olmedo, M. A. and Redondo, P. (2003), 'Treatment of venous malformations with sclerosant in microfoam form', *Archives of dermatology* **139**(11), 1409–1416.
- Caggiati, A., Bergan, J. J., Gloviczki, P., Jantet, G., Wendell-Smith, C. P., Partsch, H., on Venous Anatomical Terminology, I. I. C. C. et al. (2002), 'Nomenclature of the veins of the lower limbs: an international interdisciplinary consensus statement', *Journal of vascular surgery* **36**(2), 416–422.
- Callam, M. (1994), 'Epidemiology of varicose veins', *British journal of surgery* **81**(2), 167–173.

- Callam, M., Harper, D., Dale, J. and Ruckley, C. (1987), 'Chronic ulcer of the leg: clinical history.', *Br Med J (Clin Res Ed)* **294**(6584), 1389–1391.
- Callam, M., Ruckley, C., Dale, J. and Harper, D. (1987), 'Hazards of compression treatment of the leg: an estimate from scottish surgeons.', *British medical journal (Clinical research ed.)* **295**(6610), 1382.
- Calne, S. and Moffatt, C. (2003), 'Understanding compression therapy', *Position Document of the UK: MedicalEducation Partnership LTD* .
- Caprini, J., Partsch, H. and Simman, R. (2012), 'Venous ulcers', *Journal of the American College of Clinical Wound Specialists* **4**(3), 54–60.
- CESYS (2017), *CEBO MSA lite Tools 1.0*.
- Chandler, J. G., Pichot, O., Sessa, C., Schuller-Petrović, S., Kabnick, L. S. and Bergan, J. J. (2000), 'Treatment of primary venous insufficiency by endovenous saphenous vein obliteration', *Vascular Surgery* **34**(3), 201–214.
- Chang, C. J. and Cormier, J. N. (2013), Lymphedema interventions: exercise, surgery, and compression devices, in 'Seminars in Oncology Nursing', Vol. 29, Elsevier, pp. 28–40.
- Christensen, R. and Feng, W. (1986), 'Nonlinear analysis of the inflation of an initially flat, circular, elastic disk', *Journal of Rheology* **30**(1), 157–165.
- Clark, M. (2003), 'Compression bandages: principles and definitions', *ewma position document. Understanding compression therapy. London: Mep Ltd* pp. 5–7.
- Comerota, A. J. (2011), 'Intermittent pneumatic compression: physiologic and clinical basis to improve management of venous leg ulcers', *Journal of vascular surgery* **53**(4), 1121–1129.
- Coull, A., Tolson, D. and McIntosh, J. (2006), 'Class-3c compression bandaging for venous ulcers: comparison of spiral and figure-of-eight techniques', *Journal of advanced nursing* **54**(3), 274–283.
- Crane, J. S. and Cheshire, N. J. (2004), 'Chronic ulceration of the leg', *Surgery (Oxford)* **22**(12), 327–330.
- Crane, J. S. and Cheshire, N. J. (2008), 'Chronic ulceration of the leg', *Surgery (Oxford)* **26**(1), 13–16.
- Criqui, M. H., Denenberg, J. O., Langer, R. D., Kaplan, R. M. and Fronek, A. (2007), Epidemiology of chronic peripheral venous disease, in 'The Vein Book', Elsevier, pp. 27–37.
- Criqui, M. H., Jamosmos, M., Fronek, A., Denenberg, J. O., Langer, R. D., Bergan, J. and Golomb, B. A. (2003), 'Chronic venous disease in an ethnically diverse population: the san diego population study', *American journal of epidemiology* **158**(5), 448–456.
- Damstra, R. J., Brouwer, E. R. and Partsch, H. (2008), 'Controlled, comparative study of relation between volume changes and interface pressure under short-stretch bandages in leg lymphedema patients', *Dermatologic Surgery* **34**(6), 773–779.
- De Bruyne, P. and Dvořák, T. (1976), 'The pressure exerted by an elastic stocking and its measurement', *Medical and biological engineering* **14**(1), 94–96.
- De Buyl, F. (2001), 'Silicone sealants and structural adhesives', *International Journal of Adhesion and Adhesives* **21**(5), 411–422.

- Delis, K., Slimani, G., Hafez, H. and Nicolaides, A. (2000), 'Enhancing venous outflow in the lower limb with intermittent pneumatic compression. a comparative haemodynamic analysis on the effect of foot vs. calf vs. foot and calf compression', *European Journal of Vascular and Endovascular Surgery* **19**(3), 250–260.
- Delis, K. T., Husmann, M., Kalodiki, E., Wolfe, J. H. and Nicolaides, A. N. (2001), 'In situ hemodynamics of perforating veins in chronic venous insufficiency', *Journal of vascular surgery* **33**(4), 773–782.
- Deutsches Institut für Gütesicherung und Kennzeichnung e.V. (2008), *Medical Compression Hosiery: Quality Assurance*, ral-gz 387 edn, RAL Deutsches Institut für Gütesicherung und Kennzeichnung e.V.
- Diridollou, S., Berson, M., Vabre, V., Black, D., Karlsson, B., Auriol, F., Gregoire, J., Yvon, C., Vaillant, L., Gall, Y. et al. (1998), 'An in vivo method for measuring the mechanical properties of the skin using ultrasound', *Ultrasound in medicine & biology* **24**(2), 215–224.
- Diridollou, S., Patat, F., Gens, F., Vaillant, L., Black, D., Lagarde, J., Gall, Y. and Berson, M. (2000), 'In vivo model of the mechanical properties of the human skin under suction', *Skin Research and technology* **6**(4), 214–221.
- Dissemond, J., Assenheimer, B., Bültemann, A., Gerber, V., Gretener, S., Kohler-von Siebenthal, E., Koller, S., Kröger, K., Kurz, P., Läuchli, S. et al. (2016), 'Compression therapy in patients with venous leg ulcers', *JDDG: Journal der Deutschen Dermatologischen Gesellschaft* **14**(11), 1072–1087.
- Downie, S. P., Firmin, D. N., Wood, N. B., Thom, S. A., Hughes, A. D., Wolfe, J. N. and Xu, X. Y. (2007), 'Role of mri in investigating the effects of elastic compression stockings on the deformation of the superficial and deep veins in the lower leg', *Journal of Magnetic Resonance Imaging: An Official Journal of the International Society for Magnetic Resonance in Medicine* **26**(1), 80–85.
- Dunn, P. F. (2014), *Measurement and data analysis for engineering and science*, CRC press.
- Eberhardt, R. T. and Raffetto, J. D. (2005), 'Chronic venous insufficiency', *Circulation* **111**(18), 2398–2409.
- Eberhardt, R. T. and Raffetto, J. D. (2014), 'Chronic venous insufficiency', *Circulation* **130**(4), 333–346.
- Ebling, F., Eady, R. and Leigh, I. (1992), 'Anatomy and organization of human skin, textbook of dermatology, rh champion, jl burrington, ffg ebling, eds'.
- Edwards, J. E. and Edwards, E. A. (1940), 'The saphenous valves in varicose veins', *American heart journal* **19**(3), 338–351.
- Eklof, B. (2007), Classifying venous disorder, in 'The Vein Book', Elsevier Academic Press, San Diego, CA, pp. 111–117.
- Eklof, B., Perrin, M., Delis, K. T., Rutherford, R. B. and Gloviczki, P. (2009), 'Updated terminology of chronic venous disorders: the vein-term transatlantic interdisciplinary consensus document', *Journal of vascular surgery* **49**(2), 498–501.
- Elias, S. and Raines, J. (2012), 'Mechanochemical tumescentless endovenous ablation: final results of the initial clinical trial', *Phlebology* **27**(2), 67–72.

- Evans, C., Fowkes, F., Hajivassiliou, C., Harper, D. and Ruckley, C. (1994), 'Epidemiology of varicose veins. a review.', *International angiology: a journal of the International Union of Angiology* **13**(3), 263–270.
- Evans, C., Fowkes, F., Ruckley, C. and Lee, A. (1999), 'Prevalence of varicose veins and chronic venous insufficiency in men and women in the general population: Edinburgh vein study.', *Journal of Epidemiology & Community Health* **53**(3), 149–153.
- Falanga, V. and Eaglstein, W. (1993), 'The "trap" hypothesis of venous ulceration', *The Lancet* **341**(8851), 1006–1008.
- Falanga, V. and Eaglstein, W. H. (1986), 'A therapeutic approach to venous ulcers', *Journal of the American Academy of Dermatology* **14**(5), 777–784.
- Fan, C. M. (2005), Venous pathophysiology, in 'Seminars in interventional radiology', Vol. 22, Thieme Medical Publishers, pp. 157–161.
- Feldman, J., Stout, N., Wanchai, A., Stewart, B., Cormier, J. and Armer, J. (2012), 'Intermittent pneumatic compression therapy: a systematic review', *Lymphology* **45**(1), 13.
- Felty, C. L. and Rooke, T. W. (2005), Compression therapy for chronic venous insufficiency, in 'Seminars in vascular surgery', Vol. 18, Elsevier, pp. 36–40.
- Ferguson-Pell, M., Hagisawa, S. and Bain, D. (2000), 'Evaluation of a sensor for low interface pressure applications', *Medical engineering & physics* **22**(9), 657–663.
- Fernando, W. (2010), Manufacture of engineered compression systems using latest flat-bed knitting technology, PhD thesis, The University of Manchester.
- Finnie, A. (2000), 'Interface pressure measurements in leg ulcer management', *British journal of Nursing* **9**(Sup1), S8–S18.
- Flaud, P., Bassez, S. and COUNORD, J.-L. (2010), 'Comparative in vitro study of three interface pressure sensors used to evaluate medical compression hosiery', *Dermatologic Surgery* **36**(12), 1930–1940.
- Flour, M., Clark, M., Partsch, H., Mosti, G., Uhl, J.-F., Chauveau, M., Cros, F., Gelade, P., Bender, D., Andriessen, A. et al. (2013), 'Dogmas and controversies in compression therapy: report of an international compression club (icc) meeting, brussels, may 2011', *International wound journal* **10**(5), 516–526.
- Fowkes, F., Evans, C. and Lee, A. J. (2001), 'Prevalence and risk factors of chronic venous insufficiency', *Angiology* **52**(1_suppl), S5–S15.
- Gaied, I., Drapier, S. and Lun, B. (2006), 'Experimental assessment and analytical 2d predictions of the stocking pressures induced on a model leg by medical compressive stockings', *Journal of Biomechanics* **39**(16), 3017–3025.
- GBI-Research (2013), 'Global compression therapy market to grow significantly by 2019, with the US leading the demand', "<http://www.gbiresearch.com/media-center/press-releases/global-compression-therapy-market-to-grow-significantly-by-2019-with-the-us-leading-the-demand>". [Online; accessed 11-July-2018].
- Geerligs, M. (2006), A literature review of the mechanical behavior of the stratum corneum, the living epidermis and the subcutaneous fat tissue, Technical report, Philips Research.

- Ghosh, S., Mukhopadhyay, A., Sikka, M. and Nagla, K. (2008), 'Pressure mapping and performance of the compression bandage/garment for venous leg ulcer treatment', *Journal of Tissue Viability* **17**(3), 82–94.
- Goldman, M. P. and Weiss, R. A. (2016), *Sclerotherapy E-book: Treatment of Varicose and Telangiectatic Leg Veins*, Elsevier Health Sciences.
- Goldman, M. P., Weiss, R. A. and Bergan, J. J. (1999), *Varicose veins and telangiectasias: diagnosis and treatment*, Quality Medical Pub.
- Goode, S., Chowdhury, A., Crockett, M., Beech, A., Simpson, R., Richards, T. and Braithwaite, B. (2010), 'Laser and radiofrequency ablation study (lara study): a randomised study comparing radiofrequency ablation and endovenous laser ablation (810 nm)', *European Journal of Vascular and Endovascular Surgery* **40**(2), 246–253.
- Groves, R. (2012), Quantifying the mechanical properties of skin in vivo and ex vivo to optimise microneedle device design, PhD thesis, Cardiff University.
- Guest, J. F., Ayoub, N., McIlwraith, T., Uchegbu, I., Gerrish, A., Weidlich, D., Vowden, K. and Vowden, P. (2017), 'Health economic burden that different wound types impose on the uk's national health service', *International wound journal* **14**(2), 322–330.
- Guest, J. F., Fuller, G. W. and Vowden, P. (2018), 'Venous leg ulcer management in clinical practice in the uk: costs and outcomes', *International wound journal* **15**(1), 29–37.
- Guo, Z. (2006), Computational modelling of rubber-like materials under monotonic and cyclic loading, PhD thesis, Delft University of Technology.
- Hamdan, A. (2012), 'Management of varicose veins and venous insufficiency', *Jama* **308**(24), 2612–2621.
- Hartmann, S. (2001), 'Numerical studies on the identification of the material parameters of rivlin's hyperelasticity using tension-torsion tests', *Acta Mechanica* **148**(1), 129–155.
- Heller, J. A. and Evans, N. S. (2015), 'Varicose veins', *Vascular Medicine* **20**(1), 88–90. PMID: 25722421.
- Hendriks, F. M. (2001), Mechanical behaviour of human skin in vivo - a literature review, in 'Nat.Lab. Unclassified Report 820. Philips Research Laboratories'.
- Holschuh, B. T., Newman, D. J., Obropta, E. W. et al. (2015), 'Controllable compression garments using shape memory alloys and associated techniques and structures'. US Patent App. 14/482,365.
- Holzapfel, G. A. et al. (2001), 'Biomechanics of soft tissue', *The handbook of materials behavior models* **3**, 1049–1063.
- ISO, B. (2011), '37: 2011 rubber, vulcanized or thermoplastic—determination of tensile stress-strain properties', *British Standards Institution: London, UK*.
- Iwama, H., Suzuki, M., Hojo, M., Kaneda, M. and Akutsu, I. (2000), 'Intermittent pneumatic compression on the calf improves peripheral circulation of the leg', *Journal of critical care* **15**(1), 18–21.
- Jacquemoud, C., Bruyere-Garnier, K. and Coret, M. (2007), 'Methodology to determine failure characteristics of planar soft tissues using a dynamic tensile test', *Journal of biomechanics* **40**(2), 468–475.

- Jakel, R. (2010), 'Analysis of hyperelastic materials with mechanica-theory and application examples'.
- John, G. W., Narracott, A. J., Morris, R. J., Woodcock, J. P., Lawford, P. V. and Hose, D. R. (2007), Influence of intermittent compression cuff design on interface pressure and calf deformation: experimental results, *in* 'Engineering in Medicine and Biology Society, 2007. EMBS 2007. 29th Annual International Conference of the IEEE', IEEE, pp. 2122–2125.
- Johnson, S. (2002), 'Compression hosiery in the prevention and treatment of venous leg ulcers', *Journal of tissue viability* **12**(2), 67–74.
- Kachlik, D., Pechacek, V., Musil, V. and Baca, V. (2012), 'The deep venous system of the lower extremity: new nomenclature', *Phlebology* **27**(2), 48–58.
- Kalra, A., Lowe, A. and Al-Jumaily, A. (2016), 'Mechanical behaviour of skin: a review', *J Mater Sci Eng* **5**(4), 254–260.
- Kaplan, R. M., Criqui, M. H., Denenberg, J. O., Bergan, J. and Fronek, A. (2003), 'Quality of life in patients with chronic venous disease: San diego population study', *Journal of vascular surgery* **37**(5), 1047–1053.
- Karadi, R. L., Gow, D., Kellett, M., Denning, D. W. and O'Driscoll, R. B. (2011), 'Itraconazole associated quadriparesis and edema: a case report', *Journal of medical case reports* **5**(1), 140.
- Khatyr, F., Imberdis, C., Vescovo, P., Varchon, D. and Lagarde, J.-M. (2004), 'Model of the viscoelastic behaviour of skin in vivo and study of anisotropy', *Skin research and technology* **10**(2), 96–103.
- Kim, B., Lee, S. B., Lee, J., Cho, S., Park, H., Yeom, S. and Park, S. H. (2012), 'A comparison among neo-hookean model, mooney-rivlin model, and ogden model for chloroprene rubber', *International Journal of Precision Engineering and Manufacturing* **13**(5), 759–764.
- Kirsner, R. S. and Eaglstein, W. H. (1993), 'The wound healing process', *Dermatologic clinics* **11**(4), 629–640.
- Kolari, P. J., Peknamäki, K. and Pohjola, R. T. (1988), 'Transcutaneous oxygen tension in patients with post-thrombotic leg ulcers: treatment with intermittent pneumatic compression', *Cardiovascular research* **22**(2), 138–141.
- Komi, E. R., Roberts, J. R. and Rothberg, S. (2007), 'Evaluation of thin, flexible sensors for time-resolved grip force measurement', *Proceedings of the Institution of Mechanical Engineers, Part C: Journal of Mechanical Engineering Science* **221**(12), 1687–1699.
- Korochkina, T., Claypole, T. and Gethin, D. (2005), Choosing constitutive models for elastomers used in printing processes, *in* 'CONSTITUTIVE MODELS FOR RUBBER-PROCEEDINGS-', Vol. 4, Balkema, p. 431.
- Kosiak, M. (1959), 'Etiology and pathology of ischemic ulcers', *Arch. Phys. Med. Rehabil.* **40**, 62–69.
- Kouka, N., Nass, L. and Feist, W. (2004), 'Pharmacological and non-pharmacological management methods of dvt and pulmonary embolism', *Compression Ther. Concepts* p. 4.
- Kumar, N. and Rao, V. V. (2016), 'Hyperelastic mooney-rivlin model: Determination and physical interpretation of material constants', *Parameters* **2**(10), 01.

- Kumar, S., Samraj, K., Nirujogi, V., Budnik, J. and Walker, M. A. (2002), 'Intermittent pneumatic compression as an adjuvant therapy in venous ulcer disease', *Journal of tissue viability* **12**(2), 42–50.
- Kunimoto, B. T. (1999), 'Compression therapy: theory and practice', *Dermatologic Therapy* **9**, 63–68.
- Kurz, X., Kahn, S., Abenhaim, L., Clement, D. et al. (1999), 'Chronic venous disorders of the leg: Epidemiology, outcomes, diagnosis and management: Summary of an evidence-based report on the veines task force', *International Angiology* **18**(2), 83.
- Kurz, X., Lamping, D. L., Kahn, S. R., Baccaglini, U., Zuccarelli, F., Spreafico, G., Abenhaim, L., Group, V. S. et al. (2001), 'Do varicose veins affect quality of life? results of an international population-based study', *Journal of vascular surgery* **34**(4), 641–648.
- Lai, C. H. and Li-Tsang, C. W. (2009), 'Validation of the pliance x system in measuring interface pressure generated by pressure garment', *burns* **35**(6), 845–851.
- Laksari, K., Shafieian, M. and Darvish, K. (2012), 'Constitutive model for brain tissue under finite compression', *Journal of biomechanics* **45**(4), 642–646.
- Langer, R. D., Ho, E., Denenberg, J. O., Fronek, A., Allison, M. and Criqui, M. H. (2005), 'Relationships between symptoms and venous disease: the san diego population study', *Archives of internal medicine* **165**(12), 1420–1424.
- Lao, S. B. (2016), Wearable tactile pressure sensing for compression garments and control of active compression devices, Master's thesis, University of Waterloo.
- Latz, C. A., Brown, K. R. and Bush, R. L. (2015), 'Compression therapies for chronic venous leg ulcers: interventions and adherence', *Chronic Wound Care Management and Research* **2**, 11.
- Lebosse, C., Bayle, B., de Mathelin, M. and Renaud, P. (2008), Nonlinear modeling of low cost force sensors, in 'Robotics and Automation, 2008. ICRA 2008. IEEE International Conference on', IEEE, pp. 3437–3442.
- Lemaitre, J. (2001), *Handbook of Materials Behavior Models, Three-Volume Set: Nonlinear Models and Properties*, Elsevier.
- Lim, C. S. and Davies, A. H. (2014), 'Graduated compression stockings', *Canadian Medical Association Journal* **186**(10), E391–E398.
- Lin, S. (2016), Studies on bending, folding and buckling of soft materials, PhD thesis, RMIT University.
- Liu, R., Guo, X., Lao, T. T. and Little, T. (2017), 'A critical review on compression textiles for compression therapy: Textile-based compression interventions for chronic venous insufficiency', *Textile Research Journal* **87**(9), 1121–1141.
- Liu, R., Kwok, Y. L., Li, Y., Lao, T. T. and Zhang, X. (2007), 'Skin pressure profiles and variations with body postural changes beneath medical elastic compression stockings', *International journal of dermatology* **46**(5), 514–523.
- Liu, R., Kwok, Y. L., Li, Y., Lao, T. T., Zhang, X. and Dai, X. Q. (2005), 'Objective evaluation of skin pressure distribution of graduated elastic compression stockings', *Dermatologic Surgery* **31**(6), 615–624.

- Lord, R. S. and Hamilton, D. (2004), 'Graduated compression stockings (20- 30 mmhg) do not compress leg veins in the standing position', *ANZ journal of surgery* **74**(7), 581–585.
- Macintyre, L. (2007), 'Designing pressure garments capable of exerting specific pressures on limbs', *Burns* **33**(5), 579–586.
- Macintyre, L. (2011), 'New calibration method for i-scan sensors to enable the precise measurement of pressures delivered by 'pressure garments'', *Burns* **37**(7), 1174–1181.
- Macintyre, L., Baird, M. and Weedall, P. (2004), 'The study of pressure delivery for hypertrophic scar treatment', *International Journal of Clothing Science and Technology* **16**(1/2), 173–183.
- Magnusson, M., Nelzen, O., Risberg, B. and Sivertsson, R. (2001), 'A colour doppler ultrasound study of venous reflux in patients with chronic leg ulcers', *European Journal of Vascular and Endovascular Surgery* **21**(4), 353–360.
- Manan, N. F. A., Noor, S. N. A. M., Azmi, N. N. and Mahmud, J. (2015), 'Numerical investigation of ogden and mooney-rivlin material parameters', *ARPN Journal of Engineering and Applied Sciences* **10**(15), 6329–6335.
- Mani, R., Vowden, K. and Nelson, E. (2001), 'Intermittent pneumatic compression for treating venous leg ulcers.', *The Cochrane database of systematic reviews* (4), CD001899–CD001899.
- Mann, R., Yeong, E., Moore, M. and Engrav, L. (1997), 'A new tool to measure pressure under burn garments', *The Journal of burn care & rehabilitation* **18**(2), 160–163.
- Mariani, F. (2009), 'Compression. consensus document based on scientific evidence and clinical experiences', *Minerva Medica (Torino)* .
- Marieb, E. N. and Hoehn, K. (2007), *Human anatomy & physiology*, Pearson Education.
- Martelli, M. F. and Dusi, A. (1999), 'Implementation and validation of hyperelastic finite element models of high damping rubber bearings', *Constitutive Models for Rubber* **1**, 237.
- McGeown, J., McHale, N. and Thornbury, K. (1988), 'Effects of varying patterns of external compression on lymph flow in the hindlimb of the anaesthetized sheep.', *The Journal of physiology* **397**(1), 449–457.
- McGuckin, M., Waterman, R., Brooks, J., Cherry, G., Porten, L., Hurley, S. and Kerstein, M. D. (2002), 'Validation of venous leg ulcer guidelines in the united states and united kingdom', *The American journal of surgery* **183**(2), 132–137.
- McLaren, J., Helmer, R., Horne, S. and Blanchonette, I. (2010), 'Preliminary development of a wearable device for dynamic pressure measurement in garments', *Procedia Engineering* **2**(2), 3041–3046.
- Meissner, M. H. (2005), Lower extremity venous anatomy, in 'Seminars in interventional radiology', Vol. 22, Thieme Medical Publishers, p. 147.
- Meissner, M. H., Moneta, G., Burnand, K., Głowiczki, P., Lohr, J. M., Lurie, F., Mattos, M. A., McLafferty, R. B., Mozes, G., Rutherford, R. B. et al. (2007), 'The hemodynamics and diagnosis of venous disease', *Journal of vascular surgery* **46**(6), S4–S24.

- Michaels, J., Campbell, W., Brazier, J., Macintyre, J., Palfreyman, S., Ratcliffe, J. and Rigby, K. (2006), 'Randomised clinical trial, observational study and assessment of cost-effectiveness of the treatment of varicose veins (reactiv trial)'.
- Microlab-Electronica (2014), 'Picopress'.
URL: <http://www.microlabitalia.it/index.php?lang=en>
- Miller, K. (2004), 'Testing elastomers for finite element analysis', *Axel Products*.
- Moffatt, C. (2005), 'Four-layer bandaging: from concept to practice part 2: Application of the four-layer system', *World Wide Wounds* pp. 1–10.
- Moffatt, C. (2007), *Compression Therapy in Practice*, Vol. 1, Wound UK Publishing,.
- Moffatt, C. (2008), 'Variability of pressure provided by sustained compression', *International wound journal* **5**(2), 259–265.
- Mooney, M. (1940), 'A theory of large elastic deformation', *Journal of applied physics* **11**(9), 582–592.
- Moore, K. L., Dalley, A. F. and Agur, A. M. (2013), *Clinically oriented anatomy*, Lippincott Williams & Wilkins.
- Morris, R. J. (2008), 'Intermittent pneumatic compression—systems and applications', *Journal of medical engineering & technology* **32**(3), 179–188.
- Mosti, G. (2014), 'Compression in leg ulcer treatment: inelastic compression', *Phlebology* **29**(1_suppl), 146–152.
- Mosti, G., Iabichella, M. L. and Partsch, H. (2012), 'Compression therapy in mixed ulcers increases venous output and arterial perfusion', *Journal of vascular surgery* **55**(1), 122–128.
- Mosti, G. and Mattaliano, V. (2007), 'Simultaneous changes of leg circumference and interface pressure under different compression bandages', *European journal of vascular and endovascular surgery* **33**(4), 476–482.
- Mosti, G. and Rossari, S. (2008), 'The importance of measuring sub bandage pressure and presentation of new measuring device', *Acta Vulnol* **6**, 31–36.
- Motykie, G., Caprini, J., Arcelus, J., Reyna, J., Overom, E. and Mokhtee, D. (1999), 'Evaluation of therapeutic compression stockings in the treatment of chronic venous insufficiency', *Dermatologic surgery* **25**(2), 116–120.
- Mozes, G. and Gloviczki, P. (2007), Venous embryology and anatomy, in 'The Vein Book', Elsevier, pp. 15–25.
- Mulder, G., Robison, J. and Seeley, J. (1990), 'Study of sequential compression therapy in the treatment of non-healing chronic venous ulcers', *Wounds* **2**(3), 111–115.
- Naqvi, S., Husain, M. D., Potluri, P., Mandal, P. and Lewis, P. (2017), 'Pressure distribution under different types of blood pressure measurement cuffs', *Journal of Industrial Textiles* **47**(1), 89–103.
- Naqvi, S., Potluri, P., Mandal, P. and Lewis, P. (2018), 'Effect of different cuff types on blood pressure measurement: Variation in bp values for different cuff types', *Journal of Industrial Textiles* **47**(7), 1478–1495.

- Nelson, E. A. (2001), A study of patient and nurse factors influencing sub-bandage pressure, PhD thesis, University of Strathclyde.
- Ng, F. S.-F. (1995), 'Design of pressure garments for hypertrophic scar treatment.'
- Nicolaides, A. (2000), 'Investigation of chronic venous insufficiency: a consensus statement', *Circulation* **102**(20), e126–e163.
- Nicolaides, A., Kakkos, S., Eklof, B., Perrin, M., Nelzen, O., Neglen, P., Partsch, H. and Rybak, Z. (2014), 'Management of chronic venous disorders of the lower limbs-guidelines according to scientific evidence.', *International angiology: a journal of the International Union of Angiology* **33**(2), 87–208.
- Ogden, R. (1972), Large deformation isotropic elasticity-on the correlation of theory and experiment for incompressible rubberlike solids, in 'Proceedings of the Royal Society of London A: Mathematical, Physical and Engineering Sciences', Vol. 326, The Royal Society, pp. 565–584.
- O'Meara, S., Cullum, N., Nelson, E. A. and Dumville, J. C. (2012), 'Compression for venous leg ulcers', *Cochrane Database of Systematic Review* (11).
- O'Meara, S., Cullum, N. A., Nelson, E. A. et al. (2009), 'Compression for venous leg ulcers', *Cochrane Database Syst Rev* **1**(2), 50.
- O'Meara, S., Tierney, J., Cullum, N., Bland, J. M., Franks, P. J., Mole, T. and Scriven, M. (2009), 'Four layer bandage compared with short stretch bandage for venous leg ulcers: systematic review and meta-analysis of randomised controlled trials with data from individual patients', *Bmj* **338**, b1344.
- Pailler-Mattei, C., Bec, S. and Zahouani, H. (2008), 'In vivo measurements of the elastic mechanical properties of human skin by indentation tests', *Medical engineering & physics* **30**(5), 599–606.
- Palfreyman, S. and Michaels, J. (2009), 'A systematic review of compression hosiery for uncomplicated varicose veins', *Phlebology* **24**(1_suppl), 13–33.
- Pamplin, J. C. and Dennis, R. G. (2015), 'Method for building a dynamic compression garment'. US Patent 9,161,878.
- Partsch, B. and Partsch, H. (2005), 'Calf compression pressure required to achieve venous closure from supine to standing positions', *Journal of vascular surgery* **42**(4), 734–738.
- Partsch, H. (1991), 'Compression therapy of the legs: a review', *The Journal of dermatologic surgery and oncology* **17**(10), 799–805.
- Partsch, H. (2003), 'Understanding the pathophysiological effects of compression', *ewma position document. Understanding compression therapy. London: Mep Ltd* pp. 2–4.
- Partsch, H. (2005), 'The static stiffness index: a simple method to assess the elastic property of compression material in vivo', *Dermatologic surgery* **31**(6), 625–630.
- Partsch, H. (2006), 'Do we still need compression bandages? haemodynamic effects of compression stockings and bandages', *Phlebology* **21**(3), 132–138.
- Partsch, H. (2007), Mechanism and effects of compression therapy, in 'The vein book', Elsevier Academic Press, San Diego, CA, pp. 103–109.

- Partsch, H. (2014), 'Compression for the management of venous leg ulcers: which material do we have?', *Phlebology* **29**(1_suppl), 140–145.
- Partsch, H., Clark, M., Bassez, S., BENIGNI, J.-P., Becker, F., Blazek, V., Caprini, J., CORNU-THÉNARD, A., Hafner, J., Flour, M. et al. (2006), 'Measurement of lower leg compression in vivo: recommendations for the performance of measurements of interface pressure and stiffness', *Dermatologic Surgery* **32**(2), 224–233.
- Partsch, H., Clark, M., Mosti, G., Steinlechner, E., Schuren, J., Abel, M., BENIGNI, J.-P., COLERIDGE-SMITH, P., CORNU-THÉNARD, A., Flour, M. et al. (2008), 'Classification of compression bandages: practical aspects', *Dermatologic surgery* **34**(5), 600–609.
- Partsch, H., Mosti, G. and Uhl, J.-F. (2012), 'Unexpected venous diameter reduction by compression stocking of deep, but not of superficial veins', *Veins and Lymphatics* **1**(1), 3.
- Partsch, H., Rabe, E. and Stemmer, R. (2000), *Compression therapy of the extremities*, Éd. phlébologiques françaises.
- Pekanmäki, K., Kolari, P. and Kiistala, U. (1987), 'Intermittent pneumatic compression treatment for post-thrombotic leg ulcers', *Clinical and experimental dermatology* **12**(5), 350–353.
- Penava, Ž., Šimić-Penava, D. and Knezic, Ž. (2014), 'Determination of the elastic constants of plain woven fabrics by a tensile test in various directions', *Fibres & Textiles in Eastern Europe*.
- Piazza, G. (2014), 'Varicose veins', *Circulation* **130**(7), 582–587.
- Polliack, A., Sieh, R., Craig, D., Landsberger, S., McNeil, D. and Ayyappa, E. (2000), 'Scientific validation of two commercial pressure sensor systems for prosthetic socket fit', *Prosthetics and orthotics international* **24**(1), 63–73.
- Polygerinos, P., Lyne, S., Wang, Z., Nicolini, L. F., Mosadegh, B., Whitesides, G. M. and Walsh, C. J. (2013), Towards a soft pneumatic glove for hand rehabilitation, in '2013 IEEE/RSJ International Conference on Intelligent Robots and Systems', IEEE, pp. 1512–1517.
- Porter, J. M., Moneta, G. L. et al. (1995), 'Reporting standards in venous disease: an update', *Journal of Vascular Surgery* **21**(4), 635–645.
- Pourazadi, S., Ahmadi, S. and Menon, C. (2014), 'Towards the development of active compression bandages using dielectric elastomer actuators', *Smart Materials and Structures* **23**(6), 065007.
- Qin, Y. (2015), *Medical textile materials*, Woodhead Publishing.
- Rackl, M. (2015), Curve fitting for ogden, yeoh and polynomial models, in 'ScilabTEC, conference (Regensburg)'.
- Raju, S., Hollis, K. and Neglen, P. (2007), 'Use of compression stockings in chronic venous disease: patient compliance and efficacy', *Annals of vascular surgery* **21**(6), 790–795.
- Ramelet, A.-A. (2002), 'Compression therapy', *Dermatologic Surgery* **28**(1), 6–10.
- Rasmussen, L., Lawaetz, M., Serup, J., Bjoern, L., Vennits, B., Blemings, A. and Eklof, B. (2013), 'Randomized clinical trial comparing endovenous laser ablation, radiofrequency ablation, foam sclerotherapy, and surgical stripping for great saphenous varicose veins with 3-year follow-up', *Journal of Vascular Surgery: Venous and Lymphatic Disorders* **1**(4), 349–356.

- Renaud, C., Cros, J.-M., Feng, Z.-Q. and Yang, B. (2009), 'The yeoh model applied to the modeling of large deformation contact/impact problems', *International Journal of Impact Engineering* **36**(5), 659–666.
- Ricci, S. (2011), Chapter 1 - anatomy, in M. P. Goldman, J.-J. Guex and R. A. Weiss, eds, 'Sclerotherapy (Fifth Edition)', fifth edition edn, W.B. Saunders, Edinburgh, pp. 1 – 24.
URL: <http://www.sciencedirect.com/science/article/pii/B9780323073677000078>
- Richmand, D. M., O'Donnell, T. F. and Zelikovski, A. (1985), 'Sequential pneumatic compression for lymphedema: a controlled trial', *Archives of Surgery* **120**(10), 1116–1119.
- Rikli, D. A., Honigmann, P., Babst, R., Cristalli, A., Morlock, M. M. and Mittlmeier, T. (2007), 'Intra-articular pressure measurement in the radioulnocarpal joint using a novel sensor: in vitro and in vivo results', *The Journal of hand surgery* **32**(1), 67–75.
- Rivlin, R. (1948), 'Large elastic deformations of isotropic materials. iv. further developments of the general theory', *Philosophical Transactions of the Royal Society of London A: Mathematical, Physical and Engineering Sciences* **241**(835), 379–397.
- Rivlin, R. (1956), 'Stress-relaxation in incompressible elastic materials at constant deformation', *Quarterly of applied mathematics* **14**(1), 83–89.
- Rivlin, R. S. and Saunders, D. (1951), 'Large elastic deformations of isotropic materials. vii. experiments on the deformation of rubber', *Philosophical Transactions of the Royal Society of London A: Mathematical, Physical and Engineering Sciences* **243**(865), 251–288.
- Rose, S. and Ahmed, A. (1986), 'Some thoughts on the aetiology of varicose veins.', *The Journal of cardiovascular surgery* **27**(5), 534–543.
- Ruckley, C. (1992), 'Treatment of venous ulceration-compression therapy', *Phlebology* **7**, 22–26.
- Ruckley, C. V., Evans, C. J., Allan, P. L., Lee, A. J. and Fowkes, F. G. R. (2002), 'Chronic venous insufficiency: clinical and duplex correlations. the edinburgh vein study of venous disorders in the general population', *Journal of vascular surgery* **36**(3), 520–525.
- Sands, W. A. (2014), 'Dynamic compression for recovery in athletes', *Lower Extremity Review Magazine* .
- Sands, W. A., McNeal, J. R., Murray, S. R. and Stone, M. H. (2015), 'Dynamic compression enhances pressure-to-pain threshold in elite athlete recovery: exploratory study', *The Journal of Strength & Conditioning Research* **29**(5), 1263–1272.
- Santler, B. and Goerge, T. (2017), 'Chronic venous insufficiency—a review of pathophysiology, diagnosis, and treatment', *JDDG: Journal der Deutschen Dermatologischen Gesellschaft* **15**(5), 538–556.
- Schomburg, W. K. (2015), Introduction, in 'Introduction to Microsystem Design', Springer, pp. 1–2.
- Scott, T. E., LaMorte, W. W., Gorin, D. R. and Menzoian, J. O. (1995), 'Risk factors for chronic venous insufficiency: a dual case-control study', *Journal of vascular surgery* **22**(5), 622–628.
- Selvadurai, A. (2006), 'Deflections of a rubber membrane', *Journal of the Mechanics and Physics of Solids* **54**(6), 1093–1119.
- Shah, T. M. (2001), 'Dip molding of polyurethane and silicone for latex-free, nonallergenic products', *Medical device and diagnostic Industry* **23**(4), 75–75.

- Shahzad, M., Kamran, A., Siddiqui, M. Z. and Farhan, M. (2015), 'Mechanical characterization and fe modelling of a hyperelastic material', *Materials Research* **18**(5), 918–924.
- Shami, S., Sarin, S. and Scurr, J. (1997), 'Chronic venous insufficiency disease', *International Journal of Angiology* **6**(01), 30–48.
- Shami, S., Shields, D., Scurr, J. and Smith, P. (1992), 'Leg ulceration in venous disease.', *Postgraduate medical journal* **68**(804), 779–785.
- Shanks, R. A. and Kong, I. (2013), General purpose elastomers: structure, chemistry, physics and performance, in 'Advances in Elastomers I', Springer, pp. 11–45.
- Sharmin, E. and Zafar, F. (2012), Polyurethane: an introduction, in 'Polyurethane', InTech.
- Shingler, S., Robertson, L., Boghossian, S. and Stewart, M. (2013), 'Compression stockings for the initial treatment of varicose veins in patients without venous ulceration.', *The Cochrane database of systematic reviews* (12), CD008819–CD008819.
- Stacey, M., Jopp-Mckay, A., Rashid, P., Hoskin, S. and Thompson, P. (1997), 'The influence of dressings on venous ulcer healing—a randomised trial', *European journal of vascular and endovascular surgery* **13**(2), 174–179.
- Standring, S. and Wigley, C. (2005), 'Functional anatomy of the musculoskeletal system', *Gray's Anatomy The Anatomical Basis of Clinical Practice. 39th ed. Elsevier Churchill Livingstone* pp. 83–136.
- Stemmer, R., Marescaux, J. and Furderer, C. (1980), 'Compression therapy of the lower extremities particularly with compression stockings', *Der Hautarzt; Zeitschrift fur Dermatologie, Venerologie, und verwandte Gebiete* **31**(7), 355–365.
- Stolz, C. and Bourgeois, M. (2005), A constitutive model for the fatigue life prediction of rubber i. raoult, in 'Constitutive Models for Rubber IV: Proceedings of the fourth European Conference on Constitutive Models for Rubber, ECCMR 2005, Stockholm, Sweden, 27-29 June 2005', CRC Press, p. 129.
- Stuart, W. P., Adam, D. J., Allan, P. L., Ruckley, C. V. and Bradbury, A. W. (2000), 'The relationship between the number, competence, and diameter of medial calf perforating veins and the clinical status in healthy subjects and patients with lower-limb venous disease', *Journal of vascular surgery* **32**(1), 138–143.
- Sujendra, H., Jayaram, A., Chandan, R. and Hattaraki, G. (2018), 'Finite element modelling and simulation of rubber component in predicting hyperelastic material model', *International Research Journal of Engineering and Technology* **5**(10), 751–754.
- TBL-Plastics (2018), <https://www.tblplastics.com/platinum-vs-peroxide-silicone-tubing/>. Accessed: 2019-07-12.
- Tekscan® (2016), FlexiForce™ Standard model A201, Technical report.
- Tekscan®. (2017), Flexiforce™ standard sensors, Technical report.
- Tekscan® (2018), FlexiForce™ Standard model A201, Technical report.
- Thomas, S. (1990), 'Bandages and bandaging: the science behind the art', *Care Sci Pr.* **8**(2), 50–60.

- Thomas, S. (1997), 'Compression bandaging in the treatment of venous leg ulcers', *World Wide Wounds* .
- Thomas, S. (2003), 'The use of the laplace equation in the calculation of sub-bandage pressure', *EWMA J* **3**(1), 21–3.
- Thomas, S. and Fram, P. (1990), 'Bandages and bandaging: the science behind the art', *Care Sci Pr* **8**(2), 50–60.
- Thomas, S. and Fram, P. (2003), 'Laboratory-based evaluation of a compression-bandaging system', *Nursing times* **99**(40), 24–28.
- Tilak, D., William, C., Fernando, A., Jayawarna, D. and Chaudhury, N. H. (2006), 'Pressure Garment'.
- Tyler, D. (2015), Application of pressure sensors in monitoring pressure, in 'Materials and Technology for Sportswear and Performance Apparel', CRC Press, pp. 300–321.
- Vahapoglu, V., Karadeniz, S. and Yazici, I. (2011), 'Uniaxial tensile testing of rubber-like materials', *Experimental techniques* **35**(1), 17–23.
- Valencia, I. C., Falabella, A., Kirsner, R. S. and Eaglstein, W. H. (2001), 'Chronic venous insufficiency and venous leg ulceration', *Journal of the American Academy of Dermatology* **44**(3), 401–424.
- van Gent, W. B., Wilschut, E. D. and Wittens, C. (2010), 'Management of venous ulcer disease', *BMJ* **341**(7782), 1092–6.
- Van Langenhove, L. (2007), *Smart textiles for medicine and healthcare: materials, systems and applications*, Woodhead Publishing Series in Textiles, Woodhead Publishing.
- Vecchi, F., Freschi, C., Micera, S., Sabatini, A. M., Dario, P., Sacchetti, R. et al. (2000), Experimental evaluation of two commercial force sensors for applications in biomechanics and motor control, in '5th Ann. Conf. of Int. FES'.
- Visakh, P., Thomas, S., Chandra, A. K. and Mathew, A. P. (2013), 'Advances in elastomers', *Springer*2013 .
- Vogel, H. (1987), 'Age dependence of mechanical and biochemical properties of human skin. i: Stress-strain experiments, skin thickness and biochemical analysis', *Bioengineering and the skin* **3**(1), 67–91.
- Wang, Y. M., Cheng, L. F. and Li, N. (2006), 'Histopathological study of vascular changes after intra-arterial and intravenous injection of n-butyl-2-cyanoacrylate', *Chinese journal of digestive diseases* **7**(3), 175–179.
- Wertheim, D., Melhuish, J., Williams, R. and Harding, K. (1999), 'Measurement of forces associated with compression therapy', *Medical & biological engineering & computing* **37**(1), 31–34.
- Wildin, C., Hui, A., Esler, C. and Gregg, P. (1998), 'In vivo pressure profiles of thigh-length graduated compression stockings', *British journal of surgery* **85**(9), 1228–1231.
- Wilson, D., Apreleva, M. V., Eichler, M. J. and Harrold, F. R. (2003), 'Accuracy and repeatability of a pressure measurement system in the patellofemoral joint', *Journal of biomechanics* **36**(12), 1909–1915.

- Woodburn, J. and Helliwell, P. (1996), 'Observations on the f-scan in-shoe pressure measuring system', *Clinical Biomechanics* **11**(5), 301–304.
- Xu, Q., Pang, M., Zhu, L., Zhang, Y. and Feng, S. (2010), 'Mechanical properties of silicone rubber composed of diverse vinyl content silicone gums blending', *Materials & Design* **31**(9), 4083–4087.
- Xu, Y., Tan, C. Y. L., Wang, W. P. and Tay, E. H. (2003), 'Simulation of large membrane deformation in an electrochemical actuator', *International Journal of Computational Engineering Science* **4**(02), 205–210.
- Yamamoto, N., Unno, N., Mitsuoka, H., Saito, T., Miki, K., Ishimaru, K., Kaneko, H. and Nakamura, S. (2002), 'Preoperative and intraoperative evaluation of diameter-reflux relationship of calf perforating veins in patients with primary varicose vein', *Journal of vascular surgery* **36**(6), 1225–1230.
- Yeoh, O. (1993), 'Some forms of the strain energy function for rubber', *Rubber Chemistry and technology* **66**(5), 754–771.
- Youn, Y. J. and Lee, J. (2019), 'Chronic venous insufficiency and varicose veins of the lower extremities', *The Korean journal of internal medicine* **34**(2), 269.
- Zafar, F. and Sharmin, E. (2012), *Polyurethane*, BoD–Books on Demand.
- Zahouani, H., Pailler-Mattei, C., Sohm, B., Vargiolu, R., Cenizo, V. and Debret, R. (2009), 'Characterization of the mechanical properties of a dermal equivalent compared with human skin in vivo by indentation and static friction tests', *Skin research and technology* **15**(1), 68–76.
- Zelikovski, A., Deutsch, A. and Reiss, R. (1983), 'The sequential pneumatic compression device in surgery for lymphedema of the limbs.', *The Journal of cardiovascular surgery* **24**(2), 122–126.
- Zhang, H., Chen, Y., Zhang, Y., Sun, X., Ye, H. and Li, W. (2008), 'Synthesis and characterization of polyurethane elastomers', *Journal of Elastomers & Plastics* **40**(2), 161–177.
- Ziaja, D., Kocelak, P., Chudek, J. and Ziaja, K. (2011), 'Compliance with compression stockings in patients with chronic venous disorders', *Phlebology* **26**, 353–360.
- Zupin, Z. and Dimitrovski, K. (2010), 'Mechanical properties of fabrics from cotton and biodegradable yarns bamboo, spf, pla in weft', *Woven fabric engineering* pp. 25–46.

Appendix A

Calibration of FlexiForce[®] sensors

The standard method in calibrating the sensors is by using a set of standard weights, the detailed calibration procedure is as follows,

1. Connect the sensors to the CEBO-MSA 64 multi sensor measurement box, and open the MSA-CAL lite 1.0 software to continue the calibration process.
2. Place the sensors on a flat surface and stick with glue tape
3. Then cut a circular peg from Teflon sheet which is exactly of the same area as of the sensing area of the FlexiForce sensor (this is to concentrate the loading accurately as instructed to carry out during the calibration by the manufacturer)
4. To avoid the misplacement of the weight out of the centre of the circular sensing area of the FlexiForce sensor, cut a thin square sheet out of a clear Perspex sheet and mark the centre point of that rectangular piece of sheet. Thereafter glue the weight to this sheet using double sided tape, with the centre of the weight being marked. Then, looking through the other transparent side, adjust the weights to align with the centre point of the transparent sheet. Then draw along the base of the weight on the sheet to demarcate the base of the weight. Repeat this for weights 20g, 50g and 100g. This ensures that the weights could be put on exact same location providing the required repeatability during the calibration process.

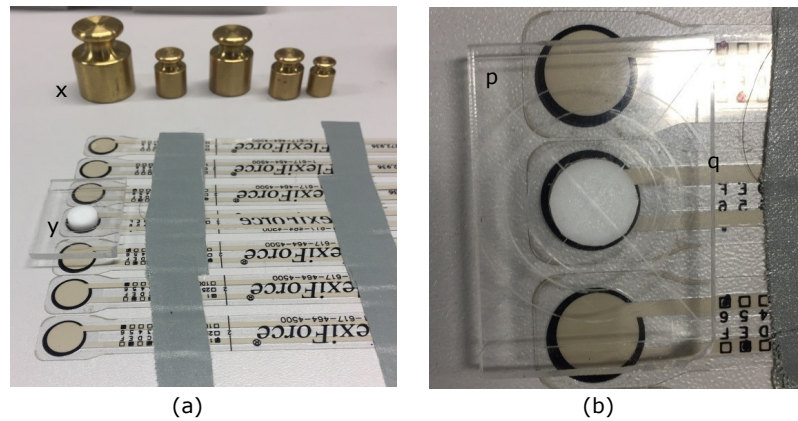


Fig. A.1 Calibration procedure for FlexiForce[®] sensors (a) placement of the Teflon peg and the Perspex sheet (x: set of standard weights, y: Teflon peg). (b) The demarcations of different weights on the sheet (p: Perspex sheet, q: demarcations).

5. Before starting of calibration, place a higher weight (e.g. 200g) on the sheet for about 3 seconds and remove it, and repeat this same procedure for three times in order to condition the sensors.
6. Start the calibration process with small weight (e.g. 20g) and step-wise increase the weight and continue the calibration
7. Then place the weight on top of the Perspex sheet, on the correct demarcation and enter the corresponding pressure value in the calibration bar height which is denoted in the software. This calibration bar changes accordance with the change of the weight .
8. After finishing calibration of one sensor, calibrate all the other sensors one by one and save the calibration file for all four sensors.

Calibration points calculation-Zwicki® tester

The pressure applied using the Zwicki® can be calculated as;

$$\text{applied pressure (mmHg)} = \frac{\text{peg weight (kg)} \times 9.81 \text{ (ms}^{-2}\text{)} + \text{Force (N)}}{71 \text{ (mm}^2\text{)}} \times 7500.638 \quad (\text{A.1})$$

Therefore, the pressure applied can be calculated as shown in Table A1.1.

Table A.1 Calculation points of the applied pressure using the Zwicki tester

Weight of the peg (g)	Weight of the peg (kg)	F (N)	Force applied by Zwicki (N)	Total Force (N)	Pressure (N/mm ²)	Pressure (mmHg)
0.92	0.00092	0.009	0.3	0.309	0.0043	32.45
0.92	0.00092	0.009	0.5	0.509	0.0071	53.53
0.92	0.00092	0.009	0.8	0.809	0.0113	85.07
0.92	0.00092	0.009	1	1.009	0.0141	106.11
0.92	0.00092	0.009	1.3	1.309	0.0183	137.65
0.92	0.00092	0.009	1.5	1.509	0.0212	158.68
0.92	0.00092	0.009	1.8	1.809	0.0254	190.23
0.92	0.00092	0.009	2	2.009	0.0281	211.26

Calibration graphs for standard weight calibration and Zwicki® tester calibration

Percent values recorded by the software against the applied pressure for standard weight calibration

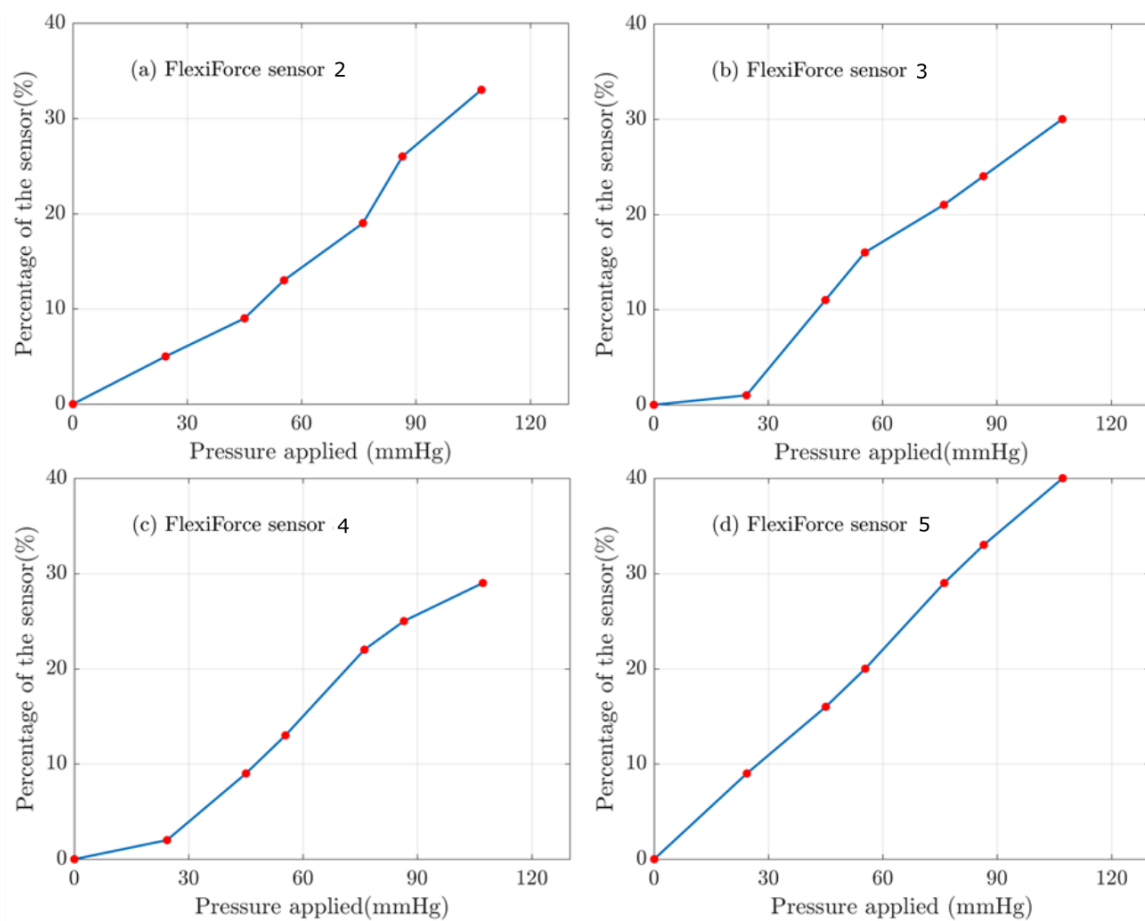


Fig. A.2 The percent values recorded by the software (% of the calibration bar) against the applied pressure used in the calibration for FlexiForce® sensors calibrated using standard weights

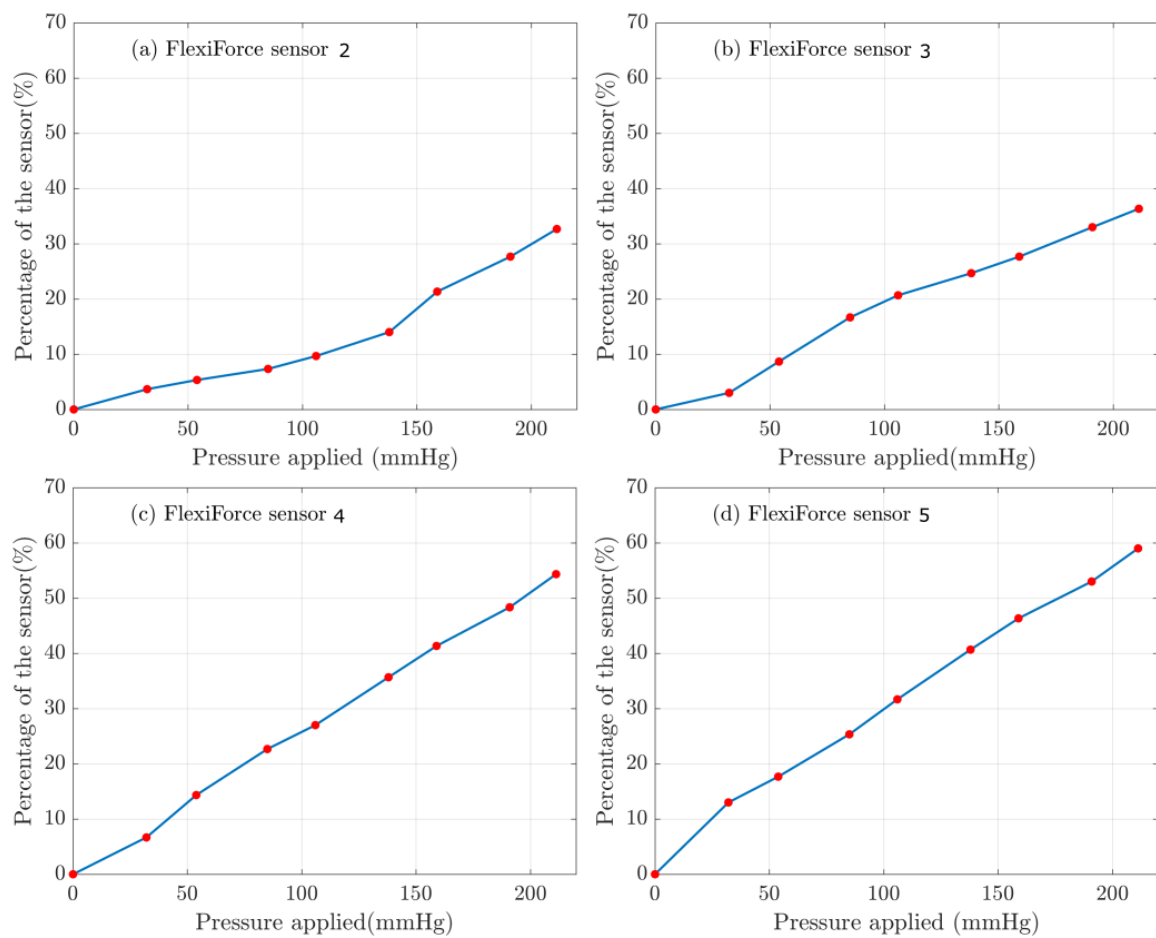


Fig. A.3 The percent values recorded by the software (% of the calibration bar) against the applied pressure used in the calibration for FlexiForce[®] sensors calibrated using Zwicki

Evaluation of FlexiForce[®] sensors against the manometer

Evaluation of FlexiForce[®] sensors against the manometer

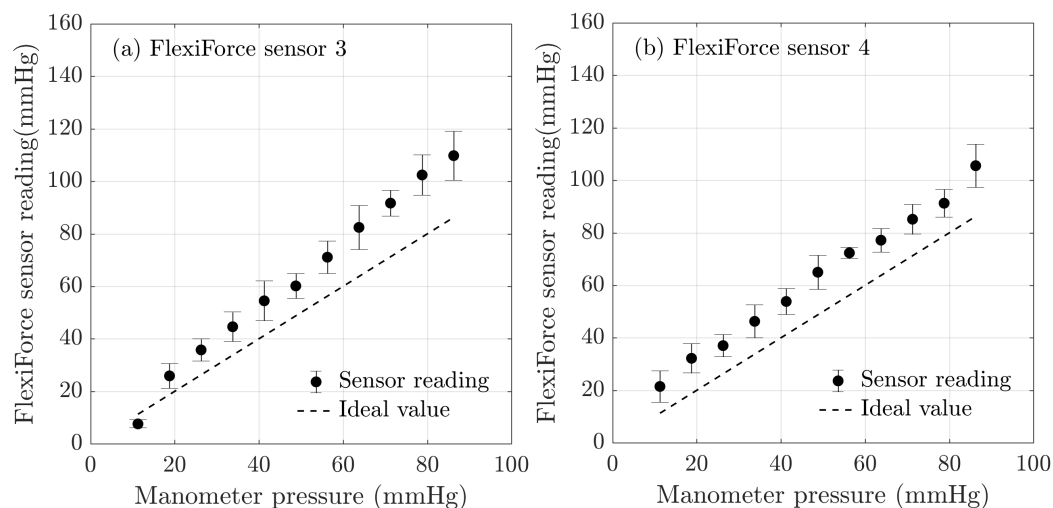


Fig. A.4 The results obtained using the bladder test, validation of FlexiForce[®] sensors readings against the manometer reading (Standard weight calibrated). The error bars represent the 95% confidence interval.

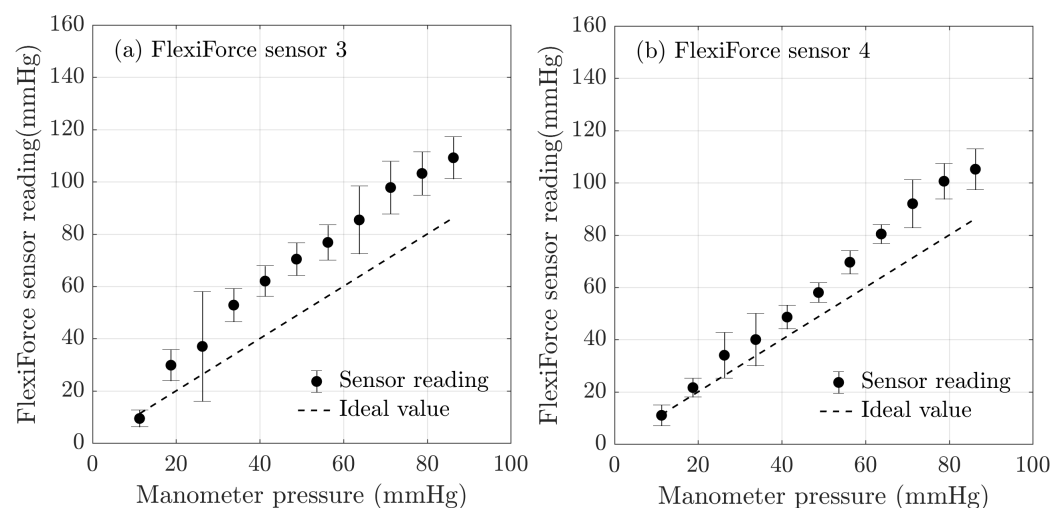


Fig. A.5 The results obtained using the bladder test, validation of FlexiForce[®] sensors readings against the manometer reading (Zwicky calibrated). The error bars represent the 95% confidence interval.

Evaluation of the face/reverse side of FlexiForce[®] sensors against the manometer

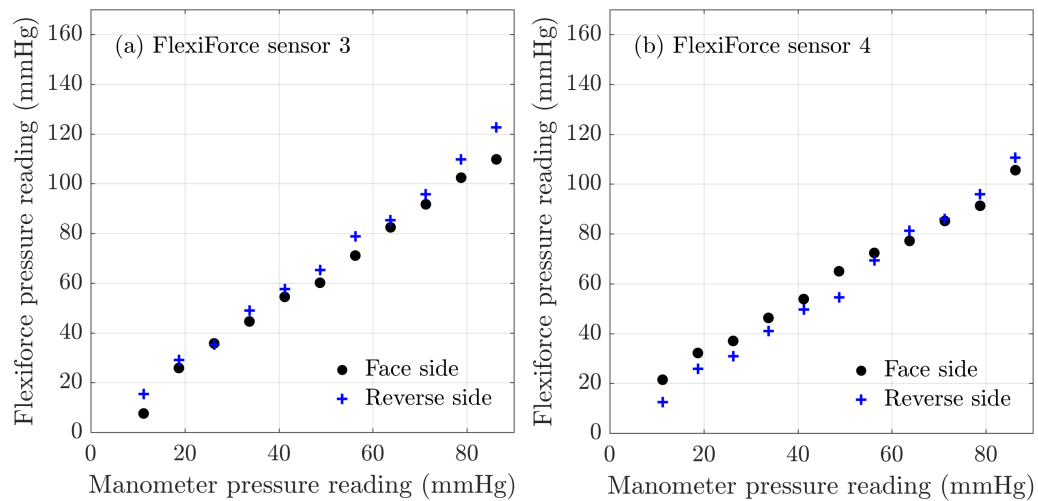


Fig. A.6 The results obtained for the face and reverse side of the FlexiForce[®] sensors readings against the manometer reading (Standard weight calibrated)

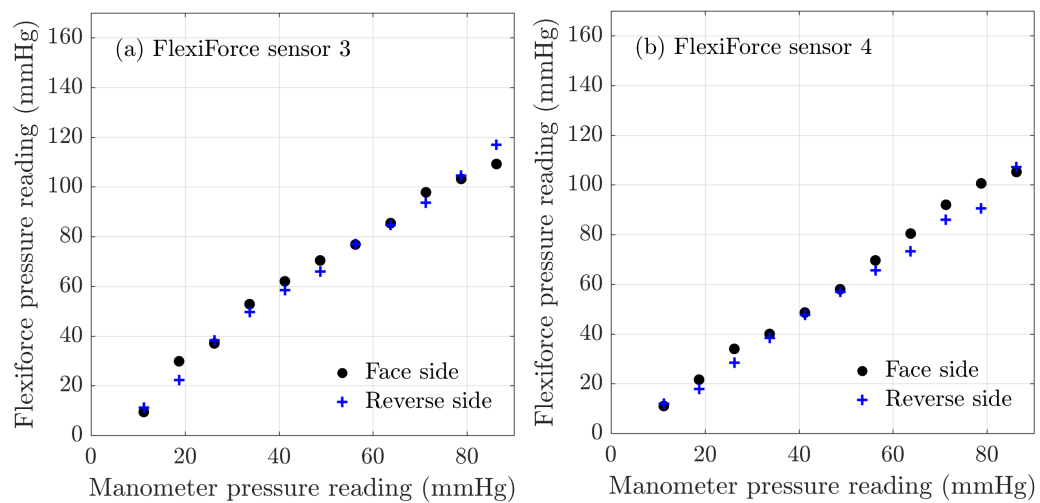


Fig. A.7 The results obtained for the face and reverse side of the FlexiForce[®] sensors readings against the manometer reading (Zwicky calibrated)

Evaluation of the second batch of FlexiForce[®] sensors

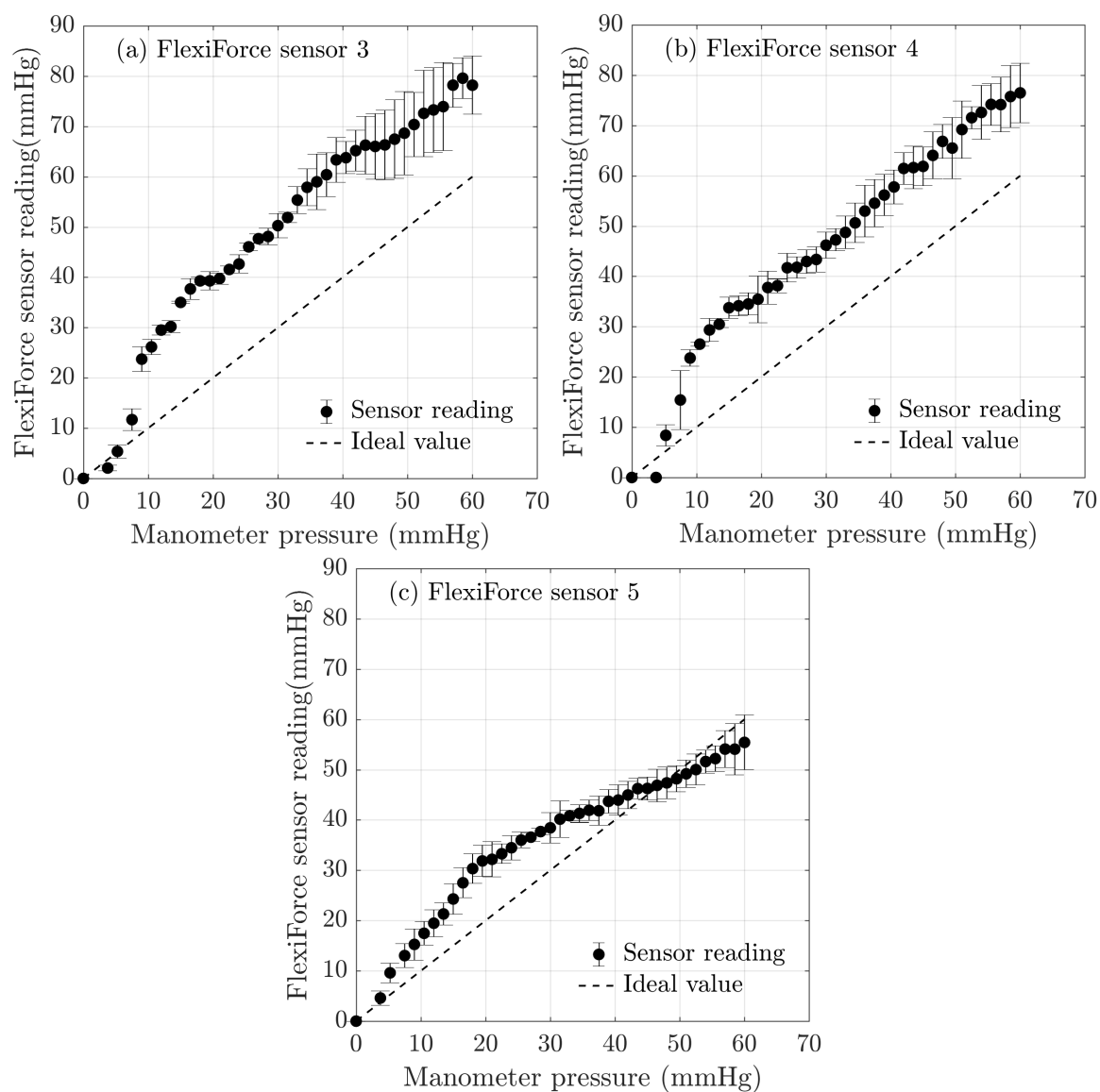


Fig. A.8 The results obtained using the bladder test, validation of FlexiForce[®] sensor (second batch) readings against the manometer (standard weight calibration). The error bars represent the 95% confidence interval

Email communications with CEBO;

Urgent Enquiry MSA-64 Box with A201,0 – 1lb

Shahidi, Arash

Thu 09/03/2017 11:41

To: Thomas Senthoff <senthoff@ubsenthoff.de>; Thomas Hoppe (thomas.hoppe@cesys.com) <thomas.hoppe@cesys.com>

Cc: Nandasiri, Hewa Madihe Annakkage 2015 (PGR) <hewa.nandasiri2015@my.ntu.ac.uk>

■ 2 attachments (106 KB)

A1.msacal2; Flexiforce-Manometer.pdf;

Dear All,

Hope everything went well for you and your family, as you are aware we are using MSA-64 BOX with the A201, 0 – 1 lb felxiforce sensor but we are having issue with the pressure collection using the sensors would it be possible to advise us regarding the following problem please,

- a) Throughout the calibration process, different sensors 1-5 are registering different value while applying different weight.
- b) After following the procedure and calibrating the sensors (1-5) the sensors are showing a different reading for the same circumstances (as mentioned can be identified throughout the calibration process too), is this what we should expect! If not what is the solution.
- c) I have tried to validate the reading against manometer but still, the big variation can be identified.

Fig. A.9 Email communications with CEBO-CEYS

Nandasiri, Hewa Madihe Annakkage 2015 (PGR)

Fri 19/05/2017 12:34

To: senthoff@ubsenthoff.de <senthoff@ubsenthoff.de>

Cc: Shahidi, Arash <arash.shahidi@ntu.ac.uk>

Dear Thomas,

The calibration was carried out independent for all the sensors.

The no load value was not in volts, since we are using the CEBO- system which converts the voltage value to the required force value which we calibrate as a pressure value. So basically this is a mmHg value.

I believe a no load calibration point would be needed here, since our measuring range is a lower one. would be better to have more calibration points in that region.

I have no data for those sensors, since we have not calibrated them.

Many thanks!

Regards,
Gayani.

From: Shahidi, Arash

Sent: 19 May 2017 10:17:59

To: Nandasiri, Hewa Madihe Annakkage 2015 (PGR)

Subject: FW: UBSenthoff

From: Thomas Senthoff [mailto:senthoff@ubsenthoff.de]

Sent: 12 May 2017 11:07

To: Shahidi, Arash <arash.shahidi@ntu.ac.uk>

Subject: UBSenthoff

Dear Arash,
please find attach some notes from Tekscan about your problem.
Let me know, if that is helpful.

Is the customer performing independent calibration for every sensor? Is the no-load value the customer specified (0.3-1.3) in units of Volts? ADC counts? The sensor's no-load resistance can vary between 5M Ω and 20M Ω or even more. If possible, I'd recommend not capturing no-load as a calibration point, because of the variance that can occur at no-load. Instead, I'd recommend the first calibration point be the lowest possible load they expect, that can be consistently applied during calibration. If capturing a no-load calibration is required for this application, I would need more information on the circuit being used in order to recommend adjustments that would accommodate a no-load calibration point.

It is impossible for me to assess whether the sensors are functioning properly based on no-load measurements. If there is some data I can see (with the sensors under loaded conditions), that would allow me to comment on functionality of the sensors.

Best regards/ Mit freundlichen Grüßen
Thomas Senthoff

Fig. A.10 Email communications with CEBO-CEYS

AMI Calibration manual

【Calibration】 in combination with the Pressure Calibration System

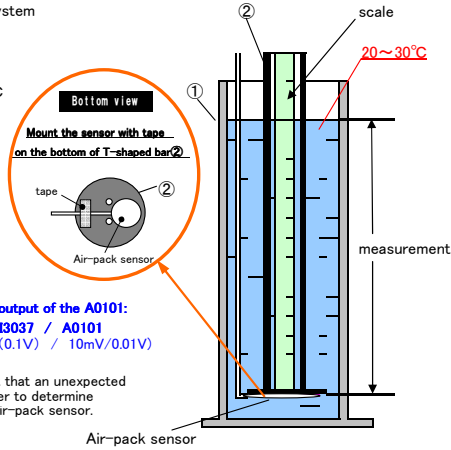
A. Calibration for Main unit and Air-pack sensor

The accuracy shown in the catalog is the accuracy to be got $20^{\circ}\text{C} \pm 5^{\circ}\text{C}$ in atmospheric temperature.

- 1) Fill the Cylinder① with warm water ($20 \sim 30^{\circ}\text{C}$) up to blue line level.
(Note that the accuracy indicated on the system may become lower than that given in the data sh of water less than 20°C)
- 2) Mount the Air-pack sensor on the bottom plate of the T-shaped bar②.
- 3) Submerge the T-shaped bar② into the cylinder①.
- 4) Measure the water depth with the scale painted on the T-shaped bar②.
- 5) Compare the value of pressure at the given water depth with the value indicated on the display for confirming the accuracy got from the system.

The pressure at the given water depth (102mmH₂O) → Measured value to be got: 1kPa (10.2gf/cm² or 7.5mmHg) → Voltage output of the A0101: AMI3037 / A0101 → 100mV(0.1V) / 10mV/0.01V

※ Proceed to the next step with Calibration B given below in the event that an unexpected error take place from the Calibration A. Also check the status in order to determine whether the error be brought about from the main unit or from the Air-pack sensor.

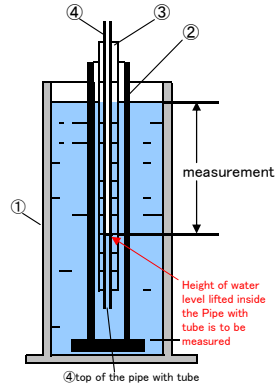


B. Calibration for Main unit

- 1) Connect the Pipe with Tube④ to the Main unit and make adjustment that the indication of output "0" on the display.
- 2) Submerge the T-shaped bar② into the cylinder①.
- 3) Insert the Scale③ into the pipe of the T-shaped bar. Adjust that the indication of water level may come to "0" while loosening a rubber ring and fix this status.
- 4) Insert the Pipe with tube④ into the hollow portion of the T-shaped bar② where the Scale③ is already mounted.
- 5) The water level inside the Pipe with tube④ is lifted by hydraulic pressure. Measure with the Scale③ the difference between the height of water level inside the Pipe with tube④ and the height of water level of the Cylinder① itself.

The pressure at the given water depth (102mmH₂O) → Measured value to be got: 1kPa (10.2gf/cm² or 7.5mmHg) → Voltage output of the A0101: AMI3037 / A0101 → 100mV(0.1V) / 10mV/0.01V

※ Return the whole main unit for our repair and readjustment provided that any errors outside the specified acceptable range.



【Units for Conversion of Output and Pressure】

AMI3037	A0101/0905	SI unit	SI unit	former unit		
DCV	DCV	hPa	kPa	(gf/cm ²)	(mmH ₂ O)	(mmHg)
0.1	0.01	10	1	10.2	102	7.5
0.0098	0.00098	0.98	0.098	1	10	0.736
0.00098	0.000098	0.098	0.0098	0.1	1	0.0736
0.0133	0.00133	1.33	0.133	1.36	13.6	1

- ①Cylinder
- ②T-shaped bar
- ③Scale
- ④Pipe with tube

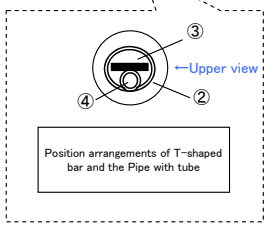
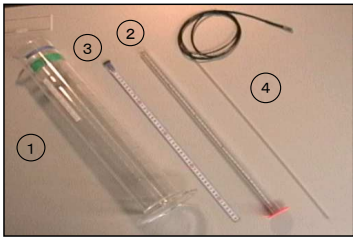
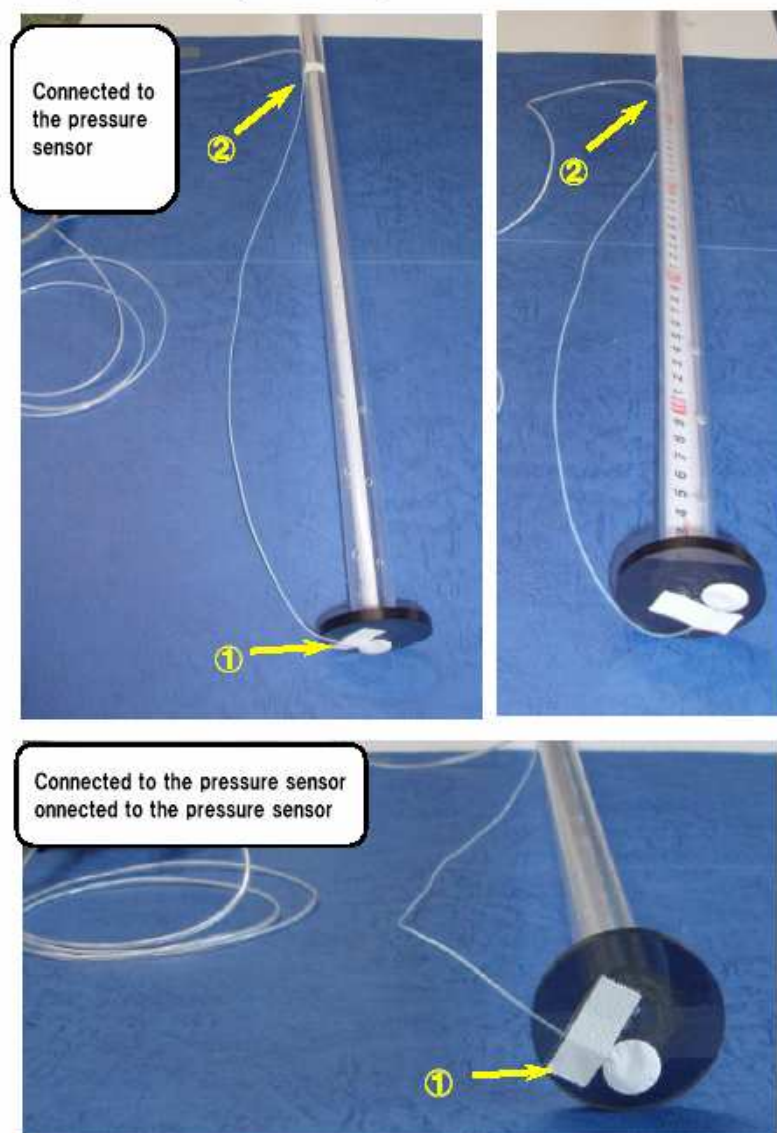


Fig. A.11 AMI Calibration manual-1

<Preparations for proofreading>



- ① Fix air pack in T-shaped bar
- ② The position whose scale can be seen

Fig. A.12 AMI Calibration manual-2

Evaluation of AMI sensors against the manometer

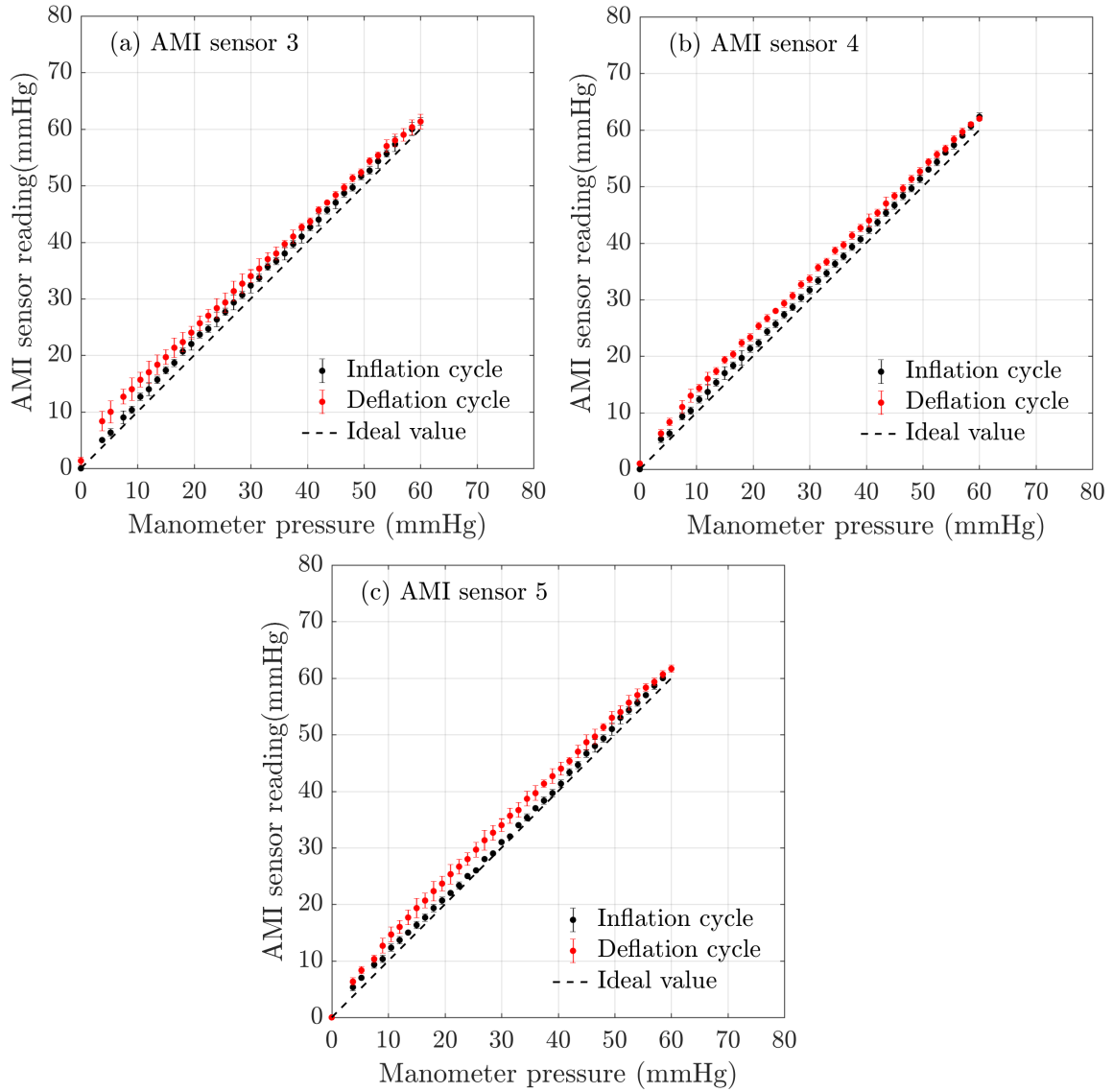


Fig. A.13 The results obtained using the bladder test, validation of AMI air-pack sensors readings against the manometer reading for inflation and deflation cycles. The error bars represent the 95% confidence interval.

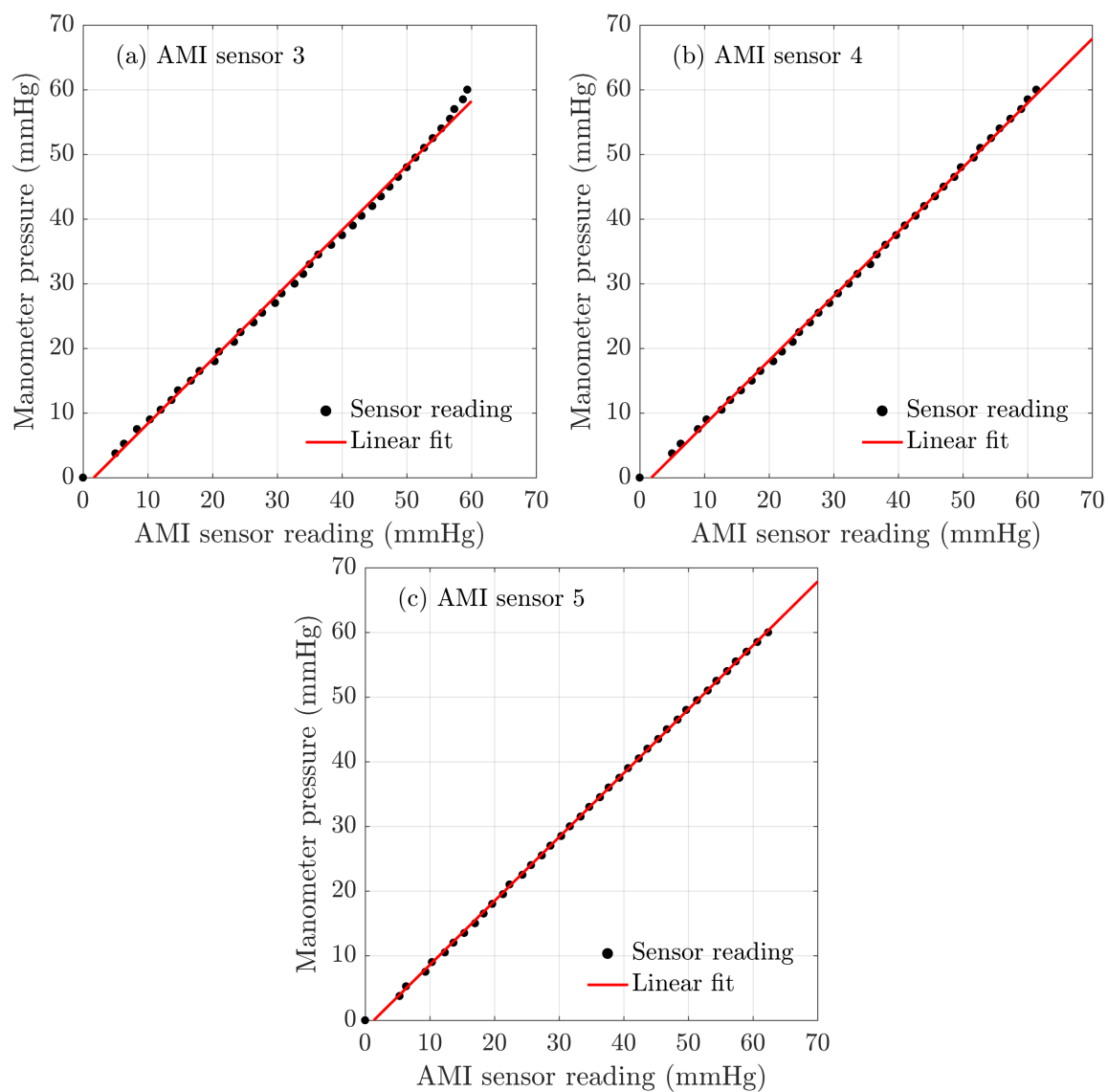


Fig. A.14 Validation of AMI air-pack sensors readings against the manometer reading- linearity relationship plot for the inflation cycle.

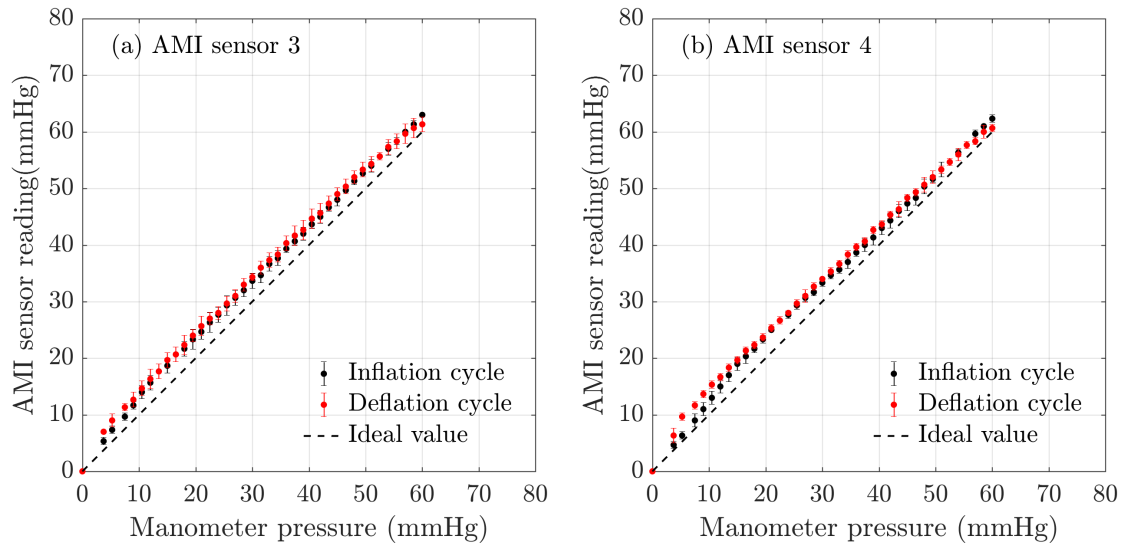


Fig. A.15 The results obtained using the bladder test, validation of AMI air-pack sensors readings against the manometer reading inflation and deflation cycles for the second batch. The error bars represent the 95% confidence interval.

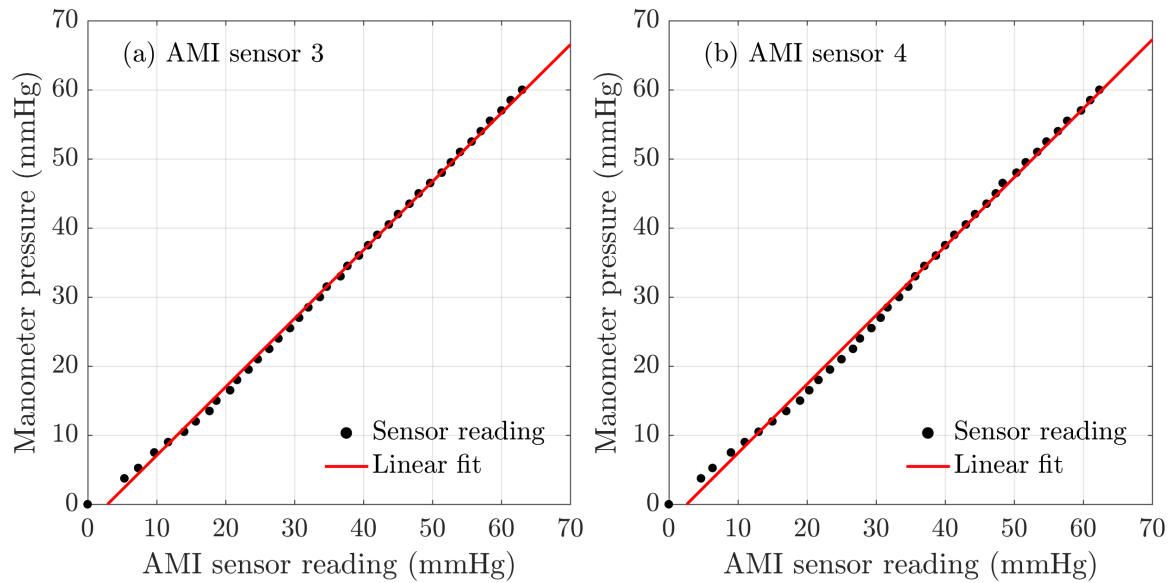


Fig. A.16 Validation of second batch of AMI air-pack sensors readings against the manometer reading-linearity plot.

FlexiForce[®] sensor user manual



FlexiForce[™]

Standard Model A201

The FlexiForce A201 is our standard sensor and meets the requirements of most customers. The A201 is a thin and flexible piezoresistive force sensor that is available off-the-shelf in a variety of lengths for easy proof of concept. These ultra-thin sensors are ideal for non-intrusive force and pressure measurement in a variety of applications. The A201 can be used with our test & measurement, prototyping, and embedding electronics, including the OEM Development Kit, FlexiForce Quickstart Board, and the ELF[™] System*. You can also use your own electronics, or multimeter.

Physical Properties

Thickness	0.203 mm (0.008 in.)
Length	191 mm (7.5 in.)** (optional trimmed lengths: 152 mm (6 in.), 102 mm (4 in.), 51 mm (2 in.))
Width	14 mm (0.55 in.)
Sensing Area	9.53 mm (0.375 in.) diameter
Connector	3-pin Male Square Pin (center pin is inactive)
Substrate	Polyester
Pin Spacing	2.54 mm (0.1 in.)

✓ ROHS COMPLIANT

* Sensor will require an adapter/extender to connect to the ELF System. Contact your Tekscan representative for assistance.

** Length does not include pins. Please add approximately 6 mm (0.25 in.) for pin length for a total length of approximately 197 mm (7.75 in.).

Benefits

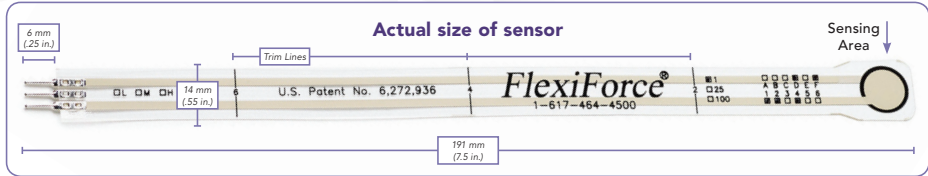
- Thin and flexible
- Easy to use
- Convenient and affordable

DS Rev F 101518

ISO 9001 Compliant & 13485 Registered



Fig. A.17 FlexiForce[®] user Manual-1



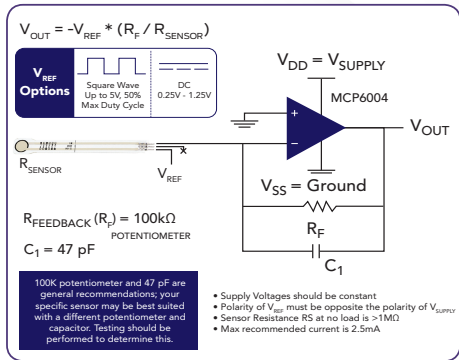
Standard Force Ranges as Tested with Circuit Shown

- 4.4 N (0 - 1 lb)
- 111 N (0 - 25 lb)
- 445 N (0 - 100 lb) †

† This sensor can measure up to 4,448 N (1,000 lb). In order to measure higher forces, apply a lower drive voltage (-0.5 V, -0.25 V, etc.) and reduce the resistance of the feedback resistor (1kΩ min.). To measure lower forces, apply a higher drive voltage and increase the resistance of the feedback resistor.

Sensor output is a function of many variables, including interface materials. Therefore, Tekscan recommends the user calibrate each sensor for the application.

Recommended Circuit



	Typical Performance	Evaluation Conditions
Linearity (Error)	< ±3% of full scale	Line drawn from 0 to 50% load
Repeatability	< ±2.5%	Conditioned sensor, 80% of full force applied
Hysteresis	< 4.5% of full scale	Conditioned sensor, 80% of full force applied
Drift	< 5% per logarithmic time scale	Constant load of 111 N (25 lb)
Response Time	< 5μsec	Impact load, output recorded on oscilloscope
Operating Temperature	-40°C - 60°C (-40°F - 140°F)	Convection and conduction heat sources
Acceptance Criteria	±40% sensor-to-sensor variation	

*All data above was collected utilizing an Op Amp Circuit. If your application cannot allow an Op Amp Circuit, visit www.tekscan.com/flexiforce-integration-guides, or contact a FlexiForce Applications Engineer.

Force reading change per degree of temperature change = 0.36%/°C (±0.2%/°F).

PURCHASE TODAY ONLINE AT WWW.TEKSCAN.COM/STORE



©Tekscan Inc., 2018. All rights reserved. Tekscan, the Tekscan logo, and FlexiForce are trademarks or registered trademarks of Tekscan, Inc.

+1.617.464.4283 | 1.800.248.3669 | info@tekscan.com | www.tekscan.com/flexiforce

Fig. A.18 FlexiForce® user Manual-2

AMI sensor user manual

	Main System						for stockings / bandages	
Models	1ch/Handy	2ch/Extend	5ch/Desktop	10ch/Desktop	1ch/Desktop	1ch/Desktop and many points are possible		
	AMI 3037-2	AMI 3037-2B	AMI 3037-5S	AMI 3037-10	A 0101-G35k-AC	A 0905-SA-35k	AMI 3037-SB-HP	AMI 3037-SB-mH
Unit of pressure	convert the voltage	convert the voltage	k Pa	k Pa	k Pa	k Pa	h Pa	(mmHg)
ch	1	2	5	10	1	1	1	1
Measuring Range	0~34.00 k Pa		0.00~34.00 k Pa		0.0~35.0 k Pa		0~350 hPa	0~263 mmHg
Air-pack(φ20)	—		—		0.0~20.0 kPa		0~200 hPa	0~150 mmHg
Measuring Accuracy in 23°C	0~14.00 ±0.1 k Pa 14.00~34.00 ±0.25 k Pa				±0.2 k Pa		±2 hPa	±1.5 mmHg
Output	1 k Pa → 0.1V (100mV)				1 k Pa → 0.01V(10mV)		—	—
Numerical display	—	—	LED 5ch	LED 10ch	LED 1 ch	LED 1 ch	LED 1 ch	LED 1 ch
Durable Pressure	up to 70 k Pa						up to 700 hPa	up to 500 mmHg
Power supply	AC100V(11VA) AA battery(1.5v×4)	supplied by the left instrument	AC100V (7VA) (10VA)		AC100V 0.5A	AC100V 0.5A	AC100V 0.5A	
Air-Cylinder	Optional attachment : AMI3037-AC/ Black, red, green, and blue					Equipped by machinery	Equipped by machinery	
Air-pack Which is connected	Standard:AMI3037-P2,AMI3037-P5/Parasol type : AMI3037-P2P,AMI3037-P5P					φ 20/?m AMI3037-SB-P3/P5	AMI3037-SB-P3/P5(φ 20/?m)	
Zero adjustment	Adjustment by screw		Adjustment by screw		Automatically		Automatically	
Applicable Environment	0~45°C RH. 25~85%						0~45°C RH. 25~85%	
External Dimensions	W92×H45×D160		W475×H160×D250		W245×H75×D175		W245×H75×D175	
Weight	0.6k g	0.6k g	8k g	8k g	2k g		2k g	
Feature	Small and a Battery	Small and a Battery	Measure 5ch at the same time	Measure 10ch at the same time	The consecutive output	The consecutive output/Many points are possible	Watch numerical value/Many points are possible	

* A0101-G35k (charge type) turned into A0101-G35k-AC (an AC power type)									
Air-Pack Model-Standard: AMI3037-P2 (Two) / AMI3037-P5 (Five) / Parasol type: AMI3037-P5P (Five) / AMI3037-P10P (Ten)									
Product number	①	②	③	④	⑤	⑥	⑦	⑧	⑨
Size (mm)	φ 15	φ 20	φ 25	φ 30	φ 8×L=28	φ 20×L=30	φ 12×L=15, φ 15×L=17	φ 12×L=15, φ 15×L=17	φ 12×L=15, φ 15×L=17
Size & Tube Length	φ15/1.5m~2m	φ20/2m~3m	φ25/2m~3m	φ30/2m~3m	1/1.5m~2m	G/2m~3m	φ12×15/1.5m	φ12×15/1.5m	φ12×15/1.5m
Parasol type (φOP)	—	φ20P/2.5m	φ25P/2.5m	φ30P/2.5m	T/1.5m~2m	GP/2.5m	φ15×17/1.5m	φ15×17/1.5m	φ15×17/1.5m
for A0905 and AMI3037-SB	—	SB φ 20/1m · 0.5m	Model A0905: Can use the special air-pack						
Max. Measuring range (Approx.)	10	20	30	38	15	20	15	15	15
Measuring accuracy (Sensitivity to soft material)	±0.15	±0.1	±0.1	±0.1	±0.2	±0.1	±0.3	±0.3	±0.3
Size Cover tape/Models	φ 47/AMI3037-PTS		φ 47/AMI3037-PTB		—				
Air Cylinder	Black(half of red)		Red	Green	Blue	Black	Red	Black	Black
Main Applications (mm)	Sphere of φ 15 or larger		Sphere of φ 20 or larger (standard)	Sphere of φ 25 or larger but with small curvature	Sphere of φ 30 or larger with small curvature	Objects of 8 in width and 28 in length or longer. For belts, flat cords, side of fingers.	Objects of 20 in width and 30 in length or longer. For fingers, etc.	Objects of 12 in width and 15 in length or longer. For fingers, etc.	Objects of 12 in width and 15 in length or longer. For fingers, etc.

Air-Pack

Standard

SB type

Parasol type

Joint φ4

Joint φ3

①

②

③

④

①

②

③

④

Pressure Calibration Unit

Models	AMI3037-CS
Calibration Range	0~4.5 kPa
Compositions	
① Fine Chemical Cylinder	φ 95 × L=500
② Scale	L=500
③ T-shaped bar	φ 50 L=500
④ Pipe with tube	φ 6 × L=500 1.5m
Weight	1kg

For the abnormal management of the measurement

AMI Techno co.,LTD.

fax : +81-3-5339-7414 3-5-3-1313, NISHI-SHINJUKU,
SHINJUKU-KU, TOKYO, 160-0023, JAPAN

E-mail: ami-tec@m2.pbc.ne.jp <http://www.ami-tec.co.jp>


«THE EXCLUSIVE OVERSEAS DISTRIBUTOR»

SANKO TSUSHO CO.,LTD.

tel: +81-3-5777-3627 fax: +81-3-5777-3629

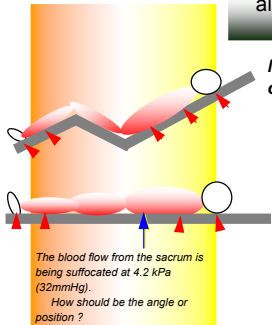
TOKYO, JAPAN E-mail: sales@sankotsusho.co.jp

Fig. A.19 AMI user Manual-1



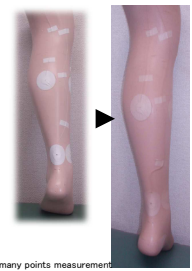
Air-pack type contact surface pressure continuously measuring system

Air-pack type : Air packed in an air-bag is put between two contacting materials and air-pressure brought about inside that air-bag is measured.




Measurement of body pressure and of pressure in its sitting attitude.

The blood flow from the sacrum is being suffocated at 4.2 kPa (32mmHg).
How should be the angle or position?




Measurement of pressure appearing in clothes.

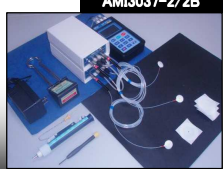
The many points measurement
The time change is measured with the sensor worn.




AMI101-G35-AC




AMI3037-10



AMI3037-2/2B



AMI3037-SB



A0905-SA

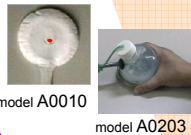
Circumferential pressure of shoes.

Living body (soft condition) can be measured.

It is possible to measure it only by pulling the cock.

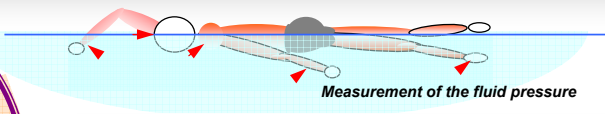
Both the living body (soft condition) and the dummy (hard condition) can be measured.

The accuracy of the measured value can be certified by the water pressure calibration method.



**Surface Pressure
Blood Flow
Skin Temperature**

model A0010 model A0203



Measurement of the fluid pressure

...Measured by water pressure calibration method...

Patented

Patent Pending

U.S.A. : U.S.Pat.5522966 July 13,1999
Europe : E.P.Pat.0831313 August 9,2000
JAPAN 3268601 January 18,2002

Air enclosure method contact pressure mensuration/PT#.2009-139649
 Cylinder-shaped expansion-style contact pressure calibration method/PT#.2008-116278

«MANUFACTURER»
AMI Techno CO.,LTD. TOKYO,JAPAN
<http://www.ami-tec.co.jp>

«THE EXCLUSIVE OVERSEAS DISTRIBUTOR»
SANKO TSUSHO CO.,LTD. TOKYO,JAPAN
 Tel: +81-3-5777-3627 E-mail: sales@sankotsusho.co.jp

Usage
 Contact pressure
 Restraint pressure
 Body pressure
 Clothes pressure
 Pressure by sitting
 Flexibility
 Calibration
 Molding of foaming materials

Fig. A.20 AMI user Manual-2

◀Reliability▶ Measurement with soft sensor for soft plane → air and soft bag → The influence on contact surface is extremely little and reproducibility is good.

This contact surface pressure measuring system is a system to measure a surface pressure of a soft material to which the sensor of this system is in contact and to correct errors in the reading to be brought about by a thermal change in the environment. This system has been approved by patent authorities in several countries in the world as a unique system to be able to effect a reliable measurement of a contact pressure of soft materials with a high reproducibility. This system does not require any special preliminary correction for the reading to be usually made before use. This system can also make a continual measurement sequentially.

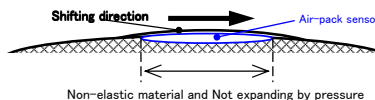
Air-pack method

An air is enclosed between two contacted surfaces and the pressure of that enclosed air is measured externally from the contacted surface. Into a flat bag made with a flexible film of a least possible elasticity, an air is enclosed in the thickness of 1mm.

Feature

- (1) It is easy to stick each part of the living body and between ruggedness of the cloth and reproducibility is good in 20mm (standard) diameter. The center part of the bag comes in contact with the point when it is too large and the situation is changeable and reproducibility worsens partial pressure it. For example, only the center of the air pack comes in contact in the ankle that the ruggedness is 30mm in diameter.
- (2) The influence of the air pack that infuse some air in 1mm in thickness becomes thinner because of pressure sinks softly of the living body and the clothes is extremely little. However, when infusing in 1.5mm in thickness and measuring it in the cylinder of $\phi 100$, the value about 1.3 times 1mm in thickness was confirmed.
- (3) The circle shape mounted to body part easily. The result change by the direction when designed besides the circle. For example, the top becomes the mean value of the lowering area high in surroundings in the measurement with the hemisphere.
- (4) In piping in the tube of 1mm that doesn't collapse, it is unaffected in the piping situation catching the transformation of the bag of the air pack (alteration in volume). The result change for a soft material such as silicon rubber in the piping situation.

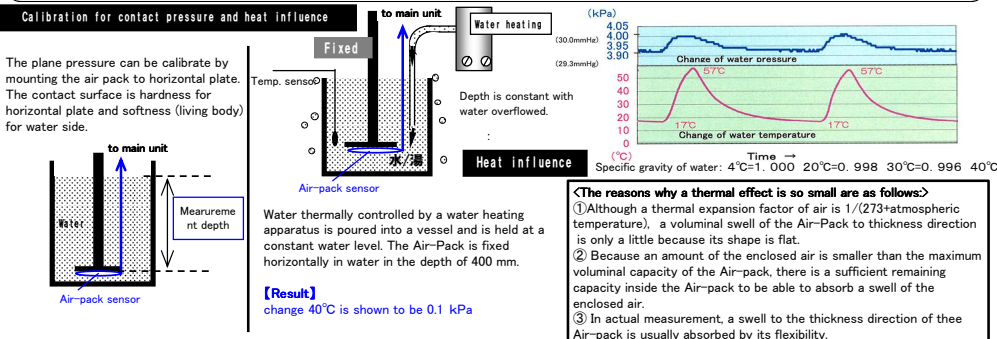
Section



Each error in measurement ①Permissible error+②Measuring area error+③Position error+④Restoration of tools material+⑤Attitude error

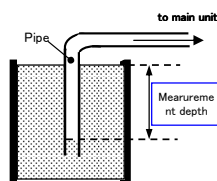
- ①Permissible error: Describes in the specification.
- ②Measuring area error: The difference of the characteristic the mounted position, the figure and the softness of the air pack sensor is caused.
- ③Position error: The value changes partially in how like hitching and a horizontal gap to match it when setting it to the measurement site when tools are installed. The error is somewhat caused though putting the sign and the line in tools in detail, and improving accuracy are necessary.
- ④Restoration of tools material: The difference of the restoration is caused by the sweat, the expansion in the rig frequency.
- ⑤Attitude error: It influences pressure in transmission and the weight shift of the material tension because of the difference among the posture angle, arm and the head position.

Note: In the measurement of body pressure to know the distribution pressure is important. However, the method of paving the seat sensor in the distribution pressure measurement and the calling contact surface and the measurements has the anxiety in reproducibility and the measurement accuracy. Non-elastic film seat enclosed between two contacted surfaces and A flexible characteristic and the contact friction are completely changed and it is not easy to call body pressure.



Calibration for pressure sensor and output

A pressure on horizontal plane corresponding to the water pressure can be got by measuring the water depth.



SI unit		Former unit			Model	AM3037-2, 5S, 10		A0101 / A0905	
hPa	kPa	(gf/cm ²)	(mmH ₂ O)	(mmHg)		DC output		DC output	
10	1	10.2	102	7.5		DC V	DCmV	DC V	DCmV
0.98	0.098	1	10	0.736		0.100	100	0.010	10
0.098	0.0098	0.1	1	0.074		0.010	9.8	0.001	0.98
1.333	0.1333	1.36	13.6	1		0.001	0.98	0.0001	0.1
						0.013	13.3	0.0013	1.3

Purpose of use for pressure measuring device

The measurement accuracy and reproducibility are confirmed the reproduction of a flexible plane contact environment. Error margin confirmation of secular distortion and confirmation of unexpected value when measuring it. It is not necessary to calibration before each measurement. * Because the standard of the contact pressure (ISO and JIS, etc.) in soft respect is not decided, the proofreading examination such as the inspecting agencies cannot be done under the present situation.

Fig. A.21 AMI user Manual-3

An air infuse to the air-pack sensor with air cylinder. And it connect to main unit and air-pack sensor mount to the body.

The air-pack sensor connect to the body in advance and wear the clothes. An air infuse to air-pack sensor with internal air cylinder by pulled the cock.

For multi point. Relay type air-pack sensor

Parasol type air-pack sensor

Main unit

DC output

(former) Accessory : Air cylinder

2 type measurement

Main unit internal model/Semi-auto air cylinder

● <1ch•3ch•5ch•7ch> Handy type/Extension AMI3037-2 (1ch) / Extension unit AMI3037-2B (2ch) Accessory : Air cylinder

Feature: 2 type power supply / The output signal is DC voltage and small main unit with dry battery (4 AA batteries) and AC adaptor (AC100v). It automatically changes to the AC adaptor when the battery consumed.

Add channel / Main unit AMI3037-2 is 1 ch and it can add each more 2 ch / 1 unit with extension unit AMI3037-2B.

Composition: ① Main unit/AMI3037-2(1ch), ② Extension unit AMI3037-2B(2ch), ③ Air cylinder/AMI3037-AMI3037-CY ④ Air-pack sensor 5pcs/AMI3037-P5, ⑤ Covering tape(200sheet)/AMI3037-PT ● Calibration set/AMI3037-CS accessory: ⑥ Press tester ● screw driver for zero adjust

Option: ● Data logging device to PC AM8051 (6ch) Accessory : software ● USB communication cable ● AC adapter (for data logger)

● <5ch•10ch> Main unit AMI3037-5S (5ch) AMI3037-10 (10ch) Accessory : Air cylinder

Feature: Main unit (10 ch desktop type) : For multi-point measurement with DC voltage output, it can measure the multi-point at one time and the data transfer to the data logger.

Composition: ① Main unit/AMI3037-10(10ch) ③ Air cylinder/AMI3037-AMI3037-CY ④ Air-pack sensor 5 pcs X 3set/AMI3037-P5 X 3 ● Covering tape(200sheet)/AMI3037-PT ● Calibration set/AMI3037-CS, accessory: ⑥ Press tester ⑦ screw driver for zero adjust

Option : ● Data logging device for PC(10ch or more)

● <1ch> Main unit with display (Auto zero adjust) A0101-G35-AC (1ch) Accessory : Air cylinder

Feature: Auto Zero Adjust: 1 ch with the output signal (DC voltage output).Auto zero adjustments after turned on the power. AC100V power supply.

Composition: ① Main unit/A0101-G35-AC(1ch) ⑨ relay tube 1. 5m ④ Air-pac sensor 3pcs/SB-φ 20/0.5m•1m ⑤ covering tape(200sheet)/AMI3037-PT ⑩ output cable ● Calibration set/AMI3037-CS, accessory: ⑥ press tester(small)

Option: ● Data logging device to PC AM8051(6ch) Accessory : software ● USB communication cable ● AC adapter (for data logger)

● <1ch> Main unit with display /DC output/Auto zero adjust) A0905-SA-35k (1ch) semi-auto air cylinder

Feature : For multipoint : Air-pack sensor previously mounted to the part and measurement tools install to the body. And the air infuse by the built-in air cylinder. Only the number of air packs repeats the measurement. Moreover, the change can be measured by being reconnected and measuring it after time passes with the air pack mounted.

Semi-auto air cylinder 2type<Black/Red> : It can select that air amount of infusion enclosed by the shape of air-pack and hardness on the measurement side. I case of Air-pack sensor φ 20, pull the red cock for soft living body with thickness 1mm and pull the black cock for hard materials with thickness 0.5mm.

Auto Zero Adjust : 1 ch with the output signal (DC voltage output).Auto zero adjustments after turned on the power.

Composition: ① Main unit/A0905-SA-35k(1ch) ⑨ relay tube 1. 5m ④ Air-pac sensor 3pcs/SB-φ 20/0.5m•1m ⑤ covering tape(200sheet)/AMI3037-PT ⑩ output cable ● Calibration set/AMI3037-CS, accessory: ⑥ press tester(small)

Option: ● Data logging device to PC AM8051(6ch) Accessory : software ● USB communication cable ● AC adapter (for data logger)

● <1ch> Mai unit with display (for multipoint) AMI3037-SB-hP (hPa) /mH (mmHg) (1ch) <stocking/bandage> semi-auto air cylinder

Feature: For multipoint : Air-pack sensor previously mounted to the part and measurement tools install to the body. And the air infuse by the built-in air cylinder. Only the number of air packs repeats the measurement. Moreover, the change can be measured by being reconnected and measuring it after time passes with the air pack mounted.

Auto Zero Adjust : 1 ch with the output signal (DC voltage output).Auto zero adjustments after turned on the power.

Composition: ① Main unit/AMI3037-SB(1ch), ⑨ relay tube 1. 5m ④ Air-pac sensor 3pcs/SB-φ 20/0.5m•1m, ⑤ Covering tape(200sheet)/AMI3037-PT, accessories: ⑥ press tester(small)

Fig. A.22 AMI user Manual-4

Picopress[®] sensor user manual

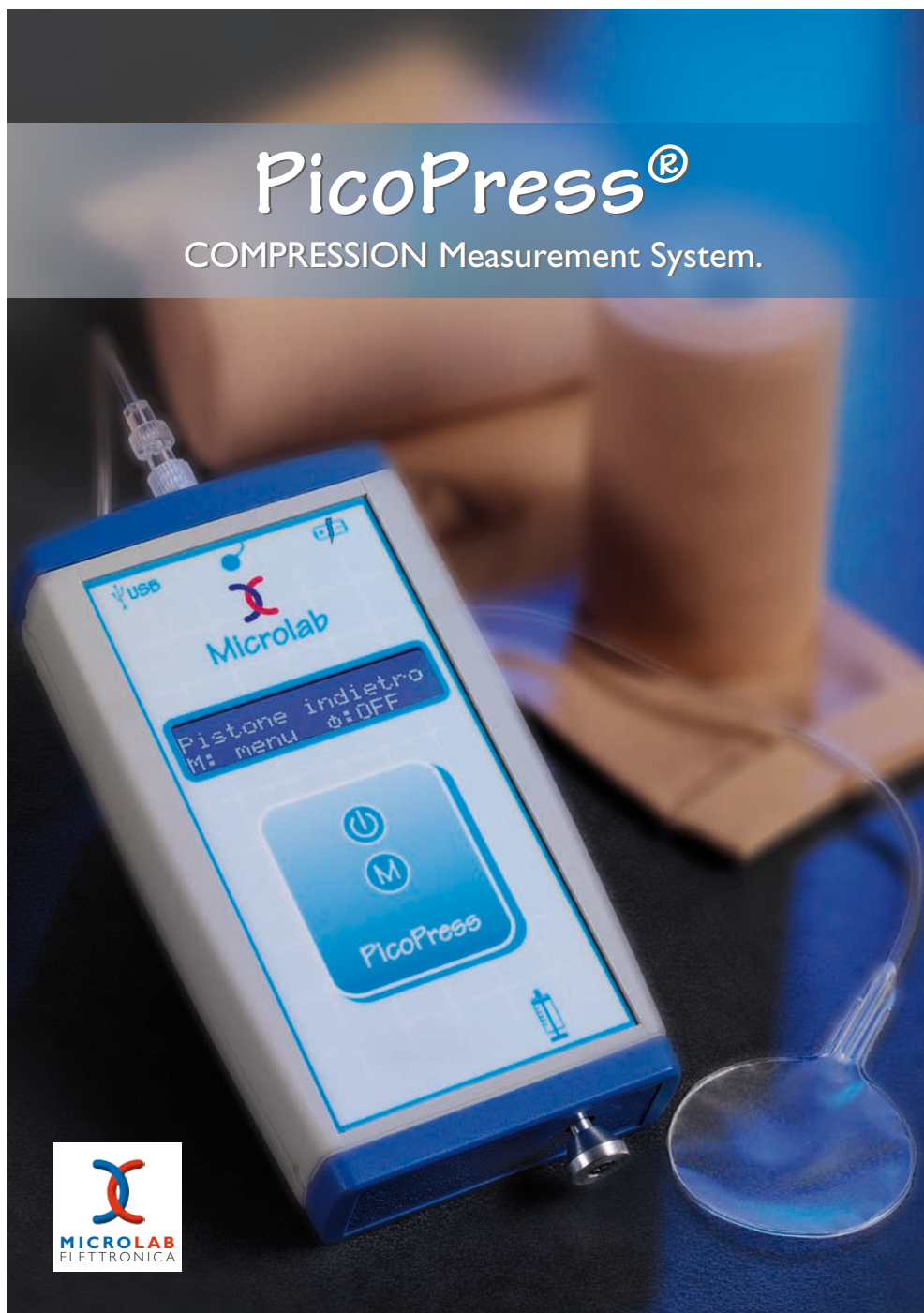


Fig. A.23 Picopress[®] user Manual-1

PicoPress®

Compression Measurement System.



Pressure measurement beneath the elastic stocking and beneath the bandage.

PicoPress Equipment
Carrying case made in soft anti-crush material
Battery charger
Technical manual
Operating software
USB connection cable.



PicoPress® was created to measure the pressure exerted by elastocompression in both static and dynamic conditions. The fact that it is so easy to use (no syringes or stopcock valves) means that it can be utilized by the patient in the comfort of his/her own home. Since the pressure can be constantly checked, patients can be monitored and it is possible to intervene immediately if the levels are abnormal. By monitoring the pressure applied by the bandage, PicoPress® provides replicable, reliable, documentable compression levels. PicoPress® does not need to be calibrated before use. Measurements can be taken repeatedly over a period of time as the sensors can be left under



the bandage. Manufactured in non-allergenic bio-compatible material, it is 200µ thick and highly adaptable to the patient's leg. PicoPress® can memorize as many as 100 readings visible on the display (autonomously without PC) and unloaded on a personal computer using a USB connection. If connected to a PC utilizing the furnished software it is possible to visualize and to record the pressure readings taken during the dynamic tests.



Visualization of the pressure curve during a dynamic test.

PicoPress® runs on high capacity batteries which, besides guaranteeing safety, make its use practically costless.

TECHNICAL CHARACTERISTICS of PicoPress®

Measurement interval:	0 ÷ 189 mm Hg
Buttons:	on / off and menu choice
Display:	16 columns liquid crystals, 2 lines
Resolution:	12 bit analog to digital converter
Languages:	Italian, English, German, French
Supply:	rechargeable internal batteries
Autonomy:	more than 5 hours of continuous use
Body:	crush proof plastic
Weight:	350 grams
Dimensions:	180 x 90 x 32 mm
Insulation:	class II type BF



COMPUTERIZED CARDIOVASCULAR DIAGNOSTIC
Via G. Rossa, 35 - 35020 Ponte S. Nicolò PD - Italy - Telefono e Telefax 049 8968179
www.microlabitalia.it - e-mail: info@microlabitalia.it



Fig. A.24 Picopress® user Manual-2

Appendix B

Pressure distribution results at different locations around the arm simulator, obtained using Oxford Pressure Monitor (OPM)

(The results were obtained from Ph.D. thesis, Shenela Naqvi, 2017, provided by Professor Tilak Dias.)

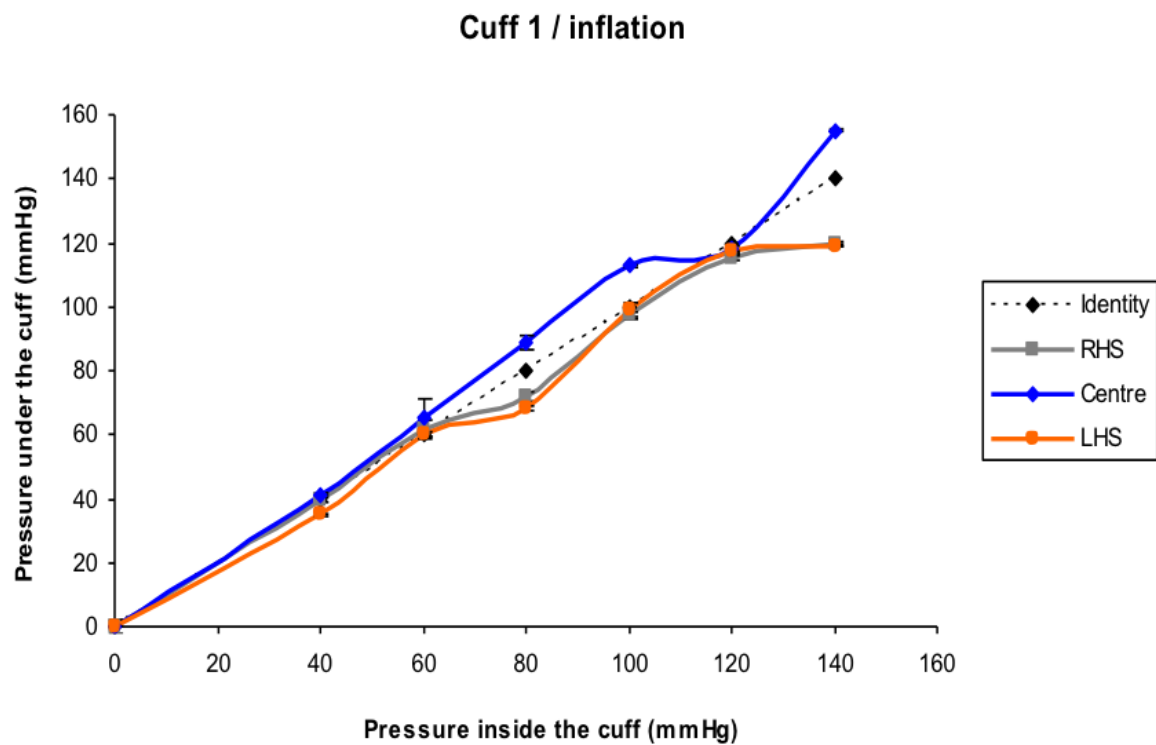


Fig. B.1 Pressure variations underneath the cuff 1 along the length

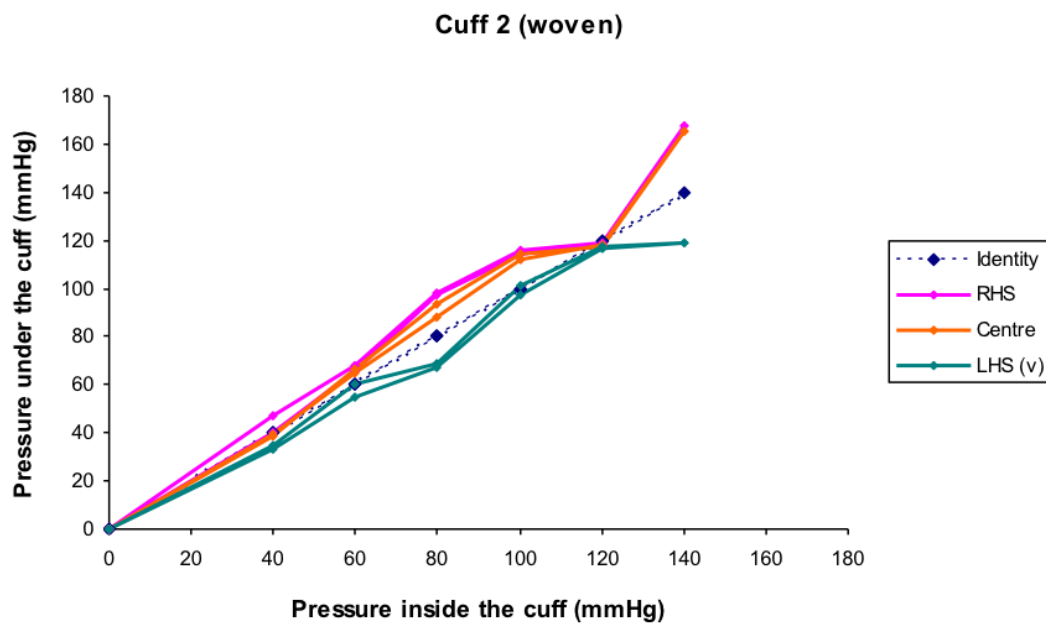


Fig. B.2 Pressure variations underneath the cuff 2 along the length

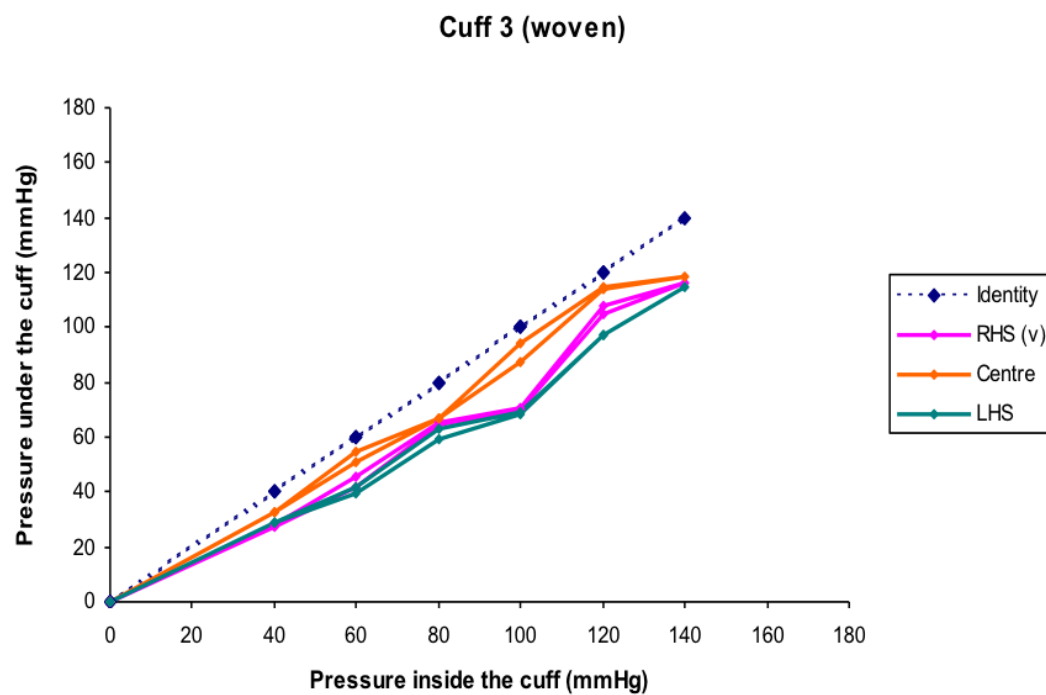


Fig. B.3 Pressure variations underneath the cuff 3 along the length

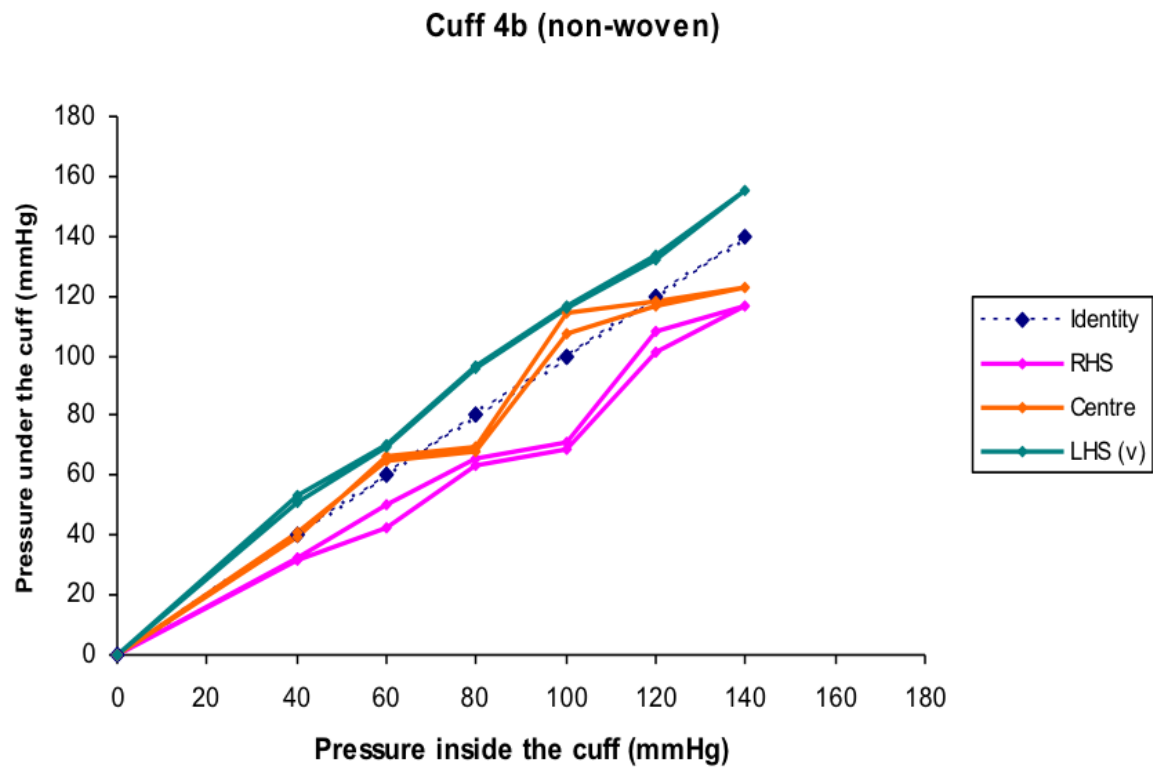


Fig. B.4 Pressure variations underneath the cuff 4 along the length

Pressure distribution results at the interface of cuff-metal cylinder during direct inflation for four different cuff types, data obtained using I-scan pressure measurement system

(Results obtained from Ph.D. thesis, Shenela Naqvi, provided by Professor Tilak Dias)

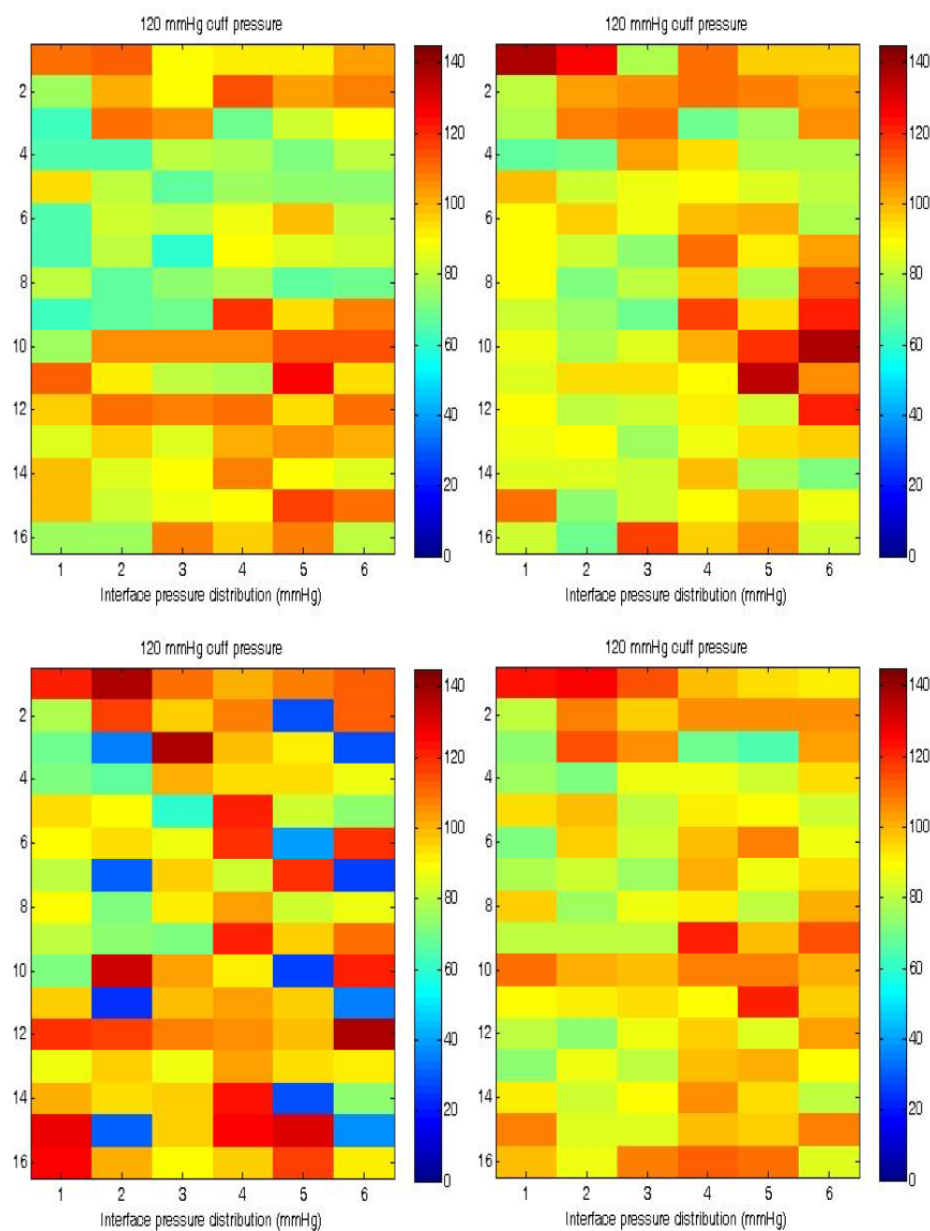


Fig. B.5 Pressure distribution at the interface of cuff-metal cylinder during direct inflation for different cuff types

Results using ANSYS Hyperelastic material curve fitting

ANSYS Hyperelastic curve fitting is a tool was used for estimating material constants for Mooney-Rivlin two parameter model and Yeoh second order model by inputting your experimental data and comparing it to the hyperelastic material models. To perform curve fitting following steps were followed; input experimental data, select a model from one of the provided hyperelastic models, perform a regression analysis, graphically view the curve-fitting results, compare the fits to the experimental data, and write the fitted coefficients to the database as nonlinear data table commands for the subsequent finite element analyses. The calculated model coefficients and goodness of fit parameters for PlatSil® Gel00 30 are listed in the Table B.1.

Table B.1 Model coefficients and fit parameter from ANSYS curve fitting results: PlatSil® Gel00 30

Sample	Mooney Rivlin two parameter model			Yeoh second order model		
	C01 (Pa)	C10 (Pa)	Residue	C10 (Pa)	C20 (Pa)	Residue
S1	23711.57	47225.09	89.01	52211.15	7.32	100.42
S2	18170.42	50797.61	94.83	53119.94	21.64	99.80
S3	19430.66	50925.78	92.92	54329.13	18.26	99.76
S4	16303.41	51916.48	98.80	53774.33	27.66	101.81
S5	18899.90	51992.32	95.20	55101.01	21.04	101.23

Email communication with the ANSYS team:

Technical Details:

Activity Description: Reply to customer

Activity Detail: Hi Gayani,

This is regarding SRs: 1637787791, 1637096707 and 1636758811. I reassigned all these SR's to myself.

I am summarizing the issue to have better understanding.

Curve fitting was done in both ANSYS & MATLAB for the same set of uniaxial test data. Different curve fits were obtained in ANSYS & MATLAB and that leads to differences in the constants obtained for the Yeoh Model.

As a sanity check, I used the constants obtained from in MATLAB, in ANSYS and got similar fit as MATLAB.

The difference can be due to curve fitting methodology. Seems like MATLAB is generating better fit than ANSYS. I will discuss with my colleagues and will file the enhancement request to improve the curve fit

Currently you can use MATLAB obtained constants directly in ANSYS for your analysis.

Hope this will help. Please let me know if you have any questions.

Regards,
Kartikeya

Thank you,
ANSYS Technical Support

Fig. B.6 Screenshot of email communication with ANSYS team

Curve fitting results for uniaxial tension tests for hyperelastic models

Mooney Rivlin two parameter model

Case1: PlatSil® Gel-OO 30 Silicone

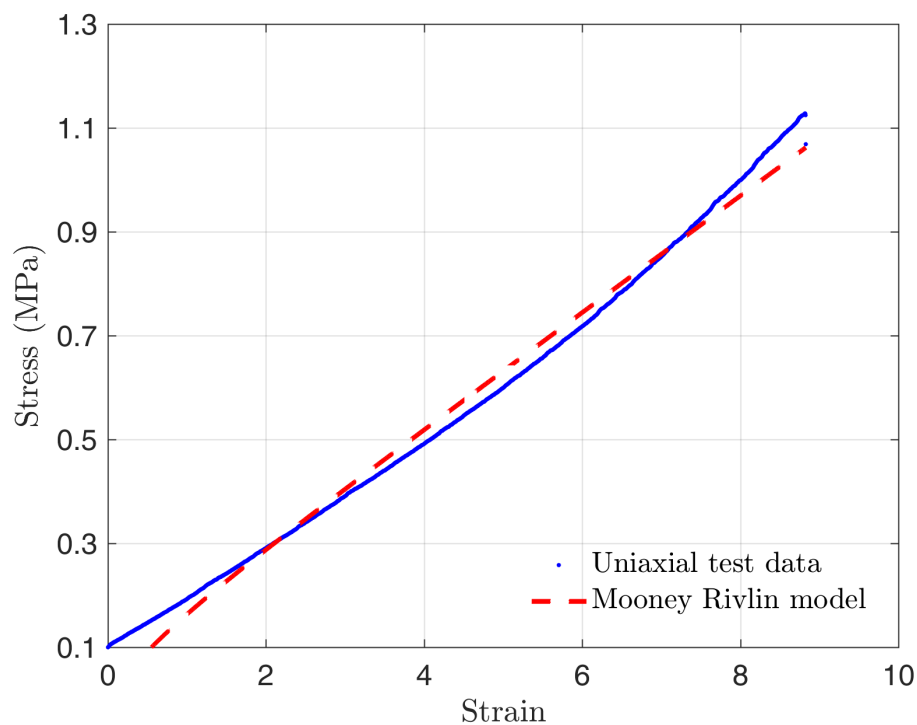


Fig. B.7 Experimental data and Mooney Rivlin two parameter model curve fit for PlatSil® Gel OO 30 -sample 2

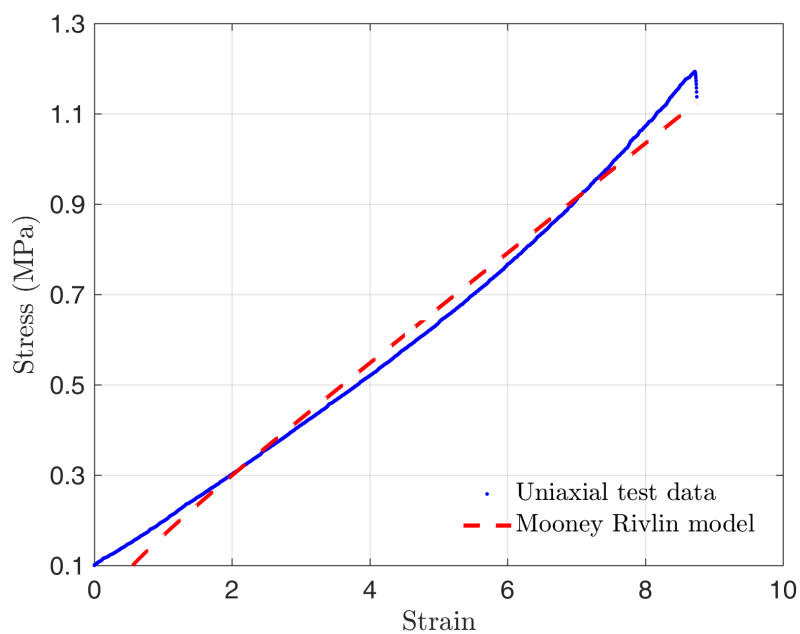


Fig. B.8 Experimental data and Mooney Rivlin two parameter model curve fit for PlatSil® Gel OO 30 -sample 3

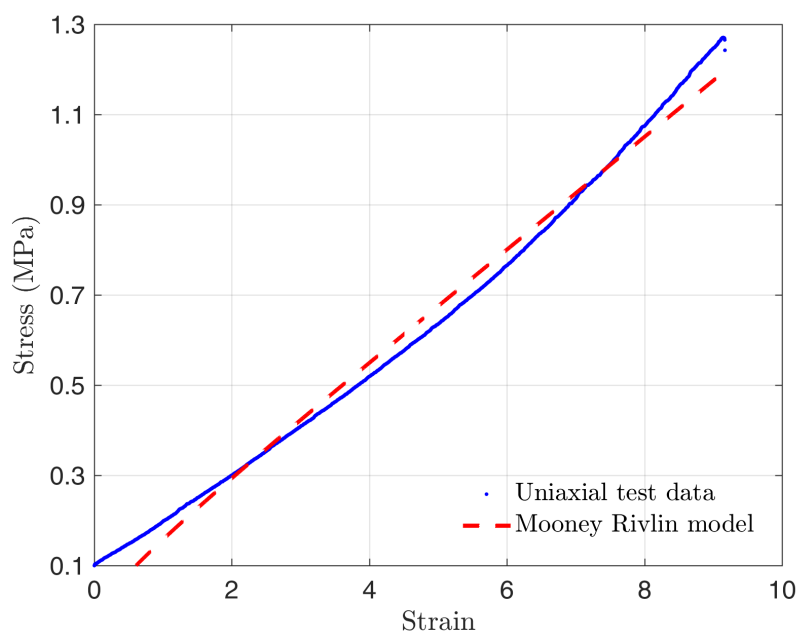


Fig. B.9 Experimental data and Mooney Rivlin two parameter model curve fit for PlatSil® Gel OO 30 -sample 4

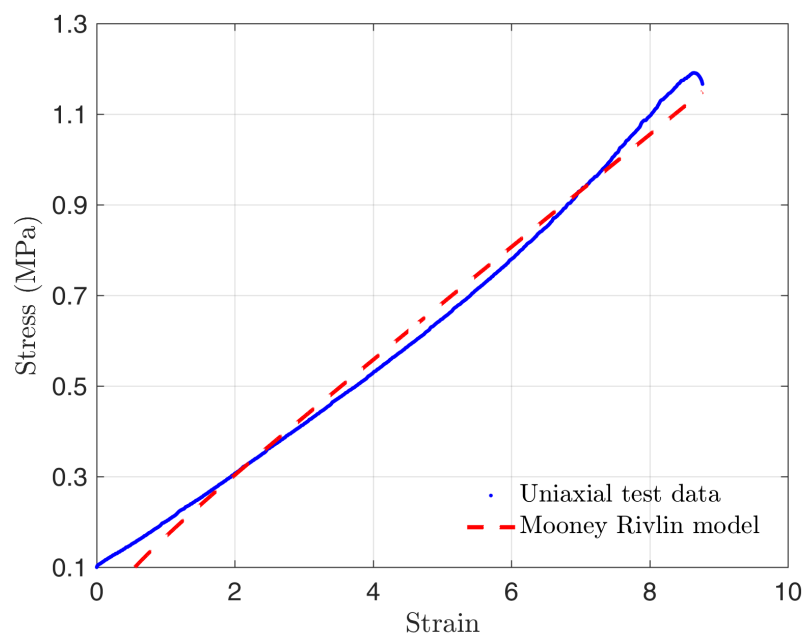


Fig. B.10 Experimental data and Mooney Rivlin two parameter model curve fit for PlatSil® Gel OO 30 -sample 5

Case2: PlatSil® Gel-A10 Silicone

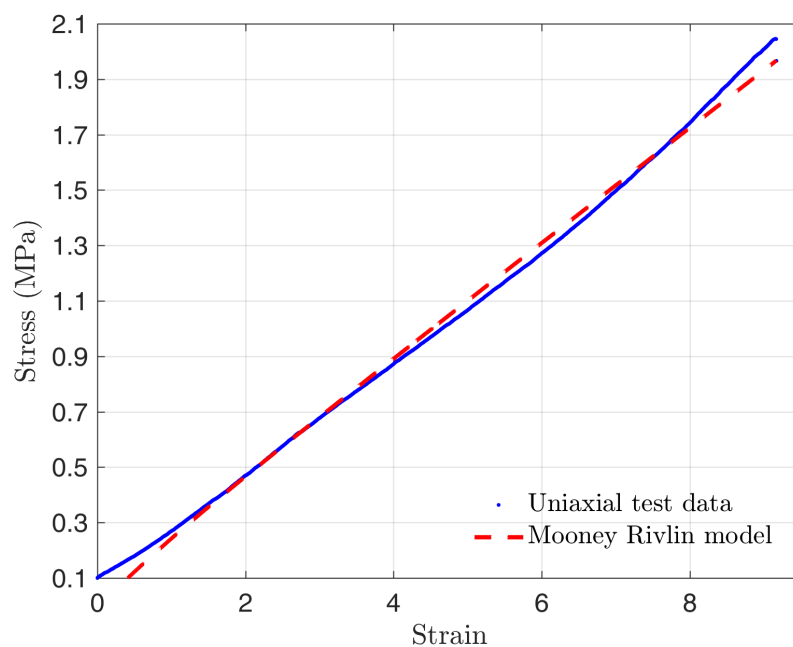


Fig. B.11 Experimental data and Mooney Rivlin two parameter model curve fit for PlatSil® Gel A10-sample 2

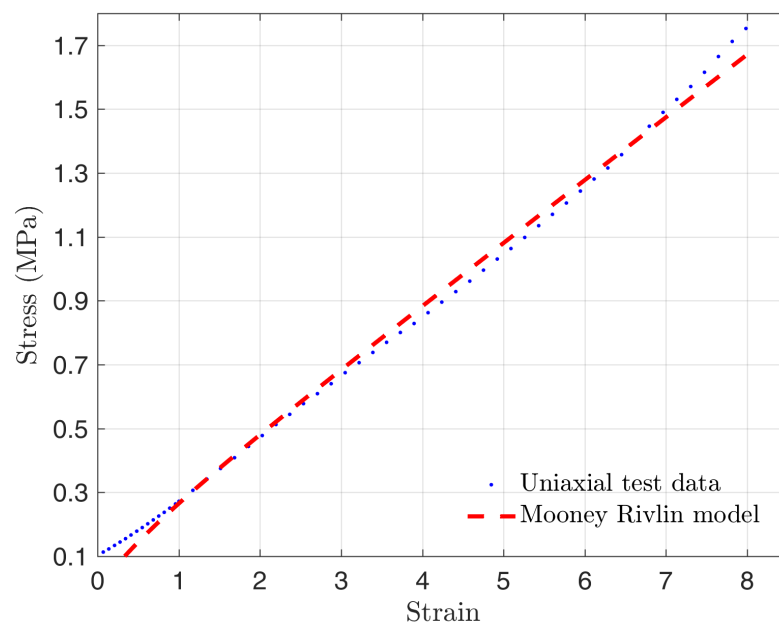


Fig. B.12 Experimental data and Mooney Rivlin two parameter model curve fit for PlatSil® Gel A10-sample 3

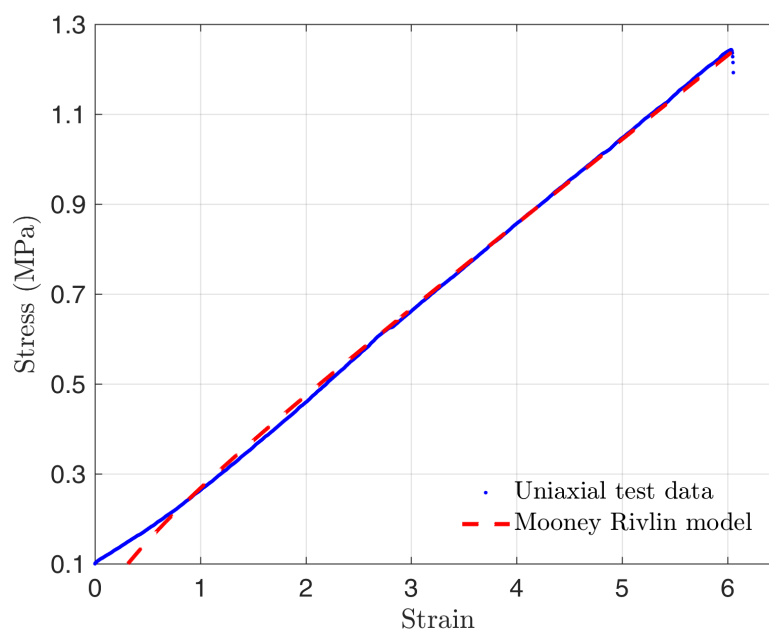


Fig. B.13 Experimental data and Mooney Rivlin two parameter model curve fit for PlatSil® Gel A10-sample 4

Yeoh second order model

Case1: PlatSil® Gel-OO 30 Silicone

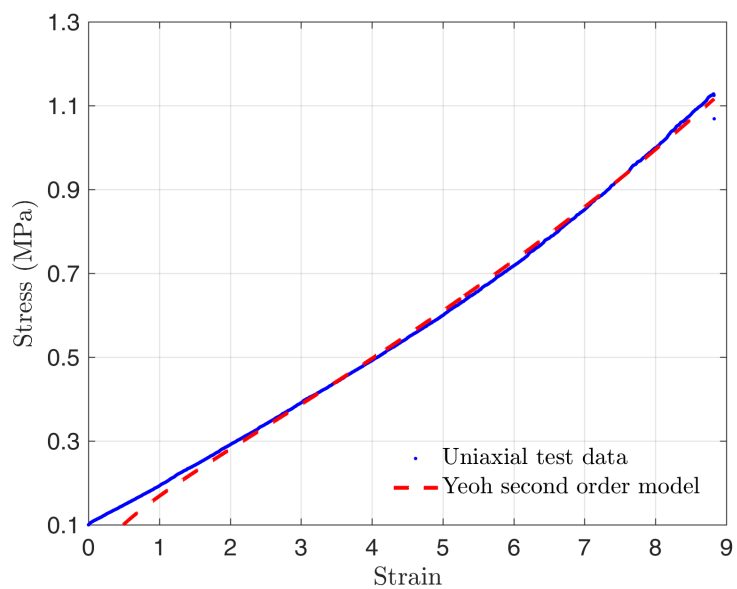


Fig. B.14 Experimental data and Yeoh second order model curve fit results for PlatSil® Gel-OO 30 – sample 2

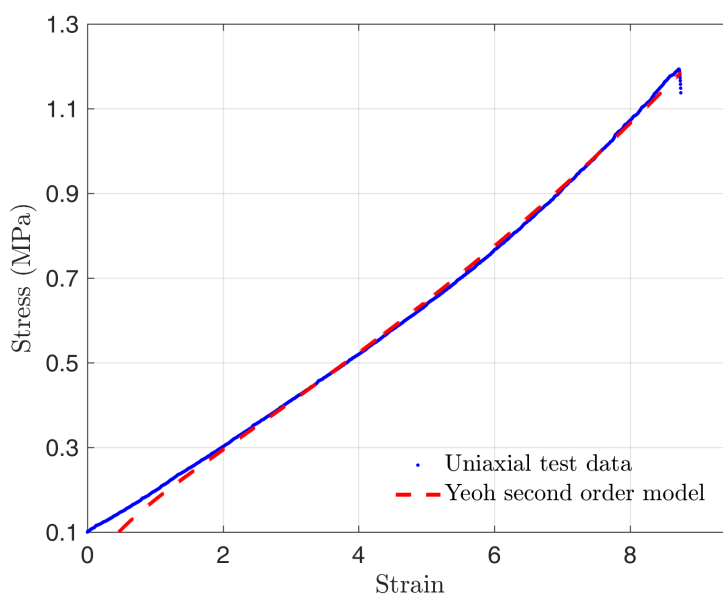


Fig. B.15 Experimental data and Yeoh second order model curve fit results for PlatSil® Gel-OO 30 – sample 3

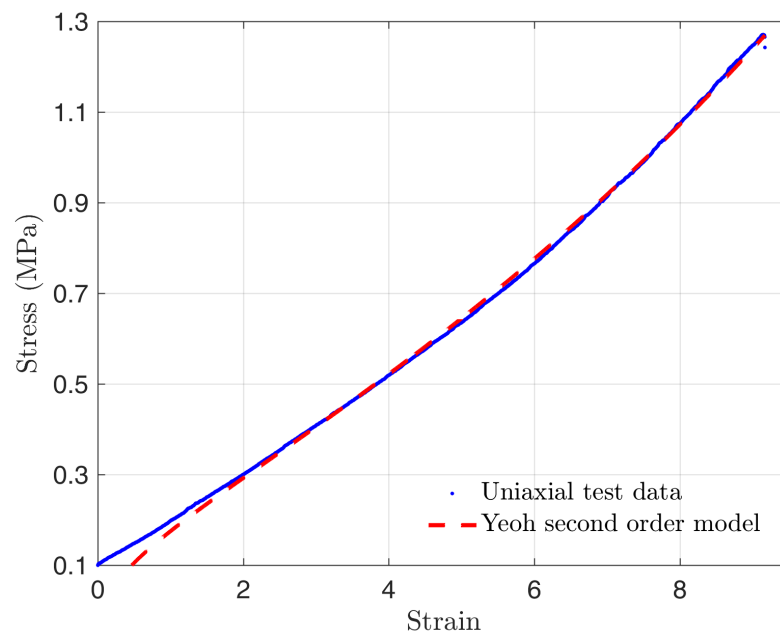


Fig. B.16 Experimental data and Yeoh second order model curve fit results for PlatSil[®] Gel-OO 30 – sample 4

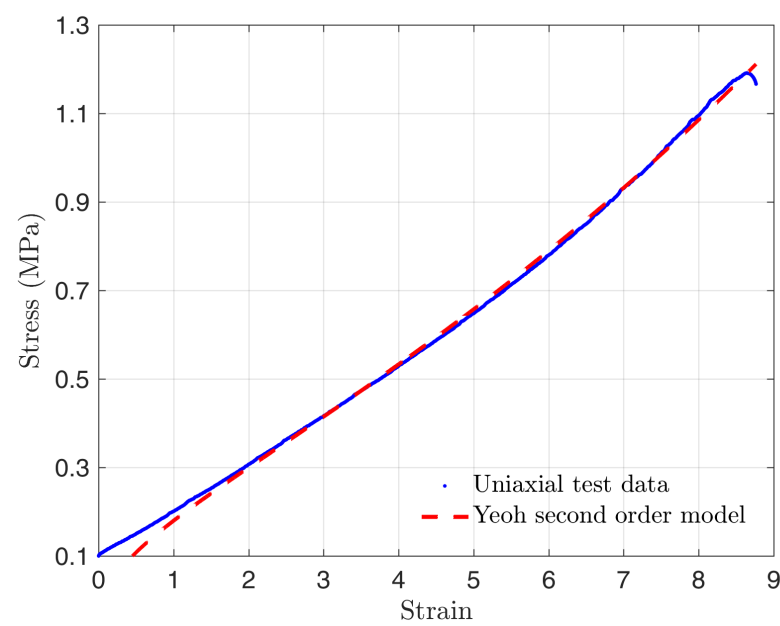


Fig. B.17 Experimental data and Yeoh second order model curve fit results for PlatSil[®] Gel-OO 30 – sample 5

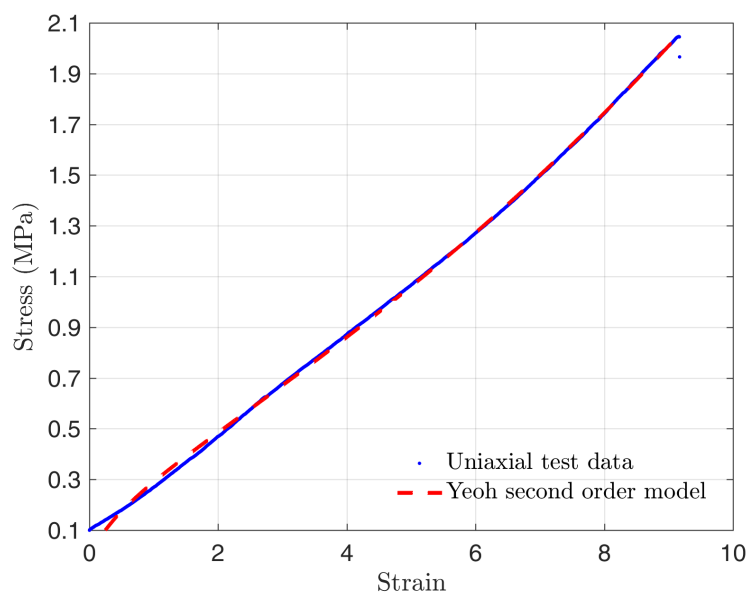
Case2: PlatSil[®] Gel-A10 Silicone

Fig. B.18 Experimental data and Yeoh second order model curve fit results for PlatSil[®] Gel-A10 – sample 2

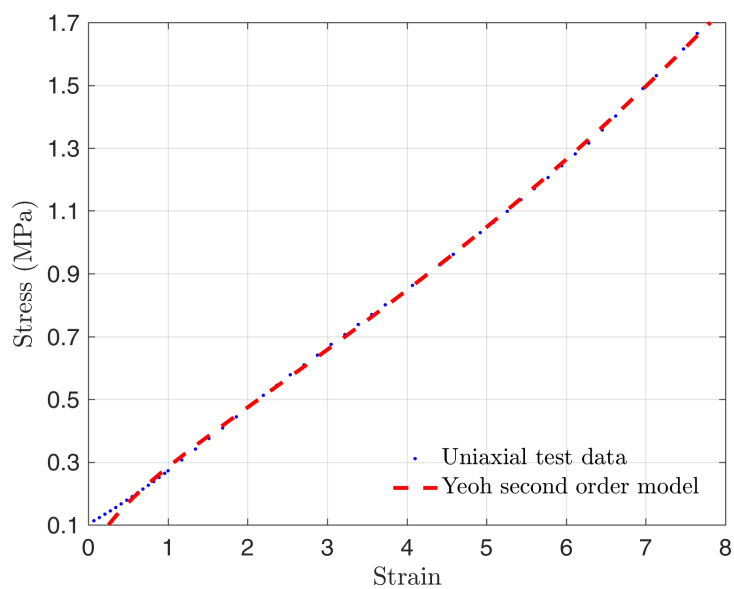


Fig. B.19 Experimental data and Yeoh second order model curve fit results for PlatSil[®] Gel-A10 – sample 3

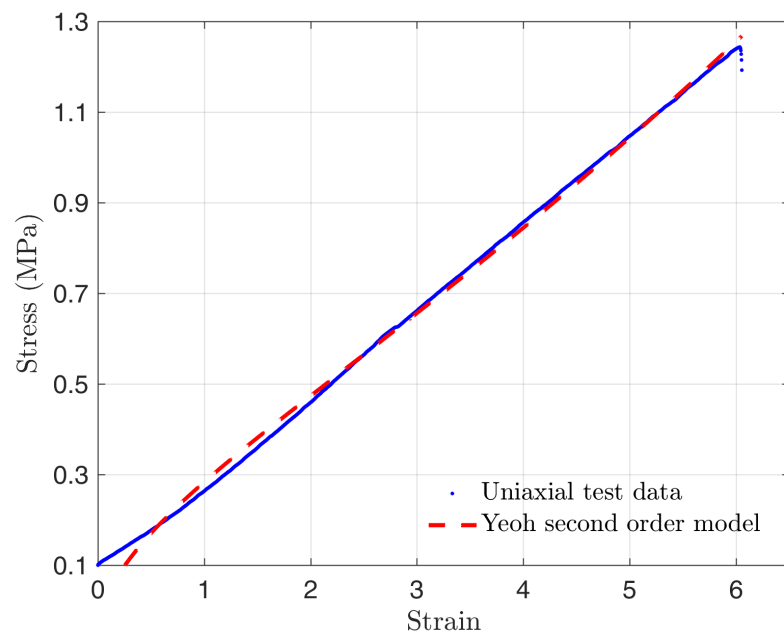


Fig. B.20 Experimental data and Yeoh second order model curve fit results for PlatSil[®] Gel-A10 – sample 4

Uniaxial test results for fabrics

Camouflage fabric

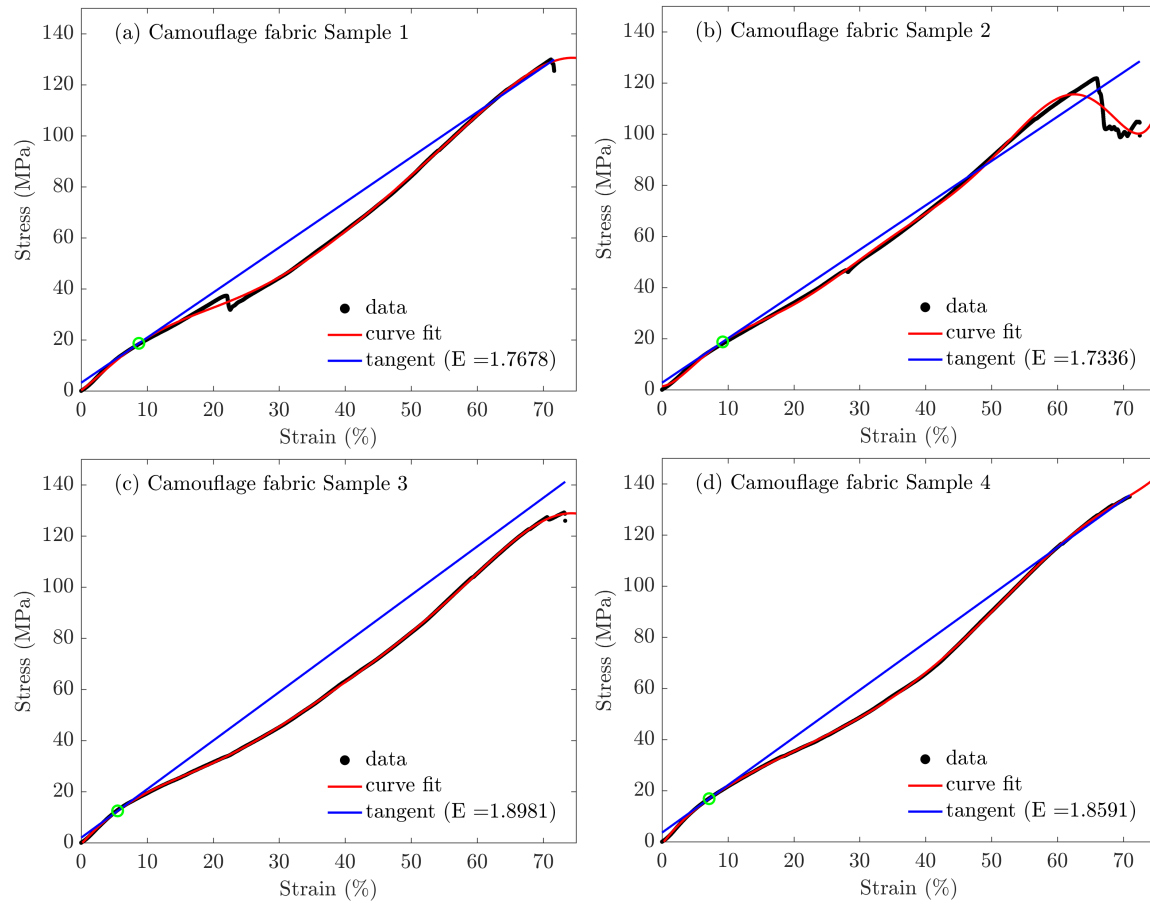


Fig. B.21 Stress strain curves for Camouflage fabric- four samples-warp direction

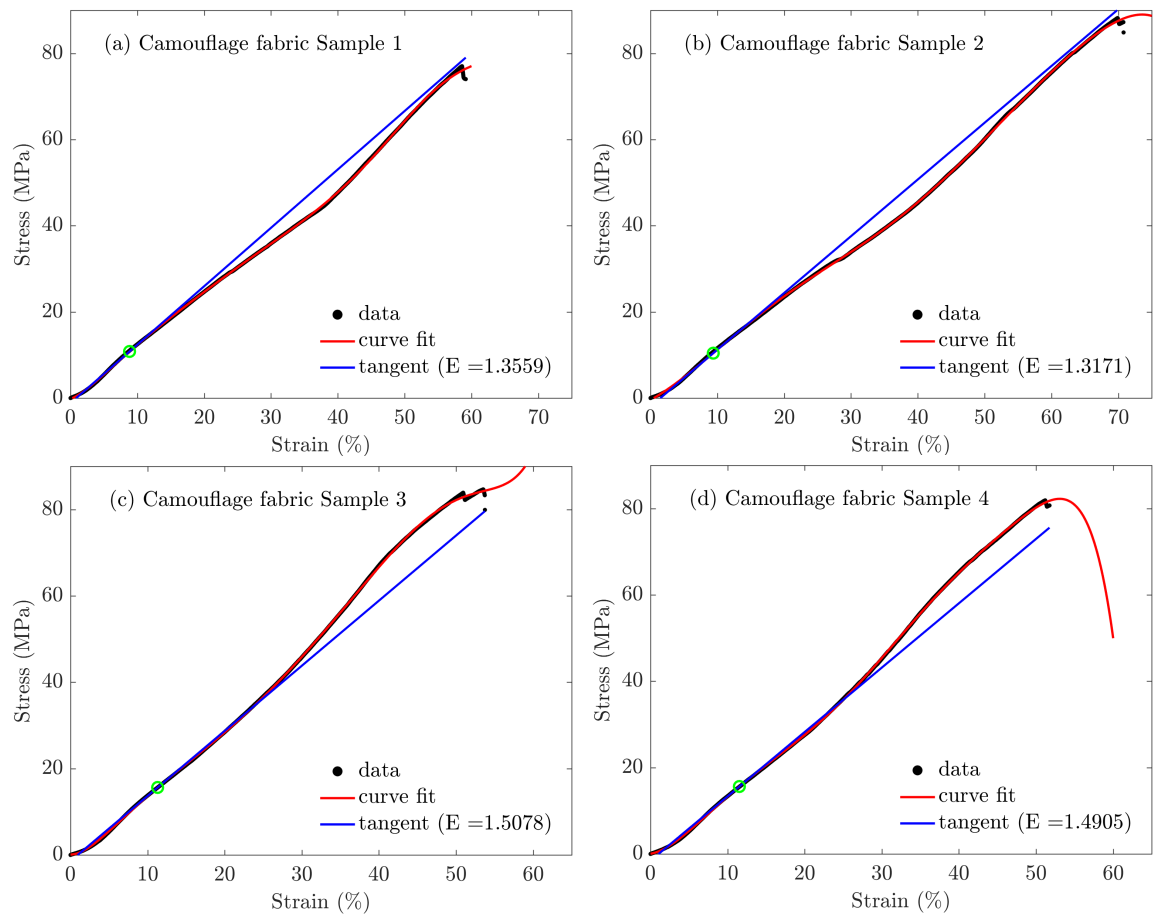


Fig. B.22 Stress strain curves for Camouflage fabric- four samples - weft direction

Greige fabric

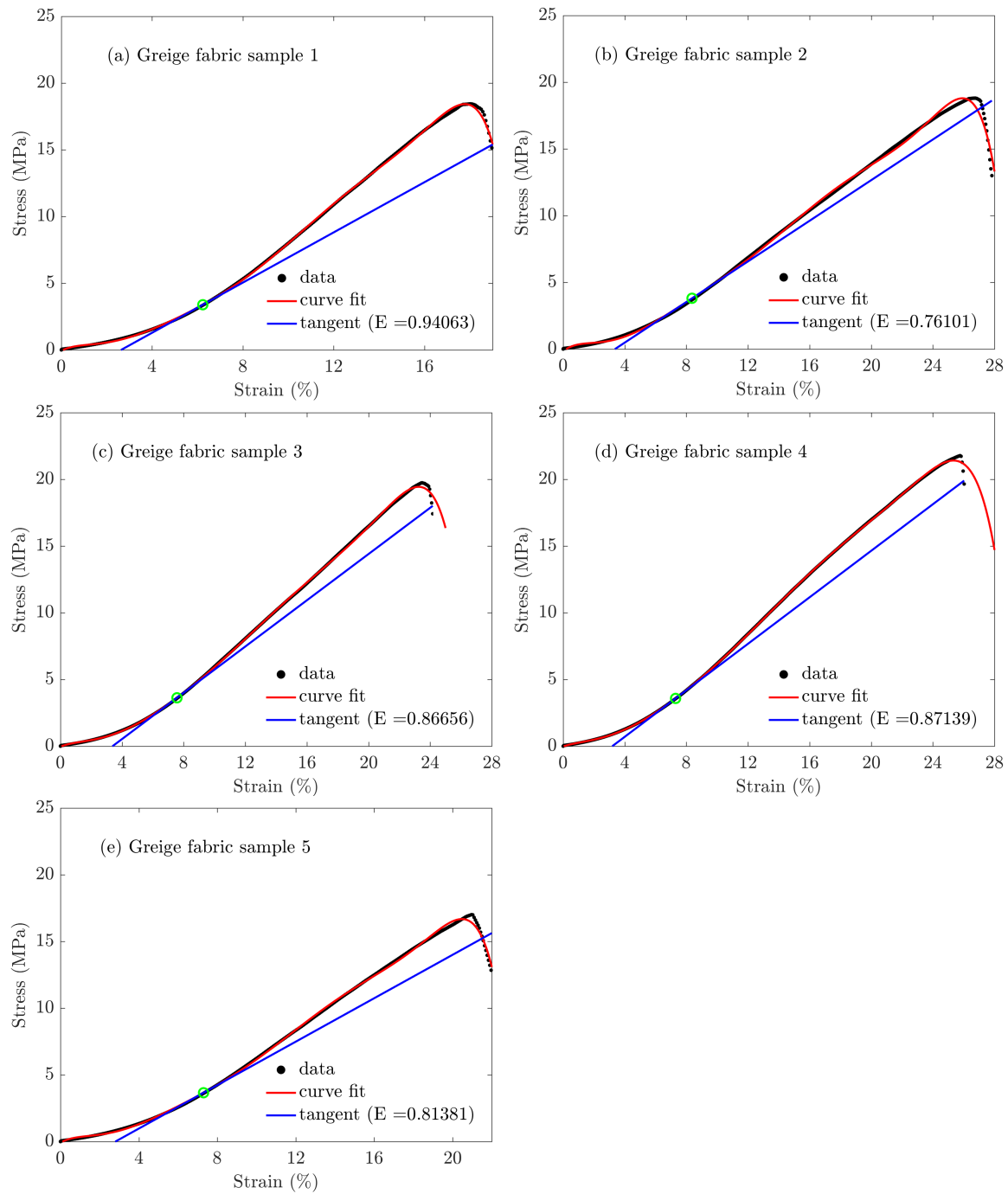


Fig. B.23 Stress strain curves for Greige fabric- four samples-warp direction

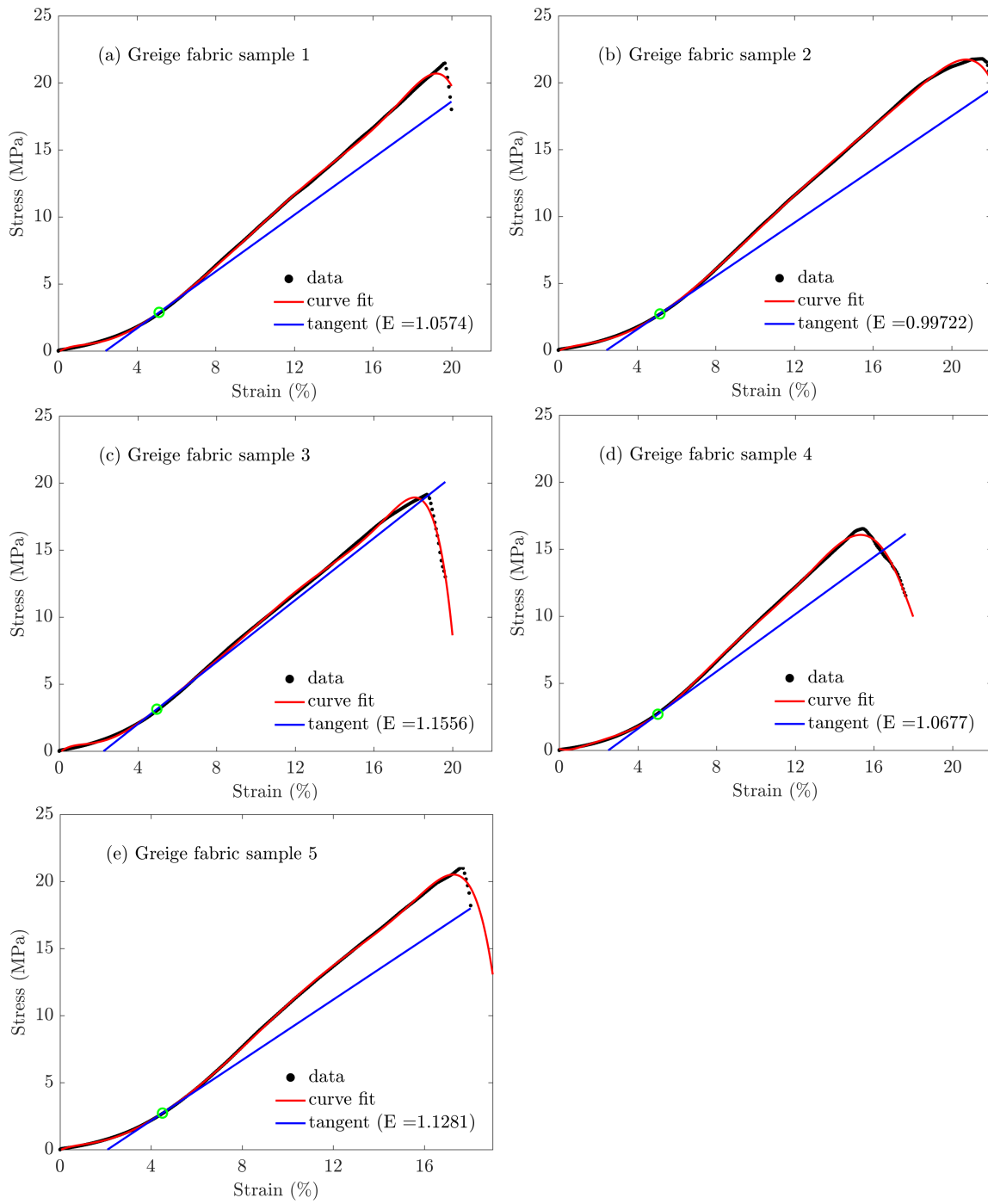


Fig. B.24 Stress strain curves for Greige fabric- four samples - weft direction

User manual for LTS 150 linear transition stage

THORLABS

LTS150 and LTS300
Long Travel Stages

User Guide



Original Instructions

HA0203T

Fig. B.25 User manual for LTS 150 linear transition stage-1

Appendix B Specifications and Accessories

B.1 General Specifications

Parameter	Value
Controller Specifications	
Microsteps per Full Step	2048
Microsteps per Revolution of Motor	409,600 (for 200 step motor)
Motor Drive Voltage	24 V
Motor Drive Power	Up to 25 W (Peak)/ 12.5 W (Avg)
Motor Speeds	Up to 3000 RPM (200 Full Step Motor)
Stage Specifications	
Bidirectional Repeatability	< $\pm 2 \mu\text{m}$
Calibrated Accuracy	< $\pm 5 \mu\text{m}$
Backlash	2 μm
Maximum Acceleration	50 mm/sec ² Horizontal, 5 mm/sec ² Vertical
Maximum Horiz Velocity	50 mm/s
Maximum Vertical Velocity	3 mm/s
Velocity Stability	$\pm 1 \text{ mm/sec}$
Max Load Capacity	15 kg Horizontal, 4 kg Vertical
Recommended Horizontal Load Capacity	< 12 kg
Minimum Achievable Incremental Movement	0.1 μm
Minimum Repeatable Incremental Movement	4 μm
Absolute On-Axis Accuracy	LTS150 20 μm LTS300 47 μm
Maximum Percentage Accuracy	LTS150 0.13 % LTS300 0.12 %
Home Location Accuracy	$\pm 0.6 \mu\text{m}$
Pitch	LTS150 0.016° LTS300 0.022°
Yaw	LTS150 0.05° LTS300 0.06°
Construction	Aluminum with precision, recirculating linear bearings
Weight	LTS150 1.9 kg (4.8 lb) LTS300 2.5 kg (5.5 lb)

Fig. B.26 User manual for LTS 150 linear transition stage-2

B.2 Motor Specifications

Parameter	Value
Step Angle	1.8°
Step Accuracy	5%
Rated Phase Current	0.85 A
Phase Resistance	5.4 Ohms
Phase Inductance	5.6 mH
Holding Torque	20 N.cm
Detent Torque	2.0 N.cm
Operating Temperature	-20°C to +40°C (Motor Specification Only)

B.3 Parts List

Part Number	Description
LTS150 and LTS150/M	Long Travel Stage with 150 mm travel
LTS300 and LTS300/M	Long Travel Stage with 300 mm travel
LTSP1 and LTSP1/M	XY Mounting Adapter Plate
LTSP2 and LTSP2/M	Vertical (Z-axis) Mounting Plate for LTS150
LTSP3 and LTSP3/M	Vertical (Z-axis) Mounting Plate for LTS300
HA0203T	Handbook

Fig. B.27 User manual for LTS 150 linear transition stage-3

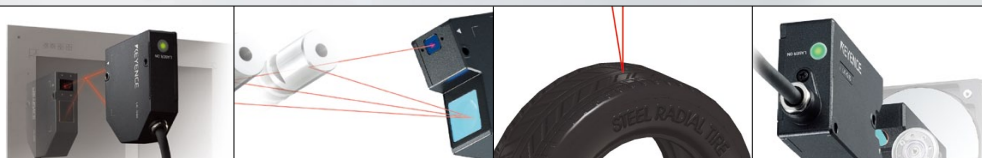
User manual for LKG laser displacement sensor



CCD Laser Displacement Sensor

GENERAL CATALOG

LK-G Series



Super Precision/High Accuracy/Long Distance
Innovative CCD Laser Displacement Sensors

High speed sampling

50 kHz

High accuracy

$\pm 0.02\%$

High repeatability

0.01 μm

Long range measurement

Max 1,000 mm (39.37")

Fig. B.28 User manual for LKG laser displacement sensor-1

LK-G Series Lineup

Overwhelming specifications achieve higher accuracy and solve previously impossible applications. Cutting-edge technology and a wide array of sensor heads offer stunning performance for any application.

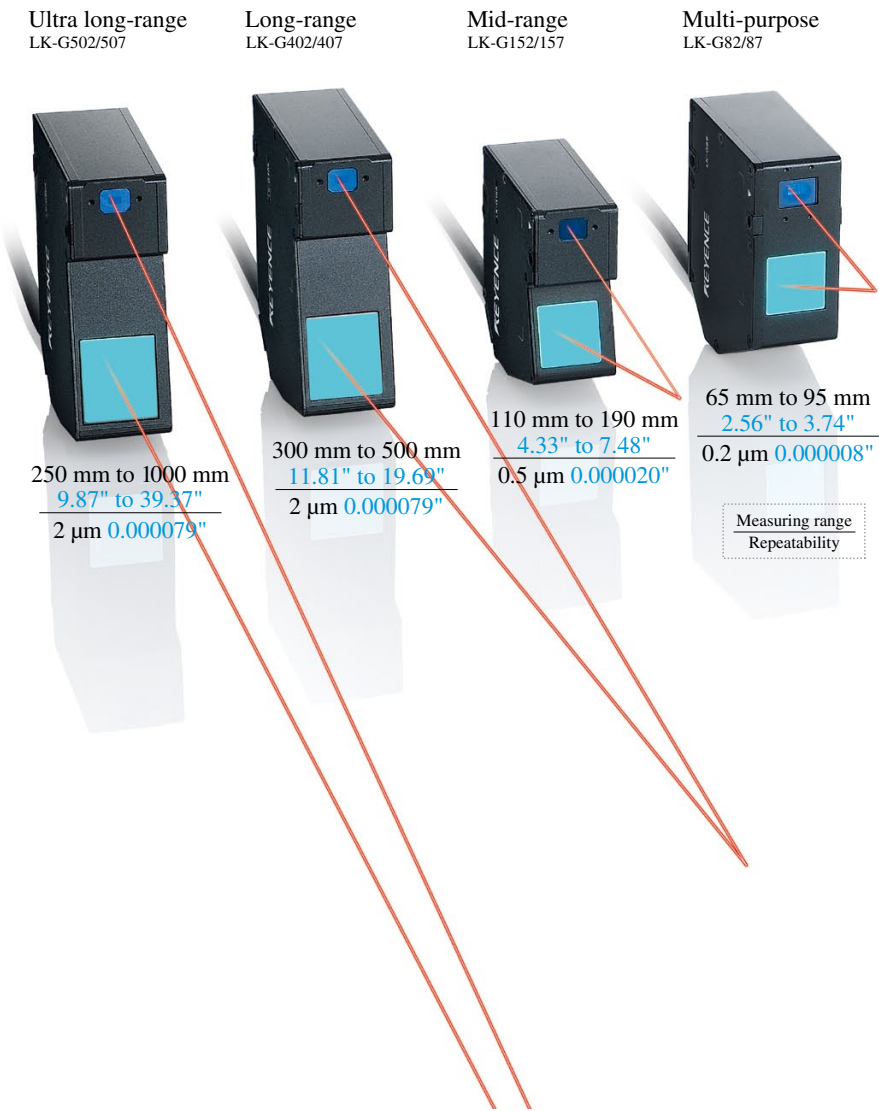
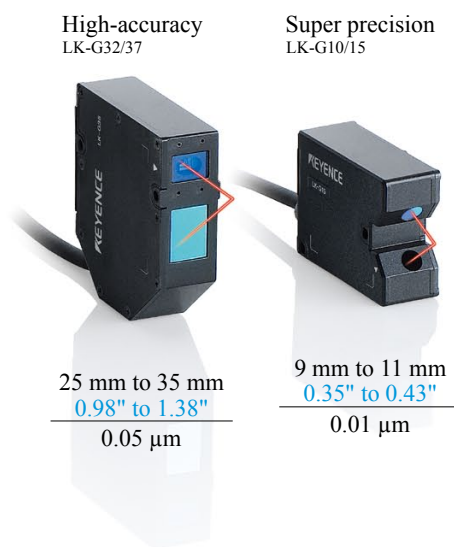


Fig. B.29 User manual for LKG laser displacement sensor-2



Multifunction controller with
built-in display and data storage



► P.6-7

Advanced Specifications

Unmatched technology has achieved specifications that are the best in the industry.



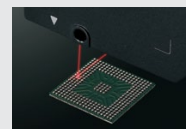
High speed sampling

50 kHz



High accuracy

$\pm 0.02\%$



High repeatability

0.01 μm

► P.8-9

Newly-developed Algorithms

Newly-developed algorithms ensure highly accurate measurement of targets that were difficult with conventional detection methods.



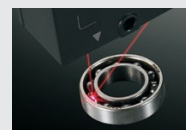
RPD algorithm

Translucent targets



Multi-ABLE control

Transparent targets

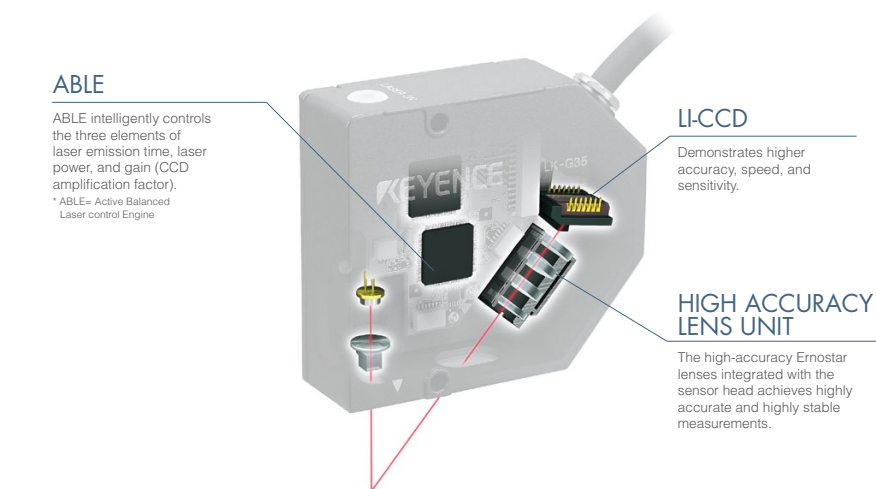


MRC algorithm

Multiple reflections

Fig. B.30 User manual for LKG laser displacement sensor-3

Advanced technology for high performance

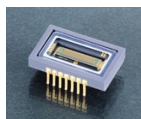
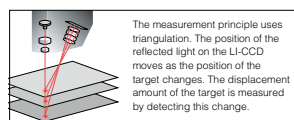


LI-CCD*

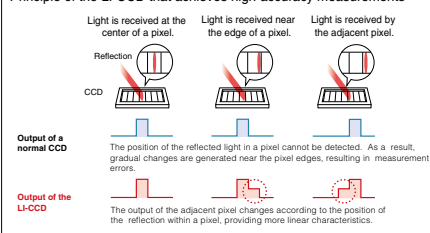
Errors in pixel edges are reduced to achieve accuracy that is two times greater than conventional models.

Since a CCD has digital output characteristics for each pixel, the errors caused by gradual outputs generated at the edge of pixels was a barrier to higher accuracy. As a countermeasure, KEYENCE has developed an LI-CCD that outputs the position of reflected light in a pixel, achieving excellent accuracy that is two times higher than conventional models. In addition, the dedicated design of the sensor has achieved a speed that is 25 times faster and a sensitivity 10 times better than conventional models.

* LI-CCD= Linearized CCD



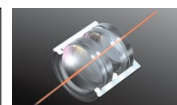
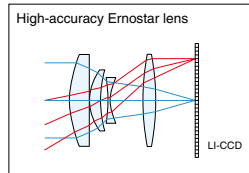
Principle of the LI-CCD that achieves high-accuracy measurements



HIGH ACCURACY LENS UNIT

Reducing errors caused by aberrations

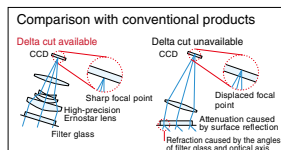
KEYENCE has designed a new light-receiving unit for concentrating reflected light onto the LI-CCD. The newly-developed, high-accuracy Ernstar lens drastically reduce spot distortion caused by aberrations. In addition, a special die-cast housing integrating the sensor head with the lenses is employed, achieving excellent rigidity.



The optical system is composed of four lenses characterized by very small aberrations. With its excellent imaging performance, light entering from various angles can be concentrated to a single point.

DELTA CUT TECHNOLOGY*

Accurate reception of reflected light from a long distance is the key to high precision. KEYENCE has reviewed the cabinet design and developed a delta cut technology that reduces reflection on a filter glass surface.

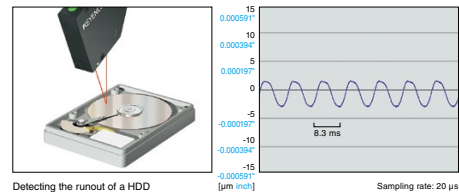


*LK-G157/G407/G507 Series

Fig. B.31 User manual for LKG laser displacement sensor-4

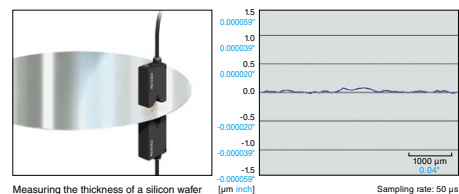
ULTRA-HIGH SPEED SAMPLING OF 50 kHz

The LI-CCD features high-speed sampling rate 25 times faster than conventional models. High-speed digital processing of signals from the LI-CCD is performed by a special waveform-processor (Digital Signal Processor), satisfying both high-speed and high-accuracy measurements. Targets traveling, rotating, or vibrating at high speed can be measured reliably.



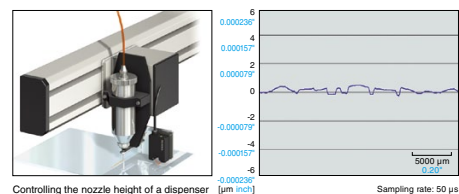
HIGH-ACCURACY OF $\pm 0.02\%$

KEYENCE has redesigned the optical system in order to achieve high-accuracy measurement. Incorporating Ernst optical systems with a LI-CCD produces excellent linearity characteristics. It precisely focuses/detects reflection from targets to provide almost double the accuracy of conventional models. Thus, the LK-G Series is designed for product miniaturization and high-accuracy measurement.



HIGH REPEATABILITY OF 0.01 μ m

The CPU, which is integrated in the sensor head, digitizes all signals sent to the controller, dramatically reducing disturbance noise. A highly rigid die-cast body is used to reduce deviations caused by temperature changes, and a LI-CCD with 10 times better sensitivity than conventional models is used to reduce signal noise. These design revisions, targeting high accuracy applications, have successfully produced a repeatability that is 20 times better than conventional models.



LONG RANGE MEASUREMENT OF 1000 mm (39.37")

Delta cut technology realizes high-accuracy measurement at a long detecting distance that is difficult with conventional models. Seven sensor heads meet a surprisingly wide measuring range from 9 mm 0.98" to 1000 mm 39.37" and a broad range of needs.

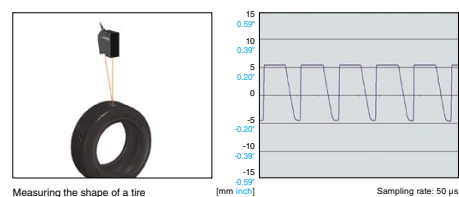


Fig. B.32 User manual for LKG laser displacement sensor-5

The ABLE function, along with newly developed measurement algorithms, provide measurement of diffuse, transparent, or translucent targets.



ABLE *

Sensing the surface conditions to control laser light intensity to the optimal level

ABLE technology senses the surface of a target and adjusts the intensity of laser light to an optimal level. ABLE intelligently controls the three elements of laser emission time, laser power, and gain (CCD amplification factor), achieving a wide adjustment range of light intensity that is up to 90 times wider than conventional models. In addition, speed is 120 times faster than conventional methods.

*ABLE=Active Balanced Laser control Engine.

Up to 90 times the adjustment range of conventional models

	Laser power	Emission time	Adjustment range
LK-G Series	8x	1662x (0.6 to 997 μs)	13296x
Conventional model	—	150x (3.2 to 480 μs)	150x

Real-time control at 120 times the speed of conventional models

	Sampling rate	Adjustment speed
LK-G Series	20 μs	0.06 ms
Conventional model	512 μs	7 ms

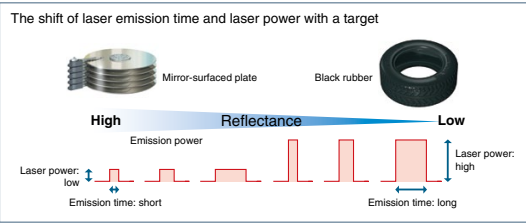


Fig. B.33 User manual for LKG laser displacement sensor-6

Multifunction controller with built-in display and data storage

Various functions with advanced specifications and unparalleled detection performance are concentrated into a compact controller.



COMPACT ALL-IN-ONE CONTROLLER SUPPORTS 2-HEAD CONNECTION

2 Ch	Large-size 2-color LED	Measurement	Judgment	Statistic
------	------------------------	-------------	----------	-----------

Two channels are available for sensor head connection, display and judgment. In addition, seven measurement modes and statistic functions are featured to support a wide range of measurement requirements.



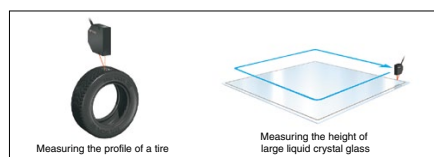
Easy-to-operate, simple setting
The current settings are displayed on a user-friendly display, which allows any user to configure the settings easily.



Featuring a large, easy-to-see 2-color LED
The ECO mode is featured to turn off the display when visual monitoring is not required.

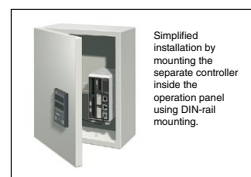
DATA STORAGE FUNCTION

65,000-point memory is integrated internally in order to store the 50 kHz ultra-high-speed sampling data. Sometimes it is necessary to enhance the tact time in obtaining data from a target traveling at high speed or to mount the unit to a device. In this case, high-speed processing of all data items is enabled by temporarily storing the data to the internal memory and retrieving the data during the period before the next measurement.



SEPARATE INSTALLATION OF THE DISPLAY AND OPERATION PANEL

The display (LK-GD500) and operation unit can be mounted on the outside of a control panel and the separate controller (LK-G3001) can be mounted inside the control panel using a DIN-rail. The separate controller (LK-G3001) can also be operated without a display*. A system with multiple channels can now be constructed at low cost.



* LK-GD500 or LK-Navigator software is required for setup.

MULTIPLE I/O REQUIRES NO OPTICAL PARTS

USB	RS-232C	Binary	I/O	Analog
-----	---------	--------	-----	--------

Five types of I/O including USB are available as standard. A wide range of needs are supported, from data gathering with a PC using USB to high-speed digital control with a PLC using binary outputs. High-speed output can be performed at 50 kHz. (Excluding the RS-232C)

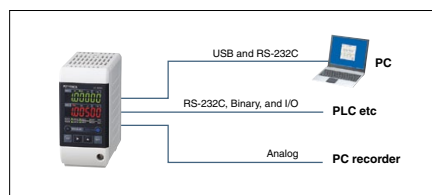
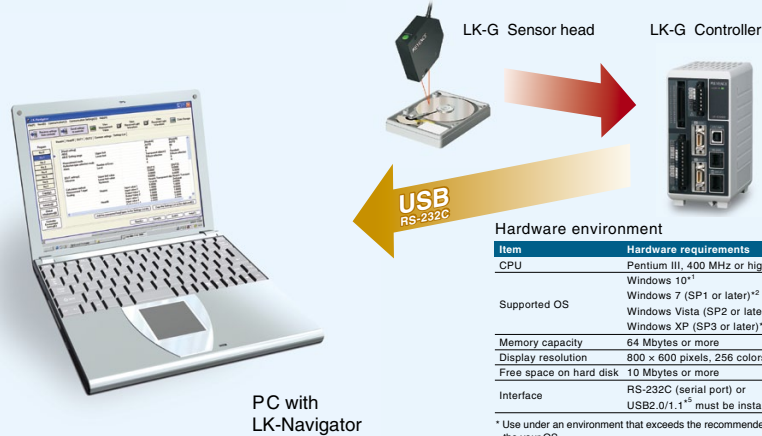


Fig. B.34 User manual for LKG laser displacement sensor-7

Simple setting and analysis on a PC

Setting support software LK-Navigator

LK-Navigator supports optimal setting of the LK-G and data gathering from a PC. Settings can be made via USB.



* Use under an environment that exceeds the recommended environment of the your OS.
*¹ Home, Pro, and Enterprise editions are supported.
*² Home Premium, Professional, and Ultimate editions are supported.
*³ Ultimate, Business, Home Premium, and Home Basic editions are supported.
*⁴ Professional and Home editions are supported.
*⁵ Connection through a USB hub is not included in the guarantee.

EASILY PROGRAM OPTIMAL SETTINGS

Simply follow the menu to select the settings. The navigator, with illustrations and explanations, allows any user to make settings easily.

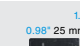
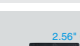


12

■ Quick set-up output ■ Quick set-up calculation between sensors

Fig. B.35 User manual for LKG laser displacement sensor-8

Selection guide

Sensor Heads

TYPE		MODEL	MEASURING RANGE	REPEATABILITY	SPOT DIAMETER
Super Precision	Small spot	LK-G10	 Measuring range $0.39^{\circ} \pm 0.04^{\circ}$ 10±1 mm	0.01 μm	$\phi 0.0008^{\circ}$ ø20 μm
	Wide beam	LK-G15			$0.0008^{\circ} \times 0.0197^{\circ}$ 20 × 500 μm
High Accuracy	Small spot	LK-G32	 Measuring range $1.18^{\circ} \pm 0.2^{\circ}$ 30±5 mm	0.05 μm	$\phi 0.0012^{\circ}$ ø30 μm
	Wide beam	LK-G37			$0.0012^{\circ} \times 0.0335^{\circ}$ 30 × 850 μm
Multi-Purpose	Small spot	LK-G82	 Measuring range $3.15^{\circ} \pm 0.59^{\circ}$ 80±15 mm	0.000008* 0.2 μm	$\phi 0.0028^{\circ}$ ø70 μm
	Wide beam	LK-G87			$0.0028^{\circ} \times 0.0433^{\circ}$ 70 × 1100 μm
Long Distance	Small spot	LK-G152	 Measuring range $5.91^{\circ} \pm 1.57^{\circ}$ 150±40 mm	0.000020* 0.5 μm	$\phi 0.0047^{\circ}$ ø120 μm
	Wide beam	LK-G157			$0.0047^{\circ} \times 0.0669^{\circ}$ 120 × 1700 μm
High-speed Long Distance	Small spot	LK-G402	 Measuring range $15.75^{\circ} \pm 3.94^{\circ}$ 400±100 mm	0.000079* 2 μm	$\phi 0.0114^{\circ}$ ø290 μm
	Wide beam	LK-G407			$0.0114^{\circ} \times 0.3268^{\circ}$ 290 × 8300 μm
Ultra Long Distance	Small spot	LK-G502	 Measuring range $19.69^{\circ} \pm 8.84^{\circ}$ 500±250/+500 mm	0.000079* 2 μm	$\phi 0.0118^{\circ}$ ø300 μm
	Wide beam	LK-G507			$0.0118^{\circ} \times 0.3740^{\circ}$ 300 × 9500 μm

Controllers

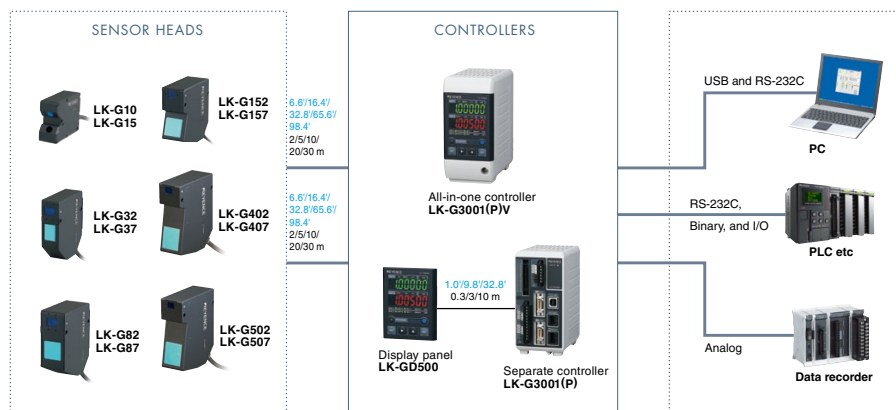
TYPE	OUTPUT	
	NPN	PNP
ALL-in-one	LK-G3001V	LK-G3001PV
Separate Display	LK-G3001	LK-G3001P

Dimming filter

For the LK-G3x/LK-G8x
LK-F1
For the LK-G15x/LK-G40x/LK-G50x
LK-F2

Fig. B.36 User manual for LKG laser displacement sensor-9

System



Specifications



Controllers

Type	All-in-one model		Separate monitor model ¹
Model	NPN	PNP	LK-G3001/LK-GD500
			LK-G3001P/LK-GD500
Display	All LK-G sensor heads are compatible		
	Maximum of 2 units		
	0.01 μm		
	±9,999.99 mm to ±9,999.99 μm (Selectable from six levels)		
Terminal block	10 times/sec		
	±10 V × 2 outputs, output impedance: 100 Ω		
	4 to 20 mA × 2 outputs, maximum load resistance: 350 Ω		
	For OUT1, non-voltage or voltage input ³		
Expansion connector	Non-voltage input ³		
	For OUT1, NPN or PNP open-collector output ²		
	For OUT1, NPN or PNP open-collector output ² (N.C.)		
	For OUT2, non-voltage or voltage input ³		
Binary	Non-voltage or voltage input ³ × 3 inputs		
	For Head A/Head B, non-voltage or voltage input ³		
	For OUT2, NPN or PNP open-collector output ²		
	For OUT2, NPN or PNP open-collector output ² (N.C.)		
RS-232C interface	Measured data output (21 bits), OUT1/OUT2 selectable, NPN or PNP open-collector output ²		
	NPN or PNP open-collector output ²		
	NPN or PNP open-collector output ²		
	Non-voltage or voltage input ³		
USB interface			
Measured data output and control input/output (Maximum baud rate: 115,200 bps, selectable)			
In conformity with USB Revision 2.0 Full speed (USB1.1 compatible)			
2 OUT simultaneous measurement, Operation, Averaging, Filter, Calibration, Measurement, AUTO ZERO, Sampling frequency setting, Mutual interference prevention, Data storage, 8-program memory, ECO mode, ABLE setting, Target setting, ABLE tuning, Selection of measurement surface of transparent target, Connection of setting support software, Selectable head-mounting, etc.			
24 VDC ±10%, Ripple: 10% (P to P) or less			
500 mA or less with 1 head/600 mA or less with 2 heads			
0 to 50°C 32 to 122°F, No condensation			
35 to 85%, No condensation			
Approx. 480 g (L/G3001V/G3001PV), Approx. 370 g (L/G3001/G3001P), Approx. 60 g (L/GD500)			

1. LK-G3001(P) can be operated singly. The measured value display and setting modifications can be performed on the display panel (LK-GD500) or via the setting support software (LK-H1W).

2. The rating of the NPN open-collector: 50 mA max. (40 V max.), residual voltage of 1 V max. The rating of the PNP open collector: 50 mA max. (30 V max.), residual voltage of 1 V max.

3. (NPN model) The rating of non-voltage input: 1 V or less ON voltage, 0.6 mA or less OFF current. (PNP model) The rating of voltage input: 10.2 V or more ON voltage (26.4 V max.) 0.6 mA or less OFF current.

Fig. B.37 User manual for LKG laser displacement sensor-10

Specifications

Sensor heads

Model	LK-G10/G15		LK-G32/G37	
Mounting mode	-		Diffused reflection	Specular reflection
Reference distance	0.39" 10 mm		1.18" 30 mm	0.93" 23.5 mm
Measuring range ¹	±0.04" ±1 mm		±0.2" ±5 mm	±0.18" ±4.5 mm
Red semiconductor laser				
Light source	Wavelength	650 nm (visible light)		650 nm (visible light)
	Laser Class	Class II (FDA CDRH 21CFR PART1040.10)		Class II (FDA CDRH 21CFR PART1040.10)
	Output	0.3 mW		0.95 mW
Spot diameter (at reference distance)	Approx. 0.0008" × 0.0197" 20 × 500 μm (G15), Approx. ±0.0008" ±20 μm (G10)		Approx. 0.0012" × 0.0335" 30 × 850 μm (G37), Approx. ±0.0012" ±30 μm (G32)	
Linearity ²	±0.03% of F.S. (F.S. ±0.04" ±1 mm)		±0.05% of F.S. (F.S. ±0.2" ±5 mm)	
Repeatability ³	0.02 μm (0.01 μm)		0.05 μm	
Sampling frequency	20/50/100/200/500/1000 μs (Selectable from 6 levels)			
LED display	Near the center of the measurement: Green lights Within the measurement area: Orange lights Outside the measurement area: Orange flashing			
Temperature characteristics	0.01% of F.S./°C (F.S. ±0.04" ±1 mm)		0.01% of F.S./°C (F.S. ±0.2" ±5 mm)	
Environmental resistance	Enclosure rating	IP67 (IEC60529)		
	Ambient luminance	Incandescent lamp or fluorescent lamp: 10,000 lux max.		
	Ambient temperature	0 to +50 °C (32 to 122 °F), No condensation		
	Relative humidity	35 to 85%, No condensation		
	Resistance to vibrations	10 to 55 Hz, multiple amplitude 0.06" 1.5 mm; two hours in each direction of X, Y, and Z		
Material	Aluminum die-cast			
Weight (including the cable)	Approx. 190 g		Approx. 280 g	

1. The range is obtained by measuring KEYENCE's standard target (ceramic).
LK-G10/G15: When the sampling rate is 20 μs, the range becomes +0.37 mm +0.01" (FAR side) to -1 mm -0.04" (NEAR side).
LK-G32/G37: When the sampling rate is 20 μs, the range becomes +1.8 mm +0.07" (FAR side) to -5 mm -0.20" (NEAR side) for diffuse reflection, and +1.6 mm +0.06" (FAR side) to -4.5 mm -0.18" (NEAR side) for specular reflection.
2. The range is obtained by measuring KEYENCE's standard target (ceramic) with the Standard mode.
3. The range is obtained by measuring KEYENCE's standard (SUS) with 4096 times of averaging at the reference distance. The range in parenthesis is the typical linearity obtained by measuring the target with 16384.

Model	LK-G82/G87		LK-G152/G157	
Mounting mode	Diffused reflection	Specular reflection	Diffused reflection	Specular reflection
Reference distance	3.15" 80 mm	2.96" 75.2 mm	5.91" 150 mm	5.81" 147.5 mm
Measuring range ¹	±0.59" ±15 mm	±0.55" ±14 mm	±1.57" ±40 mm	±1.54" ±39 mm
Red semiconductor laser				
Light source	Wavelength	650 nm (visible light)		
	Laser Class	Class II (FDA CDRH 21CFR PART1040.10)		
	Output	0.95 mW		
Spot diameter (at reference distance)		Approx. 0.0028" × 0.0433" 70 × 1100 μm (G87), Approx. 0.0028" ø70 μm (G82)	Approx. 0.0047" × 0.0669" 120 × 1700 μm (G157), Approx. 0.0047" ø120 μm (G152)	
Linearity ²		±0.05% of F.S. (F.S.= ±0.59" ±15 mm)	±0.05% of F.S. (F.S.= ±1.57" ±40 mm)	
Repeatability ³		0.000008" 0.2 μm	0.000020" 0.5 μm	
Sampling frequency		20/50/100/200/500/1000 μs (Selectable from 6 levels)		
LED display		Near the center of the measurement: Green lights Within the measurement area: Orange lights Outside the measurement area: Orange flashing		
Temperature characteristics		0.01% of F.S./°C (F.S.= ±0.59" ±15 mm)	0.01% of F.S./°C (F.S.= ±1.57" ±40 mm)	
Environmental resistance	Enclosure rating	IP67 (IEC60529)		
	Ambient luminance	Incandescent lamp or fluorescent lamp: 10,000 lux max.		Incandescent lamp or fluorescent lamp: 5000 lux max.
	Ambient temperature	0 to +50 °C (32 to 122 °F), No condensation		
	Relative humidity	35 to 85%, No condensation		
Resistance to vibrations		10 to 55 Hz, multiple amplitude 0.06" 1.5 mm; two hours in each direction of X, Y, and Z		
Material		Aluminum die-cast		
Weight (including the cable)		Approx. 380 g	Approx. 290 g	

1. The range is obtained by measuring KEYENCE's standard target (ceramic).
LK-G82/G87: When the sampling rate is 20 μs, the range becomes -0.35" -9 (NEAR side) to -0.59" -15 mm (NEAR side) for diffuse reflection, and -0.34" -8.7 (NEAR side) to -0.55" -14 mm (NEAR side) for specular reflection.
LK-G152/G157: When the sampling rate is 20 μs, the range becomes -0.87" -22 (NEAR side) to -1.57" -40 mm (NEAR side) for diffuse reflection, and -0.87" -22 (NEAR side) to -1.54" -39 mm (NEAR side) for specular reflection.
2. The range is obtained by measuring KEYENCE's standard target (ceramic) with the Standard mode.
3. The range is obtained by measuring KEYENCE's standard (SUS) with 4096 times of averaging at the reference distance. The range in parenthesis is the typical linearity obtained by measuring the target with 16384.



Fig. B.38 User manual for LKG laser displacement sensor-11

Appendix C

Manufacturing process of mini-bladder

1. Mix PlatSil® Gel-OO 30 silicone having shore OO 30 hardness (MouldLife, Suffolk, UK) was formulated by mixing part A and part B of the resin in 1:1 ratio, with 3% PlatSil® 71/73-part R retarder (MouldLife, Suffolk, UK) and then degassing the mixture for 5 minutes at room temperature until a clear liquid was formed. The liquid (degassed mixture) was then poured into the mould shown in Fig. C.1 to craft the top layer of the mini-bladder. In order to remove any air bubbles which may have formed during the pouring the unit was degassed again (5 minutes at room temperature). If the silicone level has been dropped, make sure to pour more up to the surface. If still there are tiny air bubbles use a small pin and pop them out. Then using a flat scrapper, scrape the excess silicone and create a flat surface on the top face side of the mould (Fig. C.2), (i) to (iii)). Now place the unit in the autoclave at 60°C for about 5 – 6 minutes to allow the Silicone to cure. (This step is to increase the cross-linking process, although it is a RTV polymer).

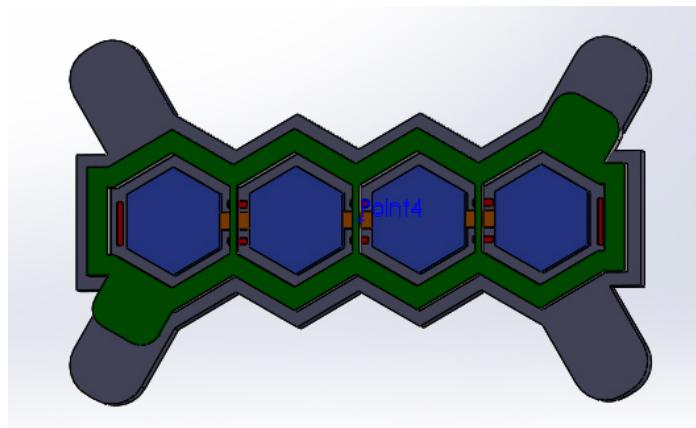


Fig. C.1 Solidworks drawing of 3D printed two-part mould of the hexagonal mini-bladder unit.

2. After the mould is removed from the autoclave, use the protruding side edges of the two moulds to pull them apart to remove the cured top part of the mould out. It should be carefully removed so that it will not tear the silicone layer.
3. Then pour PlatSil® Gel-OO 30 silicone into the base mould up to half level and pop out any air bubbles created. Then insert the piece of woven fabric on top of the Silicone layer, and gently press towards the silicone layer so that it will stick to the silicone layer (this should be carried out in a way avoiding the formation of any air bubbles). Thereafter fill the remaining half of the base mould with Silicone almost up to the edge and scrape out any excess silicone (Fig. C.2 (iv) to (vii))

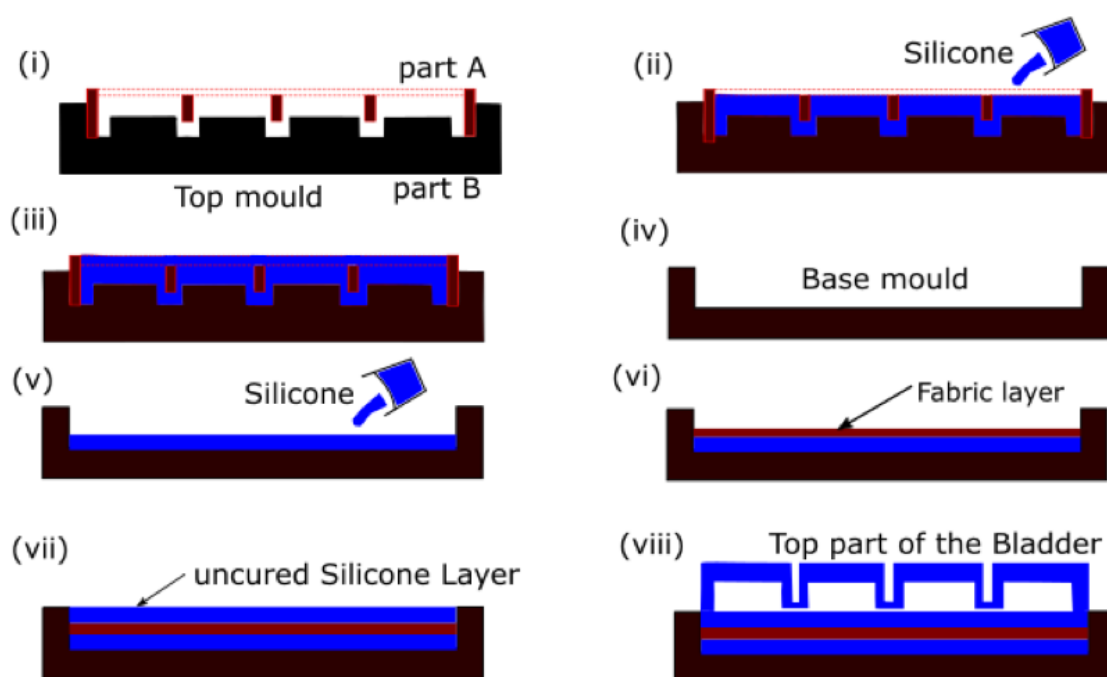


Fig. C.2 Manufacturing process of mini-bladders (i) the top mould (consisting of two parts), (ii) pouring silicone to the top mould (iii) top mould filled with silicone and removed the excess (iv) the base mould, for creating the bottom part of the bladder (v) pouring silicone half way up to the mould (vi) submerging the fabric layer (vii) pour the remaining half of silicone (viii) top part of the bladder was immersed into the base uncured silicone layer.

4. Now place the top layer of the bladder on the base mould and gently push so that it just sits over the top layer of the base silicone, without dipping too much into the layer. This will block the air channel created within the mini-bladder unit (Fig. C.2 (viii)).
5. Then place the whole bladder unit in the autoclave for another 5 – 6 minutes at 60 °C to cure the silicone. After the silicon is cured, peel off the completed mini-bladder unit from the mould.

6. To connect the air source, pierce the end of the bladder from one side using a thin metal pin
7. Insert the small straight connector through the pierced hole and seal the edges using the silicone to remove any possible leakages. Then connect the air tube to the connector and tighten to avoid leakages
8. Finally, connect the air tube to a 60 ml syringe and check whether the bladder unit have any leakages by submerging the mini-bladder unit under water and inflating. Then inspect for any air bubbles produced once inflated. If there are any leaks, seal it using Silicone and put in the autoclave to cure.

Inflation behaviour of mini-bladders

Case1: PlatSil® Gel-OO 30 Silicon – inflation/deflation height vs. air volume

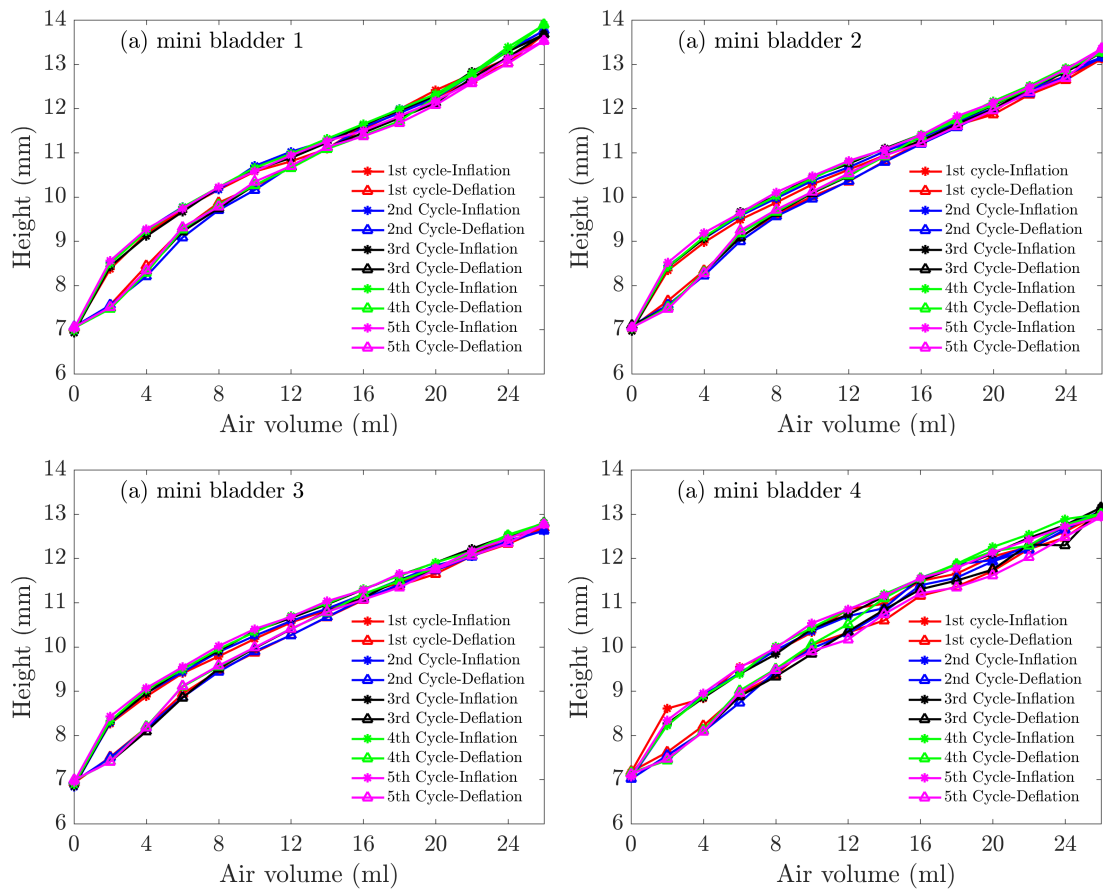


Fig. C.3 The mini-bladder unit height vs. inflating air volume, for PlatSil® Gel-OO 30, sample-1-five cycles, (a) mini-bladder 1, (b) mini-bladder 2, (c) mini-bladder 3, (d) mini-bladder 4.

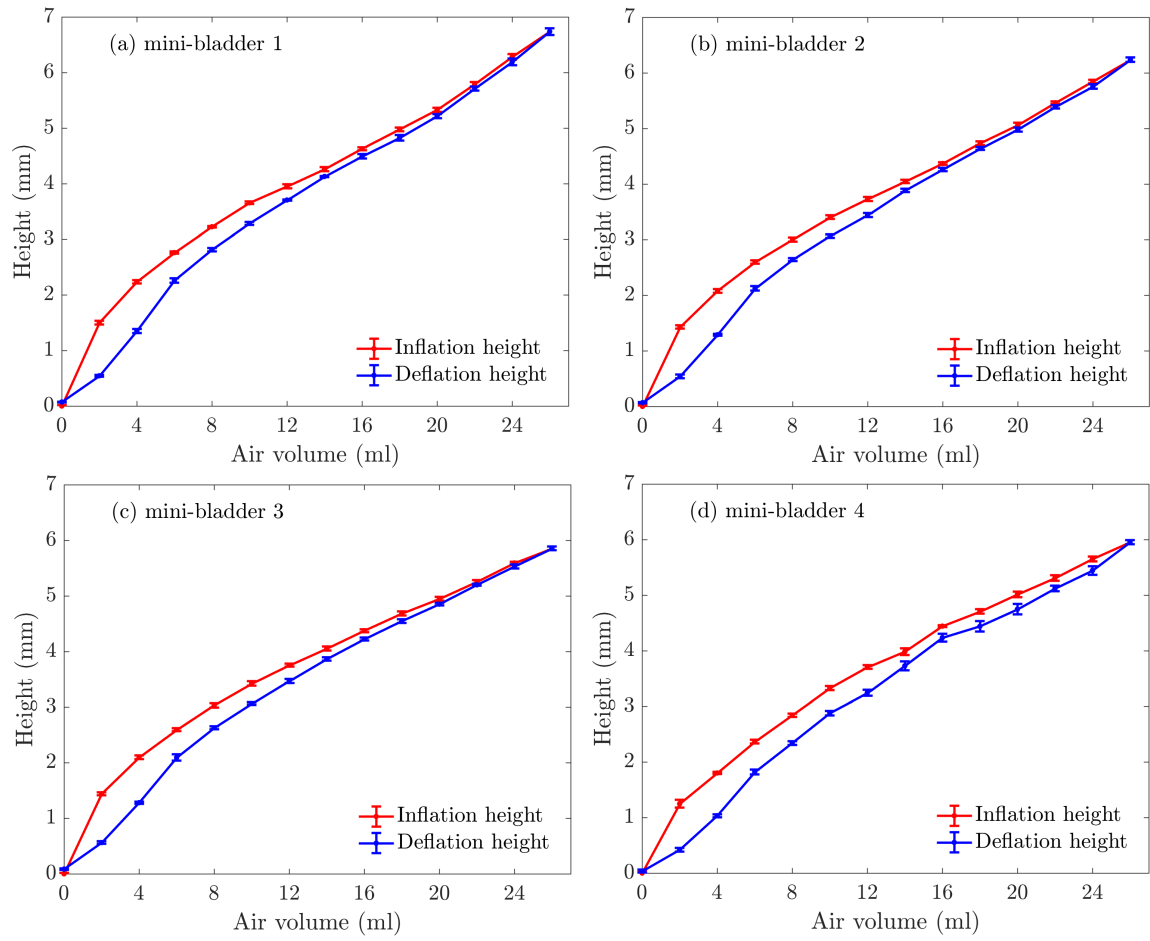


Fig. C.4 The average inflation/deflation height vs. inflating air volume, for PlatSil® Gel-OO 30, sample-1-five cycles average, (a) mini-bladder 1, (b) mini-bladder 2, (c) mini-bladder 3, (d) mini-bladder 4.

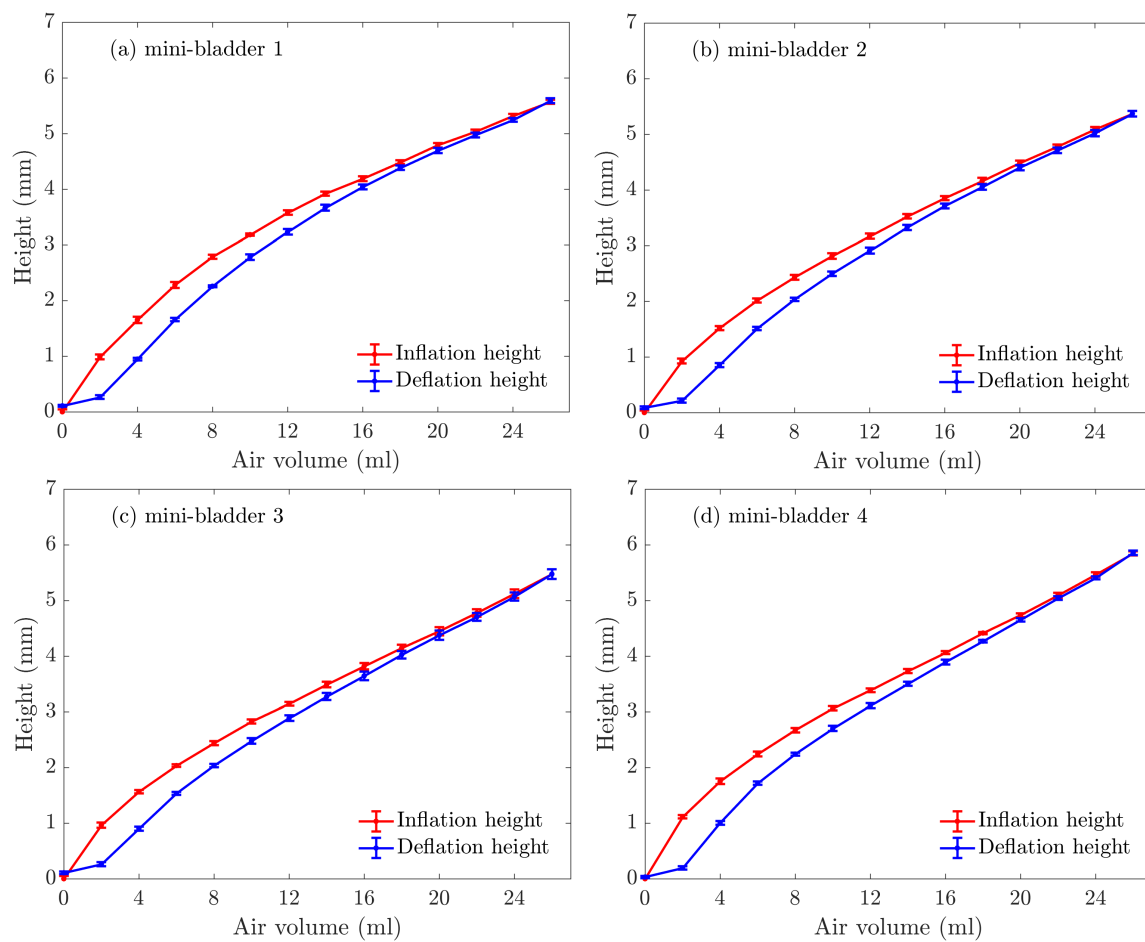


Fig. C.5 The average inflation/deflation height vs. inflating air volume, for PlatSil[®] Gel-OO 30, sample-2-five cycles average, (a) mini-bladder 1, (b) mini-bladder 2, (c) mini-bladder 3, (d) mini-bladder 4.

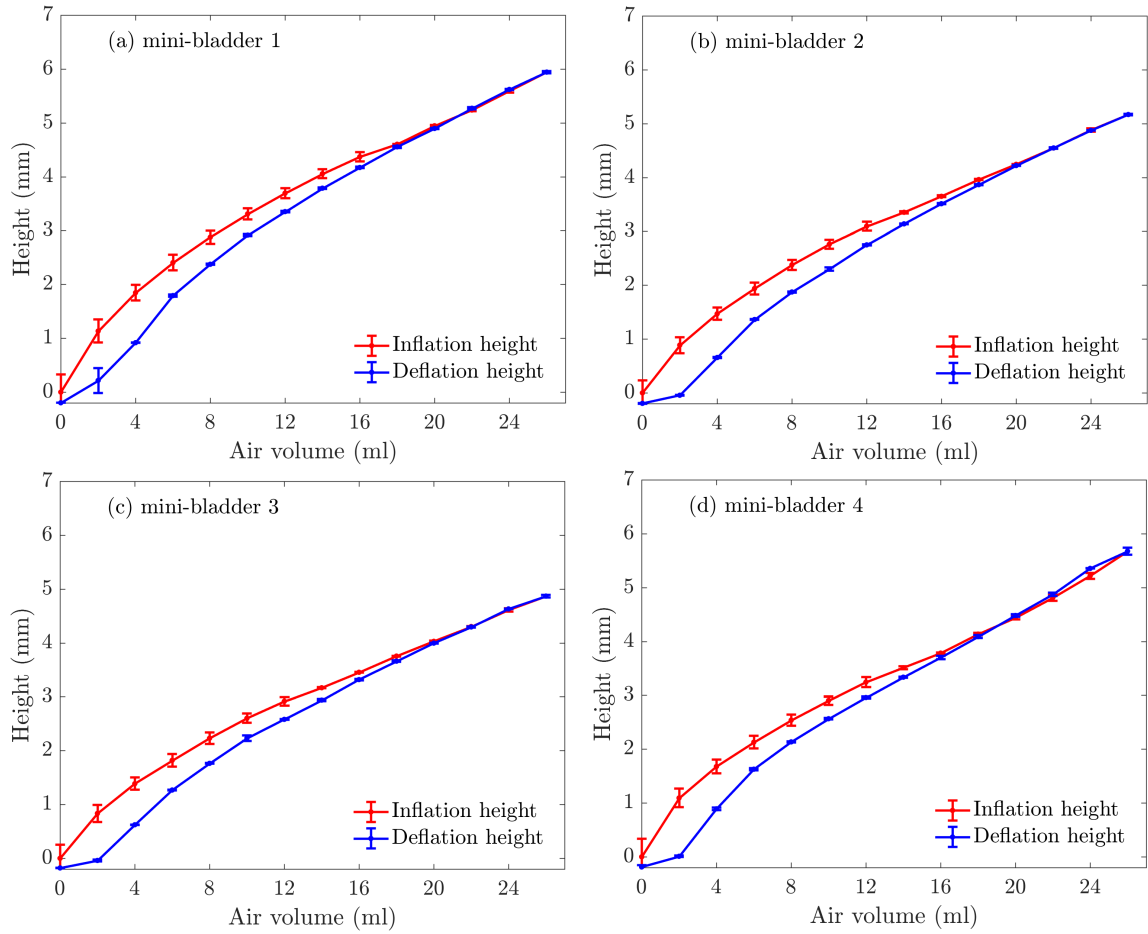


Fig. C.6 The average inflation/deflation height vs. inflating air volume, for PlatSil® Gel-OO 30, sample-3-five cycles average, (a) mini-bladder 1, (b) mini-bladder 2, (c) mini-bladder 3, (d) mini-bladder 4.

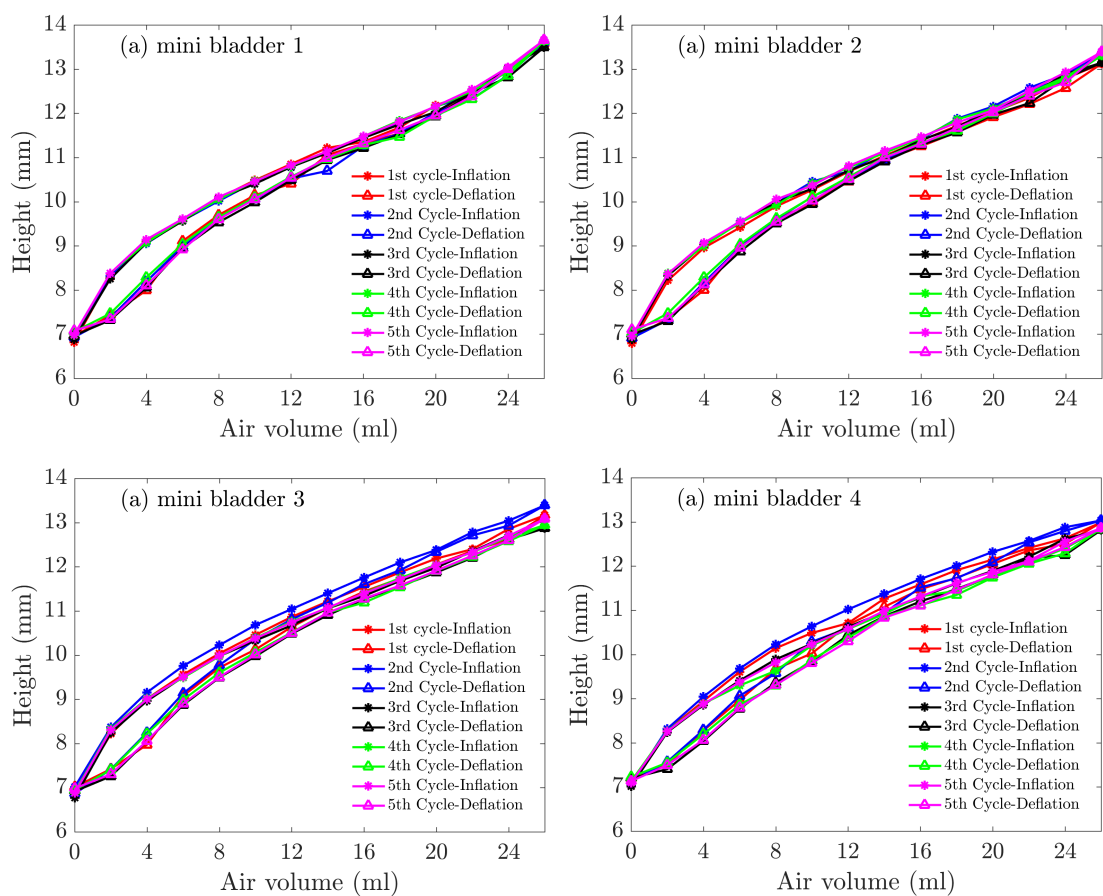


Fig. C.7 The mini-bladder unit height vs. inflating air volume, for PlatSil® Gel-OO 30, five cycles, after the sample was allowed to relax for 48 hrs., (a) mini-bladder 1, (b) mini-bladder 2, (c) mini-bladder 3, (d) mini-bladder 4

Case2: PlatSil® Gel-A-10 Silicon -inflation/deflation height vs. air volume

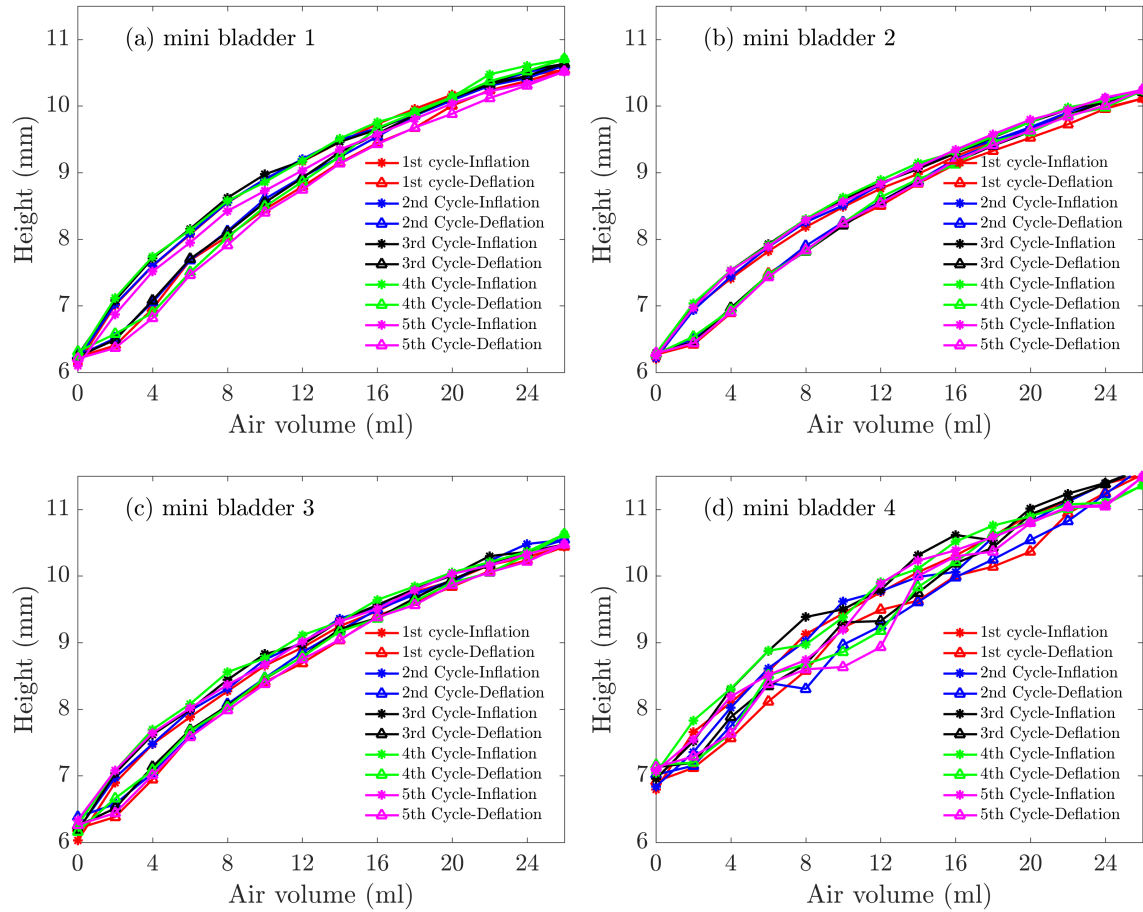


Fig. C.8 The mini-bladder unit height vs. inflating air volume, for PlatSil® Gel-A 10, sample-1-five cycles, (a) mini-bladder 1, (b) mini-bladder 2, (c) mini-bladder 3, (d) mini-bladder 4.

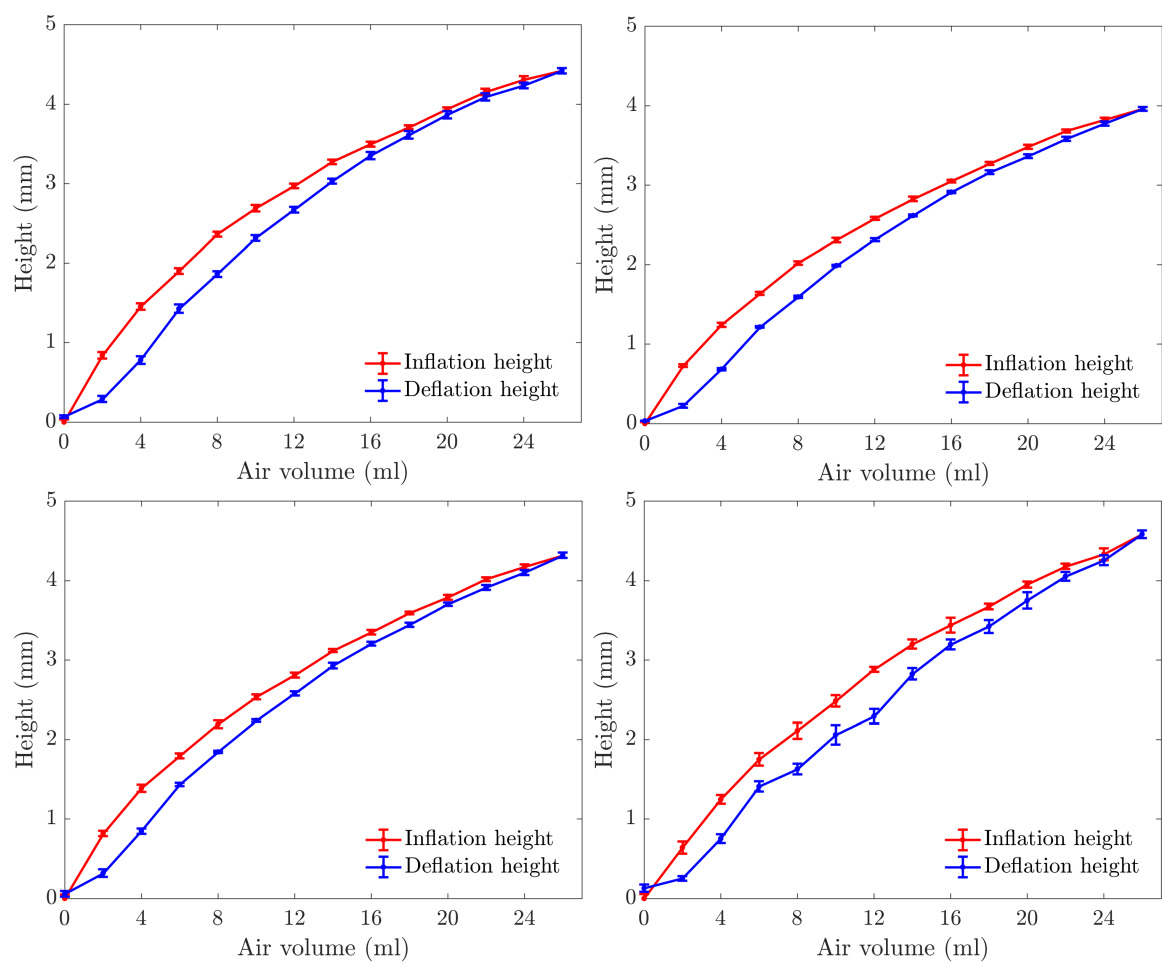


Fig. C.9 The average inflation/deflation height vs. inflating air volume, for PlatSil® Gel-A 10, sample-1-five cycles average, (a) mini-bladder 1, (b) mini-bladder 2, (c) mini-bladder 3, (d) mini-bladder 4.

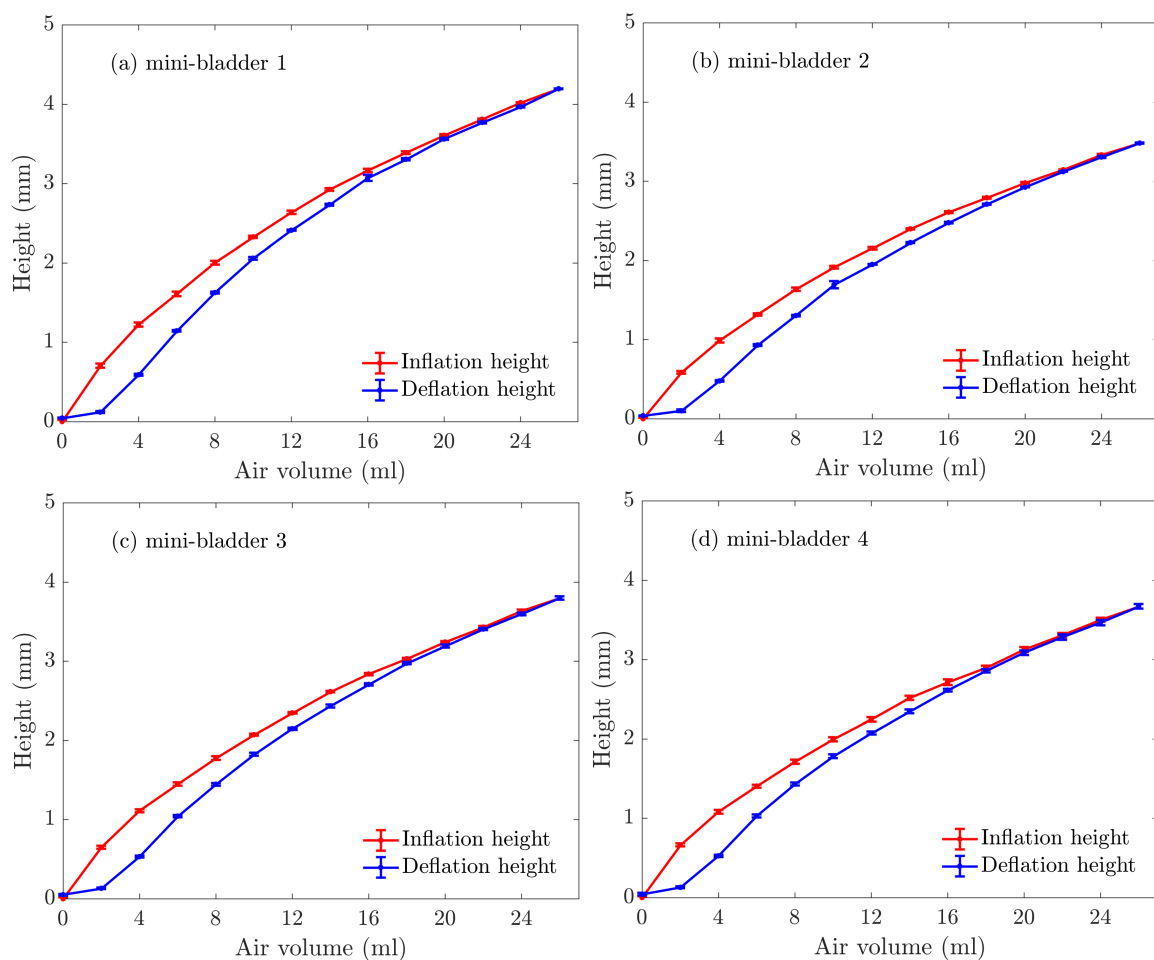


Fig. C.10 The average inflation/deflation height vs. inflating air volume, for PlatSil® Gel-A 10, sample-2-five cycles average, (a) mini-bladder 1, (b) mini-bladder 2, (c) mini-bladder 3, (d) mini-bladder 4.

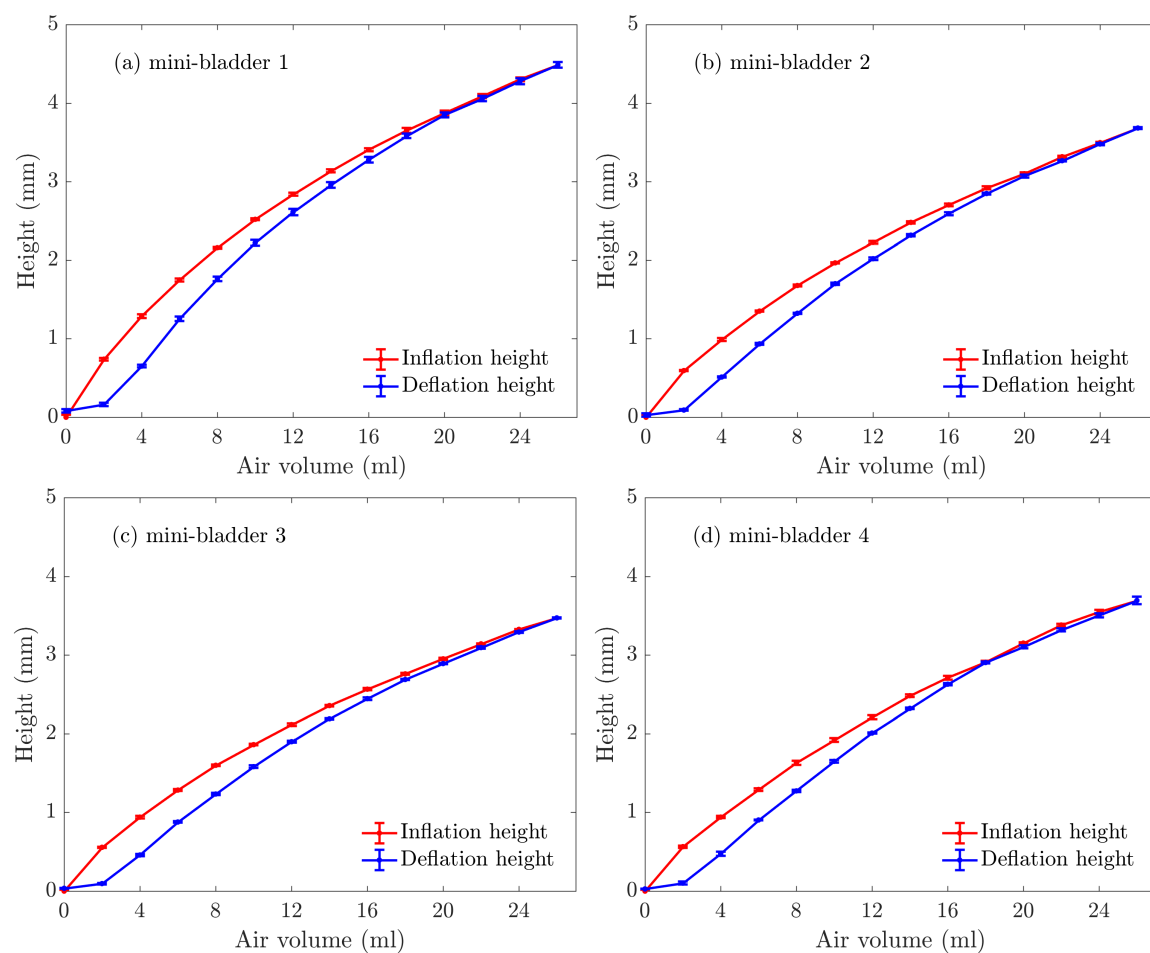


Fig. C.11 The average inflation/deflation height vs. inflating air volume, for PlatSil[®] Gel-A 10, sample-3-five cycles average, (a) mini-bladder 1, (b) mini-bladder 2, (c) mini-bladder 3, (d) mini-bladder 4.

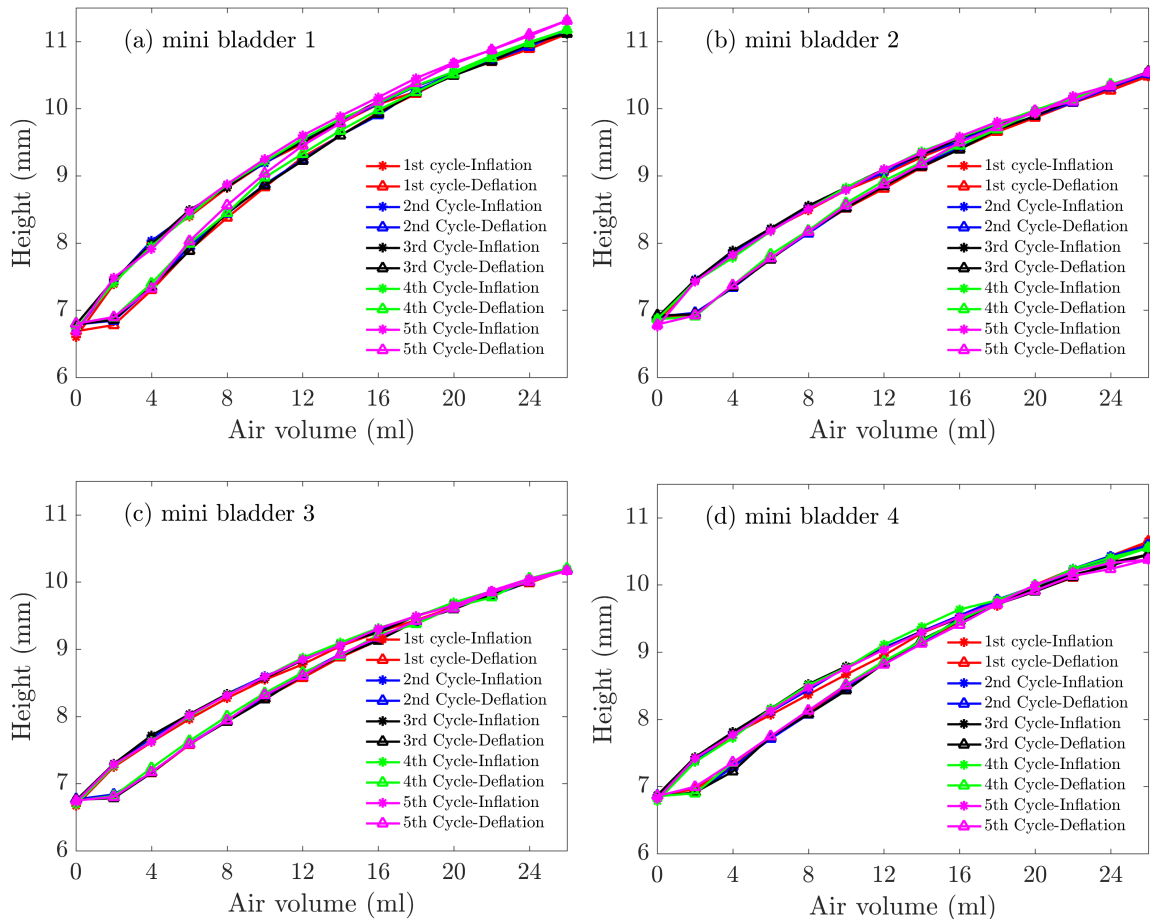


Fig. C.12 The mini-bladder unit height vs. inflating air volume, for PlatSil® Gel-A 10, five cycles, after the sample was allowed to relax for 48 hrs., (a) mini-bladder 1, (b) mini-bladder 2, (c) mini-bladder 3, (d) mini-bladder 4

Height of mini-bladder Vs inflation pressure

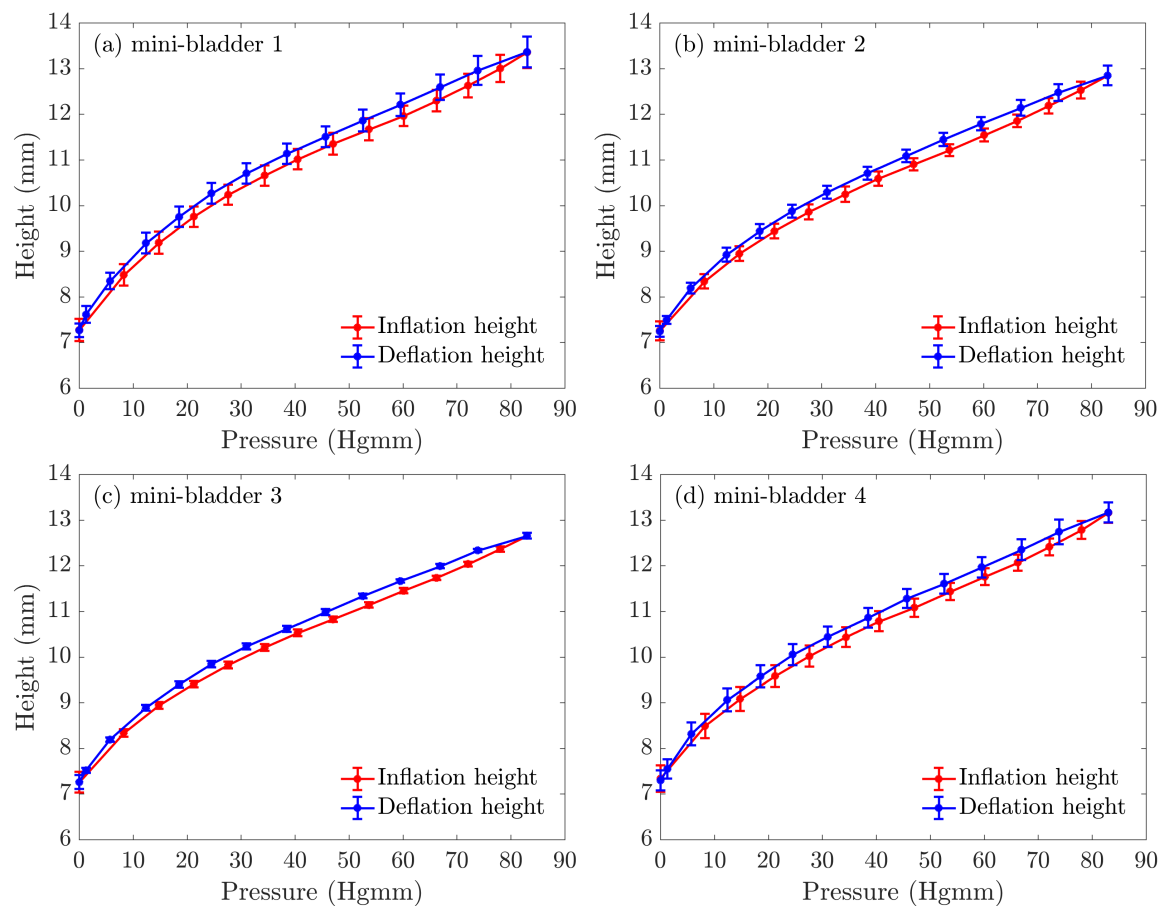


Fig. C.13 The average mini-bladder unit height vs. inflation pressure, for PlatSil® Gel-OO 30, (a) mini-bladder 1, (b) mini-bladder 2, (c) mini-bladder 3, (d) mini-bladder 4

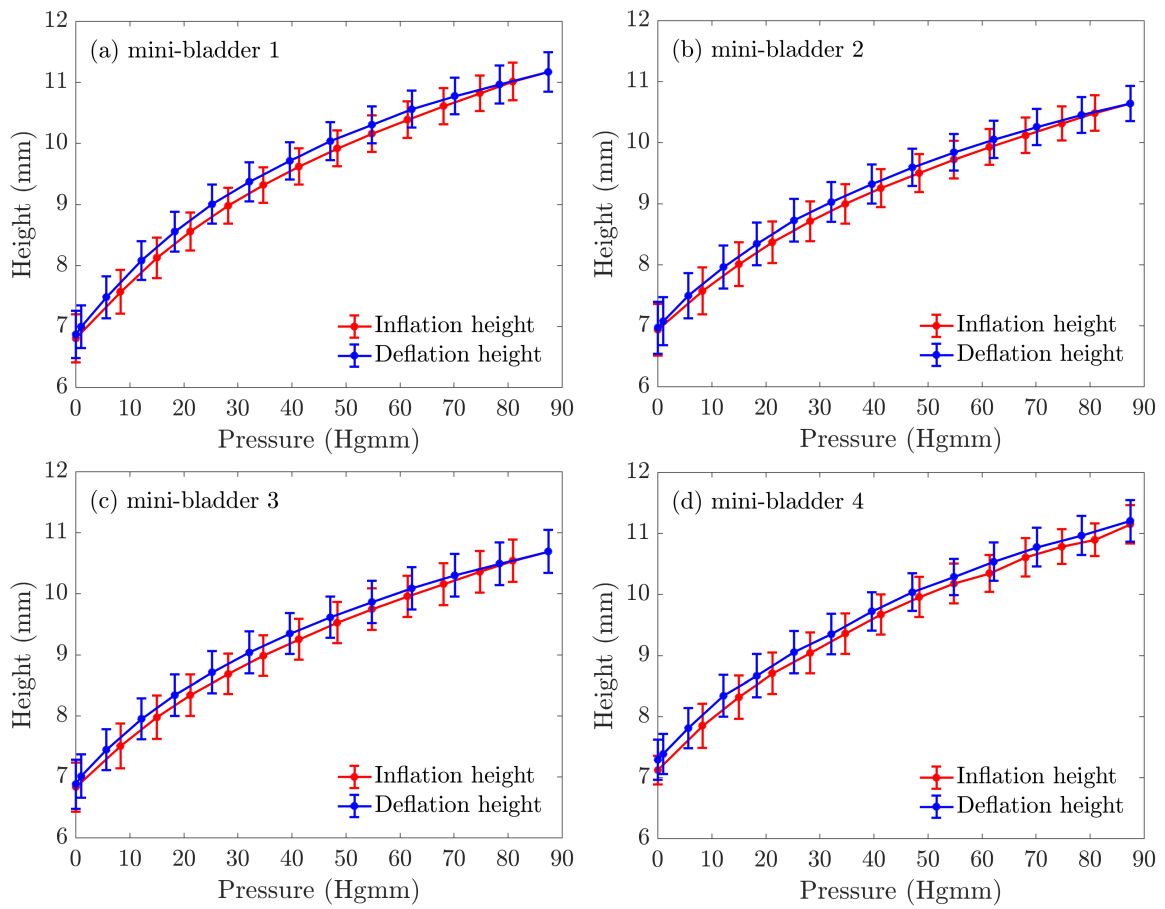


Fig. C.14 The average mini-bladder unit height vs. inflation pressure, for PlatSil® Gel-A 10, (a) mini-bladder 1, (b) mini-bladder 2, (c) mini-bladder 3, (d) mini-bladder 4

Numerical simulations for different sized hexagonal mini-bladder units and membrane thicknesses

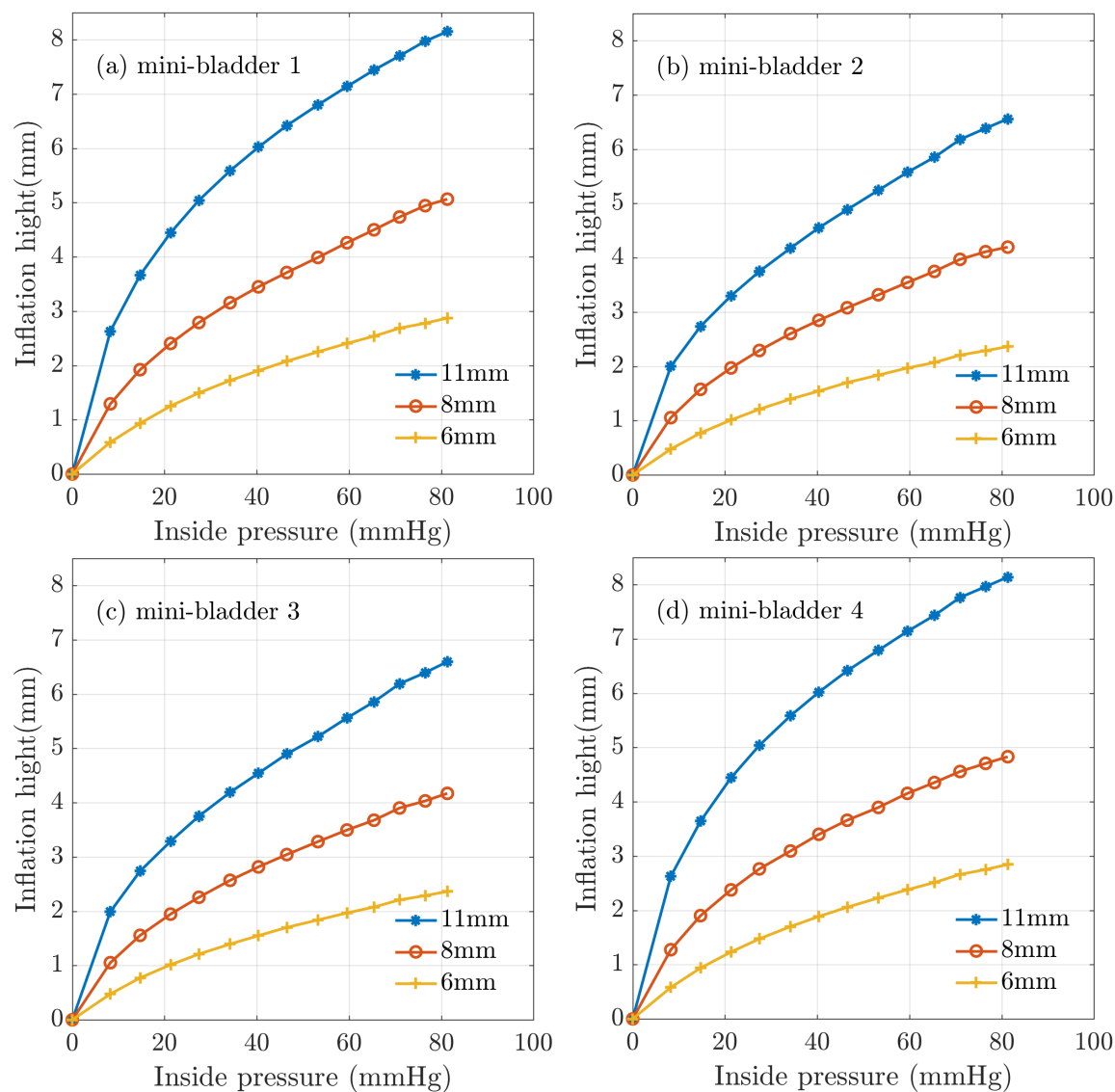


Fig. C.15 The relationship between the numerical model values (FEA) of maximum inflation height and the pressure inside mini-bladders for different sized hexagonal mini-bladder units made with PlatSil® Gel-OO 30 (a) mini-bladder 1 (b) mini-bladder 2 (c) mini-bladder 3 (d) mini-bladder 4.

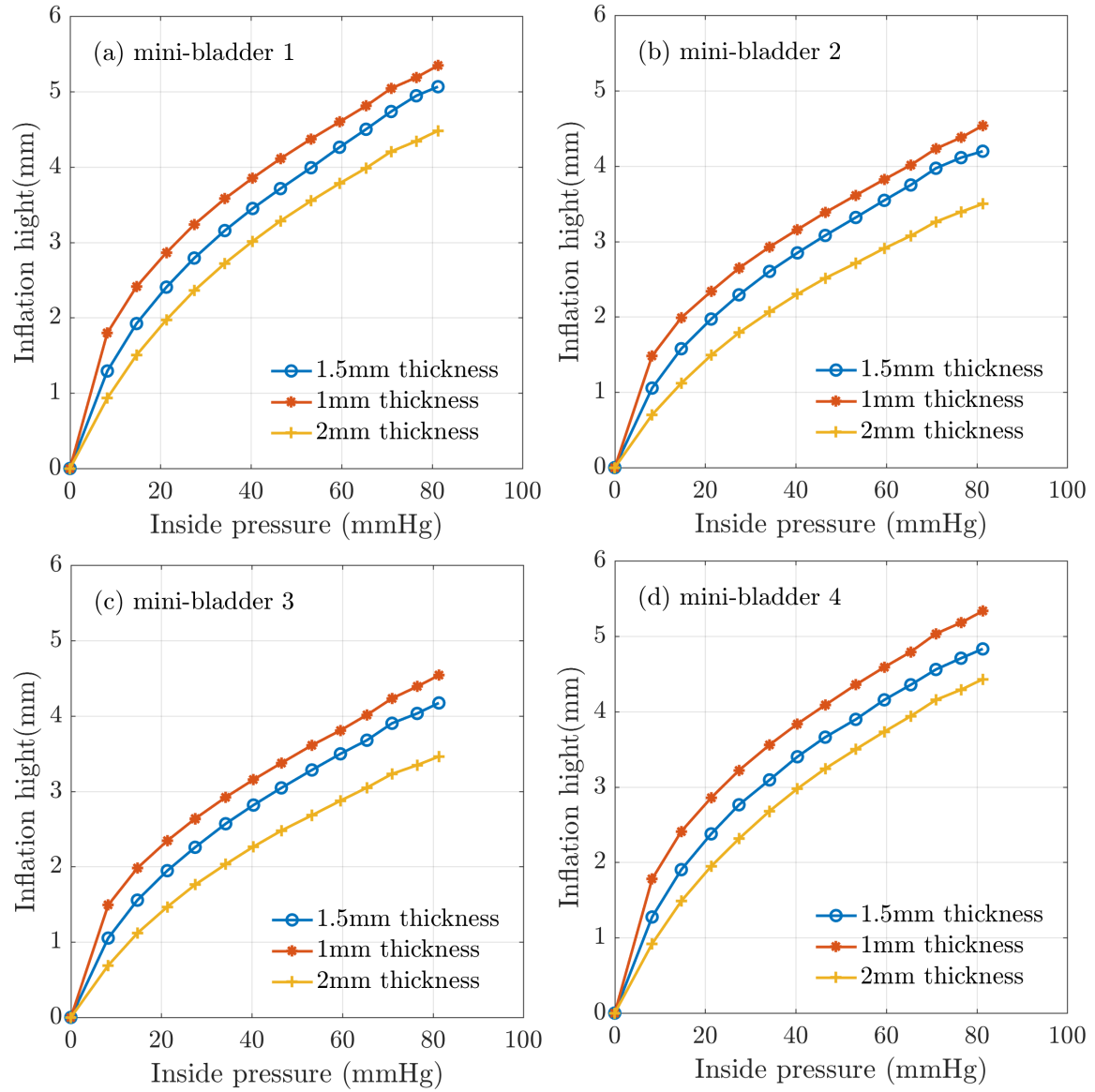


Fig. C.16 The relationship between the numerical model values (FEA) of maximum inflation height and the pressure inside mini-bladders for different membrane thicknesses of the hexagonal mini-bladder units made with PlatSil® Gel-OO 30. (a) mini-bladder 1 (b) mini-bladder 2 (c) mini-bladder 3 (d) mini-bladder 4.

Appendix D

Pressure transmission on a flat surface by mini-bladders

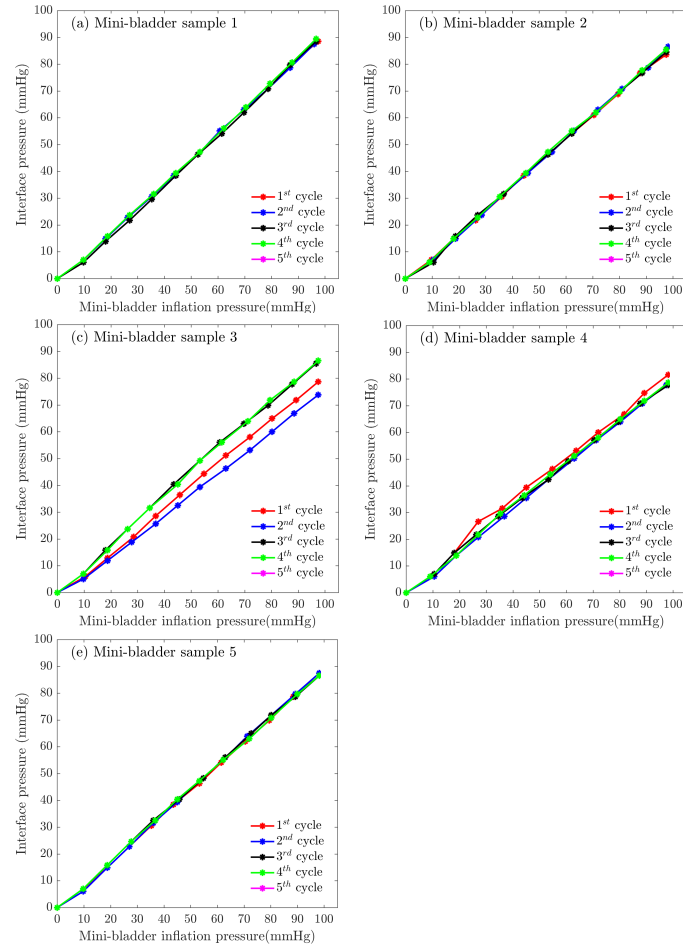


Fig. D.1 Pressure transmission on flat surface for five repeated inflation cycles for hexagonal (a) mini-bladder sample 1, (b) mini-bladder sample 2, (c) mini-bladder sample 3, (d) mini-bladder sample 4, (e) mini-bladder sample 5.

Pressure transmission on a cylindrical surface by different shaped mini-bladders

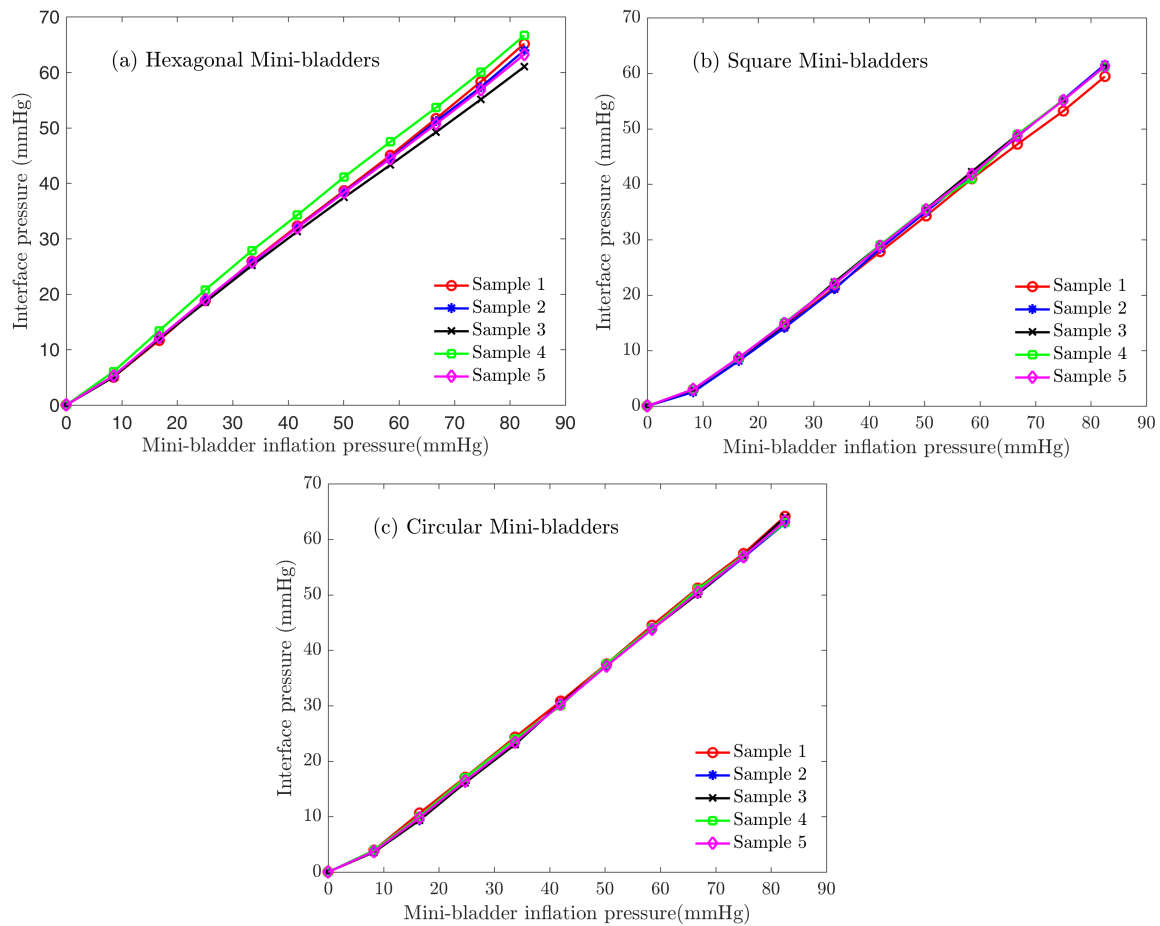


Fig. D.2 Pressure transmission on cylindrical surface for five samples (a) hexagonal shaped mini-bladders, (b) Square shaped mini-bladders, (c) circular shaped mini-bladder.

Evaluation of artificial skin and fat layers

Case 1: Tensile test results for the first skin layer samples

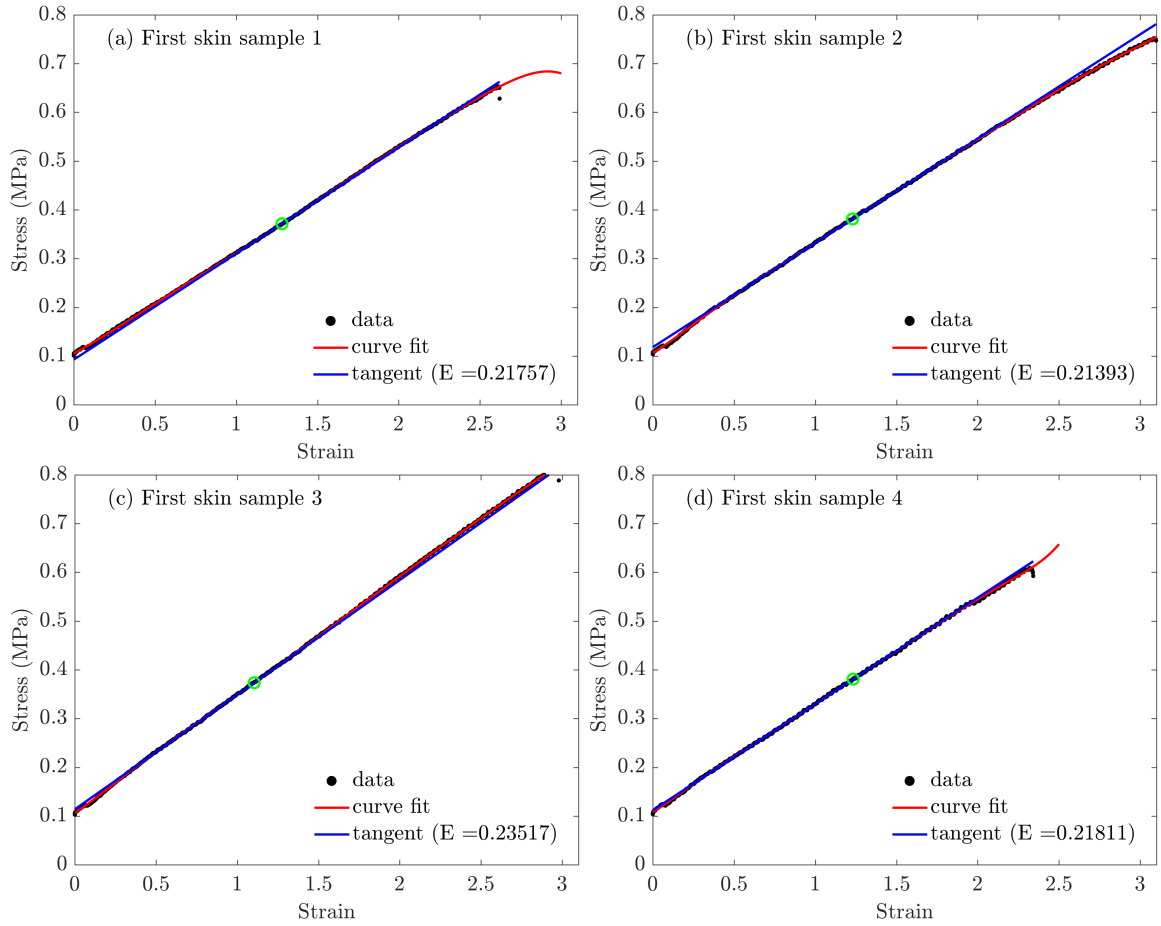


Fig. D.3 The stress, strain relationship obtained from the uniaxial tensile tests for the first skin layer (all samples), green scatter shows the place at which the tangent is drawn. The Young's modulus calculated (E) is given in legend

Case 1: Tensile test results for the first fat layer samples

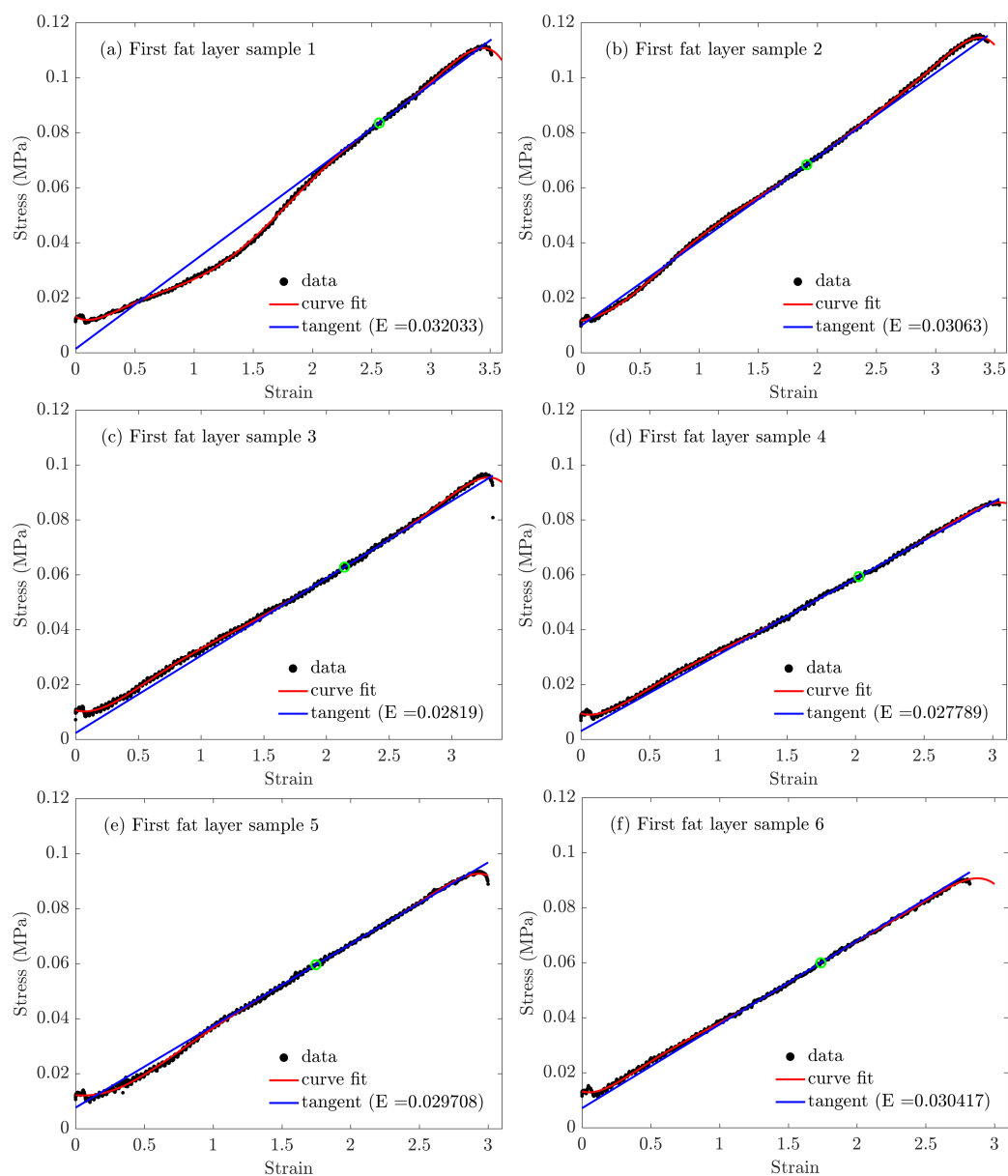


Fig. D.4 The stress, strain relationship obtained from the uniaxial tensile tests for the first fat layer (all samples), green scatter shows the place at which the tangent is drawn. The Young's modulus calculated (E) is given in legend

Table D.1 Original skin layer recipe taken from Arm R.

Component	Amount
PDMS Silicone (RTV 2-part)	
PlatSil [®] Gel- A-10 (MouldLife, Suffolk, UK)	130g each
Part A: Part B = 1:1	
Smith's Prosthetic Deadener (Polytek Development Corporation, USA distributed by MouldLife, Suffolk, UK)	69% of total PDMS weight
PlatSil [®] 71/73-part R Retarder (MouldLife, Suffolk, UK)	3% of total PDMS weight
PlatThix Thickener (Polytek Development Corporation, USA distributed by MouldLife, Suffolk, UK)	2.4% of total PDMS weight

Table D.2 Original fat layer recipe taken from Arm R.

Component	Amount
PDMS Silicone (RTV 2-part)	
PlatSil [®] Gel- A-10 (MouldLife, Suffolk, UK)	100g each
Part A: Part B = 1:1	
Silicone oil (MouldLife, Suffolk, UK)	100 % of the total PDMS weight

Table D.3 First skin layer recipe

Component	Amount
PDMS Silicone (RTV 2-part)	
PlatSil [®] Gel- A-10 (MouldLife, Suffolk, UK)	50g each
Part A: Part B = 1:1	
Smith's Prosthetic Deadener (Polytek Development Corporation, USA distributed by MouldLife, Suffolk, UK)	10% of total PDMS weight
PlatSil [®] 71/73-part R Retarder (MouldLife, Suffolk, UK)	3% of total PDMS weight
PlatThix Thickener (Polytek Development Corporation, USA distributed by MouldLife, Suffolk, UK)	2% of total PDMS weight
Polyester Flock	1% of total weight

Table D.4 First fat layer recipe

Component	Amount
PDMS Silicone (RTV 2-part)	
PlatSil [®] Gel- A-10 (MouldLife, Suffolk, UK)	50g each
Part A: Part B = 1:1	
Silicone oil (MouldLife, Suffolk, UK)	270 % of the total PDMS weight

Case 2: Tensile test results for the second skin layer samples

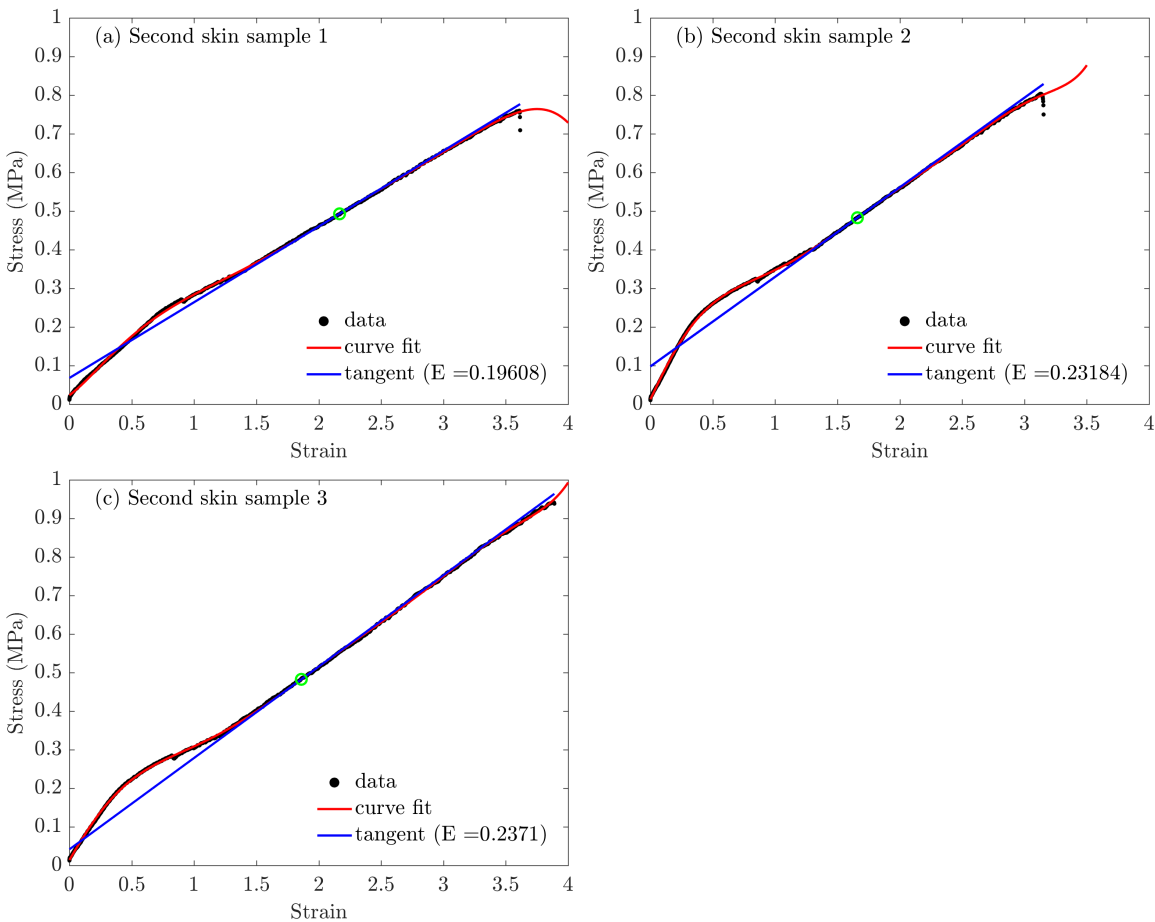


Fig. D.5 The stress, strain relationship obtained from the uniaxial tensile tests for the second skin layer (all samples), green scatter shows the place at which the tangent is drawn. The Young's modulus calculated (E) is given in legend

Case 2: Tensile test results for the second fat layer samples

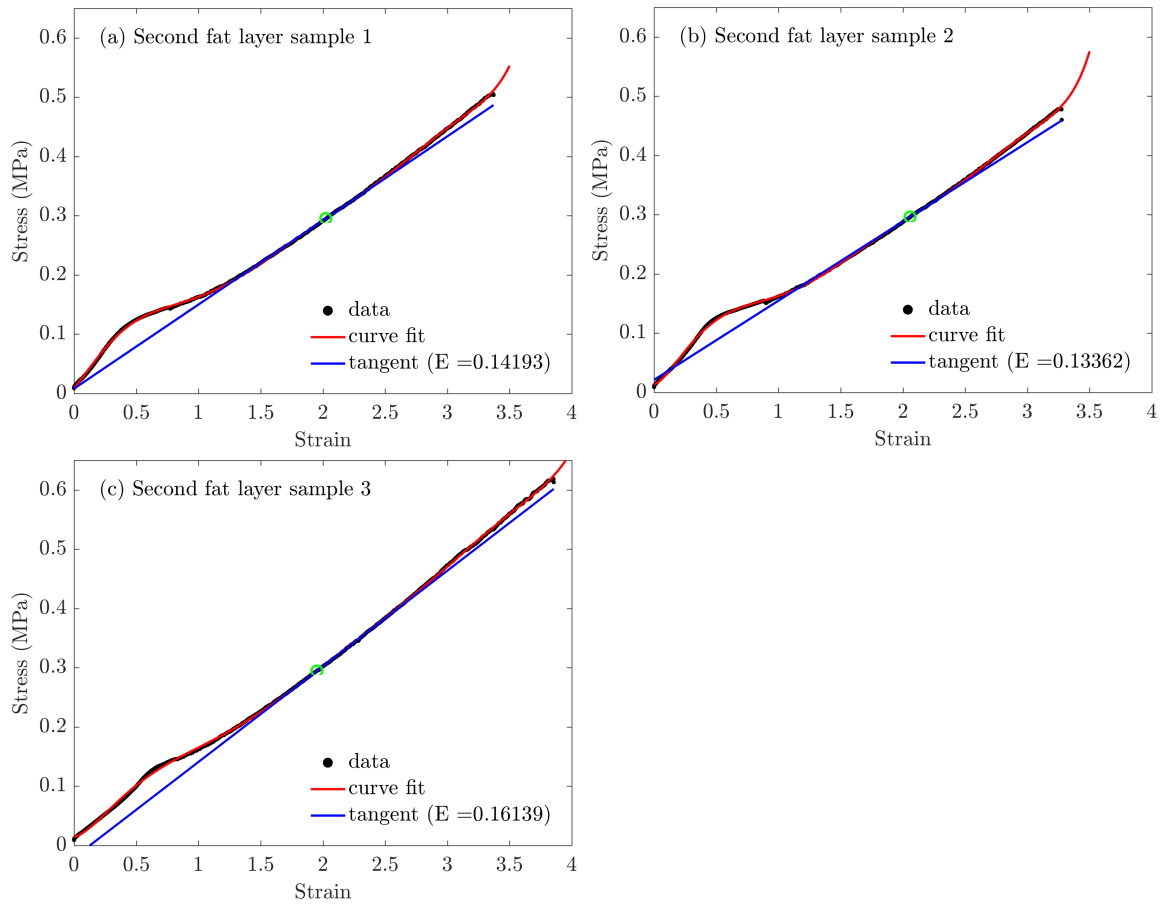


Fig. D.6 The stress, strain relationship obtained from the uniaxial tensile tests for the second fat layer (all samples), green scatter shows the place at which the tangent is drawn. The Young's modulus calculated (E) is given in legend

Table D.5 Second skin recipe

Component	Amount
PDMS Silicone (RTV 2-part)	
PlatSil [®] Gel- A-10 (MouldLife, Suffolk, UK)	50g each
Part A: Part B = 1:1	
Smith's Prosthetic Deadener (Polytek Development Corporation, USA distributed by MouldLife, Suffolk, UK)	10% of total PDMS weight
PlatSil [®] 71/73-part R Retarder (MouldLife, Suffolk, UK)	3% of total PDMS weight
PlatThix Thickener (Polytek Development Corporation, USA distributed by MouldLife, Suffolk, UK)	2% of total PDMS weight
Polyester Flock	1% of total PDMS weight

Table D.6 Second fat layer recipe

Component	Amount
PDMS Silicone (RTV 2-part)	
PlatSil [®] Gel- A-10 (MouldLife, Suffolk, UK)	50g each
Part A: Part B = 1:1	
Silicone oil (MouldLife, Suffolk, UK)	130% of the total PDMS weight

Case 3: Tensile test results for the third skin layer samples

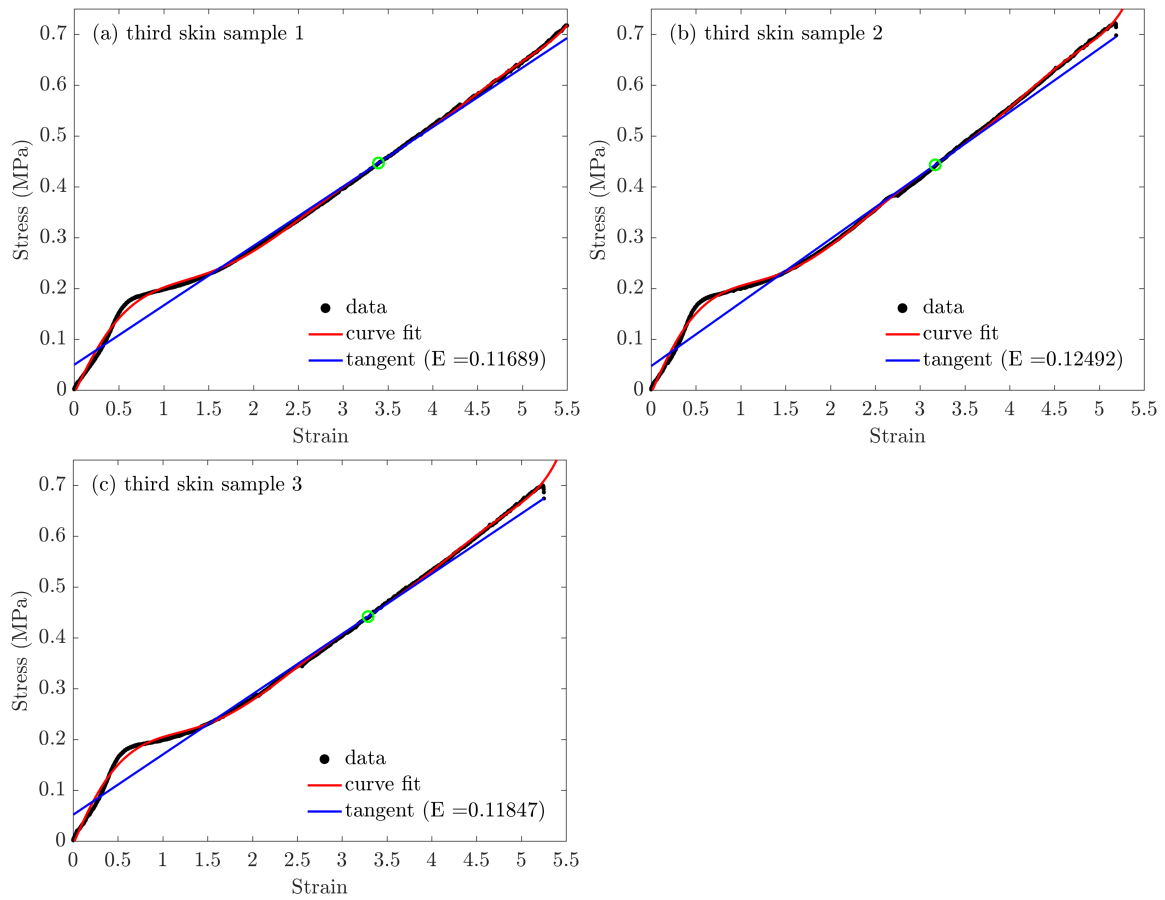


Fig. D.7 The stress, strain relationship obtained from the uniaxial tensile tests for the third skin layer (all samples), green scatter shows the place at which the tangent is drawn. The Young's modulus calculated (E) is given in legend

Case 3: Tensile test results for the third fat layer samples

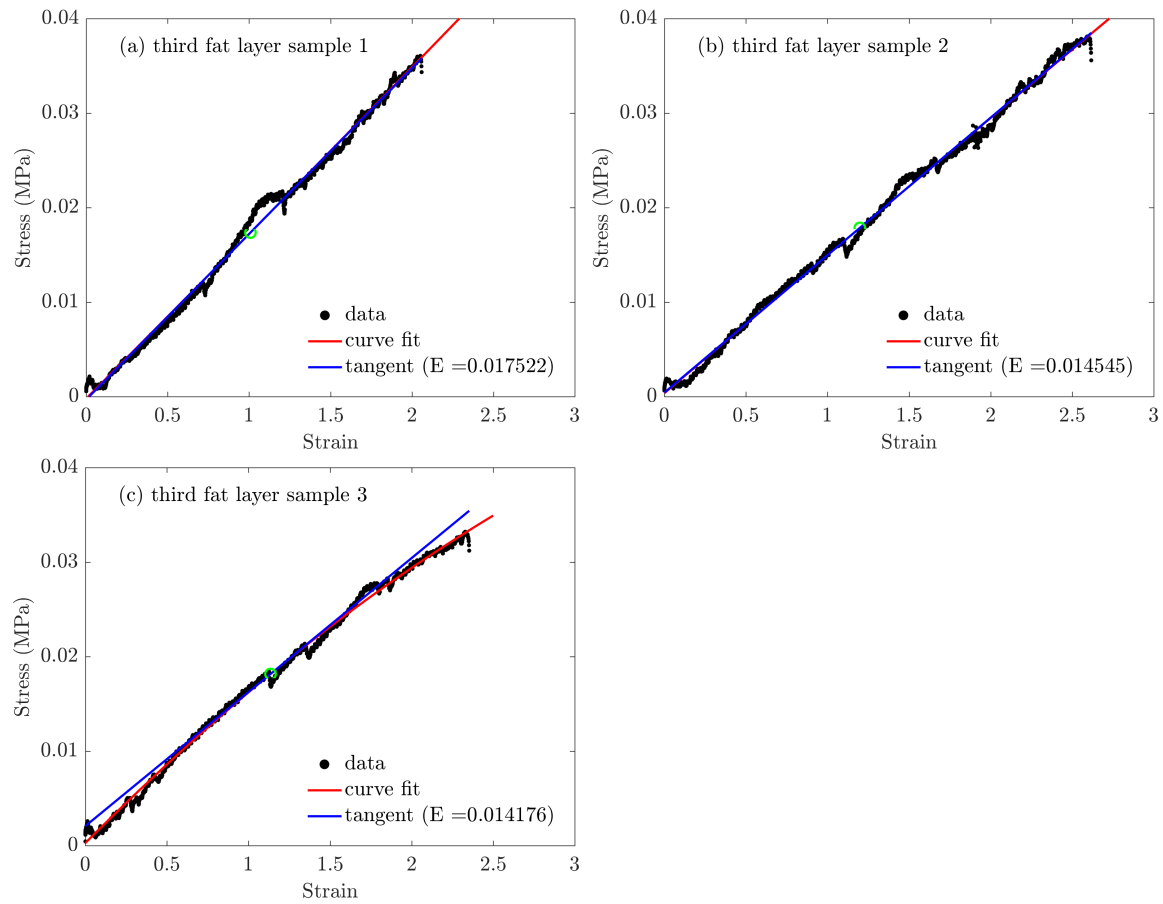


Fig. D.8 The stress, strain relationship obtained from the uniaxial tensile tests for the third fat layer (all samples), green scatter shows the place at which the tangent is drawn. The Young's modulus calculated (E) is given in legend

Table D.7 Third skin layer recipe

Component	Amount
PDMS Silicone (RTV 2-part) PlatSil [®] Gel- A-10 Part A: Part B = 1:1	50g each
Smith's Prosthetic Deadener (Polytek Development Corporation, USA distributed by MouldLife, Suffolk, UK)	18% of total PDMS weight
PlatSil [®] 71/73-part R Retarder (MouldLife, Suffolk, UK)	3% of total PDMS weight
PlatThix Thickener (Polytek Development Corporation, USA distributed by MouldLife, Suffolk, UK)	2% of total PDMS weight
Polyester Flock	1% of total PDMS weight

Table D.8 Third fat layer recipe

Component	Amount
PDMS Silicone (RTV 2-part) PlatSil [®] Gel- A-10 (MouldLife, Suffolk, UK) Part A: Part B = 1:1	50g each
Silicone oil (MouldLife, Suffolk, UK)	300% of the total PDMS weight

Calibration curves obtained for mounted AMI sensors

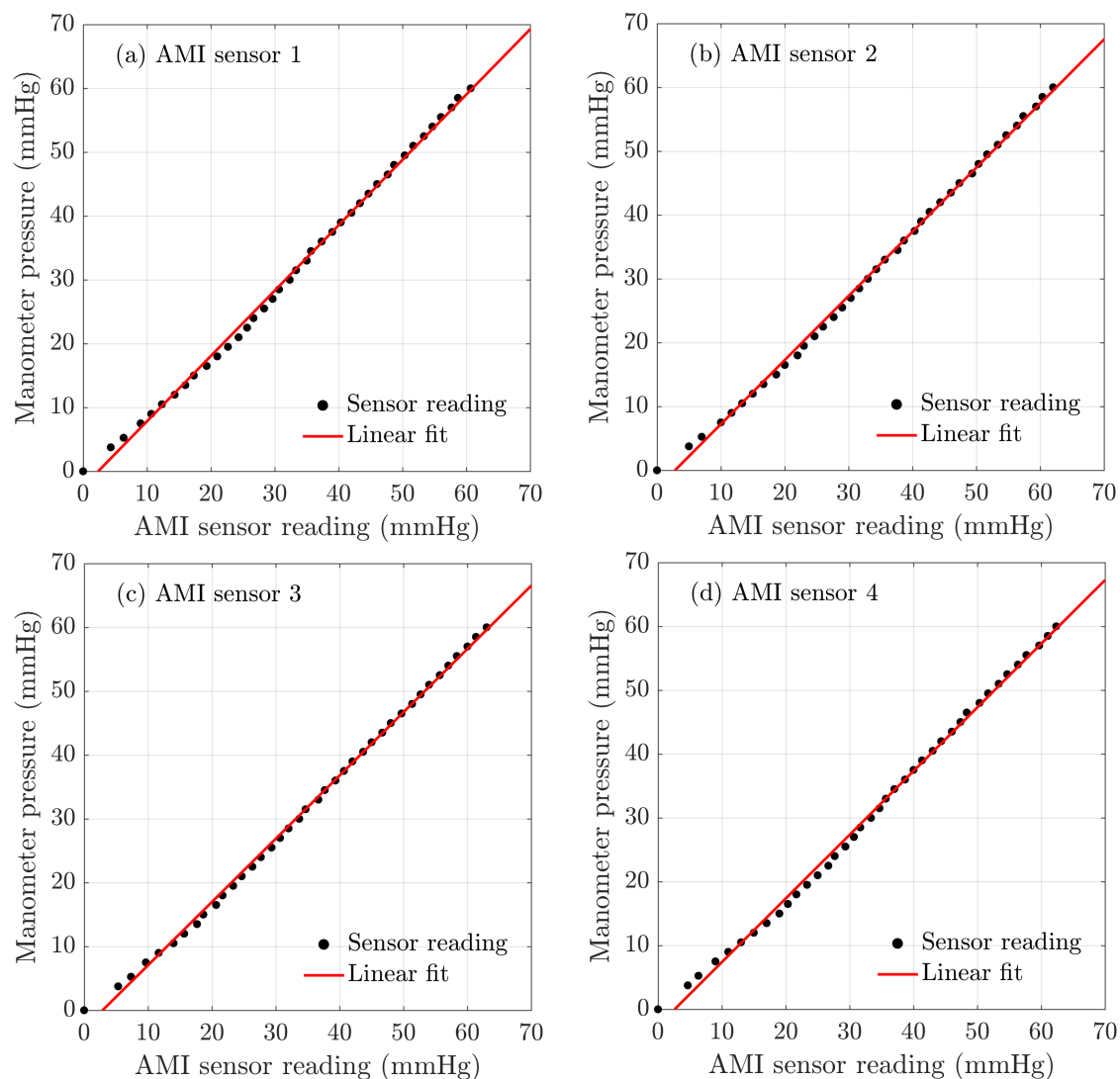


Fig. D.9 The calibration curves obtained for the four mounted AMI sensors, with their linear fits

Appendix E

Uniaxial tensile test results for the covered yarns

6437 double covered yarn

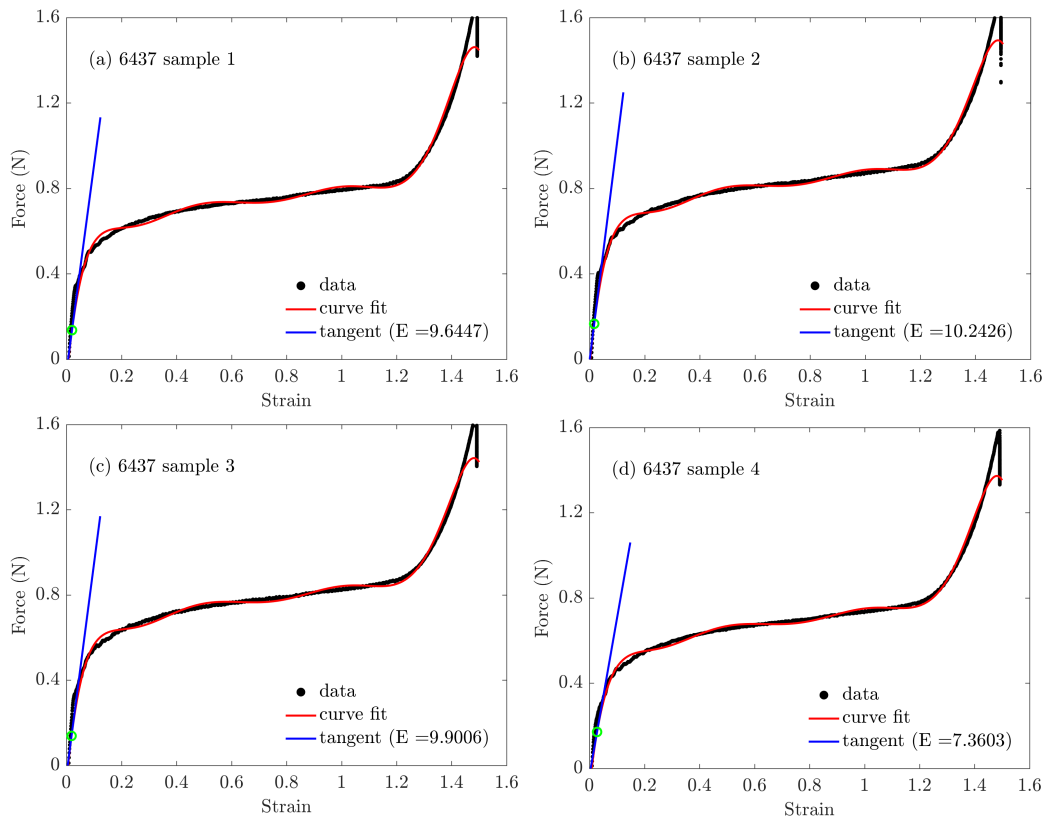


Fig. E.1 The stress, strain relationship obtained from the uniaxial tensile tests for the 6437 double covered yarn (all samples), green scatter shows the place at which the tangent is drawn. The Young's modulus calculated (E) is given in legend.

The average Young's modulus: 9.23 N/dtex (Zupin and Dimitrovski, 2010)

20030 single covered yarn

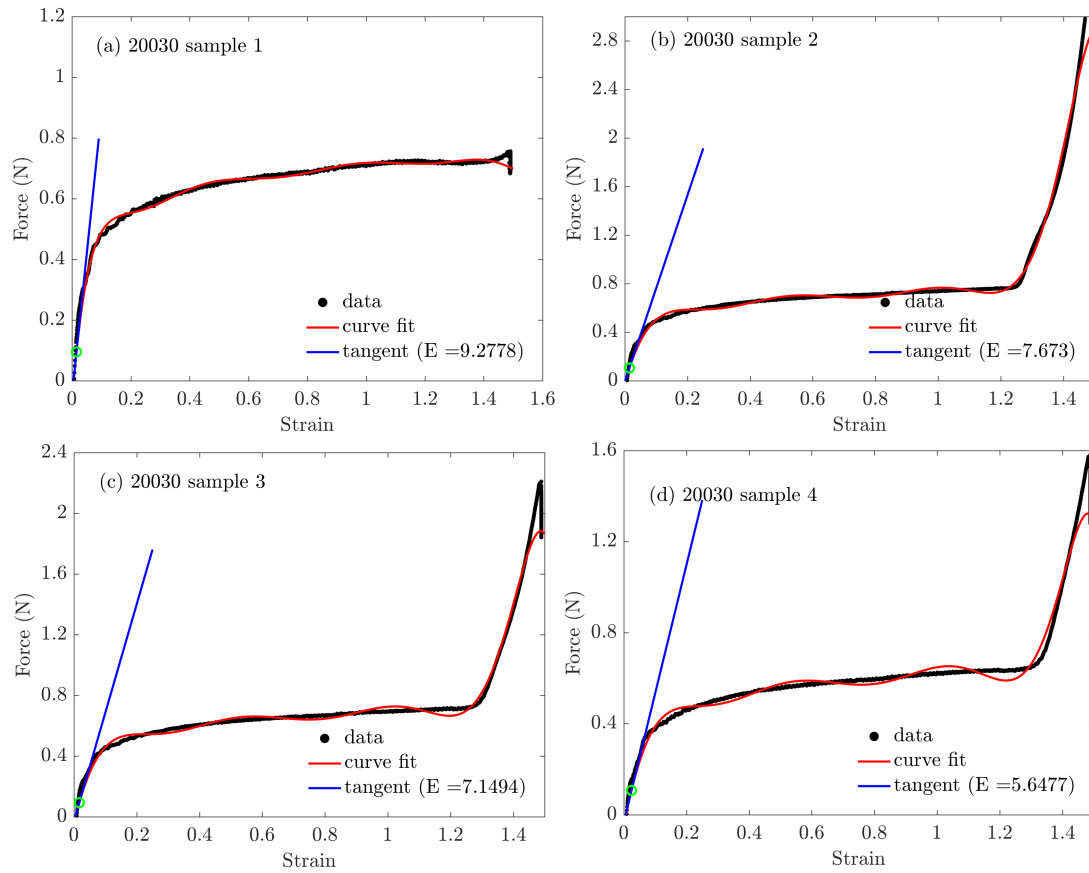


Fig. E.2 The stress, strain relationship obtained from the uniaxial tensile tests for the 20030 single covered yarn (all samples), green scatter shows the place at which the tangent is drawn. The Young's modulus calculated (E) is given in legend.

The average Young's modulus: 7.44 N/dtex (Zupin and Dimitrovski, 2010)

Z2300 single covered yarn

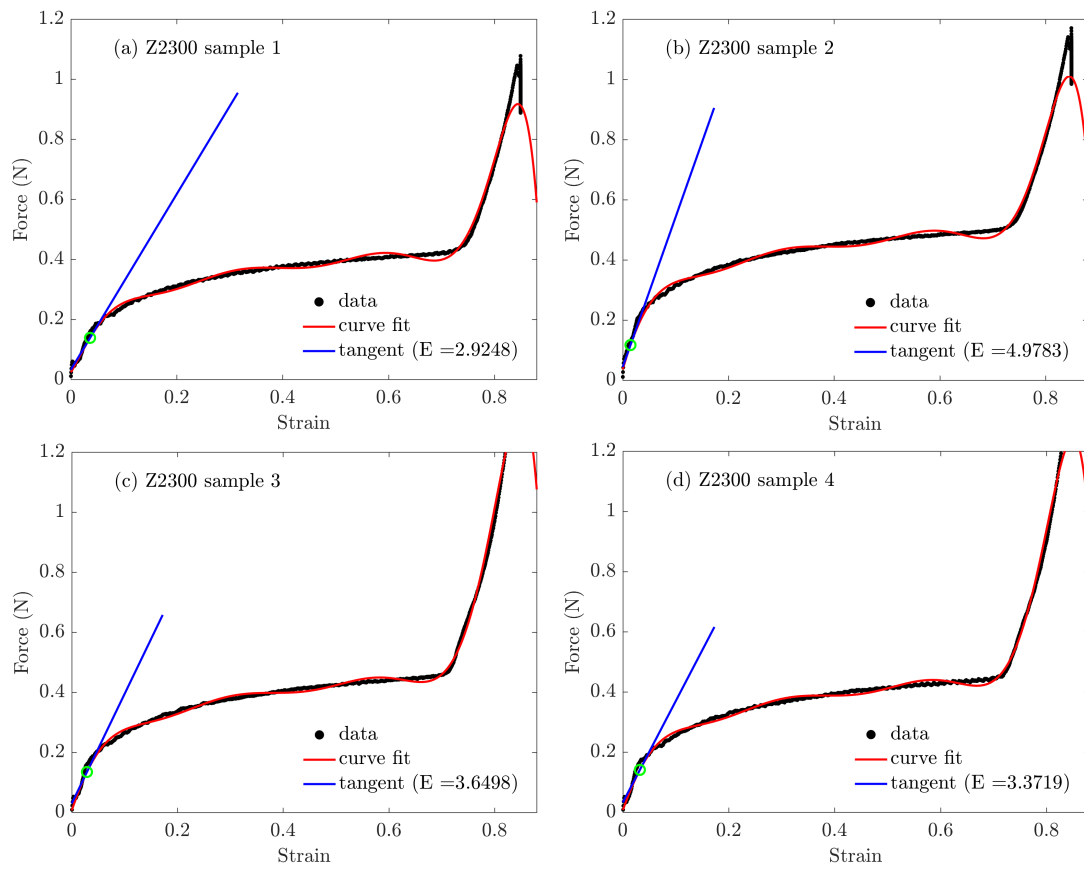


Fig. E.3 The stress, strain relationship obtained from the uniaxial tensile tests for the Z2300 single covered yarn (all samples), green scatter shows the place at which the tangent is drawn. The Young's modulus calculated (E) is given in legend.

The average Young's modulus: 3,73 N/dtex (Zupin and Dimitrovski, 2010)

Uniaxial tensile test results for the fabrics made from the covered yarns

The fabrics manufactured using the 6437 double covered yarn

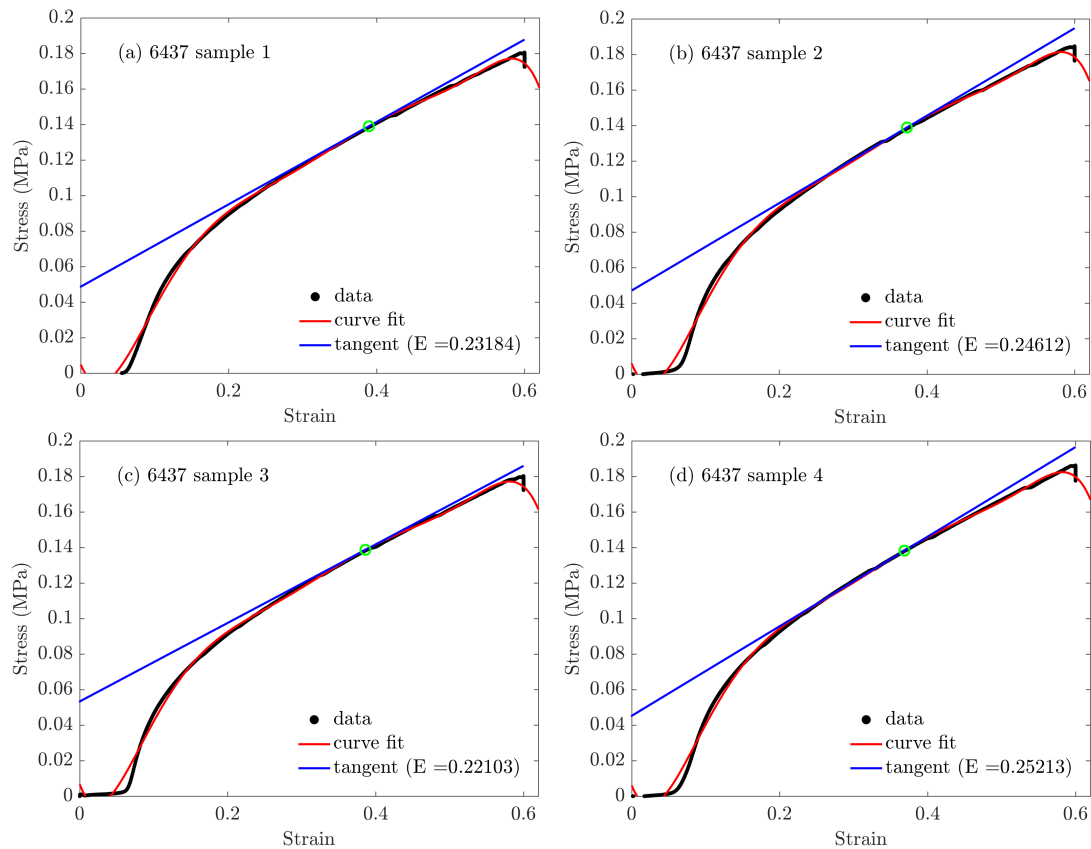


Fig. E.4 The stress, strain relationship obtained from the uniaxial tensile tests for the fabrics manufactured using 6437 double covered yarn (all samples), green scatter shows the place at which the tangent is drawn. The Young's modulus calculated (E) is given in legend.

The average Young's modulus: 0.238 MPa (Zupin and Dimitrovski, 2010)

The fabrics manufactured using the 20030 single covered yarn

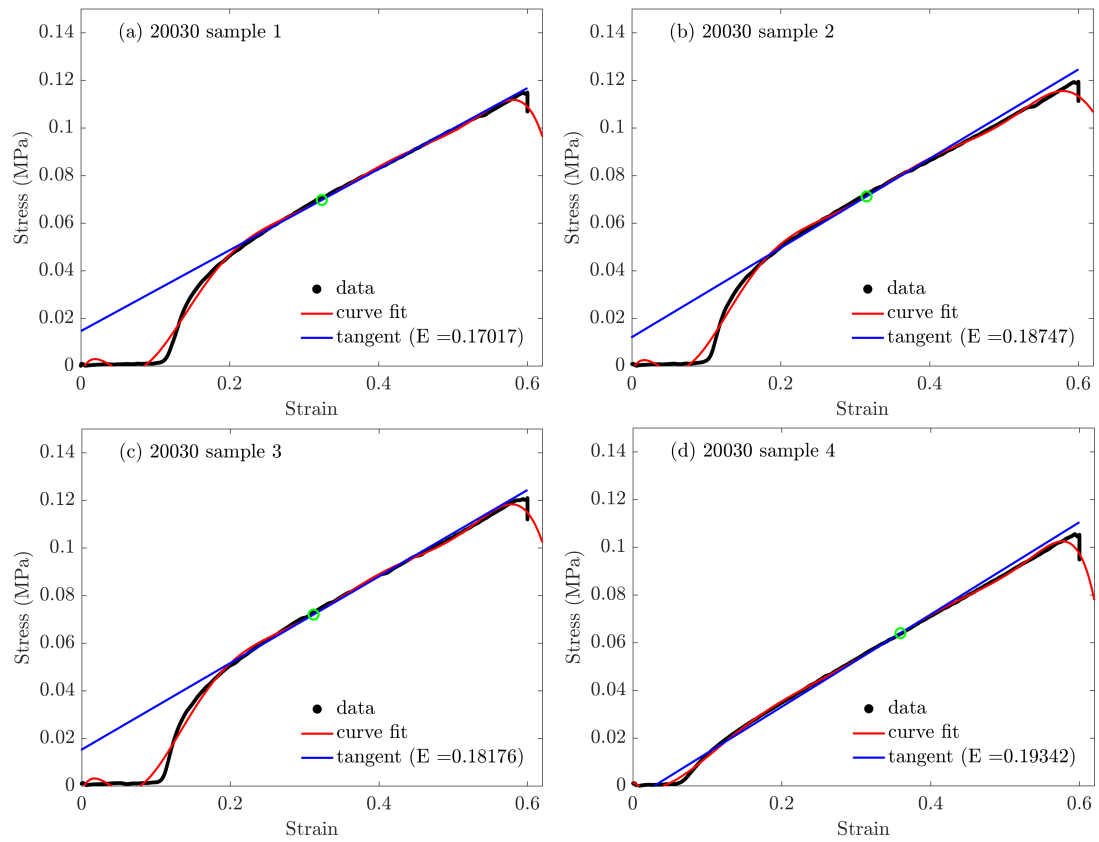


Fig. E.5 The stress, strain relationship obtained from the uniaxial tensile tests for the fabrics manufactured using 20030 single covered yarn (all samples), green scatter shows the place at which the tangent is drawn. The Young's modulus calculated (E) is given in legend.

The average Young's modulus: 0.183 MPa (Zupin and Dimitrovski, 2010)

The fabrics manufactured using the Z2300 single covered yarn

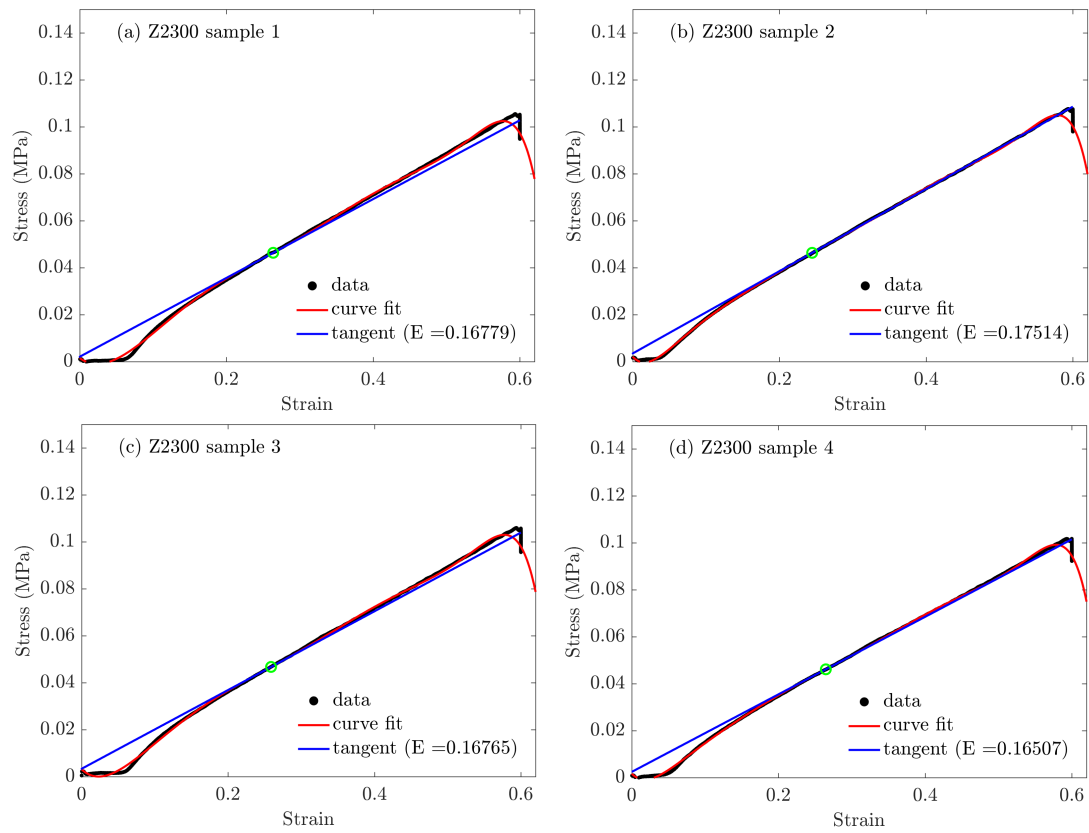


Fig. E.6 The stress, strain relationship obtained from the uniaxial tensile tests for the fabrics manufactured using Z2300 single covered yarn (all samples), green scatter shows the place at which the tangent is drawn. The Young's modulus calculated (E) is given in legend.

The average Young's modulus: 0.169 MPa (Zupin and Dimitrovski, 2010)

The detailed manufacturing process of the final mini-bladder array prototype

The detailed manufacturing process is described as follows;

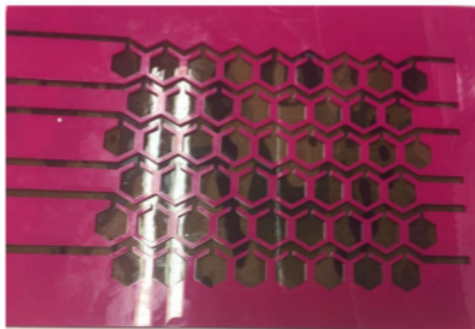
1. First a very thin layer of PlatSil[®] Gel-OO 30 is prepared which is of 0.5mm thickness. For this, a frame is prepared using thin sheets and then PlatSil[®] Gel-OO 30 is poured and then the sheet is slanted to prepare a uniform thin layer of silicone layer to remove excess of silicone. Then the layer was allowed to cure under room temperature, and when the layer is half set, a fabric panel was immersed (Fig E.7 a) into the silicone layer. Thereafter PlatSil[®] Gel-OO 30 silicone is poured on top of that to prepare another thin layer of 1mm thickness on top of the previous layer to complete the bottom layer of the mini-bladder unit (Fig E.7 b). Finally, allow the silicone layer to cure under room temperature.
2. Then place the stencil on top of the cured silicone layer to create the top layer which is the extensible layer. A layer of wax (Petroleum Jelly) is applied in the areas shown in the stencil (Fig. E.7 c) by using a paint brush in order to act as an inhibitor to prevent the silicone sticking into the areas of the air pockets (mini-bladders).. In here to get a better visibility to the area where the petroleum jelly is applied, since it originally is transparent a pigment dye of white colour is mixed. After applying petroleum jelly the unit would have the array design painted on top of the bottom silicone layer as shown in Fig. 6.12 e.
3. Then pour PlatSil[®] Gel-OO 30 silicone on top of this design to prepare a thin layer of 1.5mm thickness and allow it to set. As the inhibitors would not allow the silicone to set in areas where the inhibitor is applied, it will finally produce a prototype design with mini-bladders placed in an array as shown in Fig E.7 f. Then fix the connectors to the ends of each air channel where each row of mini-bladders are supposed to be inflated from.
4. Finally measure the length required to cover over the cylindrical surface and place two Velcro strips on both sides and bond it to the silicone layer, to give it an easy fixing and removing method (Fig. 6.13) when it is used as a sleeve.



(a)



(b)



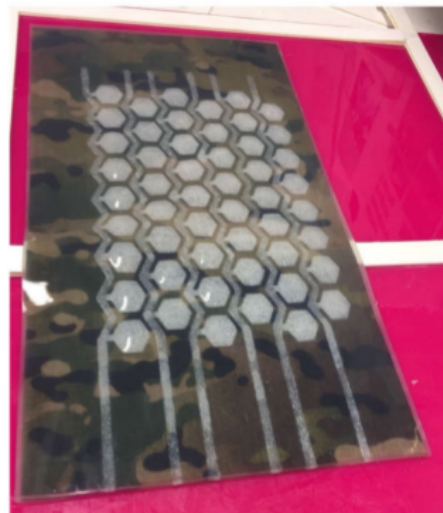
(c)



(d)



(e)



(f)

Fig. E.7 Manufacturing process of the complete mini-bladder unit.